Processing of fibre composites – challenges for maximum materials performance

Editors

B. Madsen, H. Lilholt, Y. Kusano, S. Fæster and B. Ralph

34th Risø International Symposium
on Materials Science
2013

Processing of fibre composites – challenges for maximum materials performance

Department of Wind Energy
Technical University of Denmark
Post box 49
4000 Roskilde, Denmark
www.dtu.dk

ISBN 978-87-92896-51-3

ISSN 0907-0079

Processing of fibre composites – challenges for maximum materials performance

Proceedings of the 34th Risø International Symposium
on Materials Science

2-5 September 2013

Editors

B. Madsen, H. Lilholt, Y. Kusano, S. Fæster and B. Ralph

DEPARTMENT OF WIND ENERGY
TECHNICAL UNIVERSITY OF DENMARK
ROSKILDE, DENMARK

Risø International Symposium on

Processing of fibre composites – challenges for maximum materials performance

INTERNATIONAL ADVISORY COMMITTEE

J.C. Domínguez, Spain
E.K. Gamstedt, Sweden
R. Joffe, Sweden
L. Medina, Germany
I. Partridge, United Kingdom
T. Peijs, United Kingdom
K. Pickering, New Zealand
R. Schledjewski, Austria
K. Schulte, Germany

LOCAL ORGANIZING COMMITTEE

S. Fæster
J.K. Heininge
Y. Kusano
H. Lilholt
B. Madsen
R.T.D. Prabhakaran
A.G. Thomsen

PREFACE

The challenge of the present state of fibre composite processing is to bring the various materials science disciplines together to promote technological development. High-level scientific knowledge of the physical and chemical mechanisms taking place during processing of composites is available, including detailed knowledge on the behaviour of the constituent materials, but in many cases this knowledge is not integrated and brought to practice.

Focus needs to be placed on the links between fundamental science and more practically oriented developments of processing techniques, in order to further our understanding of relationships between processing conditions and engineering properties of the final composites. Altogether, the scientific basis for development and optimization of processing of fibre composites needs to be explored to approach maximum materials performance.

This overall topic of the symposium is covered in the Proceedings book by 9 invited papers and 26 contributed papers.

Among the specific topics covered by the papers are (i) experiments and theoretical models for the analysis of resin rheology, resin cure kinetics, together with fibre assembly permeability for efficient mould filling, and optimisation of process conditions, (ii) modelling of residual stresses generated during processing for control and minimization of shape distortion, (iii) design and characterisation of the fibre/matrix interface, and the related technological techniques for surface treatment, (iv) development of techniques and analyses for the characterisation of the process controlled volumetric composition and microstructural parameters, such as length and orientation of fibres, and the related effect on composite properties, (v) compaction behaviour of fibre assemblies, (vi) new types of fibres and matrices, such as bio-based and at nano-scale, and their processing and properties, and finally, (vii) comparative studies and systems for selection, monitoring and control of processes.

The 34th International Risø Symposium on Materials Science is organized by the Department of Wind Energy, Technical University of Denmark (DTU). We want to thank all those at DTU who have assisted in the preparations for the symposium, and we gratefully acknowledge the financial support from the following foundations: Civilingeniør Frederik Leth Christiansens Almennyttige Fond, Kraks Fond, Fabrikant Mads Clausens Fond, Knud Højgaards Fond and Otto Mønsteds Fond.

S. Fæster J.K. Heininge Y. Kusano H. Lilholt
B. Madsen R.T.D. Prabhakaran A.G. Thomsen

Contents

Proceedings of the 34th Risø International Symposium on Materials Science:
Processing of fibre composites – challenges for maximum materials performance
Editors: B. Madsen, H. Lilholt, Y. Kusano, S. Fæster and B. Ralph
Department of Wind Energy, Risø Campus
Technical University of Denmark, 2013

LIMITING DELAMINATION DURING MACHINING OF FIBER REINFORCED COMPOSITES BY UNDERSTANDING INEVITABLE DAMAGE MECHANICS

Naresh Bhatnagar, G. Venugopala Rao, and Puneet Mahajan
Indian Institute of Technology, Delhi, India

ABSTRACT

Apparent facts of composite material damage mechanism in chip formation during orthogonal machining were studied experimentally and numerically for a range of fiber orientations, depths of cut and tool rake angles. A new two-phase micro-mechanical finite element (FE) model was developed. For material damage and chip formation study, fiber breakage, matrix damage and interfacial failure are considered. From the new micro-mechanical FE model the fiber failure is found to be a combination of bending and crushing for higher fiber orientations and bending alone for lower fiber orientations. Sub-surface damages are more at 30^o fiber orientation, which is primarily due to the induced stresses in the matrix (m_2) reaching failure before the adjacent fiber (f_1) fails. Interfacial failure/debonding were observed due to mixed mode fracture failure.

1. INTRODUCTION

Most of the fiber reinforced polymer (FRP) composite products are made to final component level; however, post-production removal of excess material by means of machining is often carried out to meet dimensional requirements and assembly needs. Carbon/Glass fiber reinforced polymer (CFRP/GFRP) composites are widely used in various applications, due to their high specific strength and high specific stiffness. Machining of CFRP products is difficult due to its material discontinuity, inhomogenity and anisotropic nature. Also, various damage mechanisms such as fiber pullout, fiber fragmentation, delamination, matrix burning, matrix cracking and subsurface damage lead to poor cut surface quality. Compared to the machining of metals, studies on machining of composites are few and limited in number.

The first experimental work on cutting of unidirectional carbon fiber reinforced polymer (UD-CFRP) composites was presented by Koplev, Lystrup and Vorm (1983). The machining characteristics were considered for only parallel and perpendicular fiber orientations and results were presented for chip size, cutting and thrust force variations with rake and relief angles. Crack propagation ahead of the tool tip (Mode-I) was observed during machining of laminates with 0^o fiber whereas, compression induced rupture was noticed in machining of laminates with 90^o fiber orientation. On the basis of experimental observations a combination of Mode-I and

Mode-II failure mechanism leading to chip formation was suggested by Caprino, Santo and Iorio (1997). Bhatnagar, Ramakrishnan, Naik and Komanduri (1995) ascribed fiber breakage due to axial tension as the cutting mechanism. Pwu and Hocheng (1998) suggested that the fiber breaks when the bending stresses exceed the ultimate material strength. Very few researchers have used numerical analysis to investigate the response during orthogonal machining of UD-FRP composites (Arola and Ramulu 1997; Mahdi and Zhang 2001; Arola, Sultan and Ramulu 2002; Ali and Mohamed 2009; Carlos, Xavier and Maria 2010). Most of these research work talk about the numerical simulations rather than experiments, mainly concentrated on cutting forces, influence of fiber orientation, chip formation mechanism and machining induced subsurface damage. Recently, Chinmaya and Yung (2012) presented a review article on 'Modeling of machining of composite materials'. This article provides a comprehensive review of the literature, mostly of the last 10–15 years, on modeling of machining of composite materials with a focus on the process of turning. The paper discusses modeling of both fiber reinforced and particle reinforced composites. The paper includes recent modeling work to predict cutting forces, tool–particle interaction, cutting temperatures and machined sub-surface damage.

The numerical models cited here use an equivalent homogeneous material (EHM) for modeling of orthogonal machining operation and this is probably the prime source of deviation between the experimental and numerical results, especially the thrust force. A multiphase orthogonal machining simulation was conducted for unidirectional polymeric composite by Chinmaya and Yung (2008), they simultaneous use of the Marigo brittle failure model and the cohesive zone model to describe material behavior was successful in predicting damage during machining of composites. However, there was a limitation in Chinmaya and Yung (2008) model; it does not predict damage in the matrix in the form of cracking and matrix redistribution. Since the aim of the study was to consider only fiber damage along with debonding. Nayak, Bhatnagar and Mahajan (2005) tried to correct this situation by using a model where the fiber and matrix were separately modeled rather than as an EHM for UD-GFRP composites only. Rao, Puneet and Naresh (2007) proposed a new two phase micro-mechanical FE model to estimate the chip formation mechanism in UD-GFRP composites. Matrix failure, interfacial damage initiation and propagation and also fiber failure were considered in the model.

The present article concentrates on material damage mechanism during the machining response of unidirectional carbon fiber based composites (UD-CFRP) by both experiments and numerical simulations. A new two-phase micro mechanical FE model was developed to estimate the machining response of UD-CFRP. In the micro-mechanical model matrix, interface and fiber failure are consider separately. The damage initiation and evolution in the matrix is implemented based on the material yield strain and fracture energy respectively (Iannucci and Ankersen 2006; Bahei-El-Din, Rajendran and Zikry 2004). Interface between the fiber and matrix have been studied using cohesive zone model (CZM) (Camanho and Dávila 2002). The failure of the fiber was based on the maximum principal stress at the cutting tool-work material interface. The micro-mechanical model looks at stresses in the fiber and matrix, their variation with fiber orientation, possible fracture mechanisms of the fiber, damage in the matrix, and interfacial debonding.

2. EXPERIMENTAL PROCEDURE AND OBSERVATIONS

UD-carbon fiber tapes, epoxy (LY 556) along with hardener (HY 951) are used to prepare specimens by a lay-up procedure. The test specimens of 100 mm x 50 mm x 3±0.2 mm thick with 6 ply lay-up with desired fiber orientation (15^o, 30^o, 45^o, 60^o, 75^o and 90^o) were used for orthogonal machining experiments. The fiber volume fraction of the specimen was found to be

60% by the Ignition Loss Method (ASTM D 2584). Orthogonal machining experiments for UD-CFRP laminates were performed on a vertical three axis CNC milling machine (Beaver Mill NC-5) capable of executing linear motion along three mutually perpendicular axes and one rotational motion about the vertical spindle. In the present study, solid tungsten carbide (Grade K-10) material is chosen for the cutting tool. The cutting tool is ground at a constant edge radius of 50 m and a constant relief angle of 6°. Three different rake angles were used. The tool geometry and process parameters used in the study are listed in Table 1. The specimen vice holder was mounted on a four-component piezoelectric dynamometer (KISTLER MODEL 9272), which in turn was clamped to the machine table. The longitudinal axis of the machine bed was moved at a constant speed of 0.5 m/minute to ensure orthogonal cutting conditions.

Table 1. Material, tool geometry and process parameters.

	Parameter	
UD-CFRP composites	Specimen dimensions	100 x 50 x 3 ± 0.2 mm
Tool geometry parameters	Rake angle (γ) Relief angle (α) Edge radius (r)	5º, 10º and 15º 6º 50 μm
Process parameters	Depth of cut (t) Fiber orientation (θ) Cutting speed (V)	0.1, 0.15 and 0.2 mm 15º, 30º, 45º, 60º, 75º and 90º 0.5 m/min

The chip formation mechanism was observed using a long-distance stereo zoom trinocular optical microscope. The microscope along with a charge coupled device (CCD) camera was attached in series and used to view the magnified images of the chip formation zone. Two strong light sources were used to illuminate the surface of the chip formation area. The broken chips released from the parent material were also collected and observed under a scanning electron microscope (SEM) to inspect the nature of the fiber failure and matrix cracking. To understand the material damage in the chip formation mechanism a number of successive frame images captured at 30 frames/second were analyzed using Image-Pro analysis software. These images were used to quantify the chip size and flow during the machining process. Fig. 1 shows the complete experimental set-up for both the cutting and thrust force measurements and chip formation observations.

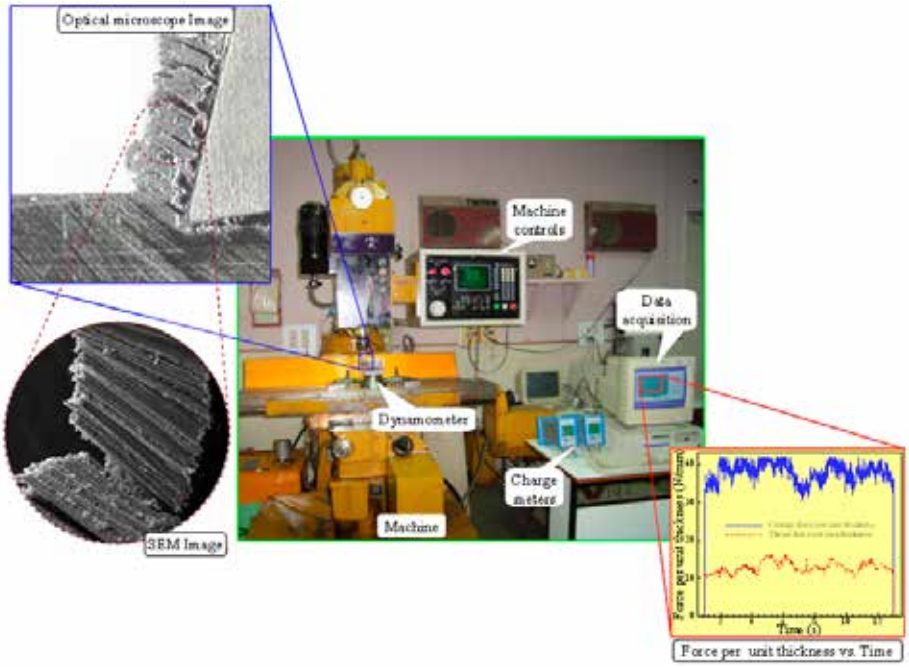

Fig. 1. Experimental set-up used for composite machining process.

3. SIMULATION PROCEDURE AND PREDICTIONS

In the present study, a new micro-mechanical finite element model was developed to estimate the response of material damage in UD-FRP composite machining process and is discussed in detail below. A parametric study by suitably varying the input variables such as tool geometry and process parameters is also performed.

3.1 Micro-mechanical Finite element model. In the micro-mechanical model, portion of the work material adjacent to the cutting tool is modelled using fiber and matrix separately, whereas, portions away from the cutting tool are modelled as equivalent homogeneous material (EHM). Two fibers, three matrix layers and two EHM regions as shown in Fig. 2 are considered in the present study. Initially the FE model had twenty layers of fiber and matrix, but simulation showed that the damage in the matrix material did not reach beyond the third matrix when the first fiber failed completely. It was therefore decided to use FE models having two fiber and three matrix layers close to the chip formation zone and the rest of the material was modelled as an EHM. The tool is assumed to be in contact with the first fiber (f_1) after the first matrix (m_1) has been removed. In the numerical model, to keep the problem tractable, only one region of the work material close to chip formation zone is modelled (2000μm x 1000μm). All the fiber and matrix regions are meshed with four-node quadrilateral elements with plane stress formulation.

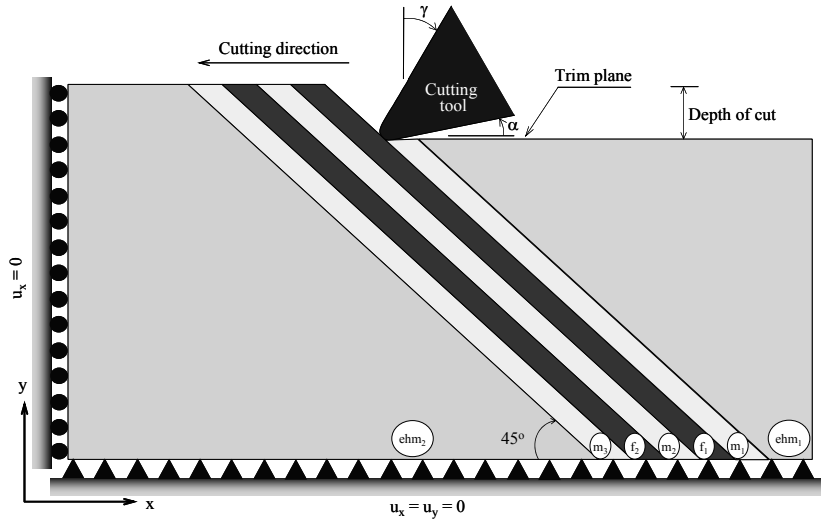

Fig. 2. Schematic view of fiber (f_1 and f_2), matrix (m_1, m_2 and m_3) and EHM (ehm_1 and ehm_2) region used in new micro-mechanical FE model for 45° fiber orientation, where 'γ' is the rake angle and 'α' is the relief angle.

Mesh convergence studies were performed and finally all fiber and matrix domains were modelled with approximately 1 µm x 1 µm element size. The EHM regions are modelled with combination of both four-node quadrilateral and three-node triangular elements. The size of the elements in the regions is 16 µm x 16 µm. The three-node triangular elements are used for the mesh transition from fine to coarse mesh. The mechanical properties of fiber, matrix and interface are taken from the available literature (Kawabata 1990; King, Blackketter, Walrath, and Adams 1992; Kozey, Hao, Vinay, and Satish 1995; DiFrancia, Ward Thomas and Claus Richard 1996; Meurs, Schrauwen, Schreurs and Peijs 1998; and Hobbiebrunken, Fiedler, Hojo, Ochiai and Schulte 2005) and these properties are presented in Table 2. The mechanical properties of the EHM zone are taken from Table 3 (i.e., macro-model properties). The machining experiments show that the velocity of cutting marginally affects the cutting forces in composites. It was therefore decided to consider the process as quasi-static and implement the same FE code. The FE code has provision for implementing damage initiation and evolution in the matrix and debonding at the interface of fiber and matrix using cohesive elements. Different FE meshes were made for the different fiber orientations and depths of cut and each model has been used with respective material properties to simulate the chip formation mechanism for each fiber orientation.

The two-phase micro-mechanical FE model essentially includes three different material (matrix, interface and fiber) failure concept, such as: i). The matrix material modelled as elastic-plastic, the damage initiation and evolution is based on the matrix yield strength and fracture energy respectively, ii). The interface between the fiber and matrix is modelled using CZM, where bi-linear, zero thickness cohesive elements are introduced at the interface and damage initiation and evolution at the fiber-matrix interface is taken into account based on the interfacial tractions and fracture energies respectively, and iii). Fiber failure is based on the induced direct stress in the fiber along or across its axis; this provides possible locations of fiber breakage due to tensile/crushing failure during the simulation.

Table 2. Mechanical properties (#) of fiber, matrix and interface used in analysis.

Material	Property	
Carbon fiber	Elastic constants (Tension)	E_1 = 235 GPa, E_2 = 14 GPa, G_{12} = 28 GPa, υ_{12} = 0.2
	Elastic constants (Compression)	E_1 = 106 GPa, E_2 = 14 GPa, G_{12} = 28 GPa, υ_{12} = 0.2
	Tensile strength	X_t = 3.59 GPa, Y_t = 0.35 GPa
	Compressive strength	X_c = 1.8 GPa, Y_c = 2.73 GPa
	Shear strength	S_{xy} = 0.38 GPa
	Diameter	d = 10 μm
Epoxy matrix	Elastic constant	E = 3.1 GPa, υ_{12} = 0.33
	Yield strength	σ_y = 27.5 MPa
	Tensile strength	σ_t = 70.3 MPa
	Fracture toughness	K_c = 0.5 MPa $m^{1/2}$
	Fracture energy	G_f = 80.6 J/m^2
Fiber-Matrix Interface	Normal strength	N = 167.5 MPa
	Shear strength	S = 21 MPa
	Fracture energy	G_{IC} = G_{IIC} = 50 N/m

#Sources: Kawabata (1990); King et al. (1992); Kozey et al. (1995); DiFrancia et al. (1996); Meurs et al. (1998); and Hobbiebrunken et al. (2005) and presently conducted experiments.

Table 3. Mechanical properties of UD-CFRP composite (EHM).

Stiffness properties				Strength properties				
E_1 (GPa)	E_2 (GPa)	G_{12} (GPa)	υ_{12}	X_t MPa	X_c MPa	Y_t MPa	Y_c MPa	S_{xy} MPa
139.4	9.5	5.8	0.24	1951	1475	47.1	188.4	74.28

3.1.1 Matrix material failure by damage initiation and evolution. The epoxy matrix exhibits elasto-plastic behavior (Hobbiebrunken et al. 2005). Young's Modulus and Poisson's ratio characterize the linear elastic behaviour. The von Mises yield criterion and isotropic hardening are used to define the plastic behaviour of the epoxy matrix. The yielding is followed by hardening until a maximum strength is reached and subsequently the matrix fails by strain softening due to onset of damage in the form of micro voids (or) micro cracks. In the elastic-plastic matrix with isotropic hardening, the damage manifests itself in two forms: softening of the yield stress and degradation of the elasticity. The damage is considered isotropic assuming that the micro cracks are initiated and propagated uniformly in all the directions. The above damage initiation and evolution model is available in ABAQUS™ FE code (Hibbit 2005).

3.1.2 Interfacial failure by cohesive zone modelling. Cohesive zone model (CZM) is a fracture mechanics approach to study the interfacial effects of either dissimilar material or in the same material when these are initially bonded together (Camanho and Davila 2002). The elements based on CZM use failure criteria that combine aspects of strength based analysis to predict the onset of the softening process at the interface and fracture mechanics to predict delamination

propagation. The main advantage of the use of cohesive elements is the capability to predict both onset and propagation of debonding without previous knowledge of the crack location and propagation direction. For pure Mode-I and Mode-II loading the bi-linear softening constitutive behaviour (Camanho and Davila 2002) is used. To predict the interfacial crack propagation under the mixed mode loading, the following criterion is used in the present study.

$$\left(\frac{G_I}{G_{IC}}\right)+\left(\frac{G_{II}}{G_{IIC}}\right)=1 \tag{1}$$

Here Mode-I or Mode-II critical fracture energy required to cause failure is G_{IC}, G_{IIC} respectively. G_I and G_{II} are the fracture energy by the traction in normal and shear directions respectively. CZM approach has been used for debonding at fiber-matrix interface during orthogonal machining of UD-CFRP composites. The interfacial properties of the present material system are taken from the literature (DiFrancia et al. 1996 and Meurs et al. 1998). Zero thickness cohesive surface elements are introduced between boundaries of elements, at the interface in a normal finite element mesh.

3.1.3 Fiber material failure by principal stress measure. The carbon fiber is assumed as an elastic and transversely isotropic material. The elements in the fiber are considered failed once the Tsai-Wu / Maximum principal stresses at the Gauss integration point reach a critical value. The fiber element loses its loading carrying capacity and its stiffness is slowly reduced to zero once the induced maximum principal stress reaches its failure strength of the fiber during the FE simulation.

4. RESULTS AND DISCUSSION

The results are arranged in two sections, Section 4.1 Experimental observation and section 4.2 Simulation predictions. The material damage mechanism in chip formation during machining is due to failure of the interface, matrix cracking and fiber breaking leading to discontinuous chip formation. Experiments also show that the size and shape of the chip depends entirely on the fiber orientation and depth of cut and to a lesser extent on the tool geometry.

4.1 Experimental observations. Experimental observations a typical flow of chip under an optical microscope is presented in detail in Fig. 3. Different stages (I, II, III, IV, V and VI) of chip blocks for 45^o fiber orientation are marked in it. Each chip block consists of group of fibers bonded with some portion of matrix material. The matrix probably also has many cracks and debonding between the fiber and matrix also occurs but these are not clearly visible with the existing magnification of the long range optical microscope. The cut portion of the chip always flows over the rake face as shown in Fig. 3. The individual blocks of chip also slide relative to each other along the fiber direction. Similar behaviour is observed in other fiber orientations also. However, the formation mechanism of the blocky chip (it is a group of broken fiber and matrix) is different for different fiber orientations. For the case of 90^o fiber orientation the chip has to rotate about 75^o (for 15^o rake angle) towards the cutting direction before releasing the final block of chip from the parent material. The large rotation leads to high interfacial shear leading to debonding between fiber and matrix and crushing of matrix into powder accompanied with tensile and shear failure of the matrix. For the case of 15^o fiber orientation the chip blocks gets released from the parent material without rotation (for 15^o rake angle). For lower chip block rotation, pure shear failure of the matrix and interface is the mode of forming the chip blocks. It is very difficult to see the cracks in the matrix and the nature of the fiber failure under the

existing optical microscope online during the machining process. To overcome this difficulty, the released chip was collected on a double adhesive tape during the machining process and was observed under a scanning electron microscope (SEM).

These observations are presented in Fig. 4 and 5; from all these figures it can be observed that, there are many cracks in the matrix material and also interfacial debonding between the fiber and matrix. Fig. 4 shows the case of 75° fiber orientation at 0.15 mm depth of cut, 5° rake angle. It shows that series of chip blocks are formed due to matrix failure and interfacial failure. Fig. 5 shows the rear surface (cut surface) of the chip for the case of 45° fiber orientation at 0.2 mm depth of cut, 15° rake angle; it indicates that the discontinuous chips are usually formed in discrete steps.

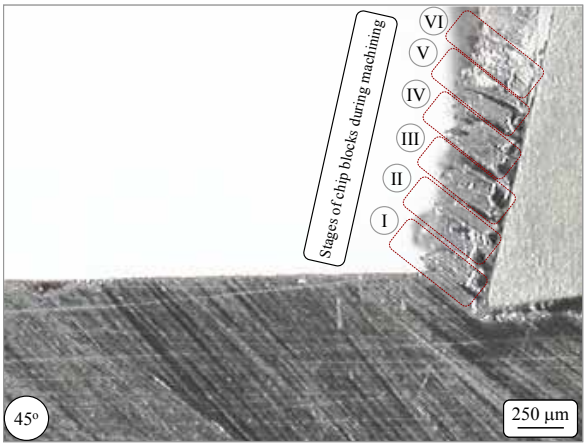

Fig. 3. Chip flow observed under the optical microscope during the machining of composite for 45° fiber orientation. (I, II, III, IV, V, VI show the various stages of chip flow).

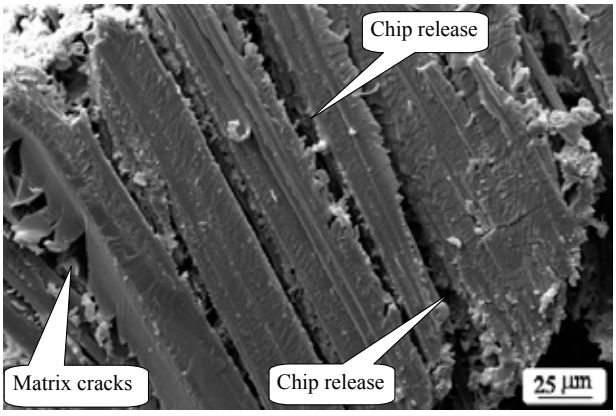

Fig. 4. SEM image of released chip for 75° fiber orientation at 0.15 mm depth of cut, 5° rake angle.

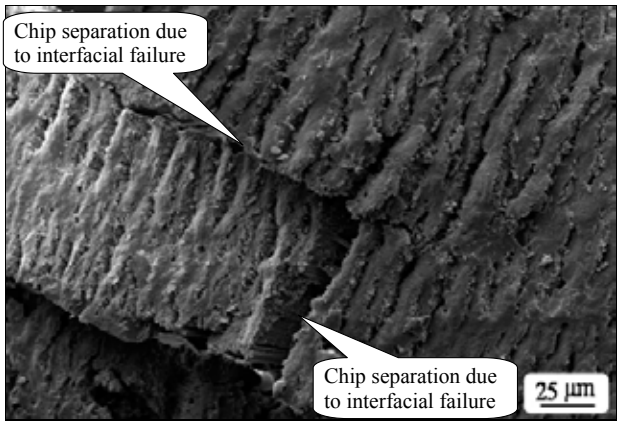

Fig. 5. SEM image of the rear surface of chip for 45° fiber orientation, 0.2mm depth of cut and 15° rake angle.

4.2 Simulation predictions.

4.2.1 Mechanism of matrix failure observations. Quantitative variation of damage in the matrix was observed when discontinuous chips are formed during machining due to the fracture failure of the fiber and matrix material. Experiments showed that the size and shape of the chip depends mainly on the fiber orientation and depth of cut and to a lesser extent on the tool geometry. During the experiments, the edge radius of the cutting tool was kept constant. The progress of damage initiation and evolution in the matrix (m_2) material for the case of the 75º fiber orientation, 0.1 mm depth of cut is shown in Fig. 6. It shows the quantitative variation of damage variable (d_m) at different locations within the same matrix. It is observed that the damage is maximum adjacent to the zone in fiber where the bending stresses are the highest.

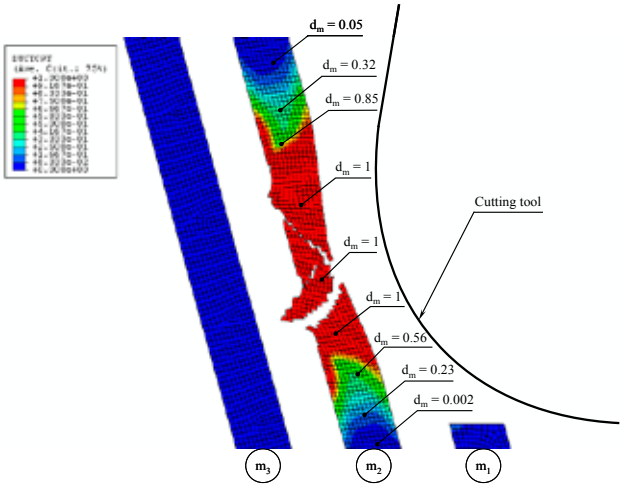

Fig. 6. Quantitative variation of damage variable at various locations in the matrix (m_2) for 75° fiber orientation (the fiber and EHM are deactivated from the original FE model for clarity).

4.2.2 Chip formation mechanism observations. The chip formation mechanism along with the sequence in which the various types of failure occurs is presented in Fig. 7(a-c). First, the interfacial damage between the fiber and matrix due to mixed mode fracture is observed at various interfaces which are supporting the work of Koplev et al. (1983) and Caprino et al. (1997). For the first interface (where the matrix has already been removed) the debonding occurs beneath the trim plane, whereas, for other interfaces it occurs above the trim plane. Subsequently, damage occurs in the matrix layer adjacent to the fiber being cut. The crushing at the tool fiber interface is caused by indentation of the fiber by the tool whereas local bending of the stiffer fiber supported by the softer matrix causes higher stresses and failure on the back side of the fiber.

For lower fiber orientations the effect of local bending, as compared to crushing in the contact region, is more significant which is also supported the earlier work of Bhatnagar et al. (1995); Arola, et al. (2002); Pwu and Hocheng (1998); Chinmaya and Yung (2008); Ali, and Mohamed (2009). Carlos, Xavier, and Maria (2010). The size of this damaged region is larger for the case of 15^o as compared to the 90^o fiber orientation. Finally element failure in the first fiber is observed. For a low orientation fiber, the failure initiates from the rear side and propagates towards the tool-fiber contact zone untill the complete fracture of the fiber occurs. For 30^o fiber orientation at 0.2 mm depth of cut, this is seen in Fig. 7(c). The damage initiation occurs initially on the rear side of this matrix (m_2) layer and propagates towards the rear side of the first fiber (f_1) forming bands at approximately $\pm 45^o$ to the fiber axis as shown for various orientations in Fig. 8(a-f).

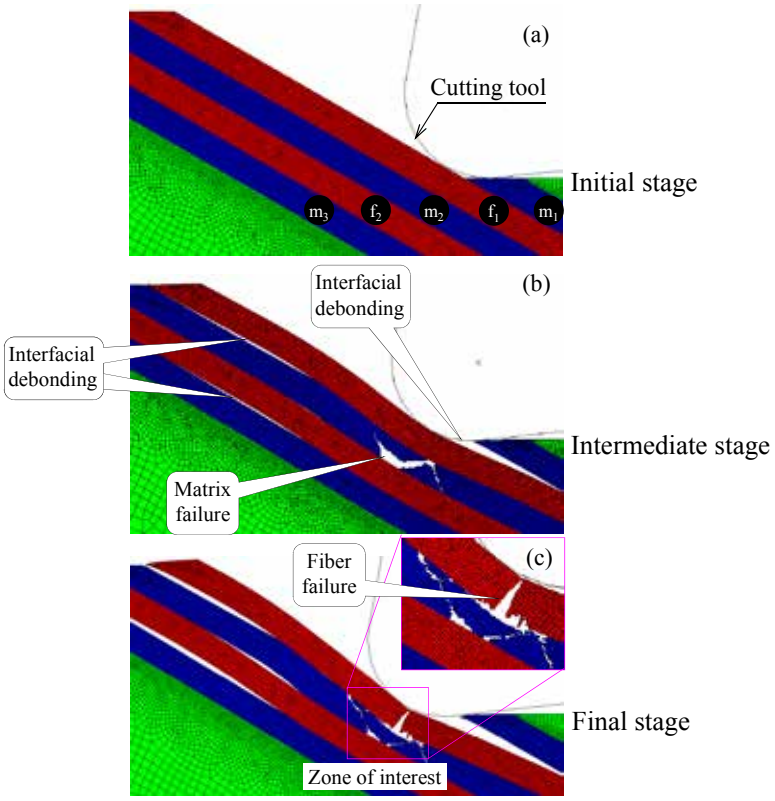

Fig. 7. Damage at the interface, matrix and fiber for 30º fiber orientation, 0.2 mm depth of cut. (a) Initial stage, (b) Intermediate stage, (c) Final stage.

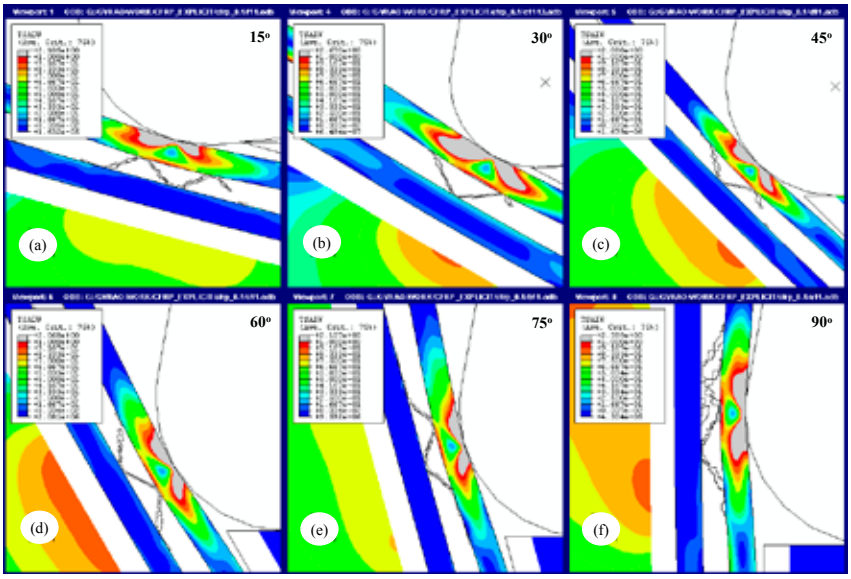

Fig. 8. Contours of Tsai-Wu stresses show the location of fiber failure for various orientations (a) 15°, (b) 30°, (c) 45°, (d) 60°, (e) 75° and (f) 90° at 0.1 mm depth of cut, 10° rake angle.

For 75° fiber orientation failure can be observed in the same fiber at both the front and rear surfaces as shown in Fig. 9(b). For 75° fiber orientation the first fiber failure is due to combination of crushing (front side) as well as tensile rupture (rear side). The crushing at the tool fiber interface is caused by indentation of the fiber by the tool whereas local bending of the stiffer fiber supported by the softer matrix causes higher stresses and failure on the back side of the fiber a similar statement made by Pwu and Hocheng (1998); Chinmaya, and Yung (2008). For lower fiber orientations the effect of local bending, as compared to crushing in the contact region, is more significant. As seen in Fig. 9(b), the simulations also show that the surface of the broken fiber is almost perpendicular to the fiber axis. This matched well with SEM image of the surface of the broken fiber, a representative of which is shown in Fig. 9(a). Moreover, the size of the broken fiber from both SEM image (Fig. 9(a)) and micro-mechanical FE model for 75° fiber orientation (Fig. 9(b)) is compared in Fig. 10.

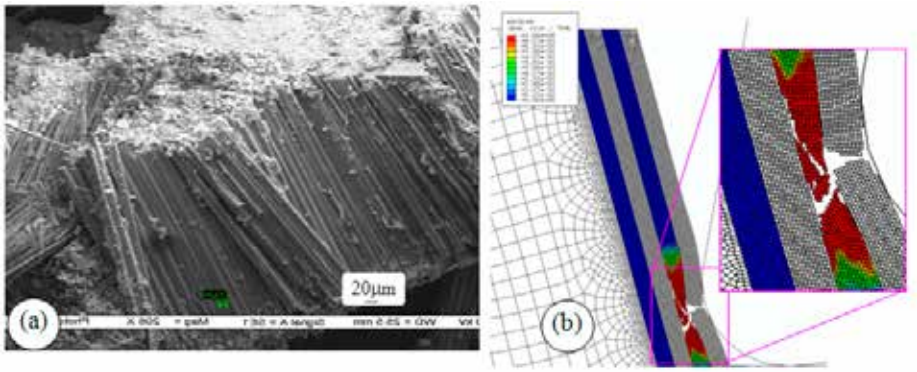

Fig. 9. Broken fiber in chip formation process, (a) SEM image, (b) Micro-mechanical FE model for 75° fiber orientation.

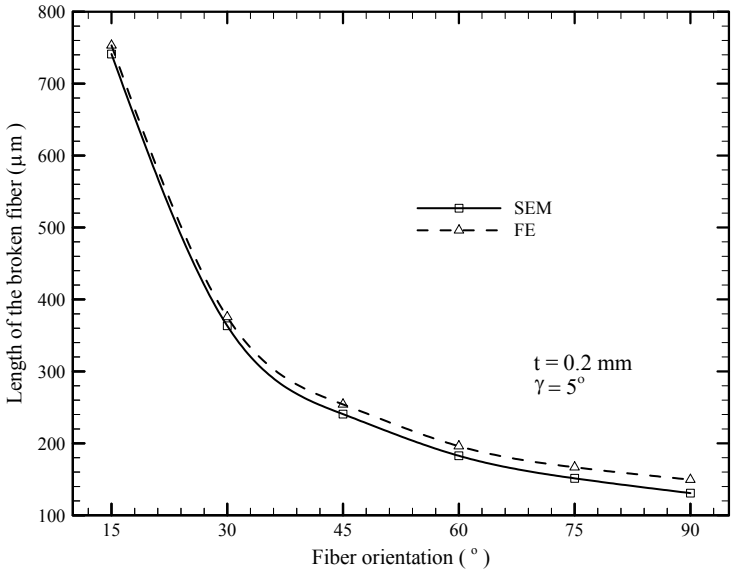

Fig. 10. Length of the broken fiber for various fiber orientations from both SEM and micro-mechanical FE model.

The chip formation mechanism is quite different for different fiber orientations. During the experiments the length of the broken fiber which is approximately equal to the chip length is measured using SEM. Powder like chip was observed at higher fiber orientation, whereas, long chip was observed at lower fiber orientation. This decrease in size with increase in fiber orientation is also seen with simulations. Fig. 10 compares the results from experiments and simulations. A good agreement between the two provides further validation of the new micro mechanical FE model. The length of the chip is approximately equal to the length of the fiber above the point where the tool first contacts the fiber. As seen from Fig. 8, for 90^o fiber orientation the tool contacts the fiber 50 μm (which is the value of the tool radius) above the trim plane whereas for 15^o fiber orientation this height is only 6.5 μm. For 0.1 mm depth of cut, the length of the fiber above the contact point is approximately 50 μm for 90^o fiber orientation and is approximately 190 μm for 15^o fiber orientation. During the simulations slipping between fiber and tool is also observed, and the initial contact zone shifts before fiber fails completely. The shifting of contact zone is more for the 15^o fiber orientation, and almost negligible for the case of 90^o fiber orientation. This slipping also effects the final chip length, although not very significantly.

4.2.3 Sub-surface damage (extent of damage below the trim plane). Matrix damage is the main mode of sub-surface damage rather than the interfacial debonding. This section is focused on only matrix damage rather than interfacial debonding. The depth of sub-surface damage below the trim plane in matrix m_1, m_2 and m_3 is given by 'h_1', 'h_2' and 'h_3' respectively. The variation of 'h_1', 'h_2' and 'h_3' with depth of cut is shown in Fig. 11. In the first matrix (m_1) adjacent to the front of the fiber being cut, the sub-surface damage is almost negligible for 15º fiber orientation and is almost constant at 58 μm for the remaining fiber orientations. The maximum damage is observed in on second matrix (m_2) next to the fiber being cut. The depth of damage in this matrix varies between 60 μm to 115 μm. In the third matrix, the damage reaches a maximum at 30º fiber orientation and decreases thereafter to zero for 75º and 90º fiber orientations which is supporting work of Chinmaya, and Yung (2008). In all the matrix elements m_1, m_2, and m_3 the

sub-surface damage was found to be maximum for the case of 30º fiber. Similar trend is observed for the remaining depths of cut also.

The sub-surface damage initiates in matrix (m_2) behind the fiber (f_1) in contact with the tool even before the tool touches the matrix. Subsequently, interfacial debonding occurs at the interface between fiber (f_1) and matrix (m_1). Both modes of damage continue until the end of the fiber (f_1) failure and extend well below the cutting plane. The sub-surface damage is maximum in the matrix m_2 as compared to 'm_1' and 'm_3' as shown in Fig. 11.

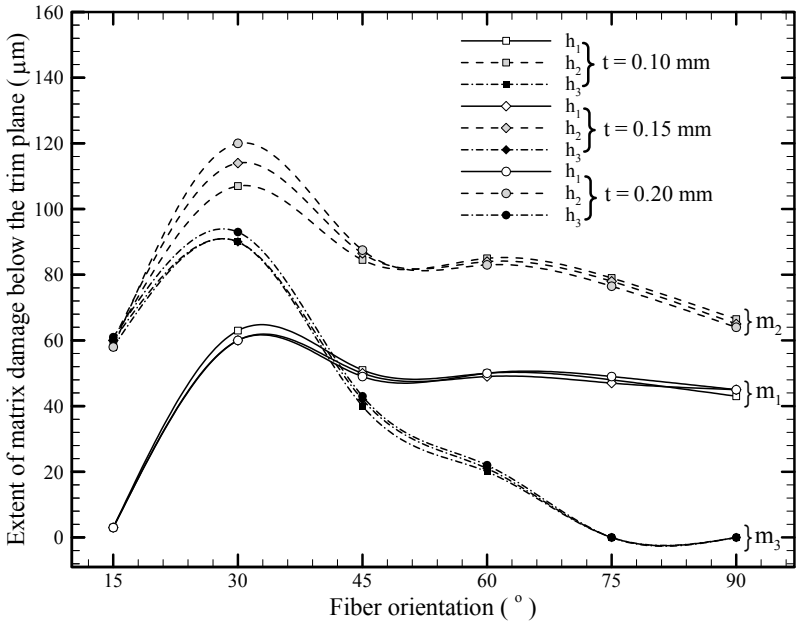

Fig. 11. Extent of damage below the trim plane (sub-surface damage) in matrix for various depths of cut and fiber orientation at 10º rake angle. where h_1, h_2 and h_3 are the damage depths measured from trim plane in the matrix m_1, m_2 and m_3 respectively.

From these results, the damage in matrix m_3 decreases with depth of cut but increases in matrix m_1 and m_2 as the depth of cut increases. For the lower fiber orientations the damage is more in m_3 as compared to m_1 and is almost same in both the matrix regions at 45º fiber orientation. For the higher fiber orientation, the damage in m_1 is almost constant but decreases when the orientation changes from 30º to 75º and remains constant thereafter. The present study shows that, matrix damage is the main mode of sub-surface damage. However, no experiments/simulations are available at a micro scale in the literature to compare present study and the following discussion is based on purely numerical simulations for which no experimental evidence is made due to infrastructure limitations of micro damage investigations.

The sub-surface damage initially increases with fiber orientation up to 30^o fiber orientation; subsequently it reduces at 45^o thereafter it is almost constant between 45^o and 90^o fiber orientation in matrix (m_1 and m_2). The damage in the third matrix (m_3) are quite low as shown in Fig. 11, and the matrix (m_3) is located away from the tool-fiber contact region and therefore stresses induced during the simulation are low. From the micro-mechanical simulation, the sub-surface damage is predominantly matrix failure as compared to the interfacial fracture and this damage is more in the second matrix (m_2) as compared to the first and third matrix. The second

matrix (m_2) directly supports the first fiber (f_1) and the external loads (due to tool movement) are directly supported on it. Sub-surface damages are more at 30^o fiber orientation, which is primarily due to the induced stresses in the matrix (m_2) reaching failure before the first fiber (f_1) fails. For other fiber orientations, similar phenomenon is not observed. This is also true for all the depths of cut and rake angles in Fig. 11. The magnitude of the sub-surface damage increases with depth of cut. However, this is significant at 30^o fiber orientation only, for other fiber orientations this is just negligible. The magnitude of the sub-surface damage is almost independent of rake angle for the lower fiber orientations (15^o, 30^o, 45^o). However, there is a slight effect of rake angle for higher fiber orientations (60^o, 75^o, 90^o). This implies that even tool rake angle may not contribute much in sub-surface damage and it is only the fiber orientation which is the most important factor.

5. CONCLUSIONS

The experimental, new micro mechanical finite element simulations on orthogonal machining of UD-CFRP composites are performed and presented in this article. The fiber breakage leads to release of blocky chip from the parent material during the orthogonal machining of UD-CFRP composites. For 90º fiber orientation both bending at fiber (f_1)-matrix (m_2) interface and crushing at cutting tool-fiber (f_1) interface cause first fiber failure. As the orientation changes from 90º to 15º, bending failure of the fiber becomes more significant. The chip formation mechanism is dominated by a combination of crushing and tensile failure of the reinforcing carbon fiber for the fiber orientation from 90º to 15º. Sub-surface damages are more at 30^o fiber orientation, which is primarily due to the induced stresses in the matrix (m_2) reaching failure before the first fiber (f_1) fails. Interfacial failure/debonding were observed due to mixed mode fracture failure.

REFERENCES

Ali M., and Mohamed El M. (2009). Finite element analysis when machining UGF-reinforced PMCs plates: Chip formation, crack propagation and induced-damage. Materials and Design, 30, 3295-3302.

Arola, D., and Ramulu, M. (1997). Orthogonal cutting of fiber reinforced composites: A finite element analysis. Int. J. Mech. Sci. 39(5), 597-613.

Arola, D., Sultan, M.B., and Ramulu, M. (2002). Finite element modeling of edge trimming fiber reinforced plastics. Transactions of ASME J. Manufact. Sci. Eng. 124, 32-41.

Bahei-El-Din, Y.A., Rajendran, A.M., and Zikry, M.A. (2004). A micromechanical model for damage progression in woven composite systems. Int. J. Solids and Struct., 41, 2307-2330.

Bhatnagar, N., Ramakrishnan, N., Naik, N.K. and Komanduri, R. (1995). On the machining of fiber reinforced plastic (FRP) composite laminates. Int. J. Mach Tools Manufact. 35(5), 701-716.

Camanho, P.P., and Dávila C.G. (2002). Mixed-mode decohesion finite elements for the simulation of delamination in composite materials. NASA/TM-2002-211737, 1-37.

Caprino, G., Santo, L., and Iorio, I.D. (1997). Chip formation mechanisms in machining unidirectional carbon fiber reinforced plastics. Proceedings of 3rd AITEM Congress, Salerno, 17-19 September 65-72.

Carlos Santiuste, Xavier Soldani, and Maria Henar Miguélez (2010). Machining FEM model of long fiber compositesfor aeronautical components. Compo. Structures, 92, 691-698.

Chinmaya R.D., and Yung C.S. (2008). Multiphase Finite Element Modeling of Machining Unidirectional Composites: Prediction of Debonding and Fiber Damage. J. Manufact. Sci. Eng. v. 130/051016-1.

Chinmaya R.D., and Yung C.S. (2012). Modeling of machining of composites: A review. Int. J. Mach tools and manufact. 57, 102-121.

DiFrancia, C., Ward Thomas, C., and Claus Richard, O. (1996). The single-fiber pull-out test 1: Review and interpretation. Compos Part A 27A, 597-612.

Hibbit, K.A.S. ABAQUS (2005). Theory and User manuals Version 6.5, ABAQUS Inc., USA.

Hobbiebrunken, T. Fiedler, B. Hojo, M. Ochiai, S. and Schulte, K. (2005). Microscopic yielding of CF/epoxy composites and the effect on the formation of thermal residual stresses. Compos. Sci. Technol. 65, 1626-1635.

Iannucci, L., and Ankersen, J. (2006). An energy based damage model for thin laminated composites. Compos. Sci. Technol. 66, 934-951.

Kawabata, S. (1990). Measurement of the Transverse Mechanical Properties of High-performance Fibers. J. Text. Inst. 81(4), 432-447.

King, T.R., Blackketter, D.M., Walrath, D.E., and Adams, D.F. (1992), Micromechanics Prediction of the Shear Strength of Carbon Fiber/Epoxy Matrix Composites: The Influence of the Matrix and Interface Strengths. J. Compos. Materials 26(4), 558-573.

Koplev, A., Lystrup, Aa. and Vorm, T. (1983). The cutting process, chips, and cutting forces in machining CFRP. Composites 14(4), 371-376.

Kozey, V.V., Hao, J. Vinay, R.M., and Satish, K. (1995). Compressive behavior of materials: Part II. High performance fibers. J. Mater. Res. 10(4), 1044-1061.

Mahdi, M., and Zhang, L. (2001). A finite element model for the orthogonal cutting of fiber-reinforced composite materials. J. Materials Proces. Technol. 113, 373-377.

Meurs, P.F.M., Schrauwen, B.A.G., Schreurs, P.J.G., and Peijs, T. (1998). Determination of the interfacial normal strength using single fiber model composites. Compos Part A 29A, 1027-1034.

Nayak, D., Bhatnagar, N., and Mahajan, P. (2005). Machining studies of UD-FRP composites Part-II: Finite Element Analysis. Machining Sci. Technol. 9(4), 503-528.

Pwu, H.Y., and Hocheng, H. (1998). Chip formation model of cutting fiber reinforced plastics perpendicular to fiber axis. Transactions of ASME J. Manufact. Sci. Eng. 120, 192-196.

Rao, V.G., Puneet M., and Naresh B. (2007). Machining of UD-GFRP Composites Chip formation mechanism. Compos. Sci. Technol. 67, 2271-2281.

Proceedings of the 34th Risø International Symposium on Materials Science:
Processing of fibre composites – challenges for maximum materials performance
Editors: B. Madsen, H. Lilholt, Y. Kusano, S. Fæster and B. Ralph
Department of Wind Energy, Risø Campus
Technical University of Denmark, 2013

DESIGNING THE FIBER-MATRIX INTERPHASE FOR OPTIMUM PERFORMANCE IN COMPOSITE MATERIALS

Lawrence T. Drzal

Composite Materials and Structures Center, 2100 Engr Bldg,
Michigan State University, East Lansing,
Michigan, 48824-1226, USA

ABSTRACT

Although fiber reinforced composite materials are routinely used in numerous applications, in many systems, the fiber-matrix interphase is the limiting factor in optimal design and use. Carbon fiber reinforced vinyl ester composite offer many potential benefits such as ambient pressure cure, low moisture absorption, and low viscosity resin transfer molding processing. The fiber-matrix interphase that forms in these systems presents a challenge because of its low adhesion. A practical solution requires not only a higher level of adhesion combined with greater energy absorption equivalent to that attainable to a carbon fiber epoxy interphase, but one which is robust and can be implemented in a manufacturing environment. This paper will present an approach based on formation of an 'engineered interphase' with a goal to develop a carbon fiber/vinyl ester interphase to increase interfacial adhesion based on a combination of chemical/mechanical bonding, coating the carbon fiber with a compatible epoxy sizing, and incorporation of nanoparticles. As part of this approach, the physical size of the resulting interphase has to be optimized as well to have maximum beneficial effect on the fiber-matrix interphase mechanical properties. The in-situ optimized CF-VE matrix adhesion and interphase mechanical properties will be related to the composite laminate properties. A description and guiding principles for this 'engineered interphase' concept will be presented.

1. INTRODUCTION

'Lightweighting' of static and dynamic structures in the aerospace, military, rail, truck, and automotive industries has been identified as a very important global strategy for the industrialized countries that has the potential for making reductions of 40%-50% in CO_2 emissions from fossil fuels. Projections of the materials necessary to achieve these levels indicate that by 2035, conventional steel usage in these structures will be reduced from 65% to 20%, while polymer composites will increase from ~5% to about 20%. The need for making larger, more complex structures coupled with the desire for reducing the time required to process and manufacture carbon fiber-epoxy composites has identified polymer systems that are

alternatives to the high performance epoxy systems. One such system is vinyl ester which can produce mechanical properties comparable to those of epoxy systems, but requiring only a low temperature out-of-autoclave cure process. That allows larger integrated carbon fiber-vinyl ester composite structures to be produced at a faster rate and with a lower capital investment in manufacturing infrastructure. The underlying assumption is that the interaction between the carbon fiber and the vinyl ester resin at the fiber-matrix interphase can be 'engineered' to provide the requisite level of adhesion and overall mechanical and durability performance competitive with carbon fiber-epoxy systems (Drzal, Sugiura and Hook 1997).

Vinyl ester matrices are based on diglycidyl ether of bisphenol-a backbone where the reactive epoxy groups are replaced with a carbon-carbon bond. Styrene is added in concentrations from 30-50% as a reactive diluent as described by Li, Yu and Yang (2008). Small amounts of peroxide initiators modified with promoters and accelerators can be added to control the polymerization reaction. The net results is a cross-linked resin that has desirable mechanical properties such as high fatigue and impact resistance, high strength per unit weight, excellent electrical and thermal insulation properties, low moisture absorption, and corrosion resistance making it suitable for most of the applications in which epoxy matrices have been used. One major deficiency however is the low adhesion of vinyl esters to carbon fibers which has a negative impact in the composite mechanical properties (Drzal and Madhukar 1993).

1.1 Factors Affecting Carbon Fiber-Vinyl Ester Adhesion. Several reasons have been identified as being contributing factors to the low adhesion to carbon fibers, (Schultz and Nardin 1994). They can be divided into chemical factors and physical factors. The chemical factors are related to the surface chemistry of carbon fibers and their lack of interaction with the vinyl ester constituents. Most carbon fibers are surface treated through an in-line anodization process optimized for maximum interaction with epoxy resins. (Drzal, Rich and Lloyd 1983). The surface treatment adds oxygen to the fiber surface and produces various chemical states including carboxylic acids, hydroxides, ketones, etc. Their overall concentration is limited to less than 15% of the carbon fiber surface area because of the morphology of the fiber surface. Vinyl ester resins will not react with the oxygen groups on the carbon fiber surface (Weitzsacker, Xie and Drzal 1997).

The surface chemistry of the carbon fiber also makes it a strong adsorbent for the constituents in the vinyl ester resins. Studies have shown that typical initiators, promoters and accelerators used in vinyl ester resins strongly adsorb on the carbon fiber surface. Likewise, styrene will strongly adsorb. The net effect is that the resulting vinyl ester cross-linked resin structure near the fiber surface after cure (i.e. in the interphase) can have properties that are quite different than the stoichiometric mixture or in the bulk away from the fiber surface (Xu 2003).

Another contributing factor to low carbon fiber-vinyl ester adhesion is the large amount of cure shrinkage than the vinyl ester resin undergoes with cure compared to an epoxy resin. Free radical cured thermosetting vinyl ester resins, typically containing 35~50% of styrene monomer as reactive diluents, have superior toughness and chemical resistance compared to unsaturated polyester. But composites of carbon fibers and vinyl ester polymers possess unexpected low mechanical properties due to low fiber-matrix adhesion (Paiva, Nardin, Bernardo and Schultz 1997). Upon cure, the volume shrinkage of vinyl ester resin is generally lower than that of unsaturated polyester resin but higher than that of epoxy resin. Vinyl ester resin can undergo as much as 5-10% volume shrinkage with cure depending on the molecular weight of the vinyl ester monomer and the content of styrene (Xu and Drzal 2003). The cure volume shrinkage can induce significant residual stresses in the fiber/matrix interphase before loading to produce a radial tensile stress as high as 90 MPa at the fiber-matrix interface acting to reduce the overall adhesion. This could be one of the most important factors that lowers the adhesion between

carbon fiber and vinyl ester resin. Conventional epoxies are known to undergo a volumetric shrinkage in the 3-5% range.

1.2 Solution: The Engineered Fiber-Matrix Interphase. Previous studies have shown that physical interactions alone do not produce a high level of adhesion. Chemical bond formation at the carbon fiber-polymer interface is necessary for good mechanical adhesion and durability. Therefore the chemical nature of the carbon fiber surface needs to be altered or the chemical nature of the vinyl ester must be changed to allow it to react with the surface treated carbon fiber surface. Second, the vinyl ester matrix volumetric shrinkage is excessive and contributes to lowering the adhesion through creating a high radial tensile force at the interface. Approaches to reducing shrinkage without reducing the modulus of the vinyl ester through alteration of the molecular structure will be required.

One of the strategies of this research is to use the low shrinkage DGEBA-T403 carbon fiber sizing to isolate the carbon fibers from the vinyl ester resin to observe the influence of the cure volume shrinkage on the fiber/matrix adhesion by comparing different vinyl ester matrices of different volume shrinkage. Shanghai Fuchem Chemical Company has developed a new-type epoxy vinyl ester resin which was claimed “free” of cure volume shrinkage (Xu 2003). One goal of this study is to gain an understanding of the matrix cure volume shrinkage on the adhesion between carbon fiber and vinyl ester matrix resin.

A constraint in adhesion improvements with carbon fibers is the adoption of new surface treatment chemistry or technology. The solution is to build on the known reactivity between epoxy and the current carbon fiber surface chemical groups (Drzal et al. 1983a). Since the majority of carbon fibers are produced with a sizing, which is selected to be compatible with an epoxy matrix, and the vinyl ester resin and DGEBA epoxy are mutually soluble, slight adjustment in the carbon fiber surface chemistry coupled with a lightly cross-linked epoxy sizing is a simple way to take advantage of carbon fiber surface chemistry and produce a surface which would be compatible with the vinyl ester resin system. Under processing conditions, some chemical binding would take place between the epoxy and the carbon fiber surface and a small amount of cross-linking agent would be added to stabilize the sized fiber surface. Under drying this thin sizing layer would vitrify and present a dry robust surface for composite prepreg manufacturing. During prepreg processing, after impregnation with the vinyl ester resin, the sizing layer will expand but not dissolve allowing the vinyl ester constituents to diffuse into and interpenetrate the sizing layer (Drzal, Rich, Koenig, and Lloyd (1983b)). Upon curing an interpenetrating network will be formed between the epoxy sizing and the vinyl ester matrix allowing for mechanical integrity and effective stress transfer in the cured composite from fiber to matrix and return (Vautard, Xu and Drzal 2010).

2. MATERIALS AND METHODS

2.1 Materials-Vinyl Ester Resin. The fibers used in this study are AS4 carbon fibers from Hexcel, Inc. with their conventional surface treatment and without any sizing. The matrix resins are Derakane 411-C50 epoxy vinyl ester resin (D411-C50) from Dow Chemical and Fuchem 891 epoxy vinyl ester resin (Fuchem891) from Shanghai Fuchem Chemicals Co., respectively. CHP-5 (diluted cumene hydroperoxide) from Witco Chemical and MEKP (methyl ethylketone peroxide) from Aldrich chemicals were used as the initiators. Both CoNap and DMA from Aldrich Chemicals were used as promoters and accelerators, respectively. Diglycidyl ether of bisphenol A (DGEBA epoxy) and Aliphatic Polyether Triamine (Jeffamine T403) were from Shell and Huntsman, respectively. Figure 1 shows the molecular structures of the epoxy vinyl ester resins, the sizing epoxy material and the cure catalysts. Molecular structure of D411-C50

and Fuchem 891 are both bisphenol A epoxy based vinyl ester but different molecular weights, about 900g/mol for D411-C50 and 1500~2000g/mol for Fuchem 891, respectively. The styrene content of D411-C50 and Fuchem891 are 50% and 35%, respectively.

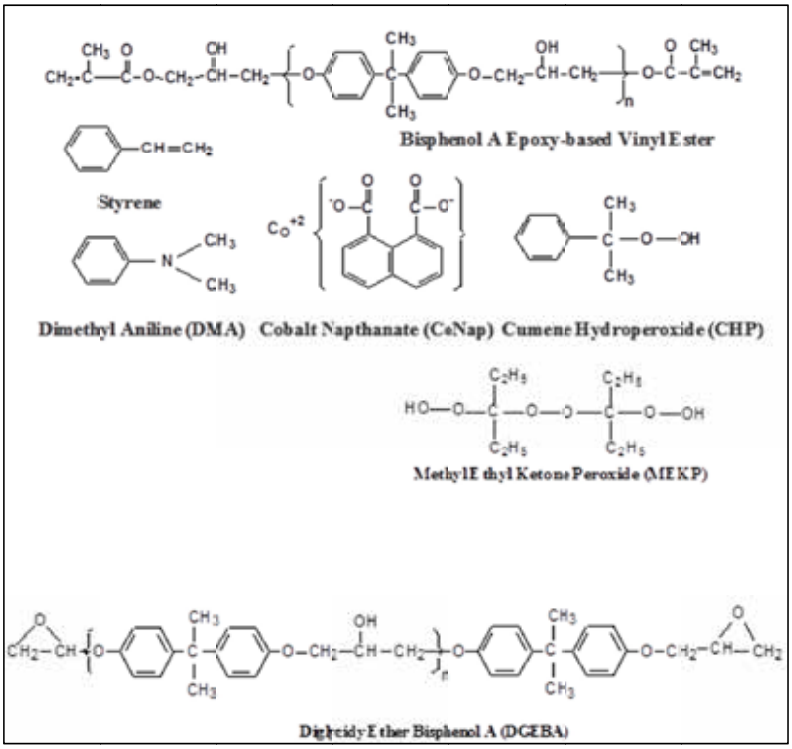

Fig. 1. DGEBA Epoxy, vinyl ester, initiator, promoter, accelerator chemical formulae.

Fuchem 891 is also a mixture of DGEBA epoxy vinyl ester and styrene. The styrene content is about 35%. Considering D411-C50 vinyl ester resin has large volume shrinkage with cure, Fuchem 891 was use in this research to quantify the influence of the cure volume shrinkage to the adhesion between carbon fiber and vinyl ester resin. The property comparison of the D411-C50 and Fuchem 891 are listed in Table 1.

Table 1. Property comparison of D411-C50 to Fuchem 891 vinyl ester.

Properties	D411-C50	Fuchem 891
DGEBA Vinyl Ester Molec Wt (g/mol)	907	1500-2000
Styrene Content	50%	35%
Tensile Modulus, E (GPa)	3.38	3.12
Tensile Strength (MPa)	79.3	75
Elongation %	5~6	4.0

2.2 Nanoparticles. Both multiwall carbon nanotubes and graphene nanoplatelets were dispersed in the sizing. The carbon nanotubes used in this study were a multi-wall carbon nanotubes (MWNTs) with a purity of 90 %, average diameter of 10 nm and average length of 1.5 μm, Nanocyl 3100 (Nanocyl S. A.). The graphene nanoplatelets (xGnP-5) were obtained from XG Sciences, Inc. and were about 5 nm in thickness with an average diameter of 5 microns. Both samples required the mixing with the use of an ultrasonic probe (Cole-Parmer 750-Watt Ultrasonic Processor with 1 inch diameter tip) set to 100 W. The obtained suspensions were very homogeneous and looked like black ink.

2.3 Volumetric Cure Shrinkage. A lab-made dilatometer was used to measure cure volume shrinkage of vinyl ester resin from liquid resin to full cure (Xu 2003a). The cure processes were the same for all samples: room temperature for 1 hour, 90°C for 1 hour and 125°C for 1.5 hours. Two different systems were used with different initiators. One is CHP-5 and the other one is MEKP. The CHP-5 cure system was based on the cure recipe for D411-C50 recommended by the manufacturer and the MEKP cure system was based on the cure recipe for Fuchem 891 recommended by the manufacturer, shown in the gray columns of Table 2. For the same initiator, the corresponding recipes, the white columns of Table 2, were calculated from the recommended recipes, the gray columns, based on the concentration of the carbon-carbon double bond, C=C.

Table 2. The catalyst recipe for the cure volume shrinkage study in vinyl ester matrices.

Initiator		Fuchem 891	D411-C50
CHP-5	CHP-5	1.40%	2.00%
	CoNap	0.21%	0.30%
MEKP	MEKP	2.00%	2.85%
	CoNap	0.10%	0.14%

2.4 Microindentation Test. In order to measure the interfacial shear strength (IFSS), the microindentation method was used (Drzal and Herrera-Franco 1993). The test was run on individually selected fibers on a polished cross-section of a composite, using a specially designed device called the Interfacial Testing System (ITS). Composite specimens were prepared by embedding a small piece of composite in a metallographic specimen, with the fibers normal to the specimen surface. The surface was grinded with sandpaper, using an increasing value of grit and then polished with 1 μm and 0.05 μm alumina particles water solutions. A diamond-tipped stylus mounted on the objective lens holder of a microscope was used to apply a force to single fibers in their surrounding matrix. The value of the IFSS was calculated using an empirical equation (1) based on a finite element analysis and adjusted by empirical data.

$$IFSS = A\frac{f_g}{d_f^2}\left(0.875696\sqrt{\frac{G_m}{E_f}} - 0.01862\ln\frac{d_n}{d_f} - 0.026496\right) \quad (1)$$

In equation (1) f_g is the load applied on the cross section of the selected fiber, G_m is the shear modulus of matrix, E_f is the tensile modulus of the fiber, d_n is the distance between the selected fiber and the nearest fiber, d_f is the diameter of the fiber and A is a conversion factor.

2.5 ThermoGravimetric Analysis (TGA). A High Resolution TGA Thermogravimetric Analyzer (TA Instruments), controlled by Thermal Advantage software was used to measure weight loss as a function of temperature. The ramp was 25 °C.min^{-1} from room temperature to 650 °C, with a resolution of 4 °C. The data were analyzed using Universal Analysis 2000

Software.

2.6 Dynamic Mechanical Thermal Analysis (DMTA). A DMTA 2980 Dynamic Mechanical Analyzer (TA Instruments), controlled by Thermal Advantage software, was used to measure the change in the loss and storage modulus as a function of temperature. The ramp was 10 °C.min^{-1} from room temperature to 150 °C. The data were analyzed using Universal Analysis 2000 Software.

2.7 Environmental Scanning Electron Microscopy (SEM). A Philips Electroscan Environmental Scanning Electron Microscope (SEM) was used for the observation of the quality of the carbon fiber coating process and the fracture profile of composites. The acceleration voltage was 20 kV and the current in the filament was set to 1.83 A. No conductive coating was deposited at the surface of the samples.

2.8 Mechanical Property Tests. Unidirectional composites at fiber volume contents of 50% were prepared with conventional VARTM prepregging using a closed mold. Single fiber fragmentation tests, Interlaminar shear strength, 0^{o} flexural tests and 90^{o} flexural tests were conducted following appropriate ASTM standards.

3. VINYL ESTER RESIN CURE VOLUMETRIC SHRINKAGE

The cure volume shrinkage depended on the resin and the type of initiator. With the same types of initiator and thermal history, the cure volume shrinkage of Fuchem 891 was the lowest. It was also much smaller with the use of MEKP at room temperature, in comparison to a cure with CHP. The cure volume shrinkage was also related to the resin molecular weight of vinyl ester monomer. The thermal history of the curing process also had an influence. For both resins, the volumetric shrinkage was much higher when the resin was cured at high temperature in comparison with a room temperature with the same composition (Table 3).

For systems cured at high temperature, the Young's modulus was measured by microindentation and the associated shear modulus was calculated. The shear modulus of samples was higher for samples cured at high temperatures (Fig. 2).

Table 3. Cure volume shrinkage as a function of the composition of resin.

Type of Resin		Fuchem 891			Derakane 411-C50		
Composition (wt%)	CHP	1.40			2.00	2.00	
	MEKP		2.00				2.85
	CoNap	0.21	0.10		0.30	0.30	0.10
Thermal Cure		1 hr 20^{o}C + 1 hr 90°C + 1.5 hr 125°C		20^{o}C	1 hr 20^{o}C + 1 hr 90°C + 1.5 hr 125°C	20^{o}C	1 hr 20^{o}C + 1 hr 90°C + 1.5 hr 125°C
Cure volume Shrinkage %		5.85	1.73	0.54	7.18	3.68	8.20

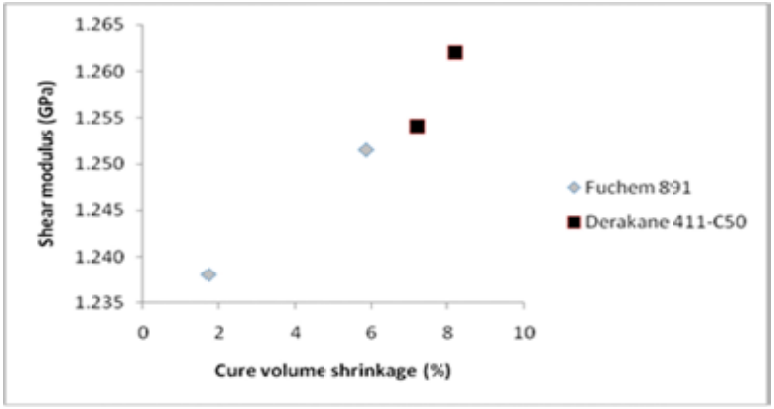

Fig. 2. Shear modulus of vinyl ester resins in function of cure volume shrinkage.

The best interfacial adhesion with AS4 carbon fibers was obtained with Fuchem 891, which had the lowest cure volume shrinkage (Fig. 2). For both resins, a trend showing that the interfacial shear strength was decreasing with increasing cure volume shrinkage could be shown. The cure volume shrinkage created some Von Mises effective stress that had a negative effect on interfacial adhesion (Ho and Drzal 1996).

The cure volume shrinkage is a significant factor affecting interfacial adhesion in carbon fiber-vinyl ester composites. That is why the composition of the resin, the choice of initiator, the molecular weight of the vinyl ester monomer and the thermal program have to be optimized. However, another way of improving interfacial adhesion can be done by inserting a third phase between the fiber and the matrix. That phase has to be malleable enough to take the stress created by the shrinkage of the matrix and not transfer it to the fiber surface. So, to counteract the residual stress created by the high cure volume shrinkage of vinyl ester resins, a slightly cross-linked epoxy coating was applied to the carbon fiber surface.

4. REACTIVE SIZING OF CARBON FIBER

4.1 Optimization of the coating process. A fiber sizing tower system was used to coat the carbon fibers with an epoxy coating (Vautard et al. 2010). The epoxy coating was made of Epon 828 + Jeffamine-T403 (43 phr). The mix was left to cure for 30 min at room temperature before being dissolved in acetone. A spool of surface treated and unsized AS4 carbon fibers was unwound and the tow went through a bath of the epoxy coating dissolved in acetone and was dried by successive exposure to two tower-shaped furnaces. The temperature inside the furnaces was fixed at 60°C and the time spent by the fibers in the furnace was roughly 1 min. The thickness of the coating was measured by TGA. The difference in mass of the coated carbon fiber before and after the 600° C exposure corresponded to the mass of the epoxy coating, which enabled the calculation of its thickness.

The thickness of the coating was directly proportional to the concentration of the sizing solution. It was found that the time spent by the fibers in the bath, which was proportional to the rotation of the winding device, did not have a major impact on the thickness of the coating (Fig. 3).

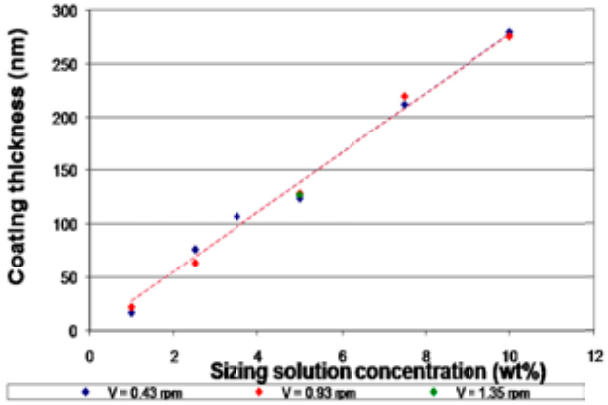

Fig. 3. Thickness of the coating as a function of the sizing solution concentration and the speed of rotation of the winding device.

The quality of the coating (uniformity, absence of resin bridges between single fibers) was checked by SEM. When the concentration of the sizing solution was ≤1 wt%, the surface of the fiber was not evenly coated, with some parts totally uncovered. A concentration of 3 wt% gave a coating that appeared to be evenly spread, without creating bridges between single fibers (Fig. 4). It was also found that for a concentration higher than 4 wt% (that is to say a coating thickness greater than 100 nm), significant bridging between fibers took place within the tow producing a tow that was hard and could not be processed. The final composition of 2.5 wt% sizing solution produced a coating of 80 nm.

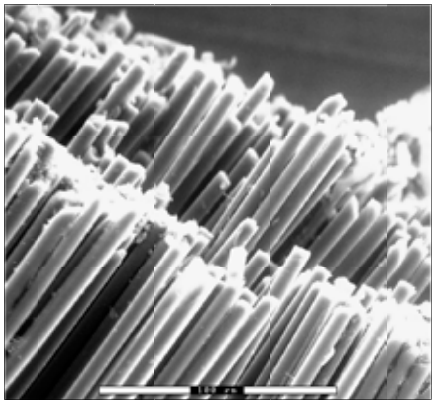

Fig. 4. SEM picture of fibers coated with an epoxy coating (concentration of sizing solution = 3 wt%).

4.2 Interactions between the epoxy coating and the components of the vinyl ester matrix. To assess the influence of a variation of the matrix composition on interfacial adhesion, the concentration of initiator (CHP), promoter (CoNap), and accelerator (DMA) were individually altered but with the same compositions of matrix were used. The values of interfacial adhesion were compared to the values obtained without the epoxy coating. The interfacial adhesion was also investigated with pure styrene and pure vinyl ester monomer.

4.2.1 Influence of the concentration of the initiator. A significant improvement of fiber-matrix adhesion as measured by the IFSS was obtained with the insertion of the epoxy coating between the carbon surface and the vinyl ester matrix (Fig. 5). There was a maximum of interfacial adhesion for a concentration of initiator of 1.5 wt% with the use of an epoxy coating.

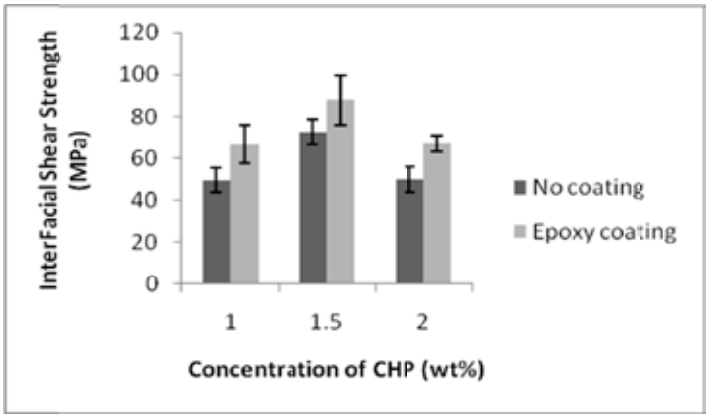

Fig. 5: Influence of the concentration of initiator on interfacial adhesion with the use of an epoxy coating.

4.2.2 Influence of the concentration of the promoter. A slight improvement of interfacial adhesion with 0.1% to 0.3% of CoNapin combination with the epoxy coating (Fig. 6) was detected however, no particular trend was noted as a function of the concentration of the promoter.

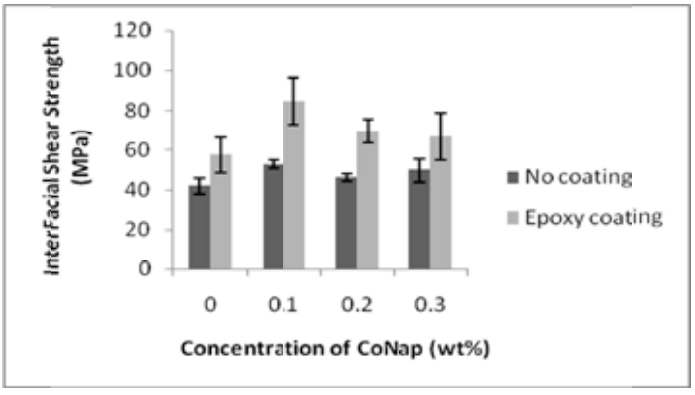

Fig. 6. Influence of the concentration of the promoter on interfacial adhesion with the use of an epoxy coating.

4.2.3 Influence of the concentration of the accelerator. A consistent increase of IFSS was found with the use of an epoxy coating (Fig. 7) but no particular trend was revealed as a function of the concentration of the accelerator.

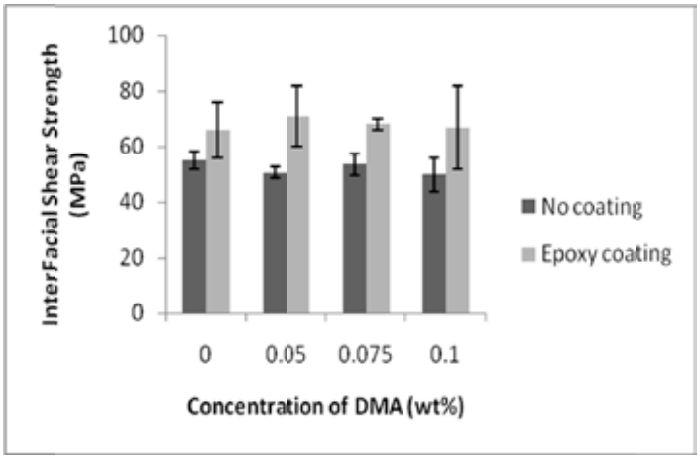

Fig. 7. Influence of the accelerator concentration on interfacial adhesion with the use of an epoxy coating.

All in all, an obvious improvement of interfacial adhesion was created by the insertion of an epoxy coating between the carbon fiber surface and the vinyl ester matrix. A slight influence of the concentration of the initiator was found but not for the promoter or accelerator. Differences in the diffusion of those components into the epoxy coating was not deemed to be responsible for the improvement.

4.2.4 Influence of monomers. Styrene and pure vinyl ester monomer were polymerized with identical thermal profiles. The concentrations of initiator, promoter, and accelerator were adjusted to be proportional to the content of carbon-carbon double bonds. The shear modulus of styrene or pure vinyl ester was measured by the microindentation test. The shear modulus of polymerized pure vinyl ester was higher than the shear modulus of polymerized styrene (Fig. 8). The shear modulus of Derakane 411-C50 was not an average value of the pure styrene and pure vinyl ester shear moduli, as it could be expected if the generalized law of mixtures was used, but it was similar to the value of the shear modulus of polymerized styrene. A lower shear modulus in the interphase could be the reason why the interfacial shear strength with AS4 carbon fibers was lower in the case of polymerized styrene (Fig. 9). With epoxy coated fibers, the values of the IFSS were ranked in a reverse order, pure styrene giving the highest value. The difference of interfacial adhesion between vinyl ester monomer and styrene was significant. The value corresponding to Derakane 411-C50 was intermediate, showing that styrene had a major influence on interfacial adhesion of Derakane 411-C50 when an epoxy coating was spread at the surface of the carbon fibers. The epoxy coating had a negative impact on the interfacial adhesion with polymerized vinyl ester.

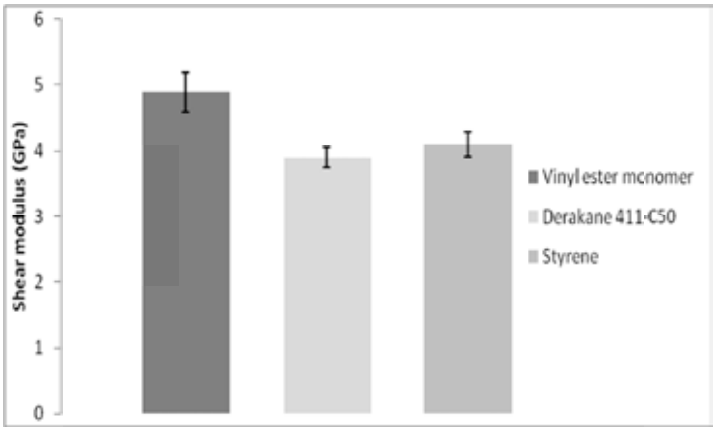

Fig. 8. Shear modulus of polymerized styrene, vinyl ester and Derakane 411-C50.

The two monomers interacted totally differently with the epoxy coating. The vinyl ester monomer did not diffuse into the epoxy coating, leading to a weak interface. On the contrary, the styrene monomer easily diffused into the epoxy coating and upon polymerization enabled the creation of an interpenetrated network, leading to a strong epoxy coating-matrix interphase. The inter-diffusion between epoxy and styrene made the epoxy coating swell, which most probably counteracted the cure volume shrinkage during the polymerization of styrene. The use of an epoxy coating also increased the level of interfacial adhesion in the case of Derakane 411-C50, which indicated that the styrene from the resin diffused preferentially in the epoxy coating and counteracted the effect of the matrix shrinkage.

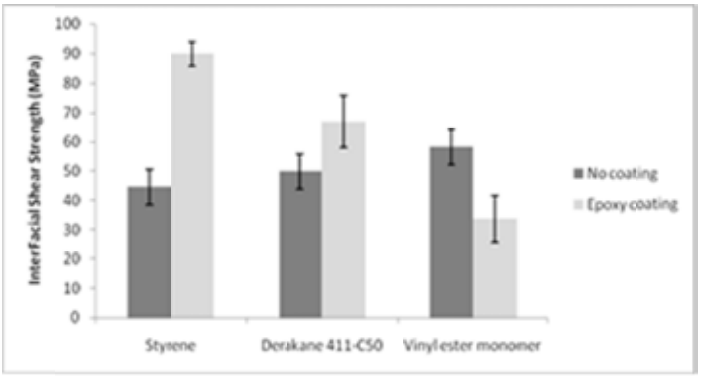

Fig. 9. IFSS of polymerized styrene, vinyl ester and Derakane 411-C50 with coated and uncoated AS4 carbon fibers.

4.2.5. Influence of the cure volume shrinkage with the use of an epoxy coating. The impact of the cure volume shrinkage on interfacial adhesion with carbon fibers was assessed in the case of epoxy coated fibers as well. For samples coated with epoxy, the value of interfacial shear strength measured by the microindentation test remained the same, while it decreased with an increase of the cure volume shrinkage in the case of uncoated fibers (Fig. 10). The coating counteracted the effect of the cure volume shrinkage. When styrene diffused in the epoxy coating, the latter expanded, which annealed the residual stress induced by the cure volume shrinkage. The chemistry and the mechanical properties of both vinyl ester resins being similar

after curing, it was assumed that the physical interactions with the carbon fiber surface and with the epoxy coating were similar. A general trend for the IFSS as a function of the cure volume shrinkage could be identified for coated and uncoated samples (Fig. 11). The respective contributions of cure volume shrinkage and the creation of covalent bonds with the carbon fiber surface could be deduced. Indeed, the difference between coated and uncoated samples with minimum shrinkage gave an assessment of the contribution of covalent bonds created between the epoxy and the carbon fibers surface. Covalent bonds do not exist between carbon fibers and vinyl ester resins. For a high volume shrinkage resin (Derakane 411-C50), the effect of residual stress was responsible for more than 50 % of the lack of interfacial adhesion between coated and uncoated fibers.

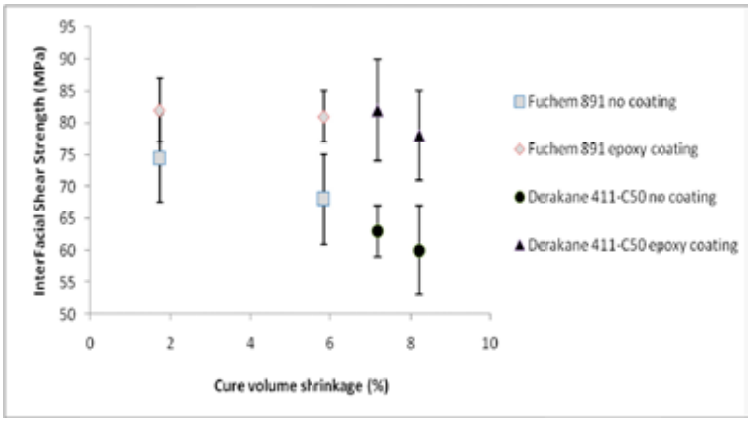

Fig. 10. Influence of cure volume shrinkage on interfacial adhesion for coated and uncoated fibers.

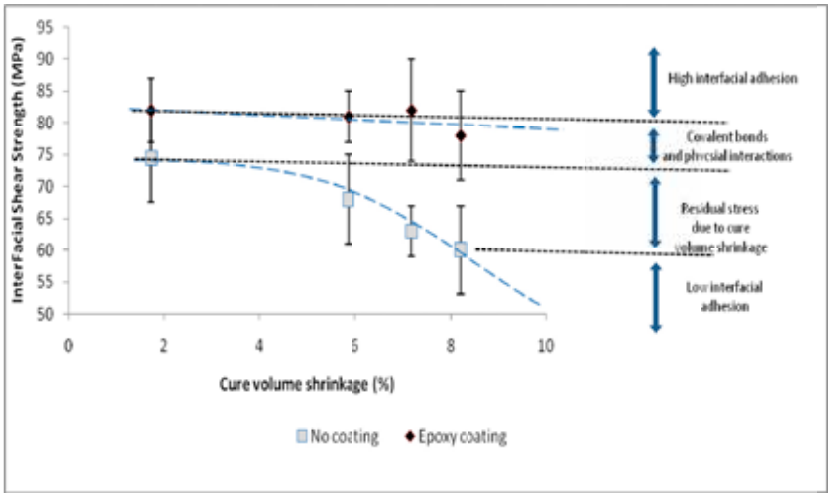

Fig.11. Assessment of the respective contributions of cure volume shrinkage and of the creation of covalent bonds at the interface on IFSS.

Optimum fiber-matrix adhesion can be obtained by properly selecting an initiator and adjusting its concentration. The initiator has indeed a direct influence on the mechanical properties and the microstructure of the matrix. An application of a lightly cross-linked amine-cured epoxy polymer on the carbon fiber surface creates a beneficial interphase between the carbon fiber and the vinyl ester matrix, resulting in an increase of the interfacial adhesion.

4.2.6 Qualitative assessment of the use of an epoxy coating on the mechanical properties of a carbon fiber-vinyl ester composite cured at high temperature. In order to confirm that low interfacial adhesion in carbon fiber-vinyl ester composites was due to the residual stress induced by the cure volume shrinkage and not by the preferential adsorption of the promoter or the accelerator on the carbon fiber surface, only the initiator was added to the resin. Derakane 510A-40, a bromated DGEBA based vinyl ester resin, was mixed with 2 wt% of CHP and cured for 2 hours at 150°C and 2 hours at 170°C. A coating of DGEBA mixed with Jeffamine T-403 (43 phr) was coated on the surface of AS4 carbon fibers. The thickness of the coating was 60 nm and it was left for 10 hours at room temperature before making contact with the matrix. Composites with a diameter of 6 mm and a fiber volume fraction of 50% were made with coated and uncoated fibers. A microindentation test was made on each composite. An obvious improvement of the IFSS was obtained with the epoxy coating (Fig. 12).

A three point flexural test was used to evaluate the composites, with a span of 30 mm between the support noses and a vertical speed of 5 $mm.min^{-1}$ for the loading nose. The fracture profile was observed by SEM. For composites made with uncoated fibers, the fracture profile was typical of a low interfacial adhesion (Fig. 13). The surface had a brush appearance with long and clean protruding fibers. Interface failure could be seen at high magnification.

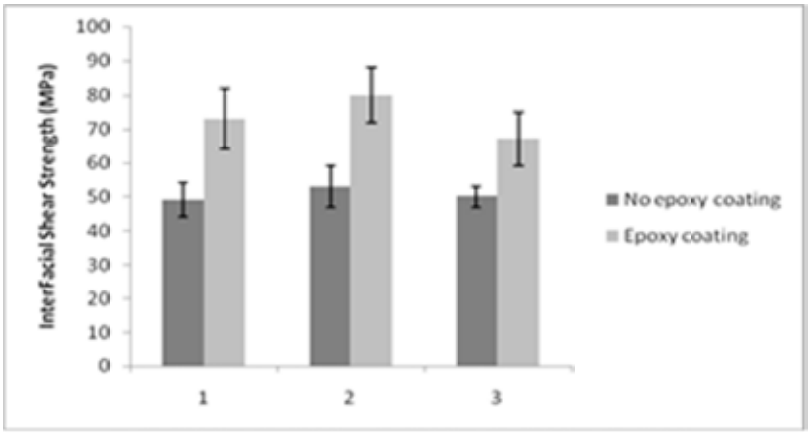

Fig. 12. Improvement of interfacial adhesion with the use of an epoxy coating for a carbon fiber-vinyl ester composite cured at high temperature.

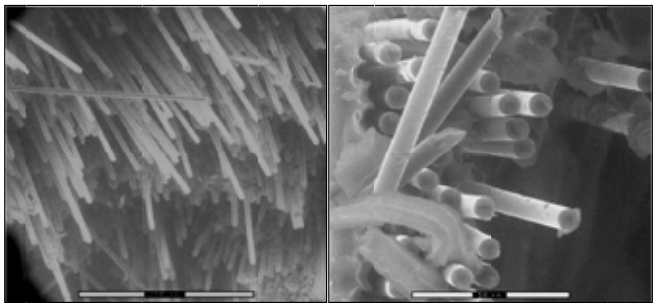

Fig. 13. SEM pictures of the fracture profile of a composite with uncoated fibers.

The fracture profile obtained with epoxy coated fibers clearly showed improved interfacial adhesion, with protruding fibers that were short and covered with pieces of matrix resin (Fig. 14). Nevertheless, some protruding fibers were still long and clean. The fracture mechanism appeared to be a mixed mode of interfacial and matrix failures. The improvement of interfacial adhesion through the use of this epoxy coating was responsible for that improvement.

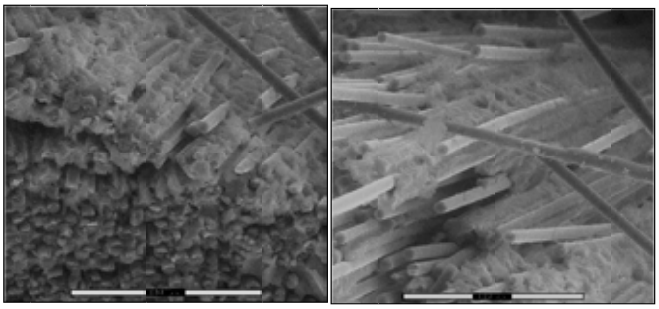

Fig. 14. SEM pictures of the fracture of a composite with epoxy coated fibers.

4.3 Determination of the optimal thickness of the coating by a finite element analysis. Using an epoxy coating improved the interfacial adhesion between carbon fibers and vinyl ester matrix (Ho et al. 1996). It is important to optimize the properties of that coating in order to get the best mechanical properties for the interphase and the composite. The influence of the coating thickness on the value of the IFSS measured by a microindentation test was evaluated with the aid of a finite element model. This finite element model was applicable when the fiber volume fraction was between 0.3 and 0.5 (Ho et al. 1996). The microindentation specimen assembly was modeled as a combination of four concentric cylindrical tubes representing the fiber, the interphase, the matrix and the composite, as shown in Fig. 15. The indenter was modeled as a rigid half-sphere. The finite element analysis of this cylindrical representative volume element required only a two-dimensional axisymmetric modeling. Because of the symmetry, only half of the cross-sectional plane was analyzed. Fixed boundary conditions were assumed at the sides of the composite. Along the axisymmetric axis (z-axis) and the bottom boundary (r-axis), roller constraints were applied. Interface elements were used between the indenter and the fiber to prevent interpenetration of the two. Coulomb friction was assumed in the indenter-fiber contact zone. A compressive load was applied to the top surface of the indenter. The boundary between the fiber and the interphase, the boundary between the interphase and the matrix, and the boundary between the matrix and the composite were all set to be continuous, which assumed perfect bonds between materials side by side.

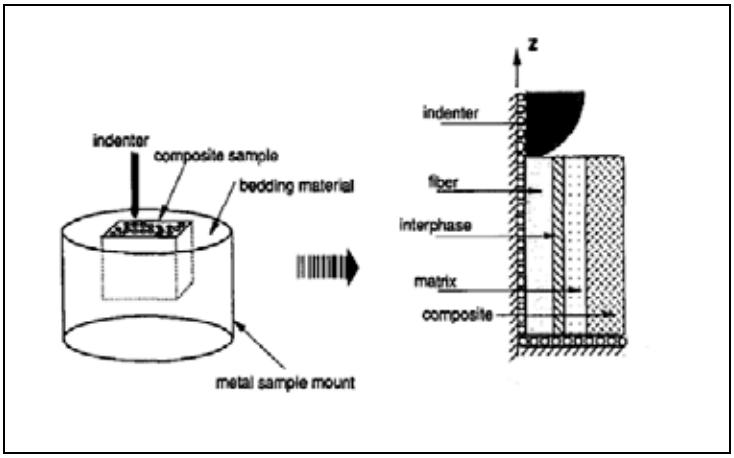

Fig. 15. Finite element model based on a four phase cylinder.

All of the materials were assumed to be homogeneous, isotropic, and elastic and no residual stress was considered. The width and length of the 2-dimensional model were 20 μm and 100 μm, respectively. The matrix thickness, which corresponded to 36 % fiber volume fraction, was 0.16 μm. The interphase was divided into 8 layers of 0.02 μm. One layer of the interphase was set to have the same properties as DGEBA. The other seven layers were set to have the same properties as Derakane 411-C50. The thickness of the matrix was 2.33 μm.

The mechanical properties of the materials used in the models are listed in Table 4. The composite properties were calculated based on the rule of mixture for a transversely isotropic composite. The models were meshed using IDEAS software. Axisymmetric four-node elements were used. The boundary conditions were set up using IDEAS software. Contact loading and calculation were carried out using ABAQUS software.

Table 4. Material properties for the baseline model used in the finite element model.

	Fiber	**Interphase**	**Matrix**	**Composite**
Tensile Modulus E (GPa)	241	2.1	3.38	85
Shear Modulus G (GPa)	96.5	0.92	1.24	32
Poisson Ratio ν	0.250	0.356	0.356	0.318

The finite element model was a simulation of the real microindentation test. The simulated values of IFSS showed that the optimal thickness for the epoxy coating was 80 nm (Fig. 16). The IFSS decreased sharply for a coating thicker than 100 nm. The tensile moduli of the pure epoxy sizing and vinyl ester matrix were 2.1 GPa and 3.38 GPa, respectively. The epoxy coating was then softer than the vinyl ester matrix, therefore, as the sizing becomes thicker, the ability of the interphase to transfer stress to the fiber was affected. This finite element analysis did not take into account the inter-diffusion between the coating and the matrix, which would certainly lead to a more efficient transfer of stress to the reinforcement. Experimental data to verify that zone of interdiffusion was characterized by a nanoindentation scratch technique.

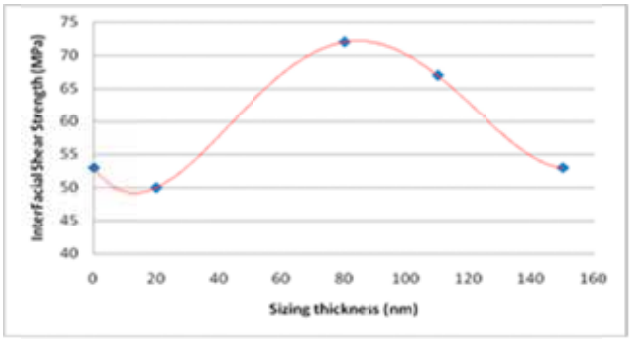

Fig. 16. Simulated IFSS in function of the thickness of the epoxy coating.

4.4. Determination of the thickness of the interdiffusion zone by a nanoindentation scratch test. The nanoindentation scratch test is a technique that determines the coefficient of friction (COF) between a nanoindenter and a material. With the same vertical load applied to the indenter, the harder the scratched material, the shallower the penetration of the indenter in that material, and the lower the COF. This technique can identify the different phases of a multi-phase material, each phase having a different COF. In the case of an interdiffusion of polymers, the value of the COF changes continuously between the values corresponding to the COF of the pure polymers, thereby highlighting the extent of the zone of interdiffusion. The thickness of the zone of interdiffusion between the epoxy coating and the vinyl ester matrix was measured to be 2.5 µm.

5. NANOPARTICLE MODIFICATION OF THE FIBER-MATRIX INTERPHASE

Analysis of the interphase region shows that ultimately the adhesion between fiber and matrix is dependent on the properties of the polymer (or polymer system) created in the interphase, in particular the dependency on the square root of the shear modulus. Variation in thermoset polymer modulus results from variation in the crosslink density. However, the crosslink density and hence the polymer modulus can only be changed over a very small range. The recent availability of nanomaterials has offered a new route to interphase modification by the incorporation of nanoparticles. For example, carbon nanotubes (CNT) ~10 nm in diameter and up to several microns in length, have been shown to have a modulus of ~ 1 TPa and a tensile strength of greater than 50 GPa. Graphene nanoplatelets (GnP) consisting of the same sp^2 graphene structure also have been shown to have similar properties. Since incorporation of these nanoparticles in polymers follows the well-known rule of mixtures, it is possible to increase the shear modulus of the interphase region by their dispersion in this region with a resulting increase in adhesion and composite mechanical properties.

Building on the interphase engineering concept it is possible to add nanoparticles to the fiber-matrix interphase. While this research is still underway, preliminary results have shown that both CNTs and GnPs can be utilized to improve interfacial and composite properties (Kamae and Drzal 2012). For example, in Fig. 17, composte data are shown for systems in which multiwall CNTs were applied to a T700 carbon fiber during the fiber 'sizing' step. The sizing thickness was held constant but the amount of CNT was varied. The interlaminar shear strength measured in a 50 volume percent carbon fiber- amine cured epoxy composite increased as much as 20% and the 90° transverse flexural strength over 10% with the addition of only 0.5 wt% of MWCNT. Compressive strength and Mode I fracture toughness also increased 28% and 10%,

respectively over the baseline system without nanoparticles.

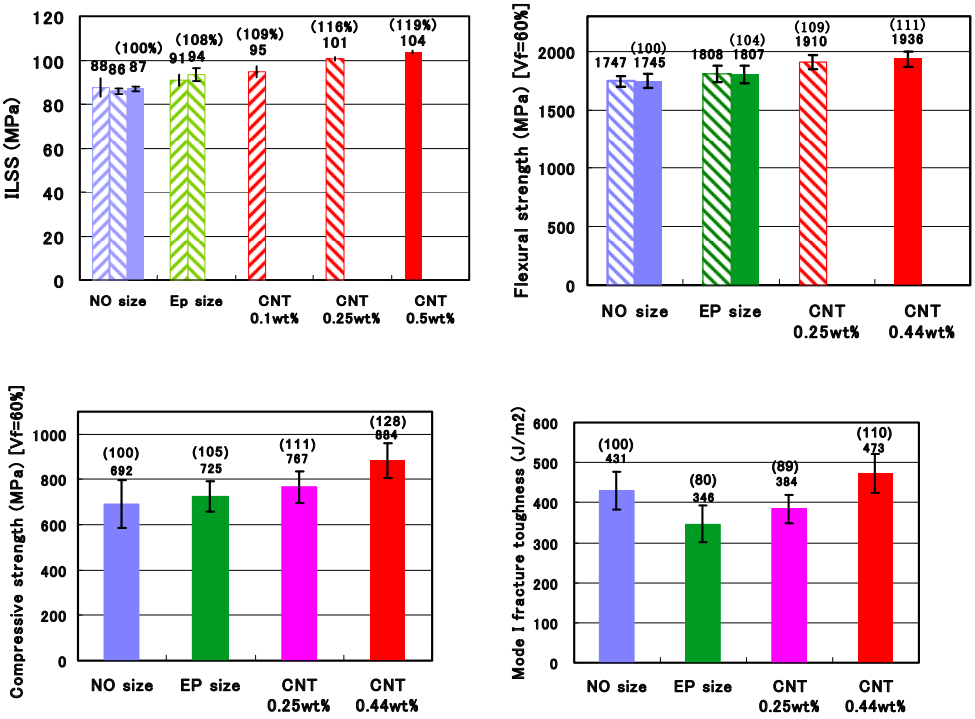

Fig. 17. Composite interlaminar shear strength (a), 90° transverse flexural strength (b), 0° compressive strength (c) and Mode I fracture toughness (d) for 50 weight % T700 carbon fiber –epoxy composites with increasing amounts of MWCNTs applied to the fiber surface.

The effect is not limited to the addition of fibrous nanoparticles. In a similar manner, GnP graphene nanoplatelets of thicknesses of ~5 nm and average diameters of 1 micron were also applied to AS4 carbon fibers in the same epoxy matrix. As shown in Fig. 18, even larger increases were measured for a 60 weight % composite using a 2 weight % application of GnP on the fiber surface. Short beam shear strength increased ~40% and 90° transverse flexural strength increased ~20%.

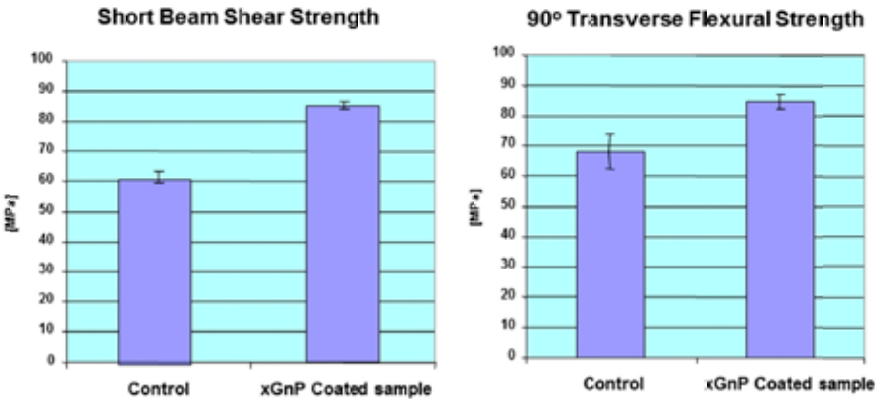

Fig. 18. Composite short beam shear strength (a) and 90° transverse flexural strength (b) for 60 weight % AS4 carbon fiber –epoxy composites with 2 weight% of GnP applied to the fiber surface.

6. CONCLUSIONS

The present study has identified the combination of causes responsible for poor adhesion between a reinforcing fiber and the polymer matrix in composite materials. These factors include: the lack of chemical bond formation between the fiber surface and the polymer; low shear modulus of the polymer in the fiber-matrix interphase region; adsorption of reactive components on the fiber surface resulting in a change in interphase polymer properties; and polymerization shrinkage resulting in radial tensile stresses at the fiber-matrix interphase.

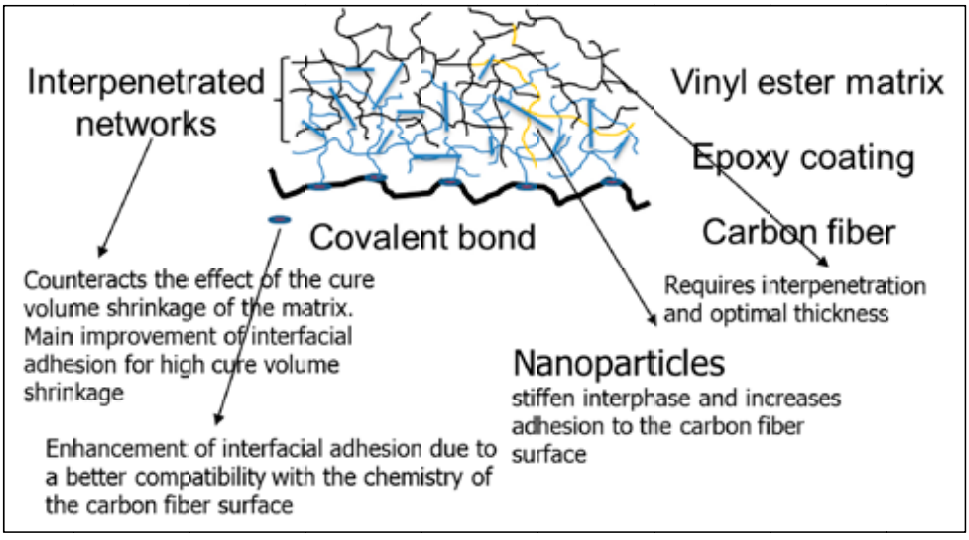

Fig. 19. Schematic of the 'Engineered Fiber-Matrix Interphase' to optimize adhesion.

As a result of an extensive study of the carbon fiber-vinyl ester interphase, an 'engineered interphase' design strategy (Fig. 19) has been proposed to overcome these factors. The essential elements of it are: *i)* chemical groups on the carbon fiber surface resulting from conventional surface treatments can be reacted with epoxy groups in a epoxy sizing; *ii)* the sizing should consist of epoxy with less than the stoichiometric amount of curing agent applied in a thickness of 70-80 nm; *iii)* the epoxy-curing agent combination is allowed to vitrify at ambient conditions giving a solid with lightly crosslinked polymer coating; *iv)* under composite prepregging conditions, the sizing will swell and the vinyl ester will diffuse into the sizing resulting in an interpenetrated network. The properties of this engineered interphase avoid segregation of polymer reactant constituents to the carbon fiber surface; counteract the radial tensile stresses resulting for high vinyl ester cure shrinkage; and provide increased fiber-matrix adhesion which improves the interface dependent composite mechanical properties. The engineered interphase also allow for incorporation of nanoparticles such as CNTs or GnPs which can further improve interfacial and composite properties.

REFERENCES

Drzal, L. T.; Rich, M.; Lloyd, P. (1983a). Adhesion of Graphite Fibers to Epoxy Matrices. I. The Role of Fiber Surface Treatment, J. Adhesion, 16, 1 30.

Drzal, L. T.; Rich, M.; Koenig, M.; Lloyd, P. (1983b). Adhesion of Graphite Fibers to Epoxy Matrices. II. The Effect of Fiber Finish, J. Adhesion, 16, 133 152.

Drzal, L. T.; Madhukar, M. (1993). Fiber-Matrix Adhesion and Its Relationship to Composite Mechanical Properties, J. Matr. Sci. 28, 569-610.

Drzal, L. T.; Sugiura, N.; Hook, D. (1997). The Polymer Interphase in Composites: Intrinsic Limitations to Adhesion, Composite Interfaces 4, 337-354.

Drzal, L. T.; Herrera-Franco, P. (2002). Measurement Methods for Fiber-Matrix Adhesion in Composite Materials. Comprehensive Adhesion Science: The Mechanics of Adhesion, Rheology of Adhesives and Strength of Adhesive Bonds A. Pocius; D. Dillard, Eds.; Elsevier, Vol. II, Chapter 17.

Ho, H.; Drzal, L. T. (1996). Evaluation of Interfacial Mechanical Properties of Fiber Reinforced Composites Using the Microindentation Method, Composites Part A, 27A, 961-971.

Kamae, T. ;Drzal, L. T. (2012). Carbon Fiber / Epoxy Composite Property Enhancement through Incorporation of Carbon Nanotube at the Fiber-Matrix Interphase – Part I. The Development of Carbon Nanotube coated Carbon Fiber and the Evaluation of Their Adhesion, Composites, Part A 43, 1569-1577.

Li P, Yu Y., Yang X. (2008). Effects of Initiator on the Cure Kinetics and Mechanical Properties of Vinyl Ester Resins. J. Appl. Polym. Sci. 109: 2539-2545.

Paiva MC, Nardin M, Bernardo CA, Schultz J. (1997). Influence of thermal history on the results of fragmentation tests on high-modulus carbon-fiber/polycarbonate model composites. Compos. Sci. and Technol. 57: 839-843.

Schultz J, Nardin M. (1994). Some Physico-Chemicals Aspects of the Fibre-Matrix Interphase in Composite Materials. J. of Adhes. 45:59-71.

Vautard, F., Xu, L. Drzal, L. T. (2010). Carbon Fiber-Vinyl Ester Interfacial Adhesion Improvement by the Use of an Epoxy Coating, pp 27-50 An Anthology of ONR Sponsored Research, I. Daniel, E. E. Gdoutos and Y. Rajapakse, editors.

Weitzsacker CL, Xie M, Drzal LT. (1997). Using XPS to Investigate Fiber/Matrix Chemical Interactions in Carbon-Fiber-reinforced Composites. Surf Interface Anal. 25: 53-63.

Xu L, Drzal LT. (2003). Influence of Matrix Cure Volume Shrinkage on the Adhesion between Vinyl Ester and Carbon Fiber. Proceedings of the 2003 Adhesion Society: 415-417.

Xu L. (2003). Interfacial Engineering of the Interphase Between Carbon Fibers and Vinyl Ester Resin. PhD Dissertation, Dept of Chemical Engineering, Michigan State University.

Proceedings of the 34th Risø International Symposium on Materials Science:
Processing of fibre composites – challenges for maximum materials performance
Editors: B. Madsen, H. Lilholt, Y. Kusano, S. Fæster and B. Ralph
Department of Wind Energy, Risø Campus
Technical University of Denmark, 2013

PROCESS CONDITIONS AND VOLUMETRIC COMPOSITION IN COMPOSITES

Bo Madsen

Composites and Materials Mechanics, Department of Wind Energy,
Technical University of Denmark, Risø Campus,
DK-4000 Roskilde, Denmark

ABSTRACT

The obtainable volumetric composition in composites is linked to the gravimetric composition, and it is influenced by the conditions of the manufacturing process. A model for the volumetric composition is presented, where the volume fractions of fibers, matrix and porosity are calculated as a function of the fiber weight fraction, and where parameters are included for the composite microstructure, and the fiber assembly compaction behavior. Based on experimental data of composites manufactured with different process conditions, together with model predictions, different types of process related effects are analyzed. The applied consolidation pressure is found to have a marked effect on the volumetric composition. A power-law relationship is found to well describe the found relations between the maximum obtainable fiber volume fraction and the consolidation pressure. The degree of fiber/matrix compatibility and the related amount of interface porosity is found to have a negligible effect on the volumetric composition. Only for the extreme case where an interface gap of 250 nm is considered to exist along the entire fiber perimeter, the porosity of the composites is noticeable above zero, but still the fiber and matrix volume fractions are only slightly changed. Air entrapment in the matrix due to non-ideal process conditions is found to have a marked effect on the volumetric composition. For composites with such type of matrix porosity, the porosity content is decreased when the fiber content is increased. Altogether, the model is demonstrated to be a valuable tool for a quantitative analysis of the effect of process conditions. Based on the presented findings and considerations, examples of future work are mentioned for the further improvement of the model.

1. INTRODUCTION

The volumetric composition in composites, their fiber, matrix and porosity content, is a fundamental characteristic for the materials performance. Micromechanical models are used to link the volumetric composition to the (mechanical) property profile of the composites. The obtainable volumetric composition of composites is however constrained by the applied

manufacturing concept, and furthermore, it is influenced by the setting of process conditions. Thus, the study of the relations between process conditions and volumetric composition in composites is central to the goal of achieving maximum materials performance.

Typically, prior to the manufacturing process, model equations for weight and volume relationships are used to convert the controlled gravimetric composition into a wanted volumetric composition. These calculations are simple if assumptions of no porosity and unlimited fiber packing ability are applied, but they become less simple for the realistic situation of composites with porosity and limited fiber packing ability. The latter situation requires however knowledge on the composite microstructure, and the compaction behavior of the fiber assembly. These parameters are included in a model for the volumetric composition in composites developed by Madsen, Thygesen and Lilholt (2007), which later on was integrated in a micromechanical model for stiffness of composites (Madsen, Thygesen and Lilholt 2009). The model has recently been used in the studies by Aslan, Mehmood and Madsen (2013) and Domínguez and Madsen (2013).

The objective of the present study is to use the volumetric composition model for a quantitative analysis of the effect of process conditions on the volumetric composition in composites. Initially, the basic definitions of gravimetric and volumetric composition in composites are presented, followed by a presentation of model concepts and key equations. Based on experimental data of composites manufactured with different process conditions, together with model predictions, three types of process related effects are analyzed: (i) *consolidation pressure*, which is a typical variable process condition, (ii) *fiber/matrix compatibility*, which is governed by e.g. the surface polarity of the two parts, and (iii) *air entrapment in matrix*, which is due to e.g. generation of volatile by-products during curing of a thermosetting resin matrix.

2. BASIC DEFINITIONS

Composite materials are typically composed of two materials parts, fibers and matrix, together with a third part, porosity, which consists of air-filled cavities within the composites. The three parts in composites are schematically illustrated in Fig. 1 showing them in their intermixed configuration (left) or visualized as discrete slabs on top of each other (right).

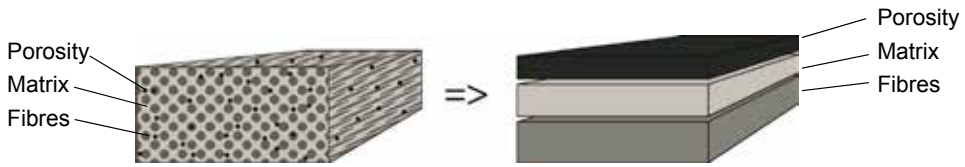

Fig. 1. Schematic illustration of the three parts in composites, fibers, matrix and porosity.

On a weight basis, composites consist of fibers and matrix, and their weight fractions sum to one:

$$m_c = m_f + m_m \quad \Rightarrow \quad 1 = \frac{m_f}{m_c} + \frac{m_m}{m_c} = W_f + W_m \tag{1}$$

where m is absolute mass, W is weight fraction, and the subscripts c, f and m are composite, fibers, and matrix, respectively.

On a volume basis, composites consist of fibers, matrix and porosity, and their volume fractions sum to one:

$$v_c = v_f + v_m + v_p \quad \Rightarrow \quad 1 = \frac{v_f}{v_c} + \frac{v_m}{v_c} + \frac{v_p}{v_c} = V_f + V_m + V_p \tag{2}$$

where v is absolute volume, V is volume fraction, and the subscript p is porosity.

Accordingly, composites are characterized by having (i) a *gravimetric composition* (W_f and W_m), which typically can be directly controlled by the ingoing masses of fibers and matrix in the manufacturing process, and (ii) a *volumetric composition* (V_f, V_m and V_p), which is influenced by the process conditions of the manufacturing process.

3. MODELS FOR VOLUMETRIC COMPOSITION

Equations for the weight/volume relations in composites are required to convert between the controllable weight fractions and the resulting volume fractions, where the latter ones govern the mechanical properties of the composites. Here follow presentations of two models for volumetric composition in composites.

3.1 Traditional model for volumetric composition. For the case of composites with *no porosity* ($V_p = 0$) and *unlimited fiber packing ability* ($V_f \in [0; 1]$), the governing equations can readily be derived:

$$V_{f*} = \frac{v_f}{v_f + v_m} = \frac{\frac{m_f}{\rho_f}}{\frac{m_f}{\rho_f} + \frac{m_m}{\rho_m}} = \frac{W_f\ \rho_m}{W_f\ \rho_m + (1 - W_f)\ \rho_f}$$

$$V_{m*} = \frac{v_m}{v_f + v_m} = \frac{\frac{m_m}{\rho_m}}{\frac{m_f}{\rho_f} + \frac{m_m}{\rho_m}} = \frac{(1 - W_f)\rho_f}{W_f\ \rho_m + (1 - W_f)\rho_f} = 1 - V_{f*} \tag{3, 4, 5}$$

$$V_{p*} = 1 - (V_{f*} + V_{m*}) = 0$$

where ρ_f and ρ_m are density of fibers and matrix, respectively. The asterisk (*) specifies the situation of no porosity and unlimited fiber packing ability. These are the equations traditionally shown in text books of composites.

3.2 New model for volumetric composition. In the more realistic case of composites *with porosity* ($V_p > 0$) and *limited fiber packing ability* ($V_f \in [0; V_{f\,max}]$ where $V_{f\,max} < 1$]), a model has been developed by Madsen et al. (2007).

The model predicts two regions of composite volumetric composition: Region A and B, which are separated by a transition point. Fig. 2 shows an example of predicted volume fractions of fibers, matrix and porosity as a function of the fiber weight fraction. The figure shows also schematized cross-sections of composites.

In Region A, where the fiber weight fraction is below a transition value, $W_{f\,trans}$, the fiber assembly is *not fully compacted* (under the operating process conditions), and the volume of matrix is *sufficient* to fill the free space between the fibers (see schematized composite cross-sections in Fig. 2). In this situation, the volumetric composition (V_f, V_m and V_p) is governed by the equations:

$$V_f = \frac{W_f\ \rho_m}{W_f\ \rho_m\ \left(1 + \sum \alpha_{pf\,(i)}\right) + \left(1 - W_f\right)\ \rho_f\ \left(1 + \sum \alpha_{pm\,(i)}\right)}$$

$$V_m = \frac{\left(1 - W_f\right) \rho_f}{W_f\ \rho_m\ \left(1 + \sum \alpha_{pf\,(i)}\right) + \left(1 - W_f\right)\ \rho_f \left(1 + \sum \alpha_{pm\,(i)}\right)} \qquad (6, 7, 8)$$

$$V_p = 1 - \left(V_f + V_m\right)$$

where $\alpha_{pf\,(i)}$ and $\alpha_{pm\,(i)}$ are so-called fiber and matrix correlated porosity factors, respectively, which control the porosity content in the composites (see Section 3.3). It can be noted that if the porosity factors are set equal to zero, then Eqs. (6) - (8) become identical to Eqs. (3) - (5) representing the simple case of no porosity.

In Region B, where the fiber weight fraction is above the transition value, $W_{f\,trans}$, the fiber assembly is *fully compacted* (under the operating process conditions), and the volume of matrix is *insufficient* to fill the free space between the fibers (see schematized composite cross-sections in Fig. 2). Since the fiber assembly is fully compacted to its minimum volume, it means that the volumetric composition is constrained by a maximum obtainable fiber volume fraction, $V_{f\,max}$. In this situation, the volumetric composition (V_f, V_m and V_p) is governed by the equations:

$$V_f = V_{f\,max}$$

$$V_m = V_{f\,max}\ \frac{\left(1 - W_f\right)\ \rho_f}{W_f\ \rho_m} \qquad (9, 10, 11)$$

$$V_p = 1 - \left(V_f + V_m\right)$$

The transition point between Region A and B, as defined by $W_{f\,trans}$, can be calculated by the equation:

$$W_{f\,trans} = \frac{V_{f\,max}\ \rho_f\ \left(1 + \sum \alpha_{pm\,(i)}\right)}{V_{f\,max}\ \rho_f\ \left(1 + \sum \alpha_{pm\,(i)}\right) - V_{f\,max}\ \rho_m\ \left(1 + \sum \alpha_{pf\,(i)}\right) + \rho_m} \qquad (12)$$

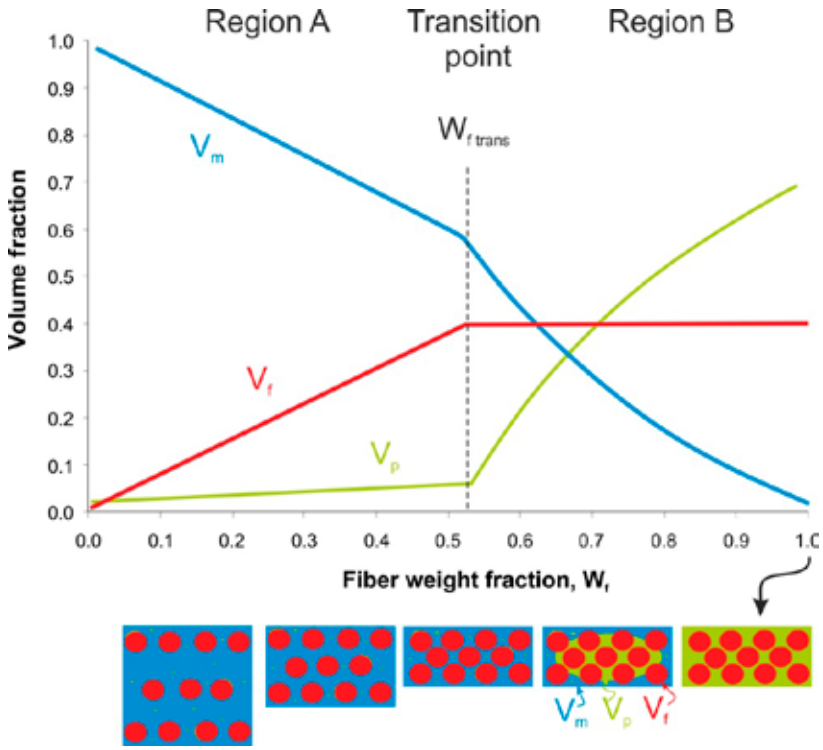

Fig. 2. Model diagram of the volumetric composition (V_f, V_m and V_p) in composites as a function of the fiber weight fraction (W_f), together with schematized composite cross sections. Color codes: red for fibers, blue for matrix, and green for porosity. (Aslan et al. 2013).

As shown in Fig. 2, at the transition point between Region A and B, the volumetric composition is characterized by the best possibly combination of high V_f and low V_p, and this typically results in composites with maximum mechanical properties (Madsen et al. 2009; Aslan et al. 2013). This is exemplified in Fig. 3 for unidirectional flax fiber/polyethylene terephthalate composites showing both the volumetric composition, and the stiffness of the composites as a function of the fiber weight fraction. The model lines predict a transition fiber weight fraction of 0.61, at which V_f is 0.53 and V_p is 0.07, and this corresponds to a maximum obtainable stiffness of the composites on 35 GPa. Thus, it is demonstrated that the transition point is valuable at giving the optimum parameters for composite design.

In general, as shown in Fig. 3, and as will be shown later, there is a good agreement between experimental data and predictions made by the developed new model for volumetric composition in composites.

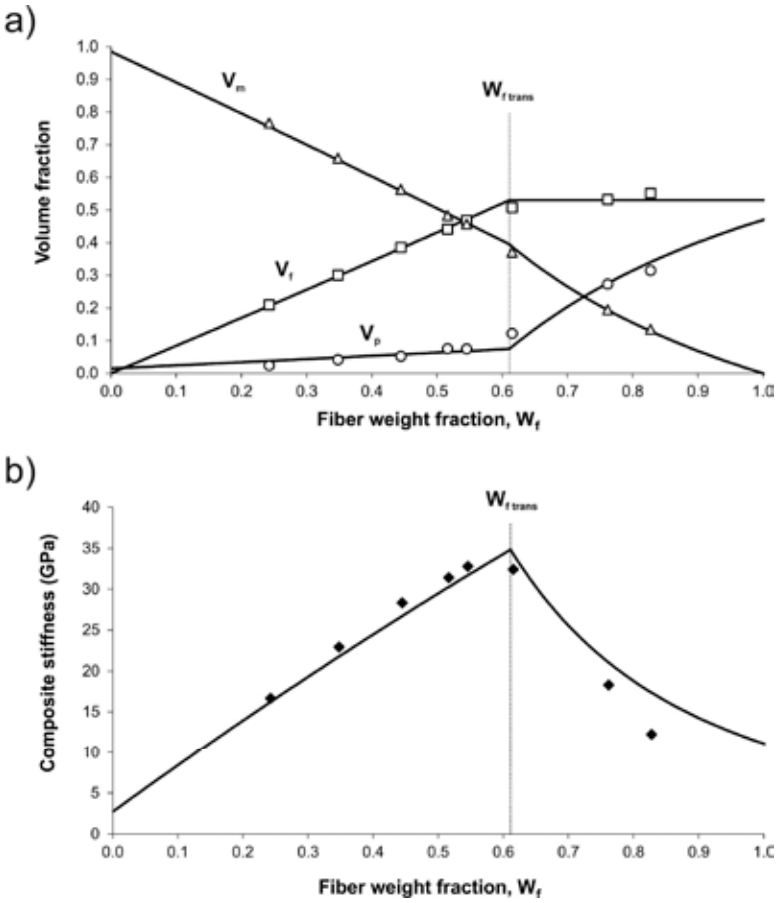

Fig. 3. Experimental data and model predictions of (a) volumetric composition (V_f, V_m and V_p) and (b) stiffness as a function of the fiber weight fraction (W_f) of unidirectional flax fiber/ polyethylene terephthalate composites. Experimental data from Aslan et al. (2013).

3.3 Identification and quantification of porosity types. In the above presented model for volumetric composition in composites, the total porosity (V_p) can be divided into a number of different types of porosity:

$$V_p = \sum V_{pf\,(i)} + \sum V_{pm\,(i)} + V_{ps} \tag{13}$$

where $V_{pf\,(i)}$ are different types of *fiber correlated porosity*, $V_{pm\,(i)}$ are different types of *matrix correlated porosity*, and V_{ps} is *structural porosity*.

The fiber and matrix correlated porosity fractions ($V_{pf\,(i)}$ and $V_{pm\,(i)}$) are assumed to be linearly related to the fiber and matrix volume fractions (V_f and V_m) via the *fiber and matrix correlated porosity factors* ($\alpha_{pf\,(i)}$ and $\alpha_{pm\,(i)}$), respectively:

$$\sum V_{pf\,(i)} = \sum \alpha_{pf\,(i)}\, V_f \quad ; \quad \sum V_{pm\,(i)} = \sum \alpha_{pm\,(i)}\, V_m \tag{14, 15}$$

The porosity factors $\alpha_{pf\,(i)}$ and $\alpha_{pm\,(i)}$ are parameters in the volumetric composition model (see Eqs. (6) and (7)).

Three different types of fiber correlated porosities have been identified:

- Fiber porosity ($V_{pf\,(1)}$), which is identified as air-filled cavities inside the fibers, i.e. fibers with a so-called lumen.
- Interface porosity ($V_{pf\,(2)}$), which is identified as air-filled cavities (gaps) at the fiber/matrix interface.
- Impregnation porosity ($V_{pf\,(3)}$), which is identified as air-filled cavities in the interior of fiber sub-assemblies (e.g. fiber bundles).

One type of fiber correlated porosity has been identified:

- Matrix porosity ($V_{pm\,(1)}$), which is identified as air-filled cavities in the matrix (e.g. entrapped air bubbles).

As indicated by Eqs. (14) and (15), each of the above-mentioned four types of porosities ($V_{pf\,(1)}$, $V_{pf\,(2)}$, $V_{pf\,(3)}$, and $V_{pm\,(1)}$) is assigned a porosity factor ($\alpha_{pf\,(1)}$, $\alpha_{pf\,(2)}$, $\alpha_{pf\,(3)}$, and $\alpha_{pm\,(1)}$). In the study by Madsen et al. (2007), analytical equations were derived to determine three out of four porosity factors:

$$\alpha_{pf\,(1)} = \frac{V_{lumen}}{1 - V_{lumen}} \qquad \text{i.e.} \qquad V_{pf\,(1)} = \alpha_{pf\,(1)}\, V_f$$

$$\alpha_{pf\,(2)} = \frac{b\,\beta\,C}{A}\frac{1}{1 - V_{lumen}} \qquad \text{i.e.} \qquad V_{pf\,(2)} = \alpha_{pf\,(2)}\, V_f \qquad (16, 17, 18)$$

$$\alpha_{pm\,(1)} = \frac{V_{matrix\ porosity}}{1 - V_{matrix\ porosity}} \qquad \text{i.e.} \qquad V_{pm\,(1)} = \alpha_{pm\,(1)}\, V_m$$

where V_{lumen} is the volume fraction of lumen in the fibers, b is the width of the interface gap, β is the interface debonding fraction of the fiber perimeter ($\beta = 1$ for fully debonded fibers), A is the cross-sectional area of the fibers, C is the perimeter of the fiber cross-section, and $V_{matrix\ porosity}$ is the volume fraction of porosity in the matrix. It should be noted that each of these parameters are physically meaningful, and they can in principle be directly measured from the microstructure of composites.

An analytical equation has however not been derived for the impregnation porosity factor ($\alpha_{pf\,(3)}$). Instead, the value of this porosity factor can be found from the slope of a linear regression line of the relation between experimental data of total porosity (V_p) and fiber volume fraction (V_f) for composites with variable fiber content (for data in Region A of the model), and by knowledge of the values of the other three porosity factors:

$$V_p = \frac{\alpha_{pf\,(1)} + \alpha_{pf\,(2)} + \alpha_{pf\,(3)} - \alpha_{pm\,(1)}}{1 + \alpha_{pm\,(1)}} V_f + \frac{\alpha_{pm\,(1)}}{1 + \alpha_{pm\,(1)}} \qquad (19)$$

Structural porosity (V_{ps}), the final part of the total porosity (see Eq. (13)), is formed due to the situation in Region B where the available matrix volume is insufficient to fill the free space in the fully compacted fiber assembly. This type of porosity is responsible for the considerable increase of the total porosity in Region B as shown in Figs. 2 and 3.

4. PROCESS CONDITIONS AND VOLUMETRIC COMPOSITION

Based on experimental data and model predictions, here follows an analysis of three types of process related effects on the volumetric composition in composites.

4.1 Effect of consolidation pressure. The applied pressure used to consolidate composite materials during manufacturing is the key important process condition used to control the resulting fiber volume fraction. Furthermore, the consolidation pressure can also be linked to the porosity content of the composites. In general, it can be expected that the higher the applied consolidation pressure, the higher the resulting fiber volume fraction, and the lower the resulting porosity content. These expected relations will be quantitatively analyzed.

In previous studies of different types of composites, series of composite plates have been manufactured with variable consolidation pressures:

- 2D random oriented flax/polypropylene composites, autoclave consolidation with pressures of 0.7 and 2.1 MPa (Toftegaard 2002; Madsen et al. 2007).
- Unidirectional flax/polyethylene terephthalate composites, press consolidation with pressures of 1.7 and 4.2 MPa (Aslan et al. 2013).
- Biaxial (± 45°) flax/epoxy composites, vacuum and autoclave consolidation with pressures of 0.1 and 0.8 MPa (Markussen, Prabharakan, Toftegaard and Madsen 2013).
- Biaxial (± 45°) glass/epoxy composites, vacuum and autoclave consolidation with pressures of 0.1 and 0.8 MPa (Markussen et al. 2013).

The experimental data of volumetric composition as function of the fiber weight fraction for the composites are shown in Figs. 4, 5, 6 and 7. Shown are also the predicted volumetric compositions using the above presented model. For means of simplicity, and to make the analysis easier to comprehend, only the results for V_f and V_p are shown in the figures. The results of the complimentary matrix volume fraction ($V_m = 1 - V_f - V_p$) are not shown. The determined model parameters used for the predictions are shown in Table 1.

For the 2D random oriented flax/PP composites (Fig. 4), there is a clear effect of the increased consolidation pressure from 0.7 to 2.1 MPa. The maximum obtainable fiber volume fraction ($V_{f\,max}$) is increased from 0.33 to 0.41, which corresponds to an increase of the transition fiber weight fraction ($W_{f\,trans}$) from 0.52 to 0.58. In the study by Madsen et al. (2009), it is reported that the corresponding maximum stiffness of the composites at $W_{f\,trans}$ is 5.8 and 6.3 GPa, respectively. In Fig. 4, it can also be observed that in Region A (for W_f below $W_{f\,trans}$), the porosity of the composites is markedly reduced when the consolidation pressure is increased, and this is quantitatively described by a decrease of the impregnation porosity factor from 0.41 to 0.19 (see Table 1). Thus, the higher pressure leads to a more efficient impregnation of the flax fiber bundles by the PP matrix.

For the unidirectional flax/PET composites (Fig. 5), the effect of the increased consolidation pressure from 1.7 to 4.2 MPa is to increase $V_{f\,max}$ from 0.53 to 0.60, which corresponds to an increase of $W_{f\,trans}$ from 0.61 to 0.68. In addition, the impregnation porosity factor is decreased from 0.12 to 0.09. Thus, these changes are comparable to the ones for the flax/PP composites, although the flax/PET composites show a relatively smaller decrease of the impregnation porosity which can be due to the already low porosity content of the low pressure composites. At $W_{f\,trans}$, the maximum stiffness of the low and high pressure composites have been reported to be 35 and 40 GPa, respectively (Aslan et al. 2013) (see also Fig. 3b).

Table 1. Determined model parameters for different types of experimental composite materials manufactured with different techniques. PET is polyethylene terephthalate, PP is polypropylene, and FA is polyfurfuryl alcohol.

	Type of composites								
	Flax/PP		**Flax/PET**		**Flax/epoxy**		**Glass/epoxy**		**Glass/FA**
Fiber orientation	2D random		Unidirectional		Biaxial (± 45°)		Biaxial (± 45°)		Biaxial (± 45°)
Fiber/matrix mixing technique	Film-stacking		Filament-winding		Vacuum infusion		Vacuum infusion		Hand-layup
Consolidation technique	Autoclave		Press		Vacuum and autoclave		Vacuum and autoclave		Vacuum
Consolidation pressure [MPa]	0.7	2.1	1.7	4.2	0.1	0.8	0.1	0.8	0.1
Maximum fiber volume fraction, $V_{f\,max}$	0.33	0.41	0.53	0.60	0.28	0.38	0.51	0.64	0.51[a]
Transition fiber weight fraction, $W_{f\,trans}$	0.52	0.58	0.61	0.68	0.33	0.45	0.70	0.80	0.69
Impregnation porosity factor, $\alpha_{pf\,(3)}$	0.41	0.19	0.12	0.09	0		0		0
Interface porosity factor, $\alpha_{pf\,(2)}$	0.01		0.01		0		0		0
Fiber porosity factor , $\alpha_{pf\,(1)}$	0.03		0.01		0.01		0		0
Matrix porosity factor, $\alpha_{pm\,(1)}$	0		0.01		0.01		0		0.10
Fiber density, ρ_f [g/cm^3]	1.54		1.59		1.52		2.60		2.62
Matrix density, ρ_m [g/cm^3]	0.91		1.36		1.15		1.15		1.36
Reference	Toftegaard 2002; Madsen et al. 2007		Aslan et al. 2013		Markussen et al. 2013		Markussen et al. 2013		Domínguez and Madsen 2013

[a] Assumed value based on the determined value for the related glass/epoxy composite.

The above presented two types of flax fiber composites are manufactured by an initial mixing of fibers and matrix by *film-stacking* or *filament-winding*, followed by consolidation of the fiber/matrix assembly by autoclave or press. These manufacturing techniques give a direct way of varying the consolidation pressure to control the volumetric composition in the composites. In contrast, this is not readily possible for the biaxial flax/epoxy and glass/epoxy composites manufactured by the *vacuum infusion* technique. In this technique, the fiber assembly is initially compacted to the consolidation level by a vacuum bag, and then the fibers are impregnated by the infused matrix. Accordingly, by using the previously used terminology for the model, composites manufactured by vacuum infusion will be exactly at the transition point where the fiber assembly is *fully compacted*, and the volume of matrix is *just sufficient* to fill the free space between the fibers, and consequently, W_f equals $W_{f\,trans}$, and V_f equals $V_{f\,max}$. Thus, for the given operating process conditions, in particular the applied vacuum pressure, the vacuum infusion technique inevitably gives composites with the best possible combination of high fiber volume fraction and low porosity content, leading to the best possible properties. This is the advantage of the vacuum infusion technique, whereas the disadvantage is the involved practical difficulties to further improve the volumetric composition, i.e. to increase the fiber volume fraction above the (rather low) value given by the vacuum pressure.

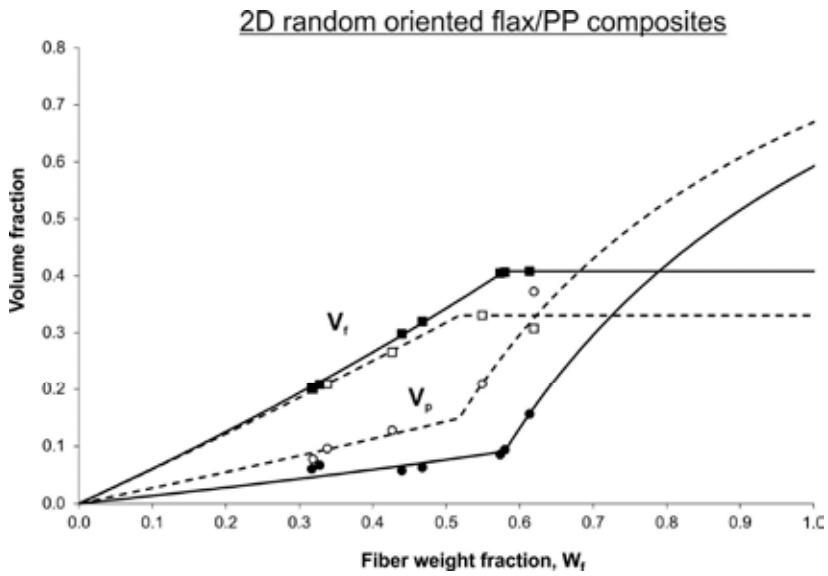

Fig. 4. Experimental data and model predictions of the volumetric composition in 2D random oriented flax/polypropylene (PP) composites manufactured by film-stacking and autoclave consolidation with low and high pressures: 0.7 MPa (open symbols, dotted lines) and 2.1 MPa (filled symbols, full lines).

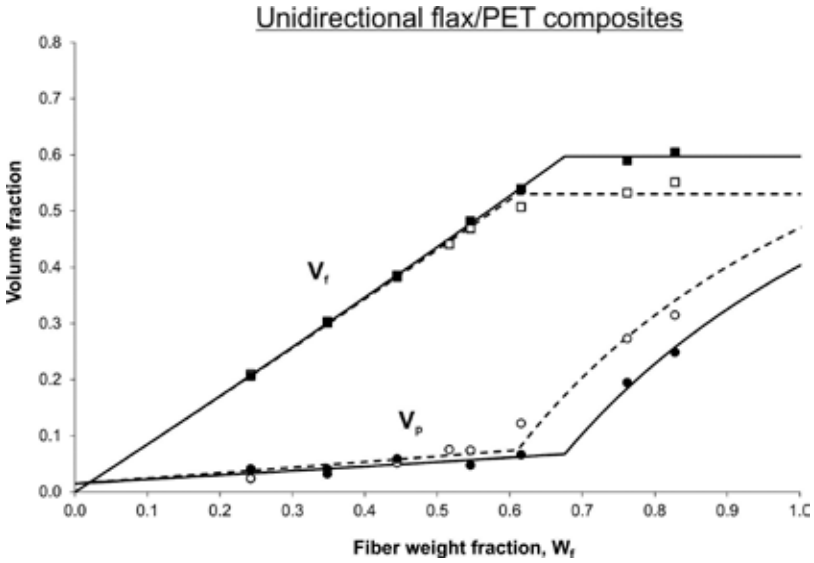

Fig. 5. Experimental data and model predictions of the volumetric composition in unidirectional flax/polyethylene terephthalate (PET) composites manufactured by filament-winding and press consolidation with low and high pressures: 1.7 MPa (open symbols, dotted lines) and 4.2 MPa (filled symbols, full lines). The results for the low pressure composites are also shown in Fig. 3.

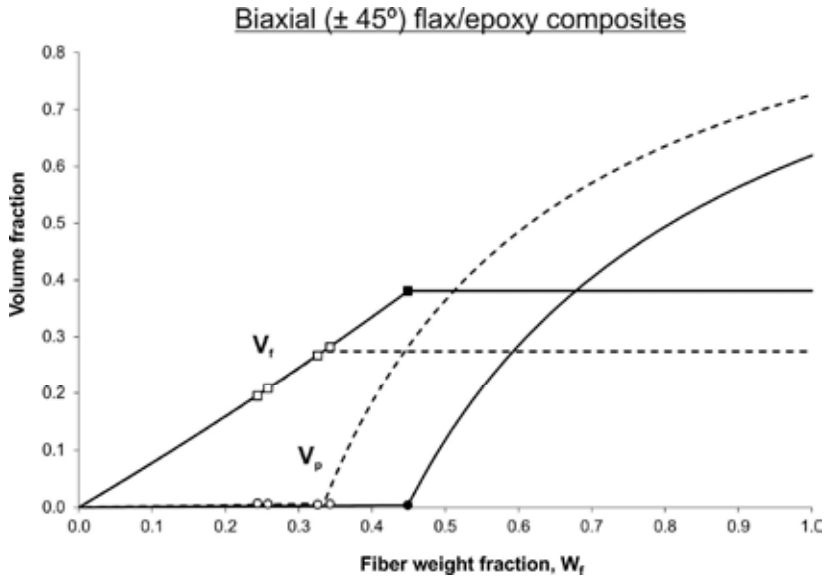

Fig. 6. Experimental data and model predictions of the volumetric composition in biaxial (± 45°) flax/epoxy composites manufactured by vacuum infusion with low and high consolidation pressures: 0.1 MPa (open symbols, dotted lines) and 0.8 MPa (filled symbols, full lines).

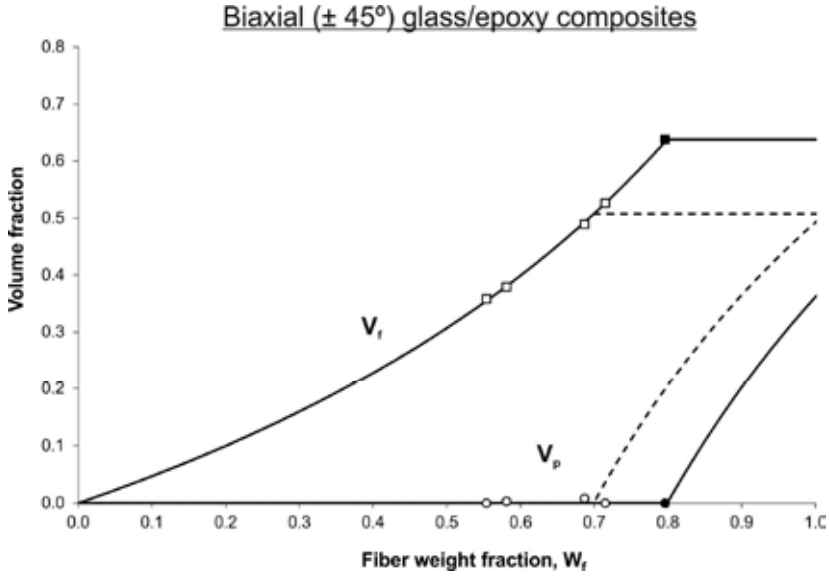

Fig. 7. Experimental data and model predictions of the volumetric composition in biaxial (± 45°) glass/epoxy composites manufactured by vacuum infusion with low and high consolidation pressures: 0.1 MPa (open symbols, dotted lines) and 0.8 MPa (filled symbols, full lines).

In the study by Markussen et al. (2013) of the biaxial flax/epoxy and glass/epoxy composites, the vacuum infusion technique was specially adapted to give composites with a different volumetric composition than the one normally given by the vacuum pressure. Composites were manufactured with (i) a lower V_f than $V_{f\,max}$ by enforcing an additional amount of matrix to the vacuum bag, and (ii) with a higher V_f than $V_{f\,max}$ by applying an additional external pressure on top of the vacuum pressure. The experimental data for the composites are shown in Figs. 6 and 7. The two groups of data points for low pressure are for composites consolidated by vacuum pressure (= 0.1 MPa), and the one data point for high pressure is for a composite consolidated by vacuum and external pressure (= 0.1 + 0.7 MPa). For both flax/epoxy and glass/epoxy composites, the low and high pressure model curves for V_f in Region A coincide, which means that if the fiber volume fraction is lowered below the value at the transition point (i.e. by enforcing an additional amount of matrix to the vacuum bag), then V_f will follow the same curve independently of the applied consolidation pressure. The increase of the consolidation pressure from 0.1 to 0.8 MPa however clearly results in an increase of V_f at the transition point (= $V_{f\,max}$) from 0.28 to 0.38 for the flax/epoxy composites, and from 0.51 to 0.64 for the glass/epoxy composites.

It can be expected that the relation between the consolidation pressure and the maximum obtainable fiber volume fraction in composites is governed by the compaction behavior of the fibers. In the literature, several studies have addressed the development of suitable models for compaction of fiber assembles (e.g. see Gutowski, Cai, Bauer, Boucher, Kingery and Wineman 1987; Simácek and Karbhari 1996; Toll 1998; Lomov and Verpoest 2000; Beil and Roberts 2002). Many of these are based on a power-law relationship:

$$V_f = a\, P^b \tag{20}$$

where P is the compaction pressure (MPa), and a and b are constants that can be related to the configuration of the fiber assembly (e.g. orientation and length of fibers), and the mechanical properties of the fibers (e.g. stiffness).

Fig. 8 presents the determined values of $V_{f\,max}$ as function of the consolidation pressure for the four types of composites (2D random flax/PP, UD flax/PET, biaxial flax/epoxy, and biaxial flax/epoxy). For each composite, a power-law relationship (Eq. (20)) has been fitted to the experimental data points. It can be observed that the curves are resembling the typical compaction curves measured for “dry” fiber assemblies, and moreover, they demonstrate the typical observed trend that (i) the packing ability is higher for glass fibers than for flax fibers (for assemblies with the same fiber orientation), and (ii) the packing ability is reduced when the fiber orientation is lowered (i.e. from unidirectional fibers to 2D randomly oriented fibers) (Madsen and Lilholt 2002).

For 2D random oriented fiber assemblies, it has been shown in theoretical studies by e.g. Toll and Manson (1995) and Toll (1998), based on geometrical and micromechanical considerations, that the exponent b in the power-law model will have a value of 1/5 (= 0.20). For unidirectional fiber assemblies, the exponent b cannot readily be determined analytically, but it has been evaluated from experimental data to be in the range 0.05 to 0.15 (Toll 1998; Madsen and Lilholt 2002). It can be observed in Fig. 8 that these theoretical values of b actually are close to the values estimated in the present study. For the biaxial glass fiber composite, which basically consists of unidirectional fiber assemblies on top of each other, the value of b is 0.11. For the unidirectional flax fiber composite, and the biaxial flax fiber composite, the value of b is about 0.15. The larger value of b for the flax fiber composites made from unidirectional fiber assemblies might be due to the twisted configuration of the flax fibers in the yarns, which means

that the fiber orientation deviates from being fully unidirectional. For the 2D random flax fiber composite, the value of b is 0.20, which is equal to the expected analytically determined value. However, in other experimental studies (Madsen and Lilholt 2002), the value of b for 2D random oriented fiber assemblies has been found to vary in the range 0.18 to 0.32. Based on observations of cross-sections of fiber assemblies, it has been indicated that the fiber dispersion (from single separated fibers to large fiber bundles) plays an important role for the measured variation in compaction behavior of 2D randomly oriented fiber assemblies (Madsen and Lilholt 2002).

Further to the above considerations of the compaction behavior of "dry" fiber assemblies, the compaction behavior of fiber assemblies during the composite consolidation process includes new parameters to be taken into account, such as the viscosity of the matrix, the lubrication of the fibers by the matrix, the elevated temperature, and the sustained pressure (creep). These parameters need to be included in the future goal of establishment of a model to relate the consolidation pressure with the maximum obtainable fiber volume fraction in composites.

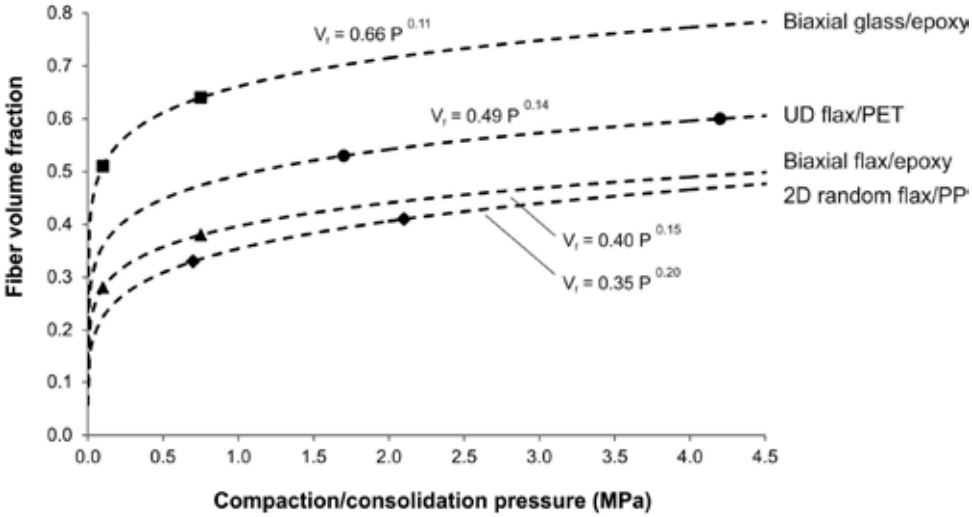

Fig. 8. Experimental data for the maximum obtainable fiber volume fraction, $V_{f\,max}$, as function of the consolidation pressure for different types of composites, together with fitted model curves (power-law relationships) for the compaction behavior of the fiber assemblies.

4.2 Effect of fiber/matrix compatibility. The compatibility between the fiber and matrix parts controls how closely the two parts can be contacted by each other in the composites. This is mainly governed by the surface polarity of the two parts. In the case of perfect fiber/matrix compatibility, intimate contact (< 1 nm) can be established between the two parts and chemical bonds (covalent, hydrogen, ionic or van der Waals) can be generated. This is the basis for obtaining a strong fiber/matrix interface bonding, which typically is considered to be essential for obtaining good mechanical properties of the composites. On the other hand, in the case of non-perfect fiber/matrix compatibility, intimate contact between the fiber and matrix parts cannot be established, and this can lead to air-filled cavities at the fiber/matrix interface regions. This so-called interface porosity can be formed both during processing of the composites, and during service of the materials due to external mechanical influences. In both cases, interface

porosity can be related to the degree of fiber/matrix compatibility.

The above presented model of volumetric composition contains parameters for quantifying the content of interface porosity in composites. In Eq. (17), the interface porosity factor ($\alpha_{pf\,(2)}$) is related to the width of the gap at the fiber/matrix interface (b), and the interface debonding fraction of the fiber perimeter (β) (where β=1 defines fully debonded fibers), in addition to parameters for the cross-sectional dimensions of the fibers. Fig. 9 shows examples of model predictions of the volumetric composition in glass fiber/epoxy composites with three realistic levels of interface porosity:

- No interface porosity, $\alpha_{pf\,(2)} = 0$ ($\beta = 0$; b = 250 nm).
- Medium interface porosity, $\alpha_{pf\,(2)} = 0.033$ ($\beta = 0.50$; b = 250 nm).
- High interface porosity, $\alpha_{pf\,(2)} = 0.067$ ($\beta = 1$; b = 250 nm).

An interface gap of 250 nm is considered to be a high, but still a realistic gap size. In the calculations, a diameter of 15 μm is used for the assumed circular glass fibers. The three other porosity factors ($\alpha_{pf\,(1)}$, $\alpha_{pf\,(3)}$, and $\alpha_{pm\,(1)}$) are set equal to zero, which means that the composites are considered to contain interface porosity only (in addition to structural porosity after the transition point). In Fig. 9, schematized cross-sections of composites with the three levels of interface porosity are shown.

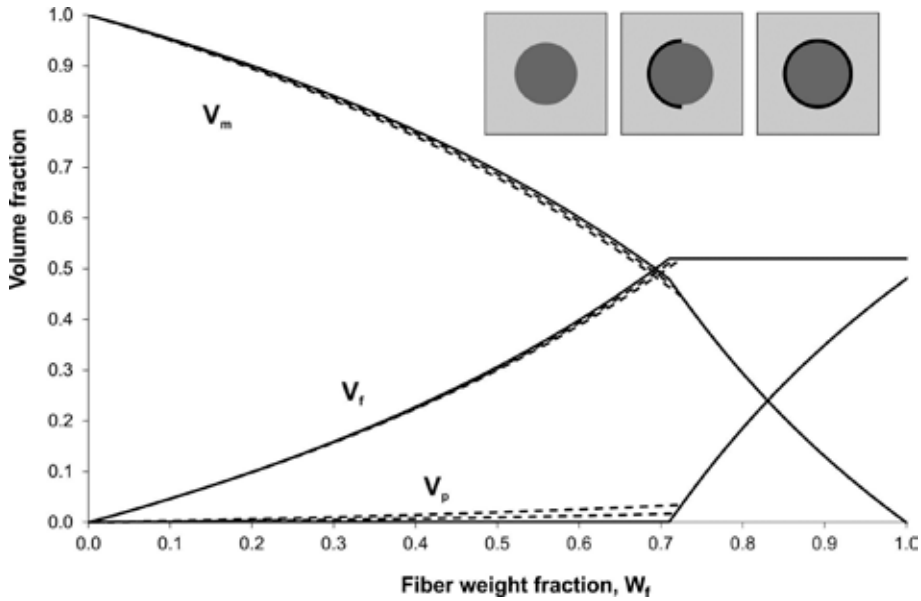

Fig. 9. Model predictions of the volumetric composition in glass fiber/epoxy composites with three levels of interface porosity. Solid lines show no porosity, and dotted lines show medium and high levels of porosity. Schematized cross-sections of the composites are shown. See more details in the text.

As can be observed in Fig. 9, the existence of interface porosity in composites has only a relatively small influence on the overall volumetric composition. Only for the case of the highest level of interface porosity where the interface gap is considered to exist along the entire fiber perimeter, the porosity of the composites is noticeable above zero (e.g. V_p is equal to 0.035 at the transition point), but still the curves for V_f and V_m are only slightly lowered.

Accordingly, as might have been expected, and is quantitatively confirmed by the model, the existence of interface porosity in composites will have a negligible effect on the volumetric composition (although it might have a large effect on the mechanical properties). Thus, the effect of changing the degree of fiber/matrix compatibility is not likely to be observed by changes of the volumetric composition in the composites.

4.3 Effect of air entrapment in matrix. The avoidance of entrapped air bubbles in the matrix is a well-known challenge in the processing of composites. The air bubbles are typically formed due to non-ideal process conditions. For thermoplastic matrix composites, entrapped air bubbles can be formed due to non-optimal settings (i.e. time, temperature, and pressure) of the melting, consolidation, solidifying processes. For thermosetting matrix composites, entrapped air bubbles can be formed due to (i) insufficient evacuation of the resin prior to fiber impregnation, (ii) inclusion of air in the resin during fiber impregnation, e.g. by roller actions in hand-layup methods, and by leakage in vacuum methods, and (iii) generation of volatile by-products, such as water, during curing of the resin.

The above presented model of volumetric composition contains parameters for quantifying the content of matrix porosity. In Eq. (18), the matrix porosity factor ($\alpha_{pm\ (1)}$) is related to the volume fraction of porosity in the matrix ($V_{matrix\ porosity}$) by a simple relationship containing only this parameter. A value for $V_{matrix\ porosity}$ can be determined by composite cross-sectional measurement of the content of air cavities in matrix-rich regions. Alternatively, a value for $V_{matrix\ porosity}$ can be determined by fitting the model to experimental data.

In the study by Domínguez and Madsen (2013), a series of biaxial glass fiber/polyfurfuryl alcohol (FA) resin composites was made by hand-layup followed by a double-vacuum bag technique. FA is a newly developed biomass-based resin (Pohl et al. 2011; Domínguez, Grivel and Madsen 2012). Water is used as solvent in the FA resin to lower the viscosity, and in addition, water is generated as by-product in the condensation reactions taking place during curing of the resin. Thus, specially adapted process conditions are required to ensure that water is removed (e.g. by evaporation) from the FA resin before it becomes trapped in the cured resin leading to air-filled cavities. The double-vacuum bag technique is specially developed for this purpose (Hou and Jensen 2008).

In the study by Domínguez and Madsen (2013), the series of glass/FA composites was made with variable amount of the impregnating FA resin. The volumetric composition in the composites was measured, and the experimental data is shown in Fig. 10. It can be seen that the composites contain a non-negligible content of porosity (V_p is in the range 0.03 to 0.08), which indicate that the process conditions can be furthermore optimized. However, it can be observed that the porosity tends to be decreased when the fiber content is increased, or expressed in another way, the porosity tends to be increased when the matrix content is increased. This tendency is interpreted as being a result of matrix porosity, which is known to be a special concern for the FA resin, as described above.

In Fig. 10, the volumetric composition model has been fitted to the experimental data of the glass/FA composites. The values of the model parameters are presented in Table 1. It is assumed that the composites contain only matrix porosity, i.e. there is no fiber porosity due to the massive nature of glass fibers, there is no interface porosity due to the high degree of compatibility between glass fibers and FA resin, and there is no impregnation porosity due to the low viscosity of the FA resin ensuring complete impregnation of the glass fiber bundles. Thus, $\alpha_{pf\ (1)}$, $\alpha_{pf\ (2)}$, and $\alpha_{pf\ (3)}$ are assumed to be equal to zero. Based on the fitted model lines in Fig. 10, the value of the matrix porosity factor, $\alpha_{pm\ (1)}$, is determined to be 0.10, leading to a value of $V_{matrix\ porosity}$ on 0.09 (Eq. (18)). Thus, in matrix-rich regions of the glass/FA

composites, the content of porosity is 0.09. In other words, a sample of neat FA resin (made by similar processing conditions) would have a porosity content of 0.09, which can be seen for the model line for V_p in Fig. 10 at $W_f = 0$ (and $V_f = 0$). This leads to a porosity content of the composites on 0.04 at the transition point.

In Fig. 10, model lines are also calculated for the case of glass/FA composites with no matrix porosity ($\alpha_{pm\ (1)} = 0$). It can be observed that the no porosity lines of V_f and V_m deviate considerably from the lines of the glass/FA composites with matrix porosity. Especially, it can be noted, as expected, that the (large) deviation between the lines for V_m is getting larger when the fiber content is decreased, whereas the (small) deviation between the lines for V_f is getter smaller. In a more practically applied context, however, the model lines in Fig. 10 for the glass/FA composites with no matrix porosity can be used to assess the potential improvement in volumetric composition (and thereby mechanical properties) of the manufactured composites if the processing conditions is furthermore optimized.

Altogether, it has been demonstrated that air entrapment in the matrix is likely to have a marked effect on the volumetric composition in the composites, and the model can be used as a tool for a quantitative analysis of the effect.

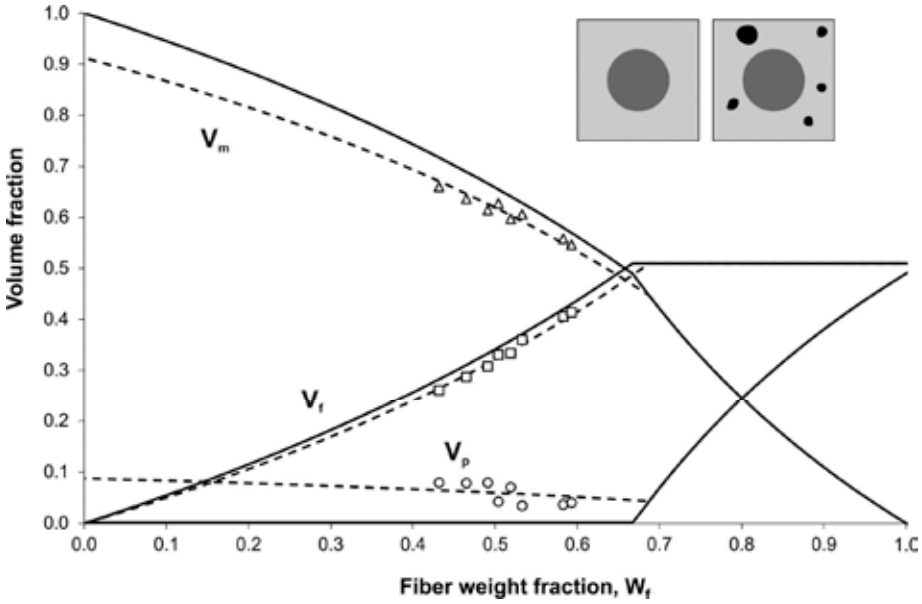

Fig. 10. Experimental data and model calculations of the volumetric composition in biaxial (± 45°) glass fiber/FA composites. Solid lines are predictions for composites with no porosity, and dotted lines are fitted to the experimental data for composites with matrix porosity. Schematized cross-sections of the composites are shown. See more details in the text.

5. CONCLUSIONS AND FUTURE WORK

A model for the volumetric composition in composites is presented, where the volume fractions of fibers, matrix and porosity are calculated as a function of the fiber weight fraction. The model includes the realistic case of composites with porosity, and limited fiber packing ability. The porosity is addressed via a number of so-called porosity factors, which can be related to the composite microstructure. The limited packing ability of the fiber assembly is addressed via the so-called maximum obtainable fiber volume fraction, $V_{f\,max}$.

The model defines two regions of composite volumetric composition, Region A and B, separated by a transition fiber weight fraction, at which the composites show the best possible combination of high fiber volume fraction and low porosity leading to composites with the best possibly mechanical properties.

Based on experimental data of composites manufactured with different process conditions, together with model predictions, a quantitative analysis is presented for three types of process related effects on the volumetric composition in composites: (i) consolidation pressure, (ii) fiber/matrix compatibility, and (iii) air entrapment in matrix.

The applied consolidation pressure used in the manufacturing process is found to have a marked effect on the volumetric composition in composites. In general, the impregnation porosity is slightly decreased, and $V_{f\ max}$ is considerably increased, when the consolidation pressure is increased. As an example, for biaxial glass/epoxy composites manufactured by vacuum infusion, $V_{f\,max}$ is increased from 0.51 to 0.64 when the consolidation pressure is increased from 0.1 to 0.8 MPa. A power-law relationship, similar to the one commonly used to describe the compaction behavior of dry fiber assemblies, is found to well describe the relation between $V_{f\ max}$ in composites and the applied consolidation pressure.

The degree of fiber/matrix compatibility and the related amount of interface porosity is found to have a negligible effect on the volumetric composition. Only for the case of a very high level of interface porosity where an interface gap of 250 nm is considered to exist along the entire fiber perimeter, the porosity of the composites is noticeable above zero, but still the fiber and matrix volume fractions are only slightly changed. Thus, the effect of changing the degree of fiber/matrix compatibility is not likely to be observed by changes of the volumetric composition.

Air entrapment in the matrix due to non-ideal process conditions is found to have a marked effect on the volumetric composition in composites. For composites with such type of matrix porosity, the porosity content is decreased when the fiber content is increased. As an example, for biaxial glass/polyfurfuryl alcohol composites manufactured by a double vacuum bag technique, the porosity content in the matrix-rich regions is determined to be 0.09. This is then the porosity content of the neat resin at zero fiber content, leading to a porosity content of 0.04 for composites with a high fiber content at the transition point.

Altogether, it is demonstrated that the presented model of volumetric composition in composites is a valuable tool for a quantitative analysis of the effect of process conditions.

Based on the findings and considerations in the present study, examples of future work can be mentioned for the further improvement of the model:

- Development of analytical model for the content of impregnation porosity in composites. This important type of porosity is related to the configuration of the fiber assembly (e.g. fiber dispersion), in addition to the matrix flow behavior.
- Development of analytical model for the relationship between consolidation pressure and

$V_{f\ max}$ in composites. Important parameters are the configuration of the fiber assembly (e.g. fiber orientation and length), the fiber mechanical properties (e.g. stiffness), and the special conditions of the composite manufacturing process (e.g. matrix viscosity, lubrication, and creep).

REFERENCES

Aslan, M., Mehmood, S., and Madsen, B. (2013). Effect of consolidation pressure on volumetric composition and stiffness of unidirectional flax fibre composites. Journal of Materials Science. 48, 3812-3824.

Beil, N.B., and Roberts, W.W. (2002). Modeling and computer simulation of the compressional behaviour of fiber assemblies. Part I: Comparison to van Wyk's theory. Textile Research Journal. 72, 341-351.

Domínguez, J.C., Grivel, J.C., and Madsen, B. (2012). Study on the non-isothermal curing kinetics of a polyfurfuryl alcohol bioresin by DSC using different amounts of catalyst. Thermochimica Acta. 529, 29-35.

Domínguez, J.C., and Madsen, B. (2013). Optimization of the operating conditions used to produce new biomass-based composite materials by the double-vacuum bag technique. In preparation.

Gutowski, T.G., Cai, Z., Bauer, S., Boucher, D., Kingery, J., and Wineman, S. (1987). Consolidation experiments for laminate composites. Journal of Composite Materials. 21, 650-669.

Hou, T.H., and Jensen, B.J. (2008). Double-vacuum-bag technology for volatile management in composite fabrication. Polymer Composites. 29, 906-14.

Lomov, S.V., and Verpoest, I. (2000). Compression of woven reinforcements: A mathematical model. Journal of Reinforced Plastics and Composites. 19, 1329-1350.

Madsen B., Thygesen A., and Lilholt H. (2007). Plant fiber composites – porosity and volumetric interaction. Composites Science and Technology. 67: 1584-1600.

Madsen, B., and Lilholt, H. (2002). Compaction of plant fiber assemblies in relation to composite fabrication. In the Proceedings of the 23rd Risø International Symposium on Materials Science. Sustainable natural and polymeric composites – Science and technology. Risø National Laboratory, Roskilde, Denmark, p. 239-250.

Madsen, B., Thygesen, A., and Lilholt, H. (2009). Plant fibre composites – porosity and stiffness. Composites Science and Technology. 69, 1057-1069.

Markussen, C.M., Prabharakan, D.R.T., Toftegaard, H.L., and Madsen, B. (2013). Biobased hybrid composites for structural applications. In preparation.

Pohl, T., Bierer, M., Natter, E., Madsen, B., Hoydonckx, H., and Schledjewski, R. (2011). Properties of compression moulded new fully biobased thermoset composites with aligned flax textiles. Plastics, Rubber and Composites. 40, 294-299.

Simácek, P., and Karbhari, V.M. (1996). Notes on the modeling of preform compaction: I-Micromechanics at the fiber bundle level. Journal of Reinforced Plastics and Composites. 15, 86-122.

Toftegaard, H. (2002). Tensile testing of flax/PP laminates. Risø Report: Risø-I-1799(EN), Risø National Laboratory, Materials Research Department, Denmark. 92 pp.

Toll, S. (1998). Packing mechanics of fiber reinforcements. Polymer Engineering and Science. 38, 1337-1350.

Toll, S., and Manson, J.-A.E. (1995). Elastic compression of a fiber network. Journal of Applied Mechanics. 62, 233-236.

Proceedings of the 34th Risø International Symposium on Materials Science:
Processing of fibre composites – challenges for maximum materials performance
Editors: B. Madsen, H. Lilholt, Y. Kusano, S. Fæster and B. Ralph
Department of Wind Energy, Risø Campus
Technical University of Denmark, 2013

MULTIPHASE FLOW AND VOID SUPPRESSION IN LIQUID COMPOSITE MOLDING

Véronique Michaud

Laboratory for Polymer and Composite Technology (LTC)
Ecole Polytechnique Fédérale de Lausanne (EPFL),
Station 12, CH 1015 Lausanne, Switzerland

ABSTRACT

The article reviews quantitative methods for void prediction and elimination in Liquid Composite Molding processes. Experimental observations related to void formation and transport during processing are first summarized, drawing from the literature and from our own work. The main physical phenomena governing multiphase fluid flow in porous media are then presented, using a continuum mechanics approach. Strategies towards solving these equations are then reviewed. Two main approaches are currently developed. One is a direct solution of the multiphase flow equations, which requires dual knowledge of how permeability varies with saturation, and how saturation varies with pressure. The other is an indirect method based on solution of saturated flow with the introduction of sink terms, representing the dual scale of the fibrous reinforcements, which requires knowledge of the flow kinetics within the tows. Even though a complete tool to simulate LCM flow and predict the location and type of porosity is still far from being available, several recent results have contributed to improve our physical understanding of LCM processes leading to porosity reduction.

1. INTRODUCTION

During composite processing by Liquid Composite Molding (LCM) techniques, a fluid precursor of the matrix phase (an uncured thermoset resin, a thermoplastic polymer or a pre-polymer) is made to infiltrate the open pore space within a reinforcement preform. Upon subsequent chemical reaction or solidification of the matrix precursor, a composite material is produced. This technique is simple in its concept, and rather cost-effective since there is no need to produce pre-impregnated materials. The infiltration process may be driven by vacuum only, or under moderate pressure applied on the fluid phase at the entrance of the preform, in both cases relieving the need for autoclaves or presses (Witik, Gaille, Teuscher, Ringwald, Michaud,

Månson, 2012). As a result, this family of techniques has gained importance in the last 20 years, and is now routinely used in many industrial applications, ranging from aerospace secondary structures (fans, propellers, brackets) to automotive, nautical, civil applications as well as wind turbine blades. Many different types of LCM have been developed, which differ by the type of mold (hard or a membrane), the resin delivery method (pressure pot or volumetric pump), the degree of preform evacuation in the initial stages of the process, and other more subtle differences described by Summerscales and Searle (2005). Underlying physical phenomena are common to all variants of the process, as are related constitutive properties of the resin and fabrics as concerns thermoset polymers, which represent the vast majority of fluids used in LCM processes.

The industrial aim to manufacture sound and homogenous parts at the lowest possible cost has driven the ambition to predict the kinetics of the process, as well as the local void and fiber content distribution within the composite, or residual strain or stress fields that may have built up in the final part. Prediction of global infiltration and curing kinetics, in turn helping to optimize mold design, injection strategies, matrix precursor pot life and viscosity, is now easily accessible with commercial numerical tools that solve the equations for flow of one fluid phase in a rigid porous medium, possibly coupled with heat transfer (for example PAM-RTM from ESI Group, or LIMS, from University of Delaware). None of the commercial tools handles void prediction or elimination, despite the fact that voids are known to degrade matrix-dominated properties of the composites, including the flexural, compressive and interlaminar shear strength, as illustrated in Refs (Judd and Wright 1978, Yoshida, Ogasa and Hayashi 1986, Tang, Lee and Springer, 1987, Madsen and Lilholt, 2003, Leclerc and Ruiz 2008). The identification and prediction of void distribution in liquid composite molding processes thus remains a challenge that is now extensively addressed in research (Park and Lee, 2011). We review here experimental observations related to void formation, evolution, and transport during LCM processes, and then present current modeling strategies aiming to address capillary effects, causes of void formation and underlying physics of multiphase flow in porous media.

2. EXPERIMENTAL OBSERVATIONS OF VOID FORMATION AND TRANSPORT IN LCM PROCESSING

A first general experimental observation is that it is difficult to reach very low porosity levels in LCM without lengthy experimental process optimization, playing with the resin velocity (through the applied pressure or flow rate), the resin initial viscosity, the placement and type of consumables (in particular the distribution media or microporous membranes in infusion processes). Once a process is stabilized, a change in fabric configuration or resin may require another (often lengthy) period of further optimization. By contrast, it is much easier to reach a very low porosity level in parts made from prepregs in an autoclave. Now, a main difference between the two situations is in the fact that prepreg processing is a consolidation process: pressure in an autoclave is applied on the entire fiber-matrix assembly, that has already been combined; if the fiber/matrix ratio is low and resin bleeding is restrained, pressure is applied on the resin phase all along the process. This helps collapse potential voids (Michaud, Sequeira-Tavares, Sigg, Lavanchy and Manson, 2006). In LCM, since the initial closing pressure of the mold or of the vacuum bag is applied on the dry fabric, the process is that of infiltration in a constrained fabric, so potentially large pressure gradients form in the resin phase, between inlet and outlet. These gradients remain until the part is filled, and may then equilibrate depending on the post-filling stage (Simacek, Heider, Gillespie and Advani, 2009). The only way to

increase the applied pressure is to use an injection-compression process, in which the resin infiltrates a dry fabric placed in a partially closed mold that is later closed once infiltration has occurred (e.g. Bickerton and Abdullah 2003, Merotte Simacek and Advani 2010); this, however, requires more complex set-ups.

In LCM voids have been shown to arise from several sources:

- insufficient flow, leaving large uninfiltrated regions that have not been reached by the flow path when filling the part,

- gas, humidity or volatiles species dissolved in the resin phase,

- gas initially present in the preform that is surrounded by flowing resin and remains trapped.

The first source of porosity is well known. It can be solved by proper design of the resin inlet and outlet locations, and by careful placement of the preform to prevent "race-tracking", i.e. the presence of preferential flow paths between the preform and the mold. Methods to reduce the occurrence of these "dry-spots" are well developed: conventional flow software tools coupled to active mold control have been designed to this end (Gokce and Advani, 2004, Matsuzaki, Koyabashi, Tadoroki, Mizutani, 2013).

The second source of void formation, namely dissolved air or volatiles, is practically solved by selecting resins with low amount of volatiles, and by carefully storing, mixing and degassing them before use (Zingraff, Michaud, Bourban and Månson, 2005).

Finally, there is trapping of air initially present in the preform. This is all the more likely to happen that most reinforcements used in LCM processes are based on textile preforms, hence are constituted of bundles of filaments, also called tows, that are woven, braided or knitted into a fabric. This creates a porous material with a binary size distribution of pores, as schematically shown in Fig. 1 (Michaud, 2012). The geometry of the textile unit cell is thus a crucial parameter, and it is possible, depending on the capillary forces at play, that flow could lead or lag in the fiber bundles, or that crossings between tows create zones of perturbed flow. Many authors have reported on this effect and have pointed out the role of the textile geometric features, and of the resin velocity on the formation and the location of voids (Patel 1995, Patel and Lee 1996a,b, De Parseval, Pillai and Advani 1997, Breard, Henzel Trochu and Gauvin 2003, Park and Lee 2011, Leclerc and Ruiz 2008). In particular, non-woven mats have been reported to behave as homogenous porous media, with low porosity, whereas woven fabrics show deviations from saturated flow behavior (Tan, Roy and Pillai 2007).

For a given plate and resin/textile combination in a given part, gradients in void content are found as a function of the position with respect to the resin inlet. In general, the void content increases with the flow distance, and is higher near the resin outlet (Lundström and Gebart, 1994). Leclerc and Ruiz (2008) attributed this increase from 2 to 6% void volume fraction in a glass fabric/epoxy material to a decrease in flow velocity with time. Others mention the positive action of resin pressure increase and additional flow introducing bubble transport near the inlet compared to the exit (Frishfeld Lundström, and Jakovics 2008, Lundström, Frishfeld and Jakovics 2010). Use of a vacuum-assisted LCM, *i.e.,* evacuating the preform before infiltration, has been shown to greatly reduce the porosity (Lundström and Gebart, 1994). In parallel, for vacuum resin infusion processes (with a soft vacuum bag and no hard top mold), the use of micro-porous membranes laid over the top of the preform, that allow air but not resin to flow out, has been shown to reproducibly decrease the void content in the final parts (Li, Krehl, Gillespie, Heider, Endrulat, Hochrein, Dunham, and Dubois, 2004).

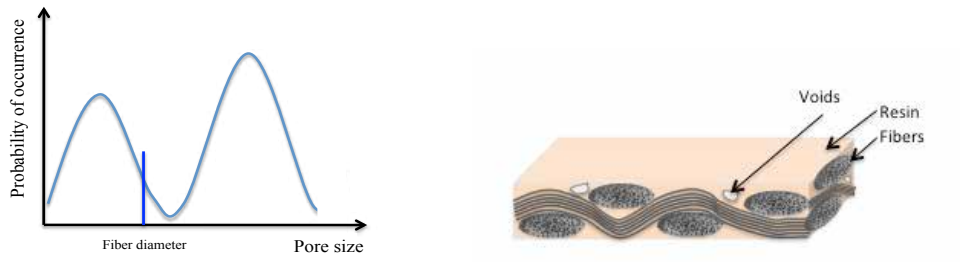

Fig. 1. Schematic of the pore size distribution in a textile fabric, left, and of the fabric architecture in the composite, right.

Regarding the amount of voids as a function of resin velocity, for a given resin/textile combination, all authors seem to converge on the idea that there exists an optimal flow velocity. This is generally expressed in terms of the (dimensionless) capillary number for the system at hand:

$$Ca = \frac{u_l \eta}{\gamma_{ma}} \tag{1}$$

where u_l is the liquid velocity, γ_{ma} is the surface tension between the matrix and the ambient atmosphere and η is the resin viscosity. Other authors (Patel et al. 1996a and b, Rohatgi, Patel and James Lee 1996) prefer to use a modified capillary number,

$$Ca^* = \frac{u_l \eta}{\gamma_{ma} \cos\theta} \tag{2}$$

where θ is the contact angle between the reinforcement and the resin, taken to be the equilibrium contact angle measured in static mode (close to 30° for epoxy resins on sized reinforcements). This was shown to collapse several data on a single master curve, for example for several model fluids such as oil or Ethylene Gylcol; however, it has also been demonstrated that for viscous systems, the relevant contact angle is for dynamic flow, with a value that strongly depends on the advancing velocity, following Tanner's law (Kistler, 1993):

$$\theta^3 - \theta_o^3 = c_T . Ca \tag{3}$$

where c_T is a coefficient which needs to be experimentally determined and θ_0 is the contact angle at thermodynamic equilibrium. Variations in contact angle that this dependence of velocity introduces can be signifant: Verrey, Michaud and Månson (2006) showed from indirect measurements that an epoxy system infiltrating a carbon fiber preform shifts from wetting to non-wetting behavior as the resin velocity, or in other words as *Ca* varies. As a result, use of *Ca* instead of *Ca** seems more appropriate, even though this may not lead to a generalized master curve for all systems.

At low *Ca* values, capillary effects dominate. Flow within the more tightly packed fiber tows

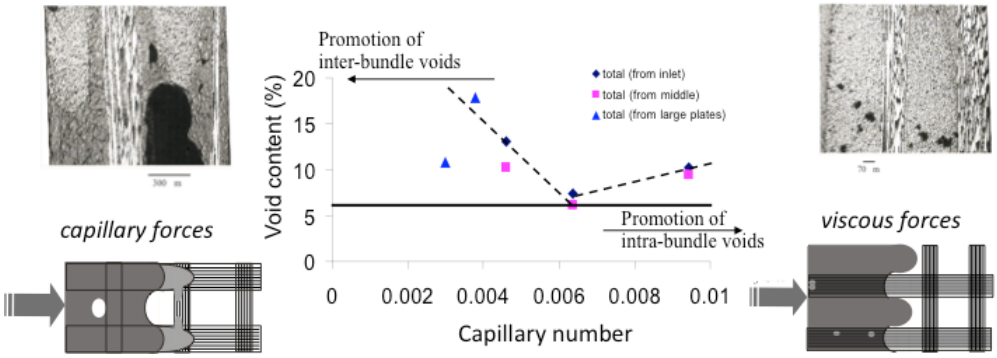

Fig. 2. Void content versus capillary number, from Zingraff et al. (2005)

therefore leads flow within wider regions (of lower capillary pressure drop) if the system is wetting. As a result, voids may be entrapped in the matrix between fiber tows. At higher *Ca* values, viscous effects dominate. This causes flow between the tows to lead ahead of flow within the tows; then, voids may remain entrapped within the fiber tows, as presented in Figure 2. Between these two values, an optimal value, Ca_{opt}, exists. For an unsaturated polyester resin infiltrating bi-directional stitched fiberglass mat, Patel (1996) found values of Ca_{opt} on the order of 10^{-1} to 10^{-2}. A similar approach was applied to LC12 low viscosity reactive thermoplastic matrices (Zingraff, Michaud Bourban and Manson 2005), with Ca_{opt} value around 0.004-0.006 in a strongly wetting system. Leclerc and Ruiz (2008) reported values of Ca_{opt}=0.008, but previous work proposed values closer to 0.01 (Ruiz, Achim, Soukane Trochu and Bréard 2006). Many of these results are gathered in the recent review article by Park and Lee (2011), who conclude that the optimal capillary number Ca_{opt} is around 10^{-3} in most cases, corresponding in practice to a resin velocity around 0.1-1mm/s.

Fabric architecture exerts an influence. For random mats, UD fabrics, and 8H satin weave, it has been shown that, at the optimal Ca value, the void content is almost nil provided the resin is properly degassed (Patel et al. 1996 a,b, Mahale, Prud'homme and Rebenfeld 1992, Rohatgi et al. 1996, Patel and James Lee, 1995, Zingraff et al. 2005). For bidirectional fabrics, higher residual void contents are generally reported, possibly because the optimal flow depends also on the tow orientation (Leclerc and Ruiz, 2008, Gourichon, Binetruy and Krawcak 2006). Ruiz and coworkers (Ruiz, Achim, Soukane, Trochu and Bréard, 2006) used a saturated flow Finite Element Model (FEM) for the prediction of infiltration kinetics, coupled with an optimization of the injection conditions to obtain a constant flow velocity across the part during impregnation, corresponding to Ca_{opt}. This practical solution allowed the use of traditional saturated flow FEM tools towards simplified void prediction. In parallel, as fluid velocities tend to be higher than the optimal value, for practical reasons, many authors have reported observations of porosity within the fiber tows, and have proposed analyses based on the notion that impregnation of the tows is delayed compared to impregnation of inter tow spaces.

Finally, it is important to mention that trapped voids can be transported by flow, and can grow or collapse, depending on the local pressure around the pores, as well as the solubility and diffusion kinetics of the entrapped gas within the resin (Babu and Pillai, 2004). Common practice teaches that additional bleeding of resin, even if this is not optimal in terms of cost or material usage, is a good practical method to reduce the void content. Lundstrom (1997) performed extensive work to analyze this practice, and proposed methods to assess the diffusion

and solubility parameters of air in a vinylester and epoxy resin. He showed that void dissolution could be effectively predicted as a function of time and local pressure. Zingraff et al. (2005) found similar results for the APLC12 monomer, a prepolymer of Polyamide 12, indicating that 30 seconds of bleeding already significantly reduced the void content in the system at hand, thanks to high diffusivity of N_2 in the prepolymer. These analyses consider the gas in the pores to behave as a perfect gas. Yamaleev and Mohan (2006) extended the analysis to a non-ideal gas law; this led to modified void reduction kinetics. More recently, Lundstrom and Frishfeld (2006, 2008) analyzed bubble formation and motion in a Non-crimp Fabric using a 3D numerical model, and confirmed the experimental findings that (i) motion of intra-tow bubbles is much slower than motion of inter-tow bubbles, that (ii) vacuum at the outlet helps to reduce void content, and that (iii) void content increases with distance from the inlet. An extension of this model to deformable fabrics (Frishfelds and Lundström 2011) showed a tendency for intra-bundle porosity to decrease when the fiber tows are deformed, and for the inter-bundle porosity to increase.

Overall, experimental observations indicate that large dry-spots or high values of porosity, above 10%, that arise from improper mold design or resin degassing are now well controlled. Residual porosity of a few vol. % is still often reported, however, due to air trapped during flow. This in turn is a function of the fabric geometrical features and of the flow front velocity, as quantified through the capillary number. This observation is still difficult to predict, and requires the need to consider multiphase flow in porous media.

3. MULTIPHASE FLOW THROUGH POROUS MEDIA

Modeling of flow kinetics and of the evolution of the liquid/air ratio distribution across the part requires solving the equations for flow of liquid, gas and solid through the porous medium constituted by the reinforcement preform. The physics of this process has been addressed for many years in other branches of engineering such as soil science and petroleum recovery (Bear 1972, Marle, 1981). Since the fibers forming the reinforcement are small compared to the part size, and the processes can often be considered as well described by considering average properties within a unit cell comprising all phases, a continuum mechanics approach is most often used. This rests on the definition of a Representative Volume Element (REV), large enough to contain representative averages of all phases, solid, liquid and gas, yet small enough to be considered as a differential element on the scale of the preform. Within the REV the model assigns only average values of relevant process parameters such as temperature or pressure. Fig. 1b provides an example of REV for a reinforcement fabric. A REV contains in the most general case what remains of the initial atmosphere, the fibers, and the liquid, in respective volume fractions V_a, V_f, V_l, such that

$$V_a + V_f + V_l = 1 \tag{4}$$

By similarity with soil mechanics, the fluid phase saturation S is defined as:

$$S = \frac{V_l}{1 - V_f} \tag{5}$$

where $(1\text{-}V_f)$ is the initial, dry preform, open porosity; S varies from 0 to 1 between a dry and a fully infiltrated (saturated) preform.

To describe the flow of liquid in a porous medium, averaged values of relevant parameters, such

as velocity or volume fraction, are used to derive equations for conservation of mass and momentum, all in a continuum mechanics approach. It is generally assumed that the densities of liquid and solid phases are constant; in most cases of non-compressible liquid fluids, this is a reasonable assumption. On the other hand this assumption loses legitimacy when infiltration by a gas is considered, which complicates equations somewhat (Scheidegger, 1974); however, this is generally not an issue in composite processing. We also assume in what follows that infiltration takes place isothermally, with no heat exchange; this is often the case in practical LCM processes, at least during the infiltration and before cure. Otherwise, one must add the energy conservation equations, together with the temperature depence of relevant parameter values. Mass conservation equations are written for the solid and the fluid phase, respectively, as:

$$\frac{\partial V_f}{\partial t} + \nabla(V_f u_s) = 0 \tag{6}$$

and:

$$\frac{\partial((1-V_f)S)}{\partial t} + \nabla((1-V_f)Su_l) = 0 \tag{7}$$

where u_s is the average local velocity of the solid, and u_l is the average local velocity of the liquid within the REV.

The momentum equation is generally written using Darcy's law (given the low values of pore-level Reynold's number):

$$(1-V_f)S(u_l - u_s) = -\frac{K}{\eta}\nabla P \tag{8}$$

where K (a function of S and V_f) is the permeability of the porous medium in ΔV, η is the liquid viscosity, and P is the pressure in the liquid. K, the permeability, is in general defined from Eq.(8) as a tensorial quantity, with units : m^2. Eq. (8) is written neglecting gravitational or other potential body forces, and is only valid provided the relevant pore-level Reynolds number, defined in relation to the average fluid velocity and the pore diameter, is less than about one: this is most often the case for polymer composite processes because polymers have comparatively high viscosity. The left-hand side of Eq. (8) is called the superficial velocity, often also called the filtration velocity, which was initially defined by Darcy as the ratio of the volumetric flow rate Q out of a porous medium, over the cross-section of this porous medium, A (Darcy, 1856). For fully saturated flow in a rigid porous medium, the filtration velocity is generally simply written as:

$$\frac{Q}{A} = u_0 = (1-V_f)u_l \tag{9}$$

Finally, having neglected inertial and body forces in both solid and liquid, stress equilibrium is written using an extension of the effective stress principle developed for partially saturated soils (Wang, 2000):

$$\nabla\sigma' - \nabla(BSP) = 0 \tag{10}$$

where σ' is the effective stress acting in the solid, counted as positive in compression and

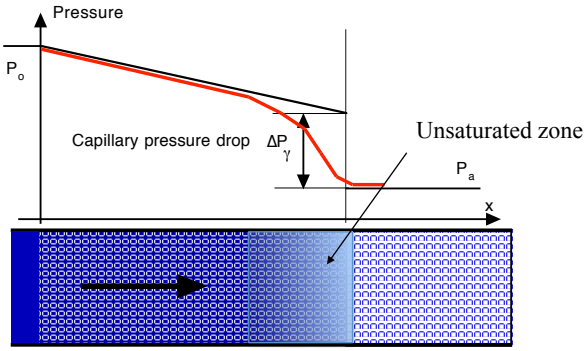

Fig. 3. Schematic of the pressure profile along the infiltration length, in black for slug-flow approach, in red for a multiphase flow approach.

averaged over a surface area comprising both solid and liquid. Initial and boundary conditions valid for each case complete the definition of the problem.

Four main characteristics of the fiber preform and the fluid thus need to be known for a solution of the problem: these are the viscosity η, the dependence of the saturation S on the local pressure P, the stress-strain behavior of the preform, and the permeability K, itself also a function of saturation S. We will focus the rest of the analysis to the case of a rigid preform; we can then ignore Eq. (10) and set u_s=0 in Eqs (6) and (8) (given that the solid remains everywhere immobile in a referencial fixed with the mold or preform). This is in first approximation valid for many LCM processes, exception made for vacuum resin infusion of low volume fraction preforms.

4. CAPILLARY EFFECTS

4.1- Saturated flow with a step boundary condition on pressure. S as defined in Eq. (5) varies from 0 to a finite value, equal to or less than 1, the precise value varying from the infiltration front to the resin inlet. Often, however, in analysis of infiltration processes the assumption is made that the saturation versus distance curve is a step-function, equal to 0 in the non-infiltrated region, and 1 in the infiltrated part. This is known as the slug-flow assumption in soil science literature (Michaud and Mortensen, 2001). All capillarity-related issues are then reduced to knowledge of the pressure boundary condition at the infiltration front, as schematically depicted in Fig. 3. Capillary phenomena in composite processing can then be simply described based on a thermodynamic analysis. The capillary pressure drop ΔP_γ, which is by definition the difference between the pressure in the preform ahead of the infiltration front and the local pressure in the fluid phase just behind the infiltration front, is then calculated from a simple energy balance as:

$$\Delta P_\gamma = -S_f \gamma_{ma} \cos\theta \tag{11}$$

where S_f is the area of matrix-fiber interface per unit volume of matrix. In Eq. (11), $\Delta P\gamma > 0$ indicates a non-wetting system whereas $\Delta P\gamma < 0$ indicates a wetting system. Similar equations introducing shape factors are also found in the literature (Ahn, Seferis and Berg 1991). As indicated earlier, since the contact angle varies with the fluid velocity, the capillary pressure

drop is found to vary with *Ca* as follows (Verrey, et al., 2006), from a wetting to a non-wetting characteristic, as represented in Fig.4 :

$$\Delta P_\gamma = -S_f \gamma_{ma} \cos\left(\sqrt[3]{c_T Ca + \theta_0^3}\right) \tag{12}$$

In the Liquid Composite Molding literature, capillary effects are generally neglected. This is because the surface tension of most resins is very low, and applied pressures rather high. Several methods have nonetheless been proposed to measure the capillary pressure drop assuming fully saturated flow, for infiltration at constant flow rate or alernatively driven by a constant applied pressure (Ahn, Seferis and Berg 1991, Verrey et al. 2006, Amico and Lekakou 2001, Li, Wang, Zhu, Gang, Li and Potter 2010); ΔP values reported all fall in the kPa range. Although this value is small (in comparision with atmospheric pressures for example), neglecting this may however lead to erroneous measurements of the permeability of fiber preforms, if so-called "unsaturated permeability" measurements (where permeability is deduced from the flow front position, and calculated neglecting the capillary pressure) are reported and compared to measurement performed in saturated conditions (where permeability is deduced from the flow rate out of a saturated preform, or where capillary effects are taken into account) (Abter et al., 2011, Breard, et al. 2003, Kim and Daniel 2007). Breard (2003) reported that the ratio R_s=K_{unsat}/K_{sat} is often below 1. This is an indication that, where measurements were conducted, the fluid *de facto* behaves as a non wetting fluid, since according to our slug-flow assumption, R_s = 1- $\Delta P_\gamma/P_i$. Nonetheless, this assumption does not allow prediction of void content, by definition (given that voids are absent from consideration). It can only be useful when using an experimentally defined condition on optimal flow to assess void content, or to assess when flow rates would correspond to ΔP_γ =0.

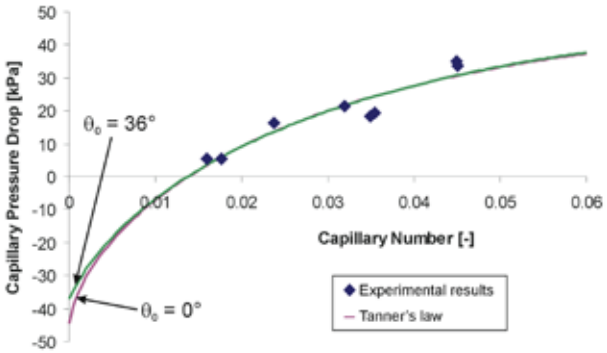

Fig.4: Capillary pressure drop as a function of the capillary number for epoxy infiltrating a carbon non-crimp fabric (from Verrey et al, 2006)

4.2- Non-saturated flow. In the more general case of multiphase flow, the saturation increases gradually. Deviations from slug-flow behavior are then observed, together with non-linear pressure gradients along the preform infiltrated length. In LCM processing research, many authors have observed several regions during infiltration: the dry fabric, a transition zone where saturation is below unity, and then a saturated region near the flow inlet; this is illustrated in Fig. 5 for infiltration of epoxy resin into a glass weave, in the case where hydrodynamic forces lead the flow (Parnas, Howard, Luce and Advani, 1995, Parseval, Pillai, Advani, 1997, Labat, Breard, Pillut and Bouquet, 2001, Labat, Grisel,

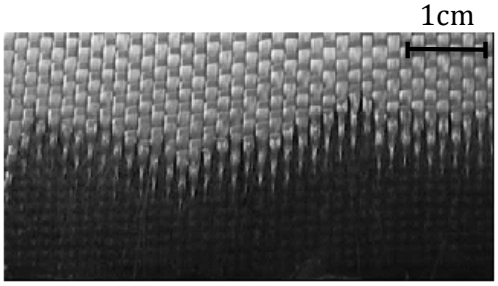

Fig. 5. Flow front during infiltration of a glass woven fabric with epoxy under constant flow rate, from Nordlund and Michaud (2012)

Breard and Bouquet, 2001, Slade, Pillai and Advani, 2001, Babu and Pillai, 2004, Nordlund and Michaud, 2012). Several strategies have been followed to solve the equations for unsaturated flow. These can be divided into two main methods. The first is to solve fully multiphase flow equations; this requires knowing the permeability as a function of saturation, as well as the saturation as a function of pressure. This is commonly done in soil science, and has been achieved in modeling other composite processes (Bear, 1972, Michaud, Compton and Mortensen, 1994, Dopler, Modaressi, Michaud, 2000, Wolfrath, Michaud, Modaressi and Månson, 2006). The second approach is to take a dual scale view of the porous preforms, in which delayed impregnation of the tows compared to the inter-tow spaces is accomplished by introducing a sink term to account for tow impregnation within a model for fully saturated flow between the bundles. Both approaches are reviewed briefly in what follows.

4.2.1 Solution of multiphase flow equations. This requires quantifying several additional parameters. The permeability K, defined in Eq. (8), is a function of the preform volume fraction, fiber arrangement and stress state, and also of the degree of fluid saturation in the preform, S. Following the approach developed in soil science, K is generally separated into two terms, $K=k_r K_s$, where the saturated permeability, K_s, is the permeability tensor of the preform for fully saturated flow, a function of the internal geometry of pores in the reinforcement only. The relative permeability, k_r, is a scalar ranging from 0 to 1, and is an increasing function of S. This parameter, inherited from methods of multi-phase flow analysis in soil science or reservoir engineering, represents the additional resistance to fluid flow created when the pore space comprises a third phase, generally air or a gas. The relative permeability thus depends on the fiber-matrix system, and is much more difficult to measure in the case of composite systems since model fluids cannot be used, or to theoretically predict given the geometrical complexity of non-saturated flow. Therefore, models are mainly semi-empirical. Several such models have been proposed and validated experimentally in soil science, and often take the general form:

$$k_r = S^n \tag{13}$$

where n is an exponent typically between 1 and 3 for particle-based soils (Spitz and Moreno, 1996) while S is considered here as the saturation in non-wetting phase (for argument's sake we consider in this section that the resin is the non-wetting phase, but it is equally possible to consider the inverse case). Alternative models introduce a parameter λ (Brooks and Corey, 1964), named the pore size distribution index:

$$k_r = S^2\left(1-(1-S)^{\frac{2+\lambda}{\lambda}}\right) \tag{14}$$

or additional parameters *L, M* and β (Van Genuchten, 1980) that are related to the shape of the *S*(*P*) saturation curve :

$$k_r = S^L\left(1-(1-S)^{\frac{1}{M}}\right)^{2M} \tag{15}$$

Breard, Henzel, Trochu and Gauvin (2003) also introduced a relative permeability law as follows:

$$k_r = \left[(1-R_S^{1/\beta})S + R_S^{1/\beta}\right]^{\beta} \tag{16}$$

where R_s is the ratio of unsaturated over saturated permeability, and β a fitting parameter.

The approach also implies that the saturation curve *S(P)* be measured for the given reinforcement/matrix system (Patel et al. 1996 a, b, Nordlund and Michaud 2012). Although this approach is standard in multi-phase flow modeling for other branches of engineering (Bear 1972, Bear and Bachmat, 1990, Scheidegger, 1974, Greenkorn, 1983, Dullien, 1979, Marle, 1981), it has seldom been used towards composite process modeling. Examples can nonetheless be found, which are either based on formulae derived from soil science (Markicevic and Djilali, 2006, Patel, 1996 a, b, Michaud, et al. 1994), have used inverse determination of *S(P)* from experiment (Dopler et al. 2000, Nordlund and Michaud 2012) or have assumed a given form of the permeability dependence (Breard, Henzel, Trochu and Gauvin, 2003, Garcia, Gaston, Chinesta, Ruiz and Trochu, 2010 and Garcia, Gascon and Chinesta, 2010). This variety of approaches is due to the difficulty in evaluating the necessary parameters with the actual matrix phase used in making composites, and to the fact that most models developed in soil science implicitly assume that capillary forces are independent of fluid velocity, which is an assumption that can be violated when high-viscosity matrices are used (Verrey, et al. 2006, Nordlund and Michaud 2012).

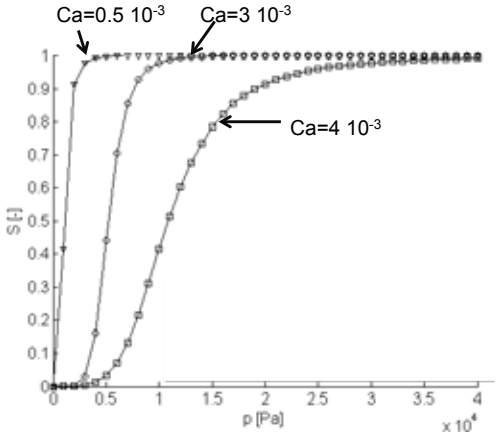

Fig. 6. Saturation curves for 3 values of the Capillary number, for infiltration of a woven glass fabric with epoxy (Nordlund and Michaud, 2012)

Static methods currently used for the measurement of saturation curves with water or oil flow may not describe these effects, since they assume that the saturation versus capillary pressure relationship is independent of the melt flow velocity. To generate data specific to composite processing, attempts have been made to dynamically measure the saturation during injection, either using electrical conductivity measurements or image analysis (Labat et al, 2001 a,b, Lawrence, Neascu and Advani 2009). Nordlund recently showed that the saturation curve for an epoxy resin infiltrating a glass fabric is indeed a function of *Ca*, as shown in Fig. 6.

4.2.2 Dual-phase approach. A different and somewhat simpler approach that has been adopted by researchers in the composites field is to separate the pore space into two populations: pores between fibers and pores between fiber tows (see Fig. 1), and then consider fully saturated fluid flow within a preform having a bulk permeability value characteristic of flow between the tow. Flow into the tows is then accounted for by introducing a sink term, as fiber bundles are gradually filled during impregnation. These sink terms, in turn, are evaluated using estimations or measurements of the local bundle permeability, by accounting for the presence of a capillary pressure drop boundary value at the local flow front inside the bundle, i.e. with a local slug flow assumption. Ingress of the resin is thus treated as a double slug-flow phenomenon, where resin infiltration is assumed to first take place in between the fabric bundles, with the resin only penetrating later and more slowly into the bundles themselves, gradually behind the infiltration front, as schematically shown in Fig. 7.

This implicitly assumes that the fluid does not wet the fabric, which as described earlier is observed when the capillary number is rather high. Parnas (Parnas and Phelan, 1991, Parnas, Salem, Sadiq, Wang and Advani 1994, Parnas 2000) was one of the first authors to introduce this two-scale infiltration model in the LCM literature. Several authors then followed, with variations in the exact solution type, or in the type of matrix material assumed (*e.g.,* addressing thermoplastic polymer infiltration), but using essentially the same approach. Adding such sink or source terms into fully saturated flow models has been shown to give fairly good agreement with experiment when adjusting appropriately the saturation rate for tow infiltration (Binetruy, Hilaire and Pabiot 1997, 1998, Gourichon 2006, Acheson Simacek and Advani 2004, Zhou, Kuentzer, Simacek, Advani and Walsh 2006, Kuentzer, Simacek Advani and Walsh 2006 and 2007, Lawrence, Neascu, Advani 2009, Bréard Henzel Trochu and Gauvin , 2003, Wolfrath et al. 2006, Bayldon and Daniel, 2009, Park and Lee 2011, Frishfeld, et al. 2011).

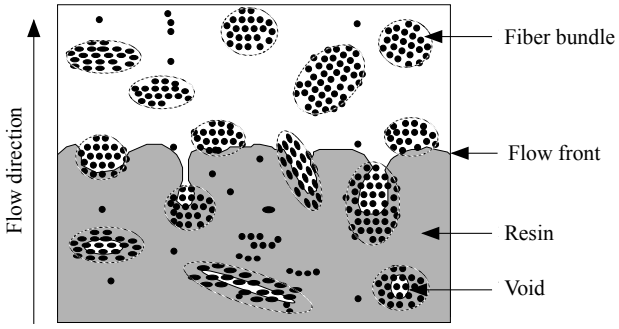

Fig. 7: Schematic of the dual scale flow, with delayed impregnation of the fiber bundles

In some recent work, the need to resort to adjustable parameters was alleviated by calculating a tow saturation rate using a local infiltration model, which can also be completed by simulating heat transfer and curing kinetics at various scales (Tan and Pillai, 2012a,b). These models have proven to be rather useful to describe the experimental observations cited in the first section of this article. Some issues remain in the choice of the model parameters, in particular of the value of capillary pressure drop within the bundles, the shape of the bundles, and also in the pressure value within the pores, either kept at a fixed value (generally zero, corresponding to evacuated preforms), or increasing with decreasing pore volume according to the perfect gas law, in turn reducing the pressure gradient driving flow in the bundles.

Recently, DeValve and Pitchumani (2013) developed a model using a unit cell approach, taking into account preform real geometrical features within a unit cell, the presence of a capillary pressure drop at the infiltration front of the tow, and 2D or 3D flow calculations using a CFD code; these simulations are not uncommon in the LCM processing field, but were so far rather geared towards the prediction of a saturated permeability value based on a unit-cell that represents the fabric architecture and its experimental variability (Verleye, Lomov, Long, Verpoest and Roose 2010, Papathanasiou et al. 2002, Nordlund , Lundstrom, 2005, Nordlund, Lundstrom, Frishfelds and Jakovics 2006, Koivu, Decain, Geindreau et al. 2010). The calculations are quite CPU-intensive but remain manageable. DeValve and Pitchumani could thus by modeling flow progression into the unit cell comprising tows, predict the saturation as a function of time over the unit cell, for constant *Ca* and *Re* experiments, and predicted a steady-state value for *S* after a given time, which implicitly arose from their choice of boundary conditions on the unit cell: constant velocity on the inlet plane, and constant pressure on the outlet plane. Predictions nonetheless successfully reproduced the experimental results of Leclerc and Ruiz (2008), showing that the void content dependency in the steady-state region as a function of *Ca* displays a minimum at an optimal *Ca* value of 0.0055. These authors could thus propose an optimal process window expressed in terms of *Re* and *Ca* for the chosen system of fabric and resin. Overall, the computational fluid dynamics approach seems promising as it removes some limitations of the more macroscopic dual-scale methods mentioned above; however, boundary conditions regarding the local wetting dynamics when fluid contacts the filaments in the bundles, and regarding the magnitude of gas pressure within the potentially entrapped voids in the bundles still remain difficult to estimate.

5. CONCLUSIONS

The presence of residual porosity in composite parts is a crucial issue that needs to be understood and controlled before reliable production of parts with LCM processes can be achieved. Most major causes are however now well controlled; these include the need to properly prepare and degas the resin, as well as the need to design the flow path so as to minimize dry-spots in the final composites. On the other hand the issue of air trapping during flow, caused by the multiphase nature of flow and enhanced by the dual-scale nature of most reinforcements, is still an active subject of research and a sensitive issue in engineering practice. As shown in this review, a multiphase flow approach, either proposing a direct solution of the flow equations knowing relevant saturation curves and relative permeability relations, or using a dual-scale description of saturated flow within a unit cell, is necessary to reach a prediction of the local saturation in the preform during flow. A multiphase flow approach enables to capture the experimentally observed effect that the flow velocity has on the amount and location of porosity during flow, and leads to predict an optimal flow rate, at which capillary and hydrodynamic forces at play in the reinforcement tend to equilibrate. This however requires knowledge of the variation of physical parameters, corresponding to the influence of saturation

on the overall permeability, and the influence of local pressure on saturation for a given flow regime, if the direct solution is chosen, or knowledge of the local preform architecture and tow saturation kinetics for a given flow regime, if the dual-scale description is chosen, that are rather difficult to quantify for a combination of resin and reinforcement. Further work is thus needed to propose practical tools to predict saturation versus position and time, and to establish practical and reliable measurement methods for the set of relevant physical parameters.

Once flow is terminated and the part is filled, other mechanisms may play a role: pores present may be transported (mostly large pores present between fiber bundles) or may dissolve and diffuse, a mechanism that is enhanced by a local pressure increase. Bleeding has been found to exert a positive action, however it is costly and time consuming. Other solutions are to add a zone of low permeability at the outlet of the preform, which slows down flow and reduces pressure gradients within the part. Many possibilities are thus still open for investigation, making investigations of physical mechanisms during flow, and the identification and quantification of relevant parameters, fruitful venues for future research.

ACKNOWLEDGEMENTS

The author wishes to thank Dr Nordlund, Dr Verrey, Dr Wolfrath, Dr Zingraff for their contributions to this research topic at the LTC over the last years. Support from the Swiss National Fund, from the Swiss commission for technology and innovation, and from the European Community is gratefully acknowledged.

REFERENCES

Abter R., J.M. Berau, C. Binetruy, L. Bizet, J. Bréard, S. Comas-Cardona, C. Demaria, A. Endruweit, P. Ermanni, F. Gommer, S. Hasanovic, P. Henrat, F. Klunker, B. Laine, S. Lavanchy, S.V. Lomov, A. Long, V. Michaud, G. Morren, E. Ruiz, H. Sol, F. Trochu, B. Verleye, M. Wietgrefe, W. Wu, G. Ziegmann (2011) Experimental determination of the permeability of textiles, a benchmark exercise, Composites part A, 42, pp.1157-1168.

Acheson JA, Simacek P, Advani SG. (2004) The implications of fiber compaction and saturation on fully coupled VARTM simulation. Composites Part A: Applied Science and Manufacturing 35:159.

Ahn, K. J., Seferis, J. C. and Berg, J. C., (1991) Simultaneous Measurements of Permeability and Capillary Pressure of Thermosetting Matrices in Woven Fabric Reinforcements, Polymer Composites, vol. 12 (3), 146-152.

Amico, S. and Lekakou, C., (2001) An experimental study of the permeability and capillary pressure in resin-transfer moulding, in Composites Science and Technology, vol. 61 1945-1959.

Babu BZ, Pillai KM. (2004) Experimental investigation of the effect of fiber-mat architecture on the unsaturated flow in liquid composite molding. J. Compos Mater. ;38:57.

Bayldon JM, Daniel IM. (2009) Flow modeling of the VARTM process including progressive saturation effects. Composites Part A-Applied Science And Manufacturing 40:1044.

Bear, J., (1972) Dynamics of fluids in porous media, Dover publications, New York.

Bear J, Bachmat Y. (1990) Introduction to Modeling of Transport Phenomena in Porous Media. Dordrecht, The Netherlands: Kluwer Academic Publishers.

Bickterton S., Abdullah MZ (2003) Modeling and evaluation of the filling stage of injection/compression moulding, Comp.Sci and Tech, 63, 1359-1375

Binetruy, C., B. Hilaire, and J. Pabiot. (1998) Tow Impregnation Model and Void Formation Mechanisms during RTM. J. of Composite Materials, 32(3): p. 223-245.

Binetruy, C., B. Hilaire, and J. Pabiot. (1997) The Interactions between Flows Ocurring inside and outside Fabric Tows during RTM. Composites Science and Technology 57: p. 587-596.

Breard J, Henzel Y, Trochu F, Gauvin R. (2003) Analysis of Dynamic Flows Through Porous Media. Part I: Comparison Between Saturated and Unsaturated Flows in Fibrous Reinforcements. Polymer Composites, 24:391.

Brooks, R.H. and A.T. Corey. (1964) Hydraulic Properties of Porous Media, Colorado State University Hydrology Papers. p. 27.

Darcy H. (1856) Les Fontaines Publiques de la Ville de Dijon. Paris: Victor Dalmont.

DeParseval Y, Pillai KM, Advani SG. (1997) A simple model for the variation of permeability due to partial saturation in dual scale porous media. Transport in Porous Media;27:243.

DeValve C and Pitchumani, R (2013), Simulation of void formation in liquid composite molding processes, Composites part A, 51, 22-32.

Dopler T, Modaressi A, Michaud VJ. (2000) Simulation of Metal Composite Isothermal Infiltration Processing. Metallurgical and Materials Transactions;31B:225.

Dullien FAL (1979). Porous Media, Fluid Transport and Pore Structure. New York: Academic Press.

Frishfelds V, Lundström TS and Jakovics A. (2008) Bubble motion through non-crimp fabrics during composite manufacturing. Composites Part A; 39(2): 243–251.

Frishfelds V., and Lundström TS, (2011) Influence of flow-induced deformations of fabrics on the formation and transport of Bubbles during Liquid Moulding Processes, Mechanics of Composite Materials, 47, n°2.

Garcia JA, Gascon LI, Chinesta F, Ruiz E and Trochu F, (2010) An efficient solver of the saturation equation in liquid composite molding processes, Int. J. Mater. Form, Supl2, S1295-1302.

Garcia JA, Gascon LI and Chinesta F, (2010), A flux limiter strategy for solving the saturation equation in RTM process simulation, Composites: Part A 41, 78–82.

Gourichon B, Binetruy C, Krawczak P. (2006) Experimental investigation of high fiber tow count fabric unsaturation during RTM. Composites Science and Technology;66:976.

Greenkorn RA. (1983) Flow Phenomena in Porous Media. New York: Marcel Dekker.

Judd NCW and Wright WW (1978). Voids and their effects on the mechanical properties of composites – an appraisal. SAMPE J, 14: 10–14.

Gokce A, and Advani SG, (2004) Simultaneous gate and vent location optimization in liquid composite molding processes, Compos Part A: Appl Sci Manuf, 35 (12) pp. 1419–1432

Kim, SK and Daniel, IM (2007) Observation of permeability dependence on flow rate and implications for liquid composite molding, Journal of Composite Materials, Volume: 41 Issue: 7 Pages: 837-849

Kistler, S. F., (1993) Hydrodynamics of Wetting, 1st ed., Wettability (J.C. Berg), Marcel Dekker Inc., 311-429.

Koivu V, Decain M, Geindreau C, et al. (2010) Transport properties of heterogeneous materials. Combining computerised X-ray micro-tomography and direct numerical simulations, International journal of computational fluid dynamics, 23, 10 713-721.Kuentzer N, Simacek P, Advani SG and Walsh S. (2007) Correlation of void distribution to VARTM manufacturing techniques. Composites Part A 38(3): 802–813.

Kuentzer N, Simacek P, Advani SG and Walsh S. (2006) Permeability characterization of dual scale fibrous porous media, Composites: Part A 37, 2057–2068

Labat L, Breard J, Pillut-Lesavre S, Bouquet G.(2001) Void fraction prevision in LCM parts. European Physical Journal-Applied Physics16:157.

Labat L, Grisel M, Breard J, Bouquet G. (2001) Original use of electrical conductivity for void detection due to injection conditions of composite materials. Comptes Rendus De L Academie Des Sciences Serie Ii Fascicule B-Mecanique;329:529.

Lawrence JM, Neacsu V and Advani SG. (2009) Modeling the impact of capillary pressure and

air entrapment on fiber tow saturation during resin infusion in LCM. Composites Part A; 40(8): 1053–1064.
Leclerc JS and Ruiz E (2008). Porosity reduction using optimized flow velocity in resin transfer molding. Composites Part A 39(12): 1859–1868.
Li M, Wang SK, Gu YZ, Zhang ZG, Li YX, Potter K.(2010) Dynamic capillary impact on longitudinal micro-flow in vacuum assisted impregnation and the unsaturated permeability of inner fiber tows. Composites Science And Technology ;70:1628.
Li W, Krehl J., Gillespie J.W.Jr. , Heider D, Endrulat M, Hochrein K., Dunham M.G., and Dubois C.J., (2004), Process and performance evaluation of the Vacuum-Assisted Process, J.Comp.Mat, 38, 20, 1803-1814.
Lundström TS and Gebart R, (1994), Influence from Process parameters on void formation in resin transfer molding, Polymer Composites, 15, n°1.
Lundström TS, Frishfelds V, Jakovics A, (2010) Bubble formation and motion in non-crimp fabrics with perturbed bundle geometry, Composites: Part A 41 83–92
Lundstrom TS. Measurement of void collapse during resin transfer moulding. Composites Part A 1997; 28(3): 201–214.
Madsen B and Lilholt H (2003) Physical and mechanical properties of unidirectional plant fibre composites – an evaluation of the influence of porosity. Compos Sci Technol 63(9): 1265–1272.
Mahale AD, Prud'homme RK and Rebenfeld L. (1992) Quantitative measurement of voids formed duringliquid impregnation of nonwoven multifilament glass networks using an optical visualization technique. PolymEng Sci 32(5): 319–326.
Markicevic B and Djilali N, (2006) Two-scale modeling in porous media: relative permeability prediction, Physics of fluids 18, 033101.
Marle C.M., (1981), Multiphase flow in porous media, Editions Technip, Paris, 254 pages.
Matsuzaki, R Kobayashi, S, Todoroki, A, and Mizutani Y (2013) Flow control by progressive forecasting using numerical simulation during vacuum-assisted resin transfer molding, Composites Part A 45 79-87.
Merotte J., Simacek P,and Advani S (2010) Resin flow analysis with fiber preform deformation in through thickness direction during Compression Resin Transfer Molding, Composites Part A, 41, 881-887.
Michaud VJ, Compton LM, Mortensen A. Capillarity In Isothermal Infiltration Of Alumina Fiber Preforms With Aluminum.(1994) Metallurgical And Materials Transactions A-Physical Metallurgy And Materials Science; 25:2145.
Michaud V and Mortensen A, (2001) Infiltration processing of fiber reinforced composites: governing phenomena, Composites part A, 32 , pp.981-996.
Michaud, V, S. Sequeira Tavares, A.Sigg, S.Lavanchy and J.-A.E. Månson, (2006) Low pressure processing of high fiber content composites, proceedings of the eight international conference on Flow processes in Composite materials, Douai.
Michaud, V (2012) Fibrous preforms and preforming, Wiley Encyclopedia of Composites. Encyclopedia of Composites, 2nd Edition, Editors: Luigi Nicolais Assunta Borzacchiello, publisher John Wiley &Sons, Hoboken, New Jersey.
Nordlund and T.S. Lundström, (2005) Numerical study of the local permeability of non-crimp Fabrics, Journal of Composite Materials, 39, 10.
Nordlund M, T.S. Lundström, V.Frishfelds, A. Jakovics, (2006) Permeability network model for non-crimp fabrics, Composites Part A, 37 , 828-835.
Nordlund M and Michaud V, (2012) Dynamic saturation curve measurement for resin flow in glass fibre reinforcement, Composites: Part A 43 333–343.
Papathanasiou, T.D., et al., (2002) Non-isotropic structured fibrous media: The permeability of arrays of fiber bundles of elliptical cross section. Polymer Composites, 23(4): 520-529.Parnas RS, Howard JG, Luce TL, Advani SG. (1995) Permeability characterization .1. A proposed

standard reference fabric for permeability. Polym. Compos;16:429.
Parnas, R. (2000) Liquid Composite Molding, Hanser Verlag, Munich, 170 pages.
Parnas RS and Phelan Jr FR. (1991) The effect of heterogeneous porous media on mold filling in resin transfer molding. SAMPE Q; 22(2): 53–60.
Parnas RS, Salem AJ, Sadiq TA, Wang H-P and Advani SG (1994), The interaction between micro-and macro-scopic flow in RTM preforms, Composite Structures, 27, 93-107.
Patel, N. and L.J. Lee. (1995) Effect of Fiber Mat Architecture on void formation and removal in liquid composite molding, Polymer Composites, 16(5), pp. 386-399.
Patel, N. and L.J. Lee. (1996a) Modeling of Void Formation and Removal in Liquid Composite Molding. Part I: Wettability Analysis. Polymer Composites 17(1): p. 96-103.
Patel, N. and L.J. Lee.(1996b) Modeling of Void Formation and Removal in Liquid Composite Molding. Part II: Model Development and Implementation. Polymer Composites 17(1): p. 104-114.
Park CH and Lee WI, (2011) Modeling void formation and unsaturated flow in liquid composite molding processes: a survey and review, J. Reinf. Plastics and Composites, 30 (119, 957-977.
Rohatgi, V., Patel, N. and James Lee, L.,(1996) Experimental Investigation of Flow-Induced Microvoids During Impregnation of Unidirectional Stitched Fiberglass Mat, Polymer Composites, vol. 17 (2), 161-170.
Ruiz E, Achim V, Soukane S, Trochu F and Bréard J. (2006) Optimization of injection flow rate to minimize micro/macro-voids formation in resin transfer molded composites.Compos Sci Technol; 66(3–4): 475–486.
Scheidegger, A.E. (1974) The Physics of Flow through Porous Media. Third ed. Toronto: University of Toronto Press.
Simacek, P., Heider D., Gillespie J.W.Jr. and Advani S, (2009), Post-filling flow in vacuum assisted resin transfer molding processes: theoretical analysis, Composites Part A, 40, 913-924.
Slade J, Pillai KM, Advani SG. (2001) Investigation of unsaturated flow in woven, braided and stitched fiber mats during mold-filling in resin transfer molding. Polym. Compos;22:491.
Spitz, K. and J. Moreno. (1996) A practical Guide to Groundwater and Solute Transport Modeling. New York, NY: John Wiley and Sons.
Summerscales, J, Searle, TJ, (2005) Low-pressure (vacuum infusion) techniques for moulding large composite structures, Proceedings of the institution of mechanical engineers, Part L-Journal of materials design and applications, Volume: 219 Issue: L1 Pages: 45-58.
Tan H, Roy T, Pillai KM. (2007) Variations in unsaturated flow with flow direction in resin transfer molding: An experimental investigation. Composites Part A-Applied Science And Manufacturing;38:1872.
Tan H, Pillai KM. (2012a) Multiscale Modeling of Unsaturated Flow in Dual-Dcale Fiber Preforms of Liquid Composite Molding I: Isothermal Flows. Composites Part A-Applied Science And Manufacturing, 43, 1, 1-13
Tan H, Pillai KM.(2012b) Multiscale Modeling of Unsaturated Flow in Dual-Dcale Fiber Preforms of Liquid Composite Molding II: Non-isothermal flows. Composites Part A-Applied Science And Manufacturing, 43, 1, 14-28.
Tang JM, Lee WI and Springer GS (1987). Effects of cure pressure on resin flow, voids, and mechanical properties. J Compos Mater 21(5): 421–440.
Van Genuchten MT. (1980) A closed form for predicting the hydraulic conductivity of unsaturated soils. Soil Sci Am Soc 892–8.
Verleye B, S. Lomov, A. Long, I. Verpoest, and D. Roose, (2010) Permeability prediction for the meso-macro coupling in the simulation of the impregnation stage of resin transfer moulding, Composites Part A, 41 pp. 29–35.
Verrey, J, Michaud V. and J.-A. E. Månson, (2006) Dynamic capillary effects in Liquid

Composite Molding with non-crimped fabrics, Composites Part A, 37 (1), pp.92-102.
Wang HF(2000), Theory of Linear Poroelasticity with Applications to Geomechanics and Hydrogeology, Princeton University Press, Princeton, NJ, 287 p.
Witik, R., Gaille F., Teuscher R., Ringwald H., Michaud V., Månson J.A.E, (2012) « The Economic and Environmental Assessment of Out-of-Autoclave Curing for Composite Materials », Journal of Cleaner Production, 29-30, pp.91-102.
Wolfrath J, Michaud V, Modaressi A, Manson JAE. (2006) Unsaturated flow in compressible fibre preforms. Composites Part A-Applied Science And Manufacturing;37:881.
Yamaleev N and Mohan R. (2006) Effect of the phase transition on intra-tow flow behavior and void formation in liquid composite molding. Int J Multiphase Flow; 32(10–11): 1219–1233.
Yoshida HT, Ogasa T and Hayashi R, (1986) Statistical approach to the relationship between ILSS and void content of CFRP. Compos Sci Technol 25(1): 3–18.
Zhou F, Kuentzer N, Simacek, P Advani S. G., Walsh S., (2006) Analytic characterization of the permeability of dual-scale fibrous porous media, Composites Science and Technology 66, 2795–2803.
Zingraff L, Michaud V, Bourban P.E. and Månson J.-A. E. (2005) Resin transfer moulding of anionically polimerized polyamide 12, Composites Part A, 36, pp.1675-1686.

Proceedings of the 34th Risø International Symposium on Materials Science:
Processing of fibre composites – challenges for maximum materials performance
Editors: B. Madsen, H. Lilholt, Y. Kusano, S. Fæster and B. Ralph
Department of Wind Energy, Risø Campus
Technical University of Denmark, 2013

NATURAL FIBRE COMPOSITES AND THEIR PROCESSING

Jörg Müssig

University of Applied Sciences Bremen, Faculty 5, Biomimetics –
The Biological Materials Group, Neustadtswall 30,
D-28199 Bremen, Germany

ABSTRACT

Throughout the last decade, intense research has been carried out in the field of natural fibre-reinforced plastics. The potential applications of natural fibre-reinforced composites (NFRC) are found in industry sectors like automotive, sports or construction. Bast fibre-reinforced composites can outperform other materials like aluminium, steel or glass fibre-reinforced polymers regarding their density related stiffness properties. The use of natural fibres as reinforcement for polymers has become increasingly important, and, owing to their different properties, the common techniques for processing fibre-reinforced plastics have to be adjusted to meet new and more demanding requirements. In the field of NFRC thermoset processing techniques are available to produce high-quality composites. The same is valid for most thermoplastic processing techniques. But the conventional compounding processes are not optimised for NFRC leading to strong fibre damage during processing. Therefore a new compounding concept for thermoplastic NFRC granules was developed: With the CMS-compounder it was possible to produce granules from long hemp fibre bundles (length > 40 mm) with fibre mass fractions ranging between 20 and 40 % in a PLA-matrix. The prepared composites have superior mechanical properties compared to conventional compounded and injection moulded samples.

1. INTRODUCTION – WHY USING NATURAL FIBRES

Faruk, Bledzki, Fink and Sain (2012) identify a growing trend to use natural fibres in plastics composites which can be explained by their flexibility during processing and high specific stiffness. NFRC are gaining more and more acceptance in structural applications, too. Over the last decades natural fibre reinforced composites have been undergoing a remarkable transformation. The composite properties as well as the part complexity increased as new fibre/polymer combinations and processes have been investigated, developed and applied to the industry (Faruk et al., 2012).

In addition to their environmental benefits, the other advantages of natural fibres include a high

stiffness and strength, with at the same time a low density (1.40 g/cm³) compared to glass (2.55 g/cm³). Natural fibre-reinforced composites have good lightweight construction potential. In the case of fracture the component breaks without rough edges and does not splinter. Disadvantages are: moisture expansion, flammability, variable quality and fibre–matrix interaction, which reduces the mechanical properties (Rowell, Sanadi, Caulfield and Jacobson, 1997; Pickering, 2008; Drzal, Mohanty, Wibowo, Misra, and Seiler, 2003; Graupner and Müssig, 2010).

The main target of a material selection process is to minimize cost while, at the same time, maintaining the mechanical properties. A systematic material selection process becomes complex if more than one criterion can be changed. With the focus on lightweight design the Ashby concept (Ashby, 2004) can help to find a suitable solution to the problem. In Figure 1 the concept for minimising the mass of two different structures for different types of loads is given. A beam under tension should be optimized with regard to the mass at fixed geometrical properties and constant load. This concept requires a material with high stiffness and low density. The ratio of (E/ρ) needs to be maximised. A mass-reduced plate under bending at fixed geometrical properties and constant load requires a material with high stiffness and a low density. The ratio of ($E^{1/3}/\rho$) needs to be maximised.

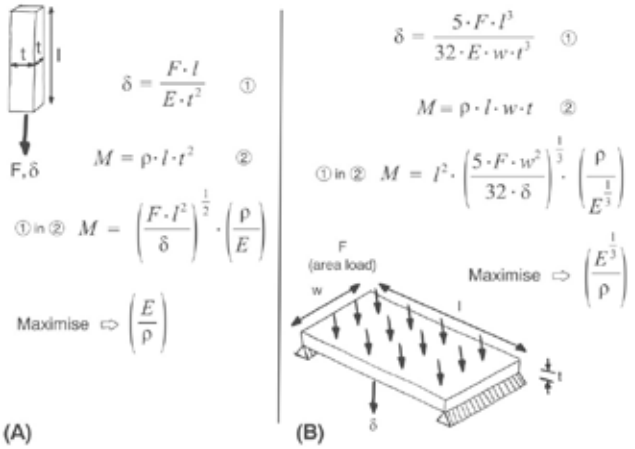

Figure 1. Combination of properties for which the ratio of stiffness to density exceed maximum values. (A) Beam under tension, maximise (E/ρ) to reduce the mass at fixed mechanical and gemetrical properties; (B) Plate under bending, maximise ($E^{1/3}/\rho$) to reduce the mass at fixed forces and geometrical properties. Adapted from Ashby et al. (2007, p. 223). δ: deflexion under load; E: Young's Modulus; ρ: density; M: mass; F: load; l: length; t: thickness; w: width.

To demonstrate the potential of NFRC for structural components the Ashby concept is applied to flax fibre-reinforced composites compared to glass, carbon fibre-reinforced composites, aluminium and steel. The following properties are used for the theoretical calculation (Verpoest, 2012):

- Aluminium: Density (2.70 g/cm³); Young's modulus (70 GPa)
- Carbon fibre: Density (1.80 g/cm³); Young's modulus (230 GPa)
- Flax fibre: Density (1.40 g/cm³); Young's modulus (65 GPa)
- Glass fibre: Density (2.55 g/cm³); Young's modulus (70 GPa)
- Polypropylene: Density (1.00 g/cm³); Young's modulus (1 GPa)
- Steel: Density (7.80 g/cm³); Young's modulus (210 GPa)

The fibre volume dependent longitudinal specific stiffness values (E/ρ), calculated by the rule of mixture, of composites compared to metals are illustrated in Figure 2.

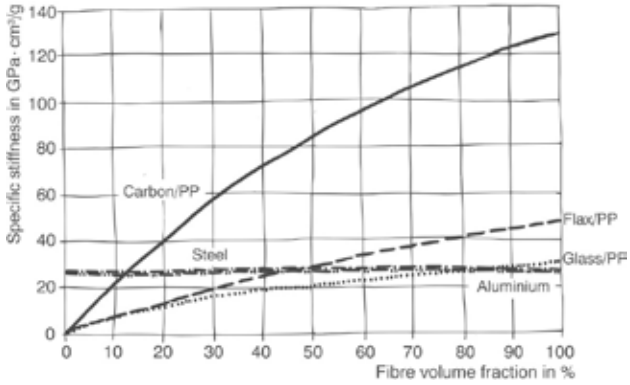

Figure 2. Fibre volume fraction dependent longitudinal specific stiffness (E/ρ) values (calculated by the rule of mixture) of composites compared to metals for the load case "beam under tension". Adapted from Verpoest (2012) and Verpoest and Baets (2012).

It is obvious that the theoretical specific stiffness of the flax/PP composite is higher compared to the value of the metals, as soon as the fibre volume exceeds 50 % (Verpoest, 2012). Flax composites reach higher (E/ρ) values compared to glass/PP if the fibre volume fraction exceeds values above 25 %. In Figure 3 the fibre volume fraction dependent longitudinal specific stiffness values ($E^{1/3}/\rho$) of composites compared to metals for the load case *plate under bending (area load)* are illustrated.

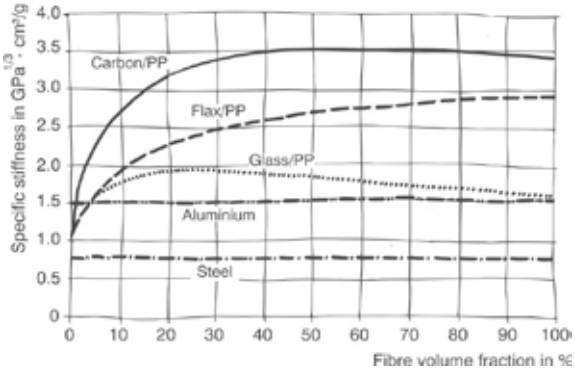

Figure 3. Fibre volume fraction dependent longitudinal specific stiffness ($E^{1/3}/\rho$) values (calculated by the rule of mixture) of composites compared to metals for the load case "plate under bending (area load)". Adapted from Verpoest (2012) and Verpoest and Baets (2012).

Through this theoretical approach of modelling, the superior properties of the carbon fibre-reinforced composites are obvious. For the flax fibre-reinforced composites the advantages become apparent especially in comparison to the glass fibre-reinforced composites (Verpoest, 2012).

2. NFRC PROCESSING – A HISTORICAL REVIEW

In particular, in the last two decades numerous studies and projects have been carried out to investigate the use of natural fibres as potential reinforcement for plastics. Although the use of NFRC is not a new concept, Hänninen and Hughes (2010) discussed that the motivation for the use of natural fibres has changed. The authors emphasise that before the introduction of man-made fibres (for composites in particular glass fibre), natural fibres (plant as well as mineral fibres) were the only reinforcement available for fibre-reinforced composites. Indeed, the processing technique associated with NFRC was well advanced even as late as the 1940's (Brown, 1947). Technical performance was one of the main reasons for using natural fibres like cotton or flax in these early composites. In view of current developments of NFRC two other aspects need to be stressed: environmental concerns and cost (Hänninen and Hughes, 2010), whereof the latter is more relevant for NFRC in the automotive industry.

Prömper (2010) stressed the important role of the automotive industry in the field of bio-based materials such as wool, cotton or leather which have been used for interior parts and seats since the beginning of industrial automobile production. The author gives a detailed overview of the development of NFRC for automotive interior applications between 1950 and 2008 in the German automotive industry and it is worth to summarize the most important conclusions as follows:

- Wood chipboards were used as decorative covering parts in automotive interiors (Fibrit process with acrylic-based resins). Since the late 1940s, these parts have become more contoured by using new developed processing techniques.

- The development of NFRC based on wood for contoured interior parts started in the early 1950s. Decorative door panels were manufactured with melamine resins.

- The development of thermosets such as phenolic or unsaturated polyester in the 1960s led to the development of simple, contoured parts reinforced with wood or cotton fibres.

- Starting in the end of the 1980s, the development of airbag systems as a safety component has changed the requirements of automotive interior NFRC parts from being simply decorative to being structural parts with relevant safety features. This development led to an adaptation of the NFRC components and the processing techniques to the changing requirements. The use of longer fibres or fibre bundles with higher mechanical properties was necessary. The type of resins changed, too. (Prömper, 2010).

Figure 4 illustrates the main development steps of NFRC for automotive interior applications between 1950 and 2008 in the German automotive industry.

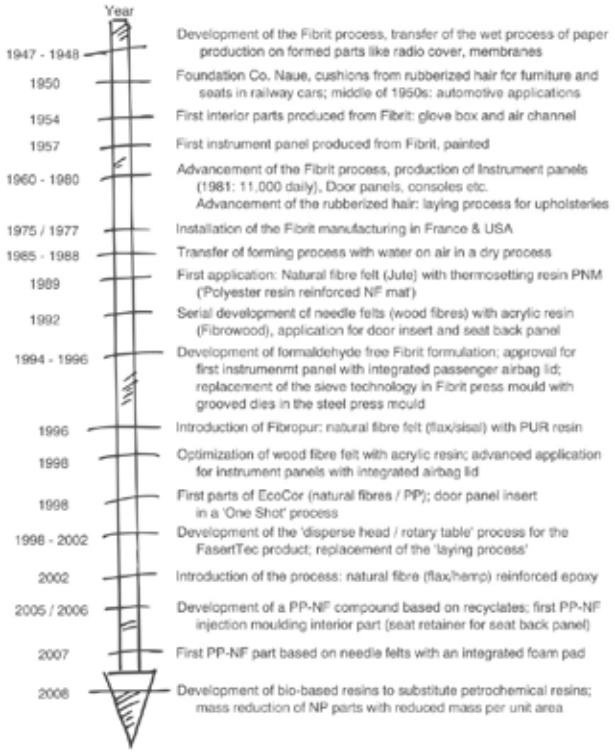

Figure 4. Timeline of NFRC between 1950 and 2008 from the viewpoint of a tier-one supplier. Adapted from Prömper (2010).

3. NFRC PROCESSING – CURRENT DEVELOPMENTS

In the last few decades, considerable efforts are made in the field of fibre-reinforced plastics. As such composites need different processes compared to unreinforced plastics the processing techniques of fibre-reinforced polymers have undergone a strong development. The use of NFRC has become increasingly important, and, owing to their different properties, the common techniques to produce NFRC have to be adjusted to meet new and more demanding requirements (Huber, Graupner and Müssig, 2010). The choice of appropriate processing techniques depends on several influencing factors such as part geometry, complexity, size, the properties of the used fibres and polymers, the fibre orientation, the quantity and quality of the product and the fact that not all processing techniques are applicable to all kinds of materials (Grove, 2006; Huber et al., 2010). Important influencing factors for choosing the adequate process are shown in Figure 5.

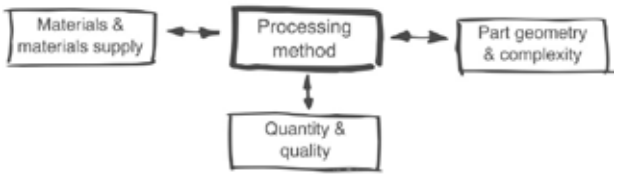

Figure 5. Important parameters for choosing the adequate process (Huber et al., 2010).

In the field of natural fibre reinforced composites the most relevant thermoset processing techniques are shown in Figure 6.

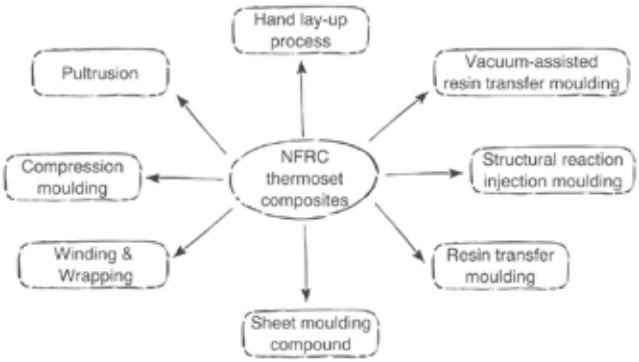

Figure 6. A selection of processing concepts relevant for NFRC thermoset composites.

The automotive industry is using mainly press moulding techniques for the production of thermoset NFRC. Other industry sectors like sports, design and construction industry are more and more aware of the advantages of NFRC. Gomina (2012) gives a nice overview of applications which are currently available on the market. All the techniques shown in Figure 6 are more or less used in these industry sectors. Some examples are as follows:

- Surfboards from company NoTox, FR ⇨ Hand lay-up (with vacuum)
- Road signs for bicycle traffic from company NPSP, NL ⇨ RTM and VARTM
- Sections for window frames from company Innobat, FR ⇨ Pultrusion
- Racing sailboats from company IDB marine, FR ⇨ Infusion moulding
- Fishing rod from company Caperlan, FR ⇨ Wrapping technique
- MAN passenger-bus body component (Müssig et al., 2006) ⇨ SMC

Thermoplastic NFRC production techniques differ from thermoset NFRC production techniques, specifically by means of higher processing temperatures and higher viscosity of the polymer. According to Ziegmann and Elsabbagh (2012) the advantages of thermoplastic NFRC compared to thermoset NFRC are: (i) lower density, (ii) easier recycling, (iii) cleaner processing, (iv) unlimited storage time, (v) formability without the need to manufacture a preform, (vi) application of welding techniques and (vii) reduced preparation time (no need for chemical reaction). Many different types of thermoplastic production techniques exist and the most important for NFRC are shown in Figure 7.

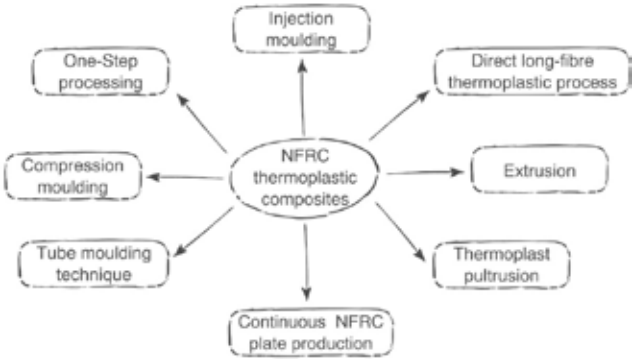

Figure 7. A selection of processing concepts relevant for NFRC thermoplastic composites.

In the automotive industry compression moulding and one-step processing are widely used production techniques. The direct long-fibre thermoplastic process (D-LFT) was used for an innovative application of natural fibres with polypropylene in underfloor protection for a passenger car (Mercedes A Class). The manufacturing process (compare Figure 8) has been initiated by Rieter Automotive, DE (Scherübl and Hintermann, 2005).

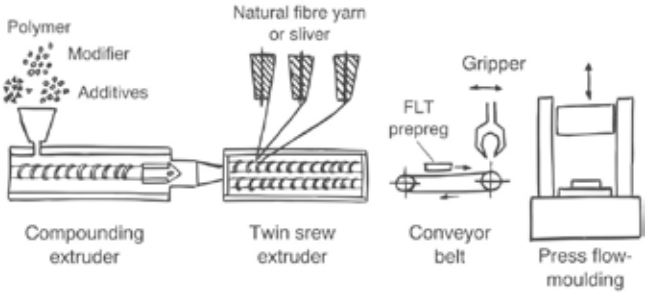

Figure 8. Process design for the production of natural fibre-reinforced thermoplastic components (LFT). Adapted from Huber et al. (2010).

Other processing techniques for thermoplastic NFRC are pultrusion (Friedrich, Evstatiev, Angelov and Mennig, 2007) and extrusion. Regarding the latter, the most important extruded NFRC material is WPC – wood plastic composite. The main application area for WPC is in construction and since the 1990's, the market for WPC has grown significantly, particularly in applications where, compared to wood products, the low maintenance and high weather resistance of WPCs are of real benefit (Hänninen and Hughes, 2010). The tube moulding technique is rarely used, but is a potentially suitable process to produce hollow tubes based, for example, on natural fibre-reinforced PLA (Dentel, Müssig and Bäumer, 2012). The continuous NFRC plate production is a relatively unknown technique, but shows a high potential for structural composite applications. The processing technique is shown in Figure 9, the further processing of the thermoplastic prepreg to moulded NFRC part is illustrated in Figure 10.

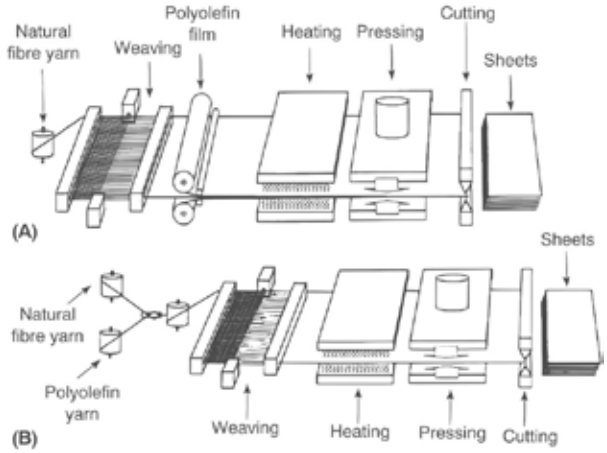

Figure 9. NFRC sheet and thermoplastic prepreg production. (A) a natural fibre weave is combined with polymer films from both sides under the influence of elevated temperature. (B) a hybrid weave is produced by combining a natural fibre yarn with a polyolefin yarn. The weave is transformed to a NFRC sheet. Adapted and adjusted from van Rooijen (2012).

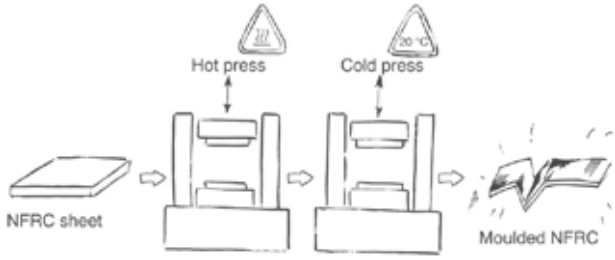

Figure 10. Thermoplastic NFRC press mould processing technique.

Injection moulding for NFRC is often called a sleeping giant in terms of market size and market potential. Based on a critical analysis there are still technical obstacles to be overcome before a fast time-to-market is achieved.

4. NFRC COMPOUNDING – A CRITICAL REVIEW

A selection of approaches for the optimisation of injection moulded NFRC is given in Figure 11. As illustrated in Figure 12, the compounding process of thermoplastic NFRC is probably the greatest challenge to overcome. In conventional compounding processes, the main bottleneck is related to the feeding of the fibres. The cut fibres can either be feed directly to the compounding systems or pelletised fibres can be used. During the last years, several new approaches to produce NFRC granules have been developed and described. Some of them will be briefly described in the following.

Figure 11. A selection of approaches for the optimisation of natural fibre-reinforced plastics (Müssig, 2011).

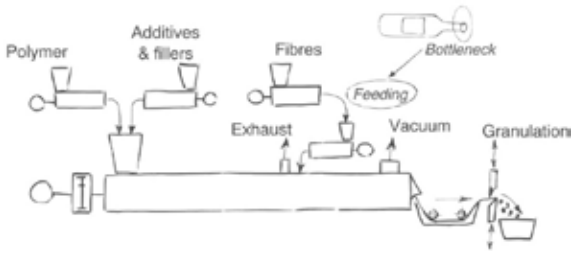

Figure 12. Process design for the production of natural fibre-reinforced thermoplastics granules with a classical extrusion process. In conventional compounding processes, the main bottleneck is related to the feeding of the fibres.

A compounding solution, which was developed for the production of regenerated cellulose fibre-reinforced thermoplastics, is illustrated in Figure 13. The so called two-step pultrusion can possibly be adapted to natural fibre yarns, but this concept demands a converting step of staple fibres into yarns before compounding. The so called Pull-Drill process (Figure 14) starts with a hybrid sliver, for example, based on flax fibre bundles and polypropylene fibres. The pulled sliver will be heated and under a continuous torsion formed into a fibre reinforced polymer strand. The strand will be chopped to granules at the end of the process. A possibility to produce granules with no shear stresses is illustrated in Figure 15. This concept is very well suited for the lab scale production of NFRC granules, and was patented by Beckmann (2001) for an industrial compounding process.

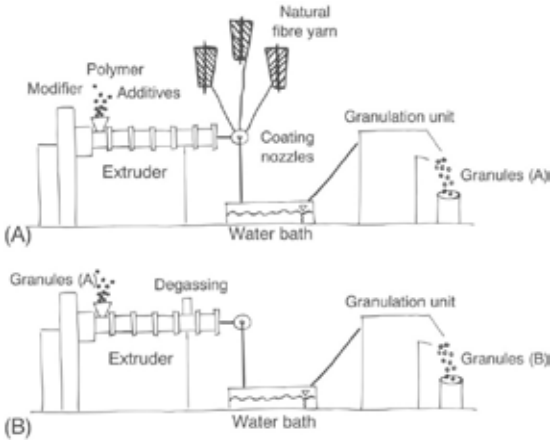

Figure 13. Process design for the production of regenerated cellulose fibre-reinforced thermoplastics (two-step pultrusion). Adapted from Haag and Müssig (2012); cf. also the process from Fraunhofer IAP, Fink, Ganster and Lehmann (2011).

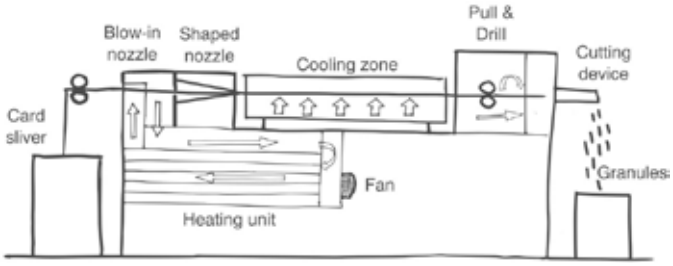

Figure 14. Process design for the production of natural fibre-reinforced thermoplastics (Pull-Drill process). Adapted from Haag and Müssig (2012) ; cf. also the process from TITK, Fink et al. (2011).

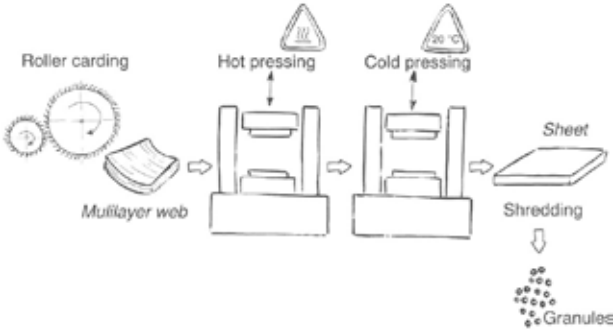

Figure 15. Roller card to form hemp fibre bundles and PLA fibres to a multilayer web; form pressing of PLA/hemp composites. Adapted from Müssig, Graupner, Oldemeyer and Mölleken (2011); cf. also the patent from Beckmann (2001).

The thermo-kinetic mixing system is illustrated in Figure 16. The technique is effective in dispersing natural fibres in thermoplastics. Addition of dispersion aids as well as coupling agents further improved the efficiency of mixing. The high shear forces during the process in the mixer decrease the lengths of fibres and fibre bundles in the final NFRC. However the improved fibre dispersion often results in improved composite properties (Rowell et al., 1997). Longer bast fibre bundles and fibre pellets are often very difficult to process with the thermo-kinetic mixing system.

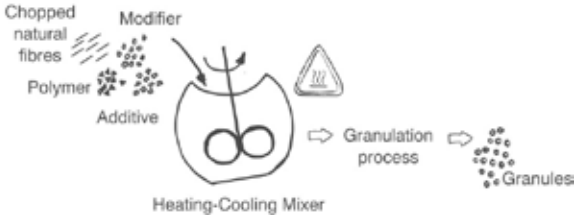

Figure 16. Process design for the production of natural fibre-reinforced thermoplastics (thermo-kinetic mixing).

Overall, it can be concluded that a universally applicable compounding method for all kinds and morphologies of natural fibres is still missing. Within the field of NFRC compounding techniques, one can identify the following as particularly important:

- Free-flowing fibres like chopped sisal with short lengths (< 3 mm) are suitable to be processed with standard compounding techniques.
- Most problems during compounding of NFRC occur because of the poor feedability of longer natural fibres.
- Some special developments for compounding of NFRC exist but are not economically in all cases, and the processes are often not flexible to use different length of fibres.
- Many standard fibre pellets are hard-pressed and cannot be separated completely during the compounding process in most cases.
- Fibre damage during compounding of NFRC occurs because of the temperature and high shear forces in most of the compounding systems.

5. A NEW COMPOUNDING CONCEPT – RESULTS & DISCUSSION

Based on the critical review on existing compounding processes, a new compounding concept was developed and realised, and still is under development in ongoing research projects. In a conventional compounding process, as illustrated in Figure 12, the main bottleneck is related to the feeding of the fibres. One of the main targets of the new natural fibre compounding concept was to solve this problem. In Figure 17 some specific targets that have already been achieved under the development program of the continuous mixing system (CMS compounder) are shown.

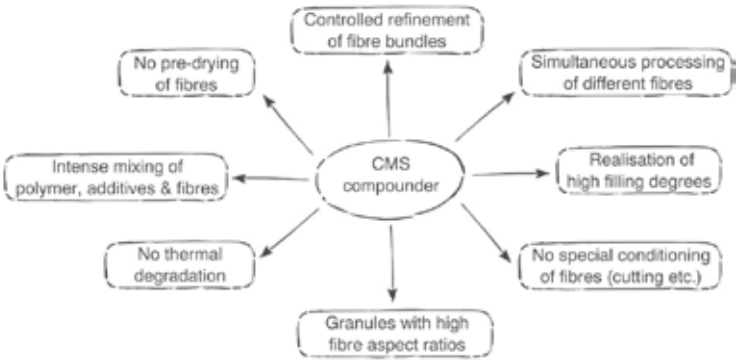

Figure 17. Examples of specific targets that have already been achieved under the development program of the CMS compounder.

With the CMS compounder granules were produced from long hemp fibre bundles (length > 40 mm) with fibre mass fractions ranging between 20 and 40 % in a PLA-matrix. Granules are further processed into test specimens with an injection moulding process described in more detail in Graupner, Ziegmann, Enzler and Müssig (2012). As reference sample neat PLA was processed in the same manner. Produced test specimens were investigated for their impact (DIN EN ISO 179) and tensile characteristics (DIN EN ISO 527). Two different types of raw hemp fibre bundles varying in fineness (Hemp KGE-02 and HempAge card sliver), were used as reinforcement. The distribution of the width of those types is shown in Figure 18.

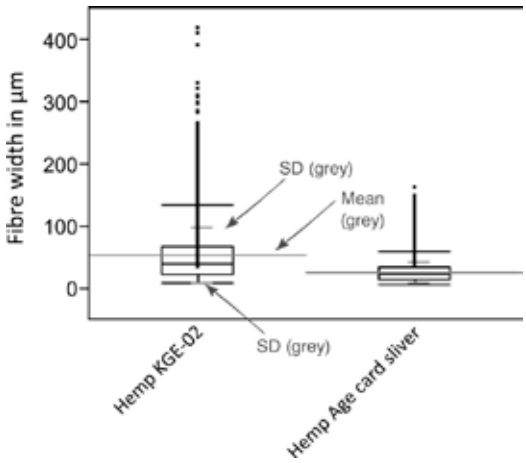

Figure 18. Box-and-whisker diagrams (black): Width of the raw hemp samples. Width measurement (mean value, standard deviation in grey): FibreShape V5.1, IST AG, CH; 4000 dpi; MM: Längen-Breitenmessung_Zoom_4000dpi_NG (Müssig and Graupner, 2013).

Hemp KGE-02 displays a average width of 53 µm and hemp age card sliver has a significant lower width of 26 µm. After injection moulding fibres were extracted from 1 g of the composites via an extraction process and were again analysed for their width and length distributions. As shown in Figure 19 the width of Hemp KGE-02 was significantly reduced to

values ranging between 23 and 25 µm due to the compounding and injection moulding process. Large fibre bundles were splitted into smaller fibre bundles and single fibres. In contrast to this the width of fibre bundles of HempAge card sliver was reduced only slightly to values of 21 – 22 µm. As shown in Figure 20, the fibres were shortened to similar lengths (178 – 211 µm) during compounding and injection moulding regardless of the fibre type and fibre mass fraction.

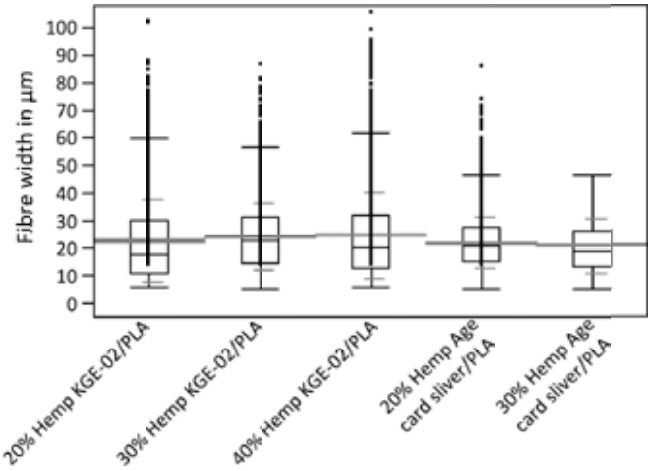

Figure 19. Box-and-whisker diagrams (black): Width extracted from the injection moulded test specimens. Width measurement (mean value, standard deviation in grey): FibreShape V5.1, IST AG, CH; 4000 dpi; MM: Längen-Breitenmessung_Zoom_4000dpi_NG (Müssig and Graupner, 2013).

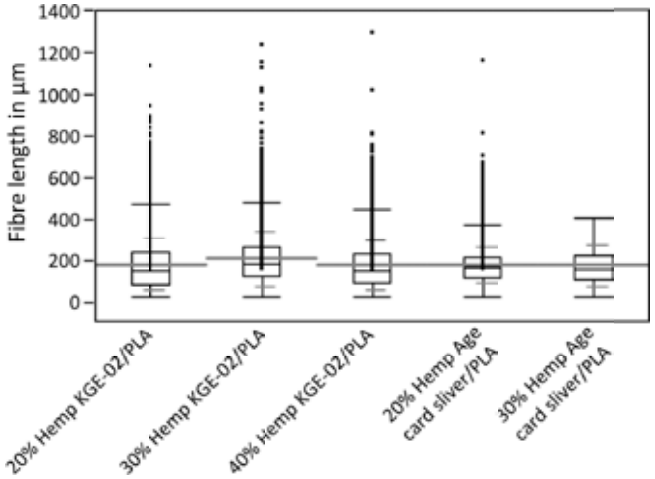

Figure 20. Box-and-whisker diagrams (black): Length of the hemp extracted from the injection moulded test specimens. Length (mean value, standard deviation in grey): FibreShape V5.1, IST AG, CH; 4000 dpi; MM: Längen-Breitenmessung_Zoom_4000dpi_NG (Müssig and Graupner, 2013).

Tensile strength values of the neat PLA-matrix and composites reinforced with 20 and 30 mass-% of both types of fibres are presented in Figure 21.

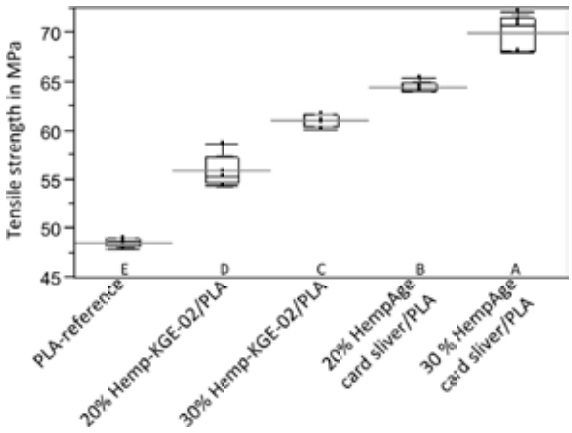

Figure 21. Box-and-whisker diagrams (black): Tensile strength of the injection moulded PLA/hemp composites (mean value, standard deviation in grey). DIN EN ISO 527; Sample 1A; l = 100 mm; Zwick Z020 / 20 kN; 2 mm/min; Video extensiometer; n = 5 (Müssig and Graupner, 2013).

It can be seen that the use of both types of hemp resulted in a significant increase in tensile strength as compared to the pure PLA matrix. An increasing fibre mass fraction also led to a significant improvement in tensile strength. Significantly higher values were achieved for composites reinforced with the stronger and stiffer hemp (HempAge card sliver). As shown in Table 1 the tensile strength of hemp/PLA composites with a fibre mass fraction of 30 % produced with the CMS compounding technique and injection moulding are clearly higher than values of flax/PLA composites produced with a standard compounding and injection moulding process. The table is not given to compare hemp with flax but to show the potential of the new compounding technique. The influence of fibre mass fractions in the range between 20 and 40 % was exemplarily investigated for composites produced with Hemp KGE-02 fibre bundles (compare Figure 22). It could be observed that the tensile strength was significantly increased with an increasing fibre content from 20 to 40 mass-%. There are only few studies that deal with the processing of such high fibre mass fractions (40 %) in the injection moulding process. In most cases, an increase in strength values is measured with an increasing fibre mass content from 20 to 30 %, while a further increase of the fibre mass fraction up to 40 % leads to a reduction of the strength values. A study by Han, Karevan, Bhuiyan, Park and Kalaitzidou (2012) deals with the analysis of injection moulded bamboo fibre-reinforced PLA composites. The authors investigated the flexural strength of the composites and determined an enhancement of flexural strength from 108 to 112 MPa by an increase in fibre mass fraction from 20 to 30 %. A fibre content of 40 mass-% led to a decrease in flexural strength to a value of 98 MPa. This is lower than the value measured for the non-reinforced PLA matrix. A similar trend was observed for regenerated cellulose fibre reinforced PLA composites. The tensile strength was enhanced with an increasing fibre mass fraction from 20 to 30 % and was reduced at a fibre content of 40 % below the value of the pure matrix (Graupner et al., 2012). The increase of tensile strength of hemp/PLA up to a fibre content of 40 mass-% shows the effectiveness that can be achieved by using the CMS compounding technique.

Table 1: Mechanical characteristics of composites produced from hemp/PLA via CMS compounding and injection moulding compared to results of injection moulded flax/PLA (results of neat PLA-matrix are given in brackets).

Composite	Fibre mass fraction in %	Tensile strength in MPa	Young´s modulus in GPa	Unnotched Charpy impact strength in kJ/m²	Reference
Hemp KGE-02/PLA	20	56 (49)	5.4 (3.1)	9.4 (10.8)	Müssig and Graupner (2013)
Hemp Age/PLA	20	64 (49)	5.3 (3.1)	11.1 (10.8)	Müssig and Graupner (2013)
Flax/PLA	20	56 (60)	6.4 (3.6)		Le Duigou et al. (2008)
Flax/PLA	20	49 (44)	5.1 (3.1)	10.5 (16)	Bax and Müssig (2008)
Hemp KGE-02/PLA	30	61 (49)	6.2 (3.1)	9.4 (10.8)	Müssig and Graupner (2013)
Hemp Age/PLA	30	70 (49)	6.6 (3.1)	11.6 (10.8)	Müssig and Graupner (2013)
Flax/PLA	30	53 (60)	7.3 (3.6)		Le Duigou et al. (2008)
Flax/PLA	30	54 (44)	6.3 (3.1)	11.0 (16.0)	Bax and Müssig (2008)

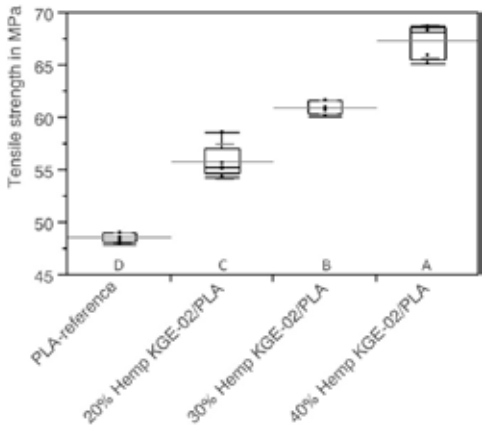

Figure 22. Box-and-whisker diagrams (black): Tensile strength of the PLA/hemp composites (KGE-02) (mean value, standard deviation in grey). DIN EN ISO 527; Sample 1A; l = 100 mm; Zwick Z020 / 20 kN; 2 mm/min; Video extensiometer; n = 5 (Müssig and Graupner, 2013).

The Young´s modulus was also significantly increased by the use of hemp fibres as compared to the pure PLA matrix. In contrast to the tensile strength no significant differences between the two different types of hemp fibres have been observed. However, the Young´s modulus was increased substantially with an increasing fibre mass content from 20 to 30 % (see Figure 23).

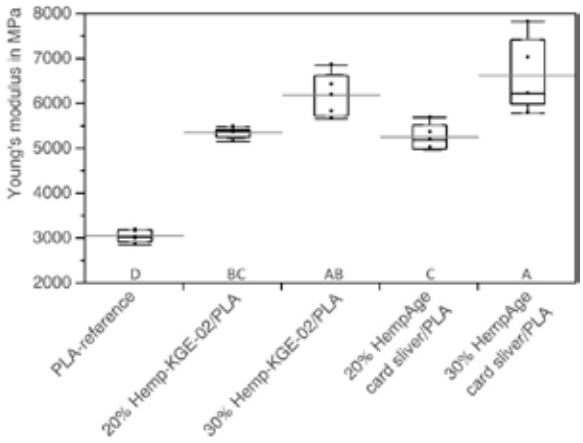

Figure 23. Box-and-whisker diagrams (black): Youngs' modulus of the injection moulded PLA/hemp composites (mean value, standard deviation in grey). DIN EN ISO 527; Sample 1A; l = 100 mm; Zwick Z020 / 20 kN; 2 mm/min; Video extensiometer; n = 5 (Müssig and Graupner, 2013).

The values are on a similar level to those of flax fibre reinforced PLA composites given in Table 1. The investigation of the influence of the fibre mass fraction (20 – 40 %) showed a significant increase of the Young´s modulus compared to the PLA reference. A significant increase of the modulus was obtained by increasing the fibre content from 20 to 30 mass-% but a further rise of the fibre content to 40 % showed no improvement of the Young´s modulus (Figure 24).

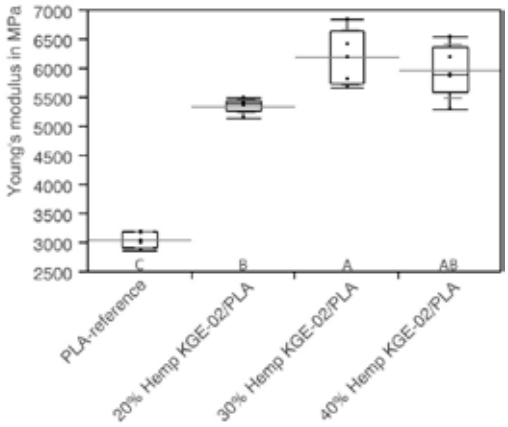

Figure 24. Box-and-whisker diagrams (black): Youngs' modulus of the PLA/hemp composites (KGE-02) (mean value, standard deviation in grey). DIN EN ISO 527; Sample 1A; l = 100 mm; Zwick Z020 / 20 kN; 2 mm/min; Video extensiometer: n = 5 (Müssig and Graupner, 2013).

As shown in Figure 25 the measurement of the unnotched Charpy impact strength showed no improvement by the use of hemp as reinforcement compared to the unreinforced PLA.

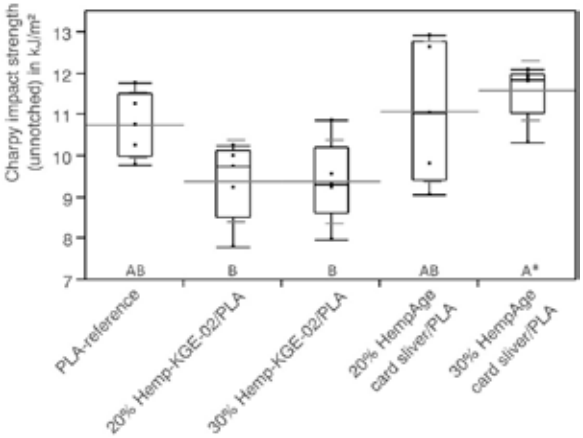

Figure 25. Box-and-whisker diagrams (black): Charpy impact (unnotched) of the PLA/hemp composites (mean value, standard deviation in grey). DIN EN ISO 179; Zwick type 5102; Pendulum: l = 225 mm; Pendulum size: 2 J; n = 5 (Müssig and Graupner, 2013).

The utilization of Hemp KGE-02 lead to lower impact strength values and the use of HempAge card sliver to an impact strength on the level of the pure PLA matrix. No significant differences were determined due to the increasing fibre content. This effect is in good agreement with values for NFCP processed with other compounding techniques. For example Bax and Müssig (2008) measured a lower impact strength of flax fibre reinforced PLA (see Table 1). This effect can be explained by the small elongation of bast fibres.

6. CONCLUSIONS

NFRC have the potential to be used as a structural material to replace technical polymers or glass fibre-reinforced plastics. Depending on the processing technique and the used fibres or the textile preforms composite properties can be adjusted within a wide range. Figure 26 shows the performance playground for flax composites. The illustration contains values for flax composites based on the different composite processing techniques. Flax fibre-reinforced composites show a high potential for a broad range of applications from injection moulded parts up to structural components. Based on the critical review on existing compounding processes, a new compounding concept was developed and realised. In a conventional compounding process the main bottleneck is related to the feeding of the fibres. With the new CMS-compounder this main problem is solved and we are able to feed fibres into the system at any length without special preparation. With the new compounding system it was possible to produce granules from long hemp fibre bundles (length > 40 mm) with fibre mass fractions ranging between 20 and 40% in a PLA-matrix. In the comprehensive survey, it was shown that the CMS compounding technique is very well suited for the compound production of long uncut fibres for further processing in an injection moulding process. The prepared composites have excellent mechanical properties, the tensile strength values are superior to samples which were produced with conventional compounding and injection moulding techniques.

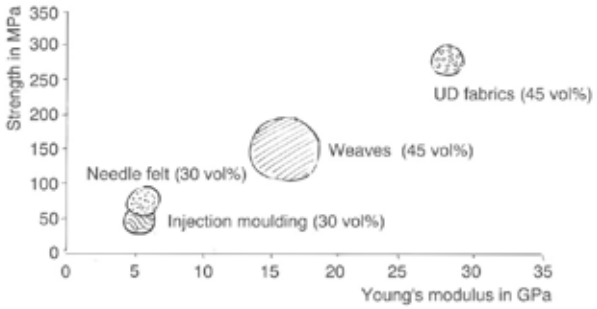

Figure 26. The performance playground for flax composites. Adapted from Verpoest (2012) and Verpoest and Baets (2012).

ACKNOWLEDGEMENTS

The author thanks Ms. Kathina Müssig for her creative work preparing most of the illustrations. I wish to thank Dipl.-Ing. (FH) Nina Graupner, Hochschule Bremen - University of Applied Sciences, Faculty 5 - Dept. for Biomimetics, The Biological Materials Group, Bremen for the close collaboration in the field of NFRC and for her critical comments.

REFERENCES

Ashby, M. F. (2004): Materials Selection in Mechanical Design. 3rd Edition. Oxford: ELSEVIER Butterworth-Heinemann, (0-7506-6168-2)

Ashby, M. F., Jones, D. R. H., Heinzelmann, M. (2007): Werkstoffe 2: Metalle, Keramiken und Gläser, Kunststoffe und Verbundwerkstoffe. 3. Auflage. Heidelberg: Spektrum Akademischer Verlag, (ISBN: 3-8274-1709-0)

Bax, B. and Müssig, J. (2008): Impact and tensile properties of PLA/cordenka and PLA/flax composites Composites Science and Technology, 68, 1601-1607

Baets, J. and Pariset, J. (2012): The range of marketed semi-finished products / preforms, how they are industrialised, and their multisector applications. In: JEC composites conference in partnership with CELC, (Organizers): FLAX AND HEMP FIBRES: A NATURAL SOLUTION FOR THE COMPOSITE INDUSTRY – High-performance operational green-chemistry solutions (Leuven, Belgium, 2012-12-04) Paris, France: JEC and CELC, CD-ROM, Conference Proceedings, 24 pages

Beckmann, F. (2001): Verfahren zum Herstellen von thermoplastisch gebundenem Naturfasermaterial in schütt- und rieselfähiger Form. Europäische Patentschrift: EP 1 307 33 B1 . – in German

Brown, W.J. (1947): Fabric Reinforced Plastics. Cleaver-Hume Press Ltd, London, UK.

Dentel, A., Müssig, J., Bäumer, R. (2012): Optimization of composites using textile structures inspired by nature. In: Technical Textiles (ISSN 0323-3243), Vol. 55, Issue 3, p. E 92 – E 93

Drzal, L.T., Mohanty, A.K., Wibowo, A., Misra, M., Seiler, B.D. (2003): Hemp fiber-reinforced cellulosic plasticbased bio-composites: physical-mechanical and morphological properties evaluation, in 7th International Conference on Woodfiber–Plastic Composites, Forest Products Society, Madison, WI, USA.

Faruk, O., Bledzki, A. K., Fink, H.-P., Sain, M. (2012): Biocomposites reinforced with natural fibers: 2000–2010. In: Progress in Polymer Science. Vol. 37, Issue 11, p. 1552 – 1596

Fink, H.-P., Ganster, J., Lehmann, A. (2011): Herausforderungen der Faserverstärkung von Polymeren aus biobasierten Monomeren. In: DECHEMA and FNR, (Organisation and Editor): DECHEMA / FNR-Workshop - Polymermonomere aus Nachwachsenden Rohstoffen - (31. Oktober - 1. November 2011, DECHEMA-Haus, Frankfurt am Main), DECHEMA, Frankfurt/Main .- in German

Friedrich, K., Evstatiev, M., Angelov, I., Mennig, G. (2007): Pultrusion of flax–polypropylene composite profiles. In: Fakirov, S. and Bhattacharyya, D.: Handbook of Engineering Biopolymers: Homopolymers, Blends and Composites. Hanser Verlag, Munich, Germany, pp. 223–235

Gomina, M. (2012): VIII – Flax & hemp composite applications. In: Reux and Verpoest (2012), pp. 141 – 162.

Graupner, N., Müssig, J. (2010): Technical Applications of Natural Fibres: An Overview. In: Müssig (2010), p. 63 – 71

Graupner, N., Ziegmann, G., Enzler, H., Müssig, (2012): In: J. Bledzki, A. K., Sperber (ed.) PLA/cellulose fibre-reinforced composites: influence of the processing procedure on the mechanical properties - compression moulding versus injection moulding - Biobased materials 9th WPC, Natural Fibre and other innovative Composites, Congress and Exhibition, Hanser Verlag, Munich, Germany

Grove, D.A. (2006): Composite processes, in Handbook of Plastic Processes, ed. by Harper C.A. John Wiley and Sons Inc., Hoboken, NJ, USA.

Haag, K., Müssig, J. (2012): Naturfaser-Pellet-Produktion – Vorstellung der technischen Analyse. In: nova Institut GmbH (Organisation) 2012: Fachtagung Naturfaserpellets. (21. Mai 2012, Maternushaus Köln, Hürth: nova-Institut GmbH, in German

Han, S. O., Karevan, M., Bhuiyan, M. A., Park, J. H., Kalaitzidou, K. (2012): Effect of exfoliated graphite nanoplatelets on the mechanical and viscoelastic properties of poly(lactic acid) biocomposites reinforced with kenaf fibers Journal of Materials Science, 47, 3535-3543

Huber, T., Graupner, N., Müssig, J. (2010): Natural Fibre Composite Processing: A Technical Overview. In: Müssig (2010), p. 407 – 421

Hänninen, T., Hughes, M. (2010): Historical, Contemporary and Future Applications. In: Müssig (2010), p. 385 – 395

Le Duigou, A., Pillin, I., Bourmaud, A., Davies, P., Baley, C. (2008): Effect of recycling on mechanical behaviour of biocompostable flax/poly(L-lactide) composites Composites: Part A: Applied Science and Manufacturing, 2008, 39, 1471-1478

Müssig, J. (2010) (Editor): Industrial Applications of Natural Fibres - Structure, Properties and Technical Applications. Chichester, United Kingdom, John Wiley and Sons, (ISBN 978-0-470-69501-1)

Müssig, J. (2011): Biobasierte polymere Verbundwerkstoffe im Automobilbau. In: DECHEMA & FNR, (Organisation and Editor): DECHEMA / FNR-Workshop – Polymermonomere aus Nachwachsenden Rohstoffen – (31. Oktober – 1. November 2011, DECHEMA-Haus, Frankfurt am Main), DECHEMA, Frankfurt/Main .- in German

Müssig, J., Graupner, N., Oldemeyer, K.-E., Mölleken, H. (2011): Hemp fibre reinforced PLA from cultivation to the final product. In: nova Institut GmbH (Organiser and Editor): 8th International Conference of the European Industrial Hemp Association. Hürth: nova-Institut GmbH, Documentation of the 8th International Conference of the European Industrial Hemp Association (EIHA). nova-Institut (Organizer), Hürth

Müssig, J., Graupner, N., Mader, A., Haag, K. (2012): Natural & Regenerated Cellulose Fibre-Reinforced Plastics. In: nova Institut GmbH (Organiser & Editor): 5th International Congress 2012 on Bio-based Plastics and Composites and Industrial Biotechnology. Hürth: nova-Institut GmbH, Documentation of the 5th International Congress 2012 on Bio-based Plastics and Composites and Industrial Biotechnology. nova-Institut (Organizer), Hürth, 33 pages

Müssig, J., Graupner, N. (2013): Injection moulded hemp fibre-reinforced thermoplastics. In:

nova Institut GmbH (Organiser and Editor): 10th International Conference of the European Industrial Hemp Association (EIHA). Hürth: nova-Institut GmbH (Organiser), Documentation, 30 pages

Müssig, J., Hughes, M. (2012): Reinforcements: fibres. In: Reux & Verpoest (2012), p. 39 – 60

Müssig, J., Schmehl, M., von Buttlar, H.-B., Schönfeld, U., Arndt, K. (2006): Exterior components based on renewable resources produced with SMC technology – considering a bus component as example –. In: Industrial Crops and Products (ISSN 0926-6690), Volume 24, Issue 2, p. 132 – 145

Pickering, K. (ed.) (2008): Properties and Performance of Natural-fibre Composites. Woodhead Publishing Limited, Cambridge, UK.

Prömper, E. (2010): Natural Fibre-Reinforced Polymers in Automotive Interior Applications. In: Müssig (2010), p. 423 – 436.

Reux, F., Verpoest, I. (Editors) (2012): Flax and Hemp fibres: a natural solution for the composite industry. First edition, Paris, France, JEC composites, prepared for JEC by the European Scientific Committee of the CELC, (ISBN 978-2-9526276-1-0).

Rowell, R. M., Sanadi, A. R., Caulfield, D. F., Jacobson, R. E. (1997): Utilization of Natural Fibers in Plastic Composites: Problems and Opportunities. In: Lignocellulosic-Plastics Composites, pp, 23 – 51

Scherübl, B.R., Hintermann, M. (2005): Use of natural-fibre reinforced plastics in automobile exteriors, in 8th International AVK–TV Conference, 27–28 September 2005, Arbeitsgemeinschaft Verstärkte Kunststoffe – Technische Vereinigung e.V. (AVK-TV), Frankfurt am Main, Germany.

van Rooijen, D. (2012): BIOPREG: Umweltfreundlich wie Holz und besser als Stahl? Vortrag zur Veranstaltung „Leichtbau der Zukunft – Biobasierte Verbundwerkstoffe“ Seminar / 3N Niedersachen Netzwerk Nachwachsende Rohstoffe (Werlte, 24. Oktober 2012) 3N (Veranst.), Werlte, .- Vortragsfolien, 45 Seiten

Verpoest, I., Baets, J. (2012): Flax and hemp fibre composites. In: JEC composites conference in partnership with CELC, (Organizers): FLAX AND HEMP FIBRES: A NATURAL SOLUTION FOR THE COMPOSITE INDUSTRY – High-performance operational green-chemistry solutions (Leuven, Belgium, 2012-12-04) Paris, France: JEC and CELC, CD-ROM, Conference Proceedings, 17 pages

Verpoest, I. (2012): I – A general introduction to composites, highlighting the advantages of flax & hemp composites. In: Reux and Verpoest (2012), pp. 15 – 37.

Ziegmann, G., Elsabbagh, A. (2012): VI – Production techniques for natural fibre polymer composites. In: Reux and Verpoest (2012), pp. 99 – 117

BIO-INSPIRED ELASTIC COMPOSITES OF NANO CRYSTALLINE CELLULOSE AND CELLULOSE BINDING RESILIN

A. Rivkin[*], S. Meirovitch[*], S. Roth[**], S. B. Arinos[*], Y. Nevo[*], O. Dgany[**], Itan Preis, D. L. Kaplan[***], O. Shoseyov[*] and S. Lapidot[****]

[*]The Robert H. Smith Faculty of Agriculture, Food and Environment, the Hebrew University of Jerusalem, Rehovot 76100, Israel
[**]Collplant Ltd. 3 Sapir St , Ness-Ziona 74140, Israel
[***]Department of Biomedical Engineering, 4 Colby Street, Tufts University, Medford, MA 02155, United States
[****]Melodea Ltd. The Robert H. Smith Faculty of Agriculture, Food and Environment, the Hebrew University of Jerusalem, Rehovot 76100, Israel

ABSTRACT

The arthropod cuticle and the plant cell wall are examples of remarkable composite materials that support survival in nature. Inspired by the elasticity of insects cuticle and the strength of plants cell wall, we hypothesized that nanocellulose and resilin composites would display useful mechanical properties featuring both strength and elasticity. *E. coli* was genetically engineered to produce recombinant resilin fused to a cellulose binding domain (Resilin-CBD) and the protein affinity to cellulose was shown. Heat and acid treatments applied on cellulose powder enabled the production of Nano Crystalline Cellulose (NCC). Two alternative methods for resilin-CBD/NCC composite production were demonstrated: The first involved resilin-CBD infusion into preformed NCC foams. The second involved the mixing of resilin-CBD with NCC suspensions that were subsequently processed into foams. Resilin-CBD/NCC composites displayed 5 to 8-fold increase in Young's modulus compared to pure resilin structures. Moreover, unlike pure NCC structures, the composites displayed a mechanical shape-memory behavior, a feature that is well-known and was observed for the pure resilin structures. This work demonstrates the advantage of the bio-inspired composite approach, which provides materials that work in a synergistic manner originating at the molecular level, thus result in enhanced mechanical properties when compared to the single polymer.

1. INTRODUCTION

1.1 Insights from natural composite materials. In nature, biomaterials usually appear in the form of composites that combine the properties of their constituents in a synergistic manner. There are numerous of high performing natural composites that may serve for us as inspiration (Lapidot, Meirovitch, Sharon, Heyman, and Shoseyov 2012). However, in order to unveil their performances, one must understand the materials molecular structure and chemistry in relation to the composite architecture arrangements. This work was inspired by two biomaterial systems: Cellulose based composites (originated from the plant kingdom) and resilin (originating from the arthropod kingdom).

1.2 Nanostructured cellulose composites. The impressive performance of natural cellulose based composites, such as found in forest trees, has sparked the imagination of scientists towards the development of new materials and applications. The basic structure of cellulose fibrils consists of highly organized crystalline domains that are linked together by less crystalline "amorphous" regions that are considered as the weak links in the fibers. Rånby (1949) was the first to show that controlled acid hydrolysis of cellulose fibers result in the degradation of the amorphous regions and the release of highly crystalline nanocellulose particles (NCC). NCC Young's modulus and tensile strength were estimated to be ~150 GPa and ~10 GPa (respectively), features that make it a promising reinforcing agent in composite systems (Sakurada, Nukushina and Ito 1962). Further technological progress was achieved by Favier, Canova, Cavaille, Chanzy, Dufresne and Gauthier (1995), who combined NCC as a reinforcing agent in latex systems. These composites showed an increase of a three orders of magnitude in the shear modulus of the latex rubbery state. Since then, several nanoscale cellulosic materials were developed (Teeri, Brumer, Daniel and Gatenholm 2007; Hubbe, Rojas, Lucia and Sain 2008; Berglund and Peijs 2010). H_2SO_4 derived NCC is of particular interest. During the hydrolysis process, the NCC are charged with sulfate groups and form stable honey-like liquid crystal suspensions that assist in the processing and manufacturing of nanostructured composites (Samir, Alloin and Dufresne 2005; Siqueira, Bras and Dufresne 2010).

1.3 Cellulose Binding Modules (CBMs). A key issue to be considered while attempting to generate biomimetic composites, is the ability to exploit the molecular recognition between the components, which defines and stabilizes the structure. One of the important molecular recognition mechanisms that evolved in nature is the presence of Carbohydrate Binding Modules (CBMs) which bind structural proteins to polysaccharide scaffolds, such as cellulose in the plant kingdom and chitin in the invertebrate kingdom. For instance: 70% of the proteins isolated from insects cuticles contained the conserved Rebers and Riddiford consensus chitin binding domain (Karouzou, Spyropoulos, Iconomidou, Cornman, Hamodrakas and Willis 2007), displaying the importance of CBMs in interfacing between the fibrous polysaccharide scaffold and the matrix proteins in the natural cuticle composite. With respect to cellulose: many microorganisms developed an array of carbohydrate degrading enzymatic complexes, termed "Cellulosome" (Bayer, Belaich, Shoham and Lamed 2004). Apart from the hydrolytic units, these complexes usually contain Carbohydrate Binding Modules (CBMs) that anchor the hydrolytic enzymatic complexes to the cellulose matrix. The first CBM that was cloned and displayed independent binding affinity to cellulose is the Cellulose Binding Domain of *Clostridium cellulovorans* bacteria (CBDclos) (Shoseyov and Doi 1990; Shoseyov, Takagi, Goldstein and Doi 1992; Goldstein, Takagi, Hashida, Shoseyov, Doi, and Segel 1993). This discovery laid the foundation for CBMs utilization in numerous biotechnological applications aiming towards cellulose fiber modifications, immobilization of proteins to cellulose and for production of cellulose-CBM fusion proteins composites (Shoseyov, Shani, and Levy 2006).

1.4 Resilin. Resilin is a polymeric rubber-like protein secreted by insects to specialized cuticle regions, in areas where high resilience and low stiffness are required for locomotion. Resilin has been identified throughout the arthropod kingdom, located within structures with cyclic locomotion where energy storage and long-range elasticity are needed, such as the flight system of locusts (Weis-Fogh 1960), and the sound producing organ of cicadas (Young and Bennet-Clark 1995). One of the most important roles of resilin is in insect jumping, and it was identified in many jumping organs of insects, such as cat fleas (*C. felis*), cicadas, planthopper insects and froghopper insects (*Philaenus*) (Bennet-Clark and Lucey 1967; Burrows, Shaw and Sutton 2008; Burrows 2009; Burrows 2010). Fleas for instance have resilin pads between the stiff cuticular struts of the metathorax above the hind legs. The froghopper and plant hopper are the champion jumpers of all insects. The jumping organ of these insect, the pleural arch, is a composite structure containing approximately 80% chitinous cuticle and 20% resilin. Burrows et al. (2008) showed that resilin by itself is not sufficient to store much energy and must act as constituent of a composite with chitin for the purpose of jumping. The mechanism requires the combination of the high elasticity of resilin with the strength of chitin in a composite manner. Therefore, it enables insects to rapidly restore body shape as well as most of the energy required for the next mechanical movement.

We have previously reported the efficient production, structural and mechanical characterization of recombinant *D. melangaster* resilin proteins (Qin, Lapidot, Numata, Hu, Meirovitch, Dekel, Podoler, Shoseyov, and Kaplan 2009). Moreover, we have demonstrated the specific chitin binding property of resilin-fused to Chitin Binding Domain (resilin-ChBD) which is important for achieving molecular interfaces between chitin and resilin. Recently, we showed that the resilin monomers and in particular exon 1, are intrinsically elastic and resilient, at the nanometric level. Moreover, we have developed novel crosslinking methods, such as citrate modified photo-Fenton, that led to highly elastic resilin matrices (Qin, Rivkin, Lapidot, Hu, Preis, Arinus, Dgany, Shoseyov and Kaplan 2011). In the current work we hypothesized that resilin containing a CBD, instead of a ChBD, will form nanocomposites with cellulose that will result in structures having enhanced mechanical properties.

2. MATERIALS AND METHODS

2.1 Production of NCC suspensions. NCC production was based on a method previously described (Bondeson, Mathew and Oksman 2006). Micro Crystalline Cellulose powder (MCC, Avicel®) was suspended in H_2SO_4 (62 wt. %) to reach 1:30 (MCC to acid weight ratio, respectively). The suspension was brought to 60 ^oC and stirred for 30 min. followed by centrifugation (10,000 rpm, 10 min.). Acidic supernatant was removed and the pellet was resuspended in deionized water (DIW). Washing and resuspension cycles were repeated 4 to 5 times, until the supernatant coming out of the centrifuge was turbid (pH~2.5). Following the final wash, NCC pellet was resuspended in DIW (to reach 2.5 wt. % final concentration) and stored (4 ^oC) till used. Finally, the white-opaque suspension was sonicated (Misonix Ultrasonic Processor XL 2015 probe sonicator 1500 V rms (max) 20 KHz (nom) (Misonix Incorporated, NY, USA) mounted with 0.5" tip operated at 80% amplitude, until the NCC suspension became optically clear.

2.2 Birefringence analysis of NCC suspensions. NCC containing vials were placed between two cross-polarizers and a tungsten lamp was served as a light source.

2.3 Transmission Electron Microscopy (TEM) of NCC. NCC suspension at concentration of 0.2% (wt. %) was applied to glow-discharged, carbon-coated copper 400-mesh grids and stained with uranyl acetate (2% w/v). The images were visualized on an FEI Tecnai-12 microscope.

Images were recorded with a SIS Megaview III camera (Electron Microscopy Unit, Weizmann Institute of Science, Rehovot, Israel).

2.4 Preparation of NCC foams. Clear NCC suspensions (2.5 wt. %) were cast into molds, frozen (-70 ^{o}C) and finally freeze dried. Dry and porous NCC foams were released from the molds for further analysis and treatments.

2.5 Scanning Electron Microscopy (SEM) of NCC foams. Foam samples were subjected to gold spattering (12mA, 6min) using S150 sputter coater (Edwards) and finally analyzed with a JEOL JEM 5410 LV microscope (Electron Microscopy Unit, Weizmann Institute of Science, Rehovot, Israel).

2.6 Construction, expression and purification of His Tag-Resilin-CBD (6H-17res-CBD). The *17-res* gene (previously described by Qin et al. 2009) was cloned by digesting pGEM-T Easy-17res plasmid with *Nco*I, *BamH*I followed by cloning of the gene into pET3d (Novagen, EMD Chemicals, Inc. CA) upstream to the *CBD* gene (previously described by Goldstein et al. 1993). The chimeric *17res-CBD* was then digested with *Nco*I, *EcoR*I and cloned into pHis-parallel3 vector. 6H-17res-CBD was expressed in *E. coli* strain BL21 (DE3) and purified by methods as previously described for 17res purification (Qin et al. 2009). Pure 17res-CBD proteins were lyophilized and stored (4^{o}C) till used.

2.7 Western blot analysis to 6H-17res-CBD. Proteins were transferred to nitrocellulose membranes using standard protocols. The proteins were detected using CBD primary antibody and anti-rabbit alkaline-phosphates conjugated secondary antibodies. The membranes were developed with BCIP/NBT (Sigma-Aldrich) reagent following standard protocols.

2.8 Analysis of cellulose binding activity of 17res-CBD. MCC dry powder was suspended in phosphate buffered saline (PBS) followed by centrifugation. The supernatant was discharged and the recovered wet MCC pellet was incubated with 17res-CBD (300:1 weight ratio, respectively) in the presence of PBS (30 min. RT. gentle shaking) followed by centrifugation. The supernatant (unbound 17res-CBD) was removed and the pellet (MCC bound 17res-CBD) was washed (X3) with PBS. Finally, supernatant and washed pellet were Sodium Dodecyl Sulfate Polyacrylamide Gel Electrophoresis (SDS-PAGE) analyzed following standard protocols.

2.9 Photo-polymerization of 17res-CBD. Photo- polymerization of 17res-CBD was based on a method previously applied on rec1-resilin (Elvin, Carr, Huson, Maxwell, Pearson, Vuocolo, Liyou, Wong, Merritt, and Dixon 2005). Lyophilized 17res-CBD was dissolved in Sodium phosphate buffer (20 mM, pH 7.5) to a desired concentration (50 to 200 mg/mL). Polymerization was performed by mixing (in dark) 17res-CBD solutions with the photo initiator $Ru(bpy)_3Cl_2$ (2 mM final) and ammonium persulfate (10 mM final), casting the solution into Teflon molds followed by exposure to halogen light (5 min).

2.10 Carbodiimide/PEG-amine based polymerization of 17res-CBD. 8-arm amine-terminated polyethylene glycol (PEG-amine), 1-ethyl-3-(3-dimethylaminopropyl) carbodiimide (EDC) and N-hydroxysuccinimide (NHS) polymerization of 17res-CBD was based on a method previously described (Ward, Kelly, Wang, Zeugolis and Pandit 2010). Lyophilized 17-res-CBD was dissolved (200 mg/mL) in sodium phosphate (20 mM, pH 7.5). Protein solutions (200 µL) were cast into ELISA plate wells (pre-treated with Sigmacote®, Sigma-Aldrich) that served as molds. The solutions were frozen (-70 ^{o}C) followed by freeze drying (Overnight) and resulted in foam formation. Foams were then infused (3 h. RT, dark) in iso-propanol (90% v/v) containing EDC (50mM), NHS (6mM) followed by second freeze drying (Overnight). Next, foams were

incubated in 8-arm amine-terminated PEG (10% w/v) in the presence of PBS (1 h. RT) followed by two washings steps with DDW. Subsequently, the foams were infused again (3 h. RT dark) with the iso-propanol (90% v/v) containing EDC (50mM) and NHS (6mM). Finally, the foams were washed with DDW and were allowed to dry (RT) till constant weight.

2.11 Production of 17res-CBD/NCC composites. Composites were prepared by two alternative methods termed: "mixed" and "infused". The “mixed” composites were prepared as follows: NCC suspension was carefully titrated to pH 7 with NaOH (1N) prior to the final sonication step. Subsequently, lyophilized 17res-CBD were dissolved (200 mg/mL) in the NCC (2.5 wt. %) suspensions. The materials were mixed and cast (250 µL) into Eppendorf tube caps that served as molds. The suspensions were frozen (-70 ^{o}C) followed by freeze drying (Appendix A. Fig A1, b). Polymerization of the resulting 17res-CBD/NCC foams was performed as described above (see 2.10). The “infused” composites were prepared as follows: NCC foams were initially produced by casting (250 µL) neutralized NCC suspension (2.5 wt. %) into ELISA plate wells followed by freezing (-70 ^{o}C) and freeze drying. Resulting cylindrical foams were rescued from the well and stored (4 ^{o}C) till used. Lyophilized 17res-CBD was dissolved (200 mg/mL) in sodium phosphate (20 mM, pH 7.5) followed by drop-wise addition to the NCC foams till fully saturated (Appendix A. Fig A1, a). Subsequently, 17res-CBD/NCC wet foams were frozen (-70 ^{o}C) and freeze dried. The polymerization was performed as described above (see 2.10).

2.12 Compression tests. Mechanical compression tests to cylindrical samples were performed using Mecmesin MultiTest 1-i computerized tensile tester (Mecmesin Ltd. Slinfold, UK) with ILC load cell (10N) set on compression test mode (2 mm/min). Prior to compression tests, samples were saturated (1 h. RT) in sodium phosphate (20 mM, pH 7.5) followed by vacuum degassing (5 min) to ensure full saturation. In order to assess the property of structure elasticity, each sample was consecutively compressed (three times) and initial lengths, Young's modulus and extensibility were compared for each test within the same sample.

3. RESULTS

3.1 Production of NCC suspensions and foams. NCC was produced by H_2SO_4 hydrolysis of 200µm MCC powder. The process involved MCC hydrolysis in controlled temperatures and acid concentration, washing cycles in water followed by sonication. A clear and transparent viscous NCC suspension (2.5 wt. %) was obtained (Fig 1a) that exhibited a liquid crystal optical property of birefringence under cross polarized light (Fig1b, right). TEM analysis to diluted NCC suspensions revealed the "whiskers" rod-like nanoparticles structures with typical dimensions of 200 nm in length and 15 nm in width (Fig 1c). NCC foams produced by casting the suspensions into molds followed by freezing and freeze drying resulted in highly porous foams (Fig 1d). SEM analysis of the opened cell NCC foams revealed networks of smooth nanopaper sheets, stacked upon each other showing highly ordered intra-structure (Fig 1e).

3.2 Cloning, expression and purification of recombinant 6H-17res-CBD. The chimeric *6H-17res-CBD* gene (Fig 2a) was composed of *D. Melnogaster* resilin exon1 17 elastic repeats (Qin et al. 2009) C-terminal fused to *C. Cellulovorans* Cellulose Binding Domain (Goldstein et al 1993) and the gene authenticity was verified by DNA sequencing (Appendix B). SDS-PAGE analysis of total bacteria showed high expression of 6H-17res-CBD following IPTG addition (Fig 2b) and western blot analysis further confirmed the 6H-17res-CBD expression (Fig 2c). Protein purification was carried out using chromatography methods (Qin et al. 2009) which resulted in highly purified 17res-CBD as shown by SDS-PAGE analysis (Fig 2d, left lane T). Protein final yields (analyzed via conventional colorimetric methods) were estimated to be ~100 mg purified res-CBD per 1L bacteria growth medium (Data not shown). Specific cellulose

binding was evident for 17res-CBD (Fig 2d, left). In contrast, cellulose binding was not evident for the 17res (that did not contain to CBD) and served as a negative control (Fig 2d, right).

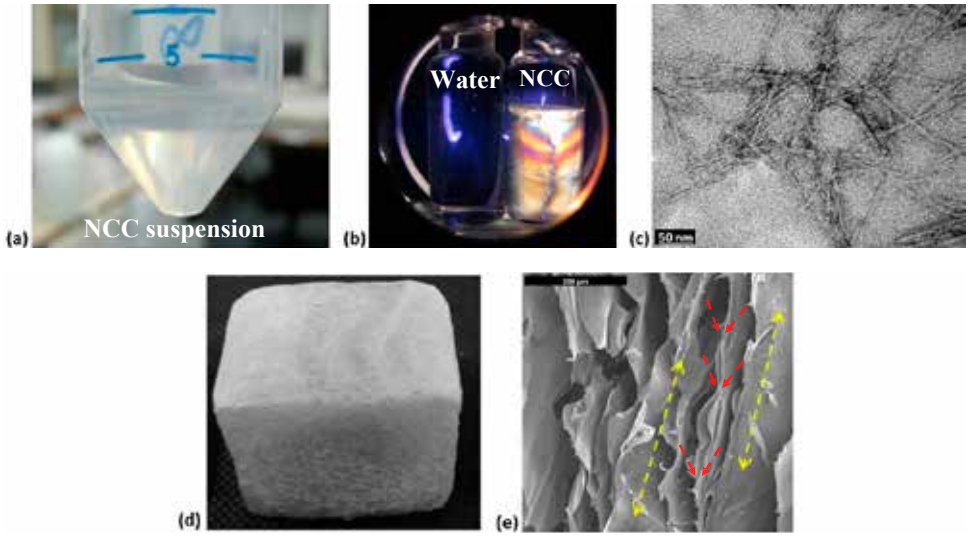

Fig. 1. Transparent NCC liquid crystal suspension (a) displays birefringence under cross polarized light (b, right) and rod-like structure revealed by TEM (c). Light-weight NCC foam (d) open cells internal order, sheet-like structure reviled by SEM (e). Red arrows mark the NCC thin sheets and yellow arrows mark the order direction of the NCC sheets.

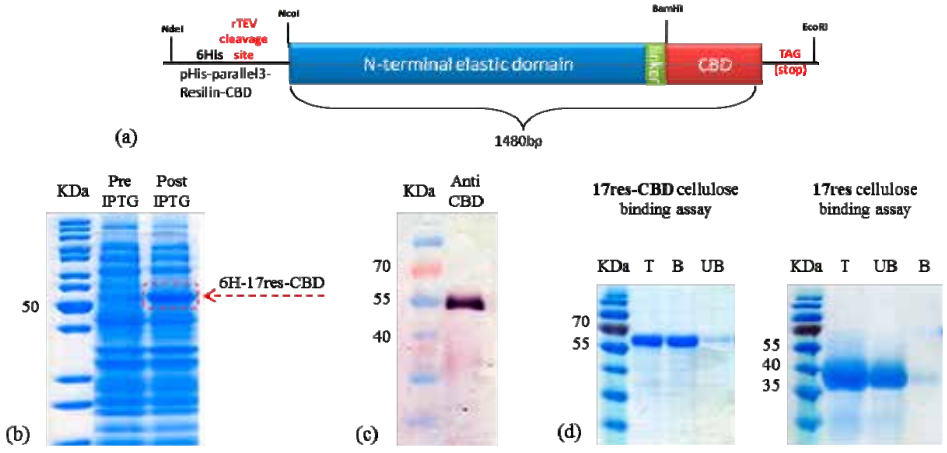

Fig. 2. Scheme of the *6H-17res-CBD* gene (a). SDS-PAGE analysis of total bacteria pre and post IPTG addition that induced 6H-17res-CBD expression (b). Western blot analysis of recombinant 17res-CBD protein against CBD primary antibody (c). SDS-PAGE analysis of cellulose binding assay to purified 17res-CBD (d, left) and to purified 17res (d, right). T; total and purified protein pre cellulose binding. B; cellulose bound proteins. UB; Unbound proteins. Mark that almost all of the 17res-CBD was found in the bound fraction showing specific binding property to cellulose (d, left, lane B) while the 17res variant showed only minimal non-specific binding to cellulose (d, right, lane B).

3.3 Production of 17res-CBD/NCC cross-linked composites. Composites were obtained using two alternative methods. The first, termed "mixed" composites involved the dissolving of a freeze dried 17res-CBD in NCC suspension followed by protein polymerization and foam processing steps. The second, termed "infused" composites involved the infusion of 17res-CBD solution in pre-formed NCC foam followed by protein polymerization and freeze drying steps. Photo-polymerization of 17-res-CBD/NCC composites by the Ru/APS system resulted in highly elastic structures (Fig 3 lower panel). However, in some cases the outer surface of the structure turned opaque and blocked the penetration of light into the foam. As a result, only the outer layer of the foam was polymerized while the inner parts remained in a solution state, resulting in an undesirable “soufflé” like structures. Due to these drawbacks, alternative routes for polymerization were sought for recombinant resilin.

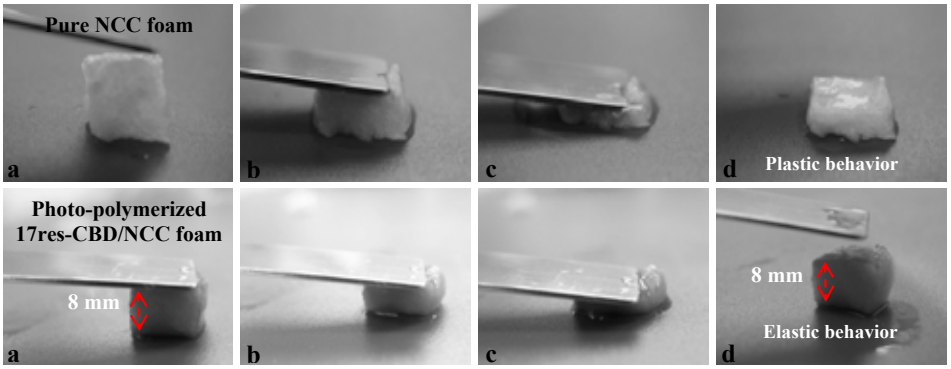

Fig. 3. Qualitative compression tests to pure NCC foams and 17res-CBD/NCC composites foam. Control NCC foam displays plastic deformation and low elasticity when compressed by spatula (Upper panel, a-d). In contrast, photo-polymerized 17res-CBD/NCC foam displays high elasticity (Lower panel, a-d).

Based on the work of Ward et al. (2010), a chemical method was developed for the polymerization of resilin and resilin/NCC composites. The method involved the activation of resilin carboxy groups (in the form of EDC/NHS active esters) and subsequently reaction with free primary amines (originated from the 8 arms PEG) to result in new amide bonds formation, thus protein crosslinking. In contrast to the photo-polymerization approach, this technique was light independent and enabled the production of highly repeatable and homogenous 17res-CBD/NCC composite foams that were also highly elastic. The composites cylindrical structure and dimensions are presented in Appendix A. Table A1. All the samples were tested for compression after being saturated in sodium phosphate buffer (20 mM, pH 7.5). Polymerized pure 17res-CBD, pure NCC foams and 17res (without the CBD)/NCC foams were also tested and served as controls.

3.4 Mechanical compression tests. Typical stress/strain curves (Fig 4) were generated from the recorded data and were used for calculation of the elastic modulus of the samples (Fig 5). During the tests, a clear difference in the performance of the samples was observed.

The calculated Young's modulus values of the pure 17res-CBD polymerized by the EDC/NHS/PEG-amine method were 6.9 kPa ± 2.3 kPa, similar to the results presented previously for the Ru-APS photo-polymerization of res1-resilin (Elvin et al. 2005). Moreover, pure 17res-CBD samples showed high elasticity and resilience and immediately recovered to their original shape following each of the three consecutive compressions. The calculated

Young's modulus values of the pure NCC foams were 16 kPa ± 4.5 kPa. However, these foams exhibited a plastic behavior (for strains >10%) and did not recover to their original shape following stress removal. (Fig 3, Fig 4; lower right corner present typical behavior under compression stress). Hence, each of the pure NCC foam was compressed only once.

Compression to 17res-CBD/NCC composites, (either “mixed” or “infused”) resulted in similar recovery and elastic behavior to the pure 17res-CBD (Fig 4). However, their calculated Young's modules were significantly higher (5 to 8-fold) with values of 26.3 kPa ±7.7 kPa for “mixed” and 56.7 kPa ± 21.4 kPa for “infused” (Fig 5). Moreover, 17res-CBD/NCC “mixed” composites generated nearly perfect overlapping stress/strain curves, like in the case of pure 17res-CBD, and the Young's modulus was insignificantly decreased. Interestingly, when 17res-CBD/NCC “infused” composites were consecutively compressed a different phenomenon was observed shown by a shift in the curves and the modulus decreased from the initial 56.7 kPa to values about 27 kPa, similar to the “mixed” composite. As mentioned above (section 3.3) 17res (without the CBD)/NCC foams were also tested for compression and served as control to the 17res-CBD/NCC composite foams. Like in the case of pure NCC foams, the 17res /NCC foams displayed plastic behavior (for strains >15%) and did not recover to the original state when the stress was removed (Fig 4, lower right corner present behavior under compression stress). Hence, like in the case of pure NCC foams 17res/NCC foams were compressed only once.

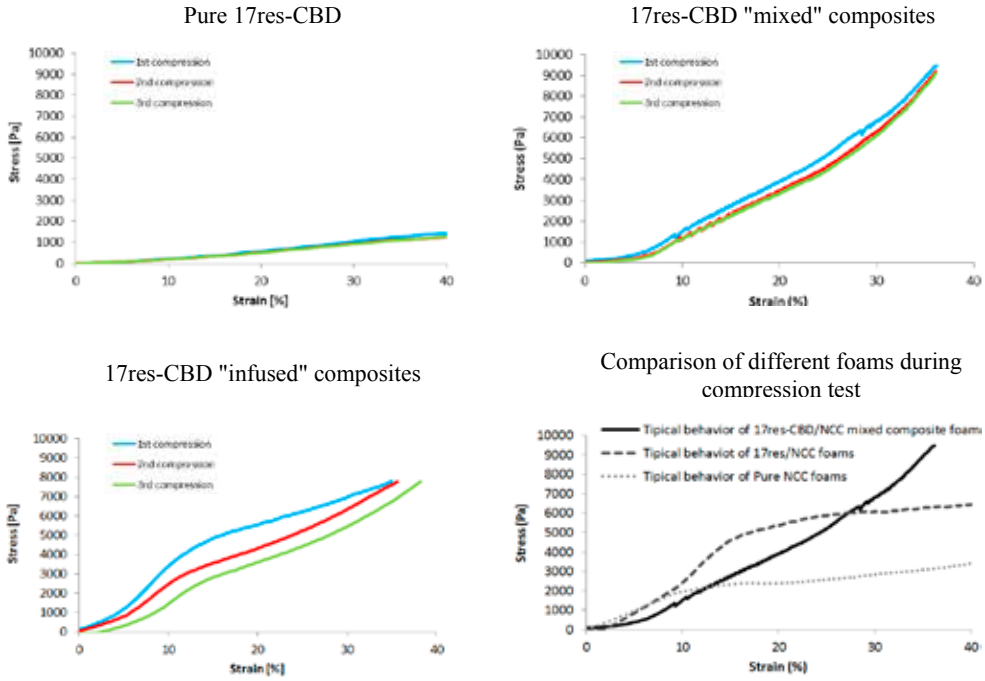

Fig. 4. Stress/strain curves of three consecutive compression tests to polymerized 17res-CBD, "mixed" and "infused" 17res-CBD/NCC polymerized composites. The blue, red and green curves represent the samples behavior at the first, second and third compression (respectively). Comparison of typical stress/strain curves of pure NCC, 17res/NCC and 17res-CBD/NCC "mixed" composite foams is presented at the lower right corner.

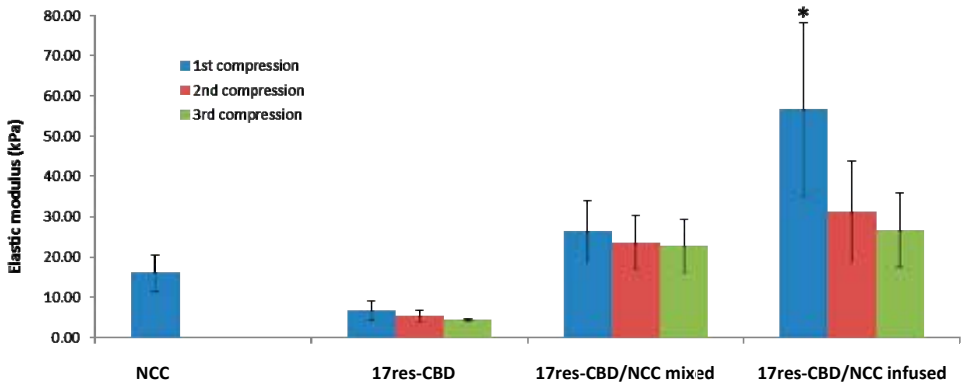

Fig. 5. Elastic modulus of the samples consecutively compressed three times. Pure NCC foams could be compressed only once without recovery. 17res-CBD and 17res-CBD/NCC "mixed" composites maintained modulus values with insignificant decrease whereas following the first compression the modulus of "infused" 17res-CBD/NCC decreased to the level of the "mixed" composites.

4. DISCUSSION

The chimeric protein 17res-CBD was successfully cloned and purified from *E. coli* and its specific affinity to cellulose was shown (Fig 2 a, d).

The Ru/APS, a visible light-dependent system mediating di-tyrosine cross-links (Elvin et al. 2005), was initially chosen for the resilin polymerization. During our research, we found that this method was not suitable for polymerizing resilin/NCC composites in the form of opaque foams or transparent suspensions. The reason for that is probably because light penetration (initiating the photo-sensitizing reaction) was possible mostly at the outer surface of the composites. Moreover, in some cases where transparent suspensions of 17res-CBD/NCC were illuminated, the outer surface became opaque and blocked the further penetration of light deeper into the sample. Hence, both "mixed" and "infused" composites were resulted in having an outer cured shell with an inner core of soluble non-cured resilin. Consequently, an alternate crosslinking method that was not light or enzyme dependent was investigated. Initially we were looking for di-tyrosine forming agents in order to emulate the natural polymerization of resilin. Recently, Charati, Ifkovits, Burdick, Linhardt and Kiick (2009) produced recombinant resilin like peptides (RLP) where the tyrosine amino acids were replaced with phenylalanine and lysine. The RLP were cross-linked via [tris(hydroxymethyl)phosphino] propionic acid forming covalent bounds with primary and secondary amines originated from RVP lysine amino acid side chines. The resulted RLP cross-linked polymers were shown to be highly elastic. Furthermore, we have previously showed by nanoindentation that resilin monomers have similar values of resilience and modulus of elasticity to the cross-linked resilin (Qin et al. 2011; Qin et al. 2009), suggesting that the resilin is intrinsically elastic at the nanometric level. Therefore, we assumed that other (and non di-tyrosine based) crosslinking methods will potentially result in highly elastic and resilient materials. Consequently, we polymerized 17res-CBD and 17res-CBD/NCC composites into highly elastic structures using the EDC/NHS/PEG-amine system (adopted from Ward et al. 2010). In this method, a multifunctional (8 arms) PEG-amine was covalently conjugated to the resilin negatively charged amino acid side chains (mediated by EDC/NHS-active esters formation).

Previous reports on the elastic modulus of resilin proteins indicated values of 2.5 kPa for recombinant resilin (Elvin et al. 2005) and 2 MPa for natural samples of dragonfly tendon (Gosline, Lillie, Carrington, Guerette, Ortlepp and Savage 2002; Vincent and Wegst 2004). In this work, 17res-CBD proteins, polymerized by EDC/NHS/PEG-amine, were calculated for elastic modulus values of 7 kPa (Fig 5). Our results are closer to those reported by Elvin et al. (2005). In addition, the fact that the elastic modulus of 17res-CBD was similar to those previously reported for recombinant resilin suggests that the addition of CBD did not alter the mechanical properties of the protein. We have previously described an alternative method for photo-polymerization of resilin utilizing the citrate modified photo-Fenton (pF) reaction. In this case, samples were shown to be highly resilient with elastic modulus values of 22.6 kPa (Qin et al. 2011). As discussed in Qin et al. (2011), pF polymerization is propelled by hydroxyl radical reaction and result in the formation of highly cross-linked complexes. Hence, may explain the higher modulus value compared to those obtained by EDC/NHS/PEG-amine or Ru/APS polymerization. A possible explanation for the significantly higher modulus of the natural resilin samples is either the presence of residual cuticular chitin that increased stiffness or different hydration levels of the tested samples. These results shed some light regarding the significantly lower modulus values of recombinant resilin samples compared with the results obtained from natural samples, but requires further investigation.

NCC liquid crystal suspensions were produced from MCC. The average dimensions of the particles were 15 nm width and 200 nm length as viewed by TEM. NCC foams were produced by suspension freezing followed by freeze drying (Fig 1, a-c). These foams were structured into laminated planes. The sheet laminated planes are micrometer in size, while the individual sheets within these features are 10-20 nm in size, about that of a single crystalline cellulose particle (Fig 1 d). NCC tends to self-assemble into nematic planes, a structure maintained when the water is removed (de Souza Lima and Borsali 2004) and under normal evaporation conditions would result in film formation. However, when the suspension is frozen a cryo-concentration affects occur, where the forming ice crystals push the cellulose nanoparticles toward each other, forcing local aggregation of the NCC while preventing them from forming a film. Therefore, a porous 3D network is formed.

Composites of NCC and recombinant 17res-CBD were produced by two routes. The first route (“mixed”) involved blending of NCC liquid crystal suspensions with concentrated protein solutions that were further polymerized. The second route (“infused") involved the initial formation of NCC 3D network foam followed by protein infusion and polymerization. Production of composites in the latter manner was in part analogous to the natural assembly of the resilin-chitin composites in nature, where the resilin is secreted and polymerized into the pre-existing chitin scaffold (Vincent et al. 2004). As discussed above, a novel method for resilin polymerization was developed, based on the EDC/NHS/PEG-amine system that enabled the production of composites that combined high strength and elasticity in a similar manner to natural resilin-chitin structure. 17res-CBD/NCC composites displayed a significant increase in Young's modulus, between 5 to 8-fold, compared to pure resilin polymers while retaining the high elasticity and the mechanical shape memory property (Fig 4 and 5). In contrast, samples prepared by the 17res variant (which did not contain the CBD) exhibited plastic deformation pattern when compression forces were applied to them. Moreover, these samples did not return to their original shape when the stress was removed, as in the case of pure NCC foam, hence could be compressed only once (Fig 4). Supported by the cellulose binding assay (Fig 2d, left), we assume that the absent of the CBD fusion partner in the 17res variant resulted in poor affinity to the NCC fibers. Hence, the 17res variant was not retained on the NCC sheets during cross-linking procedure that involved several solvent immersions and washing steps. The mechanical improvement of the 17res-CBD/NCC composites is therefore attributed to the high affinity and

more intimate interface of CBD-fused resilin to the cellulose fibers. These results also emphasize the importance of the ChBD in the assembly of the natural chitin-resilin composites within arthropods.

Composites produced by the “mixed” and “infused” methods displayed different reactions to compressive stress. The modulus of the “mixed” composites was around 26 kPa and was conserved during repetitive compressions (Fig 5). “infused” composites, produced by casting of 17res-CBD solutions on pre-formed NCC foams, were calculated for an average elastic modulus of 57 kPa (for the first compression) that was decreased to the same values as the “mixed” composites (for the second and third compression). We suggest that when the NCC are homogenously suspended in the resilin solution, as in the case of the “mixed” composites, they form a relatively random network and act as standard nanoparticle reinforcements (Samir et al. 2005). On the other hand, the pre-formation of the highly ordered 3D NCC network in the “infused” composites resulted in extra strengthening of the structure. When these structures were compressed beyond a threshold, the 3D network partially failed and the modulus dropped, although the NCC maintained some of the reinforcing affect and the composite maintained elasticity and mechanical shape memory.

The prefabricated scaffold approach presented in the ”infused” composites resembles that presented by Capadona, Van Den Berg, Capadona, Schroeter, Rowan, Tyler and Weder (2007) who prepared NCC/ethylene oxide–epichlorohydrin copolymer by forming an initial NCC scaffold that was embedded with the polymer resulting in improved mechanical properties. One of the main goals of that research was to solve the problem of equal dispersion of NCC particles in organic matrix. In the case of resilin, the hydrophilic nature of the protein enabled good dispersion as shown in the "mixed” composites. In relation to the natural resilin/cuticle composites, the results presented here emphasize the importance of the ChBD in the assembly of the natural resilin/chitin composites within arthropods and show that the fabrication method plays a major role in the final performance of the composites, as recently reviewed by Moutos and Guilak (2008).

As discussed in the introduction, Burrows et al. (2008) showed that resilin by itself is not sufficient to store the required energy for the jumping needs of insects, and must act as a composite with the chitin. The biomimetic structures that were produced in the current work demonstrate that such composites can combine high elasticity with high strength and load transfer. Such composites could withstand significantly higher stresses as in the jumping mechanism of insects compared with pure resilin. Further analysis should be performed in order to study the different properties of the materials at all length scales to provide additional insight into the performance of these materials in natural and artificial systems. Future research should also focus on tailoring the mechanical properties of such composites according to required applications, such as in biomedicine as well as in sports, automotive, construction and other fields, and as a bio-based replacement for synthetic materials.

ACKNOWLEDGEMENTS

The research was supported by the United States – Israel Binational Science Foundation (BSF) grant No. 2010456.

REFERENCES

Bayer, E.A., Belaich, J.P., Shoham, Y., and Lamed, R. (2004). The cellulosomes: multienzyme machines for degradation of plant cell wall polysaccharides. Annu Rev Microbiol. 58, 521-554.

Bennet-Clark, H., and Lucey, E. (1967). The jump of the flea: a study of the energetics and a model of the mechanism. J Exp Biol. 47, 59-76.

Berglund, L.A., and Peijs, T. (2010). Cellulose biocomposites- from bulk moldings to nanostructured systems. MRS Bull. 35, 201-207.

Bondeson, D., Mathew, A., Oksman, K. (2006). Optimization of the isolation of nanocrystals from microcrystalline cellulose by acid hydrolysis. Cellulose. 13, 171-180.

Burrows, M. (2009). How fleas jump. J Exp Biol. 212, 2881-2883.

Burrows, M. (2010). Energy storage and synchronisation of hind leg movements during jumping in planthopper insects (Hemiptera, Issidae). J Exp Biol. 213, 469-478.

Burrows, M., Shaw, S., and Sutton, G. (2008). Resilin and chitinous cuticle form a composite structure for energy storage in jumping by froghopper insects. BMC Biol. 6, 41-56.

Capadona, J.R., Van Den Berg, O., Capadona, L.A., Schroeter, M., Rowan, S.J., Tyler, D.J., and Weder, C. (2007). A versatile approach for the processing of polymer nanocomposites with self-assembled nanofibre templates. Nat Nanotechnol. 2, 765-769.

Charati, M.B., Ifkovits, J.L., Burdick, J.A., Linhardt, J.G., and Kiick, K.L. (2009). Hydrophilic elastomeric biomaterials based on resilin-like polypeptides. Soft matter. 5, 3412-3416.

de Souza Lima, M., and Borsali, R. (2004). Rodlike cellulose microcrystals: Structure, properties, and applications. Macromol Rapid Commun. 25, 771-787.

Elvin, C., Carr, A., Huson, M., Maxwell, J., Pearson, R., Vuocolo, T., Liyou, N., Wong, D., Merritt, D., and Dixon, N. (2005). Synthesis and properties of crosslinked recombinant pro-resilin. Nature. 437, 999-1002.

Favier, V., Canova, G.R., Cavaille, J.Y., Chanzy, H., Dufresne, A., and Gauthier, C. (1995). Nanocomposite materials from latex and cellulose whiskers. Polym Adv Technol. 6, 351-355.

Goldstein, M.A., Takagi, M., Hashida, S., Shoseyov, O., Doi, R.H., and Segel, I.H. (1993). Characterization of the cellulose-binding domain of the clostridium-cellulovorans cellulose-binding protein-A. J Bacteriol. 175, 5762-5768.

Gosline, J., Lillie, M., Carrington, E., Guerette, P., Ortlepp, C., and Savage, K. (2002). Elastic proteins: biological roles and mechanical properties. Philos Trans R Soc Lond B Biol Sci. 357, 121-132.

Hubbe, M., Rojas, O., Lucia, L., and Sain, M. (2008). Cellulosic nanocomposites: A review. BioResources. 3, 929-980.

Karouzou, M., Spyropoulos, Y., Iconomidou, V., Cornman, R., Hamodrakas, S., and Willis, J. (2007). Drosophila cuticular proteins with the R&R Consensus: annotation and classification with a new tool for discriminating RR-1 and RR-2 sequences. Insect Biochem Mol Biol. 37, 754-760.

Lapidot, S., Meirovitch, S., Sharon, S., Heyman, A., and Shoseyov, O. (2012). Clues for biomimietics from natural composite materials**.** Nanomedicine (Lond). 9, 1409-1423.

Moutos, F., and Guilak, F. (2008). Composite scaffolds for cartilage tissue engineering. Biorheology. 45, 501-512.

Qin, G., Lapidot, S., Numata, K., Hu, X., Meirovitch, S., Dekel, M., Podoler, I., Shoseyov, O., and Kaplan, D. (2009). Expression, cross-linking, and characterization of recombinant chitin binding resilin. Biomacromolecules. 10, 3227-3234.

Qin, G., Rivkin, A., Lapidot, S., Hu, X., Preis, I., Arinus, S.B., Dgany, O., Shoseyov, O., and Kaplan, D.L. (2011). Recombinant exon-encoded resilins for elastomeric biomaterials. Biomaterials. 32, 9231-9243.

Rånby, B.G. (1949). Aqueous colloidal solutions of cellulose micelles. Acta Chem Scand. 3, 649-650.

Sakurada, I., Nukushina, Y., and Ito, T. (1962). Experimental determination of the elastic modulus of crystalline regions in oriented polymers. J Polym Sci A Polym Chem. 57, 651-660.

Samir, M.A.S.A., Alloin, F., and Dufresne, A. (2005). Review of recent research into cellulosic whiskers, their properties and their application in nanocomposite field. Biomacromolecules**.** 6, 612-626.

Shoseyov, O., and Doi R.H. (1990). Essential 170-kda subunit for degradation of crystalline cellulose by clostridium-cellulovorans cellulase. Proc Natl Acad Sci USA. 87, 2192-2195.

Shoseyov, O., Shani, Z., and Levy, I. (2006). Carbohydrate binding modules: biochemical properties and novel applications. Microbiol Mol Biol Rev. 70, 283-295.

Shoseyov, O., Takagi, M., Goldstein, M.A., and Doi, R.H. (1992). Primary sequence-analysis of clostridium-cellulovorans cellulose binding protein-a. Proc Natl Acad Sci USA. 89, 3483-3487.

Siqueira, G., Bras, J., and Dufresne, A. (2010). Cellulosic bionanocomposites: A review of preparation, properties and applications. Polymers**.** 2, 728-765.

Teeri, T., Brumer, H., Daniel, G., and Gatenholm, P. (2007). Biomimetic engineering of cellulose-based materials. Trends Biotechnol. 25, 299-306.

Vincent, J., and Wegst, U. (2004). Design and mechanical properties of insect cuticle. Arthropod Struct Dev. 33, 187-199.

Ward, J., Kelly, J., Wang, W., Zeugolis, D.I., and Pandit, A. (2010). Amine functionalization of collagen matrices with multifunctional polyethylene glycol systems. Biomacromolecules. 11, 3093-3111.

Weis-Fogh, T. (1960). A rubber-like protein in insect cuticle. J Exp Biol. 37, 889-907.

Young, D., and Bennet-Clark, H. (1995). The role of the tymbal in cicada sound production. J Exp Biol. 198, 1001-1020.

APPENDIX A

(a) 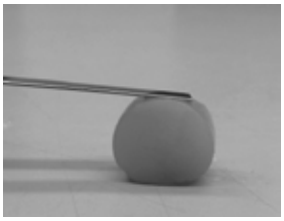 (b) 

Fig. A1. 17res-CBD/NCC composites produced by the EDC/NHS/PEG-amine procedure. "infused" 17res-CBD/NCC cylinder-shaped composite after the immersion in 17res-CBD solution (a). "mixed" 17res-CBD/NCC dry composite foams (b).

Table A1. Samples prepared for compression tests.

Sample	Diameter (mm)	Height (mm)	Number of repeats (n)
NCC	6.3±0.2	8.2±0.2	4
17res-CBD	6.9±0.5	6.6±0.8	4
NCC/17res-CBD "mixed"	8.8±0.3	5.1±0.3	3
NCC/17res-CBD "infused"	6.6±0.9	7.9±1.2	5

APPENDIX B

```
tatgtcgtactaccatcaccatcaccatcacgattacgatatcccaacgaccgaaaac
    M  S  Y  Y  H  H  H  H  H  H  D  Y  D  I  P  T  T  E  N
ctgtattttcagggcgccatgggaccggagccaccagttaactcgtatctacctccgtcc
 L  Y  F  Q  G  A  M  G  P  E  P  P  V  N  S  Y  L  P  P  S
gatagctatggagcaccgggtcagagtggtcccggcggcaggccgtcggattcctatgga
 D  S  Y  G  A  P  G  Q  S  G  P  G  G  R  P  S  D  S  Y  G
gctcctggtggtggaaacggtggacggccctcagacagctatggcgctccaggccagggt
 A  P  G  G  G  N  G  G  R  P  S  D  S  Y  G  A  P  G  Q  G
caaggacagggacaaggacaaggtggatatgcaggcaagccctcagatacctatggagct
 Q  G  Q  G  Q  G  Q  G  G  Y  A  G  K  P  S  D  T  Y  G  A
cctggtggtggaaatggcaacggaggtcgtccatcgagcagctatggcgctcctggcggt
 P  G  G  G  N  G  N  G  G  R  P  S  S  S  Y  G  A  P  G  G
ggaaacggtggtcgtccttcggatacctacggtgctcctggtggcggaaatggtggacgc
 G  N  G  G  R  P  S  D  T  Y  G  A  P  G  G  G  N  G  G  R
ccatcggacacttatggtgctcctggtggtggtggaaatggcaacggcggacgaccttca
 P  S  D  T  Y  G  A  P  G  G  G  G  N  G  N  G  G  R  P  S
agcagctatggagctcctggtcaaggacaaggcaacggaaatggcggtcgctcatcgagc
 S  S  Y  G  A  P  G  Q  G  Q  G  N  G  N  G  G  R  S  S  S
agctatggtgctcctggcggtggaaacggcggtcgtccttcggatacctacggtgctccc
 S  Y  G  A  P  G  G  N  G  G  R  P  S  D  T  Y  G  A  P
ggtggtggaaacggtggtcgtccttcggatacttacggcgctcctggtggcggcaataat
 G  G  G  N  G  G  R  P  S  D  T  Y  G  A  P  G  G  G  N  N
ggcggtcgtccctcaagcagctacggcgctcctggtggtggaaacggtggtcgtccatct
 G  G  R  P  S  S  S  Y  G  A  P  G  G  G  N  G  G  R  P  S
gacacctatggcgctcctggtggcggtaacggaaacggcagcggtggtcgtccttcaagc
 D  T  Y  G  A  P  G  G  G  N  G  N  G  S  G  G  R  P  S  S
agctatggagctcctggtcagggccaaggtggatttggtggtcgtccatcggactcctat
 S  Y  G  A  P  G  Q  G  Q  G  G  F  G  G  R  P  S  D  S  Y
ggtgctcctggtcagaaccaaaaaccatcagattcatatggcgcccctggtagcggcaat
 G  A  P  G  Q  N  Q  K  P  S  D  S  Y  G  A  P  G  S  G  N
ggcaacggcggacgtccttcgagcagctatggagctccaggctcaggacctggtggccga
 G  N  G  G  R  P  S  S  S  Y  G  A  P  G  S  G  P  G  G  R
ccctccgactcctacggacccccagcttctggatcgggagcaggtggcgctggaggcagt
 P  S  D  S  Y  G  P  P  A  S  G  S  G  A  G  G  A  G  G  S
ggacccggcggcgctgactacgataacgatgaggggatccccgaccccggcatggcagcg
 G  P  G  G  A  D  Y  D  N  D  E  G  I  P  D  P  G  M  A  A
acatcatcaatgtcagttgaattttacaactctaacaaatcagcacaaacaaactcaatt
 T  S  S  M  S  V  E  F  Y  N  S  N  K  S  A  Q  T  N  S  I
acaccaataatcaaaattactaacacatctgacagtgatttaaatttaaatgacgtaaaa
 T  P  I  I  K  I  T  N  T  S  D  S  D  L  N  L  N  D  V  K
gttagatattattacacaagtgatggtacacaaggacaaacttttctggtgtgaccatgct
 V  R  Y  Y  Y  T  S  D  G  T  Q  G  Q  T  F  W  C  D  H  A
ggtgcattattaggaaatagctatgttgataacactagcaaagtgacagcaaacttcgtt
 G  A  L  L  G  N  S  Y  V  D  N  T  S  K  V  T  A  N  F  V
aaagaaacagcaagcccaacatcaacctatgatacatatgttgaatttggatttgcaagc
 K  E  T  A  S  P  T  S  T  Y  D  T  Y  V  E  F  G  F  A  S
ggacgagctactcttaaaaaaggacaatttataactattcaaggaagaataacaaaatca
 G  R  A  T  L  K  K  G  Q  F  I  T  I  Q  G  R  I  T  K  S
gactggtcaaactacactcaaacaaatgactattcatttgatgcaagtagttcaacacca
 D  W  S  N  Y  T  Q  T  N  D  Y  S  F  D  A  S  S  S  T  P
gttgtaaatccaaaagttacaggatatataggtggagctaaagtacttggtacagcacca
 V  V  N  P  K  V  T  G  Y  I  G  G  A  K  V  L  G  T  A  P
taggatcgatccagatgtac
 *
```

DNA and protein sequence of 6H-17res-CBD. The His-tag is underlined. The wave underline marks a spacer. The double underline marks the TEV protease cleavage sequence, the cleavage site is between the grayed QG. Dashed line represents amino acids added from the cloning process. Normal font represents the 17res sequence. The native resilin linker is marked by the thick underline. The CBD is marked by bold underlined with thick wave.

Proceedings of the 34th Risø International Symposium on Materials Science:
Processing of fibre composites – challenges for maximum materials performance
Editors: B. Madsen, H. Lilholt, Y. Kusano, S. Fæster and B. Ralph
Department of Wind Energy, Risø Campus
Technical University of Denmark, 2013

PREPREG AND INFUSION PROCESSES FOR MODERN WIND TURBINE BLADES

Chris Shennan

Hexcel
Ickleton Road, Duxford,
Cambridge, CB22 4QD, UK

ABSTRACT

The different elements of wind turbine blades have been analyzed for their main function, performance requirements and drivers. Key drivers can be simplified to either performance or cost. The use of prepreg and infusion to make these blade elements has then been compared and shows, from a comparison of test laminates, that prepreg typically delivers higher mechanical performance on both glass and carbon. One of the main process differences, cure temperature, has been overcome with the introduction of M79 which cures at 70°-80°C. M79 combines this low cure temperature with a much lower reaction enthalpy allowing shorter cure cycles. This means that prepregs can now be cured in the same molds, at the same temperatures and with the same foam as used in a conventional infusion process. Although prepreg and infusion are usually used separately for making blade elements, they may also be used in combination: co-infused and co-cured using prepregs for the hard to infuse unidirectional load-carrying elements and infusion for the other elements. This can thus simplify the production process. The conclusion is that unidirectional prepregs are ideally suited for the performance driven parts of the blade such as in load carrying elements.

1. INTRODUCTION

The modern wind turbine blade comprises three main structural elements. Closest to the hub of the rotor is the root end, a massive heavily loaded structure that links to the rest of the blade. Attached to the root end is the central structural member which may be a spar or a pair of spar caps connected together via a shear web and which act as an I-beam. Both the root end and the spar caps can be many centimeters thick with the latter providing the main stiffness of the blade. This assembly is then enclosed by an aerodynamic shell which is a thinner structure, consisting of either a thin laminate or a sandwich panel construction. In addition, other elements include lightning strike protection, leading edge protection, and possibly structural health monitoring.

These three main elements of root end, spar (cap) and shell are made out of fiber-reinforced

laminate with additional use of foam as a core material for weight reduction and sandwich panel construction. By far the commonest fiber reinforcement is standard E-glass, particularly for shorter blades, while low cost large tow high strength (standard modulus) carbon fiber is increasingly used for the spar caps of longer blades, especially for blades over about 50m. Alternative high modulus glass fibers are used less often though some manufactures prefer their use to carbon which has a significantly higher cost and has sometimes been in short supply.

The dominant matrix from which the laminate is made and which is used by most wind turbine manufacturers is based on epoxy chemistry. In the case of prepreg systems, the chemistry has to be fully formulated i.e. with hardeners and all other matrix modifiers included in the matrix. Most infusion systems comprise a two part formulation with the epoxy resin in a first part and with the remaining (hardener) components in a second part. These two parts must be premixed before infusion is carried out. Polyester chemistry is also widely used.

The processes used for the construction of modern wind blades are either based on prepreg (i.e. pre-impregnated reinforcements) or infusion (i.e. dry reinforcements that are infused during manufacture) processes. Wet lamination is now much more rarely used than formerly. The fact that both prepreg and infusion are in use today exemplifies the fact that manufacturers value the attributes of each process differently.

This paper will examine some of the important characteristics of both prepreg and infusion processes. The intention is to draw comparisons between the two processes and to highlight some of the relative strengths and weaknesses of each. Some of this will be based on a qualitative comparison, but the paper includes results from an earlier quantitative comparison that was carried out in Hexcel based on both glass and carbon reinforcements.

One of the differences between prepreg and infusion systems is the cure temperature. In systems for wind energy, prepregs are typically cured at 100-120°C while infusion systems are typically cured at 60-80°C. This paper also includes some early results of a new prepreg system, M79 that can cure at 70-80°C, thus effectively eliminating a key difference between prepreg and infusion. Finally, opportunities will be described for a combination of prepreg and infusion technologies in which both matrix types are co-cured in a process that Hexcel has described as co-infusion.

2. BLADE ELEMENTS AND PERFORMANCE DRIVERS

The previous section briefly summarized the main structural elements of a typical blade which include the root end, the spar or spar caps with shear web, and the aerodynamic outer shell. The purpose of this section is to highlight some of the main functions of these elements, to understand their performance requirements, and thus the main drivers behind them.

2.1 Root end. The root of a wind blade is a heavy, thick-sectioned structure. It transfers the loads from the whole blade into the hub and as such, is highly loaded. Major design drivers include strength, stiffness and fatigue. The precise design of the root end varies between different blade manufacturers and may be fully integrated, separately constructed and even segmented. The range of designs reflects the tradeoff that is made between making the structure at low cost but heavy compared with a lower weight structure that is more expensive. Some of the most elegant designs are unfortunately the most expensive. The ideal solution is one that is of low cost but also light weight. Construction materials can include unidirectional, biax and triax reinforcements, resin and sometimes core materials.

The main practical issues with the root end reflect the critical nature of the structure and the size

(thickness). High curvature (sometimes in two directions) makes fixation of reinforcements and prepregs to the mould more difficult and deviations of fiber alignment more likely. The thick laminate requires careful control of the exotherm during cure when the heat liberated must be allowed to dissipate. The transition into the rest of the blade and especially into the load carrying elements is critical, as is the in the integration of the bushings which may be co-moulded or bonded in place.

2.2 Load-carrying elements. The main load-carrying elements include the spar caps and the shear webs which in some designs can be fused into a box-like structure of a spar. As for the root end, these structures are highly loaded and, especially near the root end, can be many centimeters thick. Major design drivers include stiffness, strength especially in compression, inter fiber failure and transverse tensile strength, and fatigue. Construction materials are dominated by the use of unidirectional glass and, increasingly carbon though this is very much dependent on the manufacturer, combined with resin. The use of carbon is much more common in longer blades, especially over 40-50m. Glass biax is also widely used.

Performance is the major driver in load carrying elements, even at the expense of increasing cost. This means that fiber alignment, wet out and porosity are critical. As for root ends, the thick laminate requires careful control of the exotherm during cure with the heat liberated being dissipated during dwells in the cure cycle. As the main structural elements of the blade, mechanical performance, quality and reproducibility are critical and require careful process control. Again the transition between the load carrying elements and the root end is critical.

The role of the shear webs is to create an I-beam like structure with the spar caps which stiffens the blade, one side being in tension while the other is in compression. Major design drivers are buckling, strength and fatigue. The structures tend to be light weight and low cost using biax reinforcements combined with resin and foam or balsa cores.

2.3 Shell. The aerodynamic shell is essentially a light weight skin with the design drivers of buckling and shear. Materials tend to be of the lowest possible cost combined with an efficient manufacturing process and a minimum finishing time. Materials are multiaxial (especially biax and triax but with some unidirectional) reinforcements, combined with resin and an extensive use of core to create lightweight sandwich panel constructions.

2.4 Summary. This brief analysis of the main structures of wind blades highlights the differences in function, performance and drivers that exist. Table 1 provides a summary of these differences.

Table 1. Summary of blade elements, functions, requirements and drivers.

Blade element	Function	Performance requirements	Main Driver
Root	a) Connect blade to hub b) Transfer loads from blade to hub	a) Highly loaded b) Provide space for bushings	*Cost versus performance*
Spar Cap	Structural integrity of blade	a) Provide stiffness b) Carry loads c) New materials	*Performance*
Shear web	Transfer shear forces between shells	Low to moderate	*Cost*
Shell	Aerodynamic efficiency	a) Surface quality b) Aerodynamic surface	*Cost*

In blade manufacturing processes today, all parts of the blade are made using all types of materials and chemistries, as summarized in the introduction. However, as blades become longer and as manufacturers search for ever more efficient ways of making blades, it is clear that materials and processes can be more selectively applied. Parts of the blade are strongly performance driven while other parts are more cost driven.

3. EXPERIMENTATION

3.1 Comparison between prepreg and infusion technologies on glass and carbon reinforcements. A study was initiated to compare the mechanical properties of closely matching laminates prepared using infusion and prepreg technologies. The study was repeated on both glass and carbon reinforcements. Panels were designed solely for mechanical testing.

3.1.1 Glass. Two typical glass prepregs were selected based on 1200 g/m^2 UD E-glass with the reference description HexPly M9.6GLT/32%/1200 (+CV)/G. Some laminates were made with pure UD, while others ('+CV') were made with an additional 50 g/m^2 non-woven glass fleece.

Infusion laminates were based on the nearest equivalent stitched UD reinforcement, LT1218 from Saertex. This reinforcement has to be stitched in order for it to have sufficient dimensional stability for infusion. The construction is shown in table 2.

Table 2. Construction of infusion reinforcement LT1218.

Construction	Areal weight [g/m²]	Tolerance [±%]	Material
0°	1152	5	E-Glass
90°	54	5	E-Glass
Stitching	12	5	PES

Infusion and prepreg laminates were prepared as 1.35 m^2 panels with the following construction which was subsequently cut up into test specimens as shown in figure 1.

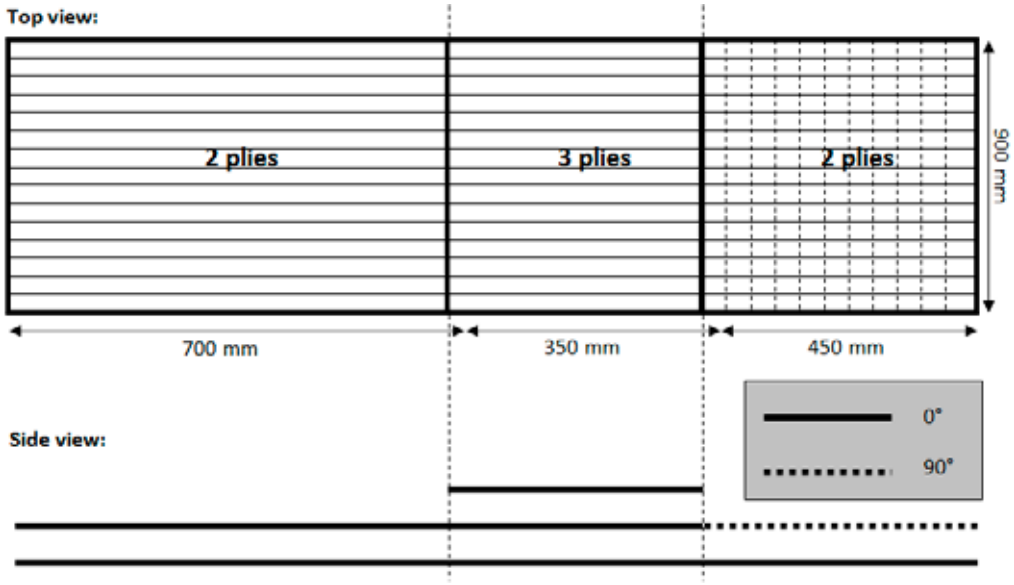

Fig. 1. Construction and layup of glass test laminates.

Infusion laminates were prepared using Epikote™ resin MGS RIM 135 from Momentive in the following construction shown in figure 2 (the VAP membrane is a semi-permeable membrane which allows the air to escape but not the resin).

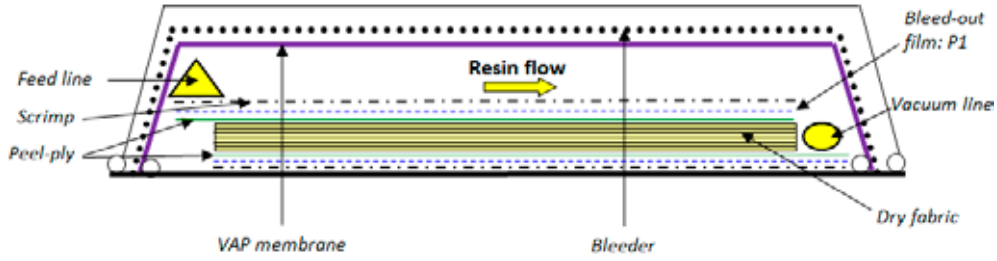

Fig. 2. Arrangement for the infusion of infusion laminates.

Prepreg laminates were prepared using the construction shown in figure 3.

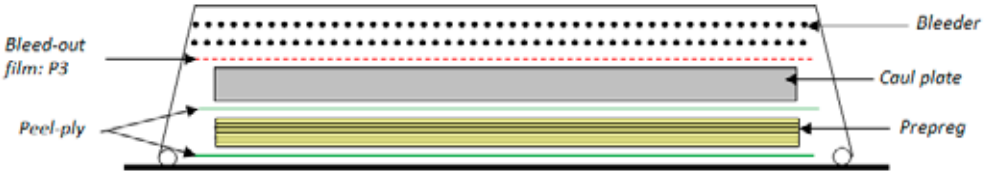

Fig. 3. Arrangement for the preparation of prepreg laminates.

Infusion and prepreg laminates were cured at 90 °C. In addition, some prepreg laminates were prepared for an effective cure at 120 °C by curing initially at 80 °C and then at 120 °C. Cure cycles are shown in figure 4.

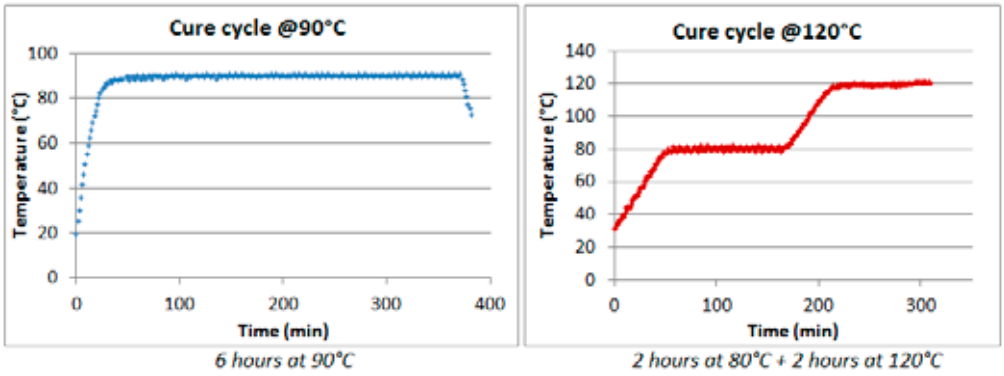

Fig. 4. Infusion and prepreg laminate cure cycles.

3.1.2 Carbon. A typical carbon prepreg was selected based on 600 g/m^2 unidirectional carbon (Toray T620) with the reference description HexPly M9.6GLT/35%/600+2P/C.

Infusion laminates were based on the nearest equivalent unidirectional reinforcement which was a plain weave 600 g/m^2 plain weave fabric with a very small amount of low crimp weft reinforcement, based on Toray T620 from Hexcel Reinforcements, Les Avenieres, France.

Infusion and prepreg laminates were prepared as 1.26 m^2 panels with the following construction which was subsequently cut up into test specimens, as shown below in figure 5.

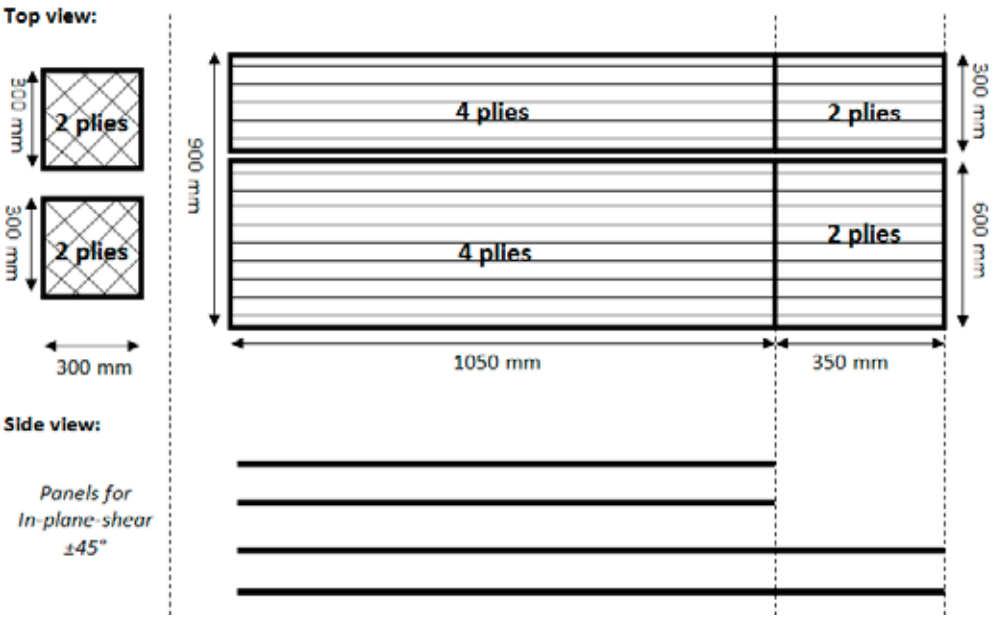

Fig. 5. Construction and layup of carbon laminates.

Other experimental details (layups, infusion resin, cure cycles) were the same as for the glass study described in section 3.1.1.

3.2 Case study comparison of co-infusion. A case study was carried out to demonstrate the feasibility of co-infusion of a combined prepreg and infusion system in which the whole system is infused and co-cured.

A typical glass prepreg was selected based on 1600 g/m^2 unidirectional E-glass with the reference description M9.6F/32%/1600+CV/G. For the infusion, an 831 g/m^2 +/- biax fabric S22EX021-00820-01270-250000 from Saertex was selected. The infusion resin was Epikote™ MGS RIM 135 with hardener RIMH 137. Divinycell H was used as an example of a typical foam.

A schematic of the layup is shown in figure 6. 20 plies of prepreg was used for the central core region. The overall length was 4 m. Figure 7 shows the resin taken up during infusion as a function of time. Infusion was complete within about 20 minutes with the consumption of about 35 kg of resin. The cure was carried out on a heated table using the cure cycle shown in figure 8, with cure taking place at 90°C for 6 hours.

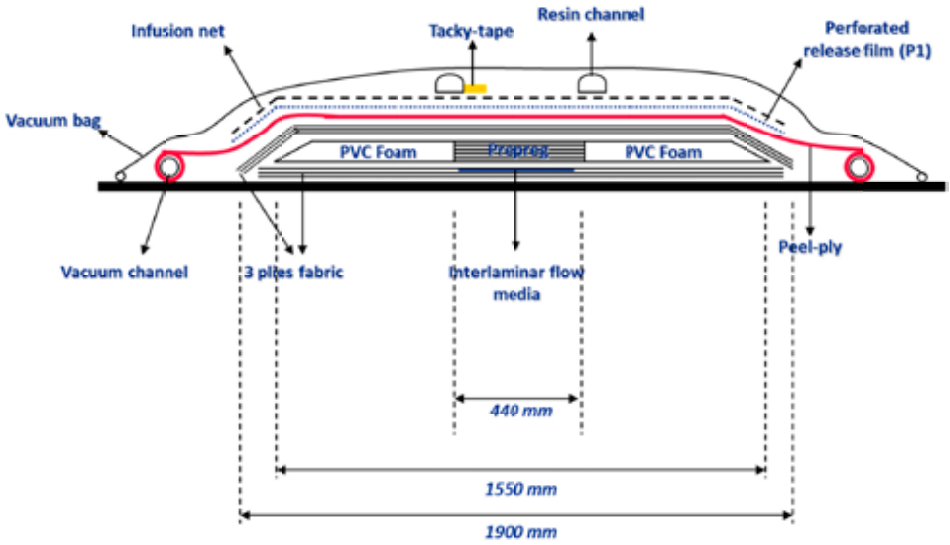

Fig. 6. Schematic diagram of the co-infusion case study.

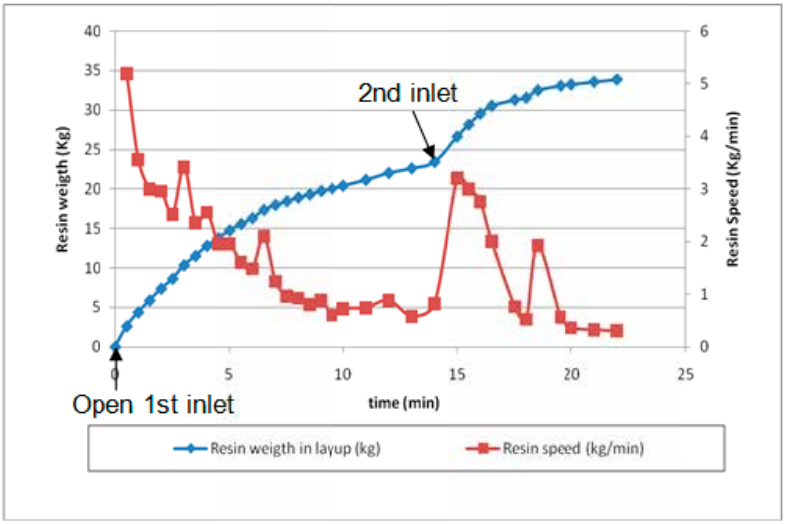

Fig. 7. Resin consumption during the co-infusion trial.

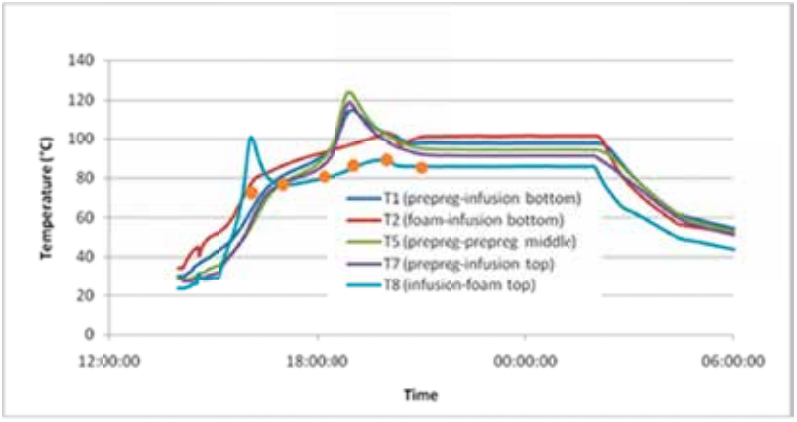

Fig. 8. Example of the cure cycle used taken from one of the sets of thermocouples used for the study.

Porosity of the final panel was assessed under an optical microscope of polished cross sections. Image analysis software was used for the calculation of voids over $0.04x10^{-6}$ m^2 as a percentage of the total laminate surface.

4. COMPARISON BETWEEN PREPREG AND INFUSION TECHNOLOGIES

The results for both glass and carbon laminates are given separately in the following sections.

4.1 Comparison on glass reinforcement. The purpose of this comparison was to establish the broad differences between comparable prepreg and infusion systems, in the absence of any other known (public) comparison. Glass laminates were prepared and cured according to the protocols

described in the section on experimentation. Table 3 gives the mechanical test results for infused laminates while table 4 gives the mechanical test results for prepreg laminates. In table 4, the results columns are labeled with the temperature of cure, and whether the reinforcement contains an additional fleece (+CV).

Table 3. Mechanical test data for infused laminates.

Test		Standard	Infusion
Tensile 0°	Strength (MPa)	ISO527	**989.6**
	Modulus (GPa)		**46.8**
Tensile 90°	Strength (MPa)		45.3
	Modulus (GPa)		5.2
Compression 0°	Strength (MPa)	EN2850B	**617.5**
	Modulus (GPa)		**47.3**
Compression 90°	Strength (MPa)		138.8
	Modulus (GPa)		15.4
Flexural 0°	Strength (MPa)	ISO14125	**1190**
	Modulus (GPa)		**28.2**
ILSS 0°	Strength (MPa)	ISO14130	45.7
IPS	Strength (MPa)	ISO14129	35.1
	Modulus (GPa)		3.3

Normalized results (60% FVF) are shown in bold in the table.

Table 4. Mechanical test data for prepreg laminates.

Test		Standard	90°C cure	90°C cure +CV	120°C cure	120°C cure +CV
Tensile 0°	Strength (MPa)	ISO527	**1125.6**	**1144.2**	**1105.5**	**1117.1**
	Modulus (GPa)		**47.1**	**45.6**	**47.7**	**45.8**
Tensile 90°	Strength (MPa)		36.6	25.3	36.3	31.2
	Modulus (GPa)		11.5	8.9	10.7	12.2
Compression 0°	Strength (MPa)	EN2850B	**846.4**	**1032.6**	**1038.6**	**931.6**
	Modulus (GPa)		**49.6**	**49**	**49**	**48.3**
Compression 90°	Strength (MPa)		149.4	186.6	159.7	173.2
	Modulus (GPa)		11.3	11	14.4	13.5
Flexural 0°	Strength (MPa)	ISO14125	**1394**	**1320**	**1299**	**1341**
	Modulus (GPa)		**35.1**	**32.5**	**32.9**	**31**
ILSS 0°	Strength (MPa)	ISO14130	78.9	54.7	77.3	55.8
IPS	Strength (MPa)	ISO14129	41.2	36.5	40.9	36.3
	Modulus (GPa)		4.2	4.2	3.9	4.2

Normalized results (60% FVF) are shown in bold in the table.

It was not the purpose of this study to provide an exhaustive analysis of the differences between the two sets of results comparing infusion and prepreg. It is acknowledged that the data set is limited and further repeat testing would be desirable. However, there are some general comments which can be made.

For 0° properties, prepreg systems provide higher mechanical properties by some 9-68%. A likely explanation for this is the difference in reinforcement. In the case of prepreg, pure unidirectional rovings are used. In the case of infusion, a stitched unidirectional fabric is used in

order to provide stability to the dry fiber. Differences in mechanical properties are likely to come from the stitching and associated crimp on the unidirectional fiber.

For 90° properties, tensile strength is higher in infusion systems. This may also be because of differences in the reinforcement where stitching in this case strengthens 90° performance. However, the opposite effect is seen on compression strength.

For ILSS and IPS, the overall matrix effects would be expected to be rather similar. Both infusion and prepreg systems often use difunctional epoxies with amine-based curatives. The effects from the reinforcement are complicated with pure unidirectional fabrics leading to higher ILSS and IPS but the addition of a fleece seems to lead to lower strengths.

4.2 Comparison on carbon reinforcement. As in section 4.1, the purpose of this comparison was to establish the broad differences between comparable prepreg and infusion systems in the absence of any other known (public) comparison. Carbon laminates were prepared and cured according to the protocols described in the section on experimentation. Table 5 gives the mechanical test results for both infused and prepreg laminates.

Table 5. Mechanical test data for both infused and prepreg laminates on carbon.

Test		Ply number	Standard	Infusion	Prepreg 90°C	Prepreg 120°C
Tensile 0° *	Strength (MPa)	2	ISO527	**2176.1**	**2670.2**	**2819.8**
	Modulus (GPa)			**130**	**125**	**128.4**
Tensile 90°	Strength (MPa)	4		33	37.9	42.9
	Modulus (GPa)			8.4	8.2	7
Compression 0°	Strength (MPa)	4	EN2850B	**902**	**1085**	**1148.2**
	Modulus (GPa)			**128.5**	**125.1**	**119.8**
Compression 90°	Strength (MPa)	4		148.6	158.3	173.6
	Modulus (GPa)			9	9.2	9.3
Flexural 0°	Strength (MPa)	4	ISO14125	**1283**	**1626**	**1700**
	Modulus (GPa)			**103.1**	**103.6**	**114.6**
ILSS 0°	Strength (MPa)	4	ISO14130	60.6	66.7	67.6
IPS	Strength (MPa)	2	ISO14129	32.2	39.6	39.2
	Modulus (GPa)			4.2	4	3.9

Normalized results (60% FVF) are shown in bold in the table.

As before, it was not the purpose of this study to provide an exhaustive analysis of the differences between the two sets of results from infusion and from prepreg. It is acknowledged that the data set is limited and further repeat testing would be desirable. However there are some general comments which can be made.

For 0° properties, prepreg systems provide higher mechanical properties by about 20-30%. As for glass systems, a likely explanation is in the differences between the reinforcements. In the case of prepreg, pure unidirectional carbon was used. In the case of infusion, a lightly woven fabric was used. Although the crimping effect had not been thought to be as severe as for a stitched fabric, there does seem to be a significant difference from the unwoven unidirectional reinforcement used in prepreg.

For 90° properties, ILSS and IPS, prepreg systems consistently deliver higher properties. In these cases when compared with the glass comparison, there seems to be no enhancement of

infused systems from the 90° fiber; there is no added 50 g/m^2 fleece; and the matrix systems are also of a comparable type.

5. A NEW MATRIX FOR LOW TEMPERATURE CURE

Prepreg has a number of advantages when compared with infusion. In wind energy applications, one of the main disadvantages is that while infusion materials are typically cured at 70-80°C, prepreg materials are more normally cured at 110°-120°C although they can be cured at other temperatures as well. This temperature difference can in turn lead to specific requirements for foam core, mold design, and cure cycle control. The range of temperatures at which the different materials can cure is given below in figure 9. The figure compares several generations of Hexcel prepreg matrix systems with the year of their introduction, as well as the associated reaction enthalpies. The opportunity exists for a lower temperature curing prepreg material, preferably curing at 70°-80°C which thereby eliminates this difference from infusion systems.

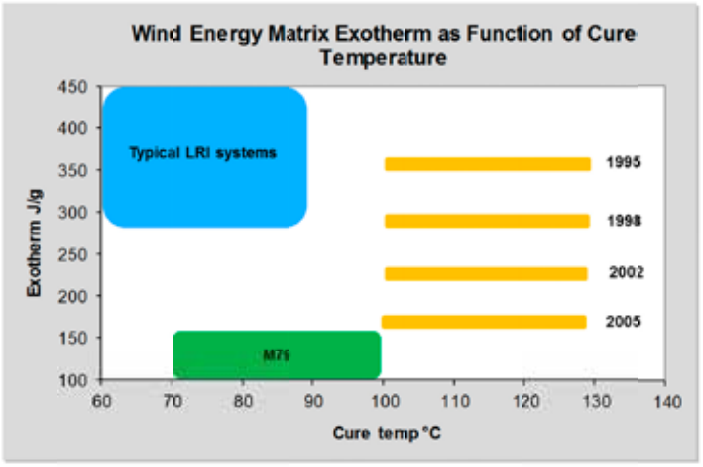

Fig. 9. Comparison of infusion and prepreg systems: cure temperature ranges and expected reaction enthalpies.

In 2013, Hexcel introduced a new low temperature curing prepreg called M79 which cures at 70°-80°C (as well as at higher temperatures) and which retains the long outlife of other wind energy prepregs. This matrix is also included in figure 9. For the first time, this new matrix eliminates the cure temperature difference between infusion and prepreg materials. First details were published in May 2013 (Shennan 2013) and a short summary of the main characteristics is given in table 6.

Table 6. Summary of the main properties of M79.

Property	Value
Cure time at 70°C	10 hours
Cure time at 80°C	6 hours
Outlife	>2 months
Reaction enthalpy	100-120 J/g
Static mechanical properties	Similar to current M9 family
Product form	Same as current M9 family
Manufacturing process	Same as current M9 family

The reaction enthalpy of M79 at 100-120 J/g is unusually low for prepreg matrices, and is exceptionally low when compared with infusion matrices which are commonly over 300 J/g. The significance of this is seen most clearly when having to cure thick laminate sections such as in the spar cap or root end of a wind blade or in any other large heavyweight composite section. In such thick sections, the cure cycle must be carefully managed to control the temperature growth during cure which is a function that includes the rate of heating, chemistry type and exotherm (reaction enthalpy) in what are virtually adiabatic conditions. Lower reaction enthalpies lead to shorter optimized cure cycles which are important for higher productivity of the large structures being made. Figure 10 shows how reaction enthalpies have reduced in the last 18 years.

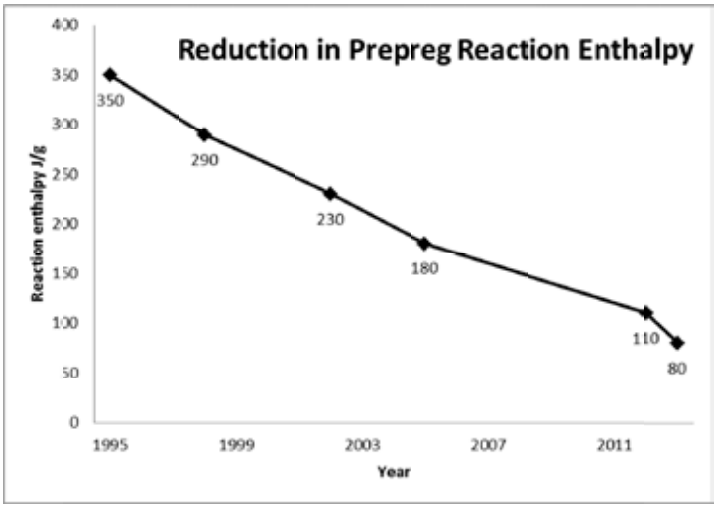

Fig. 10. Reduction in reaction enthalpies for wind energy prepreg matrices between 1995 and 2013.

6. CO-INFUSION: COMBINATIONS OF PREPREG AND INFUSION

Prepreg and infusion have different and sometimes complementary strengths. Instead of the choice having to be 'either/or', a third option is to combine the materials in a common structure and in a process which can be described as 'co-infusion'. In such a structure, prepreg should typically be used as the major unidirectional/ load carrying element which is often thicker, harder to infuse and with the higher mechanical properties. Infusion of dry reinforcements can then be used for the remaining structure.

An excellent example of a structure than is suitable for co-infusion is the combination of a spar cap and shell of a wind turbine blade. The reinforcement of the spar cap can be either glass or carbon, while the shell reinforcement is usually a combination of multiaxial fabrics, typically 600 g/m^2 +/-45° biax (BB600) and 1200 g/m^2 0,+/-45° triax (LBB1200).

This concept was tested on a 4x2 m scale using a unidirectional glass prepreg for the simulated spar cap while using an 831 g/m^2 dry reinforcement for the simulation of the rest of the structure. Full details of the protocol are described in the section on experimentation.

The infusion was completed very quickly, in about 20 minutes, and consumed about 30 kg of resin. The fast infusion was not surprising given that the unidirectional fiber had been pre-impregnated as prepreg. After curing, the panel was de-moulded and is shown below in figure 11.

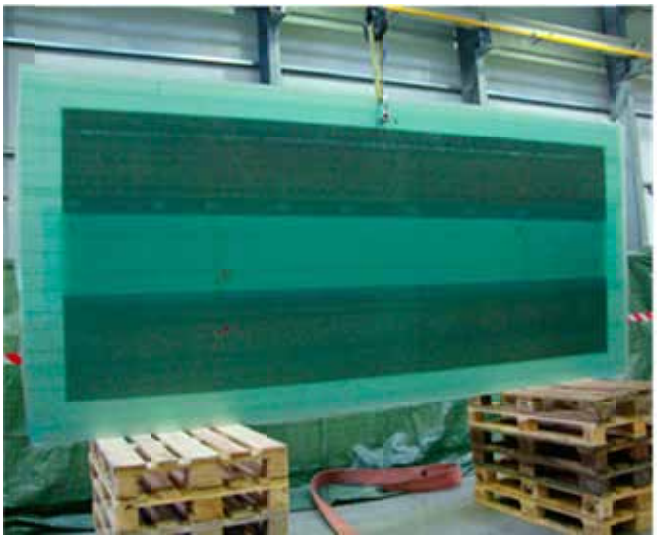

Fig. 11. Co-infusion panel after cure and demoulding.

Laminate quality was assessed and showed a low level of porosity with glass transition temperatures (Tg) that reflected the base resin chemistry used for the respective parts of the panel (typically, prepregs yield higher glass transition temperatures than infusion systems). A summary is given in Table 7.

Table 7. Summary of laminate quality from co-infusion panel.

Fiber Volume (%)		50
Porosity (%)	Side	0,7
	Middle	1,5
Tg (°C)	Top	75
	Middle	120
	Bottom	75

The conclusion from this case study is that prepregs can be co-infused with dry reinforcements very successfully, achieving acceptable levels of porosity and glass transition temperature. A fuller evaluation of the mechanical properties was carried out at a later date on test laminates

(Hexcel internal work). This showed that, depending on the laminate structure, results were typically between those expected from infusion and prepreg systems.

A prerequisite for successful co-infusion is that both infusion and prepreg materials must be cured at the same temperature. Either infusion materials can be cured at higher than normal temperatures with standard prepregs, for instance at 90+°C, or prepregs can be used that have been developed to cure at the lower temperatures of cure of infusion materials i.e. 70°-80°C. It is in this context that the introduction of M79 is very timely because it enables cure at 70°-80°C as has been mentioned in the previous section.

6. FURTHER DISCUSSION AND CONCLUSIONS

The analysis of blade materials and processes identified that all parts of the blade can be made using several types of materials and chemistries. However, as blades become longer and as manufacturers search for ever more efficient ways of making blades, materials and processes can be more selectively applied. Parts of the blade are strongly performance driven while other parts are more cost driven.

The comparison between prepreg and infusion technologies showed that prepreg seems to give significantly higher mechanical properties overall when compared with infusion, on glass and on carbon reinforcements. The most obvious explanation for this lies in the differences in unidirectional reinforcement used. In unidirectional prepreg, pure rovings or bobbins of fiber are used. In the case of glass materials for infusion, they are stitched, and thereby crimped. In the case of carbon reported in this paper, a low crimp woven reinforcement was used but again, this has some crimp and seems to lead to a qualitatively similar difference between prepreg and infusion. As was stated earlier, it was not the purpose of the study to provide an exhaustive analysis of the differences, and it is acknowledged that the data set is limited.

In wind energy applications, one of the main disadvantages of prepreg is that while infusion materials are typically cured at 70-80°C, prepreg materials are more normally cured at 110°-120°C although they can be cured over a wider temperature range. This can in turn lead to specific requirements for foam core, mold design, and cure cycle control. M79 has recently been introduced as a material for large structures such as wind blades and which cures at 70°-80°C. It also has a much lower reaction enthalpy than from infusion systems, thereby enabling shorter cure cycles. Mechanical properties compare favorably with conventional prepreg systems. M79 thus eliminates the difference in cure temperatures in the range of 70°-80°C.

There are also other differences between prepregs and infusion materials. Unidirectional prepreg is very cost competitive because the cost of manufacture is offset by the additional cost of unidirectional reinforcements used for infusion. However, the same cost of manufacture makes multiaxial prepregs more expensive in terms of pure product cost.

Infusion of multiaxial materials, particularly of glass, is straightforward because the open structure of the reinforcement assists the flow of resin. However infusion of carbon is harder. It is very difficult to obtain consistent and complete infusion of thick unidirectional carbon sections. Prepregs are by definition pre-impregnated and so can deliver a higher quality much more reliably in these sections.

This suggests that prepreg is ideally suited to those parts of the blade that are most driven by performance which includes both the root end and the load carrying elements such as the spar caps or spar. For those parts of the blade that are most heavily cost but not performance driven,

infusion can be the more efficient process- except, for instance, where cure cycle is an issue because of exotherm control.

In some parts of the structure, the process can be further simplified by using combinations of prepreg and infusion in a process termed co-infusion. This enables prepreg and dry reinforcements to be laid up in a single process step, followed by co-infusion and co-cure. An excellent example of where this could be used is with pure unidirectional prepreg for a spar cap being laid up in a shell of infused multiaxial reinforcement.

Different manufacturers will doubtless continue to have their preferred processes for the manufacture of wind blades. But the differences between infusion and prepreg processes have narrowed. There are now M79 prepregs available that cure in the same mould constructions, with the same foams, and at the same cure temperatures as used for infusion while combinations of prepregs and infusion can be used in the same process of co-infusion and co-cure.

REFERENCES

Shennan, C.D. (2013). Characterization of prepreg materials for wind turbine blades. SAMPE 2013 Long Beach, California, USA.

Proceedings of the 34th Risø International Symposium on Materials Science:
Processing of fibre composites – challenges for maximum materials performance
Editors: B. Madsen, H. Lilholt, Y. Kusano, S. Fæster and B. Ralph
Department of Wind Energy, Risø Campus
Technical University of Denmark, 2013

CONTINUUM MECHANICS OF COMPOSITES PROCESSING: FIBRE BED BEHAVIOUR

Staffan Toll

KTH Royal Institute of Technology
10044 Stockholm, Sweden

ABSTRACT

Assemblies of parallel fibres for the reinforcement of composite materials are strongly anisotropic and display a complex variety of responses in different directions, ranging from simple elasticity to granular flow depending on the orientation and mode of deformation. To describe this behaviour, in a single consistent theory, we propose a new constitutive structure which combines a *hyper*elastic response based on a strain energy potential, for the volumetric mode and extension in the fibre direction, with a *hypo*plastic response based on a stress energy potential, for the transverse and longitudinal shear modes. The resulting constitutive equation is objective and thermodynamically consistent. All parameters involved have a simple physical meaning and are measurable and estimable. Examples are provided to illustrate the response in shear, compression and their combinations.

1. INTRODUCTION

In the continuum modelling of composites forming, one deals with a fibre preform that is either dry or fully or partially impregnated with resin. In either case a constitutive model of the preform is needed. Several types of preform structure, such as a prepreg stack or non-crimp fabric, can be represented by combination of layers of a unidirectional fibrous medium, henceforth called a *fibre bed*. Such a material, illustrated in Figure 1, has, at best, a transversely isotropic symmetry about the fibre axis $\mathbf{n}$.

In many cases, the preform is mainly being compressed. Thus much of the past research focused on volumetric response. Elastic models were proposed by Curiskis and Carnaby (1985), Cai and Gutowski (1992), Chen, Cheng and Chou (2001), and others. One of the simplest results is the power law, obtained by analogy with random fibre networks (Toll 1998),

$$p = kE\phi^{\beta}, \tag{1}$$

where p is pressure, E is the fibre elastic modulus, ϕ is the fibre volume fraction and k and β are constitutive parameters.

To model more complicated processes, involving 3D forming, such as pre-forming operations or press forming, one needs a full tensorial constitutive equation including in-plane deformations, shear modes and anisotropy. Cai and Gutowski (1992) proposed a transversely isotropic model for an aligned fibre bed, treating the axial and transverse deformations as elastic and the shear mode as Newtonian. Their model is, however, not easily formulated as a tensorial constitutive equation, due to its combination of viscous and elastic responses. Wysocki, Toll, Larsson and Asp. (2010) proposed a hyperelastic model, which is simplistic, but has the advantage of a simple form:

$$\boldsymbol{\sigma} = -kE\phi^{\beta}\mathbf{I} + G(\mathbf{b} - \mathbf{I}) + 2\phi EH(e)e\mathbf{nn}, \tag{2}$$

where $\boldsymbol{\sigma}$ is the Cauchy stress tensor, $\mathbf{n}$ is the fibre director (see figure 1), e is the longitudinal strain[1], $\mathbf{b}$ is the Finger tensor, and H is the Heaviside step function (in practice a continuous approximation). I express this in an Eulerian frame because it will be appropriate later on. The first term above is the power law volumetric response (1), the second term is an isotropic Neo-Hookean contribution, heuristically introduced to model the shear response, and the last term is a linear elastic response to fibre elongation. The rationale of the last term is that if the fibres are nearly straight and parallel, the tensile response should be given by the tensile properties of the fibres themselves, and the compressive axial response is considered negligible, due to fibre buckling.

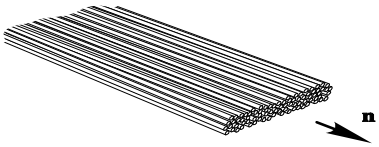

Figure 1: Unidirectional fibre bed with director $\mathbf{n}$.

Elasticity is, however, not usually enough. Somashekar, Bickerton and Bhattachayya (2012) showed that cyclic compression leads after a few cycles to a repeatable state, characterised by a stationary hysteresis loop. Recently Cheng, Kelly and Bickerton (2012) used rate independent elastoplasticity to construct an 8-parameter model and managed to capture the uniaxial cyclic compression response of various fibreglass fabrics. The latter is probably the most useful model so far.

A limitation of all those approaches is their simplistic description of the shear response. Shearing, more than any other mode, activates the mechanism of frictional slip, and thus exposes a behaviour best described as granular flow. Granular solids are known for a peculiar type of path dependent elasticity, cf. Norris and Johnson (1997) or, in the context of random fibrous materials, Alkhagen and Toll (2007), and a plasticity behaviour which cannot be described by standard conservative elastoplasticity. The state-of-the-art theory for modelling such behaviour is *hypoplasticity*, introduced and developed in geomechanics (Kolymbas 2000).

Standard hypoplasticity is isotropic and strain-rate independent, leading to an evolution equation of the form (Lanier, Caillerie, Chambon, Viggiani, Bésuelle and Desrues 2004),

$$\dot{\boldsymbol{\sigma}} = \mathbb{L}(\boldsymbol{\sigma}) : \mathbf{d} - \mathbf{N}(\boldsymbol{\sigma})\,\|\mathbf{d}\| + \mathbf{w}\boldsymbol{\sigma} - \boldsymbol{\sigma}\mathbf{w}, \tag{3}$$

[1] $e = \lambda - 1$ with $\lambda^{-2} = \mathbf{n} \cdot \mathbf{b}^{-1}\mathbf{n}$

where $\mathbb{L}$ and $\mathbf{N}$ are isotropic functions of the stress, $\mathbf{d}$ and $\mathbf{w}$ are the symmetric and skew parts of the spatial velocity gradient and $\|\mathbf{d}\| = \sqrt{\mathrm{tr}\mathbf{d}^2}$ is the Euclidean norm of $\mathbf{d}$. Equation (3) is rate independent because it is homogeneous of degree 1 in the velocity gradient. A shortcoming of this formulation is that, due to the absence of energy potential, there is no guarrantee of non-negative dissipation. Only recently, Toll (2011) derived the full class of thermodynamically consistent hypoplasticity, by introducing a stress energy potential.

The purpose of the present paper is to provide a thermodynamically consistent theory for the complete space of deformation modes and introduce the most adequate models for each deformation mode—linear elasticity for axial elongation, power-law hyperelasticity for the volumetric mode and hypoplasticity for the shear modes. Restriction is made to transversely isotropic symmetry and rate independence.

2. GENERAL CONSTITUTIVE STRUCTURE

In its unloaded state, the material is assumed to have transversely isotropic symmetry about the fibre axis $\mathbf{n}$. The material is further assumed to be elastic under purely volumetric deformation, as well as under axial stretching in the fibre direction. Any shear deformation, however, will be governed by frictional interaction of a granular-solids nature. To allow for these fundamentally different responses, we split the Cauchy stress tensor $\boldsymbol{\sigma}$ into two partial stress tensors: a hyperelastic stress $\boldsymbol{\sigma}_\circ$ and a hypoplastic stress $\boldsymbol{\sigma}_*$:

$$\boldsymbol{\sigma} = \boldsymbol{\sigma}_\circ + \boldsymbol{\sigma}_*. \tag{4}$$

The hyperelastic stress is due to transverse compression and longitudinal extension of the fibre bed, and is therefore linked directly to the volume fraction ϕ and fibre stretch λ,

$$\boldsymbol{\sigma}_\circ = \mathcal{F}\left(\phi, \lambda, \mathbf{n}\right). \tag{5}$$

The hypoplastic stress is due to frictional shear forces within the fibre bed, and will be described in the spirit of granular solids (cf. Kolymbas 2000), by means of a differential law:

$$\dot{\boldsymbol{\sigma}}_* = \mathcal{G}\left(\phi, \boldsymbol{\sigma}_*, \mathbf{n}, \mathbf{l}\right) + \boldsymbol{\omega}\boldsymbol{\sigma}_* - \boldsymbol{\sigma}_*\boldsymbol{\omega}, \tag{6}$$

where $\mathbf{l}$ is the velocity gradient, with symmetric and skew symmetric parts $\mathbf{d}$ and $\mathbf{w}$. The material spin $\boldsymbol{\omega}$, should naturally follow the rotation of the fibre axis, such that

$$\boldsymbol{\omega}\mathbf{n} = \dot{\mathbf{n}}. \tag{7}$$

Axially, any objective rotation is admissible, and a sensible choice is the simple co-rotation,

$$\mathbf{n}\cdot\mathbf{e} : \boldsymbol{\omega} = \mathbf{n}\cdot\mathbf{e} : \mathbf{w}. \tag{8}$$

Combining these features leads to the total spin

$$\boldsymbol{\omega} = \mathbf{w} + \mathbf{dnn} - \mathbf{ndn}. \tag{9}$$

The resulting objectivity of the evolution law (6) may be verified in the usual way.

The hyperelastic stress consists of the longitudinal normal stress $\mathbf{nn} : \boldsymbol{\sigma}_*$ and the transverse mean stress $\frac{1}{2}\left(\mathbf{I} - \mathbf{nn}\right) : \boldsymbol{\sigma}_*$, while the hypoplastic stress is the shear stress along and across $\mathbf{n}$. Thus

$$\boldsymbol{\sigma}_\circ = \boldsymbol{\sigma}_\circ : \left[\frac{1}{2}\left(\mathbf{I}-\mathbf{nn}\right)\otimes\left(\mathbf{I}-\mathbf{nn}\right) + \mathbf{nnnn}\right] \tag{10}$$

and

$$\boldsymbol{\sigma}_*\colon \mathbf{nn} = \mathbf{0}, \qquad \boldsymbol{\sigma}_*\colon \mathbf{I} = \mathbf{0}. \tag{11}$$

We finally introduce a free energy *per unit volume* as follows:

$$\check{\psi} = \check{\psi}_\circ\left(\boldsymbol{\sigma}_\circ, \mathbf{n}\right) + \check{\psi}_*\left(\boldsymbol{\sigma}_*, \mathbf{n}\right), \tag{12}$$

where each of the contributions $\check{\psi}_\circ$ and $\check{\psi}_*$ is positive definite. Because of the relation (5) the hyperelastic energy $\check{\psi}_\circ$ may just as well be written as a strain energy function. Thus

$$\check{\psi} = \check{\psi}_\circ\left(\phi, \lambda\right) + \check{\psi}_*\left(\phi, j_3, j_4\right), \tag{13}$$

where j_3 and j_4 are two of the *physical* joint invariants of $\boldsymbol{\sigma}_*$ and $\mathbf{n}$ (cf. Spencer 1992):

$$j_3 = \mathbf{n}\cdot\boldsymbol{\sigma}_*^2\mathbf{n}, \tag{14}$$

$$j_4 = \frac{1}{2}\mathrm{tr}\boldsymbol{\sigma}_*^2 - \mathbf{n}\cdot\boldsymbol{\sigma}_*^2\mathbf{n}, \tag{15}$$

where j_3 measures the longitudinal shear stress and j_4 the transverse shear stress. A full description should include, an additional invariant measuring the relative orientation between the planes of longitudinal and transverse shear stress,

$$j_5 = \frac{1}{3}\mathrm{tr}\boldsymbol{\sigma}_*^3, \tag{16}$$

which is ommitted here for simplicity.

3. DISSIPATION INEQUALITY

The rate of free energy may now be developed as

$$\begin{aligned}
\dot{\check{\psi}} &= \frac{\partial\check{\psi}_\circ}{\partial\phi}\dot{\phi} + \frac{\partial\check{\psi}_\circ}{\partial\lambda}\dot{\lambda} + \frac{\partial\check{\psi}_*}{\partial\phi}\dot{\phi} + \frac{\partial\check{\psi}_*}{\partial\boldsymbol{\sigma}_*}:\dot{\boldsymbol{\sigma}}_* + \frac{\partial\check{\psi}_*}{\partial\mathbf{n}}\cdot\dot{\mathbf{n}} \\
&= -\frac{\partial\check{\psi}_\circ}{\partial\phi}\phi\mathrm{tr}\mathbf{d} + 2\frac{\partial\check{\psi}_\circ}{\partial\lambda^2}\lambda^2\mathbf{nn}:\mathbf{d} - \frac{\partial\check{\psi}_*}{\partial\phi}\phi\mathrm{tr}\mathbf{d} + \frac{\partial\check{\psi}_*}{\partial\boldsymbol{\sigma}_*}:\mathcal{G} \\
&\qquad + \frac{\partial\check{\psi}_*}{\partial\boldsymbol{\sigma}_*}:\left(\boldsymbol{\omega}\boldsymbol{\sigma}_* - \boldsymbol{\sigma}_*\boldsymbol{\omega}\right) + \frac{\partial\check{\psi}_*}{\partial\mathbf{n}}\cdot\dot{\mathbf{n}} \\
&= \left(-\frac{\partial\check{\psi}_\circ}{\partial\phi}\phi\mathbf{I} + 2\frac{\partial\check{\psi}_\circ}{\partial\lambda^2}\lambda^2\mathbf{nn}\right):\mathbf{d} - \frac{\partial\check{\psi}_*}{\partial\phi}\phi\mathrm{tr}\mathbf{d} + \frac{\partial\check{\psi}_*}{\partial\boldsymbol{\sigma}_*}:\mathcal{G}.
\end{aligned} \tag{17}$$

The spin-dependent last two terms of $(17)_2$ cancel identically, which is seen by developing the fifth term and using the identity (7):

$$\frac{\partial\check{\psi}_*}{\partial\boldsymbol{\sigma}_*}\colon\left(\boldsymbol{\omega}\boldsymbol{\sigma}_* - \boldsymbol{\sigma}_*\boldsymbol{\omega}\right) = -2\left(\frac{\partial\check{\psi}_*}{\partial j_3} - \frac{\partial\check{\psi}_*}{\partial j_4}\right)\mathbf{n}\cdot\boldsymbol{\sigma}_*^2\dot{\mathbf{n}} = -\frac{\partial\check{\psi}_*}{\partial\mathbf{n}}\cdot\dot{\mathbf{n}}. \tag{18}$$

The dissipation inequality,

$$\boldsymbol{\sigma}:\mathbf{d} - \check{\psi}\mathrm{tr}\mathbf{d} - \dot{\check{\psi}} \geq 0, \tag{19}$$

becomes

$$\left[\boldsymbol{\sigma}_\circ - 2\frac{\partial\check{\psi}_\circ}{\partial\lambda^2}\lambda^2\mathbf{nn} + \left(\frac{\partial\check{\psi}_\circ}{\partial\phi}\phi - \check{\psi}_\circ\right)\mathbf{I}\right] : \mathbf{d} + \boldsymbol{\sigma}_* : \mathbf{d} + \left(\frac{\partial\check{\psi}_*}{\partial\phi}\phi - \check{\psi}_*\right)\mathrm{tr}\mathbf{d} - \frac{\partial\check{\psi}_*}{\partial\boldsymbol{\sigma}_*} : \mathcal{G} \geq 0. \quad (20)$$

The square bracketed term must vanish because it is independent of $\boldsymbol{\sigma}_*$. We thus obtain the hyperelastic response function $\mathcal{F}$ as well as a dissipation condition for $\mathcal{G}$:

$$\mathcal{F} = \left(\check{\psi}_\circ - \frac{\partial\check{\psi}_\circ}{\partial\phi}\phi\right)\mathbf{I} + 2\frac{\partial\check{\psi}_\circ}{\partial\lambda^2}\lambda^2\mathbf{nn}, \quad (21)$$

$$\boldsymbol{\sigma}_* : \mathbf{d} + \left(\frac{\partial\check{\psi}_*}{\partial\phi}\phi - \check{\psi}_*\right)\mathrm{tr}\mathbf{d} - \frac{\partial\check{\psi}_*}{\partial\boldsymbol{\sigma}_*} : \mathcal{G} \geq 0. \quad (22)$$

To develop a specific constitutive law, we must now specify the free energy functions $\check{\psi}_\circ$ and $\check{\psi}_*$ and the evolution law $\mathcal{G}$.

4. STRAIN ENERGY FUNCTION

For the hyperelastic response we adopt the strain energy function of Wysocki et al. (2010), which is Hookean in positive axial extension and power-law elastic in the volumetric mode:

$$\check{\psi}_\circ(\phi,\lambda) = \frac{kE_f}{\beta-1}\phi^\beta + \frac{1}{4}\phi E_f Z(\lambda-1), \quad (23)$$

where

$$Z(x) = xH(x) \quad (24)$$

and $H(x)$ is the Heaviside step function. Thus the Z-function is equal to its argument if the latter is positive and zero otherwise. Differentiation of this energy function into equation (21) yields the response function

$$\mathcal{F}(\phi,\lambda,\mathbf{n}) = -kE_f\phi^\beta\mathbf{I} + \phi E_f Z(\lambda-1)\mathbf{nn}. \quad (25)$$

5. STRESS ENERGY FUNCTION

At sufficiently small isochoric strains we expect the fibre bed to be linear elastic with longitudinal and transverse shear moduli G_L and G_T that scale with the bulk modulus, i.e.,

$$G_L = G_{fL}\phi^\beta, \quad (26)$$

$$G_T = G_{fT}\phi^\beta, \quad (27)$$

where the constants G_{fT} and G_{fL} should be of the same order as the intrinsic fibre modulus E_f. Let us thus consider a simple stress energy function that is locally linear elastic:

$$\check{\psi}_*(\phi,j_3,j_4) = \frac{1}{2}\left(\frac{j_3}{G_L} + \frac{j_4}{G_T}\right) = \frac{1}{2\phi^\beta}\left(\frac{j_3}{G_{fL}} + \frac{j_4}{G_{fT}}\right). \quad (28)$$

This energy function possesses some rather attractive properties. By differentiation of (28) and application of the chain rule, we obtain the relation

$$\frac{\partial\check{\psi}_*}{\partial\boldsymbol{\sigma}_*} : \boldsymbol{\sigma}_* = 2\left(\frac{\partial\check{\psi}_*}{\partial j_3}j_3 + \frac{\partial\check{\psi}_*}{\partial j_4}j_4\right) = \frac{1}{\phi^\beta}\left(\frac{j_3}{G_{fL}} + \frac{j_4}{G_{fT}}\right) = 2\check{\psi}_* \quad (29)$$

and, similarly,

$$\frac{\partial \check{\psi}_*}{\partial \phi}\phi = -\frac{\beta}{2\phi^\beta}\left(\frac{j_3}{G_{fL}} + \frac{j_4}{G_{fT}}\right) = -\beta\check{\psi}_*. \tag{30}$$

6. EVOLUTION LAW

Now consider an evolution law of the hypoplastic form

$$\mathcal{G}\left(\phi, \boldsymbol{\sigma}_*, \mathbf{n}, \mathbf{l}\right) = \mathbb{L}\left(\phi, \mathbf{n}\right) : \mathbf{d} - \boldsymbol{\sigma}_* R\left(\phi, \boldsymbol{\sigma}_*, \mathbf{d}, \mathbf{n}\right), \tag{31}$$

where the linear operator $\mathbb{L}\left(\phi, \mathbf{n}\right)$ is a transversely isotropic tensor and $R\left(\phi, \boldsymbol{\sigma}_*, \mathbf{d}, \mathbf{n}\right)$ is a scalar dissipation function. We shall require that $\mathbb{L}\colon \mathbf{d}$ be non-dissipative, so that a purely elastic shear response is at all possible. This implies the condition

$$\boldsymbol{\sigma}_* : \mathbf{d} - \frac{\partial \check{\psi}_*}{\partial \boldsymbol{\sigma}_*} : \mathbb{L} \colon \mathbf{d} = 0. \tag{32}$$

As a consequence, introducing (31) into (22) and using (32), the total dissipation becomes

$$\frac{\partial \check{\psi}_*}{\partial \phi}\phi\mathbf{I} : \mathbf{d} + \frac{\partial \check{\psi}_*}{\partial \boldsymbol{\sigma}_*} : \boldsymbol{\sigma}_* R\left(\phi, \boldsymbol{\sigma}_*, \mathbf{d}, \mathbf{n}\right) - \check{\psi}_* \mathrm{tr}\mathbf{d} \geq 0. \tag{33}$$

Due to the properties of the stress energy function (29) and (30), and $\check{\psi}_* \geq 0$, the dissipation condition (33) reduces to

$$R \geq \frac{1}{2}\left(\beta + 1\right)\mathrm{tr}\mathbf{d}. \tag{34}$$

This result can be understood as follows. A decrease in stiffness gives an increase in energy, for a given stress state So when β is positive, i.e. the material stiffens on compression, some shear stress must be relaxed upon expansion, or negative dissipation would occur. Physically such stress relaxation occurs through slip at contacts as the contact pressure is released. A perhaps unphysical feature of the present formulation is that repeated compression and expansion will eventually dissipate all of the stress (cf. the numerical examples below). This behaviour is a consequence of the limited state space chosen, and could be remedied by introducing history dependent state variables in the stress energy function. Now inequality (34) implies that, while shear dissipation is "optional", dilational dissipation is mandatory, regardless of what dissipative mechanisms are considered. Equations (32) and (34) will form a solid basis for constructing $\mathbb{L}$ and R, respectively.

7. LINEAR OPERATOR

Equation (32) implies that the linear operator is defined by the stress energy potential $\check{\psi}_*$ through the relation

$$\frac{\partial \check{\psi}_*}{\partial \boldsymbol{\sigma}_*} : \mathbb{L} = \boldsymbol{\sigma}_*. \tag{35}$$

along with the transversely isotropic symmetry and the form of $\boldsymbol{\sigma}_*$. Being transversely isotropic, $\mathbb{L}$ must have the form[2]

$$\begin{aligned} \mathbb{L}\left(\phi, \mathbf{n}\right) \;=\; & A\left(\mathbf{I}\bar{\otimes}\mathbf{I} + \mathbf{I}\underline{\otimes}\mathbf{I}\right) + B\mathbf{I}\otimes\mathbf{I} + C(\mathbf{I}\otimes\mathbf{nn} + \mathbf{nn}\otimes\mathbf{I}) \\ & + D(\mathbf{I}\bar{\otimes}\mathbf{nn} + \mathbf{I}\underline{\otimes}\mathbf{nn} + \mathbf{nn}\underline{\otimes}\mathbf{I} + \mathbf{nn}\bar{\otimes}\mathbf{I}) + E\mathbf{nnnn}, \end{aligned} \tag{36}$$

[2]The open products are defined as $\mathbf{a}\otimes\mathbf{b} = a_{ij}b_{kl}e_ie_je_ke_l$, $\mathbf{a}\bar{\otimes}\mathbf{b} = a_{ik}b_{kl}e_ie_je_ke_l$, $\mathbf{a}\underline{\otimes}\mathbf{b} = a_{il}b_{jk}e_ie_je_ke_l$.

where the coefficients A, B, C, D, E are functions of ϕ. Due to (11) $\mathbb{L}$ must also have the properties

$$\mathbf{nn} : \mathbb{L} = \mathbf{0} \quad \text{and} \quad \mathbf{I} : \mathbb{L} = \mathbf{0}, \tag{37}$$

which yields

$$A = C = -B, \qquad E = -(3A + 4D). \tag{38}$$

Thereby (36) reduces to

$$\begin{aligned} \mathbb{L}(\phi, \mathbf{n}) &= A\left[(\mathbf{I}\bar{\otimes}\mathbf{I} + \mathbf{I}\underline{\otimes}\mathbf{I}) - \mathbf{I}\otimes\mathbf{I} + (\mathbf{I}\otimes\mathbf{nn} + \mathbf{nn}\otimes\mathbf{I})\right] \\ &\quad + D\left(\mathbf{I}\bar{\otimes}\mathbf{nn} + \mathbf{I}\underline{\otimes}\mathbf{nn} + \mathbf{nn}\underline{\otimes}\mathbf{I} + \mathbf{nn}\bar{\otimes}\mathbf{I}\right) - (3A + 4D)\mathbf{nnnn}. \end{aligned} \tag{39}$$

Using the proposed energy function we have

$$\frac{\partial \check{\psi}_*}{\partial \boldsymbol{\sigma}_*} = \frac{1}{2}\phi^{-\beta}\left[G_{fT}^{-1}\boldsymbol{\sigma}_* + \left(G_{fL}^{-1} - G_{fT}^{-1}\right)(\boldsymbol{\sigma}_*\mathbf{nn} + \mathbf{n}\boldsymbol{\sigma}_*\mathbf{n})\right]. \tag{40}$$

Introducing (39) and (40) into the condition (35) yields

$$A = G_{fT}\phi^{\beta}, \tag{41}$$

$$D = (G_{fL} - G_{fT})\,\phi^{\beta}, \tag{42}$$

and the linear operator is found to be

$$\begin{aligned} \mathbb{L}(\phi, \mathbf{n}) &= \phi^{\beta}\left[G_{fT}\left(\mathbf{I}\bar{\otimes}\mathbf{I} + \mathbf{I}\underline{\otimes}\mathbf{I} - \mathbf{I}\otimes\mathbf{I} + \mathbf{I}\otimes\mathbf{nn} + \mathbf{nn}\otimes\mathbf{I}\right)\right. \\ &\quad + (G_{fL} - G_{fT})\left(\mathbf{I}\bar{\otimes}\mathbf{nn} + \mathbf{I}\underline{\otimes}\mathbf{nn} + \mathbf{nn}\underline{\otimes}\mathbf{I} + \mathbf{nn}\bar{\otimes}\mathbf{I}\right) \\ &\quad \left. - (4G_{fL} - G_{fT})\mathbf{nnnn}\right]. \end{aligned} \tag{43}$$

8. CONSISTENT DISSIPATION FUNCTION

Contact slip may occur either by raising the tangential force or by lowering the normal force. On the continuum scale we associate tangential forces with shear stress and normal forces with pressure, and thus distinguish between plastic dissipation (due to shear overload) and decompression dissipation (due to pressure release). For the decompression dissipation we simply use the necessary dissipation given by the inequality (34). For the plastic dissipation we associate the tangential forces with shear stress invariants j_3 and j_4, and the normal forces with the pressure $kE_f\phi^{\beta}$ and introduce a slip stress function,

$$\zeta = \zeta(\phi, j_3, j_4, j_5), \tag{44}$$

such that

$$R = Z(\boldsymbol{\nabla}\zeta : \mathbb{L} : \mathbf{d}), \tag{45}$$

where $\boldsymbol{\nabla}\zeta = \partial\zeta/\partial\boldsymbol{\sigma}_*$ and the Z-function is defined in equation (24). The argument of the Z-function is the rate of increase of the slip stress function ζ due to the elastic stress rate. The resulting dissipation function becomes

$$R = \frac{1}{2}(\beta + 1)\,Z(\mathrm{tr}\mathbf{d}) + Z(\boldsymbol{\nabla}\zeta : \mathbb{L} : \mathbf{d}). \tag{46}$$

This form is *homogeneous of order 1*, which implies that the constitutive model will be rate independent.

The specification of the slip stress function may be done in any number of ways. Here we shall consider a simple Coulomb-type behaviour,

$$\zeta = \frac{1}{kE_f\phi^\beta}\sqrt{\frac{j_3}{\mu_3^2}+\frac{j_4}{\mu_4^2}}. \tag{47}$$

Then

$$\begin{aligned}\boldsymbol{\nabla}\zeta &= \frac{\partial\zeta}{\partial j_3}\frac{\partial j_3}{\partial\boldsymbol{\sigma}_*}+\frac{\partial\zeta}{\partial j_4}\frac{\partial j_4}{\partial\boldsymbol{\sigma}_*} \qquad (48)\\ &= \frac{1}{2kE_f\phi^\beta}\left(\frac{j_3}{\mu_3^2}+\frac{j_4}{\mu_4^2}\right)^{-1/2}\left[\left(\frac{1}{\mu_3^2}-\frac{1}{\mu_4^2}\right)(\boldsymbol{\sigma}_*\mathbf{nn}+\mathbf{n}\boldsymbol{\sigma}_*\mathbf{n})+\frac{1}{\mu_4^2}\boldsymbol{\sigma}_*\right].\end{aligned}$$

From equation (43), using $\mathrm{tr}\boldsymbol{\sigma}_* = \boldsymbol{\sigma}_*\colon\mathbf{nn} = 0$, we obtain

$$\begin{aligned}\mathbb{L}\colon\mathbf{d} &= \phi^\beta\left[G_{fT}\left(2\mathbf{d}+\mathbf{I}\otimes\mathbf{nn}:\mathbf{d}-(\mathbf{I}-\mathbf{nn})\,\mathrm{tr}\mathbf{d}\right)\right. \qquad (49)\\ &\quad \left.+\,2\left(G_{fL}-G_{fT}\right)(\mathbf{dnn}+\mathbf{ndn})-(4G_{fL}-G_{fT})\,\mathbf{nnnn}:\mathbf{d}\right],\\ \boldsymbol{\sigma}_*:\mathbb{L}:\mathbf{d} &= \phi^\beta\left\{2G_{fT}\boldsymbol{\sigma}_*\colon\mathbf{d}+4\left(G_{fL}-G_{fT}\right)\mathbf{n}\cdot\boldsymbol{\sigma}_*\mathbf{dn}\right\}, \qquad (50)\\ (\boldsymbol{\sigma}_*\mathbf{nn}+\mathbf{n}\boldsymbol{\sigma}_*\mathbf{n}):\mathbb{L}:\mathbf{d} &= 4\phi^\beta G_{fL}\mathbf{n}\cdot\boldsymbol{\sigma}_*\mathbf{dn}. \qquad (51)\end{aligned}$$

Combining (48) with (50) and (51) yields

$$\boldsymbol{\nabla}\zeta:\mathbb{L}:\mathbf{d} = \frac{1}{kE_f}\left(\frac{j_3}{\mu_3^2}+\frac{j_4}{\mu_4^2}\right)^{-1/2}\left[2\left(\frac{G_{fL}}{\mu_3^2}-\frac{G_{fT}}{\mu_4^2}\right)\mathbf{n}\cdot\boldsymbol{\sigma}_*\mathbf{dn}+\frac{G_{fT}}{\mu_4^2}\boldsymbol{\sigma}_*\colon\mathbf{d}\right]. \tag{52}$$

9. NUMERICAL EXAMPLES

The constitutive equations developed above may be summarised as follows:

$$\begin{aligned}\boldsymbol{\sigma}_\circ &= -kE_f\phi^\beta\mathbf{I}+\phi E_f Z\left(\lambda-1\right)\mathbf{nn}, \qquad (53)\\ \dot{\boldsymbol{\sigma}}_* &= \mathbb{L}\colon\mathbf{d}-\boldsymbol{\sigma}_*\left[\frac{1}{2}\left(\beta+1\right)Z\left(\mathrm{tr}\mathbf{d}\right)+Z\left(\boldsymbol{\nabla}\zeta:\mathbb{L}:\mathbf{d}\right)\right]\\ &\quad +2\mathrm{sym}\left(\mathbf{w}\boldsymbol{\sigma}_*-\boldsymbol{\sigma}_*\mathbf{dnn}+\boldsymbol{\sigma}_*\mathbf{ndn}\right), \qquad (54)\end{aligned}$$

with $\mathbb{L}\colon\mathbf{d}$ given by equation (49) and $\boldsymbol{\nabla}\zeta:\mathbb{L}:\mathbf{d}$ by equation (52). Numerical integration of equation (54) was performed using the simple quadratic algorithm

$$\boldsymbol{\sigma}_{n+1} = \boldsymbol{\sigma}_{n-1}+2\dot{\boldsymbol{\sigma}}_n\Delta t, \tag{55}$$

where Δt is the timestep. Reasonable elastic parameters for carbon fibre roving were chosen as follows: Based on literature data (Kim, McCarthy and Fanucci 1991; Toll 1998): $kE_f = 500$, $\beta = 14.5$. The intrinsic elastic modulus is taken to be $E_f = 2\times10^5$MPa and the intrinsic shear moduli were set to $G_{fL} = 0.1E_f$ and $G_{fT} = 0.01E_f$. The friction coefficients where set to $\mu_3 = 0.5$ (longitudinal) and $\mu_4 = 0.1$ (transverse). All examples use a constant strain step of $\|\mathbf{d}\|\,\Delta t = 10^4$, which is quite sufficient for convergence.

Figure 2 plots the transverse pressure $-\sigma_{33}$ $(= -\sigma_{22})$, vs volume fraction, ϕ, in biaxial cyclic compression. Being hyperelastic, this response is completely reversible with no sign

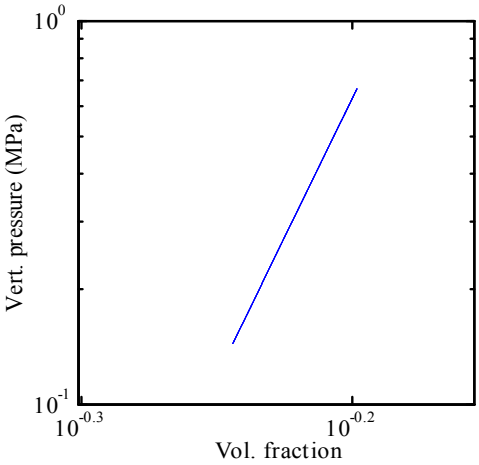

Figure 2: Biaxial transverse compression.

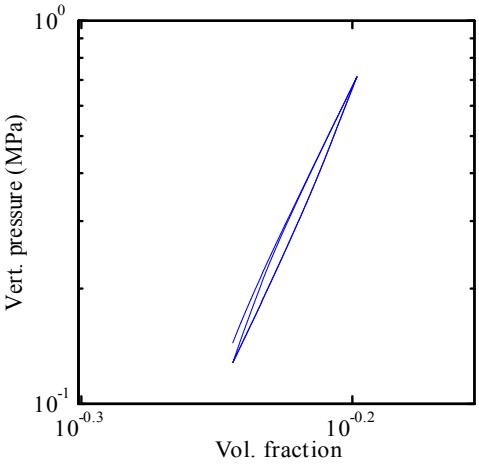

Figure 3: Uniaxial compression.

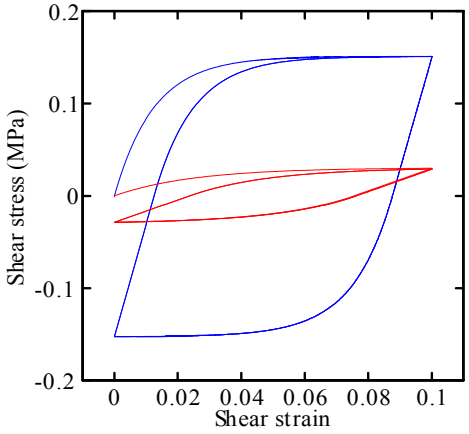

Figure 4: Longitudinal and transverse shear.

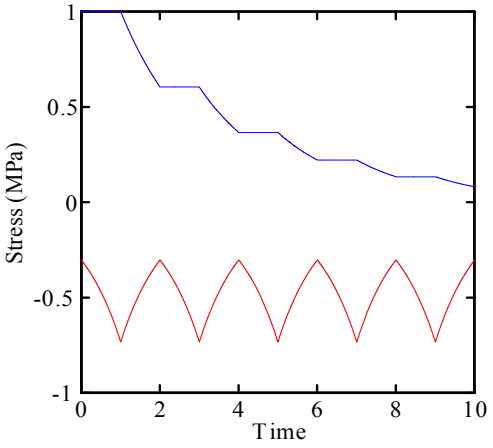

Figure 5: Relaxation of shear stress on decompression. Upper σ_{13}; lower σ_{33}.

of hysteresis. Figure 3 shows the same thing for uniaxial compression. Two cycles are shown for a compression strain of 10%, starting at $\phi = 0.57$, the process is stationary already after two cycles, so all further cycles coincide with the second cycle. The hysteresis is due to the shear component involved in the uniaxial compression mode. Figure 4 plots the shear stress response in longitudinal and transverse shear. Two cycles are shown for a shear strain of 10% at $\phi = 0.6$. Again the process is already stationary after two cycles. Figure 5 shows the relaxation of a shear stress, σ_{13} (upper curve), originally at 1 MPa, during 5 cycles of 3% biaxial transverse compression and decompression starting at $\phi = 0.6$. The lower curve shows the compression stress, σ_{33} ($= \sigma_{22}$). Notice that no shear stress relaxation takes place during the compression cycles, because of the positive compression rate and the absence of any shear rate. It may be worth recalling that this theory is rate-independent, so all the curves are invariant under any change of timescale.

10. CONCLUDING REMARKS

The present theory is intended as a structure and a framework for future modelling, rather than a model ready for use. We know at least two additional phenomena that will need to be introduced in order to accurately represent true behaviour: (1) Rate dependence, due to the lubricating effect of resin and sizing, can be introduced by making the response function $\mathcal{G}(\phi, \boldsymbol{\sigma}_*, \mathbf{n}, \mathbf{l})$ inhomogeneous in $\mathbf{l}$, for example by adding one or more terms of other degrees in $\mathbf{l}$. (2) Volumetric inelasticity may be introduced by making the hypoplastic stress $\boldsymbol{\sigma}_*$ non-deviatoric and introducing a suitable volumetric contribution into the linear operator $\mathbb{L}$. Both of those effects are thus readily accomodated within the structure, and it is the intention of the author to do so in future work.

Another important limitation of the present theory is that the slip function as well as the stress energy function is indifferent to the orientation of longitudinal shear stress (i.e., the angle of the plane of longitudinal shear stress relative to the principal directions of the transverse shear stress). This implies, for example, that slip due to a longitudinal shear stress under, say, uniaxial compression occurs at the same stress level regardless of whether the plane of longitudinal shear is parallel or perpendicular to the compression axis. This can be solved by including an additional stress invariant, j_5, but at the expence of considerable added complexity.

The axial spin, equation (8), was chosen here as a simple Jaumann-type co-rotation. It is well known that this spin yields oscillating stress response at steady flow (cf. Zhou and Tamma 2003). More sophisticated spins, such as the logarithmic spin (Xiao, Bruhns and Meyers 1997), can of course be used if requried. The Jaumann spin has, however, the advantage of simplicity. Notice, however, that the non-axial part of the spin is dictated by the rotation of the fibre axes, which must be affine due to the continuity of the fibres.

The separation made here between hyperelastic and hypoplastic parts of the response is not necessary—the evolution law (6) is general enough to describe the full response. The benefit of this separation is that we retain the familiar structure of nonlinear elasticity for that part of the response which is elastic, while introducing a differential structure only where it is needed.

ACKNOWLEDGEMENT

This work was financed by the Swedish Research Council (VR).

REFERENCES

Alkhagen, M., and Toll, S. (2007). Micromechanics of a compressed fibre mass. ASME J. Appl. Mech. 74, 723-731.

Cai, Z., and Gutowski, T. (1992). The 3-D deformation behaviour of a lubricated fiber bundle. J. Composite Materials 26, 1207-1237.

Chen, B., Cheng, A.H.-D., and Chou, T.-W. (2001). A nonlinear compaction model for fibrous preforms. Composites Part A 32, 701-707.

Cheng, J.J, Kelly, P.A., and Bickerton, S. (2012). A rate-independent model thermo-mechanical constitutive model for fiber reinfoircements. J. Composite Materials 46, 247-256.

Curiskis, J.I., and Carnaby, G.A. (1985). Continuum mechanics of the fibre bundle. Textile Res. J. 55,334–344.

Kim, Y.R, McCarthy P., and Fanucci, J.P. (1991). Compressibility and relaxation of fiber reinforcements during composite processing. Polymer Composites 12, 13–19.

Kolymbas, D. Introduction to hypoplasticity. (2000). Advances in Geotechnical Engineering and Tunneling. Vol 1, Balkema, Rotterdam.

Lanier, J., Caillerie, D., Chambon, R., Viggiani, G., Bésuelle, P., and Desrues, J. (2004). A general formulation of hypoplasticity. Int. J. Numer. Anal. Meth. Geomech., 28, 1461–1478.

Norris, A.N., and Johnson, D.L. (1997). Nonlinear Elasticity of Granular Media. ASME J. Appl. Mech. 64, 39–48.

Somashekar, A.A., Bickerton, S., and Bhattachayya, D. (2012). Modelling the viscoelastic stress relaxation of glass fibre reinforcements under constant compaction strain during composites manufacturing. Composites Part A 43, 1044-1052.

Spencer A.J.M. (1992). Plasticity theory for fibre.reinforced composites. J. Eng. Mech. 26, 107–118.

Toll, S. (1998). Packing mechanics of fiber reinforcements. Polymer Engineering and Science 38, 1337–1350.

Toll, S. (2011). The dissipation inequality in hypoplasticity. Acta Mech. 221, 39–47.

Wysocki, M., Toll, S., Larsson R, and Asp, L. (2010). Anisotropic and tension-compression asymmetric model for composites consolidation. Composites Part A 41, 284-295.

Xiao, H. Bruhns, O.T., and Meyers, A. (1997). Hypo-elasticity model based upon the Logarithmic Stress Rate. J. Elasticity 47, 51–68.

Zhou, X., and Tamma, K.K. (2003). On the applicability and stress update formulations for corotational stress rate hypoelasticity constitutive models. Finite Elements in Analysis and Design, 39, 783–816.

Proceedings of the 34th Risø International Symposium on Materials Science:
Processing of fibre composites – challenges for maximum materials performance
Editors: B. Madsen, H. Lilholt, Y. Kusano, S. Fæster and B. Ralph
Department of Wind Energy, Risø Campus
Technical University of Denmark, 2013

NEW FASTENER SYSTEM FOR LAMINATED COMPOSITES BY FE-BASED SHAPE MEMORY ALLOY

H. Yasuda, O. C. Namli, Y. Liang and M. Taya

Center for Intelligent Materials and Systems,
Department of Mechanical Engineering, University of Washington,
Box 352600 Seattle Washington 98195-2600, USA

ABSTRACT

We propose a new fastener system which consists of a simple pin and washer made of Fe-based shape memory alloy (Fe-SMA). This fastener system creates the clamping force and seals a fastener hole due to the reverse martensite to austenite phase transformation of Fe-SMA. In order to estimate the stress at the boundary between the proposed pin and a fastener hole, we constructed an analytical model using Eshelby's theory. In addition, three point bending test on aluminum plates and carbon fiber composite plates, which were clamped by the proposed fastener system, was conducted to verify the effectiveness of the proposed new fastener method.

1. INTRODUCTION

Advanced composites have been used increasingly in the modern airplane and other energy infrastructures such as wind turbine blades. Those composite parts of the airplane structures must be jointed together either by bonding or fasteners. Bolted joints are widely used as fasteners because of low cost and mature technology. Although aerospace engineers already ensure that fastened joints do not reduce the efficiency on the structure, the problem could be more severe with composite materials than with conventional metals because composites are relatively brittle and have very little capacity to redistribute loads. Great efforts have been done on many special designs of fasteners for composites, like HUCK-TITE (Niu 2010). One of the common yet important aspects of using those fasteners is to use very small hole size clearance or even interference fit. Some fasteners include sleeves for interference fit to prevent damage of composite during assembly. This is because loose fits result in poor fatigue life of composite joints (Niu 2010). Hesse et al. (2004) developed NiTi SMA based clamping-force actuator in a bolted joint. This actuator has the advantage to re-tighten the joint and to prevent structure failure in loosed bolted joints, however, it cannot fill the clearance hole which is very important for the polymeric composite structure. Furthermore, the cost of NiTi actuators can be high. Instead of using complex fasteners possible with sleeves to create the interference fit, we

propose using simple design and low cost of joint made of iron based shape memory alloy (Fe-SMA, e.g. Fe-Mn-Si) as a replacement. Fe-SMAs have been developed in decades since Sato et al. (1982) found martensitic transformation fcc(γ) ↔ hcp(ε) in Fe-30Mn-1Si alloy. A great review of various Fe-SMAs was also reported (Sato et al. 2006). Although Fe-SMAs have about 4% recovery-strain and wide transformation temperature ranges, where the shape memory properties are not suitable for two-way operations as NiTi SMA, Fe-SMAs became very important recently in many practical applications such as pipe joints, fishplate for crane rail, and so on (Sato et al. 2006). In addition, Fe-SMAs have advantages in commercial production due to their inexpensive constituent elements and availability of the mass-production facilities that are readily used for the production of stainless steels. Further improvement has been made to add other elements in Fe-Mn-Si SMAs to improve material properties and shape recovery strain (Kajiwara et al. 2001;Watanabe et al. 2002). It was found that Fe-SMAs become high corrosion-resistant by adding Cr and Ni (Jiang et al. 1995; Otsuka et al. 1990), which is very important if Fe-SMAs are used for joints in harsh environment.

In this paper, we will discuss about the property of Fe-SMA based on experiments focusing on their strain recovery. Due to its unique property, we designed a new Fe-SMA fastener system. This joining method has advantages over conventional bolts and nuts fastener system while increasing its fatigue life. To measure the effectiveness of the new joint design, we conducted three point bending test on both aluminum plates and carbon fiber composite plates which were clamped by Fe-SMA pins and washers. Also, an analytical model based on Eshelby's theory is developed to estimate the stress around a fastener hole.

2. ANALYTICAL MODEL FOR NEW FE-SMA JOINT

The Fe-SMA joint is composed of a pin and a washer as illustrated in Fig.1. When the Fe-SMA pin and washer are heated over the austenite start temperature, the pin shortens in length while expand in diameter and the washer shrinks in diameter due to the martensite to austenite reverse phase transformation. Therefore, the Fe-SMA joint creates the clamping force and provides additional benefits to seal the hole in radial direction, strengthen the laminate structure, reduce slippage of lamination during external loading, and importantly increase fatigue life of the jointed composites. It is noted here that the surface of the proposed pins and washers are smooth, i.e., without any teeth, thus, its fatigue life is much better than the traditional bolts and nuts which have teeth.

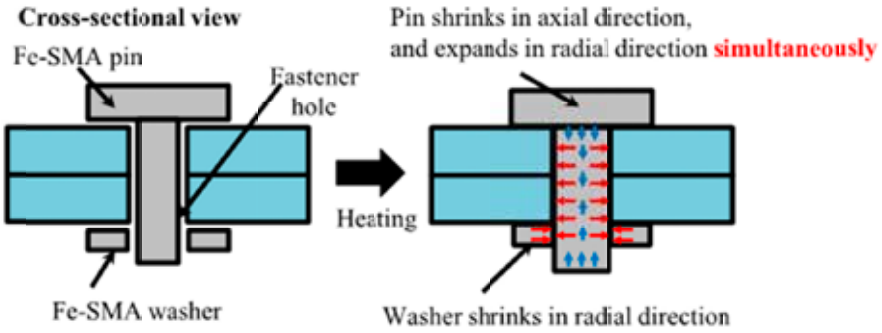

Fig. 1. Schematic illustration of Fe-SMA pin and washer joining method.

An analytical model based on the Eshelby's inhomogeneity inclusion problem (Fig.2) is developed to estimate the stresses due to swelling of the Fe-SMA pin in the laminated structure. Compared with Fig.1, the inhomogeneity Ω in Fig.2 represents the Fe-SMA pin while the matrix D-Ω represents the laminated structure such as aluminum or polymeric composite plates.

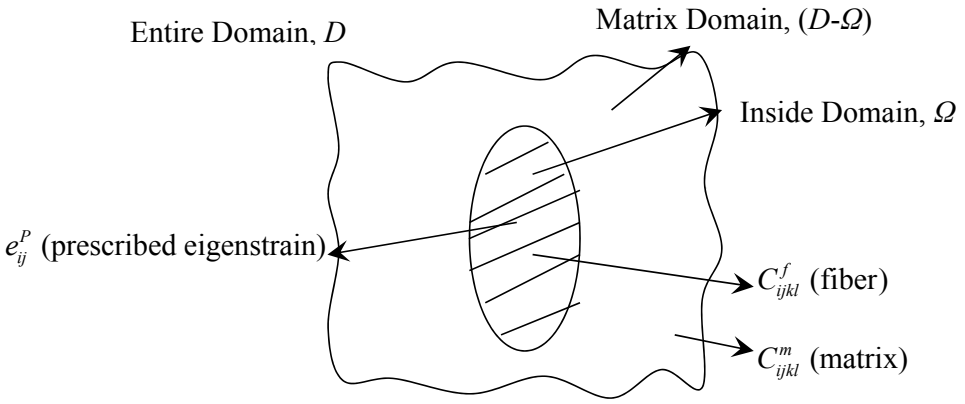

Fig. 2. Analytical model based on Eshelby's inhomogeneity inclusion problem with the prescribed eigenstrain e^p (Taya, 2005).

As shown in Fig.2, the inhomogeneity Ω has a given uniformly prescribed eigenstrain e^p and the stress in the fiber is (Mura 1982):

$$\sigma_{ij}^{f} = C_{ijkl}^{f}\left(e_{kl}^{f} - e_{kl}^{p}\right) = C_{ijkl}^{m}\left(e_{kl}^{f} - e_{kl}^{*}\right) \tag{1}$$

$$e_{kl}^{f} = S_{klmn}e_{mn}^{*} \tag{2}$$

where C, S and e are stiffness, Eshelby's tensor and strain tensor, respectively. The superscripted f and m mean fiber and matrix, respectively. The stiffness tensor C which is assumed to be isotropic for simplicity, can be expressed as

$$C_{ijkl} = \lambda\delta_{ij}\delta_{kl} + \mu\left(\delta_{ik}\delta_{jl} + \delta_{il}\delta_{kj}\right) \tag{3}$$

where λ and μ are Lame constants, and δ is Kronecker delta. By substituting Eq. (2) and (3) into (1), and setting k = l, it yields

$$\lambda^{f}\delta_{ij}\left(S_{kkmn}e_{mn}^{*} - e_{kk}^{p}\right) + 2\mu^{f}\left(S_{ijmn}e_{mn}^{*} - e_{ij}^{p}\right) = \lambda^{m}\delta_{ij}\left(S_{ijmn}e_{mn}^{*} - e_{kk}^{*}\right) + 2\mu^{m}\left(S_{ijmn}e_{mn}^{*} - e_{ij}^{*}\right) \tag{4}$$

In Eq.(4), only e^* is unknown. Because the pin embedded in the laminated structure is transverse isotropic, $e_{11}^{*} = e_{22}^{*}$. By assigning i,j = 1,1 and 3,3 to Eq.(4), two equations are formed as

$$C_{11}e_{11}^{*} + C_{12}e_{33}^{*} = F \tag{5}$$

$$C_{21}e_{11}^{*} + C_{22}e_{33}^{*} = G \tag{6}$$

where

$$C_{11} = \left(S_{1111} + S_{2211} + S_{3311} + S_{1122} + S_{2222} + S_{13322}\right)\left(\lambda^f - \lambda^m\right) + \left(S_{1111} + S_{1122}\right)\left(2\mu^f - 2\mu^m\right) + 2\lambda^m + 2\mu^m \tag{7}$$

$$C_{12} = \left(S_{1133} + S_{2233} + S_{3333}\right)\left(\lambda^f - \lambda^m\right) + S_{1133}\left(2\mu^f - 2\mu^m\right) + \lambda^m \tag{8}$$

$$C_{21} = \left(S_{1111} + S_{2211} + S_{3311} + S_{1122} + S_{2222} + S_{13322}\right)\left(\lambda^f - \lambda^m\right) + \left(S_{3311} + S_{3322}\right)\left(2\mu^f - 2\mu^m\right) + 2\lambda^m \tag{9}$$

$$C_{22} = \left(S_{1133} + S_{2233} + S_{3333}\right)\left(\lambda^f - \lambda^m\right) + S_{3333}\left(2\mu^f - 2\mu^m\right) + 2\mu^m + \lambda^m \tag{10}$$

$$F = \lambda^f\left(e_{11}^p + e_{22}^p + e_{33}^p\right) + 2\mu^f e_{11}^p \tag{11}$$

$$G = \lambda^f\left(e_{11}^p + e_{22}^p + e_{33}^p\right) + 2\mu^f e_{33}^p \tag{12}$$

Hence, the fictitious eigenstrains (e_{11}^* and e_{33}^*) can be solved from Eq.(5) and (6) as

$$e_{11}^* = \frac{C_{22}F - C_{12}G}{C_{11}C_{22} - C_{12}C_{21}} \tag{13}$$

$$e_{33}^* = \frac{-C_{21}F + C_{11}G}{C_{11}C_{22} - C_{12}C_{21}} \tag{14}$$

The inhomogeneity Ω is assumed as the elliptical cylinder. Therefore, the Eshelby's tensor, S can be determined where $a_1 = a_2$ and $a_3 = \infty$ (Mura 1982), for example,

$$S_{1111} = \frac{1}{2\left(1-\nu_m\right)}\left(\frac{a_2^2 + 2a_1a_2}{\left(a_1 + a_2\right)^2} + \left(1 - 2\nu_m\right)\frac{a_2}{\left(a_1 + a_2\right)}\right) = \frac{5 - 4\nu_m}{8\left(1-\nu_m\right)} \tag{15}$$

e^p is known due to the thermal expansion,

$$e^p = e^p\begin{bmatrix} 1/2 \\ 1/2 \\ -1 \\ 0 \\ 0 \\ 0 \end{bmatrix} \tag{16}$$

Therefore, Eq. (7) to (12) can be further simplified as

$$C_{11} = \frac{\lambda^f - \lambda^m}{1-\nu_m} + \frac{\mu^f - \mu^m}{1-\nu_m} + 2\left(\mu^m + \lambda^m\right) \tag{17}$$

$$C_{12} = \frac{\nu_m\left(\lambda^f - \lambda^m\right)}{1-\nu_m} + \frac{\nu_m\left(\mu^f - \mu^m\right)}{1-\nu_m} + \lambda^m \tag{18}$$

$$C_{21} = \frac{\lambda^f - \lambda^m}{1-\nu_m} + 2\lambda^m \tag{19}$$

$$C_{22} = \frac{\nu_m\left(\lambda^f - \lambda^m\right)}{1-\nu_m} + 2\mu^m + \lambda^m \tag{20}$$

$$F = \mu^f e^p \tag{21}$$

$$G = -2\mu^f e^p \tag{22}$$

The close form solution of fictitious eigenstrain can be derived from Eq. (13) to (22),

$$e_{11}^* = e_{22}^* = \frac{C_{22}F - C_{12}G}{C_{11}C_{22} - C_{12}C_{21}} = \frac{\left(3\lambda^f + 2\mu^f\right)\nu_m + \left(3\lambda^m + 2\mu^m\right)\left(1-2\nu_m\right)}{2\mu^m\left(1+\nu_m\right)\left(\mu^m + \mu^f + \lambda^f\right)}\mu^f e^p \tag{23}$$

$$e_{33}^* = \frac{-C_{21}F + C_{11}G}{C_{11}C_{22} - C_{12}C_{21}} = -\frac{\left(3\lambda^f + 2\mu^f\right) + \left(3\lambda^m + 2\mu^m\right)\left(1-2\nu_m\right)}{2\mu^m\left(1+\nu_m\right)\left(\mu^m + \mu^f + \lambda^f\right)}\mu^f e^p \tag{24}$$

The above strain components can be transformed to the polar coordinates (r, θ, z). Equations (23) and (24) coincide with the results by Mikata and Taya (1985) who used the mismatch strain due to the difference of thermal expansion coefficients between the fiber and matrix, while e^p in the case of Fe-SMA pin is prescribed eigenstrain. Furthermore, from Eq.(1), the stresses in the fiber are

$$\sigma_{11}^f = \sigma_{22}^f = \left(\frac{\left(\lambda^f + \mu^f\right)\left(3\lambda^m + 2\mu^m\right)\left(1-2\nu_m\right)}{2\mu^m\left(1+\nu_m\right)\left(\mu^m + \mu^f + \lambda^f\right)} - 1\right)\mu^f e^p \tag{25}$$

$$\sigma_{33}^f = \left(\frac{\lambda^f\left(3\lambda^m + 2\mu^m\right)\left(1-2\nu_m\right)}{2\mu^m\left(1+\nu_m\right)\left(\mu^m + \mu^f + \lambda^f\right)} + 2\right)\mu^f e^p \tag{26}$$

Again, Eqs. (25) and (26) coincide with the results by Mikata and Taya (1985).

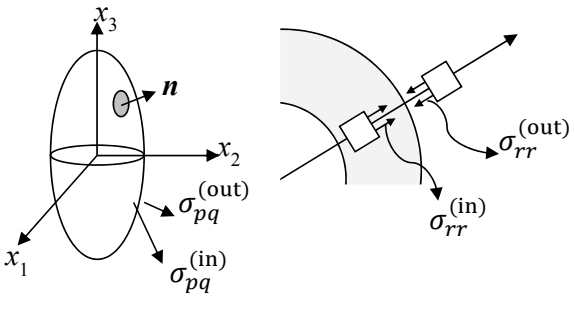

Fig. 3. Analytical model base on Walpole-Hill-Mura Jump Condition.

Next, the stress just outside the fiber can be estimated by Walpole-Hill-Mura jump condition, Fig.3 (Mura 1982; Mikata and Taya 1985),

$$\sigma_{pq}^{(out)} = \sigma_{pq}^{(in)} + C_{pqmn}^{m}\left(-C_{klij}^{m} e_{ij}^{*} n_l n_n \frac{\left(\lambda^m + 2\mu^m\right)\delta_{km} - \left(\lambda^m + \mu^m\right) n_k n_m}{\mu^m\left(\lambda^m + 2\mu^m\right)} + e_{mn}^{*} \right) \tag{27}$$

where $\boldsymbol{n}$ is the unit outer-normal vector on the inclusion surface. Therefore, stresses, $\sigma_{11}^{(out)}$ ($\sigma_{11}^{(out)} = \sigma_{22}^{(out)}$) and $\sigma_{33}^{(out)}$, just outside the fiber are

$$\sigma_{11}^{(out)} = \sigma_{11}^{(in)} - 2\mu^m\left(\frac{-\nu^m}{\left(1-\nu^m\right)} e_{ii}^{*} + \frac{\nu^m}{\left(1-\nu^m\right)} e_{ij}^{*} n_i n_j + \frac{\nu^m}{\left(1-\nu^m\right)} e_{ii}^{*} n_1 n_1 + 2e_{1i}^{*} n_1 n_i - \frac{1}{\left(1-\nu^m\right)} e_{ij}^{*} n_i n_j n_1 n_1 - e_{11}^{*} \right) \tag{28}$$

$$\sigma_{33}^{(out)} = \sigma_{33}^{(in)} - 2\mu^m\left(\frac{-\nu^m}{\left(1-\nu^m\right)} e_{ii}^{*} + \frac{\nu^m}{\left(1-\nu^m\right)} e_{ij}^{*} n_i n_j + \frac{\nu^m}{\left(1-\nu^m\right)} e_{ii}^{*} n_3 n_3 + 2e_{3i}^{*} n_3 n_i - \frac{1}{\left(1-\nu^m\right)} e_{ij}^{*} n_i n_j n_3 n_3 - e_{33}^{*} \right) \tag{29}$$

For the case of the Fe-SMA pin as the elliptical cylinder, $\boldsymbol{n}$ only points out in the radial direction (x_1 and x_2), therefore, by assigning $\boldsymbol{n}$ = (1,0,0) Eqs.(28) and (29) yield

$$\sigma_{11}^{(out)} = \sigma_{11}^{(in)} \tag{30}$$

$$\sigma_{33}^{(out)} = \sigma_{33}^{(in)} - 2\mu^m\left(\frac{-\nu^m}{\left(1-\nu^m\right)} e_{22}^{*} - \frac{1}{\left(1-\nu^m\right)} e_{33}^{*} \right) \tag{31}$$

The coordinate system can be easily transformed into the polar one (r, θ, z). By substituting Eqs. (23) ~ (26) into Eqs. (28) ~ (29), the stresses just outside the fiber can be solved numerically.

The case studies of the above analytical model are performed by using Al 6061 as the matrix and Fe-Mn-Si SMA as the fiber, where the input material properties are listed in Table1. The prescribed eigenstrain, e^p, of 3.5% is used. Table 2 shows the numerical results from the analytical model, and we compared them with the results obtained from the finite element analysis(FEA) focusing on the components of stresses in the r and θ directions. The results of the induced stresses in Fe-SMA pin and just outside the pin prediected by the Eshelby's model agree well with the FEM analysis.

Table 1. Isotropic material properties for matrix and fiber at room temperature.

	Matrix (Al-6061)	Fiber (Fe-Mn-Si SMA)
Young's Modulus (GPa)	70	167.5
Poisson's Ratio	0.33	0.359
Shear Modulus (GPa)	26.3	62.3
Lame constant, λ	51.1×10^9	157×10^9
Lame constant, μ	26.3×10^9	61.6×10^9

Table 2. Results.

	e^p	$e^*_{rr} = e^*_{\theta\theta}$	$\sigma^f_{rr} = \sigma^f_{\theta\theta}$	$\sigma^{(out)}_{rr} = \sigma^{(out)}_{\theta\theta}$
Eshelby	3.5%	3.35%	−230MPa	−230MPa
FEA	3.5%	–	−297MPa	−297MPa

3. EXPERIMENT

3.1 Material properties of Fe-based shape memory alloys. The shape memory effect of Fe-SMAs can be further improved when the alloys experience the applied strain and heat treatment several times, which is called the training process (Sato et al. 2006). We applied 6% strain to the dog-bone shape (rectangular cross-section) plate specimen followed by heat treatment in which the specimen was heated at 600°C for 10 minutes, and this process was repeated four times. Fig.4(a) shows the results of the tensile test in which the tensile specimen (Fe-28Mn-6Si-5Cr) experienced four-times training. The specimen exhibits about 3.5% recovery strain when heated from room temperature to 350°C after the training process.

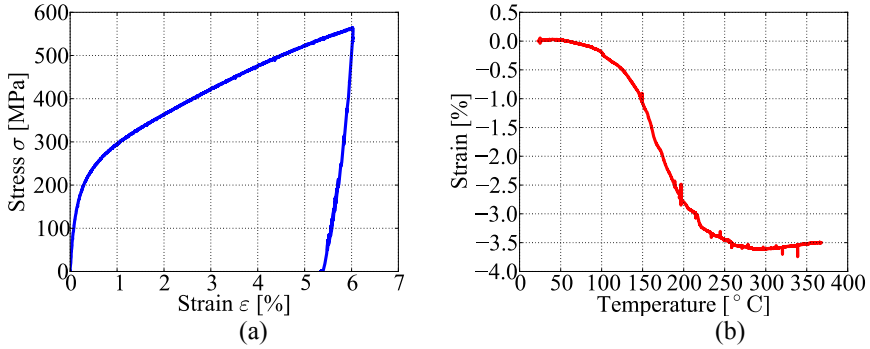

Fig. 4. (a) Stress-strain curve of Fe-28Mn-6Si-5Cr alloys after the training process, (b) followed by applying heat under stress free conditions and observe the strain recovery during heating.

The martensite transformation and reverse transformation is observed in different temperature range under different constant applied stress. If the Fe-SMA phase transformation is characterized, it will provide four phase transformation temperatures: M_s , M_f (martensite start and finish) and A_s , A_f (austenite start and finish). For austenite phase to martensite phase:

$$\xi = 1 - \exp\left[a^M \left(M_s - T\right) + b^M \sigma\right] \tag{32}$$

$$a^M = \frac{\ln(0.01)}{M_s - M_f}$$
$$b^M = \frac{a^M}{C^M} \tag{33}$$

For martensite phase to austenite phase:

$$\xi = 1 - \exp\left[a^M \left(A_s - T\right) + b^A \sigma\right] \tag{34}$$

$$a^A = \frac{\ln(0.01)}{A_s - A_f}$$
$$b^A = \frac{a^A}{C^A} \tag{35}$$

where C_M and C_A are the slope of the M_s and A_f lines in the σ-T diagram, respectively. By using the above constitutive equations, one can calculate the volume fraction of martensite ξ, from eq.(32) or (34), then the Young's modulus of the Fe-SMA with such ξ, can be calculated from the following simple rule of mixtures formula:

$$E = \left(1 - \xi\right) E_A + \xi E_M \tag{36}$$

where E_A and E_M are the Young's modulus of the Fe-SMA with 100% austenite phase and 100% martensite phase, respectively.

3.2 Fe-SMA pin and washer fastener applied to laminated plates. To verify the effectiveness of Fe-SMA pins and washers, three-point bending experiments were conducted. Both aluminum and carbon fiber composite plates were used. As shown in Fig.5, two Fe-SMA pins (14mm in diameter) were inserted into holes (150mm apart) of two aluminum plates (400 × 64 × 12mm). The plates were clamped by heating Fe-SMA pins and washers over 350°C where the training process was applied to both pins and washers. When the applied force reached about 20kN, the aluminum plates were under the plastic deformation as shown in Fig.5(b). When 25kN was applied, both Fe-SMA joints were still intact and held the laminated plates very well, even though the aluminum plates were bent permanently.

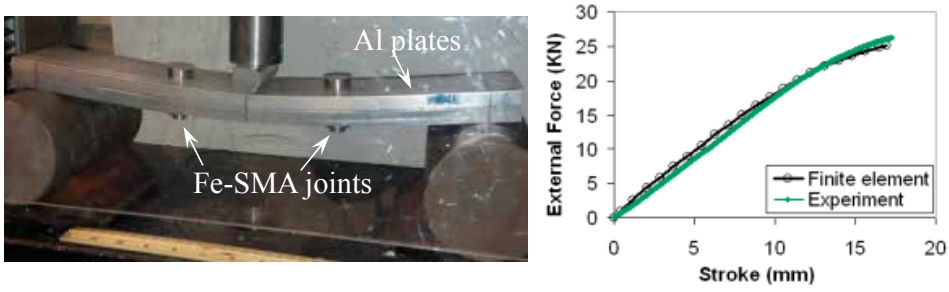

(a) (b)

Fig. 5. (a) Three pint bending experiment on aluminium plates, and (b) the test results.

The similar test was done on the case of carbon fiber composite plates (composite layup; 0°, +45°, 90°, –45°, –45°, 90°, +45°, 0°) as shown in Fig.6(a). Two Fe-SMA pins (6mm in diameter) were 80mm apart in the composite plates (308×45×5.7mm). During the three-point test, the carbon fiber composite plates start to break when the external force is about 4.5kN. The maximum tensile bending stress on the composite plate is estimated by the finite element analysis about 740MPa when the displacement is 26mm, which corresponds to the first sudden loss of force in Fig.6(b). However, both Fe-SMA joints were also intact without any separation between pins and washers.

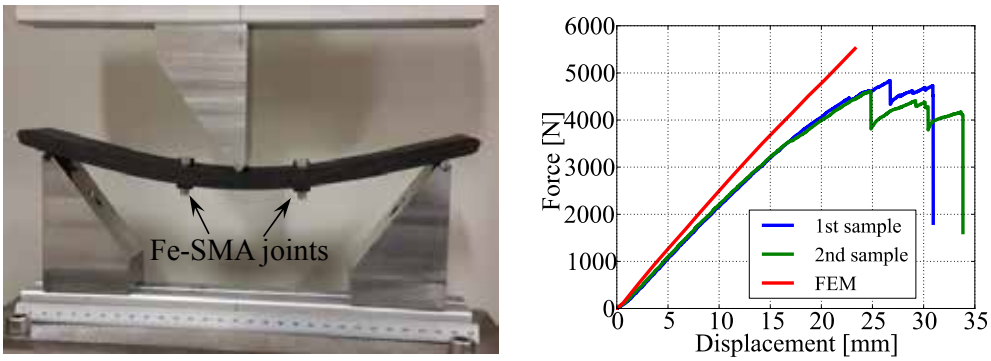

Fig.6. (a) Three point bending test on carbon fiber composite plates, and (b) its test results.

4. DISCUSSION

Wada et al. (2006) examined the behavior of Fe-Mn-Si based shape memory alloy under constant stress, and the relationship between the applied constant stress and the shape recovery temperature. The martensite transformation or reverse transformation is triggered when certain energy (ΔG) is applied to SMA (Fig.7). Under the constant stress applied to oppose the reverse transformation, SMA requires not only ΔG but also energy of applied stress ΔE for the reverse transformation, which shifts A_s temperature to A'_s. By using the analytical model based on the Eshelby's inclusion problem, the stresses around the pin and the fastener hole can be estimated. These stresses and the phase diagram can be used as the key parameters to design the Fe-SMA joints.

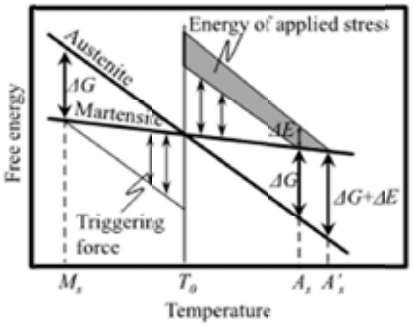

Fig. 7. Schematic illustration of phase transformation under applied stress (Wada et al. 2006)

It is noted in Fig. 4(b) that the heating of the Fe-SMA pin and washer up to 250 C is adequate in securing the recovery strain of up to 3.5%. where the heating could be done by applying Joule heating for a relatively short time, thus, this would not damage the polymeric composite next to the hole. Therefore, high recovery strain at even lower temperature than 250 C is preferable and this could be done by changing the material compositions and the training process (Sato et al. 2006).

5. CONCLUSIONS

We proposed a new simple fastener system by using Fe-based shape memory alloys, which consists of simple pins and washers and is secured by applying heat. The effectiveness of the proposed fastener system is demonstrated by three-point bending tests on both aluminum and polymeric composite laminated plates. The advantage of this system is that the Fe-SMA pin will swell in diameter to fill the gap of the clearance holes, therefore it does not damage the fastener hole during the assembly and it can be effective to enhance the fatigue life of the composite structure. Furthermore, the cost of the Fe-SMA is modest due to their inexpensive constituent elements and availability of the mass-production facilities as compared with NiTi SMA.

ACKNOWLEDGEMENTS

This work was supported by a partly a contract from Boeing Commercial Company, JCATI funding and the funding from Nabtesco. We are thankful for Mr. T. Maruyama of Awaji Materia who provided the Fe-SMA materials.

REFERENCES

Hesse, T., Ghorashi, M., and Inman, D. J. (2004). Shape Memory Alloy in Tension and Compression and its Application as Clamping-Force Actuator in a Bolted Joint: Part 1 - Experimentation. *Journal of Intelligent Materials Systems and Structures,* 15(8), 577-587.

Jiang, B. H., Sun, L., Li, R., and Hsu, T. Y. (1995). Influence of austenite grain size on γ-ε martensitic transformation temperature in Fe-Mn-Si alloys. *Scripta Metallurgica Et Materialia,* 33(1), 63-68.

Kajiwara, S., Liu, D., Kikuchi, T., and Shinya, N. (2001). Remarkable improvement of shape memory effect in Fe-Mn-Si based shape memory alloys by producing NbC precipitates. *Scripta Materialia,* 44(12), 2809-2814.

Mikata, Y., and Taya, M. (1985). Stress Field in a Coated Continuous Fiber Composite Subjected to Thermo-Mechanical Loadings. *Journal of Composite Materials*, 19(6), 554-578.

Mura, T. (1982). *Micromechanics of defects in solids* (M. Nijhoff, The Hague) Chapter 1 and 2.

Niu, M.C.Y (2010). *Composite airframe structures: Practical design information and data*, (Conmilit Press, Hong Kong), Chapter 5.

Otsuka, H., Yamada, H., Maruyama, T., Tanahashi, H., Matsuda, S., and Murakami, M. (1990). Effects of alloying additions on Fe-Mn-Si shape memory alloys. *Isij International,* 30(8), 674-679.

Sato, A., Chishima, E., Soma, K., and Mori, T. (1982). Shape memory effect in $\gamma \rightleftarrows \epsilon$ transformation in Fe-30Mn-1Si alloy single crystals. *Acta Metallurgica,* 30(6), 1177-1183.

Sato, A., Kubo, H., and Maruyama, T. (2006). Mechanical Properties of Fe-Mn-Si Based SMA and the Application. *Materials Transactions,* 47(3), 571-579.

Taya, M. (2005). *Electronic Composites*, Cambridge University Press, Cambridge, UK.

Wada, M., Naoi, H., and Tsukimori, K. (2006). Shape recovery characteristics under constant stress on FeMnSi based shape memory alloy. *Journal of the Japan Society for Technology of Plasticity*, 47(545) 522-526. (in Japanese)

Watanabe, Y., Miyazaki, E., and Okada, H. (2002). Enhanced Mechanical Properties of Fe-Mn-Si-Cr Shape Memory Fiber/Plaster Smart Composite. *Materials Transactions,* 43, 974-983.

QUANTIFYING REINFORCING EFFICIENCY OF NANOCELLULOSE FIBRES

Yvonne Aitomäki and Kristiina Oksman

Composite Centre Sweden, Division of Materials Science, Luleå University of Technology, Sweden

ABSTRACT

Cellulose nanofibres are found in all plants and have the potential to provide a sustainable biobased material source. These nanofibres can be used for reinforcing polymers and thus as structural materials. Very promising results have been reported for different nanocomposites but to compete with existing materials, it is important to understand what progress has been made towards structural materials using nanocellulose. To do this the reinforcing efficiency of the stiffness and strength of nanocellulose in different nanocomposites has been calculated for a number of reported nanocellulose fibre based composites. For the stiffness this is done by back-calculating a reinforcing efficiency factor from a Halpin-Tsai model and laminate theory. For the strength efficiency, two models are used: a classic short fibre composite model and a network model. The results show that orientation is key to the stiffness efficiency, as shown by the high efficiency of aligned natural fibres. The stiffness efficiency is, as expected, high in soft matrices but in stiff matrices, the network effect of the nanofibres is possibly limiting their reinforcing potential. The strength efficiency results show that in all the nanocomposites evaluated the network model is closer to predicting strength than the short fibre composite model. The correlation between the network strength and the composite strength suggest that much of the stress transfer is from fibre to fibre and strong nanocomposites depend heavily on having a strong network. Also noted is that in composite processing a good impregnation of the nanofibers is also seen as an important factor in the efficiency of both strength and stiffness.

1. INTRODUCTION

Cellulose nanofibres have been shown to have good reinforcing effect in polymers as shown in a number of reviews of the subject (Hubbe, Rojas, Lucia, and Sain (2008), Siro and Plankett (2010), Siqueira, Bras and Dufresne (2010)) This is particularly noteworthy in composites at temperatures beyond the glass transition temperature of the polymer even with concentrations as low as 6%. These biobased nanofibres can be extracted from agricultural waste and other cellulose by-products, and if their properties can be exploited in materials such as biobased

composites, they can provide an excellent alternative to petroleum-based materials. A large number of different combinations of matrix and nanocellulose fibres at different fibre volume concentrations have been tested and the number of publications on these nanocomposites has increased exponential over the last decade (see Fig. 1). Comparison between the different nanocomposites is difficult due to the range of different matrices used and the differences in their fibre volume fractions.

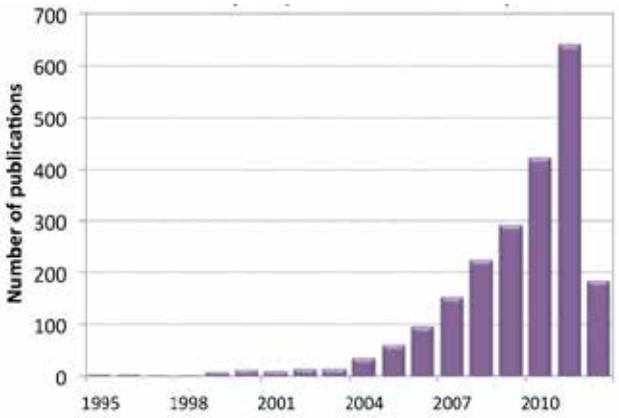

Fig. 1 Publications in the field of cellulose nanocomposites based on result returned from the Web of Science database in April 2012 with the Boolean search string 'Cellulos* AND (nanocompos* OR nanofib* OR nanowhis* OR nanocrystals*)'.

In this paper, the aim is to provide a tool for comparing different nanocomposites by calculating the reinforcing efficiency of the stiffness and strength. The model used here for stiffness efficiency is based on composite models both Halpin-Tsai and rule of mixtures. The strength efficiency has been calculated both using a short-fibre composite model and a network model.

2. THEORY

2.1 Stiffness Efficiency

The stiffness efficiency is calculated based on the use of composite laminar theory (CLT) with the stiffness of each layer calculated based on the Halpin-Tsai equation or the rule of mixtures equation.

The stiffness of the unidirectional ply, E_1, is calculated from Halpin-Tsai equation such that

$$E_1 = E_m \frac{1+\zeta\eta V_f}{1-\eta V_f} \tag{1}$$

where

$$\eta = \frac{E_f/E_m - 1}{E_f/E_m + \zeta}, \tag{2}$$

and where E_f is the elastic modulus of the fibre, E_m is the elastic modulus of the matrix, V_f is the

fibre volume fraction and ζ is the efficiency of the reinforcement. Once this is calculated, it is used in the CLT for a quasi-isotropic material with the layup [45/-45/0/90]. The other independent material constants required for the calculation are the transverse modulus of the unidirectional ply, E_2, its shear modulus, G_{12} and its Poisson's ratio, ν_{12}.The equations used for these constants are given in the appendix.

Rather than fixing the ζ to a shape factor and setting it to twice the aspect ratio, as is usually done for short fibre composites, in this case, ζ is used as an efficiency parameter. This efficiency, ζ is back-calculated from the experimentally measured stiffness of the composite. A high value for ζ is obtained when the composite approaches a Voigt's model of behaviour where the strain is constant and when the stiffness is dominated by the stiffness of the fibres. This typically occurs in laminates with unidirectional continuous fibres. Short-fibre composites can also achieve high efficiency and the longer the fibres the higher the efficiency, asymptotically approaching the continuous fibre limit. However in short-fibre composites, the efficiency will also depend on the interface between the fibre and the matrix.

The back-calculation is done by using a search function. A value of ζ in the Halpin-Tsai model is initially set, the stiffness of the unidirectional sheet is calculated, and then the CLT is used to calculate the stiffness of the composite. The value of ζ is changed until the value of the quasi-isotropic composite model equals the experimental measured Young's modulus of the composite.

The general values for the elastic parameters used to back-calculate ζ are shown in Table 1. The specific values used for calculating the efficiencies from selected cellulose nanocomposites reported in the literature are shown in Table 2. The search algorithm used is a Matlab implementation of the optimisation route described by Forsythe, Malcolm and Moler (1976).

Table 1: Material constant values used in the all the calculation of reinforcing efficiency and fibre efficiency for the cellulose nanocomposites.

Property	Symbol	Value
Longitudinal Young's modulus of the nanofibre	E_f	138 GPa
Transverse Young's modulus of the nanofibre	E_{f2}	25 GPa
Poisson ratio of the nanofibre	ν_f	0.3
Shear modulus of the nanofibre	G_f	1.7 GPa
Poisson ratio of the matrix polymer	ν_m	0.3

Table 2: Specific material properties from selected cellulose nanofibre and fibre mats used in the calculation of reinforcing efficiency and fibre efficiency. In the table GF stands for glass fibres, CNF for cellulose nanofibres from plants and BC for cellulose nanofibres from bacteria.

Matrix	Fibre type	E_m (GPa)	V_f %	Reference	Key
Epoxy	Flax (uni)	3.1	42	Oksman (2001)	1
Epoxy	GF [0/90]	2.9	60	Nyström and Aitomäki (2012)	2
Epoxy	GF [+45/-45]	2.9	60	Nyström and Aitomäki (2012)	2
Starch	CNF	0.0016	61	Svagan, Samir and Berglund (2007)	3
Chitosan	CNF	1.4	17	Hassan, Hassan, and Oksman (2011)	4
Epoxy	BC	2.8	43	Yano, Sugiyama, Nakagaito, Nogi, Matsuura, Hikita, and Handa (2005)	5
Polyurethane (PU)	BC	0.19	43	Juntaro, Ummartyotin, Sain, and Manuspiya (2012)	6
Hydroxethyl Cellulose (HEC)	CNF	0.95	62	Sehaqui, Zhou, and Berglund (2011)	7
Epoxy	BC	2.98	49	Lee, Tammelin, Schulfter, Kiiskinen, Samela, and Bismarck (2012)	8
Melamine Formaldehyde (MF)	CNF	8.3	79	Henriksson and Berglund (2007)	9
Polylactic acid (PLA)	CNF	2	15	Tingaut, Eyholzer, and Zimmermann (2011)	10

The parameter, ζ, gives a measure of efficiency of the fibres in a particular matrix. It is also useful to be able to measure the efficiency of the fibres themselves and this can be done by using the rule of mixtures equation.

The stiffness of a composite based on the rule of mixtures is given by:

$$E_1 = \eta_f E_f V_f + (1 - V_f) E_m \tag{3}$$

where η_f is the fibre efficiency. This efficiency, η_f, can be back calculated using a similar procedure as for ζ. For this an initial estimate of the η_f, is made and the stiffness of the unidirectional layer calculated from Eq. 3. This unidirectional laminate stiffness E_1 is then used to calculate the stiffness of the composite using CLT. As with ζ , the value of η_f is changed until the calculated value of the stiffness of the composite matches that of the experimentally measured stiffness.

2.2 Strength Efficiency

The strength of the composite, σ_c, is calculated from a rule of mixture equation given by Fu and Lauke (1996) such that

$$\sigma_c = \eta_{os} \eta_{ls} \sigma_f V_f + (1 - V_f) \sigma_{mf} \tag{4}$$

where

$$\sigma_{mf} = \sigma_f \frac{E_m}{E_f} \tag{5}$$

and where σ_f is the fibre strength, η_{ls} is the fibre length efficiency factor and η_{os} is the orientation factor.

In the application of this model to nanocomposites we assume that the fibres are orientated in the 2D plane, and as such $\eta_{os}=3/8$. In the case of the flax and glass fibre, for unidirectional fibres, $\eta_{os}=1$, for [0 90], $\eta_{os}=1/2$ and for [-45 +45] $\eta_{os}=1/2$.

From Kelly and Tyson (1965) we have that η_{ls} is dependent on a critical length, which is used to take into account the end effects of short fibres. Hence

$$\eta_{ls} = \begin{cases} 1 - l_c/2l & l > l_c \\ l_c/2l_c & l > l_c \end{cases} \tag{6}$$

where

$$l_c = \frac{\sigma_f d}{2\tau} \tag{7}$$

Here, l and d are the length and diameter of the fibre and τ is the interface shear strength, (IFSS).

In nanocomposites, direct measurements of the interface shear strength are currently not possible. To be able to make some approximation of the critical length and subsequently the strength of the composite, we assume that there is a perfect interface between the fibre and the matrix. Hence we let $\tau=\tau_m$, where τ_m is the shear strength of the matrix. However, the shear stress of the matrix in the nanocomposites discussed here are rarely reported hence we assume that $\tau=\sigma_m$, where σ_m is the matrix tensile strength of the matrix. This provides an upper limit to the value of τ_m and thus a lower limit to the value of l_c. Hence, we can say that the critical length must be at least this value.

The strength efficiency is calculated differently to the stiffness efficiency. Here the measured strength, reported in different studies, is simply compared to the theoretical strength, as calculated from Eqs. 4-7. The strength efficiency is the fraction the measured strength is of the theoretical strength. In the calculation of the strength the parameter values set out in Table 2 were used. Included in the table is the measured strength, σ_{av}. In all cases, the fibre strength, σ_f, was set as 2000 MPa. This is estimated as the lowest possible strength of cellulose nanofibres and is based on the strength from single fibre tests of flax fibres, which are made up of bundles of aligned CNFs. These fibres have maximum values of 1800 MPa (Anderson, Sparnis, Joffe and Wallström, (2005)). The flax fibres have an alignment angle of 6-10° (Morton and Hearle, (1993)) hence the strength was increase to 2000 MPa to compensate for this.

An alternative method for obtaining a theoretical value of the cellulose nanofibre composite strength is to use a rule of mixtures equation based on network strength. Hence

$$\sigma_c = \sigma_n V_f + (1 - V_f)\sigma_{mf} \tag{8}$$

where σ_n is the strength of the network. The other parameters have been previously described.

Table 3: Values for parameters used for cellulose nanofibre composites

Matrix	Nanofibre type	σ_{mf} (MPa)	l (μm)	d (μm)	l/d	l_c (μm)	σ_{av} (MPa)	V_f %
Starch	CNF	0	3	0.03	100	85.7	160	61
Chitosan	CNF	20	3	0.01	300	5.7	193	17
Epoxy	BC	41	3	0.03	100	1.5	325	43
PU	BC	3	3	0.03	100	1.9	151	43
HEC	CNF	14	3	0.03	100	0.7	181	59
Epoxy	BC	43	3	0.03	100	0.4	102	49
MF	CNF	120	3	0.03	100	1.0	108	79
PVA	CNF	29	3	0.03	100	3.8	10	15

3. RESULTS

The theoretical stiffness and strength efficiency were calculated for selected bionanocomposite reported in the literature. To provide a reference for these values the stiffness and strength efficiencies were also calculated for a natural fibre composite and glass fibre composites with different layups and are shown in Fig. 2. The number in front of the composite names matches that in Table 2 so the details and references for these composites can be identified.

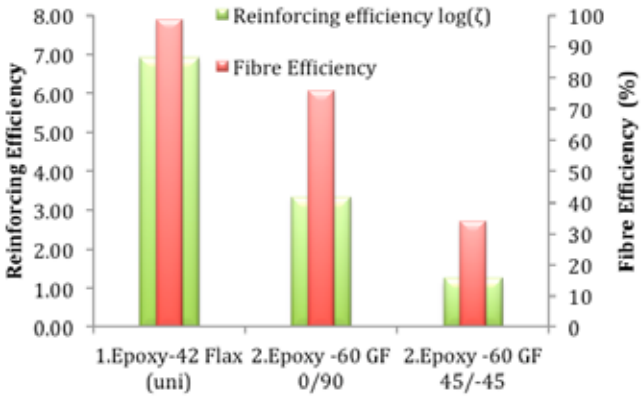

Fig. 2 Plot of the reinforcing efficiency of a natural fibre reinforced composite and two glass fibre composites with different layups. The green bars represent the values of the log of the reinforcing efficiency ζ and the red bars are the fibre reinforcing efficiency η_f. To identify the composites and where they are reported, the key number is set in front of the material names and matches those set out in Table 2.

In the plot of reinforcing efficiency, the logarithm of ζ is plotted. The reason is that as the behaviour of the composite approaches that of the Voigt model, $\zeta \to \infty$. This exponential increase as the limit is approached is therefore better represented by $\log(\zeta)$. The rule of mixtures efficiency has a linear behaviour and hence no additional function is applied. The plot shows that the fibre efficiency and the reinforcing efficiency are both high for the unidirectional flax fibres. The high fibre efficiency means that the stiffness in the composite approximately equals the product of fibre volume concentration and fibre stiffness. The high reinforcing efficiency means the composite is approaching a state of constant strain in the composite, and the strain in the matrix is restricted by the fibres. In fact a maximum value of η_f and ζ means the composite behaves according to the Voigt model. Very low fibre efficiency, as $\eta_f \to 0$ indicates a very poor interface between the matrix and the fibres resulting in the matrix bearing the load. Hence in the worst case the fibres act as voids instead of reinforcing fibres. Low reinforcing efficiency however is where the composite behaves according to the Reuss model. This means that the fibres and matrix undergo equal stress and hence the strain is dominated by the matrix strain.

The effect on the reinforcing efficiency of the fibres not being aligned with the load can be clearly seen in Fig. 2. Hence despite the fact that the decomposition of forces is taken into account by the CLT, the misalignment means that the fibres do not restrict the matrix in the same way and the reinforcing efficiency is lower for the [+45/-45] than the [0/90] layup. It is to be expected then that randomly orientated fibres, such as those in the bionanocomposites will have a lower fibre efficiency and reinforcing efficiency than GF composites with a [0/90] layup i.e. below 73%. This is because of the fibre direction and because the interface between the epoxy and the glass fibres of the composite whose stiffness is shown in Fig 2. is very good since the glass fibre sizing has been particularly developed for this composite.

Fig. 3 shows the fibre efficiency and reinforcing efficiency calculated for selected nanocomposites. Here it can be seen that the fibre reinforcing efficiency is below 73% for the all nanocomposites except one, the epoxy and BC bionanocomposite produced and tested by Yano et al. (2005). This result is unexpectedly high especially since the nanofibre stiffness is overestimated at 138 GPa. A possible explanation of this is that volume fraction is underestimated possibly combined with a preferred orientation to the network formed by the BC. It also suggests that the way in which the crystalline cellulose in the BC nanofibres is arranged is such that the stiffness of the crystalline cellulose dominates the nanofibre stiffness. It can also be seen that two of the three BC based composites have higher fibre efficiencies than the CNF based composites. Comparing the processes used in the BC/epoxy composite from Yano et al. (2005) and that prepared by Lee et al. (2012), it can be seen that care was taken to preserve the BC network laid down by the bacteria in the study by Yano et al. (2005). However, Lee et al. (2011) used bacteria cellulose that was crushed and mixed, and hence the original BC network was disordered and therefore is more similar to the CNF network. This suggestion is supported by a study by Nakagaito et al. (2005) who found when the BC network is disrupted the resulting network is similar in morphology and mechanical properties to CNF networks. In addition, Lee et al. (2012) used vacuum infusion of the dry BC network over the period of up to 2 hours to manufacture the composite whereas Yano et al. (2005) impregnated the BC network over a period of 12 hours.

The results for the reinforcing efficiency in Fig. 3 show that composites with starch and polyurethane (PU), both of which are soft matrices, give high values. At the other end of the scale, the stiffest matrix studied, melamine formaldehyde (MF), gave a negative result for the reinforcing efficiency. This is most likely explained by the fact that the fibres form bonds to form a network hence rather than a combination of the stiffness of the fibres and the matrix, the stiffness of the composite is dominated by the stiffness of the fibres network. As the network

stiffness is greater than the starch/nanofibre combination, the efficiency appears high. In contrast, in the case of the MF/nanofibre, the network stiffness is lower than this combination of matrix and fibre and as a result the reinforcing efficiency is low. It is also interesting to note that the reinforcing efficiency of the majority of CNF bionanocomposites with matrices stiffer than the HEC do not reach the efficiency of short fibre composites. This can be found from the fact that ζ has been empirically established as twice the aspect ratio for short fibre composites (Halpin and Kardos, (1976)). If we assume a minimum aspect ratio of 100, as is commonly expected of nanofibres (width 30 nm, length 3000 nm), then $\zeta=2l/d=2\cdot100$. Plotting the log of this gives us a line at a reinforcing efficiency of 2.3, which is the reinforcing efficiency that would be expected of a short fibre composite. It can also been seen here that the BC based composites by Yano et al. (2005) and by Juntaro et al. (2012) have higher reinforcing efficiency than the CNF based composites with the exception of the starch based composite, whose high efficiency has already been explained. These high values are partially due to the increase in fibre efficiency but it could also be due to the greater porosity in BC, compared to the CNF network, which would allow a better impregnation of the network.

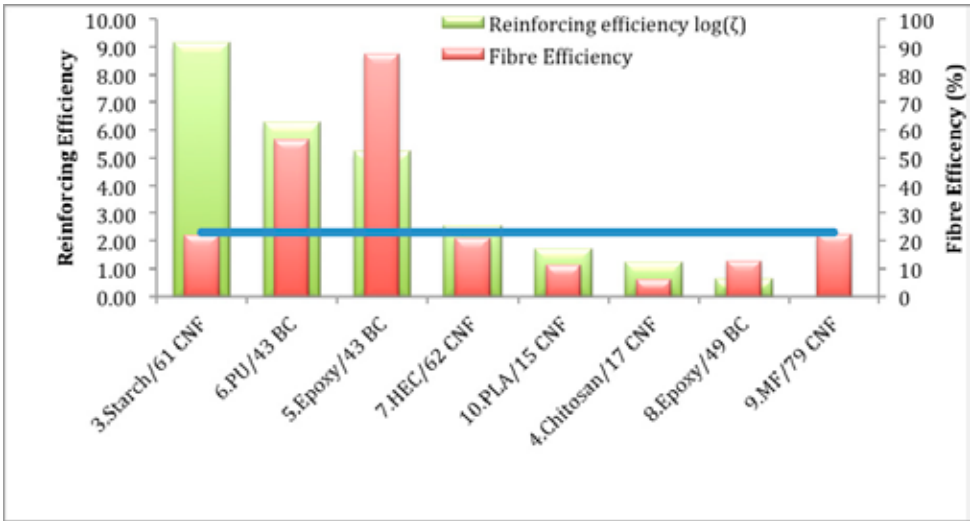

Fig. 3 Plot of the reinforcing efficiency of selected bionanocomposites reported in the literature. The green bars represent the values of the log of the reinforcing efficiency ζ and the red bars are the fibre reinforcing efficiency η_f. The blue line is where ζ is $\log(2l/d)$ and l/d is the aspect ratio of nanofibres.

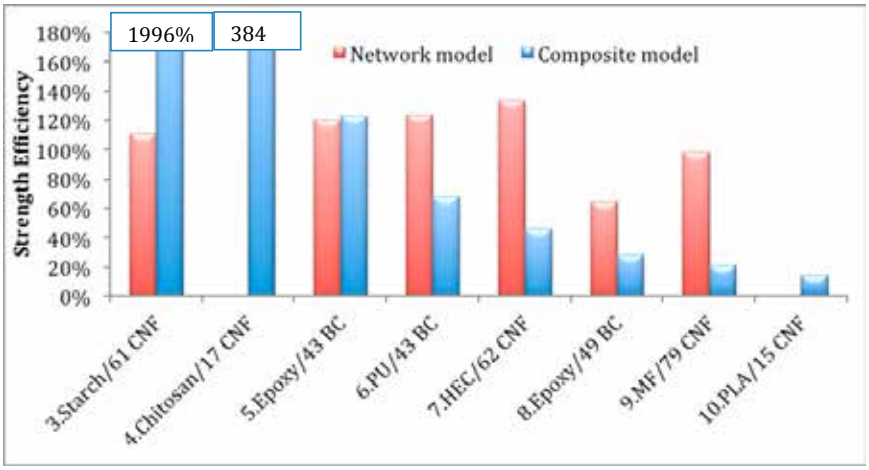

Fig. 4 Plot of the strength efficiency based on the composite model and the network model calculated for selected bionanocomposites reported in the literature.

The strength efficiency results for the same nanocomposites used for the calculation of the stiffness efficiency are shown in Fig. 4. The inaccuracy of the theoretical efficiency is clearly seen for the composites with weak matrices. The model depends on the value of l_c that is calculated from the value of the interlaminar shear strength of the matrix,τ. Where the ratio of the fibre strength σ_f to τ is very high, as is the case with weak matrices then the critical length is very high. This means the first condition of equation 6 is not met and the model predicts a very low strength. It is possible that τ is much higher than the rough estimate used here, which was based on the strength of the matrix. These higher values could be due to the molecular interaction between the nanofibres and the polymer chains. Unfortunately, τ is very difficult to measure.

The network model although based on a very simple rule of mixtures of the matrix and the network strength, it seems to be a better prediction of the strength of these nanofibre composites. This suggests that the strength of the nanocomposites is heavily dependent on the strength of the dry network. This also implies that the stress transfer is through the network and not through the matrix in high volume fraction cellulose nanofibre composites. The disadvantage with the network model is that low volume fraction network cannot be measured hence there are no values available for the polylactic acid (PLA) based composite or the chitosan based composite. Comparing the nanocellulose composites using the network model, we can see that the addition of the matrix has had a positive effect on the strength for all but the MF based composite and the epoxy /BC composite from Lee et al. (2012). The MF based composite is neutrally affected and no strength is lost, however the composite by Lee et al. (2012) appears to underperform. This is possibly due to a lack of good impregnation of the composite.

4. CONCLUSIONS

The reinforcing efficiency and fibre efficiency provides a tool to compare the stiffness efficiency of different nanocellulose composites. It shows that the network effect appears to be advantageous to soft matrices but the results suggest that composites with stiffer matrices do not benefit as much from this network effect. The results also show that the composites based on bacterial cellulose exploits the both the fibre properties and the matrix properties in terms of

stiffness and strength, if processing conditions allow good impregnation and if the original network is not destroyed. This is thought to be because the BC forms a porous network that can be more easily impregnated than the CNF networks and due to the structure of the network produced by the bacteria. It appears however, that CNF based composites do not exploit the fibre properties as well as these BC composites. Orientation is a key to high efficiency in fibre composites and the isotropic nature of the nanofibre composites will reduce their efficiency.

The strength efficiency calculations show that the current implementation of the composite model does not capture the behaviour of the strength of cellulose nanocomposites. The correlation between the network strength and the composite strength suggest that much of the stress transfer is from fibre to fibre and strong nanocomposites depend heavily on having a strong network, at least for composites with high fibre volume fractions. In most cases the matrix had a positive effect on the network strength. However, the results indicate that good impregnation is required.

ACKNOWLEDGEMENTS

The authors wish to thank Bio4Energy for the financial support for this work.

REFERENCES

Andersons, J., Sparnins, E., Joffe, R., and Wallström, L. (2005). Strength distribution of elementary flax fibres. Composites science and Technology, 65(3):693–702.

Forsythe G. E., Malcolm M. A., and Moler C. B. (1976). Computer Methods for Mathematical Computations. Prentice-Hall.

Fu, S.-Y. and Lauke, B. (1996). Effects of fiber length and fiber orientation distributions on the tensile strength of short-fiber-reinforced polymers. Composites Science and Technology, 56(10):1179 – 1190.

Halpin, J. C. and Kardos J. L. (1976). The halpin-tsai equations: A review. Polymer Engineering and Science, 16(5):344–352.

Hassan M., Hassan E., and Oksman K. (2011). Effect of pretreatment of bagasse fibers on the properties of chitosan/microfibrillated cellulose nanocomposites. Journal of Materials Science, 46(6):1732–1740.

Henriksson M. and Berglund L. A. (2007) Structure and properties of cellulose nanocomposite films containing melamine formaldehyde. Journal of Applied Polymer Science, 106(4):2817–2824.

Hubbe, M. A., Rojas, O. J., Lucia L. A., and Sain M. (2008) Cellulosic nanocomposites: A review. BioRes, 3(3):929–980.

Juntaro, J., Ummartyotin, S., Sain M., and Manuspiya H. (2012). Bacterial cellulose reinforced polyurethane- based resin nanocomposite: A study of how ethanol and processing pressure affect physical, mechanical and dielectric properties. Carbohydrate Polymers, 87(4):2464

Kelly, A. and Tyson, W. (1965). Tensile properties of fibre-reinforced metals: Copper/tungsten and copper/molybdenum. Journal of the Mechanics and Physics of Solids, 13(6):329 – 350.

Lee, K.-Y., Tammelin, T., Schulfter, K., Kiiskinen, H., Samela, J., and Bismarck, A. (2012). High performance cellulose nanocomposites: Comparing the reinforcing ability of bacterial cellulose and nanofibrillated cellulose. ACS Applied Materials and Interfaces, 4(8):4078–4086.

Morton W. E. and Hearle J. (1993). Physical properties of textile fibres. Textile institute.

Nakagaito, A. N., Iwamoto, S. and Yano, H. (2005). Bacterial cellulose: the ultimate nano-scalar cellulose morphology for the production of high-strength composites. Applied Physics A:

Materials Science and Processing, 80(1):93–97.
Nyström, B. and Aitomäki, Y. (2012). Structural biobased composite processed by vacuum infusion using flax fibres and biobased epoxy. In 12th International Conference on Biomaterials: Transition to Green materials, Niagara Falls, Canada May 6-8.
Oksman K. (2001) High quality flax fibre composites manufactured by the resin transfer moulding process. Journal of Reinforced Plastics and Composites, 20(7):621–627.
Sehaqui H., Zhou Q., and Berglund L. A. (2011). Nanostructured biocomposites of high toughness-a wood cellulose nanofiber network in ductile hydroxyethylcellulose matrix. Soft Matter, 7:7342–7350.
Siqueira, G., Bras, J., and Dufresne, A. (2010). Cellulosic bionanocomposites: A review of preparation, properties and applications. Polymers, 2:728–765.
Siro I. and Plackett D. (2010) Microfibrillated cellulose and new nanocomposite materials: a review. Cellulose, 17(3):459–494.
Svagan, A. J., Samir, M. A. S. A., and Berglund, L. A. (2007). Biomimetic polysaccharide nanocomposites of high cellulose content and high toughness. Biomacromolecules, 8(8):2556–2563.
Tingaut P., Eyholzer C., and Zimmermann T. (2011). Functional Polymer Nanocomposite Materials from Microfilbrillated Cellulose In Advances in Nanocomposite Technology 2011 Ed. A. Hashim, (Intech) 319–334.
Yano H., Sugiyama, J., Nakagaito, A. N., Nogi, M., Matsuura, T., Hikita, M., and Handa, K. (2005). Optically transparent composites reinforced with networks of bacterial nanofibers. Advanced Materials, 17(2):153– 155.

APPENDIX

The other independent material constants required for the CLT are the transverse modulus of the unidirectional ply, E_2, its shear modulus, G_{12} and its Poisson's ratio, ν_{12}. The following calculations are used for these constants.

$$E_2 = E_m \frac{1+\zeta\eta V_f}{1-\eta V_f} \tag{A.1}$$

where

$$\eta = \frac{E_{2f}/E_m - 1}{E_{2f}/E_m + 1} \tag{A.2}$$

and where E_{2f} is the transverse fibre Young's modulus. The values for the parameters are given in the text.

Similarly,

$$G_{12} = G_m \frac{1+\zeta\eta V_f}{1-\eta V_f} \tag{A.3}$$

where

$$\eta = \frac{G_{12f}/E_m - 1}{G_{12f}/E_m + 1} \tag{A.4}$$

and since the matrix is isotropic $G_m=E_m/(2(1+\nu_m))$. Here, G_{12f} is the shear modulus of the fibre and ν_m is the Poisson's ratio of the matrix.

Poisson's ratio, ν_{12} was simply set to 0.3 as both the Poisson's ratio of the fibre and matrix was set to 0.3.

Proceedings of the 34th Risø International Symposium on Materials Science:
Processing of fibre composites – challenges for maximum materials performance
Editors: B. Madsen, H. Lilholt, Y. Kusano, S. Fæster and B. Ralph
Department of Wind Energy, Risø Campus
Technical University of Denmark, 2013

NUMERICAL AND SEMI-ANALYTICAL MODELLING OF THE PROCESS INDUCED DISTORTIONS IN PULTRUSION

I. Baran*, P. Carlone**, J.H. Hattel* and G.S. Palazzo**

* Technical University of Denmark, Department of Mechanical Engineering, Denmark
** University of Salerno, Department of Industrial Engineering, Via Giovanni Paolo II, 84084, Fisciano, Italy

ABSTRACT

The geometrical changes of the processed material (process induced distortions) are a critical issue in pultrusion, since they affect the process dynamics (mainly the pull force), as well as the mechanical properties and geometrical precision of the final product. Hence, a detailed understanding of the mechanical behavior generating the distortions during the process is eventually required. In the present study, two different modelling approaches are implemented and compared to calculate the development of the distortions during the pultrusion of a graphite/epoxy composite rod. In both cases, the temperature and the degree of cure distributions are obtained from the thermo-chemical analysis, using a finite element and a finite volume approach, respectively. Process induced distortions have been computed solving a sequential stress-strain finite element model, in the former case. In the latter, the transient distortions are inferred adopting a semi-analytical procedure, i.e. post processing numerical results by means of analytical methods. The predictions of the process induced distortion development using the aforementioned methods are found to be qualitatively close to each other. Furthermore, the location of the detachment between the heating die and the part due to shrinkage is also investigated.

1. INTRODUCTION

Pultrusion is a continuous manufacturing process used to realize constant cross sectional composite profiles. In recent years, the pultrusion process experienced a remarkable growing within the composite industry, due to its cost-effectiveness, automation and quality of products. Nowadays the process is widely used to manufacture highly strengthened structures such as wind turbine blades, window profiles, door panels, and reinforcement beams for concrete. In a pultrusion process, the fibers/mats are first impregnated by the (thermoset or thermoplastic) matrix material by means of a resin bath or employing a resin injection chamber. The wet out reinforcements then enter the forming and curing die where the heat activates the exothermic

reaction process. The cured profile is continuously advanced via a pulling system to the cut-off saw and finally is cut to the desired length. A schematic view of the pultrusion process is depicted in Fig. 1.

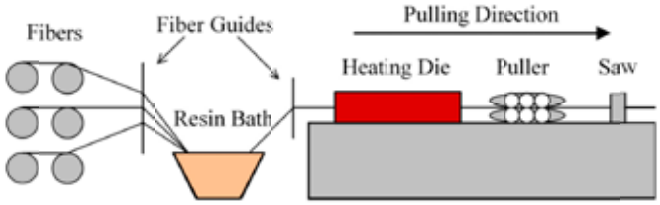

Fig. 1. Schematic view of the pultrusion domain for the composite rod.

Process induced shape distortions may be important for pultruded products such as window frames and fencing panels due to their desired high geometrical precision. Hence, one of the challenges in a pultrusion process is avoiding or reducing the development of process induced distortions. The transient distortions during process arise due to several mechanisms [Svanberg and Holmberg (2001), Wisnom, Gigliotti, Ersoy, Campbell and Potter (2006), Bogetti and Gillespie Jr (1992), Johnston (1997)]: (i) the mismatch in the coefficient of thermal expansion (CTE) of the matrix material and the fibers, (ii) the chemical shrinkage of the matrix material, (iii) the tool-part interaction and (iv) the temperature and the degree of cure gradients through the composite thickness due to non-uniform curing. Several numerical models have been presented in the literature, in order to achieve a better understanding of the pultrusion process [Baran, Tutum, and Hattel (2012a), Baran, Tutum, and Hattel (2012b), Baran, Tutum, and Hattel (2012c), Baran, Tutum, and Hattel (2013a), Baran, Tutum, and Hattel (2013b), Baran, Tutum, Nielsen and Hattel (2013), Carlone, Palazzo and Pasquino (2006), Carlone and Palazzo (2007), Carlone and Palazzo (2008), Joshi and Lam (2001), Joshi, Lam and Win Tun (2003), Liu, Crouch, and Lam (2000), Tutum, Baran and Hattel (2013), Valliappan, Roux, Vaughan, and Arafat (1996)].

In the present paper, two different approaches to the computational simulation of the pultrusion process have been proposed, compared and discussed. The aim of both models is to predict thermo-chemical aspects as well as process induced transient distortions in a conventional pultrusion process of a graphite/epoxy rod. The first model (Model-1) is based on the sequential coupling of a 3D Eulerian thermo-chemical model together with a 2D quasi-static plane strain mechanical analysis. The resin elastic modulus development is calculated by means of the cure hardening instantaneous linear elastic (CHILE) approach [Johnston (1997)], which is a valid pseudo-viscoelastic approximation of the linear viscoelasticity. A finite element scheme has been used to solve both boundary value problems. The second model (Model-2) is based on a semi-analytical procedure: a computational fluid dynamics (CFD) finite volume approach is employed to derive the 3D distribution of temperature and degree of cure into the processing material, while the process induced distortion are inferred post-processing numerical results by means of analytical methods. The paper is structured as follows: in Section 2 the theoretical formulation and the adopted solution strategies for the thermo-chemical boundary value problem are exposed, while in Section 3 the implemented procedure for distortion computing are detailed. Numerical outcomes are reported, compared and discussed in Section 4, briefly highlighting the most relevant conclusions in Section 5.

2. THERMO-CHEMICAL MODEL

Even if pultrusion is conceptually a very simple process, its dynamics are affected by several important aspects, such as heat and mass transfer, resin reaction and phase changes, voids growth or dissolution, interaction between the processing material and the heating die and stress-strain development. All the aforementioned issues are strictly related to thermo-chemical phenomena, which, from a modelling point of view, can be formulated in terms of energy and species balances. In more detail, the temperature distribution into the processing material can be inferred solving the following form of the energy equations:

$$\rho C_p \left(\frac{\partial T}{\partial t} + u\frac{\partial T}{\partial x_3}\right) = k_{x_1}\frac{\partial^2 T}{\partial x_1^2} + k_{x_2}\frac{\partial^2 T}{\partial x_2^2} + k_{x_3}\frac{\partial^2 T}{\partial x_3^2} + q \tag{1}$$

where T is the temperature, t is the time, u is the pulling speed (along the x_3 direction), ρ is the density, C_p is the specific heat and k_{x1}, k_{x2} and k_{x3} are the thermal conductivities along x_1, x_2 and x_3 directions, respectively. Lumped material properties are used and assumed to be constant throughout the process.

The generative term q at the second member of Eq. 1 is related to the internal heat generation due to the exothermic resin reaction or conversion, i.e. the crosslinking of polymeric chains, quantified by means of the degree of cure α. Rigorously speaking, α is defined as the ratio between the reacted species and the total reactive species at the beginning of the process, however, for convenience, it is commonly quantified considering some reaction dependent parameter, such as the released heat. Following this assumption, the degree of cure can be written as the ratio between the amount of heat H_t, evolved up to the time t, to the total heat of reaction H_{tr} (for $\alpha = 1$). As a consequence, considering that the reinforcing fibers do not contribute to the generative term and indicating the reaction rate (first derivative of the degree of cure with respect to time) as R_r it follows:

$$q = \left(1 - V_f\right)\rho_r H_{tr} R_r, \tag{2}$$

where V_f is the fiber volume fraction and ρ_r is the resin density.

Several kinetics models have been proposed and discussed in the inherent literature to describe the evolution of the cure reaction. In the present investigation the well-established n-order model has been adopted [Valliappan et al. (1996)], assuming an Arrhenius type dependence on the absolute temperature:

$$R_r(\alpha, T) = \frac{\partial \alpha}{\partial t} = \frac{1}{H_{tr}}\frac{dH(t)}{dt} = K_0 exp\left(-\frac{E}{RT}\right)(1-\alpha)^n. \tag{3}$$

The above equations have been solved using a finite element scheme in Model-1. The evaluation of degree of cure and reaction rate has been obtained by means of iterative in-house developed routines implemented into the commercial software ABAQUS (version 6.11, 2011), until the matching of a temperature and degree of cure tolerance. In Model-2 a finite volume approach has been employed, defining the degree of cure as an additional volumetric scalar variable, whose transport equation, in the aforementioned hypothesis, can be written as:

$$\left(\frac{\partial \alpha}{\partial t} + u\frac{\partial \alpha}{\partial x_3}\right) = R_r. \tag{4}$$

Eqs. (1-4) have been solved by means of the commercial package ANSYS-CFX for Model-2.

3. CALCULATION OF THE DISTORTIONS

Model-1. The evolutions of the process induced displacements in transverse directions are predicted using a 2D plane-strain model [Baran et al. (2013)]. In this model, the cross section of the part is assumed to move along the pulling direction of the process while tracking the corresponding temperature and degree of cure profiles calculated in the 3D thermo-chemical simulation. In other words, a 3D Eulerian thermo-chemical model is coupled with a 2D plane strain Lagrangian mechanical model. The corresponding transient distortions are calculated based on the temperature and the cure distributions together with the corresponding glass transition temperature (T_g) of the cross section by using the quadratic plane-strain elements in ABAQUS. The instantaneous resin elastic modulus (E_r) development during the process is calculated using the CHILE approach [Johnston (1997)], as follows:

$$E_r = \begin{cases} E_r^0 & T^* < T_{C1} \\ E_r^0 + \frac{T^* - T_{C1}}{T_{C2} - T_{C1}}(E_r^\infty - E_r^0) \quad for & T_{C1} \le T^* \le T_{C2} \\ E_r^\infty & T^* > T_{C2} \end{cases}, \tag{5}$$

where E_{r0} and $E_{r\infty}$ are the uncured and fully cured resin moduli, respectively. T_{C1} and T_{C2} are the critical temperatures at the onset and completion of the glass transition, respectively, T^* represents the difference between the instantaneous resin glass transition temperature (T_g) and the resin temperature, i.e. $T^* = T_g - T$ [Johnston (1997)]. The evolution of the T^* is given by:

$$T^* = T_g - T = (T_g^0 + \alpha_{Tg} \cdot \alpha). \tag{6}$$

The effective mechanical properties of the composite are calculated by using the self-consisting field micromechanics (SCFM) approach which is a well-known technique in the literature [Bogetti and Gillespie Jr (1992)]. User-subroutines in ABAQUS are used for the calculation of the transient distortions as used in [Baran et al. (2013)].

Model-2. The basic assumption of this model is that the section of the processing material varies along the pultrusion die, preserving the position of its axis of gravity (barycenter), following the approach proposed in [Joshi and Lam (2001)]. The virtual dimension (radial in this case) of *i*-th control volume can be computed multiplying its initial value times the correction factor:

$$\delta_{c,i} = V_r \delta_{r,i} + V_f \delta_{f,i}, \tag{7}$$

being $\delta_{r,i}$ and $\delta_{f,i}$ the variation of a unit dimension of the *i*-th volume entirely filled respectively with resin or fiber materials:

$$\delta_{r,i} = \left(1 + \varepsilon_r (T_i - T_0)\right) \cdot \left(1 - \frac{\gamma_r \alpha_i}{100}\right)^{1/3}, \tag{8}$$

$$\delta_{r,i} = \left(1 + \varepsilon_f (T_i - T_0)\right). \tag{9}$$

In the above equation ε_r represents the thermal expansion coefficient and γ_r is the percentage volumetric shrinkage of the fully cured ($\alpha = 1$) resin. Repeating the calculation one finally has:

$$\Delta_{r,i} = r_i \left(\delta_{c,i} - 1\right). \tag{10}$$

The total displacement Δ_r can be evaluated extending Eq. 10 to the whole radius. In particular, if the virtual section of the processing composite results greater than the internal die section, i.e.

the pultruded is compressed into the die, perfect thermal contact is assumed. When the shrinkage effect prevails, inducing the detachment of the material from the die, an additional thermal contact resistance (TCR) is induced between the die and the composite. An iterative procedure connecting the thermochemical model with the dimensional change model has been used, until a temperature criterion is satisfied.

4. RESULTS AND DISCUSSIONS

The 3D thermo-chemical simulation of the pultrusion of a UD graphite/epoxy composite rod is carried out. Only a quarter of the pultrusion domain, seen in Fig. 2, is modelled due to symmetry. Instead of using the die and the heaters in the numerical model, the measured die wall temperature [Valliappan et al. (1996)] is applied to the outer surface of the rod for the length between 0-915 mm (i.e. inside the die). At the symmetry surfaces adiabatic boundaries are defined in which no heat flow is allowed across the boundaries. At the post die region, the exterior surface of the pultruded rod is exposed to ambient temperature (27 ^{o}C) assuming a temperature dependent convective heat transfer coefficient. The length of the post die region ($L_{post\text{-}die}$ in Fig. 2) is determined to be approximately 1370 mm [Valliappan et al. (1996)]. Material properties and the resin kinetic parameters are listed in Table 1 and Table 2, respectively. The parameters used in the CHILE approach for Model-1 are given in Table 3. The pulling speed is set to 5 mm/s. The inlet temperature of the composite part is assumed to be the resin bath temperature of 38 ^{o}C [Valliappan et al. (1996)] and the matrix material at the die inlet is assumed to be uncured (α = 0). In the present study, the total volumetric shrinkage of the epoxy resin is assumed to be 4% [Joshi and Lam (2001)].

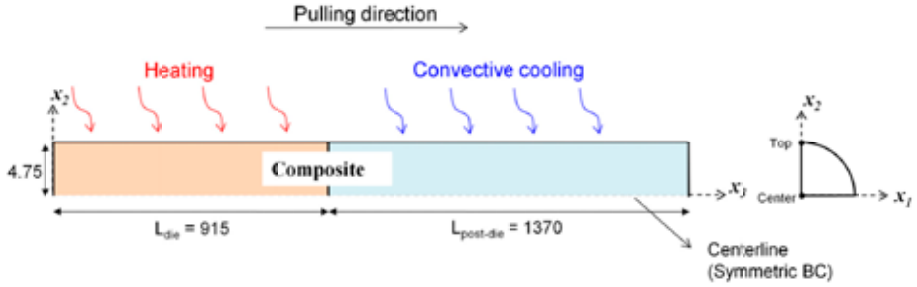

Fig. 2. Schematic view of the pultrusion domain for the composite rod. All dimensions are in mm.

Table 1. Material physical properties and concentration

Material	ρ [kg m^{-3}]	c_p [J kg^{-1} K^{-1}]	k_{x3} [W m^{-1} K^{-1}]	$K_{x1,x2}$ [W m^{-1} K^{-1}]	ε_r [°C^{-1}]	Vol. fraction
Resin	1260	1255	0.2	0.2	4.5E-5	0.378
Fiber	1790	712	66	11.6	7.2E-6	0.622

Table 2. Resin kinetics and rheological parameters

K_0 [s^{-1}]	E [J mol^{-1}]	n	H_{tr} [J kg^{-1}]
19.14 E+4	60.5 E+3	1.69	323.7 E+3

Table 3. Parameters used in the CHILE model (Eq. 5) [Baran et al. (2013)].

E_r^0 [MPa]	E_r^∞ [MPa]	T_{C1} [°C]	T_{C2} [°C]	T_g^0 [°C]	α_{Tg}
3.447	3.447E+3	165	215	0	380

The calculated centreline temperature and degree of cure profiles are shown in Fig. 3. It is seen that the predicted results match quite well with the available experimental data in [Valliappan et al. (1996)]. This shows that the present numerical schemes in Model-1 and Model-2 are stable and converged to a reliable solution. The temperature of the composite part becomes higher than the die wall temperature after approximately 380 mm from the die inlet due to the internal heat generation of the epoxy resin. At that point the peak increase rate of degree of cure is obtained. The maximum composite temperature is calculated approximately as 205 °C. At the post die region, the degree of cure is increased slightly which indicates that the curing still takes place after the die exit. This fact was also observed in [Valliappan et al. (1996)]. The centerline degree of cure is increased from 0.838 (at the die exit) to 0.867 (at the end of the process) which corresponds to a percentage increase of approximately 3.3%.

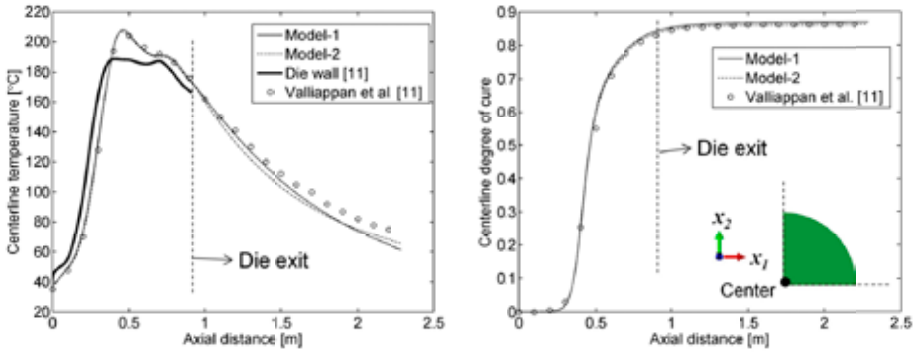

Fig. 3. The centerline temperature (*left*) and degree of cure (*right*) distributions.

The transient distortions are calculated using the obtained temperature and degree of cure distributions in Model-1 (2D plane strain FE model) and Model-2 (1D semi analytical model). The results are depicted in Fig. 4 for the displacement evolution of the outer surface of the composite rod, i.e. the top point in Fig. 4. It is seen that the mechanical assumptions in the semi-analytical model (Model-2) with access to the calculated temperature and degree of cure developments are sufficient to obtain a trend for the transient distortions similar to the ones calculated by the finite element method (FEM) (Model-1) for the circular composite part. However, there is a significant deviation between the calculated displacements especially at the post die region in Model-1 and Model-2. As aforementioned, the SCFM approach is used in Model-1 which calculates the effective composite mechanical properties. This approach captures the mechanical response of the composite quite well [Bogetti and Gillespie Jr (1992)] such that the fibers dominate the longitudinal properties, on the other hand the transverse properties is controlled by the matrix material. For instance, the longitudinal and the transverse moduli at the end of the process are found to be approximately 130 GPa and 10 GPa, respectively in Model-1, which agrees well with typical values given in [Zenkert and Battley (2009)] for a UD carbon/epoxy with a fiber volume fraction of 60%. For the virtual displacement calculation in the transverse direction in Model-2, homogenization of the fibers and the epoxy resin variations

is considered (Eq. 7) in terms of fiber volume fraction. Hence, the transient displacement levels are calculated relatively smaller in Model-2 if compared to Model-1. The stiffness of the epoxy resin is changed after vitrification according to the CHILE approach (see Eq. 5), hence this may cause a larger deviation in the displacement evolution at the post-die region as compared to the inside of the heating die. Inside the heating die, the simplified 1D model (Model-2) is able to predict the transient distortions with reasonable accuracy. The virtual detachment point at the die-part interface, which can be defined as the "zero" displacement during the process, is seen from Fig. 4. The detachment is found to be approximately 540 mm in Model-1 and 580 mm in Model-2 which is a good agreement between the two models. The residual displacement of the top point in Fig. 4 is calculated approximately as -0.025 mm and -0.017 mm for Model-1 and Model-2, respectively.

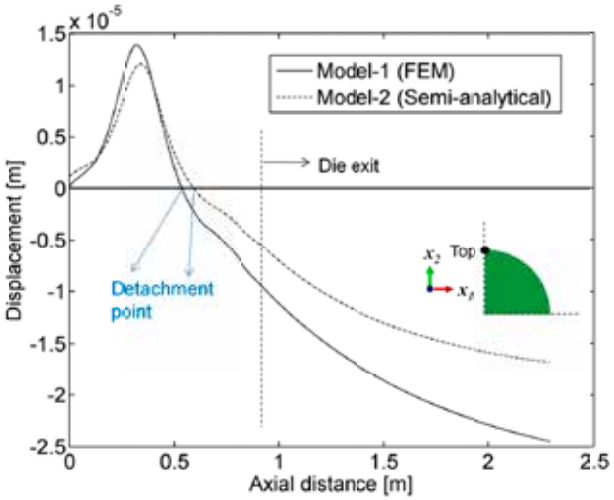

Fig. 4. The process induced transient displacements in the x_2-direction.

5. CONCLUSIONS

In the present work, the transient distortions were predicted using a 2D plane strain FE model (Model-1) and a 1D semi-analytical model (Model-2). The temperature and the degree of cure distributions are first calculated at steady state and good agreement was found between the two models. Using these temperature and degree of cure profiles, the transverse displacement evolution of the composite surface was predicted. A similar trend of development was obtained using the two models since the process induced variations were defined based on the thermal expansion and chemical shrinkage. The displacement levels in Model-2 were found to be close to the ones obtained in Model-1 inside the heating die. For the post die region, the deviation between the two results has become larger since the effect of the matrix material on the distortion behavior in the transverse direction is more pronounced in Model-1 as compared to Model-2.

ACKNOWLEDGEMENTS

This work is a part of DeepWind project which has been granted by the European Commission (EC) under FP7 program platform Future Emerging Technology.

REFERENCES

Baran, I., Tutum, C.C., and Hattel, J.H. (2012a). Optimization of the thermosetting pultrusion process by using hybrid and mixed integer genetic algorithms. App. Compos. Mat. DOI: 10.1007/s10443-012-9278-3.

Baran, I., Tutum, C.C., and Hattel, J.H. (2012b). Reliability estimation of the pultrusion process using the first-order reliability method (FORM). App. Compos. Mat. DOI: 10.1007/s10443-012-9293-4.

Baran, I., Tutum, C.C., and Hattel, J.H. (2012c). Probabilistic thermo-chemical analysis of a pultruded composite rod. In: Proceedings of the 15th European Conference on Composite Materials (Venice, Italy, 24-28 June 2012).

Baran, I., Tutum, C.C., and Hattel, J.H. (2013a). The internal stress evaluation of the pultruded blades for a Darrieus wind turbine. Key Eng. Mat. 554-557, 2127-2137.

Baran, I., Tutum, C.C., and Hattel, J.H. (2013b). The effect of thermal contact resistance on the thermosetting pultrusion process. Compos. Part B: Eng. 45, 995-1000.

Baran, I., Tutum, C.C., Nielsen, M.W., and Hattel, J.H. (2013). Process induced residual stresses and distortions in pultrusion. Compos. Part B: Eng. 51, 148-161.

Bogetti, T. A., and Gillespie Jr, J. W. (1992). Process-induced stress and deformation in thick-section thermoset composite laminates. J. Compos. Mater. 26 (5), 626–660.

Carlone, P., Palazzo, G.S., and Pasquino, R. (2006). Pultrusion manufacturing process development by computational modelling and methods. Math. Comput. Model. 44, 701-709.

Carlone, P., and Palazzo, G.S. (2007). Pultrusion manufacturing process development: Cure optimization by hybrid computational methods. Comput. Math. Appl. 53, 1464–1471.

Carlone, P., and Palazzo, G.S. (2008). Viscous pull force evaluation in the pultrusion process by a finite element thermo-chemical rheological model. Int. J. Mater. Form. 1, 831–834.

Johnston, A. (1997). An Integrated Model of the Development of Process-Induced Deformation in Autoclave Processing of Composites Structures. (Ph.D. thesis, The University of British Columbia, Vancouver).

Joshi, S.C., Lam, Y.C., and Win Tun, U. (2003). Improved cure optimization in pultrusion with pre-heating and die-cooler temperature. Compos. Part A: Appl. S. 34, 1151-1159.

Joshi, S.C., and Lam, Y.C. (2001). Three-dimensional finite-element/nodal-control-volume simulation of the pultrusion process with temperature-dependent material properties including resin shrinkage. Compos. Sci. Technol. 61, 1539–1547.

Liu, X.L., Crouch, I.G., and Lam, Y.C. (2000). Simulation of heat transfer and cure in pultrusion with a general-purpose finite element package. Compos. Sci. Technol. 60, 857-864.

Svanberg, J.M., and Holmberg, J.A. (2001). An experimental investigation on mechanisms for manufacturing induced shape distortions in homogeneous and balanced laminates. Compos. Part A: Appl. S. 32, 827–838.

Tutum, C.C., Baran, I., and Hattel, J.H. (2013). Utilizing multiple objectives for the optimization of the pultrusion process. Key Eng. Mat. 554-557, 2165-2174.

Valliappan, M., Roux, J.A., Vaughan, J.G., and Arafat, E.S. (1996). Die and postdie temperature and cure in Graphite/Epoxy composites. Compos. Part B: Eng. 27, 1-9.

Wisnom, M.R., Gigliotti, M., Ersoy, N., Campbell, M., and Potter, K.D. (2006). Mechanisms generating residual stresses and distortion during manufacture of polymer–matrix composite structures. Compos. Part A: Appl. S. 37, 522-529.

Zenkert, D., and Battley, M. (2009). Laminate and sandwich structures: Foundations of fibre composites (Polyteknisk Forlag, Denmark, 2nd Edition).

Proceedings of the 34th Risø International Symposium on Materials Science:
Processing of fibre composites – challenges for maximum materials performance
Editors: B. Madsen, H. Lilholt, Y. Kusano, S. Fæster and B. Ralph
Department of Wind Energy, Risø Campus
Technical University of Denmark, 2013

3D THERMO-CHEMICAL-MECHANICAL ANALYSIS OF THE PULTRUSION PROCESS

I. Baran*, J.H. Hattel* and Cem C. Tutum**

* Technical University of Denmark, Department of Mechanical Engineering, Denmark
** Michigan State University, Department of Electrical and Computer Engineering, East Lansing, MI, USA

ABSTRACT

In the present study, a 3D Eulerian thermo-chemical analysis is sequentially coupled with a 3D Lagrangian quasi static mechanical analysis of the pultrusion process. The temperature and degree of cure profiles at the steady state are first calculated in the thermo-chemical analysis. In the mechanical analysis, the developments of the process induced stresses and distortions during the process are predicted using the already obtained temperature and degree of cure profiles together with the glass transition temperature. The predictions of the transverse transient stresses and distortions are found to be similar as compared to the available data in the literature. Using the proposed 3D mechanical analysis, different mechanical behaviour is obtained for the longitudinal stress development as distinct from the stress development in the transverse directions. Even though the matrix material is in a liquid state before entering the die (the degree of cure is zero), it is found that there exists longitudinal stresses at the mid-section which indicates that the already pulled material has an effect on the longitudinal stress evolution even before entering the die.

1. INTRODUCTION

Pultrusion is one of the cost efficient composite manufacturing processes in which constant cross sectional continuous fiber reinforced plastic (FRP) profiles are produced. Recently, pultruded structures are foreseen to have potential for the replacement of conventional materials used in the construction industry. More specifically, the application of pultruded composite rods is significantly increasing for reinforcements of concrete elements in the construction industry. This has lead to an increased need for a detailed understanding of the mechanical behavior as well as the failure mechanism of the profile. A schematic view of the pultrusion process is depicted in Fig. 1.

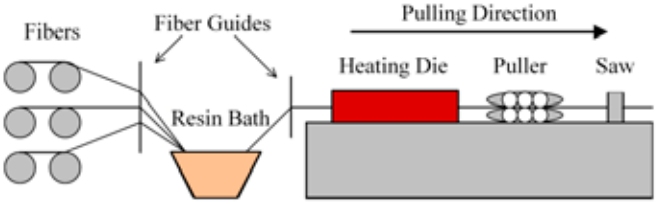

Fig. 1. Schematic view of the pultrusion domain for the composite rod. Fibers/mats and resin matrix are pulled together in the pultrusion direction by pullers through the heated die and then the cured composite is cut by a saw system.

Process induced residual stresses and shape distortions may be important for pultruded products such as reinforcement profiles in the construction industry, stiffeners for wind turbine blades, window frames and fencing panels. Hence, the process induced variations should be controlled or avoided during process which may arise due to the certain mechanisms [Svanberg and Holmberg (2001), Wisnom, Gigliotti, Ersoy, Campbell and Potter (2006), Bogetti and Gillespie Jr (1992), Johnston (1997)]: (i) the mismatch in the coefficient of thermal expansion (CTE) of the matrix material and the reinforcement material (fibers, mats etc.), (ii) the chemical shrinkage of the matrix material, (iii) the tool-part interaction and (iv) the temperature and the degree of cure gradients through the composite thickness due to non-uniform curing. In order to have a better understanding of the pultrusion process, several numerical models have been developed in the literature [Baran, Tutum, and Hattel (2012a), Baran, Tutum, and Hattel (2012b), Baran, Tutum, and Hattel (2012c), Baran, Tutum, and Hattel (2013a), Baran, Tutum, and Hattel (2013b), Baran, Tutum, Nielsen and Hattel (2013c), Chachad, Roux, Vaughan, and Arafat (1995), Carlone, Palazzo and Pasquino (2006), Carlone and Palazzo (2007), Carlone and Palazzo (2008), Joshi, Lam and Win Tun (2003), Liu, Crouch, and Lam (2000), Tutum, Baran and Hattel (2013)].

In the present work, the 3D process induced transverse stresses and distortions are predicted using the finite element method (FEM) for the pultrusion of a glass/epoxy square beam. The temperature and the cure degree distributions are calculated in the 3D thermo-chemical simulation. By using these distributions, the 3D transient stresses and distortions are calculated by means of the cure hardening instantaneous linear elastic (CHILE) approach [Johnston (1997)], which is a valid pseudo-viscoelastic approximation of the linear viscoelasticity.

2. THERMO-CHEMICAL MODEL

2.1 Numerical Implementation. In the thermo-chemical model, the energy equations for the square composite beam and the die block domains given in Eq. 1 and Eq. 2, respectively, are solved in order to calculate the temperature field.

$$\rho_c Cp_c \left(\frac{\partial T}{\partial t} + u \frac{\partial T}{\partial x_3} \right) = k_{x_1,c} \frac{\partial^2 T}{\partial x_1^2} + k_{x_2,c} \frac{\partial^2 T}{\partial x_2^2} + k_{x_3,c} \frac{\partial^2 T}{\partial x_3^2} + q \tag{1}$$

$$\rho_d Cp_d \frac{\partial T}{\partial t} = k_{x_1,d} \frac{\partial^2 T}{\partial x_1^2} + k_{x_2,d} \frac{\partial^2 T}{\partial x_2^2} + k_{x_3,d} \frac{\partial^2 T}{\partial x_3^2} \tag{2}$$

where T is the temperature, t is the time, u is the pulling speed, ρ is the density, Cp is the specific heat and k_{x1}, k_{x2} and k_{x3} are the thermal conductivities along the x_1, x_2 and x_3 directions,

respectively. The subscriptions *c* and *d* correspond to composite and die, respectively. Lumped material properties are used and assumed to be constant throughout the process. The internal heat generation (q) [W/m^3] due to the exothermic reaction of the epoxy resin can be expressed as [Chachad et al. (1995), Baran et al. (2013c)]:

$$q = (1 - V_f)\rho_r H_{tr} \left[R_r(\alpha)\right]_e \tag{3}$$

where V_f is the fiber volume fraction and H_{tr} is the total heat of reaction, ρ_r is the density of epoxy resin, α is the degree of cure and $[R_r(\alpha)]_e$ is the effective cure rate, i.e. dα/dt, expressed as [Chachad et al. (1995), Baran et al. (2013c)]

$$\left[R_r(\alpha)\right]_e = K_o \exp(-\frac{E}{RT})(1-\alpha)^n \cdot f(\alpha, T) \tag{4}$$

where K_o is the pre-exponential constant, E is the activation energy, R is the universal gas constant and n is the order of the reaction (kinetic exponent). K_o, E, H_{tr} and n can be obtained by a curve fitting procedure applied to the experimental data evaluated using differential scanning calorimetry DSC [Chachad et al. (1995)]. $f(\alpha,T)$ is the diffusion factor which accounts for the glass transition effect defined as [Johnston (1997)]:

$$f(\alpha, T) = \frac{1}{1 + \exp[C(\alpha - (\alpha_{C0} + \alpha_{CT} T))]} \tag{5}$$

where C is a diffusion constant, α_{C0} is the critical degree of cure at T = 0 K and α_{CT} is a constant for the increase in critical α with T [Johnston (1997)]. The relation of the effective resin kinetics equation can be expressed as [Baran et al. (2013c)]

$$\frac{\partial \alpha}{\partial t} = \left[R_r(\alpha)\right]_e - u\frac{\partial \alpha}{\partial x_3} \tag{6}$$

where it is the expression in Eq. 6 which is used in the numerical model.

For the 3D thermo-chemical simulation of the pultrusion process, user defined sub-routines in a commercial finite element software ABAQUS (version 6.11, 2011) are used in order to obtain the temperature and degree of cure fields.

2.2 Model description. The 3D thermo-chemical simulation of the pultrusion of a UD glass/epoxy based square beam is carried out. Only a quarter of the pultrusion domain is modelled due to symmetry. The details of the model geometry and the dimensions are given in Fig. 2. Material properties are listed in Table 1. The resin kinetic parameters are [Chachad et al. (1995), Baran et al. (2013c)]: H_{tr} = 324 (kJ/kg), K_0 = 192000 (1/s), E = 60 (kJ/mol), n = 1.69, C = 30, α_{C0} = -1.5 and α_{CT} = 0.0055 (1/K). At the symmetry surfaces adiabatic boundaries are defined in which no heat flow is allowed across the boundaries. The remaining exterior surfaces of the die are exposed to ambient temperature (27 ^{o}C) with a convective heat transfer coefficient of 10 W/(m^2 K) except for the surfaces located at the heating regions. Similarly, at the post die region, convective boundaries are defined for the exterior surfaces of the pultruded profile. The length of the post die region (L_{conv} in Fig. 2) is determined to be approximately 13.7 m [Baran et al. (2013c)] which results in a total length of approximately 14.6 m (L_{die}+L_{conv}, Fig. 2) for the composite part.

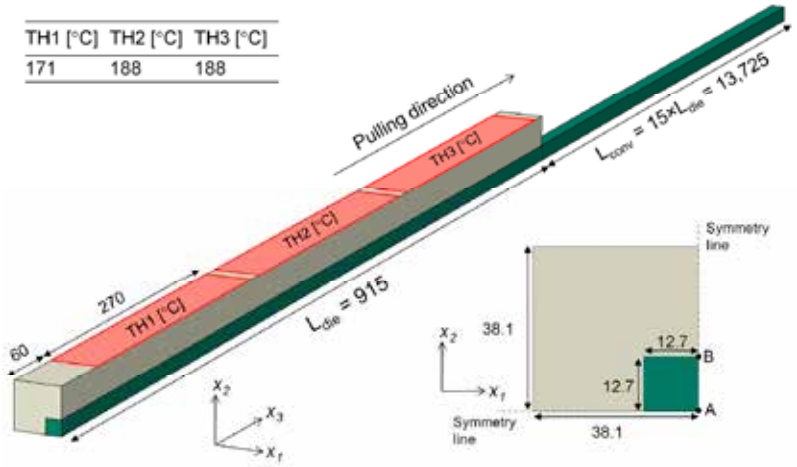

Fig. 2. Schematic view of the pultrusion domain for the square beam. All dimensions are in mm.

Table 1. Material Properties [Chachad et al. (1995)].

Material	ρ (kg/m^3)	Cp (J/kg K)	k_{x_3} (W/m K)	k_{x_1} , k_{x2} (W/m K)
Composite (V_f = 63.9%)	2090.7	797.27	0.9053	0.5592
Die (steel)	7833	460	40	40

3. THERMO-CHEMICAL-MECHANICAL MODEL

3.1 Numerical implementation. The effective mechanical properties of the composite are calculated by using the self consistent field micromechanics (SCFM) approach which is a well known technique in the literature [Bogetti and Gillespie Jr (1992)]. The instantaneous resin elastic modulus development during the process is calculated using the CHILE approach. The glass transition temperature (T_g) is calculated using Di Benedetto equation [Johnston (1997)]. An incremental linear elastic approach is implemented utilizing user-subroutines in ABAQUS for the calculation of the residual stresses and distortions as used in. In the present study, the total volumetric shrinkage of the epoxy resin is assumed to be 6% [Baran et al. (2013c)].

3.2 Model description. The developments of the 3D process induced stresses and distortions are predicted using a 3D thermo-chemical-mechanical model. In this model, the 3D composite part defined in Section 2 is assumed to move along the pulling direction of the process while tracking the corresponding temperature and degree of cure profiles already calculated in the 3D thermo-chemical simulation. In other words, a 3D Eulerian thermo-chemical model is coupled with a 3D quasi-static Lagrangian mechanical model. The die surfaces are not included in the proposed 3D mechanical model. A mechanical symmetry boundary condition (BC) is applied at the symmetry surfaces (see Fig. 2) in the x_1 and x_2-directions.There is no applied mechanical BC at the ends of the composite part in the x_3-direction, i.e. a free-free BC is applied at the end surfaces in the x_3-direction. The corresponding stresses and distortions are calculated based on the temperature and the cure distributions together with the corresponding glass transition temperature (T_g) of the composite part by using the 3D quadratic elements in ABAQUS.

4. RESULTS AND DISCUSSIONS

In order to reflect the 3D thermo-chemical-mechanical behavior of the process more precisely and correctly, the mid-section of the composite part is considered since the pultrusion is a continuous process, i.e. there is always material inside the heating die during the process. The details of the mid-section are shown in Fig. 3 in which a schematic view of the movement of the part in the pulling direction is depicted. It should be noted that the tracking of the mid-section starts at $x_3 \approx -7.3$ m and ends at $x_3 \approx 7.3$ m. The pulling speed is set to 20 cm/minute.

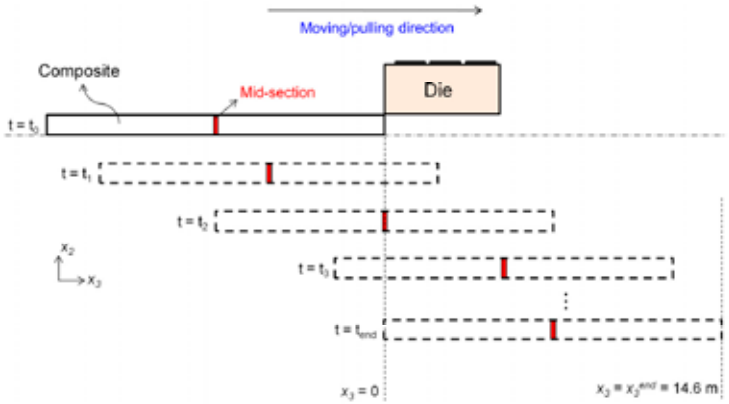

Fig. 3. Schematic view of the movement of the part in the pulling direction and the positioning of the mid-section. The sizes of the die and the part are not scaled.

The transient temperature and degree of cure distributions at the mid-section are shown in Fig. 4 for the inner region (point A) and the outer region (point B). It is seen that until the mid-section enters the heating die, the temperature remains constant as the resin bath temperature of 30°C and the degree of cure remains uncured, i.e. $\alpha = 0$. The non-uniform temperature and degree of cure profiles are obtained especially inside the die, such that the point B cures earlier than the point A since it is closer to the die having heaters on top of it. This shows that the internal heat generation of the matrix material plays a more important role for the inner region (point A). The maximum temperature and degree of cure value obtained inside the composite are approximately 217°C and 0.97, respectively (for point A).

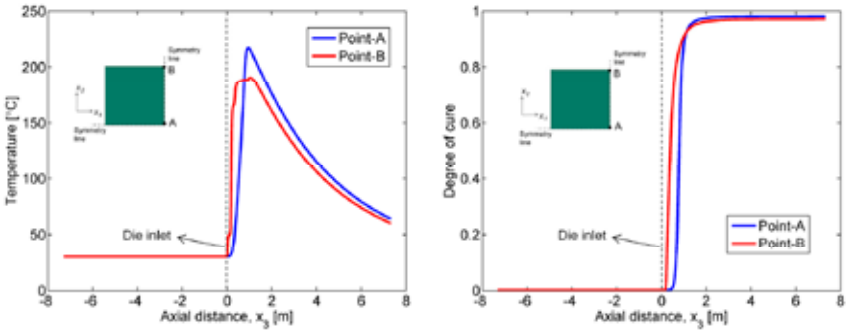

Fig. 4. The temperature (*left*) and degree of cure (*right*) distributions at the mid-section for point A and point B.

The non-uniform temperature and degree of cure distributions promote the process induced residual stresses and distortions [Bogetti and Gillespie Jr (1992)]. The evolutions of the transient stresses at the mid-section (Fig. 3) are given in Fig. 5 for point A and point B. In Fig. 5, S11, S22 and S33 are the normal stresses in the x_1-direction (horizontal, transverse), the x_2-direction (vertical, transverse) and the x_3-direction (longitudinal), respectively. It is seen that until the mid-section enters the die, there are almost no transverse stresses, i.e. S11 and S22 (Fig. 5a,b). This shows that the already pulled material (e.g. the front end of the product) has no effect on the stress development at the mid-section. Inside the die, the stress levels are relatively small because the matrix material has not enough stiffness to build up the stresses. The outer regions closest to the die cure first which make them a little constrained by the inner region during shrinkage. Due to this, a residual compression is found in these regions [Baran et al. (2013c)].

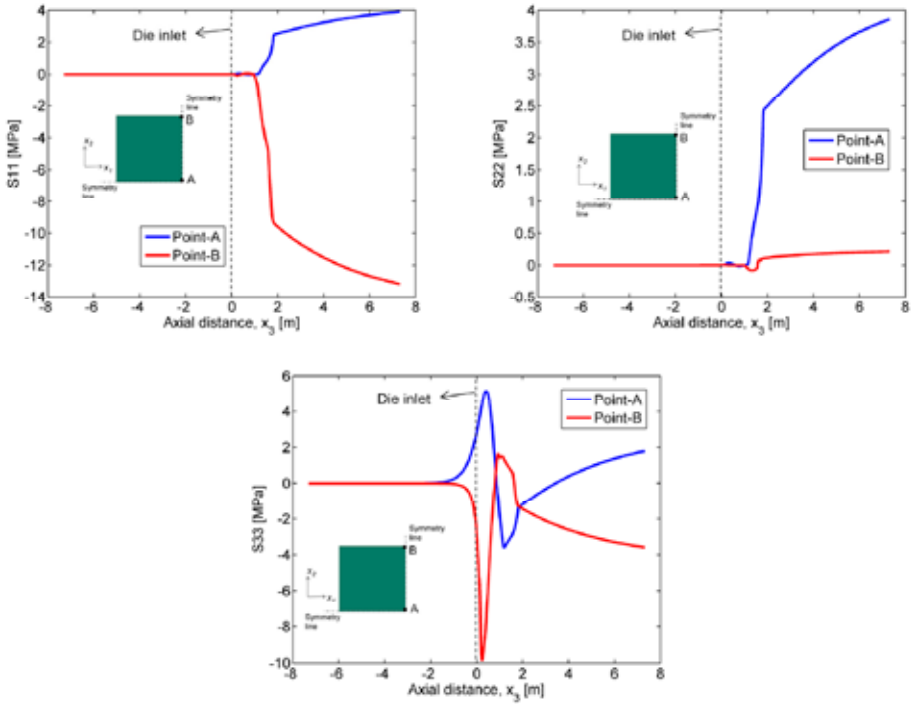

Fig. 5. The transverse transient stress S11 (a), S22 (b) and the longitudinal stress S33 (c) evolutions at the mid-section for point A and point B.

Regarding the longitudinal stress development (S33) in the pulling or fiber direction, different mechanical behaviour is obtained as distinct from the stress development in the transverse directions (S11 and S22). Even though the matrix material is in a liquid state before entering the die (the degree of cure is zero), it is found that there exists longitudinal stresses at the mid-section which can be seen in Fig. 5c. This indicates that the already pulled material has an effect on the longitudinal stress evolution at the mid-section even before entering the die. However, as mentioned before, this 3D effect is not pronounced in the transverse directions. It is important that the 3D effect in the longitudinal direction is only captured by using the full 3D mechanical model. The longitudinal stress levels calculated for S33 (Fig. 5) are found to be relatively small as compared to S11 and S22 because the process induced strains in the longitudinal direction are

smaller than the ones in the transverse directions. The fibers in the pulling directions restrict the process induced strain built-up in the longitudinal direction; hence, this provides lower process induced stresses in the longitudinal direction (S33).

The evolution of the displacement profile at the mid-section for point B in the x_2-direction (U2) is shown in Fig. 6. It is seen that the part starts expanding while entering the die owing to the increase in temperature and the exclusion of the die surfaces in the present 3D mechanical model. It should be noted that the initial pressure condition of the part before entering the heating die is not taken into account which may affect the stress and displacement field. It is seen from Fig. 6 that the cure shrinkage takes place after approximately 0.5 m from the die inlet which results in a decrease in the displacement value. After that point, the point B shrinks until the end of the process due to cure together with convective cooling at the post die region.

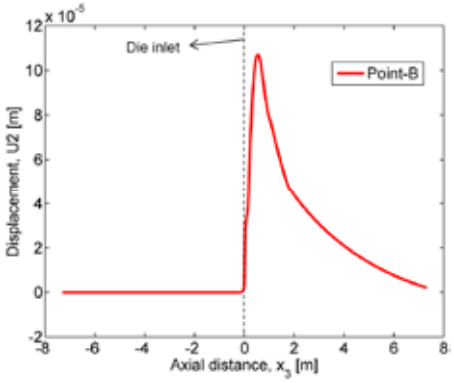

Fig. 6. Displacement of the point B in x_2-direction (U2) for the mid-section of the part

5. CONCLUSIONS

In the present work, a 3D Eulerian thermo-chemical model was sequentially coupled with a 3D quasi-static Lagrangian mechanical model for the pultrusion process simulation of a square UD glass/epoxy composite beam. The CHILE approach was implemented for the calculation of the instantaneous resin modulus development. The effective mechanical properties of the composite are calculated using the SCFM method. The transient stress and displacement evolutions are predicted incorporating the temperature and degree of cure profiles. The trend of the transverse stress development was found to be similar as predicted in [Baran et al. (2013c)]. Regarding the longitudinal stress prediction, the effect of the already pulled material on the stress development at the mid-section was investigated in the 3D mechanical model. Longitudinal process induced stresses were found to exist before entering the heating die due to the 3D effect. This is one of the important aspects of the proposed 3D mechanical model which would be very useful for the calculation of the pulling as well as frictional forces during the process. Apart from the transient stresses, the displacement evolution of the product was predicted which would be crucial for pultruded products such as window frames and fencing panels due to their desired high geometrical precision. Hence, the proposed 3D thermo-chemical-mechanical model has the potential for controlling or avoiding the development of process induced shape distortions.

ACKNOWLEDGEMENTS

This work is a part of a DeepWind project which has been granted by the European Commission (EC) under FP7 program platform Future Emerging Technology.

REFERENCES

Baran, I., Tutum, C.C., and Hattel, J.H. (2012a). Optimization of the thermosetting pultrusion process by using hybrid and mixed integer genetic algorithms. App. Compos. Mat. DOI: 10.1007/s10443-012-9278-3.

Baran, I., Tutum, C.C., and Hattel, J.H. (2012b). Reliability estimation of the pultrusion process using the first-order reliability method (FORM). App. Compos. Mat. DOI: 10.1007/s10443-012-9293-4.

Baran, I., Tutum, C.C., and Hattel, J.H. (2012c). Probabilistic thermo-chemical analysis of a pultruded composite rod. In: Proceedings of the 15th European Conference on Composite Materials (Venice, Italy, 24-28 June 2012).

Baran, I., Tutum, C.C., and Hattel, J.H. (2013a). The internal stress evaluation of the pultruded blades for a Darrieus wind turbine. Key Eng. Mat. 554-557, 2127-2137.

Baran, I., Tutum, C.C., and Hattel, J.H. (2013b). The effect of thermal contact resistance on the thermosetting pultrusion process. Compos. Part B: Eng. 45, 995-1000.

Baran, I., Tutum, C.C., Nielsen, M.W., and Hattel, J.H. (2013c). Process induced residual stresses and distortions in pultrusion. Compos. Part B: Eng. 51, 148-161.

Bogetti, T. A., and Gillespie Jr, J. W. (1992). Process-induced stress and deformation in thick-section thermoset composite laminates. J. Compos. Mater. 26 (5), 626–660.

Chachad, Y.R., Roux, J.A., Vaughan, J.G., and Arafat, E. (1995). Three-dimensional characterization of pultruded fiberglass-epoxy composite materials. J. Reinf. Plast. Comp. 14, 495-512.

Carlone, P., Palazzo, G.S., and Pasquino, R. (2006). Pultrusion manufacturing process development by computational modelling and methods. Math. Comput. Model. 44, 701-709.

Carlone, P., and Palazzo, G.S. (2007). Pultrusion manufacturing process development: Cure optimization by hybrid computational methods. Comput. Math. Appl. 53, 1464–1471.

Carlone, P., and Palazzo, G.S. (2008). Viscous pull force evaluation in the pultrusion process by a finite element thermo-chemical rheological model. Int. J. Mater. Form. 1, 831–834.

Johnston, A. (1997). An Integrated Model of the Development of Process-Induced Deformation in Autoclave Processing of Composites Structures. (Ph.D. thesis, The University of British Columbia, Vancouver).

Joshi, S.C., Lam, Y.C., and Win Tun, U. (2003). Improved cure optimization in pultrusion with pre-heating and die-cooler temperature. Compos. Part A: Appl. S. 34, 1151-1159.

Liu, X.L., Crouch, I.G., and Lam, Y.C. (2000). Simulation of heat transfer and cure in pultrusion with a general-purpose finite element package. Compos. Sci. Technol. 60, 857-864.

Svanberg, J.M., and Holmberg, J.A. (2001). An experimental investigation on mechanisms for manufacturing induced shape distortions in homogeneous and balanced laminates. Compos. Part A: Appl. S. 32, 827–838.

Tutum, C.C., Baran, I., and Hattel, J.H. (2013). Utilizing multiple objectives for the optimization of the pultrusion process. Key Eng. Mat. 554-557, 2165-2174.

Wisnom, M.R., Gigliotti, M., Ersoy, N., Campbell, M., and Potter, K.D. (2006). Mechanisms generating residual stresses and distortion during manufacture of polymer–matrix composite structures. Compos. Part A: Appl. S. 37, 522-529.

Proceedings of the 34th Risø International Symposium on Materials Science:
Processing of fibre composites – challenges for maximum materials performance
Editors: B. Madsen, H. Lilholt, Y. Kusano, S. Fæster and B. Ralph
Department of Wind Energy, Risø Campus
Technical University of Denmark, 2013

ANALYSIS OF COMPOSITION AND MICROSTRUCTURAL UNIFORMITY OF HYBRID GLASS/CARBON FIBRE COMPOSITES

Justine Beauson, Christen Malte Markussen and Bo Madsen

Composites and Materials Mechanics, Department of Wind Energy,
Risø Campus, Technical University of Denmark,
DK-4000 Roskilde, Denmark

ABSTRACT

In hybrid fibre composites, the intermixing of the two types of fibres imposes challenges to obtain materials with a well-defined and uniform microstructure. In the present paper, the composition and the microstructural uniformity of hybrid glass/carbon fibre composites mixed at the fibre bundle level are investigated. The different levels of compositions in the composites are defined and experimentally determined. The composite volume fractions are determined using an image analysis based procedure. The global fibre volume fractions are determined using a gravimetrical based method. The local fibre volume fractions are determined using volumetric calculations. A model is presented to predict the interrelation of volume fractions in hybrid fibre composites. The microstructural uniformity of the composites is analysed by the determined variation in composite volume fractions. Two analytical methods, a standard deviation based method and a fast Fourier transform method, are used to quantify the difference in microstructural uniformity between composites, and to detect and quantify any repeating pattern in the composite microstructure.

1. INTRODUCTION

Hybrid fibre composites consisting of two types of fibres (e.g. glass and carbon fibres) are attracting scientific and industrial interest due to the potential synergistic effect of having reinforcement fibres with different properties. The so-called "hybrid effect" is explored on a mechanical basis (e.g. to have longer fatigue life, and larger compression strength), and, equally important, it is explored for economic reasons to improve the materials cost-performance. Earlier work has addressed hybrid fibre composites by analysing the difference in failure strain and dimensions between the two reinforcement fibres with respect to improved composite strength (Aveston and Kelly 1980). Later on, in the 1990'ies, within an EU Framework Programme (JOULE) with participation from Risø National Laboratory, Denmark, studies were performed on the manufacturing and testing of hybrid composites for wind turbine rotor blades.

Recently, the hybrid fibre concept has been addressed in a number scientific studies (e.g. Hermann et al. 2006, Hillermeier 2009, Zhang et al. 2012), forming also a central element in a current Danish technology project (Blade King).

By their nature, composites are heterogeneous materials due to the dispersion of discrete fibres in a continuous matrix. For conventional composites consisting of a single type of fibres, fibre/matrix preforms and composite manufacturing techniques have been developed to produce materials with a well-defined and uniform microstructure. Hence, this allows for the use of representative geometrical models of the microstructure (so-called representative volume elements) for the analysis and modelling of the (mechanical) properties of the composites. This supports the use of composites in highly demanding structural applications, such as rotor blades for wind turbines. However, in the case of hybrid fibre composites consisting of two fibre types, the intermixing of the two fibres will impose challenges to obtain a similar high degree of microstructural uniformity to allow reliable analysis and modelling of properties. Different fibre intermixing levels can be defined: fibre-fibre, bundle-bundle and ply-ply, and each level bring forward specific microstructural characteristics.

In the present paper, based on experimental data from a number of manufactured hybrid glass/carbon fibre composites, the microstructure of the composites is studied by two aspects. The first one is related to the composition of the composites, i.e. volume fractions of the two composite phases, the two fibre types and the matrix, and with focus on establishing a model for their interrelations. The second one is related to the microstructural uniformity of the composites, and with focus on the variation in volume fractions of the two composite phases.

2. MATERIALS AND METHODS

Plates of hybrid and non-hybrid fibre composites were made with the same type of glass fibre roving (Hybon2026 - PPG FibreGlass, 2447 tex) and the same type of carbon fibre roving (PANEX35 - Zoltek, 3645 tex). One type of preform was used, uniaxial fibre assemblies made by filament-winding, and with variable number of glass and carbon rovings to have composites with different composition and microstructure. The composite plates were made with vacuum infusion using epoxy (DowAirstone) as matrix, and the plates had dimensions of 450 mm x 475 mm x thickness of the plate (see Table 1). Fig. 1 shows the cross section of the eight manufactured composite plates, and Table 1 summarizes their specifications. In the table, β is the hybrid fibre *weight* mixing ratio:

$$\beta = \frac{m_{f\,carbon}}{m_{f\,carbon} + m_{f\,glass}} \tag{1}$$

where m_f is the mass of fibres. Likewise, a hybrid fibre *volume* mixing ratio γ can be defined, and the relation between β and γ can be established:

$$\gamma = \frac{v_{f\,carbon}}{v_{f\,carbon} + v_{f\,glass}} \tag{2}$$

$$\gamma = \frac{\rho_{f\,glass} \cdot \beta}{\rho_{f\,glass} \cdot \beta + \rho_{f\,carbon}(1-\beta)} \tag{3}$$

where v_f is the volume of fibres, and ρ_f is the density of fibres. The calculated values of γ shown in Table 1 are based on a glass fibre density of 2.58 g/cm^3, and a carbon fibre density of 1.83 g/cm^3, which were measured by pycnometry.

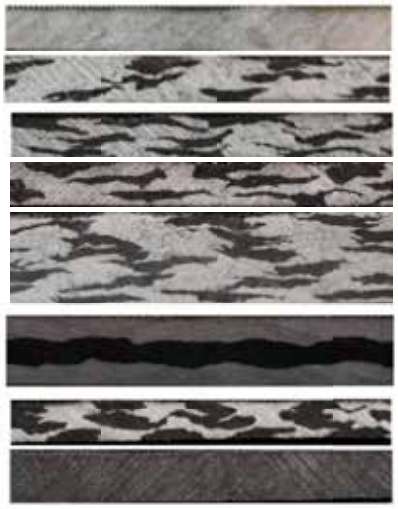

Fig. 1. Cross sections of the hybrid and non-hybrid glass/carbon fibre composites.

Table 1. Specifications of the manufactured hybrid and non-hybrid glass/carbon fibre composites.

Composite plate code	Number of preform layers	Plate thickness [mm]	Hybrid fibre weight mixing ratio, β	Hybrid fibre volume mixing ratio, γ
CXG-01	10	3.0	0.00	0.00
CXG-06	3	3.4	0.21	0.27
CXG-03	3	3.1	0.28	0.35
CXG-02	3	3.2	0.28	0.35
CXG-07	6	5.8	0.28	0.35
CXG-10	6	6.1	0.28	0.35
CXG-05	4	3.1	0.44	0.53
CXG-04	6	3.5	1.00	1.00

2.1 Determination of composition. In the present paper, three levels of compositions in the hybrid fibre composites are defined and determined. In Fig. 2a, a hybrid composite composed of glass and carbon fibres is schematically represented, and used to illustrate the definitions:

- *Composite volume fraction* V_c, which is exemplified in Fig. 2b with the volume of the carbon fibre composite region in black, in relation to the total volume of the hybrid composite framed in red. V_c will be assessed by an image analysis procedure.
- *Global fibre volume fractions* V_f, which is exemplified in Fig. 2c with the volume of the carbon fibres in black in relation to the total volume of the hybrid composite framed in red. V_f will be measured with the conventionally applied gravimetrical based method.
- *Local fibre volume fractions* V_f^*, which is exemplified in Fig. 2d with the volume of the carbon fibres in black in relation to the volume of the carbon fibre composite framed in red. V_f^* will be calculated with Eq. (7) detailed hereafter.

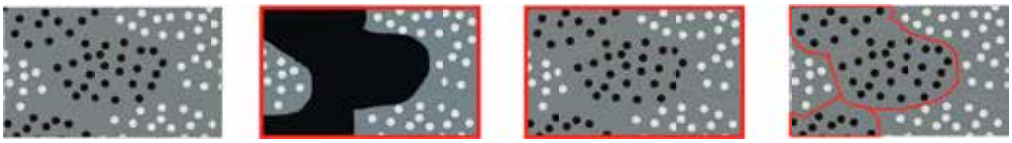

a) b) c) d)

Fig. 2. The three levels of compositions in hybrid fibre composites: a) general view of hybrid composite with glass fibres (white) and carbon fibres (black) in a common matrix (grey), b) composite volume fraction, c) global fibre volume fraction, and d) local fibre volume fraction. The volumes (or areas) framed in red indicate the reference volumes. The three compositions are exemplified by the carbon fibres.

The definitions of the above-mentioned three levels of compositions in hybrid composites, and their relationship are given here (exemplified by carbon fibres):

$$V_{c\,carbon} = \frac{v_{c\,carbon}}{v_{c\,carbon} + v_{c\,glass}} \quad \text{(composite volume fraction)} \tag{4}$$

$$V_{f\,carbon} = \frac{v_{f\,carbon}}{v_{f\,carbon} + v_{f\,glass} + v_{matrix}} \quad \text{(global fibre volume fraction)} \tag{5}$$

$$V^*_{f\,carbon} = \frac{v_{f\,carbon}}{v_{f\,carbon} + v^*_{matrix}} \quad \text{(local fibre volume fraction)} \tag{6}$$

$$V_{f\,carbon} = V^*_{f\,carbon} \cdot V_{c\,carbon} \tag{7}$$

where the asterisk (*) defines the local non-hybrid composite region in the hybrid fibre composite (see Fig. 2d). In these definitions, the porosity content in the composites is assumed to be zero.

Here follows descriptions of the experimental methods used to determine V_c and V_f in the manufactured hybrid fibre composites.

To determine the composite volume fractions (V_c), samples with widths in the range 20 - 50 mm, transverse to the fibre direction, were cut from the composite plates, and the cross sections were grinded and polished in several steps in order to get a smooth surface.

Grayscale images of the samples were taken using an optical microscope with a motorized XY stage. The software *DeltaPix* was used to calculate how many images were needed to cover the cross sectional area of the samples, and the stage was automatically moved by the software. In addition, the stitching of the captured images was performed automatically by the software.

The grayscale images were then prepared for image analysis with the procedure illustrated in Fig. 3. The grayscale image of the hybrid composite, as exemplified in Fig. 3a, is composed of dark grey regions which are the carbon fibre composite phase, and light grey regions which are the glass fibre composite phase. The first step in the procedure is to adjust the contrast, see Fig. 3b. Then, the regions of glass fibre composite are selected using the *Quick selection tool* in *Adobe Photoshop*. This tool is an interactive segmentation tool, which will partition the image based on user provided input, texture information (colours) and/or edge information (contrast). In the *Quick selection tool,* the users input is provided through a brush stroke tool that enables in the present case to select the glass fibre composite regions, see Fig. 3c. Finally, the contrast is adjusted to get a binary image, see Fig. 3d. An example is given in Fig. 4 with the composite

plate CXG-07.

In the obtained binary images, the number of pixels having a value of 1 was counted using a routine in *Mathematica*. This number is divided with the total number of pixels in the image to give *area fractions*, which are assumed to be equal to *volume fractions*, because of the uniaxial nature of the composites, i.e. it is assumed that each observed unit in the transverse cross section is extending continuously in the longitudinal direction.

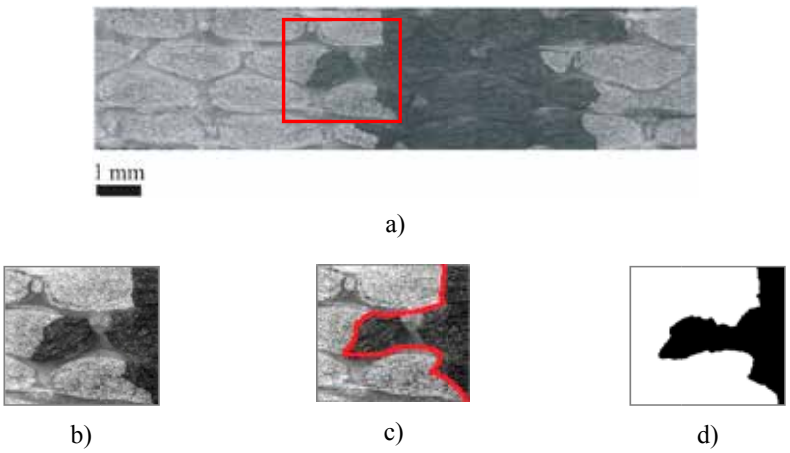

Fig. 3. Image preparation: a) original grayscale image of hybrid fibre composite, where the red box shows: b) the adjustment in contrast, c) the selection process with *Photoshop*, and d) the final binary image.

Fig. 4. Hybrid glass/carbon fibre composite with β = 0.28 and γ = 0.35 (CXG-07): original grayscale image (top), and resulting binary image (bottom).

The global fibre volume fractions (V_f) in the composites were determined using a gravimetrical based method. This method consists of weighing of samples in successive steps. The composite samples are first dried and weighed in air. Then, the samples are sealed and weighed in water. The epoxy matrix is then removed by burning at 450 °C in a nitrogen environment. The resulting assembly of carbon and glass fibres are weighed. Finally, the carbon fibres are removed by burning at 625 °C in air, and the remaining glass fibres are weighed.

Finally, the local fibre volume fractions (V_f^*) in the composites were calculated using Eq. (7) with the experimentally determined values of V_c and V_f.

In principle, the local fibre volume fractions could also be determined directly by image analysis. However, this method presents one major difficulty, which is the selection of

representative local areas. Fig. 5 shows examples of three selected areas in a glass fibre composite region. The local glass fibre volume fractions are found to vary from about 0.40 to 0.60.

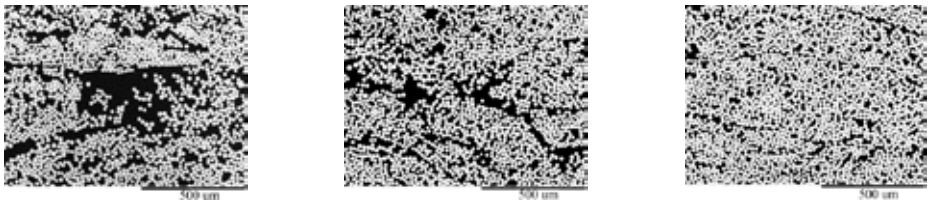

a) $V^*_{f\,glass} = 0.42$ b) $V^*_{f\,glass} = 0.54$ c) $V^*_{f\,glass} = 0.63$

Fig. 5. Examples of determined local glass fibre volume fractions in three areas of a glass fibre composite region.

2.2. Determination of microstructural uniformity. As indicated by the images in Fig. 1, the composition of the hybrid fibre composites will be varying depending on the location and size of the selected cross sectional area. As an example, the composite CXG-06 shows large areas of glass composite rich regions, which means that at certain cross sectional areas of the composite, the glass fibre composite volume fraction is very high (approaching 1.0).

To describe the variation in composition of the composites, V_c is determined in rectangular cross sectional areas, i.e. windows, with a width of 0.1 mm, and with a height equal to the height of the image, i.e. from one edge to the other edge of the sample. V_c is determined in windows successively moved from one end (left side) to the other end (right side) of the image. This result in a curve showing V_c as a function of the position across the sample (see example in Fig. 10).

In order to quantify the microstructural uniformity of the composites, the determined variation in V_c is then analysed using two different methods: *a standard deviation based method*, and *a fast Fourier transform method.* The two methods will be explained in details later on.

3. COMPOSITION OF HYBRID COMPOSITES

3.1. Composite volume fractions and global fibre volume fractions. The obtained binary images of the hybrid glass/carbon fibre composites are shown in Fig. 6, and the determined values of V_c and V_f are summarized in Table 2.

Table 2. Determined composite volume fractions and global fibre volume fractions in the manufactured hybrid and non-hybrid glass/carbon fibre composites.

Composite plate code	β	$V_{c\,carbon}$	$V_{c\,glass}$	$V_{f\,carbon}$	$V_{f\,glass}$
CXG-01	0.00	0.00	1.00	0.00	0.59
CXG-06	0.21	0.30	0.70	0.15	0.41
CXG-03	0.28	0.36	0.64	0.20	0.38
CXG-02	0.28	0.35	0.65	0.20	0.37
CXG-07	0.28	0.39	0.61	0.21	0.38
CXG-10	0.28	0.39	0.61	0.21	0.38
CXG-05	0.44	0.54	0.46	0.28	0.31
CXG-04	1.00	1.00	0.00	0.53	0.00

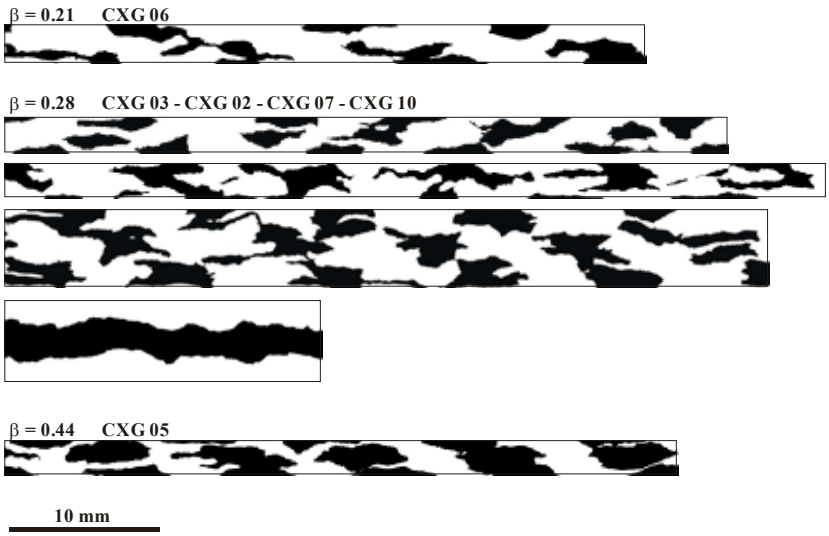

Fig. 6. Binary images of the hybrid glass/carbon fibre composites.

The variation in the results due to the sensitivity of the applied image analysis procedure was tested. The main source of error in the procedure to determine V_c comes from the objectivity of the operator when the *Quick selection tool* is used to manually detect the border between the two composite regions. This effect was tested by repeating three times the procedure on the same image. The results are shown in Fig. 7, and it can be observed that the difference between the determined values of V_c is negligible.

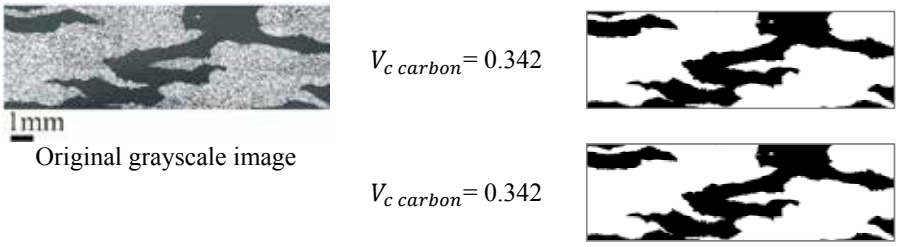

Fig. 7. Results obtained for the sensitivity testing of the image analysis procedure. The procedure was repeated three times on the same image to determine V_c.

3.2. Local fibre volume fractions. From Eq. (7), the local carbon and glass fibre volume fractions, $V^*_{f\,carbon}$ and $V^*_{f\,glass}$ are calculated based on the experimental data in Table 2. The results are summarized in Table 3.

Table 3. Calculated local glass and carbon fibre volume fraction in the manufactured hybrid glass/carbon fibre composites.

Composite plate code	$\boldsymbol{V^*_{f\,carbon}}$	$\boldsymbol{V^*_{f\,glass}}$
CXG-06	0.50	0.59
CXG-03	0.56	0.59
CXG-02	0.57	0.57
CXG-07	0.54	0.62
CXG-10	0.54	0.62
CXG-05	0.56	0.62
Average	**0.54**	**0.60**

It can be realized that the fibre volume fractions determined with the gravimetric method for the non-hybrid composites, CXG-04, containing only carbon fibres, and CXG-01, containing only glass fibres (see Table 2), can be compared to the calculated local carbon and glass fibre volume fractions in the hybrid composites.

The fibre volume fraction of CXG-04 is 0.53, and this compares well to the mean value on 0.54 for the calculated local carbon fibre volume fractions. Similarly, the fibre volume fraction of CXG-01 is 0.59 and this compares well to the mean value on 0.60 for the calculated local glass fibre volume fractions.

Thus, the local fibre volume fractions in the hybrid composites can be closely approximated by the fibre volume fractions determined in the related non-hybrid composites. In other words, it is demonstrated that the values of the local fibre volume fractions in hybrid composites can be determined a priori by manufacturing of the two non-hybrid fibre composites, and by determining the fibre volume fractions in these composites.

4. MODEL FOR COMPOSITION OF HYBRID COMPOSITES

Hereafter follows the derivation of model equations for the interrelation of volume fractions in hybrid composites. The equations can be used to calculate the global fibre volume fractions (V_f) and composite volume fractions (V_c) as a function of the hybrid fibre volume mixing ratio (γ), and with the local fibre volume fractions (V_f^*) as input parameters.

To derive the model equations, some useful support equations can be established on beforehand:

- $\gamma = \frac{v_{f\,carbon}}{v_{f\,carbon} + v_{f\,glass}} = \frac{1}{\frac{v_{f\,glass}}{v_{f\,carbon}} + 1}$
- $\frac{v_{f\,glass}}{v_{f\,carbon}} = \frac{1}{\gamma} - 1 = \frac{1-\gamma}{\gamma}$
- $1 - \gamma = 1 - \frac{v_{f\,carbon}}{v_{f\,carbon} + v_{f\,glass}} = \frac{v_{f\,glass}}{v_{f\,carbon} + v_{f\,glass}}$

The equation for the *global carbon fibre volume fraction* is derived as follows:

$$V_{f\ carbon} = \frac{v_{f\ carbon}}{v_c} = \frac{v_{f\ carbon}}{v_{c\ glass} + v_{c\ carbon}} = \frac{1}{\frac{v_{c\ glass}}{v_{f\ carbon}} + \frac{v_{c\ carbon}}{v_{f\ carbon}}} = \frac{1}{\frac{v_{f\ glass}}{V^*_{f\ glass}} \cdot \frac{1}{v_{f\ carbon}} + \frac{1}{V^*_{f\ carbon}}}$$

$$V_{f\ carbon} = \frac{1}{\frac{1}{V^*_{f\ glass}} \cdot \frac{1-\gamma}{\gamma} + \frac{1}{V^*_{f\ carbon}}} \tag{8}$$

The equation for the *global glass fibre volume fraction* is derived in the same way:

$$V_{f\ glass} = \frac{v_{f\ glass}}{v_c} = \frac{v_{f\ glass}}{v_{c\ glass} + v_{c\ carbon}} = \frac{1}{\frac{v_{c\ glass}}{v_{f\ glass}} + \frac{v_{c\ carbon}}{v_{f\ glass}}} = \frac{1}{\frac{1}{V^*_{f\ glass}} + \frac{v_{f\ carbon}}{V^*_{f\ carbon}} \cdot \frac{1}{v_{f\ glass}}}$$

$$V_{f\ glass} = \frac{1}{\frac{1}{V^*_{f\ glass}} + \frac{1}{V^*_{f\ carbon}} \cdot \frac{\gamma}{1-\gamma}} \tag{9}$$

The porosity content is assumed to be 0, and the *global matrix volume fraction* is therefore calculated as follows:

$$V_{matrix} = 1 - V_{f\ carbon} - V_{f\ glass} \tag{10}$$

The equations for the *carbon and glass composite volume fractions* are derived as follows:

$$V_{c\ carbon} = \frac{v_{c\ carbon}}{v_c} = \frac{v_{c\ carbon}}{v_{c\ glass} + v_{c\ carbon}} = \frac{1}{\frac{v_{c\ glass}}{v_{c\ carbon}} + 1} = \frac{1}{1 + \frac{v_{f\ glass}}{V^*_{f\ glass}} \cdot \frac{V^*_{f\ carbon}}{v_{f\ carbon}}}$$

$$V_{c\ carbon} = \frac{1}{1 + \frac{V^*_{f\ carbon}}{V^*_{f\ glass}} \cdot \frac{1-\gamma}{\gamma}} \tag{11}$$

$$V_{c\ glass} = \frac{v_{c\ glass}}{v_c} = \frac{v_{c\ glass}}{v_{c\ glass} + v_{c\ carbon}} = \frac{1}{1 + \frac{v_{c\ carbon}}{v_{c\ glass}}} = \frac{1}{1 + \frac{v_{f\ carbon}}{V^*_{f\ carbon}} \cdot \frac{V^*_{f\ glass}}{v_{f\ glass}}}$$

$$V_{c\ glass} = \frac{1}{1 + \frac{V^*_{f\ glass}}{V^*_{f\ carbon}} \cdot \frac{\gamma}{1-\gamma}} \tag{12}$$

In the equations (8) - (12), γ is used as the independent variable. It is however more appropriate to use β as the independent variable, since the two fibre types most typically is mixed by their weights in the hybrid fibre preforms. Thus, β is typically accurately controlled, and known for a given preform. The relation between γ and β is given by Eq. (3).

In Figs. 8 and 9, the model equations (8) – (12) are plotted for the hybrid glass/carbon fibre composites. The used values of local carbon and glass fibre volume fractions are 0.53 and 0.59, respectively, which are the values determined from the non-hybrid composites (CXG-04 and CXG-01). The experimental data of the hybrid composites (Table 2) is shown together with the model lines.

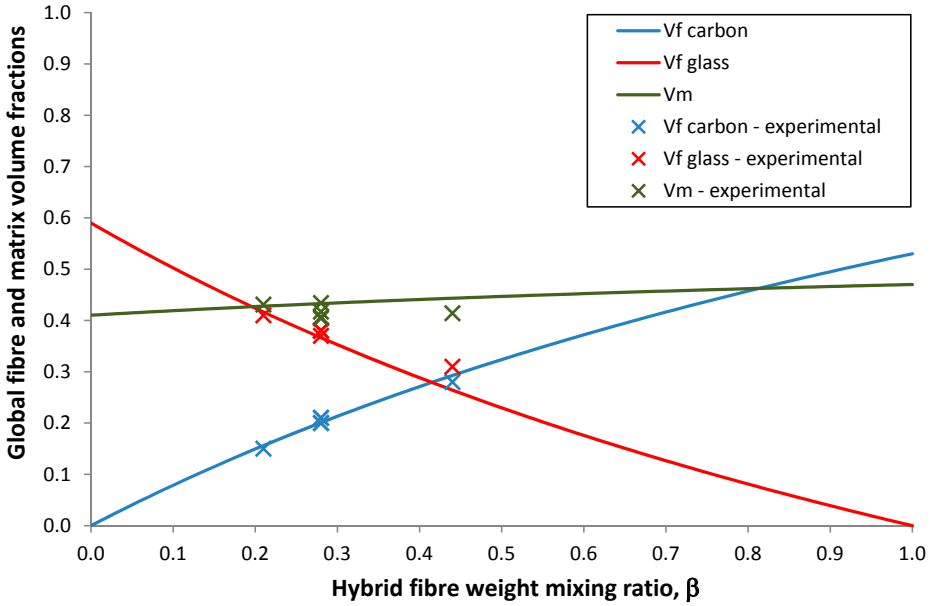

Fig. 8. Global fibre and matrix volume fractions in hybrid glass/carbon fibre composites as function of the hybrid fibre weight mixing ratio (β), model predictions and experimental data.

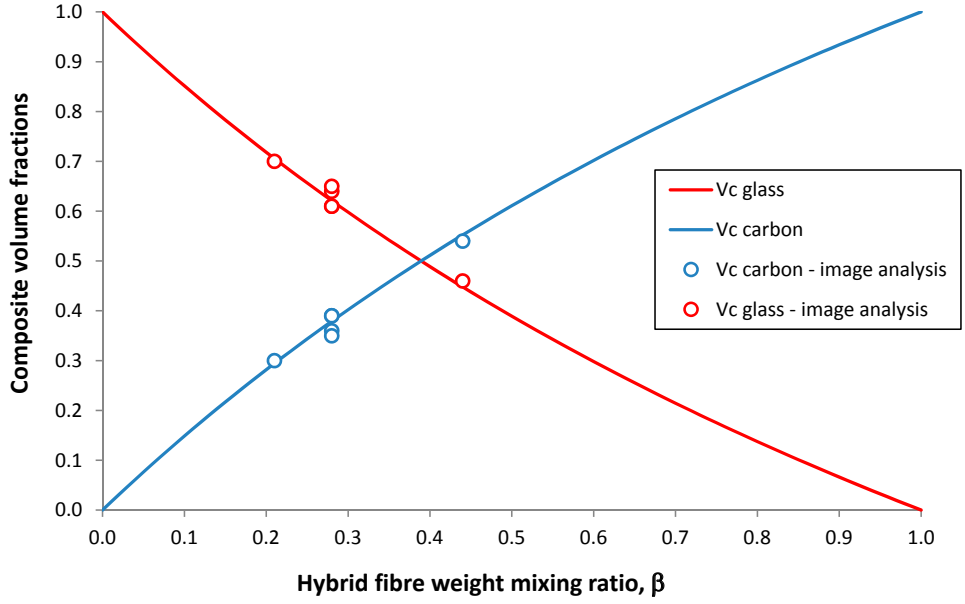

Fig. 9. Composite volume fractions in hybrid glass/carbon fibre composites as function of the hybrid fibre weight mixing ratio (β), model predictions and experimental data.

As can be observed in Figs. 8 and 9, there is generally a good agreement between the model lines, and the experimental data points. Thus, it is demonstrated that *the model equations are useful for the prediction of the composition in hybrid fibre composites, and thereby for the design of hybrid composites with wanted property profiles*.

5. MICROSTRUCTURAL UNIFORMITY OF HYBRID COMPOSITES

For the analysis of the microstructural uniformity, the two composites CXG-05 and CXG-10 were selected since they have a marked difference in their microstructure (see Fig. 6). CXG-05 has a *bundle-bundle* structure, and CXG-10 has a *ply-ply* structure. The image of CXG-10 is about half the width of the image of CXG-05 (about 20 vs. 40 mm), and it was therefore prolonged by stitching together twice the same image.

The first step in the quantification of the microstructural uniformity is to present the variation in the composite composition from one end of the composite sample to the other.

The results of the determined $V_{c\ glass}$ for every 0.1 mm of the two composites are shown in Fig. 10, where the composition is plotted against the position across the sample (or image). The dashed straight lines in Fig. 10 show the average $V_{c\ glass}$ values (which are similar to the ones in Table 2):

$$V_{c\ glass\ bundle-bundle} = 0.46 \quad \text{and} \quad V_{c\ glass\ ply-ply} = 0.61$$

The bundle-bundle curve is oscillating from about 0.2 to about 0.8, and the ply-ply curve is oscillating from about 0.5 to about 0.7. In each case, the difference between the two extreme values gives an indication of the dispersion of $V_{c\ glass}$, which reflects how constant the composition is across the composite. It is therefore clear that the ply-ply composite has a roughly constant composition compared to the bundle-bundle composite.

Other indications given in Fig. 10 for the bundle-bundle composite are the presences of glass composite rich regions ($V_{c\ glass} > 0.8$) and carbon composite rich regions ($V_{c\ glass} < 0.2$). The distance between these consecutive regions can roughly be estimated to 4 mm. Thus, one can say that the bundle-bundle composite is varying between two very different composite compositions within few millimetres across the sample.

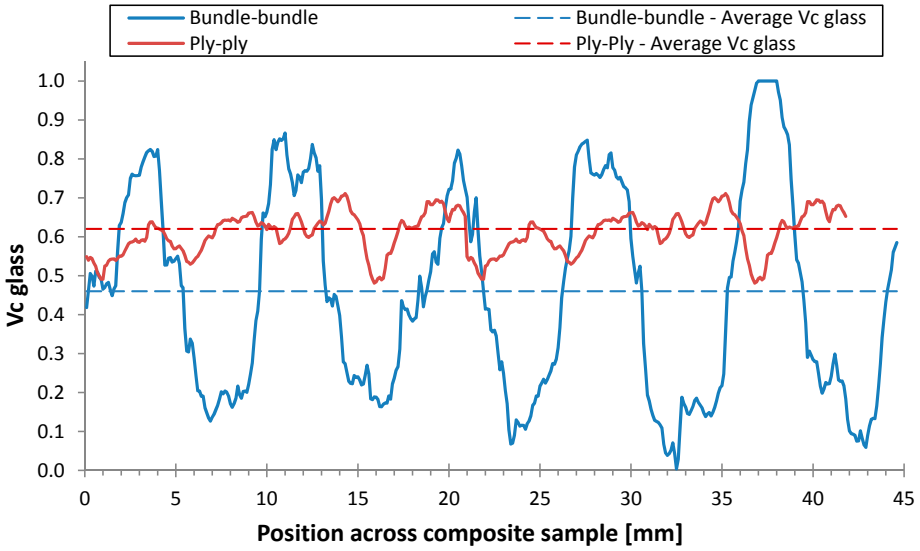

Fig. 10. Glass composite volume fraction ($V_{c\ glass}$) as function of position across the composite sample for composites with a bundle-bundle structure (CXG-05) and with a ply-ply structure (CXG-10). Shown are also average values.

In order to analyse the observed variation in V_c, and thereby to be able to quantify the microstructural uniformity, two methods are presented.

It can be realized that the variation in the determined values of V_c (see Fig. 10) depends on the width of the cross sectional windows used to determine V_c. It can be expected that the smaller the width of the cross sectional windows, the larger the variation of the determined values of V_c. This qualitative expectation will be quantified by *a standard deviation based method*, where a parameter D is calculated for a given width of the cross sectional windows (k) to represent the deviation in V_c from the overall (true) value of V_c.

$$D(k) = \sqrt{\frac{\sum_{i=1}^{n}\left(X_i - \bar{X}\right)^2}{n-1}} \tag{13}$$

where X_i are the determined values of V_c for all possible locations of a cross sectional window with a width of k (in mm) across the composite sample, $\bar{X}$ is the overall V_c determined for the entire sample (or image), i.e. $\bar{X}$ is equal to the average values shown in Fig. 10. The parameter n is the number of all possible locations of a cross sectional window with a width of k across the composite sample (or image). The parameter D is named *characteristic deviation* to designate that the parameter is not used in the normal statistical meaning of a standard deviation.

The parameter k and the width of the composite sample (or image) have to be a multiple of 0.1 mm, and the parameter n can then be calculated:

$$n = width\ of\ composite\ sample \cdot 10 - k \cdot 10 + 1 \tag{14}$$

The presented method can be exemplified on the image in Fig. 6 of the hybrid composite with

the bundle-bundle structure (CXG-05), where the width of the image is 44.5 mm, and the overall V_c for the glass fibre composite phase is determined to be 0.46.

- For a cross sectional window width of 0.1 mm (k = 0.1 mm), there will be n = 445 possible locations of the window. On each of these n locations, V_c is determined, and then D is calculated by Eq. (13) to be 0.27. Thus, for a window width of 0.1 mm, the characteristic deviation of V_c can be stated to be 0.46 ± 0.27.
- For a cross sectional window width of 4.0 mm (k = 4.0 mm), there will be n = 406 possible locations of the window. On each of these n locations, V_c is determined, and then D is calculated by Eq. (13) to be 0.18. Thus, for a window width of 4.0 mm, the characteristic deviation of V_c can be stated to be 0.46 ± 0.18.

By varying k stepwise from the minimum window width (= 0.1 mm) to the maximum window width (= width of the image – 0.1mm, where n = 2), a curve can be established showing D as a function of k.

In Fig. 11, the curves for D as a function of k are shown for the bundle-bundle composite and the ply-ply composite (CXG05 and CXG10). Firstly, it can be observed that the deviations in V_c are smaller for the ply-ply composite. As an example, for a window width of 4 mm, the characteristic deviations of V_c are 0.46 ± 0.18 and 0.61 ± 0.02 for the bundle-bundle composite and the ply-ply composite, respectively. Accordingly, V_c will therefore vary from about 0.28 to 0.64 for the bundle-bundle composite depending on the location of the 4 mm cross sectional window, whereas V_c will only vary from about 0.59 to 0.63 for the ply-ply composite.

From this first observation, one can say that the presented method is able *to quantify the difference in microstructural uniformity between composites*.

Secondly, it can be observed in Fig. 11 that for the bundle-bundle composite, the curve is clearly oscillating, whereas for the ply-ply composite, the curve is more flat. This indicates that the bundle-bundle composite contain a repeating pattern in the microstructure, whereas the ply-ply composite does not contain such a pattern.

In Fig. 11, the bundle-bundle curve shows a first minimum at a width of 8.9 mm, and the following minimum values are roughly at a multiple of this value, located at 17.1 mm and 25.7 mm. These values are easily and precisely determined. Thus, at every about 9 mm, the composition of the composite has gone through a glass composite rich region, and a carbon composite rich region. The same observation can be made from the results in Fig. 10. It can be realised that for samples with widths equal to a multiple of the width of the repeating pattern, the variation in V_c is at a minimum. In contrast, for samples with widths equal to a multiple of half the width of the repeating pattern, the variation in V_c is at a maximum.

From this second observation, one can say that the presented method is able *to detect and quantify any repeating pattern in the microstructure of composites.*

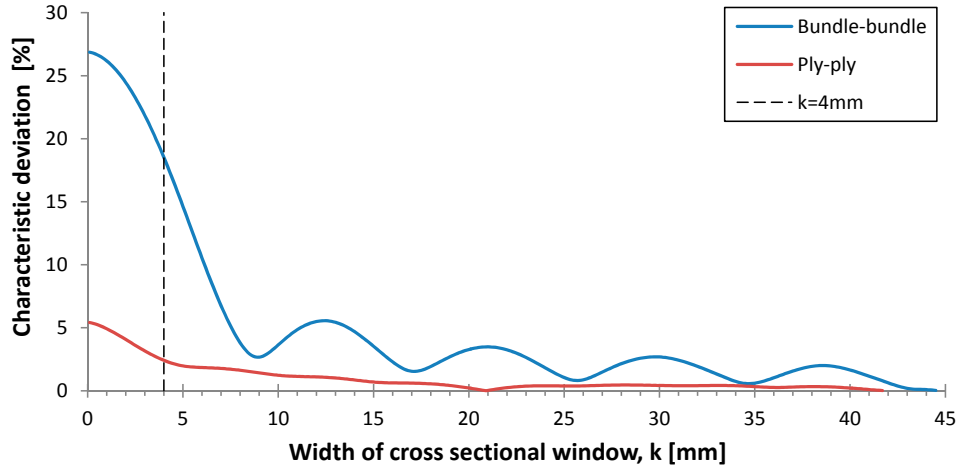

Fig. 11. Characteristic deviation of V_c as a function of width of the cross sectional window, obtained by the standard deviation based method. Results are shown for a composite with a bundle-bundle structure, and for a composite with a ply-ply structure.

In order to analyse further the observed variation behaviour in Fig. 10, a second method was used, a *fast Fourier transform method*. For that method, the two curves in Fig. 10 were considered as oscillating signals from which fundamental frequencies could be determined, and the Fourier transforms were calculated using the fast Fourier transform function in *Excel.*

The results obtained by this method are presented in Fig. 12, and show the frequency magnitude as a function of frequency range. It can be observed that the bundle-bundle curve shows a clear first peak at a frequency of 0.117 mm^{-1}, which correspond to a period of 8.5 mm. The ply-ply curve does not show any noteworthy peak. The period found for the bundle-bundle curve corresponds well to the results obtained by the standard deviation based method.

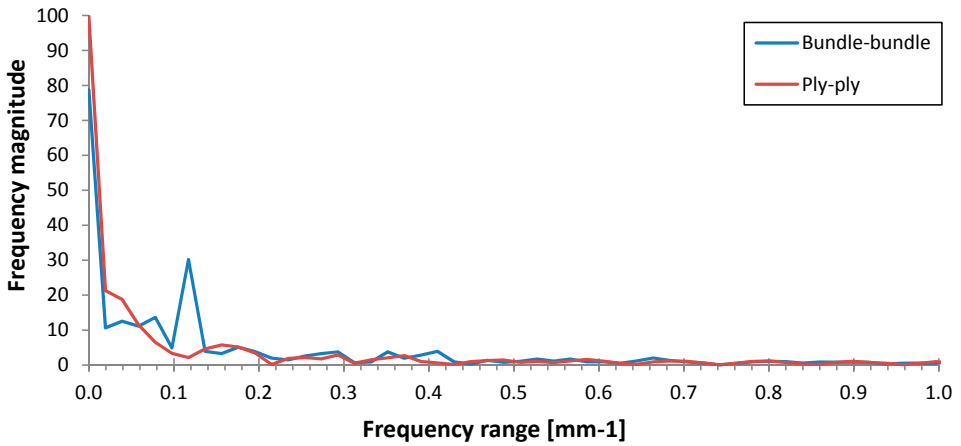

Fig. 12. Frequency magnitude as a function of frequency range obtained by the fast Fourier transform method. Results are shown for a composite with a bundle-bundle structure, and for a composite with a ply-ply structure.

6. CONCLUSIONS

The three levels of compositions in hybrid fibre composites were defined, experimentally determined and analysed. A model for the volume fractions in hybrid composites was presented, and used for the analysis of the experimental data. Good agreement between model predictions and experimental data was observed. Two quantification methods were implemented to analyse the microstructural uniformity of the composites. The methods were demonstrated to be well suitable to quantify the difference in microstructural uniformity between composites, and to detect and quantify any repeating pattern in the composite microstructure.

ACKNOWLEDGEMENTS

This work was conducted in a research project (Blade King, 2008 - 2013) sponsored by the Danish National Advanced Technology Foundation. The authors would like to thank Tom Løgstrup Andersen and Hans Lilholt for valuable advices and support in the manufacturing of composites, and analysis of data.

REFERENCES

Aveston J., Kelly A. (1980). Tensile first cracking strain and strength of hybrid composites and laminates. Phil. Trans. R. Soc. Lond. A, 294: 519-534.

Hermann T.M., Locke J.E. (2006). Fabrication, testing, and analysis of anisotropic carbon/glass hybrid composites. Technical report, Sandia, Lockheed Martin Company, for the United States Department of Energy's National Nuclear Security Administration, USA.

Hillermeier W. (2006). New composite hybrid reinforcements for the wind turbine industry. JEC Composites Magazine. No 49, June 2009.

Zhang J., Chaisombat K., He S., Wang C.H. (2012). Hybrid composite laminates reinforced with glass/carbon woven fabrics for lightweight load bearing structures. Materials and Design, 36: 75-80.

Proceedings of the 34th Risø International Symposium on Materials Science:
Processing of fibre composites – challenges for maximum materials performance
Editors: B. Madsen, H. Lilholt, Y. Kusano, S. Fæster and B. Ralph
Department of Wind Energy, Risø Campus
Technical University of Denmark, 2013

SELECTION OF ENVIRONMENTAL SUSTAINABLE FIBER MATERIALS FOR WIND TURBINE BLADES - A CONTRA INTUITIVE PROCESS?

Morten Birkved*, Andrea Corona*, Christen Malte Markussen** and Bo Madsen**

*Department of Management Engineering, Division for Quantitative Sustainability Assessment, Lyngby Campus, Technical University of Denmark
**Department of Wind Energy, Section of Composites and Materials Mechanics, Risø Campus, Technical University of Denmark

ABSTRACT

Over the recent decades biomaterials have been marketed successfully supported by the common perception that biomaterials and environmental sustainability de facto represents two sides of the same coin. The development of sustainable composite materials such as blades for small-scale wind turbines have thus partially been focused on the substitution of conventional fiber materials with bio-fibers. The major question is if this material substitution actually, is environmental sustainable. In order to assess a wide pallet of environmental impacts and taking into account positive and negative environmental trade-offs over the entire life-span of composite materials, life cycle assessment (LCA) can be applied. In the present case study, four different types of fibers (carbon, glass, flax and carbon/flax mixture) are compared in terms of environmental sustainability and cost. Applying one of the most recent life cycle impact assessment methods, it is demonstrated that the environmental sustainability of the mixed carbon/flax fiber based composite material is better than that of the flax fibers alone. This observation may be contra-intuitive, but is mainly caused by the fact that the bio-material resin demand is by far exceeding the resin demand of the conventional fibers, and since the environmental burden of the resin is comparable to that of the fibers, resin demand is in terms of environmental sustainability important. On the other hand is the energy demand and associated environmental impacts in relation to the production of the carbon and glass fibers considerable compared to the impacts resulting from resin production. The ideal fiber solution, in terms of environmental sustainability, is *hence* the fiber composition having the lowest resin demand and lowest overall energy demand. The optimum environmental solution hence turns out to be a 70:30 flax:carbon mix, thereby minimizing the use of carbon fibers and resin. On top of the environmental sustainability assessment, a cost assessment of the four fiber solutions was carried out. The results of the economical assessment which turns out to not complement the environmental sustainability, pin-point that glass fibers are the most effective fiber material.

1. INTRODUCTION

The purpose of the present case study is to perform a screening LCA facilitating benchmarking of four different wind turbine blade types, with the aim of illuminating the environmental sustainability performance of bio-composites such as flax based composites and bio-based resin relative to conventional composites such as carbon and glass fiber epoxy based composites.

The dominating industrial and scientific focus on bio-based composite materials (Müssig 2010; Pickering 2008; Mohanty, Misra, Lawrence 2005) are mainly concerned with the technical performance of the materials, but the sustainability of these new materials needs to be addressed as well. The study at hand addresses the environmental issues by presenting the results of a quantitative comparative sustainability assessment of four prototype small-scale wind turbine blades differing only in type and amount of fiber reinforcement material, i.e. conventional and bio-based and/or in the type of resin, a conventional epoxy resin and a bio-based epoxy resin. All blades were designed for being used in a wind turbine car concept (Gaunaa, Øye, Mikkelsen 2009).

Quite a number of LCAs on wind power technology have been published over the last two decades. LCAs of wind power technologies found in the existing literature most often focuses on the comparison of the environmental burdens of different life cycle stages of a wind turbines and/or comparison of complete turbines of various sizes (Davidsson, Höök, Wall 2012). Many of these studies highlight the fact that blades are one of the most environmental burdensome parts of a wind turbine. Still LCAs on wind turbine blades are rare.

A few publications involving comparative LCAs of various blade types or bio-based composites for blades have been identified. One of the most recent publications addressing LCA of materials for blades focuses on the application of nano-carbon for reinforcement (Mergula, Lowrie, Khana, Bakshi 2010). A further "grey" literature publication focuses on the application of bamboo for the blades (Xu, Qin, Zhang 2009). These two publications are as far as we know the only publications assessing the environmental performance of wind turbine blades applying LCA.

As conventional reinforcement, a typical carbon fiber fabric was selected, and as bio-based reinforcement, a commercial flax fiber fabric was selected. Both fiber fabrics were impregnated with a bio-based epoxy resin with "typical" mechanical properties, but sourced from bio-waste. In a previous study, a full technical documentation was done of the mechanical properties of the three composite materials combinations: carbon/epoxy, flax/epoxy and hybrid carbon/flax/epoxy composites (Bottoli, Pignatti 2011). From this, finite element models were constructed to dimension the small-scale wind turbine blades. Manufacturing was done using vacuum infusion to ensure high quality and reproducibility corresponding to industrial standards.

Initially a comparative LCA was carried out (Markussen, Birkved, Madsen 2013) and based on this assessment it was concluded that further analysis and inclusion of glass fiber reinforcement (currently the most used reinforcement for wind turbine blades) was needed in order to evaluate the environmental trade-offs between carbon and flax fiber reinforcement in the hybrid blade. To assess these scenarios a mechanical modeling approach was applied.

2. METHODS

The product system model was set-up in GaBi 4.4 (PE 2011a), and built based on readily available commercial unit processes from either the GaBi professional database (PE 2011b) or

the Ecoinvent database (Swiss Centre for LCI 2011). The parameterized model is illustrated in Fig. 1. The product system model covers all relevant life cycle stages of the blade's life cycle from extraction of raw materials, such as crude oil for the epoxy resin, to fuels for waste disposal (here incineration with energy recovery) of the blades. The experimental input for the model are the material quantities consumed during manufacture of the blade prototypes.

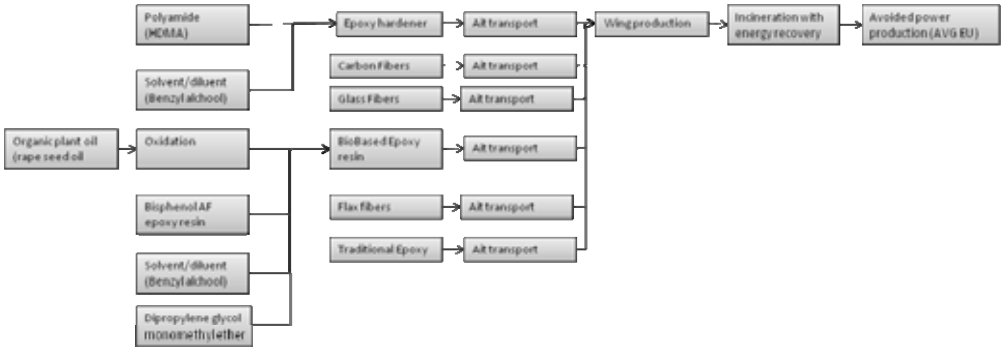

Fig. 1: Product system model.

Due to lack of experimental data, a sequence of assumptions had to be made in order to quantify the composition of both the resin and the hardener. Further explanation of these assumptions and the allocations needed to develop the product system model are presented in Markussen et al. (2013). All estimation work relating to model construction and model parameterization is by the authors considered to reflect the actual conditions as well as possible, and hence are the uncertainties relating to the estimation work and assumptions as low as possible. It is important to keep in mind that the uncertainties relating to the estimation work are approximately equally large for all blade type scenarios, and hence are the overall ratios between the impact potentials of the blade types therefore considered to have a considerable lower uncertainty than the absolute impact potentials (i.e. many of the uncertainties being the same for all blade types, will equal out by the comparison).

In a comparative LCA the same functional unit is used. In the present case study, all the blades have to meet the same stiffness requirements. For the first three scenarios (carbon, flax and hybrid 50/50) a full mechanical analysis of the blades was performed (Bottoli, Pignatti 2011); however, for the glass and the hybrid blades with mixing ratios different than 50:50, no mechanical analyses have been performed.

To obtain the same stiffness of the blades, the Ashby's methodology was used (Ashby 2011). This material selection methodology allows varying the material of an object maintaining the design requirements. In this case, the blade was compared to a beam in order to have a deflection less than the maximal deflection constrain and minimizing the mass. These design requirements are the same as those used to perform the mechanical analysis. The resulting masses serve as inputs for the product system model.

In this case, the Ashby's material index is: $I = \frac{E^{1/2}}{\rho}$ (1)

Hence to obtain the mass of a glass fiber blade with the same flexural stiffness as the other blades, the following equation was used.

$$m_g = \left(\frac{E_r}{E_g}\right)^{1/2} \frac{\rho_g}{\rho_r} m_r \quad (2)$$

where E (GPa) is the elastic modulus of the material, ρ (g/cm^3) is the density and m (g) is the mass of the blade. The subscript r is referring to the reference material, while g is referring to the glass composite blade. The calculation has been performed with both carbon and flax blades as reference material. The results are presented in Table 1. In order to evaluate the accuracy of the applied mechanical model, the 50:50 carbon:flax blade scenario is evaluated to avoid that large errors are introduced due to the applied mechanical performance assessment approach.

Table 1: Mechanical performance evaluation results of the "pure" composite materials (materials with only one fiber type).

Material	E (GPa)	ρ (g/cm^3)	Mass, real (g)	Mass, calculated (g)
Glass	38	1.88		495 (f) 500 (c)
Carbon	100	1.50	246	243
Flax	20	1.25	454	458

The results obtained for the flax and the carbon blade indicate that no large error is introduced using this simple mechanical performance assessment approach. To obtain the mass of the glass fiber needed on the inside of the composite, the law of mixture was used, assuming a fiber volume fraction (V_f) of 0.50.

The same approach was applied to calculate the weight of the hybrid composite blades with different flax fiber contents (Table 2).

Table 2: Weight of the hybrid blades, and weight of the fiber and resin demands.

% of flax fiber	Blade mass (g)	Carbon fiber mass (g)	Flax fiber mass (g)	Epoxy mass (g)
0 %	246	155	0	91
10 %	257	139	15	103
20 %	270	124	31	115
30 %	283	109	47	128
40 %	299	94	63	142
50 %	316	80	80	157
60%	337	65	98	174
70%	361	51	118	193
80 %	389	35	140	214
90 %	424	18	166	240
100 %	453	0	191	263

For the assessment of the environmental impacts induced by the different blade designs, the ReCiPe Life Cycle Impacts Assessment (LCIA) methodology was applied (Goedkopp et al. 2013). ReCiPe is within the LCA community considered to be one of the most recent and complete LCIA methodologies (Markussen et al. 2013). In the present case study, the Hierarchical assessment perspective is used, since it is the assessment perspective representing an "average political orientation".

This ReCiPe methodology allows for assessment both on midpoint and endpoint level. In this study, the results are presented at endpoint level or as aggregated endpoints in the form of single score combining all the endpoint categories.

3. RESULTS

The product system model assessment results are presented in Figs. 2 and 3.

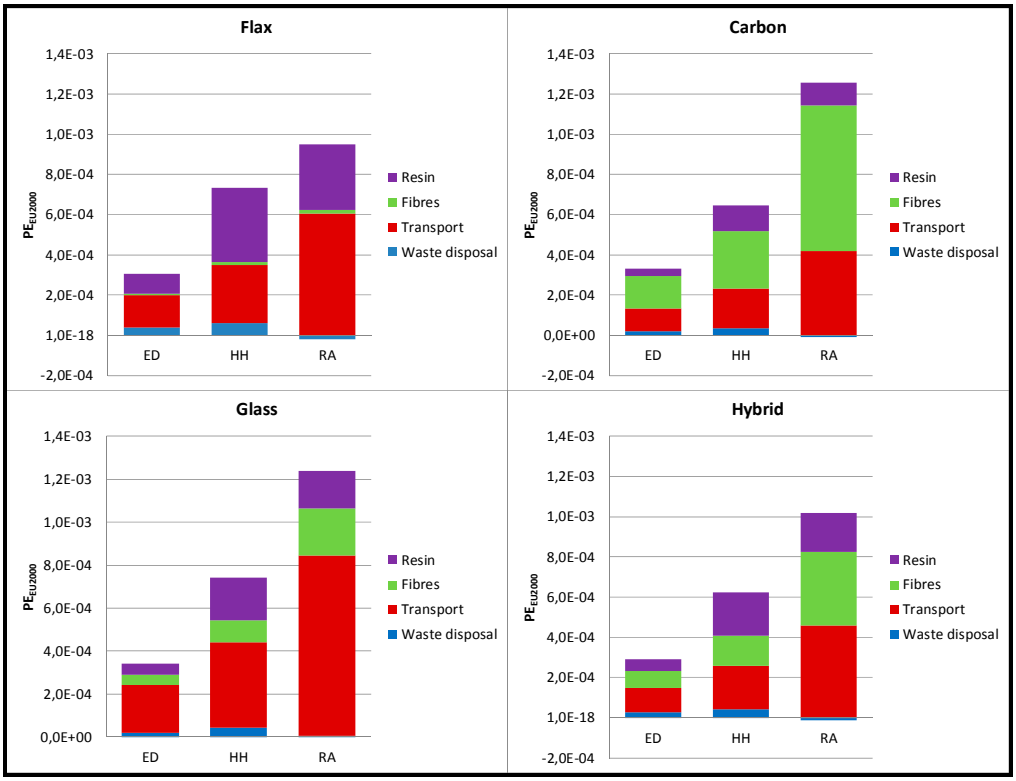

Fig. 2: Impact assessment results at endpoint level for all blade types obtained applying the ReCiPe impact assessment methodology on each blade alternative, applying the Hierarchist result assessment perspective, presented according to product system activity ED = Ecosystem damage, HH = Human Health damage, RA=Resource depletion damage.

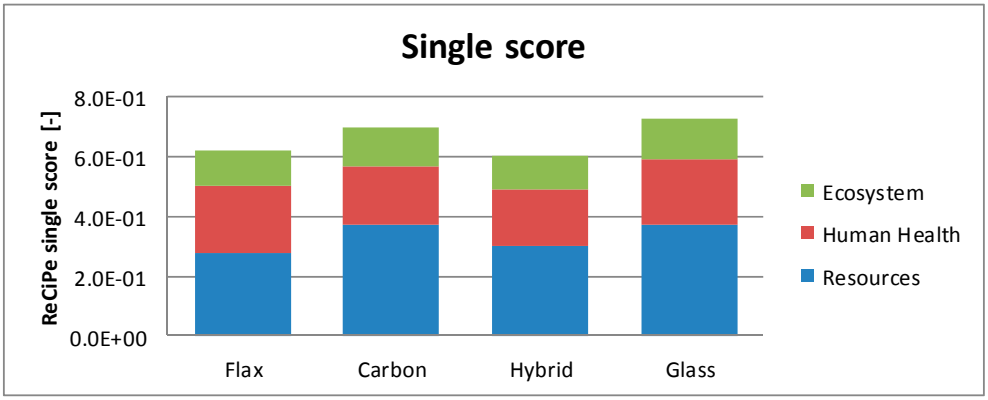

Fig. 3: Impact assessment results on endpoint level for all blade types obtained applying the ReCiPe impact assessment methodology on each blade alternative, applying the Hierarchist result assessment perspective.

In order to illustrate the differences between the bio-based blades and the glass fiber blade, in terms of their contributions to the specific endpoint or single score, the results are also presented in Δ-LCA result form. According to the Δ-LCA result interpretation approach, only the differences in impacts are highlighted, by calculating the differences in contributions to impact categories as:

$$\Delta IP_i = IP\left(flax/hybrid\right)_i - IP\left(glass\right)_i$$

where ΔIP_i is the difference of the specific endpoint impact category, and IP_i is the endpoint impact category of the specific blade scenario.

The results of the Δ-LCA between bio-based and glass fiber blades are presented in Fig. 4. For further in-depth information about the Δ-LCA and the carbon and flax blades, see Markussen et al. 2013.

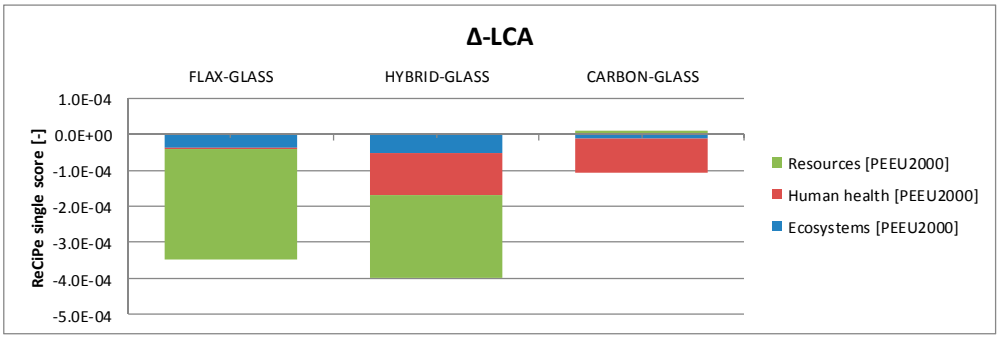

Fig. 4: Impact assessment result difference on endpoint level for all blade types obtained applying the ReCiPe methodology on each blade alternative, applying the Hierarchist result assessment perspective.

The environmental performance of the hybrid blade varies according to the amount of flax fibers applied. The results on the hybrid blade assessment are presented in Fig. 5.

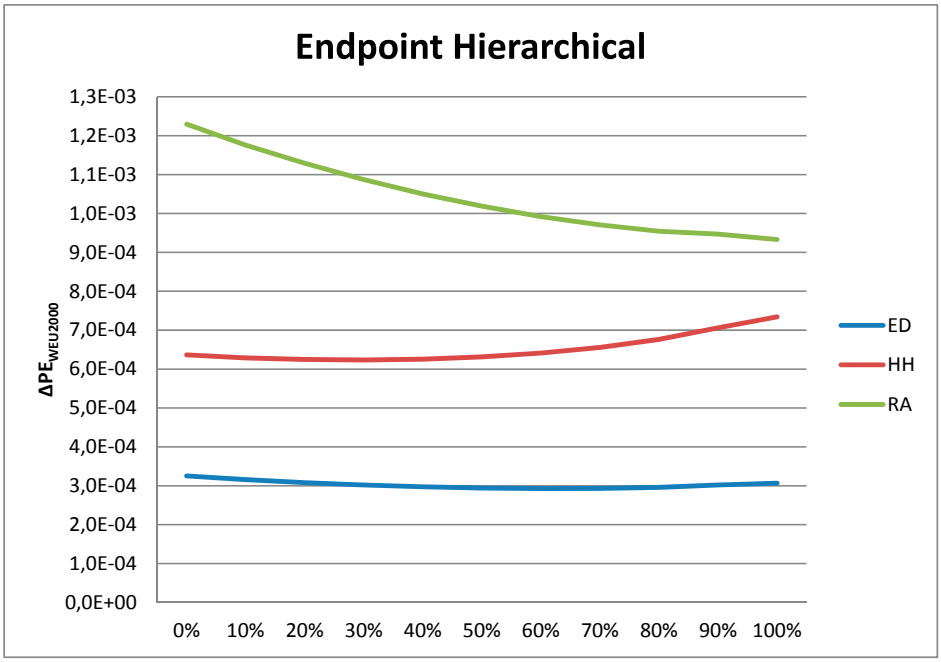

Fig. 5: Impact assessment result for the hybrid blade applying different flax contents on midpoint level obtained applying the ReCiPe impact assessment methodology on each blade alternative, applying the Hierarchist result assessment perspective.

The impacts from different fiber ratios of the hybrid blade are presented in Fig. 6.

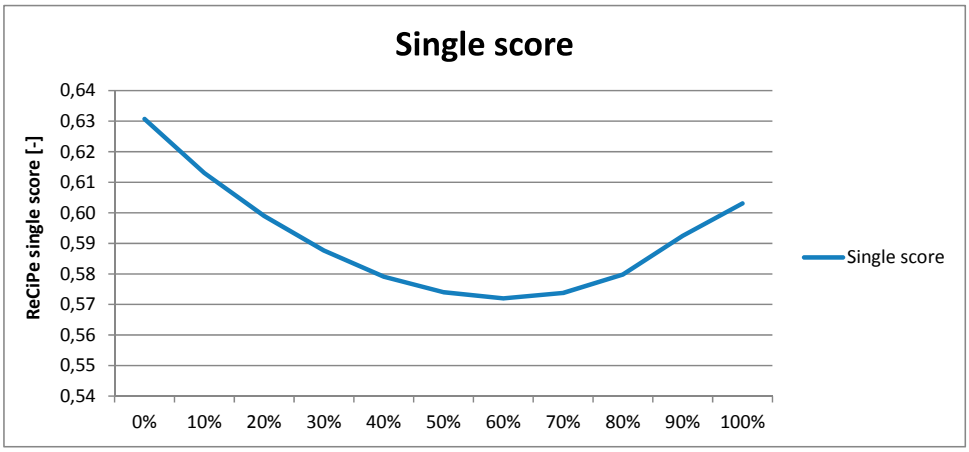

Fig. 6: Impact assessment result for the hybrid blade applying different flax contents on single score level obtained applying the ReCiPe impact assessment methodology on each blade alternative, applying the Hierarchist result assessment perspective.

In Fig. 7, the prices/costs of the hybrid blades are presented applying different fiber ratios. The material prices originate from Bottoli and Pignatti (2012), and are related to the prototype scale. Although the prices do not represent the true price in an industrial massive scale production, the prices are considered representative on a relative scale.

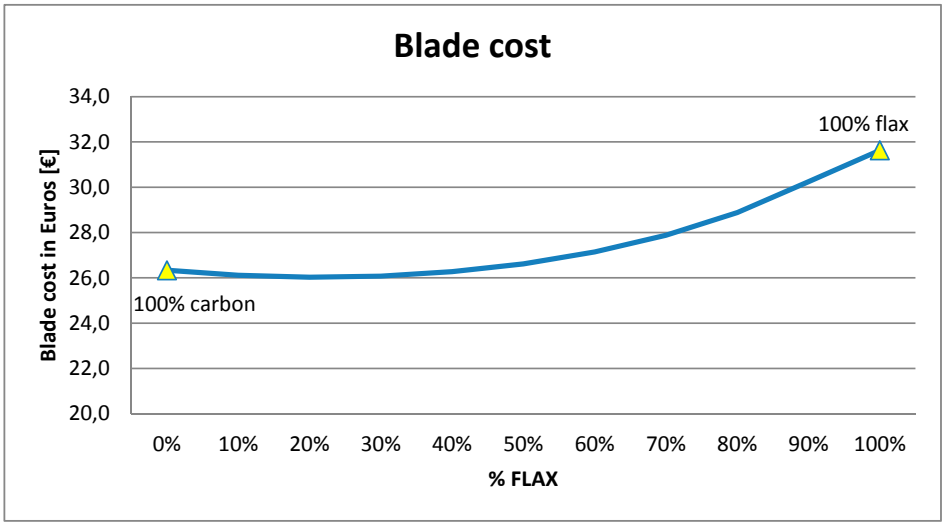

Fig. 7: Hybrid blade cost in Euros as a function of the ratio of flax applied.

In Fig. 8, the results are shown for Δ-LCA comparing a flax blade made with bio-based resin and one with conventional epoxy resin.

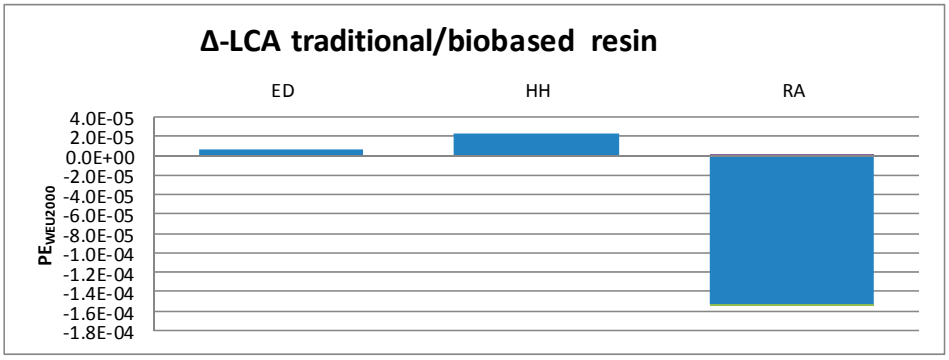

Fig. 8: Impact assessment results on both endpoint level comparing the impact of a flax blade with conventional resin and bio-resin.

4. DISCUSSION

A general view on the LCA results on the four different materials as presented in Figs. 1-3 clearly indicate that the hybrid blade has the best environmental performance. This observation is in accordance with the fact that the hybrid blade combines the low non-renewable resource depletion related with the flax fibers, the high specific stiffness of this blade type, and the low resin uptake of the carbon fibers.

On the other hand, the glass fiber blade has the worst environmental performance (see Figs. 1-3). This is because the production process for glass fibers in general is more environmentally burdensome than the one for flax fibers, and comparable burdensome to the one for carbon fibers. Additionally the glass fibers itself has poor specific stiffness, necessitating a higher mass in order to obtain the same flexural stiffness as the other alternative. The high mass of the glass fiber blade type further increases the environmental burden of the transport phase. For a detailed analysis of the carbon, flax, and hybrid 50-50 scenario, see Markussen et al. (2013).

Focusing on the Δ-LCA results (Fig. 4) it is observed that all the other materials perform better than the glass blade. Compared to the flax blade, the glass blade has higher a contribution to Resource Depletion. This is caused by the production process and the transport process (flax fibers are assumed produced in Europe, while carbon and glass fibers are produced in China).

In Fig. 4, the hybrid/glass blade comparison reflects the same issues; however in addition there is a higher contribution to Human Health damage for the glass fiber blade mainly caused by the difference in mass between the two blade types, which causes an increase in the emissions related to the transport stages. This pattern is also observed for the carbon/glass blade comparison.

The carbon/glass blade comparison reveals no large differences in terms of Resource Depletion since both of the fiber production forms require considerable amounts of energy.

The single score results on the hybrid blade covering different flax:carbon ratios indicate that there is a minimum for the single score, as presented in Fig. 6. The optimal solution is a ratio of 70% of flax fibers and 30% of carbon fibers.

As presented in Fig. 5, by increasing the amount of flax fibers leads to a decrease in the Resource Depletion; however, on the other hand, since flax fibers have a low volume fraction, the more flax fibers require more resin. Increasing the amount of resin implies that Human Health damage is increasing since Human toxicity is mainly related to the production and use of the epoxy resin.

As observed in Fig. 7, there is a minimum cost of the hybrid composites. This minimum cost solution seems to have the same flexural performance as the other alternatives, and it takes place at approx. 20% flax fibers and 80% carbon fibers. The price of flax fibers is high because there is only a small demand for this product. Carbon fibers on the other hand have over the last decade shown a remarkable decrease in price mainly caused by the high demand for this product.

As presented in Fig. 8, the application of a bio-based resin reduces the overall environmental burden of a blade. Flax blades however have the highest resin uptake among all the blade alternatives compared in the present case study.

5. CONCLUSIONS

In the study at hand, it has been demonstrated that the optimum material in terms of environmental sustainability performance, is a hybrid solution consisting of 70% flax fibers and 30% carbon fibers. This ratio is however not the cheapest hybrid alternative.

At the same time, it has been demonstrated that in terms of cost, the optimum solution is a 20% flax and 80% carbon hybrid solution.

Despite the fact that the optimum solutions in terms of environmental performance and cost are different, the data uncertainty related to the assessment does not allow for judgment of whether the two optima are different or not.

The use of a bio-based epoxy resin shows an increase in the environmental performance. This is an interesting observation, since despite being of "bio" origin these materials still have a considerable environmental burden.

REFERENCES

Ashby, M. (2011). Materials selection in mechanical design. 4th edition. Elsevier, Oxford, UK.

Bottoli, F. and Pignatti, L. (2011). Design and processing of structural components in biocomposites materials - case study: rotor blades for wind turbine cars. Master thesis, Technical University of Denmark.

Davidsson, S., Höök, M. and Wall, G. (2012). A review of life cycle assessments on wind energy systems. The International Journal of Life Cycle Assessment, 17(6), 729–742.

Gaunaa, M., Øye, S. and Mikkelsen, R.(2009). Theory and design of flow driven vehicles using rotors for energy conversion. To be published.

Markussen, C.M., Birkved, M. and Madsen, B. (2013). Quantitative sustainability assessment of conventional and bio-based composite materials: a case study of a small-scale wind turbine blade. Submitted to Wind Energy.

Mergula, L.-A., Lowrie, G.W., Khana, V. and Bakshi, B.R. (2010). Comparative life cycle assessment: Reinforcing wind turbine blades with carbon nanofibers. IEEE International Symposium on Sustainable Systems and Technology (ISSST).

Mohanty, A., Misra, M. and Lawrence, D.T. (2005). Natural fibers, biopolymers and biocomposites. Florida: CRC Press.

Müssig, J. (2010). Industrial applications of natural fibres - structure, properties and technical applications. United Kingdom: Wiley.

PE (2011a). GaBi 4.4. Compilation 4.4.131.1. Stuttgart, Germany: PE International - Software-System and Databases for Life Cycle Engineering.

PE (2011b). Professional Database version 4.131. Stuttgart, Germany: PE International - Software-System and Databases for Life Cycle Engineering.

Pickering, K. (2008). Properties and performance of natural fibre composites. Cambridge, England: Woodhead Publishing Limited.

Swiss Centre for LCI (2011). Ecoinvent v. 2.2. St-Gallen, Switzerland: Swiss Centre for Life Cycle Inventories.

Xu, J., Qin, Y. and Zhang, Y. (2009). Bamboo as a potential material used for windmill turbine blades. Master thesis, Roskilde University, Denmark.

Proceedings of the 34th Risø International Symposium on Materials Science:
Processing of fibre composites – challenges for maximum materials performance
Editors: B. Madsen, H. Lilholt, Y. Kusano, S. Fæster and B. Ralph
Department of Wind Energy, Risø Campus
Technical University of Denmark, 2013

INTERPHASE STUDIES IN NATURAL FIBRE COMPOSITES

H. Brodowsky and E. Mäder

Leibniz-Institut für Polymerforschung Dresden eV, Hohe Str. 6,
D- 01069 Dresden, Germany

ABSTRACT

Natural fibres are a valuable reinforcement material because of their low density and attractive specific properties at low price, combined with recycleability and renewability. Studies of natural fibres as reinforcement for polylactic acid or an epoxy resin matrix are presented, focusing on interphase strength improvement. This study focuses on the investigation of interphases, as natural fibres such as jute, flax, or hemp in composites have poor compatibility towards a hydrophobic polymer matrix, resulting in weak interfaces and poor mechanical properties of the composites. This may in part be overcome by the use of surface modification, or in the case of reinforced polypropylene matrix by additional maleation of the matrix. Hereby, the mechanical properties of the resulting materials have been significantly improved.

1. INTRODUCTION

Technological progress demands ever more efficient materials. In recent years, sustainability issues have gained more attention. Natural fibre reinforced composites are ideal materials to meet these two requirements simultaneously. Natural fibres combine low density and attractive specific properties at low price with recycleability and renewability.

Plant based fibres may be derived from the stem or bast (e.g. flax, hemp), the flower (cotton) or the leaf (abaca, sisal) of the plants. The fibre properties depend not only on the fibre type but also on the growing conditions of the plant, the site of extraction, the retting process, leading to a scatter in the fibre properties. The load bearing components of the fibre are cellulose microfibrils, fibres also contain lower molecular hemicellulose or pectins.

For a maximum performance of natural fibre reinforced composites, a significant drawback of natural fibres must be overcome: The interphase between the hydrophilic fibre and the hydrophobic polymer matrix is often weak. This needs to be modified in order to obtain a strong interphase. The fibre needs to be tailored according to the matrix in mind. As the cellulose exposes OH-moieties on the surface, many of the chemical modifications known from glass fibre reinforcement should also be appropriate. For glass fibers, the processing routes are well

known for many polymer matrix materials and may be adopted to natural fibres. One difference is that in the industrial process, glass surface modification is performed via sizing the glass fibres online during the production process immediately after leaving the bushing. Naturals fibres need to be stripped of their low molecular parts e.g. by hydroxide treatments or mercerization in order to enable modification.

As a polymer matrix, Polylactic acid (PLA) derived from corn starch was chosen. For this matrix, known modifications lead to improvements but cannot lead to interphase strengths comparable to those of polypropylene (PP) or polyamide (PA) matrix systems. In combination with the natural fibres, this leads to an all-bio composite.

2. MATERIALS AND METHODS

Composites are prepared by various processing routes. Bamboo is obtained as powder made up of typically 400 µm x 50 µm pieces from Bamboo Fibre Technologies (France). Variations of treated powder are compounded with PLA (Ingeo2003D, NatureWorks LLC) and injection moulded into plates or test specimens. The surface modifications include de-waxing of fibres by soaking in 1wt% NaOH for 2 h followed by washing and neutralizing, sizing the fibres with an aqueous solution containing coupling agents such as silanes (3-aminopropyltriethoxysilane, APS or 3-glycidoxypropyltrimeth-oxysilane, GPS) or maleic acid, or film formers such as chitosan or epoxy dispersion. The PLA is compounded with dicumyl peroxide (DCP) for improved bonding. Jute yarn / epoxy microcomposites with differently treated fibres (treatment: NaOH, silanes as described for bamboo) are made on an institute-built embedding device.

The influence of modified interphases in natural fibre composites is studied in compression shear tests and transverse tension tests as well as Charpy impact test. Besides, the interfacial adhesion strength of single fibre composites is evaluated by a pull out test. It is carried out on a self-made pull-out device with a force accuracy of 1 mN, and a loading rate of 0.01 µm/s. The maximum force required for pulling the fibre out of the matrix and the embedded length were determined from the force-displacement curves. The adhesion bond strength between the fibre and the matrix is characterized by the values of the apparent interfacial shear strength (τ_{app}). The fracture surfaces of the fibres after pull-out are studied by scanning electron microscopy (SEM) and atomic force microscopy (AFM).

3. RESULTS AND DISCUSSION

The single fibre pull-out test was used to determine the quality of interfacial bonding between differently treated or conditioned jute fibres and the epoxy matrix. This micro-mechanical test is very sensitive to variations of interfacial adhesion. For untreated fibres, the apparent interfacial shear strength between the jute fibre and the epoxy matrix was determined as $\tau_{app} = 43 \pm 9$ MPa. An AFM study of the fracture surface (Fig. 1a) shows compact structures as of a waxy surface. The fracture is expected to occur within the weakly cohesive cementing layer, which covers the untreated fibre and consists of low molecular weight fats, lignin, pectin and hemicellulose.

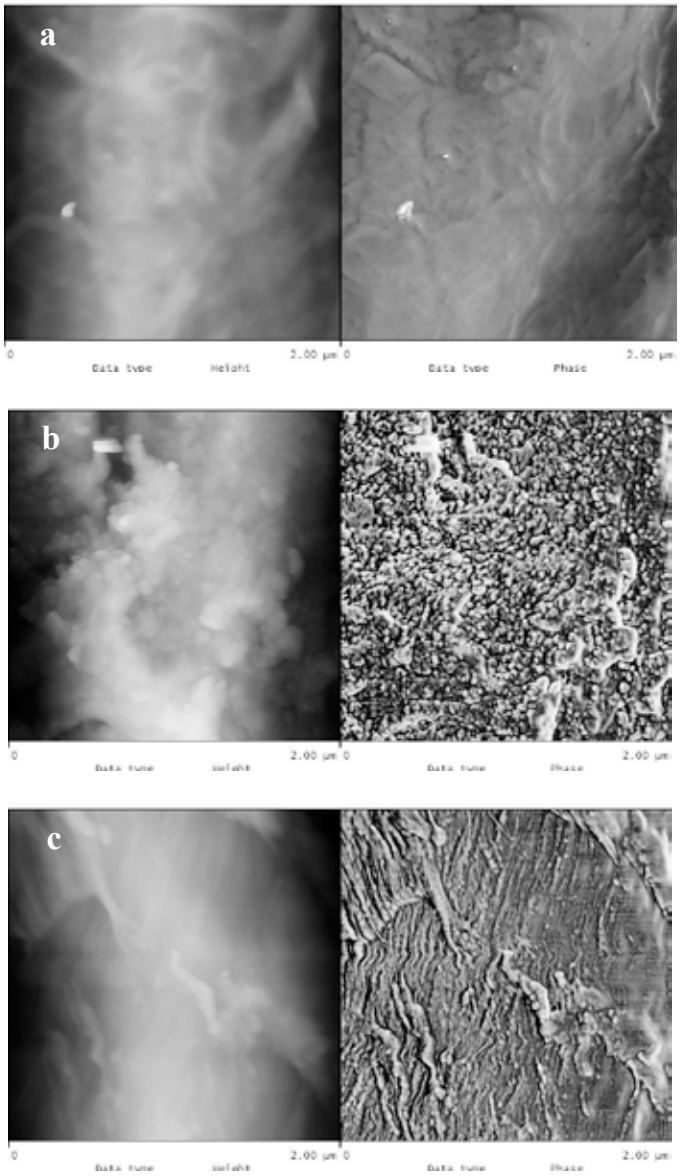

Fig. 1. AFM images of fracture surfaces of jute fibres pulled out of an epoxy matrix. The fibres were untreated (a) treated with NaOH (b) or NaOH treated followed by sizing with APS (c).

Alkaline treatment of the fibre increases the apparent shear strength τ_{app} by 40% to 61 ± 12 MPa (Doan et al. 2012). The AFM surface image (Fig. 1b) shows an agglomeration of 30 nm and 200 nm structures which are randomly arranged. A high surface roughness often corresponds to higher fracture energies. Removing the said cementing layer is the aim of the NaOH fibre treatments. It also provides a rougher fibre surface and improves the wettability (Doan et al. 2012). This enhances the interfacial shear strengths of jute / epoxy model micro-composites significantly as compared to untreated fibre micro-composite.

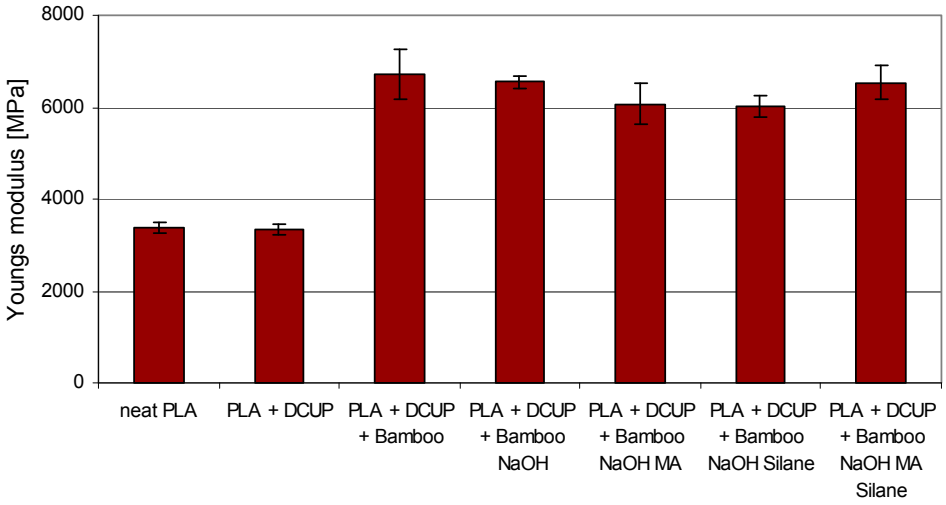

Fig. 2. Young's modulus of PLA and bamboo powder reinforced PLA with different surface modifications

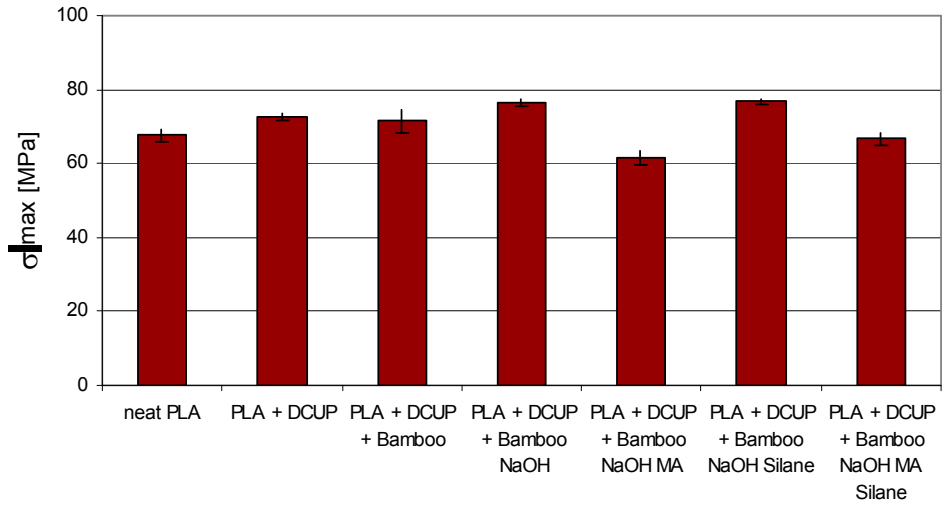

Fig. 3. Tensile strength of PLA and bamboo powder reinforced PLA with different surface modifications

Silane treatments enhance the adhesion strength further. The apparent interfacial shear strength of the epoxy composite based on NaOH/APS treated fibres was increased by 49%, as compared to untreated fibres. This compares well to jute / epoxy composites where fibres with the same treatments were arrayed by stitching and then embedded in an epoxy matrix (Doan et al. 2012). NaOH treated jute fibre exhibits a porous structure on the fibre surface, the sizing components such as coupling agents can penetrate into the pores and form a mechanically interlocked coating on the fibre surfaces. In the AFM micrographs, the fracture surface reveals a cross-hatched structure of the crystalline cellulose exposed after peeling-off the surface layer (Fig. 1c). The bonding must therefore be strong enough to induce cohesive fracture within the jute fibre in contrast to the adhesive fracture seen in the interface of the NaOH treated fibre composites

(Doan et al. 2012, Doan et al. 2007).

In jute / PP single fibre model composites, the interfacial shear strength can be doubled via the maleation of the matrix (Doan et al, 2006). Such a matrix modification is technologically convenient. For PLA, no appropriate polymeric modifier is commercially available. So the fibres were modified and treated with various bonding agents. As fibre, bamboo powder with 400 µm length was used, corresponding roughly to a typical fibre length of injection moulded glass fibre reinforced thermoplastics.

Bamboo powder was surface treated with NaOH and then with bonding agents (maleic acid, GPS). It is compounded into PLA in a twin screw extruder (ZSE 27 MAXX, Leistritz, Germany), DCP peroxide is added together with the PLA, the modified fibres are added downstream to reduce fibre shorteing. Reinforcing the PLA with 30 wt% bamboo powder almost doubles the Youngs modulus (Fig. 2). As the Young's modulus is determined at strains so low that local failure should not occur, the adhesion strength of the interphase does not play a role: the moduli are independent of the surface treatment. However, they influence the tensile strength. Adding DCP, a peroxide with a reaction temperature of 160°C, to the neat PLA leads to an increased tensile strength of the injection moulded specimens by 10% (Fig. 3). Adding unmodified bamboo powder does not improve the tensile strength, unless the powder is alkali treated first. A silane treatment slightly improves the tensile strength further whereas a treatment with maleic acid decreases the tensile strength of bamboo powder composites, the decrease is less pronounced if silane is present.

Compounding peroxide into the PLA increases the toughness due to random chain length and cross linking reactions. As expected, the toughness decreases upon addition of the bamboo powder. Here, the treatments of the powder have a large effect: as in the tensile strength, best results are optained for alkali/silane treated bamboo composites, the improvement is less pronounced in maleic acid treated powder composites (Fig. 4).

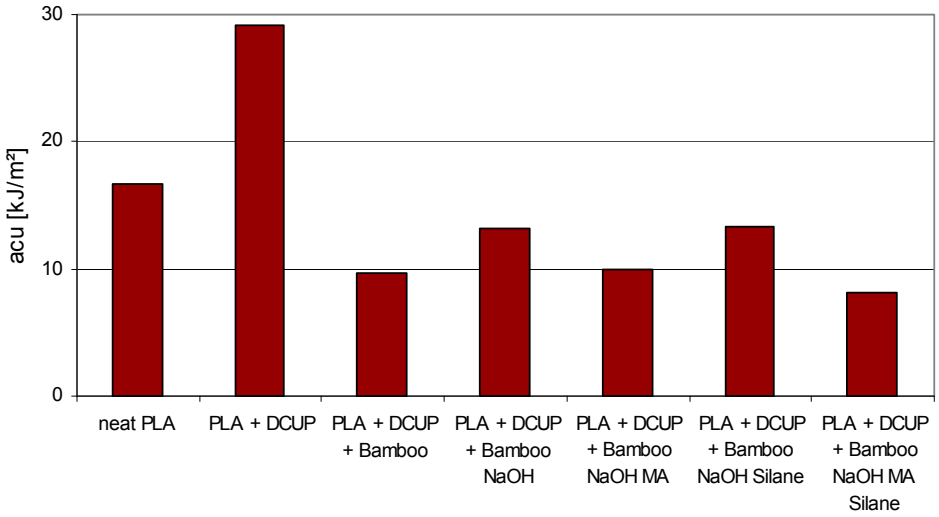

Fig. 4. Charpy impact toughness (a_{cu}) of PLA and bamboo powder reinforced PLA with different surface modifications

4. CONCLUSIONS

Natural fibre surface treatments alter the fibre properties in terms of morphology, topography, adhesion as well as of bonding ability towards a specific matrix and thereby affect the interphase properties. Especially the presence of silane coupling agents leads to improved adhesion in the interphase, through chemical bonds between, on the one hand, the fibre and silane coupling agent/film former and, on the other hand, the coupling agent/film former and the matrix.

As well known, a similar effect is obtained by maleating the matrix in PP / jute composites: This is a technologically easy way to enable the formation of a covalent bond between fibre and matrix. In thermoplastic matrix materials made from sustainable resources, the aim is to form as strong an interphase as that resulting from the maleated PP. Generally, the interphase needs to be tailored according to the matrix. When trying to make composites out of bio-products such as natural fibre reinforced PLA, the specific interphase formation needs further improvement. Although the interphase material makes up only a relatively small fraction of the total mass, these functional interphases influence the composite properties significantly.

.

ACKNOWLEDGEMENTS

The authors would like to thank Dr. Thi-Thu Loan Doan for valuable work on the jute epoxy composites and helpful discussions.

REFERENCES

Doan, T.T.L.; Brodowsky, H; Mäder, E. (2012). Jute fibre/epoxy composites: Surface properties and interfacial adhesion, *Compos.Sci.Technol*. **72** (10), pp.1160-1166, ISSN: 0266-3538.

Doan, T.T.L.; Brodowsky, H; Mäder, E. (2007). Jute fibre/polypropylene composites II. Thermal, hydrothermal and dynamic mechanical behaviour, *Compos.Sci.Technol*. **67** (13), pp. 2707–2714, ISSN: 0266-3538.

Doan, T.T.L.; Gao, S.L.; Mäder, E. (2006). Jute/polypropylene composites I. Effect of matrix modification, *Compos Sci Technol*; **66** (2), pp 952-963, ISSN: 0266-3538.

Proceedings of the 34th Risø International Symposium on Materials Science:
Processing of fibre composites – challenges for maximum materials performance
Editors: B. Madsen, H. Lilholt, Y. Kusano, S. Fæster and B. Ralph
Department of Wind Energy, Risø Campus
Technical University of Denmark, 2013

DETERMINATION OF THE GEL POINT OF A POLYFURFURYL ALCOHOL RESIN AND CHARACTERIZATION OF ITS CURING RHEOKINETICS

Juan Carlos Domínguez[1] and Bo Madsen[2]

[1]Department of Chemical Engineering, Complutense University of Madrid, Avda. Complutense s/n, 28040 Madrid, Spain
[2]Department of Wind Energy, Section of Composites and Materials Mechanics, Technical University of Denmark, Risø Campus, Frederiksborgvej 399, DK-4000 Roskilde, Denmark

ABSTRACT

The determination of the gel point of a resin is a key in order to design and optimize the manufacturing process of composite materials. In this work, the gel point of a biobased polyfurfuryl alcohol (FA) resin has been determined by rheological isothermal tests at different curing temperatures. The obtained gel times using three different amounts of catalyst (2, 4 and 6 % wt.) were correlated to temperature by the Macosko model; to predict the gel time at any temperature within the studied range. Furthermore, the evolution of the complex viscosity of the FA resin after its gel point has been studied as a function of the amount of catalyst and temperature. The rate of viscosity change was compared to the rate of viscosity change during the pre-gel stage, and a clear reduction was observed. Thus, the two different curing stages (pre-gel and post-gel) can be clearly identified by the rheological behavior of the resin system. The evolution of the viscosity has been modeled using widely used rheokinetic models. Finally, since rheological properties such as viscosity and complex modulus (G^*) are highly sensitive to the molecular weight of a polymeric system, and they can be used as indicators of the degree-of-cure of a resin, the measured complex modulus of the FA resin has been used to determine degree-of-cure profiles for FA resins with different amounts of catalyst, and at a range of temperatures.

1. INTRODUCTION

The preparation of composite materials to achieve both an optimization of the manufacturing process and the final properties of the composites depending on the application requires basic knowledge of the properties of the constituent materials. Thus, the study of polymers and fibers employed as matrix and reinforcements of composite materials is of great importance. In the case of thermosetting polymers, the analysis of its kinetics of curing, and the evolution of its

properties during crosslinking of the polymer, and the transitions that may occur, gelling and vitrification, are crucial.

The gel point of a resin is defined as the point at which the behavior of the resin is more similar to a solid than to a liquid, i.e. its flow behavior is changed, and it is considered that all the polymer chains are linked together forming a polymeric network. At this point, the kinetics of the curing reactions are commonly changed compared with the pre-gel stage; e.g. the curing rate is typically reduced. The gel times of a resin under different conditions (e.g. amount of catalyst and temperature) can be obtained through rheological tests. The five criteria normally used in the literature to detect the gel point by a rheological technique are: (i) the cross-over point of the elastic modulus (G') and the viscous modulus (G'') (Tung and Dynes, 1982), (ii) the point at which tan(δ) becomes independent of the frequency (Winter, 1987), (iii) the maximum of tan(δ) (Cadenato et al., 1997), (iv) the crossing point between the tangent line of the elastic modulus curve and the baseline G'=0 (Martin et al., 2000), and finally (v) the onset of decrease in the rate of growth of the viscous modulus during the polymer cure (Harran and Laudouard, 1985).

In the present work, a study of the curing process of a biobased polyfurfuryl alcohol (FA) resin was carried out using rheology as the analysis technique. The study includes determining the gel point of the resin, using the above-mentioned first two criteria, in addition to determining the gel time dependence with amount of catalyst and temperature. Furthermore, profiles of the degree-of-cure of the resin *vs.* time were obtained through a rheological variable such as the complex modulus, and the rheokinetics for the post-gel stage were determined.

2. EXPERIMENTAL PROCEDURE

Rheological runs were performed using an AR Rheometer 2000 (TA Instruments©) with a 25 mm diameter upper plate and a peltier lower plate. Normal force was zeroed and fixed during the tests to prevent contact loss between the sample and plates. Five isothermal curing runs of the FA resin in the three temperature ranges 65 – 85 ºC, 55 – 75 ºC and 50 – 70 ºC (using a 5 ºC increment) for 2, 4 and 6 % wt. amounts of catalyst, respectively, were carried out for 60 min. The frequencies employed were from 1 to 10 Hz (6 frequencies equally separated on a logarithm scale), and with a 0.1 % strain. For the isothermal curing runs, a 20 ºC.min^{-1} heating ramp from a starting temperature of 20 ºC was programmed in order to reach the various curing temperatures. The samples were first stabilized at 20 ºC for 2 min before the heating ramp was started. All rheological measurements were performed within the linear viscosity region of the FA resin. Three replicates were used for each experimental setting.

3. RESULTS AND DISCUSSION

The gel point of the FA resin was obtained by applying the criterion of the cross-over point of the elastic modulus (G') and the viscous modulus (G'') at a single frequency (1Hz), and the criterion of the point at which tan(δ) becomes independent of the frequency, i.e. when the value of the tangent is equal for all the tested frequencies. An example of this is shown in Figure 1.

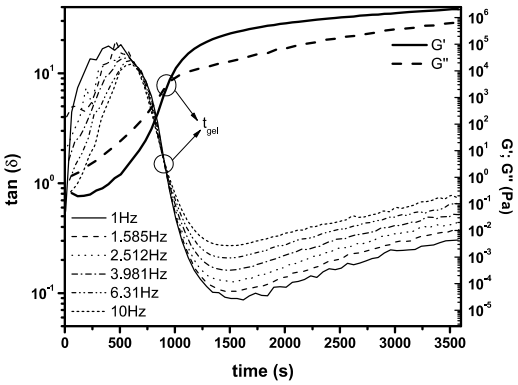

Fig. 1. Determination of gel time using the cross-over point of the elastic and storage modulus (at 1 Hz), and the point at which tan(δ) becomes independent of the frequency for a FA resin with 2 % wt. amount of catalyst and at a temperature of 75 ºC.

In the case of the second criterion, i.e. when tan(δ) becomes independent of the frequency, it was observed that at high temperatures and high amounts of catalyst, the values of gel time obtained for the three different replicates showed large variation. This second criterion was therefore rejected, and the cross-over of the moduli was taken as the most reliable criterion.

The average value of the gel time obtained for the FA resin at the tested temperatures and amounts of catalyst were determined (Table 1). The natural logarithm of the inverse of the gel times is plotted *vs.* the inverse of the absolute temperature in Figure 2.

Table 1. Gel times for FA resin for different amounts of catalyst and temperatures determined using the two criteria: cross-over of the moduli and independent value of tan(δ).

Amount of catalyst	**Temperature (ºC)**	**t_{gel} (s) cross-over**	**t_{gel} (s) tan(δ)**
2 % wt.	65	2544 ± 253	2641 ± 75
	70	1425 ± 8	1461 ± 28
	75	1056 ± 226	936 ± 21
	80	657 ± 44	666 ± 5
	85	448 ± 103	457 ± 6
4 % wt.	55	1875 ± 126	2004 ± 134
	60	1204 ± 21	1235 ± 27
	65	744 ± 18	754 ± 8
	70	452 ± 25	455 ± 3
	75	297 ± 1	—
6 % wt.	50	1579 ± 191	—
	55	911 ± 63	—
	60	555 ± 33	—
	65	347 ± 56	—
	70	230 ± 13	—

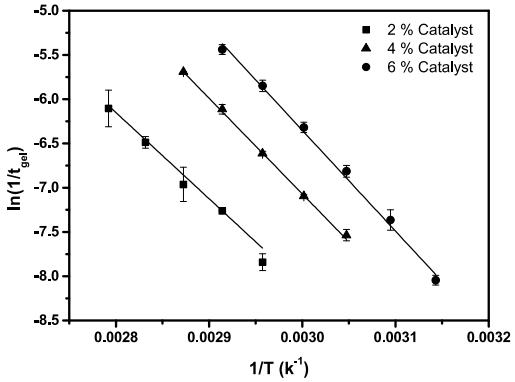

Fig. 2. Logarithm of the inverse of the gel time vs. inverse of the temperature for FA resins with the three amounts of catalyst, together with fitted model lines according to the Macosko model.

The Macosko model (Mussatti and Macosko, 1973), as described by Eq. (1), which relates the gel time to the temperature, was fitted to the results as shown in Figure 2.

$$1/t_{gel} = C \cdot \exp\left(-\Delta E_k / R \cdot T\right) \tag{1}$$

The activation energy of the process (E_k) together with the frequency factor (ln(C)) were obtained for the different amounts of catalyst. Both parameters consistently increased as the amount of catalyst was increased, as shown in Table 2.

Table 2. Calculated parameters of the Macosko model.

Amount of catalyst	Ln (C)	ΔE_k (kJ.mol^{-1})	R^2	σ
2 % wt.	21.1 ± 2.1	81.0 ± 5.9	0.984	1.058
4 % wt.	25.4 ± 0.2	90.0 ± 0.5	1.000	0.549
6 % wt.	27.8 ± 1.1	94.8 ± 2.9	0.995	1.133

In the case of the determined values of the activation energy, there is a clear difference when using the low 2 % wt. amount of catalyst (ΔE_k = 81 kJ.mol^{-1}) compared to the higher 4 and 6 % wt. amounts of catalyst (ΔE_k about 92 kJ.mol^{-1}). This same tendency was also found for the curing activation energies obtained by DSC by the Belichmeier method – also a single point method – in previous work by the authors (Domínguez and Madsen, 2011). The smaller difference found between 4 and 6 % wt. amounts of catalyst suggests that a maximum of the curing rate is approached. Altogether, as demonstrated by the quality of the fits shown in Figure 2, it is proven that the Macosko model is quite suitable to be used to predict the gel time of the FA resin at the temperatures commonly used in the manufacturing of FA resin composite materials (Domínguez and Madsen, 2013).

Once the dependence of the gel point of the FA resin on temperature for each of the used amounts of catalyst was determined, the evolution of the degree-of-cure during the post-gel stage was estimated by monitoring a rheological variable such as the complex modulus (G^*) using Equation (2).

$$\alpha(t) = \frac{\log(G^*(t)) - \log(G^*(t_{\alpha=0}))}{\log(G^*(t_{\alpha=1})) - \log(G^*(t_{\alpha=0}))} \quad (2)$$

This model is one of the different models proposed in the literature for the estimation of the degree-of-cure (Domínguez et al., 2010). The degree-of-cure is related to the increase in the logarithm of the complex modulus throughout the curing process, i.e. from the modulus measured for the uncured resin to the modulus measured for the fully cured resin. In the present study, if the FA resin was not fully cured at the end of the test, the complex modulus of the fully cured resin was estimated by Eq. (2) using the determined complex modulus at the gel-point ($G^*(t_{gel})$) and the previously determined degree-of-cure at the gel point ($\alpha(t_{gel})$) on 0.50 for the FA resin (Domínguez et al., 2012; Guigo et al., 2007). The complex modulus used to calculate the obtained degree-of-cure of the FA resin corresponds to a frequency of 1 Hz, which is the same frequency employed in the gel point determination. The evolution of the degree-of-cure of the FA resin is shown in Figure 3 for the three amounts of catalyst, and at a temperature of 65 ºC.

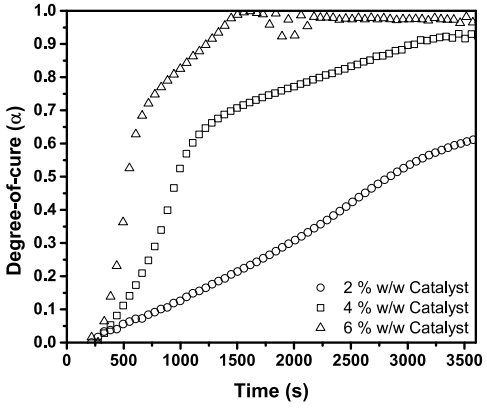

Fig. 3. Evolution of the degree-of cure of the FA resin at 65 ºC.

The degree-of-cure of the FA resin reached at the end of the performed experiments, i.e. after an hour of curing (3600 seconds, see Figure 3) under isothermal conditions, for each of the temperatures and amounts of catalyst is shown in Table 3. For those trials in which the resin has been fully cured, the average time required to reach final cure has also been determined.

Table 3. Reached degree-of-cure of the FA resin at different temperatures and amounts of catalyst.

Temperature [ºC]	Amounts of catalysts		
	2 % wt.	4 % wt.	6 % wt.
50	—	—	0.727 ± 0.020
55	—	0.710 ± 0.018	1.000 (3382 ± 160)*
60	—	0.832 ± 0.010	1.000 (2238 ± 168)*
65	0.661 ± 0.035	0.908 ± 0.030	1.000 (1478 ± 142)*
70	0.809 ± 0.068	1.000 (2243 ± 4)*	1.000 (950 ± 122)*
75	0.862 ± 0.012	1.000 (1586 ± 1)*	—
80	0.882 ± 0.023	—	—
85	0.972 ± 0.050	—	—

* Time (s) required to fully cure the FA resin.

All the obtained degree-of-cure profiles of the FA resin, as exemplified in Figure 3, show a marked change in the slope at a given time interval, and this is due to a change in the kinetics of the curing process. This change occurs once the FA resin exceeds the degree-of-cure at the gel point, which is determined in previous studies to be approximately 0.50 (Domínguez et al., 2012; Guigo et al., 2007), and this is in good agreement with the results shown in Figure 3. The observed reduction of the curing rate after the gel point is in agreement with previously results showing a tendency for the activation energy to be reduced in the proximity of the gel point (Domínguez et al., 2012). Thus, it is shown that in the case of FA resins, the study of curing kinetics must be split in two stages, pre-gel and post-gel, applying for each stage the most suitable models for the determination of the curing kinetic parameters.

The cure kinetics models applied to the complex viscosity measured beyond the gel point of the FA resin are the four- and six-parameter Arrhenius models, which are described by Equations (3) and (4), respectively:

$$\mathrm{Ln}\left(\eta^{*}(t)\right) = \mathrm{Ln}\left(\eta^{*}_{\infty}\right) + \frac{\Delta E_{\eta}}{R \cdot T} + t \cdot k_{\infty} \cdot \exp\left(\frac{-\Delta E_{k}}{R \cdot T}\right) \tag{3}$$

$$\mathrm{Ln}\left(\eta^{*}(t,T)\right) = \mathrm{Ln}\left(\eta^{*}_{\infty}\right) + \frac{\Delta E_{\eta}}{R \cdot T} + \frac{\phi}{n-1} \cdot \mathrm{Ln}\left(1 + (n-1) \cdot t \cdot k_{\infty} \cdot \exp\left(\frac{-\Delta E_{k}}{R \cdot T}\right)\right) \tag{4}$$

where η^{*} is the complex viscosity at absolute temperature T, η^{*}_{∞} is the reference viscosity at "infinite temperature", ΔE_{η} is the Arrhenius activation energy for viscosity, t is the curing time, R is the universal gas constant, k_{∞} is the kinetic constant analogue of η^{*}_{∞}, and ΔE_{k} is the kinetic activation energy analogue to ΔE_{η}, φ is a proportionality factor (φ) and n is the reaction order.

The curing parameters of the FA resin for its post-gel stage were calculated by applying a minimization algorithm of residual sum of squares (RSS) using Matlab. The obtained results for the Arrhenius four- and six-parameter models are shown in Table 4, together with the calculated total error (including all three replicates) of the model for all the temperatures tested.

Table 4. Determined values for the parameters of the four and six-parameter Arrhenius models.

Model	Catalyst	$-\Delta E_k$ (kJ/mol)	$\mathrm{Ln}(k_\infty)$	ϕ	n	MSE*
Arrhenius 4p.	2 %	—	—	—	—	—
	4 %	62.1	16.51	—	—	0.898
	6 %	58.9	15.95	—	—	0.695
Arrhenius 6p.	2 %	104.4	32.79	0.62	1.40	0.897
	4 %	79.9	23.96	0.88	1.27	0.180
	6 %	60.5	17.23	0.92	1.17	0.136

*Mean Square Error.

As expected, the Arrhenius four-parameter model cannot predict correctly the behavior of the complex viscosity of the FA resin since this model is only valid for linear increasing viscosity behavior. This is revealed by the high total error evaluated through the MSE values calculated for the 4 and 6 % wt. amounts of catalyst. In the case of the 2 % wt. amount of catalyst, the model was applied to the data but the curing parameters provided by the model were meaningless, and they are therefore not shown in Table 4. A clearly curved evolution of the

logarithm of the complex viscosity of the FA resin was found, as exhibited in Figure 4, and therefore a more sophisticated version of the Arrhenius model was required to obtain suitable predictions, namely the Arrhenius six-parameter model.

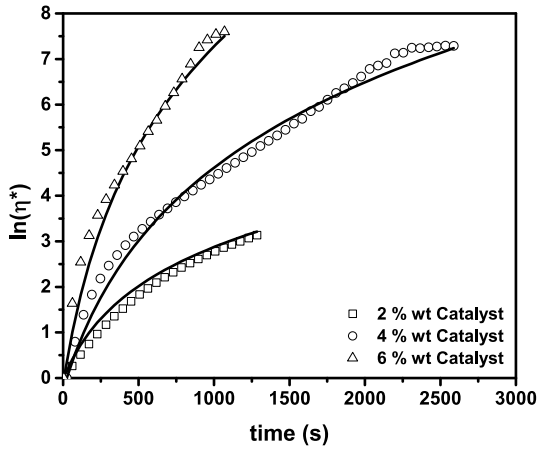

Fig. 4. Post-gel evolution of the logarithm of the complex viscosity of the FA resin at 65ºC. Experimental data (symbols) and model predictions by the Arrhenius six-parameter model (lines).

The Arrhenius six-parameter model can predict the behavior of the complex viscosity of the FA resin during the post-gel curing stage quite correctly, as shown in Figure 4. In particularly, good predictions are found for the 4 and 6 % wt. amounts of catalyst as shown by the low MSE values (Table 4). In contrast, the MSE value for the 2 % wt. amount of catalyst is higher, and close to the values obtained for the four-parameter model. This is expectedly due to the scattered values of the complex viscosity found for high temperatures (80-85 ºC) when a 2 % wt. amount of catalyst was used. These scattered values can be explained by the possible small gradients of the catalyst in the resin (i.e. non-perfect mixing), and the effect of these gradients becomes more significant at high temperatures, and thereby at high curing rates.

4. CONCLUSIONS

The following conclusions can be extracted from the present study:

- The gel time of a FA resin with different amounts of catalyst was measured at different temperatures by a rheological technique. The Macosko model was successfully applied to the experimental data. The model allows predicting gel times of the FA resin when using any of the tested amounts of catalyst, and within the range of the tested temperatures.

- The evolution of the degree-of-cure of the FA resin was estimated under isothermal conditions by a rheological analysis of its curing process, and by monitoring only rheological variables. Two curing stages were found, and they were clearly marked by the gelation of the resin, i.e. pre- and post-gel stages. This confirms the results found in a previous study of the curing process of the FA resin.

- The rheokinetic parameters of the FA resin curing process were calculated for two of the

three amounts of catalyst used, 4 and 6 % wt., by the Arrhenius six-parameter model, which was found to be the most suitable model. The modeling of the curing process when a 2 % wt. catalyst was used could not be conducted satisfactorily.

ACKNOWLEDGEMENTS

The authors are grateful for the support from "Ministerio de Educación" (Spanish Government) for financial support (Programa Nacional de Movilidad de Recursos Humanos del Plan Nacional de I-D+i 2008-2011). The research has been funded by the European Community's Seventh Framework Programme (FP7/2007-2013) under grant agreement nº 210037 (WOODY).

REFERENCES

Cadenato, A., Salla, J.M., Ramis, X., Morancho, J.M., Marroyo, L.M., Martn, J.L., (1997). Determination of gel and vitrification times of thermoset curing process by means of TMA, DMTA and DSC techniques TTT diagram. J. Therm. Anal. Calorim. 49, 1429-1433.

Domínguez, J.C., Alonso, M.V., Oliet, M., Rojo, E., Rodríguez, F., (2010). Kinetic study of a phenolic-novolac resin curing process by rheological and DSC analysis. Thermochim. Acta. 498, 39-44.

Domínguez, J.C., Grivel, J.C., Madsen, B., (2012). Study on the non-Isothermal curing Kinetics of a polyfurfuryl alcohol bioresin by DSC using different amounts of catalyst. Thermochim. Acta. 529, 29-35.

Domínguez, J.C., Madsen, B., (2011). Furolite 050915A resin. Curing behaviour and chemorheology. Un-published Report, (DTU, Roskilde).

Domínguez, J.C., Madsen, B., (2013). Optimization of the Operating Conditions Used to Produce New Biomass-Based Composite Materials by the Double-Vacuum Bag Technique. In Preparation.

Harran, D., Laudouard, A., (1985). Caractérisation de la gélification d'une résine thermodurcissable par méthode rhéologique. Rheol. Acta. 24, 596-602.

Martin, J.S., Laza, J.M., Morrás, M.L., Rodríguez, M., León, L.M., (2000). Study of the curing process of a vinyl ester resin by means of TSR and DMTA. Polymer. 41, 4203-4211.

Mussatti, F.G., Macosko, C.W., (1973). Rheology of network forming systems. Polym. Eng. Sci. 13, 236-240.

Tung, C.Y.M., Dynes, P.J., (1982). Relationship between viscoelastic properties and gelation in thermosetting systems. J. Appl. Polym. Sci. 27, 569-574.

Winter, H.H., (1987). Can the gel point of a cross-linking polymer be detected by the (G')-(G") crossover. Polym. Eng. Sci. 27, 1698-1702.

Proceedings of the 34th Risø International Symposium on Materials Science:
Processing of fibre composites – challenges for maximum materials performance
Editors: B. Madsen, H. Lilholt, Y. Kusano, S. Fæster and B. Ralph
Department of Wind Energy, Risø Campus
Technical University of Denmark, 2013

HIGH PERFORMANCE BASALT FIBRES: INVESTIGATION OF FIBRE PROPERTIES AND MODIFIED INTERPHASES IN EPOXY COMPOSITES

T. Förster*, J.W. Liu* and E. Mäder*,**

*Department of Composites, Leibniz-Institut für Polymerforschung Dresden e.V., Hohe Strasse 6, 01069 Dresden, Germany
** Institute of Materials Science, Technische Universität Dresden, Helmholtzstrasse 7, 01069 Dresden, Germany

ABSTRACT

The mechanical properties of basalt fibres were studied by single fibre tensile tests in the initial state and after heat treatment. The Young's modulus and tensile strength of basalt fibres are compared to those of glass and carbon fibres. The topic of fibre sizing is discussed adapted to fibre type and matrix compatibility. Furthermore, the strengthening effect due to tailored sizings and properties of basalt fibres after heat treatment are presented.

1. INTRODUCTION

Besides the size and design of rotor blades, growing interests in types of applied reinforcement fibres are in discussion driven predominantly by the efficiency of wind turbines. Attractive are high performance fibres having a moderate price level. Growing high technology fields, such as wind power and automotive manufacturing, have initiated new approaches in the development of fibreizable glass compositions as well as alternative yarns or fibre manufacturing technologies. Forming continuous fibres from basalt-like rock material belongs to the latter one and could be a potential substitute to glass fibres in the process chain of rotor blade manufacturing.

Basalt is a volcanic rock, which offers the possibility to manufacture reinforcement fibres analogously to glass fibre manufacturing by well-known melt spinning process. Basalt fibres are sometimes discussed as natural fibres due to their raw material sources. However, the quality of fibres strongly depends on the processing technology. According to Novitskii and Efremov (2011) two techniques are available: modular and multioperator technology, which differ in the size of the bath furnace and number of spinneret feeders. Nevertheless, fibreizing itself is a complex process, which is affected by multiple factors. Challenging research tasks exist in fields

of processing as well as fundamental works of tailored interphase design. Especially, the fibre design due to a wittingly raw material selection of basalt constituents becomes a key technology.

As early as 1963, Andreevskaya and Plisko (1963) investigated Young's modulus of model basalt fibres by frequency method. The experimentally determined values of 13-18 µm model basalt fibres were about 9230 kg/mm² (91 GPa). Subramanian and Austin reported values of moduli, varying between 78 to 90 GPa, measured by thin-line ultrasonics (Subramanian and Austin 1978; Subramanian and Austin 1980). The authors pointed out that the modulus of basalt fibres is higher than the obtained value of E-glass fibres. Today, basalt fibre manufacturer's data differ between 84 and 110 GPa. The density of basalt fibres is reported in the range of 2.6 to 2.8 g/cm³.

2. EXPERIMENTAL

Single fibre tensile tests were conducted under air-conditioning (temperature 23°C, rel. humidity 50 %) by using a Favigraph semi-automatic testing device (Textechno, Mönchengladbach, Germany) equipped with a 1 N load cell. The cross head velocity was 25 mm/minute and the gauge length was 50 mm. The fineness of each selected fibre was determined by using the vibroscope method in accordance with ASTM D 1577. 50 single fibres were tested for the determination of the average values. The density of fibres was not experimentally determined. Thus, 1.8 g/cm³ for carbon fibres, 2.5 g/cm³ for glass fibres and 2.8 g/cm³ for basalt fibres are taken as a basis for tensile tests (Fig. 1).

Heat treatment was managed by storing fibres in an oven (L5/11 Nabatherm) for 5h at 500°C and 600°C, respectively, in air.

Young's moduli of fibres at a strain range of 0.5-1.0 % were determined by single fibre tensile tests at different gauge lengths (20, 35, 50 and 80 mm). The results are influenced by the clamp equipment leading in a dependence of modulus on gauge length. Liu (2008) showed two different approaches to correct this effect. Generally, the influence of the clamps becomes less important with increasing gauge length. In this work, the Young's modulus was estimated by Equation (1).

$$E_m = E_f + \frac{C}{l_{fo}} \tag{1}$$

where E_m is the measured modulus value, E_f is the calculated modulus value, l_{fo} is the gauge length of fibre and C is a constant. C was determined by fitting Equation (1) in the plot of E_m against l_{fo}.

Unidirectional basalt fibre/epoxy composites were manufactured by filament winding and vacuum assisted resin infusion. The compression shear test (CST) was performed to characterize interphasial properties. A scheme of specimen loading is included in Fig. 4. Unidirectional basalt fibre/epoxy composites, specifically CST specimens, were tested before and after immersion for 72 h in boiling water. Basalt fibres used for manufacturing the composite are surface modified: sizing 1 and sizing 2 were applied during the fibrezing process. Basically, sizing 1 and sizing 2 are sizing formulations compatible for epoxy matrices. For the experimental study, the main formulation was retained; only the type of coupling agent was varied. Sizing 1 includes 3-glycidyloxypropyl-trimethoxysilane and sizing 2 N-Vinylbenzyl-N(2-aminoethyl)-3-aminopropylpolysiloxan (both supplied by Evonik).

Fibre content of BF/EP composites, namely sample sizing 1 and sizing 2, is 60 and 56 vol% respectively. The matrix system was based on an epoxy resin and hardener (Epikote RIMR135 and Epikure RIMH137, weight ratio 100:30, both Momentive).

3. RESULTS AND DISCUSSION

Fig. 1 shows the tensile strength as a function of strain of several glass, basalt and carbon fibres evaluated by single fibre tensile test. Glass fibre includes E-glass as well as advanced glass samples like S-glass, ECR-glass and AR-glass. Linear regression is added to point out the stress-strain proportionalities of basalt fibres compared to glass fibres. Investigated carbon fibres show high tensile strengths and small strain values. The measured tensile strength is about 4000 MPa and the measured modulus about 204 GPa. Basalt fibres compared to glass fibres reveal similar behaviour with exception of the S-glass sample. The measured tensile strength of S-glass[1] sample is 4600 MPa and the measured modulus 86 GPa.

Apart from that, the stress-strain proportionalities, as estimates for Young's modulus seem to be slightly advantageous comparing basalt and glass fibres. Table 1 summarizes measured moduli E* of investigated S-glass, E-glass and basalt fibre.

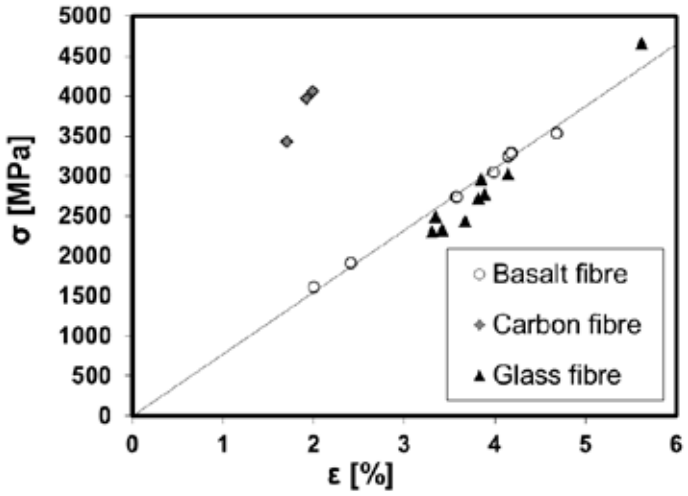

Fig. 1. Tensile strength-strain behaviour of carbon, glass and basalt fibres. Standard deviation of σ: 617 - 837 MPa (Carbon fibre); 227-740 MPa (Basalt fibre) and 147-528 MPa (Glass fibre). Standard deviation of ε: 0.29 -0.39 % (Carbon fibre); 0.34-0.96 % (Basalt fibre) and 0.22-0.80 % (Glass fibre).

[1] Specifically, S2-glass (AGY) was investigated.

Table 1. Young's moduli E* values determined in the strain range of 0.5-1.0 % (Gauge length: 50 mm; densities: 2.8 g/cm³ (Basalt), 2.5 g/cm³ (S-glass and E-glass)).

Fibre	Basalt	S-glass	E-glass
E* (0.5-1.0 % Strain) [GPa]	82 ± 1	86 ± 1	72 ± 1

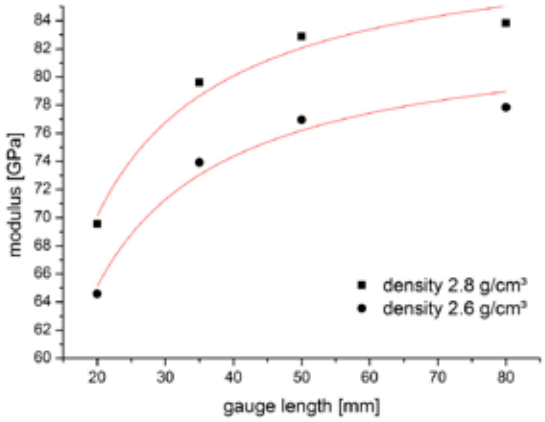

Fig. 2. Dependencies of determined tensile modulus of a basalt fibre sample on gauge length and fibre density (standard deviation: < 2 GPa).

Equation (1) was applied to calculate Young's modulus. Fig. 2 shows data points of a basalt fibre sample for different fibre densities. The calculated moduli are 84±1 GPa for 2.6 g/cm³ and 90±1 GPa for 2.8 g/cm³. In comparison, the calculated modulus of E-glass fibre is 76±1 GPa based on a density value[2] of 2.6 g/cm³. The experiments verify an advantage of basalt fibres compared to E-glass fibres in tensile modulus of about 10-16 %. However, knowledge of exact fibre densities is essential.

The protective effect of a sizing during the drawing process is significant. Fig. 3 shows mean tensile strength of unsized and sized basalt fibres. The tensile strength of unsized fibres is only about 1200 MPa. The unsized fibres were wetted by water, which was applied as sizing. The tensile strength of sized fibres is much higher. In Förster, Mäder and Heinrich the defect healing efficiency of sizing is discussed. In this work we showed that the coupling agent within a sizing offers potential to increase the fibre tensile strength, even surpassing a mean value of 3276 MPa.

Furthermore, Fig. 3 reveals the tensile strength after a heat treatment of 5 h and a temperature of 500°C. The absolute tensile strength value of the unsized fibres remains nearly unchanged. Moreover, enhanced temperature treatment due to a further increase of annealing temperature up to 600°C did not influence significantly the tensile strength.

[2] Density of E-glass fibres is reported in the range of 2.54 -2.67 g/cm³ by Wallenberger and Bingham (2010).

Heat treatment experiments were also performed with sized basalt fibres. However, after a heat treatment of 5h and a temperature of 600°C the fibre tensile strength could not be determined. Probably, the sizing supports sintering of filaments and the fibres are damaged during the preparation for a single fibre tensile test due to the separation of single filaments. A further thorough investigation of an extended temperature region as well as new and better suited sizing formulations is underway. A further challenging aspect is a second sizing application after heat treatment.

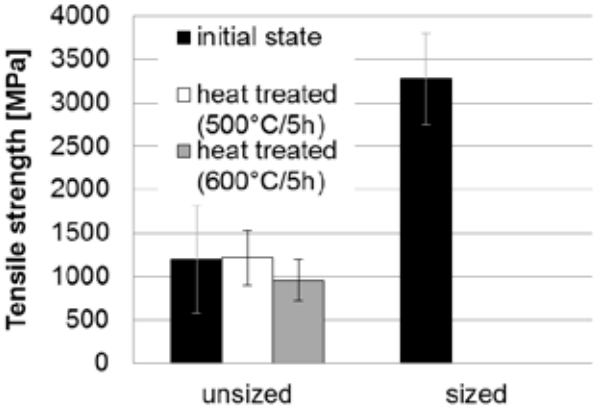

Fig. 3. Tensile strength (mean values) of unsized, sized and heat treated basalt fibres.

It is well known, modifying the interphase of composite materials is an appropriate method to increase the mechanical performance of composites. Surface modification of basalt fibres is a further key technology in the rather young basalt fibre manufacturing.

The composition of the surfaces of unsized and silanized basalt fibres were studied by XPS in previous work (Förster, Mäder, Jesson and Watts 2013) and pointed out that, in spite of the very complex chemical composition of basaltic glass fibres, the surface is dominated by silica and aluminium. Bonding is expected due to reaction of coupling agent and hydroxyl groups on basalt fibre surface. Coupling agents are an essential ingredient of sizings due to their ability to react or interact with fibre surface as well as with the polymeric matrix. Both investigated types of silanes are supported to be effective for epoxy matrices.

Fig. 4 compares the shear strength of investigated samples. Initial shear strength is 52 ±1 MPa (sizing 1) and 57 ±1 MPa (sizing 2). After 72 h immersion in boiling water the compression shear strength is significantly decreased. However, sizing 2 proved to be advantageous. It is supposed, that the nature/structure of coupling agent (e.g. aromatic or aliphatic silane, chain length) contributes to the improved performance.

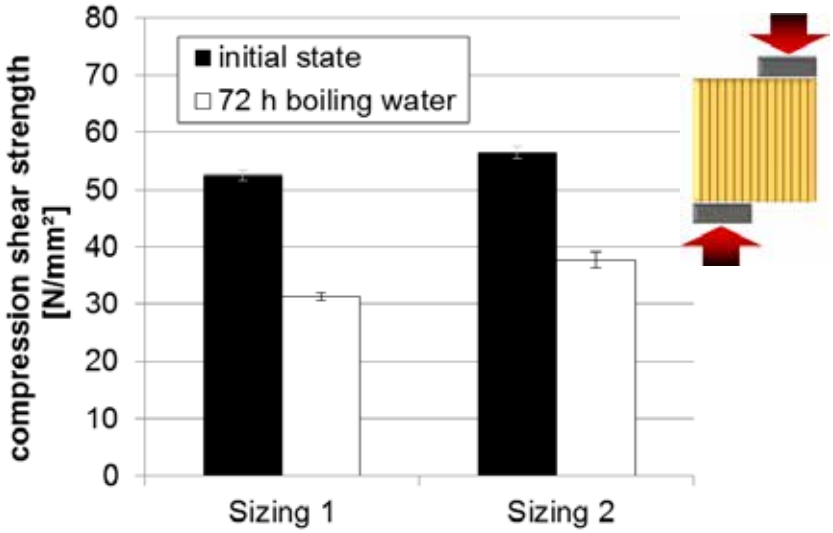

Fig. 4. Compression shear strength of unidirectional basalt fibre/epoxy composites before and after 72 h immersion time in boiling water.

4. CONCLUSIONS

In this study the potential of the new reinforcement fibres made out of basalt rocks is evaluated. The single fibre tensile test results show that the performance of basalt fibres is advantageous compared to E-glass fibres. Considering an increased Young's modulus of basalt fibres, a suited substitution of glass fibres by basalt fibres in rotor blade manufacturing might be envisaged. However, the determination of the Young's moduli requires both exact information about the basalt fibre density and exact experimental determination as well as suited tensile test conditions for single fibre tests.

Furthermore, besides the variation of the constituents of the basalt raw material the stress-strain behaviour of basalt fibres achieved different performance levels. Sizing and processing of basalt fibres seem to be key factors to exhaust the potential of basalt fibres. Surface and interphase modifications of basalt fibre are able to improve the fibre performance as well as composite performance.

ACKNOWLEDGEMENTS

The authors are indebted to Rosemarie Plonka, Janett Hiller, Tim Krülle, Karsten Scheibe for experimental assistance and helpful discussions.

The authors would like to express their thank to Keramikinstitut Meißen for excellent co-operation and to Bundesministerium für Wirtschaft und Technologie (BMWi) for funding within the project ZIM-KF 2022809 SU0.

REFERENCES

Andreevskaya, G.D and Plisko, T.A. (1963). Some physical properties of continuous basalt fibres. Glass and Ceramics, 20 (8). 418-420.

Förster, T, Mäder, E. and Heinrich, G. (submitted). Defect healing efficiency of sizings on surface flaws of glass and basalt fibres.

Förster, T, Mäder, E., Jesson, D. A. and Watts, J.F (2013). Surface analyses of basalt fibres: Tailoring the interphase of "green" fibre reinforced composites. 19th International Conference on Composite Materials (ICCM 19) Montreal, Canada

Liu J. (2008). Untersuchung von Verbundwerkstoffen mit Basalt- und PBO-Faser-Verstärkung. PhD Thesis, Technische Universität Dresden.

Novitskii, A. G. and Efremov, M. V. (2011). Some Aspects of the manufacturing process for obtaining continuous basalt fibre. Glass and Ceramics, 67 (11-12), 361-365.

Subramanian, R. V. and Austin H. F.(1978). Basalt Fibers In. Handbook of Fillers and Reinforcements for Plastics 1978. Eds. S. Katz and J.V. Milewski, (Van Nostrand Reinhol New York) 504.

Subramanian R.V. and Austin H. F. (1980). Silane coupling agents in basalt-reinforced polyester composites. International Journal of Adhesion and Adhesives, 1 (1), 50-54.

Wallenberger, F. and Bingham P. A. (2010) Fiberglass and Glass Technology: Energy-friendly Compositions and Applications (New York Dordrecht Heidelberg London).

Proceedings of the 34th Risø International Symposium on Materials Science:
Processing of fibre composites – challenges for maximum materials performance
Editors: B. Madsen, H. Lilholt, Y. Kusano, S. Fæster and B. Ralph
Department of Wind Energy, Risø Campus
Technical University of Denmark, 2013

MONITORING OF FIBRE LENGTH DEGRADATION DURING PROCESSING OF SHORT-FIBRE COMPOSITES BY USE OF X-RAY COMPUTED TOMOGRAPHY

E. K. Gamstedt[1], T. Joffre[1], A. Miettinen[2] and F. Berthold[3]

[1] Department of Engineering Sciences, Uppsala University, Box 534,
SE-751 21 Uppsala, Sweden
[2] Department of Physics, University of Jyväskylä, Box 35 (YFL),
FI-40014 Jyväskylä, Finland
[3] Innventia AB, Packaging Solutions, Box 5604,
SE-114 86 Stockholm, Sweden

ABSTRACT

The mechanical properties in the fibre direction of composites are mainly attributed to the fibre slenderness, or aspect ratio. Composites with long, slender and oriented fibres are more costly and difficult to manufacture than composites with short fibres. A trade-off between performance and processability is usually required, and dependent on the intended application. Injection-moulded short-fibre composites are used in high-volume applications, with short processing cycles and lesser demands on the load carrying capacity. However, if the mechanical properties could be improved, injection-moulded composites could be used in mechanically more demanding applications. Thus, if the fibre length could be retained or not severely degraded during various processing steps towards the injection-moulded component, a stiffer and stronger composite product could be obtained. In the case of short-fibre composites, wood fibres are gaining increased use due to their renewability, availability, low density and limited wear on processing tools, as compared with glass fibres. The processing steps for injection moulded wood-fibre composites include: 1. Pulping, 2. Commingling, 3. Extrusion, 4. Pelletizing, 5. Injection moulding. In order to tune the processing parameters systematically for retained fibre length, it would be useful to investigate the step-wise degradation of the original fibre length distribution throughout the processing chain, to focus on the unit that degrades the fibres the most. The development of X-ray micro-computed tomography and three-dimensional image analysis methods has given us an improved tool for quantifying the microstructure of small samples, such as fibre length distribution, without going through the tedious process of digesting the polymer matrix and measuring the length of individual fibres. In the present project, the fibre length degradation has been monitored through the processing steps in injection-moulded wood pulp-fibre reinforced polylactide. Significant fibre length degradation can be observed, which was also quantified by image analysis. In particular, the extrusion step was found to result in a significant fibre length reduction.

1. INTRODUCTION

Wood pulp fibres are readily available as a renewable reinforcement for composite materials. The fibre length (individual tracheid cell length) is about 4 mm for softwood fibres. With a diameter of about 25 μm, the relatively high aspect ratio makes these fibres interesting from a reinforcement perspective. The fibres are still sufficiently short to be used in melt processing of thermoplastic-matrix composites, and result in considerable less wear of tools and dies than e.g. short glass fibres. However, the fibres are still worn down to very small aspect ratios; sometimes even to particle size, with aspect ratios around two. With a particle-like geometry the wood fibres are acting as a filler rather than as a reinforcement. Strength could even be lower than that of the neat matrix if the cellulose fibre segments are too short. For sufficiently long fibre segments, i.e. a couple of times longer than the ineffective length of stress-build up at the end of an oriented embedded fibre, the desired reinforcement can be achieved. In a complicated melt processing procedure, there are several steps that individually contribute to the degradation of the initial fibre length, and hence also to the inferior mechanical properties. In this study, we focus on the manufacture of injection-moulded wood pulp-fibre reinforced polylactide, i.e. an entirely renewable and biodegradable composite material. The fibre length distribution is quantified step-by-step along the processing line. If the step which results in the most severe fibre degradation could be identified, measures could be taken to mitigate and treat the fibres more gently at this step to retain some if its slenderness. Of course, there is a balance between processability and mechanical performance, and some fibre length reduction must be acceptable in order to keep the high production rate of injection-moulded composite products leading to low manufacturing costs.

The quantification of fibre length distributions in composites has traditionally been done by chemically dissolving the matrix and studying a dilute fibre suspension with optical microscopy. The fibre length distribution can then be quantified either manually by measuring the fibre lengths one by one, or using two-dimensional image analysis software. The dissolution and optical microscopy procedures are direct, but rather time consuming. Fibre lengths in water suspensions could be more swiftly characterized by on-line systems where the projected dimensions of individual fibres are measured as they flow in a controlled manner, one by one, through a capillary tube. The Innventia FiberMaster (Karlsson and Fransson, 1994) and Kajaani Fiberlab (Cöpür and Makkonen, 2007) are examples of such equipment.

X-ray micro-computed tomography (XμCT) is a non-destructive method to assess the three-dimensional structure of a sample from two-dimensional X-ray projection images. After computational processing of the projection images, a three-dimensional array of X-ray attenuation coefficients is obtained. For many materials, especially non-diffractive ones, the attenuation coefficient correlates with local density of the material. The method essentially produces a density map of the sample, as visualised in Fig. 2a. Recent development of XμCT methods has conveyed the composite research community with a non-destructive technique capable of characterizing the geometry of fibres inside the composite material sample. With the aid of 3D image analysis, it is possible to quantify fibre length and orientation distributions from the reconstructed 3D images, as shown by Luengo Hendriks (2010) and Miettinen et al. (2012, 2013). Some interesting previous studies on this general topic include the work by Alemdar et al. (2009), who showed that XμCT can be used to quantify the dimensions of wood and flax fibre in polypropylene matrix. In that case the Image-Pro Plus software was used to indentify the Weibull parameters of the size distributions of the fibres.

2. EXPERIMENTAL PROCEDURES

Materials: The natural fibres used for making the composites are bleached sulphite wood fibre, which were laboratory cooked and bleached at Innventia AB. The matrix material is polylactic acid (PLA). PLA is thermoplastic aliphatic polyester manufactured from starch-rich renewable resources such as maize, sugar beets or wheat. For a biopolymer, PLA has decent physical and mechanical properties, making it a candidate for substitution of certain petrochemical thermoplastics. Due to the good adhesion to cellulose fibres, it has been proven to be suitable to use PLA as matrix material in pulp-fibre composites (Huda et al., 2006a and 2006b). The PLA fibres used here were PLA 01 quality delivered from Unitika (1.7 dtex, 1 mm length). In some cases the PLA fibres were first run through a pulp screen (Wennbergsil) and dried at room temperature in order to facilitate filament release.

Manufacturing: Commingled wood fibre/PLA mats were manufactured using a laboratory scale dynamic sheet former. The polymer and wood fibres were evenly distributed, preventing the fibres aggregating to larger bundles. The extrusion experiments were run on a 40 mm co-rotating twin screw extruder, Werner & Pfleiderer ZSK40. The material was run through the extruder either once or twice (see Fig. 1). In order to quantify the fibre length degradation it might be interesting to run the same process several times. Moreover, the pellets obtained after two extrusions were less rough and thus easier to process (see Fig. 1). After extrusion the extrudates were cooled in water and led to a chopper to produce pellets. After pelletizing the material was dried in an oven at 50°C for several hours. Extrudates were also broken into smaller bits using a hammer mill. The amount of PLA in produced material was kept constant at 70 wt%. After drying the pellets were fed into an injection moulding machine equipped with a multiple die containing profiles for dogbone shaped specimens. At each step of the process, samples have been taken off for XμCT.

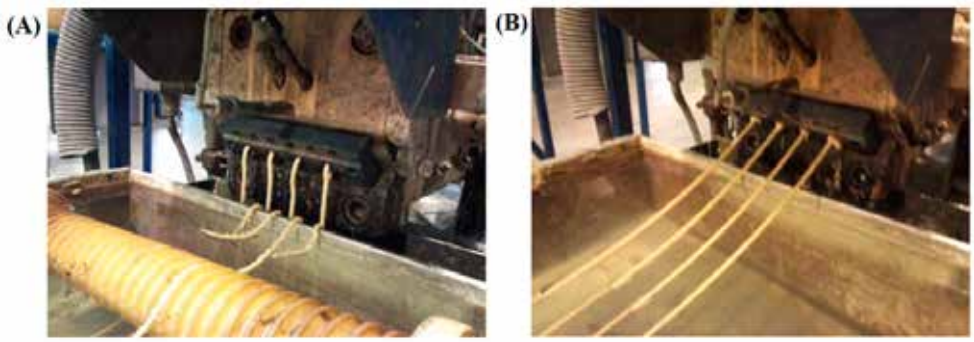

Fig. 1. Extrudates as they leave the extruder, after (A) one pass, and (B) after two passes through the extruder. Note that the apparent quality of the extrudates is improved after a second pass. The improved processability is at the cost of shortened fibre length.

X-ray micro-computed tomography: To prepare the composite samples for the XμCT imaging, a rotary tool was used to carve the sample into a cylinder with radius of approximately 1 mm. The cylinder was then glued to the top of a carbon fibre tube that serves as a sample holder. To scan pulp fibres and commingled fibres, no specific sample preparation was needed; a bundle of fibres was simply glued on top of a glass tube acting as a sample holder. The XμCT imaging was done using Xradia microCT-400 tomograph with approximately 1 μm resolution. The results are visualized in Fig. 2a.

Image analysis: To separate the fibres from the matrix in the three dimensional images, a variance weighted mean filter was first applied in order to attenuate noise in the images. The images were then thresholded. Objects having volume smaller than 5000 voxels were considered as noise and removed. The result of these operations is presented in Fig. 2b. The length of the fibres was measured using path opening method with flexible line segments as structuring elements. This method, described by Luengo Hendriks (2010) and Miettinen et al. (2012), is suitable to detecting and measuring lengths of lines that are not perfectly straight and is thus used here to measure the fibre length distribution. The method can also be used for other purposes such as fibre orientation distribution and thickness measurement (see e.g. Chinga-Carrasco et al., 2011).

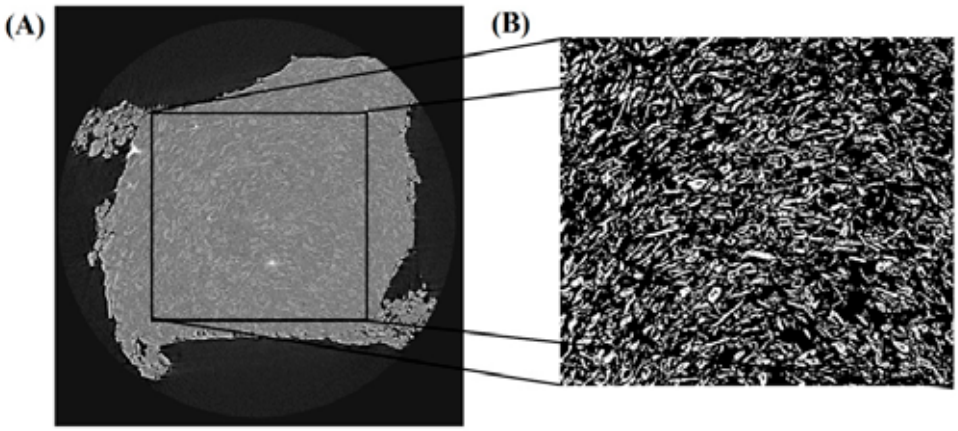

Fig. 2. Visualisation of a slice of the three dimensional images, (A) just after reconstruction, and (B) after image segmentation. Width of the image is approximately 1 mm.

3. RESULTS AND DISCUSSION

Softwood tracheids have a native length of up to 4 mm (e.g. Bardage, 2001). These fibres are inevitably shortened during each of the following processing steps towards the wood-fibre composite. The wood is chipped, pulped, commingled with the thermoplastic fibres, extruded once or twice, pelletized, and finally injection moulded to form a fibre-composite component. There are examples of the final wood segments acting as particles in the composite material, rather than the desired elongated reinforcing units. The fibre length has then been shortened two orders of magnitude, which certainly have negative implications on the mechanical properties. Oksman et al. (2009) investigated the fibre length degradation and concomitant tensile properties of injection-moulded composites based on a number of different types of natural fibres in polypropylene matrix. The fibre fragmentation was dependent on the species of natural fibres. Some natural fibres are more brittle and likely to break during processes than others.

In Fig. 3, images of wood pulp fibres are shown before and after composite manufacture. Although the fibres have become shorter in the pulping process, compared with the green state, the significant length degradation arises somewhere during the course of the composite manufacturing process. With the image analysis methods described above, it is possible to quantify the length distribution at different process stages.

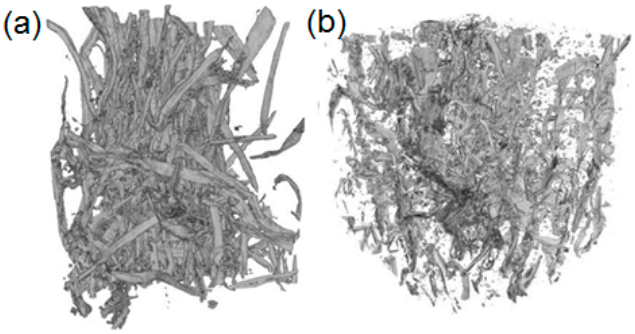

Fig. 3. Visualisation of XμCT images of (a) a dry and unimpregnated bundle of pulp fibres, and (b) pulp fibres in a composite sample. The width of the structure is approximately 1 mm in both figures.

It can be noticed in Fig. 4(a) that the fibre length distribution is already significantly shifted to short segments in comparison to what is expected for mildly pulped fibres. This length degradation is further worsened after the injection moulding step, as shown in Fig. 4(b). The average fibre lengths was found to be 300 μm for the once extruded material, 150 μm for the twice extruded material, and finally 160 μm for the injection moulded material. Consequently, it can be concluded that the second extrusion step, as shown in Fig. 1(B), significantly reduced the fibre length, although the appearance and processing properties are improved. The effect of the second extrusion is about the same as the final injection moulding step. The obtained values are in the same order and show similar trends as those obtained by Nyström et al. (2007) for chemothermomechanical pulps in injection-moulded polypropylene-matrix composites. Our lower values can be attributed to the resulting embrittlement in the sulphite cooking process, as compared to kraft or thermomechanical pulps.

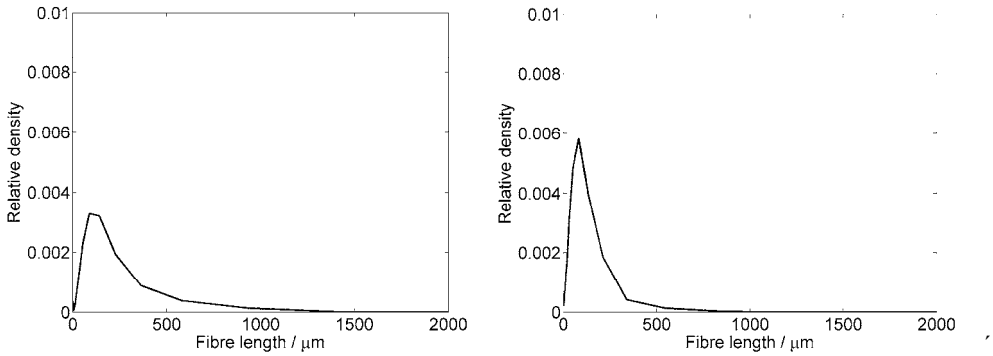

Fig. 4. Fibre length distributions after (a) extrusion, and after (b) extrusion and injection moulding.

Nyström (2007) have reported a rather comprehensive study in her thesis on the effects of the processing parameters on the strength of natural fibre composites. She found that the extrusion speed at the compounding stage, and the injection speed and temperature at the injection-moudling stage had the highest impact on the tensile properties, which is controlled by the fibre

aspect ratio for natural-fibre composites with rather weak interfacial coupling, such as the case of polypropylene matrix systems.

4. CONCLUSIONS

It was possible to use X-ray microtomography to assess the microstructure of wood fibre composite. A first result of this study is that the fibres are highly damaged during the manufacturing process of wood fibre composite. The fibre length distribution was characterized at various processing steps of injection-moulded wood-pulp reinforced PLA composites, and will be comprehensively presented in a forthcoming publication. At the current stage, it can concluded that the extrusion step severely reduces the fibre lengths, impairing the mechanical properties. XμCT has been shown as a relatively convenient method to quantify the internal fibre length distribution of cellulose fibre composites in a non-destructive manner.

ACKNOWLEDGEMENTS

The authors wish to thank Formas and the WoodWisdom-NET project 'WoodFibre3D' for financial support. The project was coordinated by Bjørn Steinar Tanem (SINTEF Materials and Chemistry).

REFERENCES

Bardage, S.L. (2001). Three-dimensional modeling and visualization of whole Norway spruce latewood tracheids. J Wood Fib. Sci. 33, .627-638.

Alemdar, A., Zhang, H., Sain, M., Cescutti, G. and Müssig, J. (2008). Determination of fiber size distributions of injection moulded polypropylene/natural fibers using X-ray microtomography. Adv. Eng. Mater. 10, 126-130.

Chinga-Carrasco, G., Miettinen, A., Luengo Hendriks, C.L., Gamstedt, E.K., and Kataja, M. (2011). Structural characterisation of kraft pulp fibres and their nanofibrillated materials for biodegradable composite applications. In: Nanocomposites and Polymers with Analytical Methods, Cuppoletti, J. (Ed.), InTech Open Access Publisher, 18 p.

Cöpür, Y., and Makkonen, H. (2007). Precision and accuracy studies with Kajaani fiber length analyzers. J Appl. Sci. 7, 1043-1047.

Huda, M.S., Drzal, L.T., Misra, M., and Mohanty, A.K. (2006a). Wood fiber reinforced poly (lactic acid) composites: Evaluation of the physicomechanical and morphological properties. J. Appl. Polym. Sci. 102, 4856-4869.

Huda, M.S., Drzal, L.T., Mohanty, A.K., and Misra M. (2006b). Chopped glass and recycled newspaper as reinforcement fibers in injection molded poly (lactic acid) (PLA) composites: A comparative study. Comp. Sci. Technol. 66, 1813-1824.

Karlsson, H., Fransson, P.I. (1994). STFI Fibermaster gives papermakers new muscle - New knowledge concerning fiber shape can be the key to paper of the future. Svensk Papperstidning, 97, 26-28.

Luengo Hendriks, C.L. (2010). Constrained and dimensionality-independent path openings. IEEE Trans. Image Process. 19, 1587-1595.

Miettinen, A., Luengo Hendriks, C., Chinga-Carrasco, G., Gamstedt, E.K,. and Kataja, M. (2012). A non-destructive X-ray microtomography approach for measuring fibre length in short-fibre composites. Compos. Sci. Technol. 72, 1901-1908.

Miettinen, A., Joffe, R., Madsen, B., Nättinen, K., and Kataja, M. (2013). Quantitative analysis of length-diameter distribution and cross-sectional properties of fibres from three-dimensional tomographic images. Proceedings of 34th Risø International Symposium on

Materials Science.
Nyström, B. (2007). Natural Fiber Composites: Optimization of Microstructure and Processing Parameters. Licentiate Thesis, Department of Applied Physics and Mechanical Engineering, Luleå University of Technology.
Nyström, B., Joffe, R., and Långström, R., (2007). Microstructure and strength of injection molded natural fiber composites. J. Reinf. Plast. Comp. 26, 579-599.
Oksman, K., Mathew, A.P., Långström, R., Nyström, B., and Joseph, K. (2009). The influence of fibre microstructure on fibre breakage and mechanical properties of natural fibre reinforced polypropylene. Compos. Sci. Technol. 69, 1847-1853.

Proceedings of the 34th Risø International Symposium on Materials Science:
Processing of fibre composites – challenges for maximum materials performance
Editors: B. Madsen, H. Lilholt, Y. Kusano, S. Fæster and B. Ralph
Department of Wind Energy, Risø Campus
Technical University of Denmark, 2013

EFFECT OF PROCESSING ON FRACTURE OF BINDERFREE ALL-CELLULOSE COMPOSITES

S. Goutianos[1], R. Arévalo[2], B.F. Sørensen[1] and T. Peijs[2]

[1]Department of Wind Energy, Section of Composites and Materials Mechanics, Technical University of Denmark, Risø Campus, DK-4000 Roskilde, Denmark
[2]Queen Mary, University of London, Centre of Materials Research, School of Engineering and Materials Science, Mile End Road, E1 4NS London, UK

ABSTRACT

Binderfree all-cellulose composites were prepared by a mechanical refinement process that allows the formation of intramolecular hydrogen bonds between the cellulose molecules during the drying process. The extent of this hydrogen bond network strongly depends on the duration of the refinement process. The fracture properties are studied at five different refining times. Due to the non-linear mechanical response of the binderfree all-cellulose composites, a method is first developed to obtain the fracture properties (fracture resistance and mode I cohesive law). The method uses a Double Cantilever Beam (DCB) sandwich specimen loaded with pure bending moments and it is based on the J integral. It is found that an increase of the refining times results a) in an increase of the crack initiation fracture energy and in a decrease of the steady-state fracture energy, and b) in an increase of the mode I peak cohesive traction.

1. INTRODUCTION

Natural fibre reinforced composites are attractive due to environmental and economical reasons. Thus, extensive research has been carried out over the last decades to improve their mechanical properties (Heijenrath and Peijs 1996; Van de Weyenberg, Ivens, De Coster, Kino, Baetens and Verpoest 2003). The attractiveness of natural fibres as an alternative reinforcement comes from their relatively high specific properties (Singleton, Baillie, Beaumont and Peijs 2005) and their eco-friendly performance when compared to traditional fibres such as glass fibres (Bos and Donald 1999).

Since natural fibres are based on renewable resources, the eco-performance of natural fibre composites is mainly controlled by the polymer matrix (Shen and Patel 2008). In waste management, one of the most favourite end-of-life options is recycling, which is limited in

natural fibre composites even if recyclable polymers such as polypropylene are used (Peijs 2003). If natural fibres are combined with a biodegradable matrix, such as polyhydroxybutyrate (PHB), polylactic acid (PLA) and starch, an additional disposal option becomes available through composting.

To address the environmental impact of the polymer matrix, self-reinforced fully recyclable cellulose composites, in which both the fibre and the matrix are composed of the same material have been developed in recent years (Nishino, Matsuda, and Hirao 2004; Gindl and Keckes 2005; Soykeabkaew, Nishino and Peijs 2009). These developments were based on the concept of all-polymer composites such as all-polypropylene composites (Ward and Hine 1997; Cabrera, Alcock, Loos and Peijs 2004). In all-polymer composites, both the fibre and the matrix are chemically identical resulting in excellent interfacial compatibility. Moreover, as these are mono-materials, fully recyclable and environmentally friendly materials with good mechanical properties can be obtained.

Two different approaches have been developed to manufacture all-cellulose composites: a) conventional impregnation methods of cellulose matrix into cellulose fibres (Nishino, Matsuda, and Hirao 2004; Grunert and Winter 2002) and b) selective dissolution methods where the skin of cellulose fibre is partially dissolved to form the matrix phase that bonds the fibres together (Nishino and Arimoto 2007). However, in both approaches, non-environmentally friendly solvents are used.

An alternative approach to create strong all-cellulose materials is to explore the potential of intramolecular bonding between cellulose molecules as in paper materials. In these processes the intrinsic bonding capability between cellulose fibres is used to enhance the Van der Waals or hydrogen bonded network. The key aspect to obtain materials with high mechanical properties is to increase the intramolecular-bonding network, which is achieved by increasing the specific-surface area of the fibres. A promising way to increase the cellulose network density is through the use of nanocelluloses (Berglund and Peijs 2010). However, nanofibres are often very costly. Thus, a different method was developed by Zellform GmbH, which involves the mechanical refinement of raw cellulose material (such as plant fibers or waste paper) into a sub-microfiber pulp having an increased degree of intramolecular bonding between the fibrils, which after drying and compaction in a hot-press results in a binderfree all-cellulose composite.

The mechanical properties of these composite products were found to outperform many conventional natural fibre composites in terms of stiffness and strength. These mechanical properties were found to increase with increasing the fibre refinement, due to the increase in network density (Arévalo, Achilli and Peijs 2013). In the present work, the fracture properties of these materials are examined as a function of the refinement time. The focus is to a) measure the fracture resistance / cohesive laws and b) observe the failure mechanisms during crack growth. Crack growth in cellulose networks can be complicated by the occurrence of crack bridging during crack growth and it resembles the fracture of paper (Isaksson and Hägglund 2007).

Such a toughening mechanism gives rise to fracture resistance with crack extension (R-curve behaviour) (Suo, Bao and Fan 1992) and therefore the fracture of these materials should not in general be characterised in terms of Linear Elastic Fracture Mechanics (LEFM). Instead, the fracture process zone can be modeled by non-linear fracture mechanics. The analysis followed is based on the J integral approach (Rice 1968) and a Double Cantilever Beam (DCB) sandwich specimen loaded with pure bending moments is used. Usually, in fracture mechanics analysis, the material outside the fracture process zone is assumed to be elastic. However, all-cellulose composites have a non-linear response and therefore it is necessary to take account of this non-linearity when calculating the fracture resistance. Thus, a general J integral based testing

approach, inspired by the work of Thouless, Kafkalidis, Ward and Bankowski (1997) who used the I integral, is first developed to obtain fracture resistance from the DCB experiments. It should be noted that the use of the J integral for materials having non-linear stress-strain relationship is allowed as long as there is no unloading of any material point so that the non-linear stress-strain behaviour can be considered as being a non-linear elastic material.

2. BASIC MECHANICS

The fracture properties are determined by the use of the DCB sandwich specimen shown in Fig. 1. It consists of the all-cellulose composite glued inside the grooves of two steel beams that are mounted on a special fixture (described in Section 3), which applies pure bending moments (Sørensen, Horsewell, Jøgensen, Kumar and Engbæk 1998). The fracture resistance can be calculated by evaluating the path independent J integral along a path over the external boundaries of the specimen.

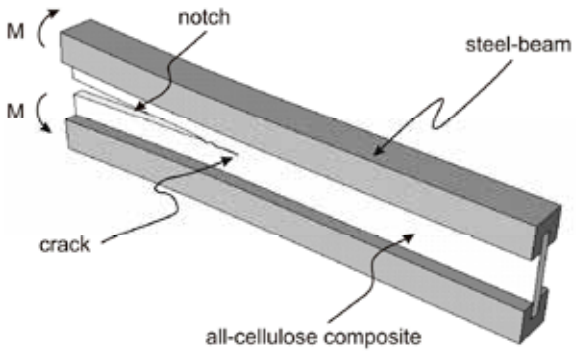

Fig. 1. Double Cantilever Beam (DCB) sandwich specimen loaded with pure bending moments.

To evaluate the two dimensional J integral, the non-uniform cross-section of the specimen (Fig.1) has to be transformed to an approximate equivalent cross-section of uniform width, B (the width of the steel beams). This can be achieved if the Young's modulus of the all-cellulose composite, E_2, is modified according to (Goutianos, Arévalo, Sørensen and Peijs 2013):

$$\mathrm{E}_2^* = \eta\left(1 + \mathrm{I}_o + \frac{\mathrm{I}_o}{\Sigma}\right)\mathrm{E}_2 \tag{1}$$

where $\Sigma = \mathrm{E}_2 / \mathrm{E}_1$ with E_1 the Young's modulus of the steel beams, $\eta = b/B$ with b the width of the all-cellulose composite, and I_o a non-dimensional constant given by:

$$\mathrm{I}_o = \frac{\rho - \rho^2 + \rho^3/3 - 2\rho\Delta + \rho^2\Delta + \rho\Delta^2}{\xi^3/3 + \xi^2 + \xi - \xi\Delta^2 - 2\xi\Delta + \xi\Delta^2} \tag{2}$$

where $\xi = h/H$ with $2h$ the height of the all-cellulose composite and H the height of the steel beam, $\rho = t/H$ with t the depth of the groove (Fig. 1), and Δ the normalised position of the neutral axis.

The modified cross-section allows an evaluation by the two dimensional J integral along a path along the external boundaries of the specimen as shown in Fig. 2.

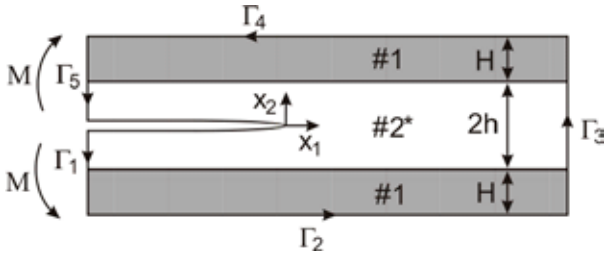

Fig. 2. Two-dimensional specimen representation and J integral path along the external boundaries.

The uni-axial tensile behaviour of the all-cellulose composites was found to be described by (Goutianos et al. 2013):

$$\sigma_{11} = \alpha_1 \varepsilon_{11} + \alpha_2 \varepsilon_{11}^2 \tag{3}$$

where α_1 is approximately equal to the Young's modulus of the all-cellulose composite. Eq. 3 is scaled according to Eq. 1. Then, the J integral solution for the sandwich specimen of Fig. 2 is given by (Goutianos et al. 2013):

$$J = -\frac{E_1 \hat{\varepsilon}^2}{\eta \Delta^2}\left(-\Delta^2 H + \Delta H^2 - \frac{H^3}{3}\right) - \frac{\alpha_1 \hat{\varepsilon}^2}{\eta \Delta^2}\left(-\frac{h^3}{3} - h^2(\Delta - H - h) - h(\Delta - H - h)^2\right) -$$

$$-\frac{4\alpha_2 \hat{\varepsilon}^3}{3\eta \Delta^3}\left(-\frac{h^4}{4} - h^3(\Delta - H - h) - \frac{3h^2}{2}(\Delta - H - h)^2 - h(\Delta - H - h)^3\right) \tag{4}$$

where $\hat{\varepsilon}$ is a function of the applied moment M. Since the J integral I is path independent, the local J integral surrounding the fracture process zone is equal to the J integral from Eq. 4, and thus the mode I cohesive law is given by (Sørensen and Jacobsen 2009):

$$\sigma = \frac{dJ_{loc}}{d\delta^*} \tag{5}$$

3. EXPERIMENTAL

3.1 Materials and Processing. The binderfree all-cellulose composites were based on flax fibres, with the process described in detail in Arévalo et al. (2013). The process involves a refining treatment stage where the flax fibres are cut and fibrillated in a highly dilute water suspension (2% cellulose). This suspension was subsequently filtered and dewatered to partially remove the water and to obtain the desired consistency for the subsequent compaction and drying steps. This fibre pulp was subjected to a room temperature pressing operation (10 bar) where further removal of water took place (~50% water content). This precursor was then finally dried in a hot-press where the application of pressure (40-80 bar) in combination with moderate heat (140^{o}C) allowed the complete removal of all retained water, leading to well compacted flat

panels. An increase in refining time results in all-cellulose composites with improved mechanical properties in terms of Young's modulus and strength. In the present work, 5 different refining times were chosen. Representative SEM micrograpahs of the prepared specimens (before fracture) are shown in Fig. 3. An increase of the refining time results in an increased fibre fibrillation e.g. the number of fibrils increases and their size (length and cross section) decreases.

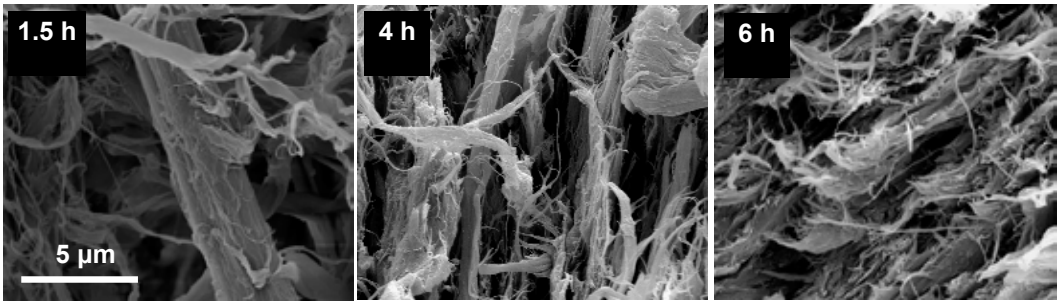

Fig. 3. SEM micrographs of the binderfree all-cellulose composites with a refining time of 1.5h, 4h, and 6h, respectively.

3.2 Specimen geometry. Rectangular specimens with a central notch along the biggest dimension were cut from all cellulose composite plates at dimensions approximately 10 mm x 65 mm x b mm. The width b varied from 1.2 to 2 mm depending on the refining time. The notch length (Fig. 1) was 25 mm and the height was approximately 1 mm. Further, a sharp crack was sawed manually at the root of the notch with a root radius less than 1.5 µm. The all-cellulose composite were then placed inside the grooves of two steel beams and glued using a two-part epoxy adhesive (Scotch-WeldTM DP460 from 3M).

3.3 Loading arrangement and instrumentation. The pure bending moments are applied to the DCB specimen using a special fixture (Sørensen et al. 1998), which can be operated inside the chamber of an environmental scanning electron microscope (ESEM) for in situ observation of the crack growth. In an ESEM the specimens need not be coated with conductive layers as in a conventional SEM where the new surfaces created by crack growth "charge up" and cannot be observed in detail. All the tests were conducted at room temperature and at a vapour pressure of 50 Pa. The fixture was mounted on the XY Z stage of the microscope (Zeiss Evo 60 EP-SEM) and thus by translating the stage in the specimen plane (XY) the crack growth increments could be measured.

3.4 Loading procedure. The DCB specimens were subjected to a monotonically increasing loading inside the ESEM. Images of the initial crack tip were recorded at different applied moments. As the moment increases, the end-opening of the crack tip increases. These openings represent the opening of the crack tip fracture process zone. At a certain moment, crack growth takes place. The moment was further increased and the images were recorded to measure the end-opening. These openings describe the bridging zone. The loading was stopped, when the steady-state fracture resistance was reached.

4. RESULTS

Representative fracture resistance curves as a function of the end-opening are shown in Fig. 4. The fracture resistance increases from a relatively low value, corresponding to failure process

zone at the crack tip, to a steady-state level, as the bridging zone evolves. The fracture resistance steady-state value decreases with increasing the refining time. The end-opening at which the steady-state is attained is almost independent of the refining time. The initial slope of the fracture resistance curves, up to end-openings less than 5 μm, describe the crack tip fracture process zone. The steeper slope is observed for a refining time of 6h and decreases with decreasing the refining time. The enhanced fibrillation at 6h results in a more extensive hydrogen-bonded network between the fibrils. Such a strong network structure would result in a higher fracture resistance for crack initiation (steeper initial slope in Fig. 4). For end-openings larger than approximately 5 μm, the fracture resistance curves describe the bridging failure mechanism which is controlled by the length of the fibres and the adhesion between them, i.e. short fibres (6h refining time) are less effective in bridging the crack faces and therefore the increase in fracture resistance is less pronounced.

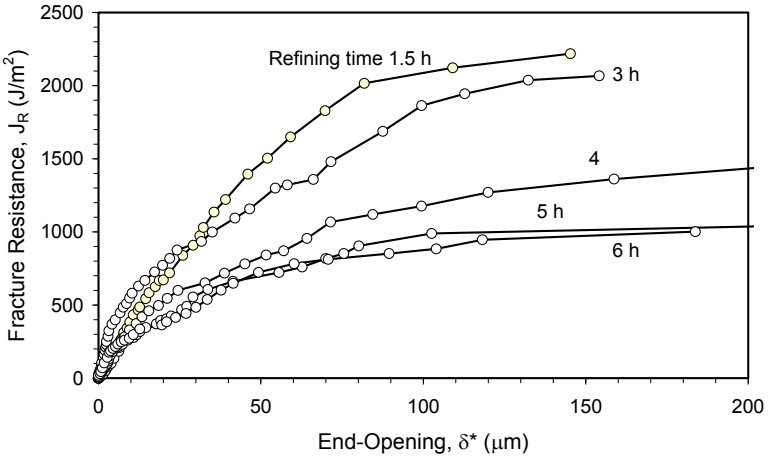

Fig. 4. Effect of the refining time on the fracture resistance, J_R.

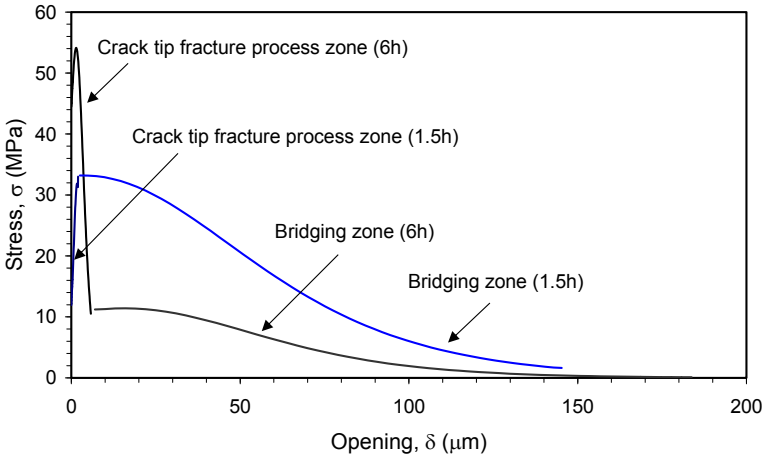

Fig. 5. Examples of cohesive laws for refining times 1.5h and 6h, respectively.

In order to obtain the cohesive laws from the fracture resistance curves of Fig. 4, the experimental data are first fitted with a non-linear function and the differentiated with respect to the end-opening (Goutianos et al. 2013). For each curve the experimental data are split in two parts. The fist part corresponds to the opening of the crack tip fracture process zone, and the second part to the bridging zone. The transition point is determined from observations during the in-situ experiments. The representative cohesive laws for 1.5h and 6h are given in Fig. 5. The peak cohesive stress is significantly higher for 6h refining time than 1.5h. However, the traction in the bridging zone is higher for the shorter refining time (1.5h).

Fig. 6 shows as an example of the observations made by performing the experiments inside the chamber of the ESEM. In Fig. 6 extensive fibre bridging can be seen for binderfree all-cellulose composites with a refining time of 1.5h because the flax fibres are larger in size (length and diameter). Such large fibres can effectively bridge the crack faces even for large crack openings. This can explain the higher steady-state fracture resistance (see Fig. 4) and higher cohesive tractions in the bridging zone (Fig. 5).

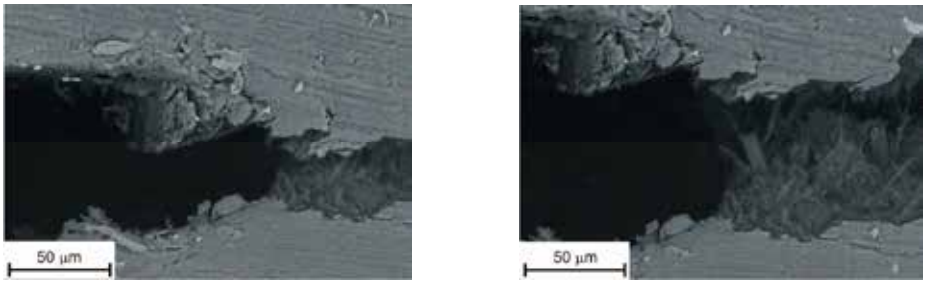

(a) (b)

Fig. 6. Backscatter electron micrographs showing the end-opening of the fracture process zone at increasing applied moment for 1.5 h refining treatment.

5. CONCLUSIONS

The fracture properties of binderfree all-cellulose composites with different levels of fibre fibrillation were studied. A general J integral based method for mode I fracture mechanics characterisation taking account of the non-linear response of the all-cellulose composites was developed using DCB sandwich specimens loaded with pure bending moments. The experiments were performed inside an environmental scanning electron microscope to observe the failure mechanisms, determine the crack initiation, and measure the crack length. It was found that:

a) The fracture resistance for crack initiation and peak cohesive stress both increase with increasing fibre fibrillation. This is due to the presence of a stronger Van der Waals or hydrogen bonded network structure in all-cellulose composites with higher refining time.
b) The steady-state fracture resistance decreases with increasing fibre fibrillation. An increase in refining time results not only in a reduction in fibre diameter but also in shorter fibres and thus in a lower fracture resistance with increasing refining times.

ACKNOWLEDGEMENTS

The authors wish to thank Ove Rasmussen (Department of Physics, DTU) for assistance with specimen preparation. RA was supported by the Technology Strategy Board (TSB) funded REFLECT project. BFS was supported by DCCSM, Grant No. 09-067212 from the Danish

Council for Strategic Research.

REFERENCES

Arévalo, R., Achilli, L, and Peijs, T. (2013). Binderfree all-cellulose composites. In preparation.

Berglund, L. A. and Peijs, T. (2010). Cellulose biocomposites - from bulk moldings to nanostructured systems. MRS Bulletin 35, 201–207.

Bos, H. L. and Donald, A. M. (1999). In situ ESEM study of the deformation of elementary flax fibres. Journals of Materials Science 34, 3029-3034.

Cabrera, N., Alcock, B., Loos, J., and Peijs, T. (2004). Processing of all-polypropylene composites for ultimate recyclability, Proceedings of the Institution of Mechanical Engineers, Part L: Journal of Materials: Design and Applications 218, 145–155.

Gindl, W., and Keckes, J. (2005). All-cellulose nanocomposite, Polymer 46, 10221–10225.

Goutianos, S., Arévalo, R., Sørensen, B. F., and Peijs, T. (2013) Effect of processing conditions on fracture resistance and cohesive Laws of binderfree all-cellulose composites. In preparation.

Grunert, M. and Winter, W. T. (2002). Nanocomposites of cellulose acetate butyrate reinforced with cellulose nanocrystals, Journal of Polymers and the Environment 10, 27–30.

Heijenrath, R. and Peijs, T. (1996). Natural-fibre-mat-reinforced thermoplastic composites based on flax fibres and polypropylene. Advanced Composites Letters 5, 81-85.

Isaksson, P., and Hägglund, R. (2007). Evolution of bond fractures in a randomly distributed fiber network. International Journal of Solids and Structure 44, 6135–6147.

Nishino, T., Matsuda, I., and Hirao, K. (2004). All-cellulose composite. Macromolecules 37, 7683–7687.

Nishino, T. and Arimoto, N. (2007). All-cellulose composite prepared by selective dissolving of fiber surface. Biomacromolecules 8, 2712–2716.

Peijs, T. (2003). Composites for recyclability. Materials Today 6, 30-35.

Rice, J. R. (1968). A path independent integral and the approximate analysis of strain concentrations by notches and cracks, Journal of Applied Mechanics 35, 379–386.

Shen, L., and Patel, M. K. (2008). Life cycle assessment of polysaccharite materials: A review. Journal of Polymers and the Environment 16, 154–167.

Singleton, A. C. N., Baillie, C. A., Beaumont, P. W. R. and Peijs, T. (2005). On the mechanical properties, deformation and fracture of a natural fibre/recycled polymer composite. Composites Part B: Engineering 36, 245-255.

Soykeabkaew, N., Nishino, T., and Peijs, T. (2009). All-cellulose composites of regeneratedcellulose fibres by surface selective dissolution, Composites Part A: Applied Science and Manufacturing 40, 321–328.

Suo, Z., Bao, G., and Fan, B. (1992). Delamination R-curve phenomena due to damage. Journal of the Mechanics and Physics of Solids 40, 1–16.

Sørensen, B. F., Horsewell, A., Jøgensen, O., Kumar, A. N., Engbæk, P. (1998). Fracture resistance measurement method for in situ observation of crack mechanisms, Journal of the American Ceramic Society 81, 661–669.

Sørensen, B .F., and Jacobsen, T. K. (2009). Characterizing delamination of fibre composites by mixed mode cohesive laws. Composites Science and Technology 69, 445-456.

Thouless, M., Kafkalidis, M., Ward, S., and Bankowski, Y. (1997). Toughness of plastically-deforming asymmetric joints, Scripta Materialia 37, 1081–1087.

Van de Weyenberg, I., Ivens, J., De Coster, A., Kino, B., Baetens, E., and Verpoest, I. (2003). Influence of processing and chemical treatment of flax fibres on their composites. Composites Science and Technology 63, 1241-1246.

Ward, I. M. and Hine, P. J. (1997). Novel composites by hot compaction of fibers. Polymer Engineering & Science 37, 1809–1814.

Proceedings of the 34th Risø International Symposium on Materials Science:
Processing of fibre composites – challenges for maximum materials performance
Editors: B. Madsen, H. Lilholt, Y. Kusano, S. Fæster and B. Ralph
Department of Wind Energy, Risø Campus
Technical University of Denmark, 2013

3D PERMEABILITY MEASUREMENTS WITH AN INDUSTRIAL APPROACH

T. M. Green*, J. Eman*
and A. George**

*Swera SICOMP AB, PO Box 271, SE-941 26 Piteå, Sweden
**Brigham Young University, School of Technology, 265Q CTB,
Provo, UT84602, USA

ABSTRACT

For industrial purposes in composite manufacturing, a straightforward method to determine 3D permeability in fibrous material is sought for. Nedanov and Advani (2002) presented a solution for point infusion of a material stack to determine the three permeability components. Although, computing the three permeability components might be a taxing task. Here, we propose a ratio simplification method to greatly simplify the calculation of the permeability components and apply the method to homogenously sheared and unsheared material stacks.

1. INTRODUCTION

As the composites industry continues to grow, the demand for simulation tools grows ever larger to speed up process optimization. Flow simulation of liquid composite molding (LCM) processes in composites manufacturing reduces prototyping time. LCM flow simulation is commonly based on Darcy's Law, which requires the permeability (K) of the reinforcement material to be characterized. Some LCM variant processes such as resin transfer molding (RTM) are dominated by in-plane flow which only required the in-plane components (K_{xx}, K_{yy}). But in other LCM variants that use flow distribution media, such as the vacuum infusion process (VI) for example, the through-thickness flow is the most time-consuming path. Therefore, accurate simulation of these processes requires also the through-thickness permeability component (K_{zz}).

Some advances have been made in flow simulation of VI such as coupling it with compressibility, as described by George, Ahlborn, El-Ghareeb, Drechsler (2011a) and Modi (2008), and also including capillary forces (George et al 2011a). But K_{zz} measurement remains a more significant problem because of the lack of a standardized measurement method, the high scatter in results, as well as the high sensitivity of the flow velocity to K_{zz} variation. Many reported measurement methods force 1D flow through the thickness. Some involve 1D flow in a compression cell, enabling continuous measurement of K_{zz} and compressibility at a range of

fiber contents (v_F) (Comas-Cardona, Binetruy, Krawczak, 2007). The well-known problem of race tracking is the greatest weakness of 1D K_{zz} methods. In addition, the saturated flow and high pressures usually applied can cause flow phenomena inaccurate to industrial VI.

Nedanov and Advani (2002) suggested a single point infusion method through a stack of dry plies as simple test setup for K_{zz} measurement. All three major K components can be determined from the flow dimensions of one experiment that resembles actual processing and discards the race-tracking issue. The unique challenge with such a K_{zz} measurement in unsaturated flow is that observations of the flow-front are impeded by the fabric it-self, compared to in-plane measurements. Flow perturbation often occurs from embedded sensors, and non-intrusive methods (ultrasound, mass flow measurement, etc.) require expensive equipment and calibration work. By using a transparent mould base, the time (t_F) at which the flow reaches the bottom of the mould can be measured. The resulting K calculation has been shown to be sufficiently accurate when based on only this one data point (Nedanov and Advani 2002).

Flow disturbances near the inlet are common for all K measurement methods. The point infusion method is no exception. As with 2D radial testing, the shape of the flow-front is constricted by the tube and needs some distance to develop into the correct geometry (Weitzenböck, Shenoi, Wilson, 1999). Related to this is the point singularity phenomena; tow-based fabrics will have different initial flow patterns based on the x/y location of the inlet tube, e.g. how many channels or stitches the inlet covers. But this error is also assumed to be mitigated far from the inlet. Therefore, the sample needs to be sufficiently thick and wide to achieve a well-developed 3D hemispherical flow-front.

The low pressures and wetting flow of such a test ensure that the capillary effects are similar to typical industrial processing. But this also complicates the data analysis as K must be evaluated independent of these. Infusion under a vacuum bag is the simplest implementation of this test, but adds the complication of variable mould thickness (i.e. compressibility).

George, Pickett, Sirtautas and Drechsler (2012) proposed a ratio simplification to Nedanov and Advani (2002) method, which approximates the solution and only requires solving for a single variable. The same relationship was applied by Liu, Parnas and Giffard (2007) to simplify data analysis for 2D testing. The isotropic permeability reduces to a function of the ellipsoid shape:

$$K = K_{zz} (r_x * r_y / r_z^2) \quad (1)$$

The dimensionless hemispherical flow radius then reduces to 1. All other variables are evaluated in the same way as Nedanov and Advani (2002). This reduces the optimization problem to a single variable, which is mathematically straightforward to solve. This method was verified by George et al. (2012). It was found that the ratio simplification produced the same values for K_{xx}, K_{yy}, and K_{zz}.

George et al. (2012) numerical solution assumes constant pressure gradients and porosity. In reality, pressure gradients in the flow front vary along the axes. Also, compressibility changes the porosity along the filled regime under a vacuum bag, which causes further changes in the pressure gradients. These effects are highly coupled with each other and the Darcian flow. To further investigate the effects of shearing on K_{zz} this study have adapted the picture frame test for shearing a material stack.

2. EXPERIMENTATION

Test samples (150 mm x 150 mm) of various reinforcement materials were prepared for point infusion testing. A bindered uni-directional (UD) weave (272 g/m2) was used as the baseline material. This was tested in two different orientations: first, with all tows in parallel (UD) and second as a quasi-isotropic, QI layup (0/+45/90/-45). Three different preforming treatments were tested with the QI stacks: untreated, heated to 130°C, and heated to 130°C while under a bag and 1 bar vacuum. "NCF1," a biax bindered NCF of 548 gsm was also tested (untreated, UD). Other non-crimp fabrics (NCF), braids, and tailored fiber placement (TFP) fabrics were also included in this study and are described in George (2011b). All of the tested materials consist of HTS40 carbon fiber tows. All materials were stacked with sufficient layers to achieve a compressed thickness of approximately 10 mm.

VI point infusion tests were performed on the weave using paraffin oil, with a few selected tests of QI stacks being infused at 120°C with Hexcel RTM 6. The other materials were all infused with Hexion RIM235. Most samples were compressed to 1 bar vacuum for the infusion. Some selected weave samples were infused at 0.5 bar vacuum. For some of the materials from George (2011b), only one test was performed on each. For all other materials and treatments, three to seven replicates were performed and the results averaged.

The in-plane major axis radii (r_x, r_y) and t_F were recorded at the moment the fluid first appeared at the bottom of the sample. Measuring the wetted experimental thickness (r_z) under a vacuum bag is not straightforward. Considering the ellipsoid flow shape at t_F, r_z should be the thickness of the sample directly under the inlet. But this is difficult to measure as the inlet tube is in the way. An estimate was made by waiting some minutes after t_F and then measuring the thickness at a point away from the center where the flow front along the bottom has just past. This gives a minimum r_z as the measurement represents a fully lubricated material at a minimal resin pressure (P_R). P_R on the top of the sample would be slightly higher directly under the tube. But as P_R drops quickly through the thickness in a 3D infusion, and v_F changes little for all but the highest P_R, this difference was neglected.

To examine the effects of shearing a picture frame, for uniform shearing were ordered. Normally a picture frame is mounted in an Instron to measure the stress required to shear a single ply. Here the focus is to understand the impact on K_{zz} when several plies are sheared, compacted and pre-formed. Therefore some modifications were done to the ordered picture frame compared to a "standard" picture frame. Here, the four moving arms are mounted on a support frame with a tensioning screw; cf. Fig 1. To pinch the plies down to the moving frame, four separate aluminium bars are placed on top of the plies and clamped with three welding tongs on each side. Material stacks of 16 ply UD were laid up with the zero direction parallel to two of the arms in the quadratic frame, i.e. starting position. The clamped material stack was then sheared before consolidation at 1 bar and 120°C in the same manner as for the unsheared samples described previously (George et al. 2012). From the stack four test samples (150 mm x 150 mm) was cut out and point infused. Three different shear angles of the 16 plies reinforcement stack have been tested; 9.6°, 11.1° and 13.2°, corresponding to a displacement of lower picture frame joint of 48, 55 and 65 mm, respectively.

Fig 1: The delivered Trellis frame for shearing of multiple ply lay ups. The four moving arms are mounted on a support frame with a tensioning screw for controlling the shear angle of the plies. Above the Trellis frame one welding tong and one clamping bar is visible.

3. RESULTS

The resulting r_x, r_y and t_F were used to calculate the K tensor using the ratio-simplified model. To evaluate the effects of the lag in bulk flow, George et al. (2012) calculated the K_{zz} results a 2nd time with both the x and y flow fronts reduced by 3 mm in order to evaluate the effects of capillary pressure, P_{cap}. The calculations were made a 3rd time with ΔP increased by the estimate for P_{cap}. The results for all tests with the UD-weave are presented in Fig. 2, normalized to 60% v_F by the Kozeny-Carman equation. The differences between the modelling methods are small. Reducing the flow front 3 mm in r_x and r_y only decreases the resulting K_{zz} by ~ 5% which is deemed insignificant in comparison to the scatter in results. The farthest flow front is therefore assumed, as this agrees with the practice of measuring t_F at the farthest z flow length. As P_{cap} is thought to be significant at low v in these experiments the P_{cap} model is used throughout the rest of this paper.

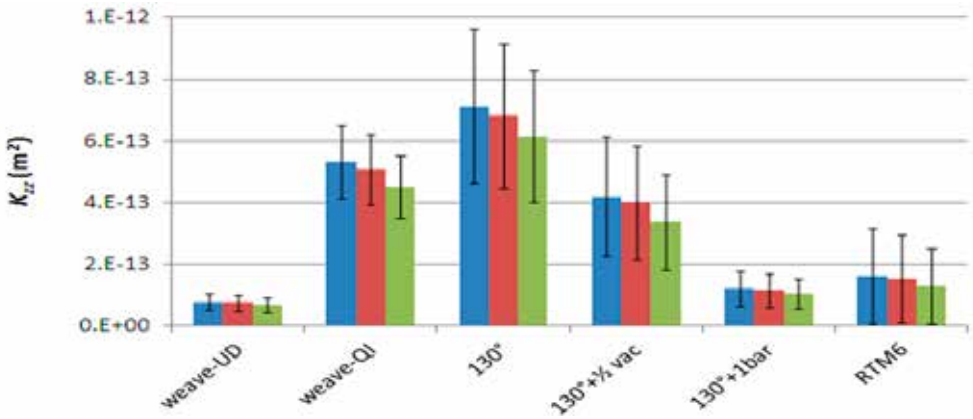

Fig 2: K_{zz} (60% v_F) by model and test: blue = simple; red = 3mm lag; green = P_{cap} modified.

The half vacuum tests (at 0.5 bar) were run to see if a relationship between K and v_F could be determined similar to practice in 1D K_{zz} testing by simply changing the sample thickness (Comas-Cardona et al. 2007). Lowering v_F should result in a higher K, but the results showed no significant difference from full vacuum (actually slightly lower K). Under a vacuum bag, it is hard to achieve significantly different thicknesses, as the thickness changes little from 0.5 bar to 1 bar compaction. Furthermore, it is suspected that capillary pressure forces will modify the flow with increasing severity as the mechanically applied pressure is significantly decreased in this way.

Fig. 2 compares all three resultant permeability components, normalized to 60% v_F. Since only one point-infusion test was performed for the five right-most materials in Fig. 2, a standard deviation (s) of 100% was assumed. The weave tests with RTM6 also resulted in s ~ 100% over three replicates, indicative of the challenges of implementing this test in an oven. Otherwise, s ranged from 8 to 55% for the other tests. The in-plane K proved to be 5 to 100x K_{zz} for these materials; TFP-UD being the lowest ratio (high stitching content) and the bindered weave being the highest ratio (combination of binder plugging channels and no z-direction stitching). The QI layup of the weave resulted in a five times higher K_{zz} than the UD layup. This is attributed to the greater inter-tow z-direction channelling in the QI lay-up.

From the experiments with sheared material stacks it was found that the permeability for the non-sheared UD fabric is five times lower than for the QI material stacks. When shearing the material stacks with the picture frame it was found that K_{zz} is about 21 to 52 % less than for the non-sheared UD results, depending on the shear angle. As it may be presumed, the 9.6° resulted in a K_{zz} half of the unsheared state. Interesting to notice is that lowest permeability and spread in results, is achieved for the intermediate shear angle of 11.1°. When increasing the shear angle to 13.2°, the average permeability in K_{zz} increases to an intermediate value; see Figure 3.

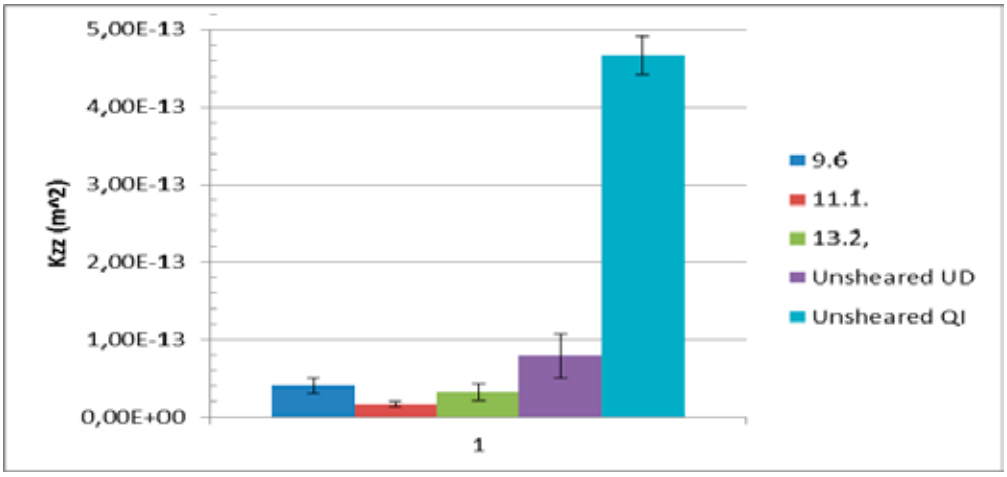

Fig 3: The resulting K_{zz} for sheared UD material stacks compared to unsheared UD and QI material stacks. 9.6° shearing results in K_{zz} 4.1±0.9*10^{-14} m^2, the corresponding result for 11.1° and 13.2° is 1.8±0.2*10^{-14} m^2 and 3.2±1.0*10^{-14} m^2. For the unsheared UD the resulting K_{zz} is 8.0±1.2*10^{-14} m^2 and for the QI 47±0.2*10^{-14} m^2.

4. CONCLUSIONS

A simplified method to determine the permeability for industrial purposes have been presented and applied to several material stacks. Comparison has been performed between conventional 1D permeability tests and a point infusion method. It is found that the presented method present reasonably good results for a simple experimental set-up and calculations.

ACKNOWLEDGEMENTS

This study was funded by Sweden's NFFP5-KOMPLETT and EU's FP-7 INFUCOMP.

REFERENCES

Comas-Cardona, S., Binetruy, C. and Krawczak, P. (2007). Unidirectional Compression of Fibre Reinforcements. Part 2: A continuous permeability tensor measurement. Composites Science and Technology 67 638-645.

George, A., Pickett, A. Sirtautas, J. and Drechsler, K. (2012). Optimization of 3D Wetting Permeability Measurements. Proc. of the Flow Processes in Composite Materials (FPCM – 11).

George, A., Ahlborn, H., El-Ghareeb, M., Drechsler, K., and Heider, D. (2011a). Compressibility Modeling and Validation for Coupled Flow Simulation. Proc. of the 18th International Conference on Composite Materials (ICCM18).

George, A. (2011b). Optimization of Resin Infusion Processing for Composite Materials. PhD thesis (University of Stuttgart).

Liu, Q., Parnas, R.S. and Giffard, H.S. (2007). New set-up for in-plane Permeability Measurement. Composites: Part A 38 954-962.

Modi, D. (2008). Modeling and Active Control of the Vacuum Infusion Process for Composites Manufacture. PhD thesis (University of Nottingham).

Nedanov, P.B. and Advani, S.G. (2002). A Method to Determine 3D Permeability of Fibrous Reinforcements. Journal of Composite Materials 36(2) 241-254.

Weitzenböck, J.R., Shenoi, R.A. and Wilson, P.A. (1999). Radial flow permeability measurement. Part A:Theory. Composites: Part A 30 781-796.

Proceedings of the 34th Risø International Symposium on Materials Science:
Processing of fibre composites – challenges for maximum materials performance
Editors: B. Madsen, H. Lilholt, Y. Kusano, S. Fæster and B. Ralph
Department of Wind Energy, Risø Campus
Technical University of Denmark, 2013

NUMERICAL ANALYSIS OF MICROMECHANICAL ASPECTS IN SHORT FIBRE COMPOSITES

I. Ioannou[1], A. Hodzic[2], I. Gitman[1], C. Soutis[3] and M.A. Almaadeed[4]

[1] Department of Mechanical Engineering, The University of Sheffield, Sheffield, UK
[2] Advanced Manufacturing Research Centre, The University of Sheffield, Sheffield, UK
[3] Aerospace Research Institute, The University of Manchester, Manchester, UK
[4] Materials Technology Unit, Qatar University, P. O. Box: 2713, Doha, Qatar

ABSTRACT

This study aims to investigate the influence of micromechanical parameters in randomly reinforced composites using numerical simulations and analytical models. The composite material in this study consists of a blend of thermoplastic polymer and glass fibres. The micromechanical parameters under investigation are Aspect Ratio (AR) and Fibre Orientation (FO). Mechanical and thermal properties were derived under the concept of Unit Cell (UC) and Representative Volume Element (RVE). In order to mimic the nature of stochastic composite micro-geometry, an algorithm was developed in order to create realisations of random inclusions with different aspect ratios and inclusion orientations. Finite element calculations were carried out and an average homogenisation method was applied in order to calculate the effective properties by measuring local stresses and local strains. Models were developed for three normalised (by inclusions length) sizes that were investigated through a statistical hypothesis and verification by Chi Square (CS) test (Gitman and Askes 2007). Analytical models were considered in order to compare them with numerical results. Three main families of analytical models were considered. The bounds method by implementing the general Voigt and Reuss bounds and Hashin Shtrikman bounds, the semi empirical model of Halpin Tsai (Fu, Lauke, Mai 2009) and the mean field method by considering the Eshelby model (Eshelby 1957) and the Mori Tanaka model (Mori and Tanaka 1973). The contribution of aspect ratio is discussed for the cases of aligned, misaligned and randomly oriented fibres, and for mechanical and thermal properties.

1. INTRODUCTION

The investigated material is a discontinuous short fibre composite. The reinforcing agent is short glass fibre and the matrix is a blend of thermoplastic polymers. According to Fu et al. (2009) the mechanical behaviour of short fibre reinforced composite (SFRC) mainly depends on three parameters: fibre aspect ratio, fibre orientation and volume fraction from which the first

two depend on the manufacturing process of the composite. Injection moulding and extrusion compounding processes are the major methods for the industrial manufacture of short fibre composites (Astrom 1997).

The industry currently favours replacement of traditional engineering materials with short fibre polymer composites. Utilisation of SFRC has expanded due to the relative ease and low cost of manufacturing on a large scale and the improved properties of these composites. Hence, there is a need for more understanding of the effect of the micromechanical parameters affecting the macroscopic behaviour of the thermoplastic composites.

This study aims to characterise a two phase composite material consisting of glass fibre inclusions in a polymer blend matrix. Properties under investigation are longitudinal and transverse effective stiffness, effective shear modulus, longitudinal and transverse thermal conductivity and coefficient of thermal expansion (CTE). Numerical models were developed using the concept of RVE in a four step procedure.

1. The creation of geometry by an algorithm which ensures non-intersection of the inclusions and the periodicity of the geometry. Fibres are simulated as elliptical inclusions and the aspect ratio is assumed to be equal to the ratio of major to minor axes of the ellipses,
2. The analysis of RVE in the linear elastic regime,
3. The implementation of an averaging homogenisation technique, and
4. The implementation of a statistical evaluation.

The Finite Element simulations were developed using Abaqus and the geometry was created in Matlab and introduced to Abaqus through Python scripting. The minimum size of RVE was to be determined. For each size, five different realisations were created in order to investigate the dependency of results with RVE size. The evaluation of size was conducted by chi square tests which ensured, with an accuracy of 95%, that the effective results of the analysis were independent of the stochastic parameters (position and orientation).

Results of all the effective properties are presented for representative sizes as a function of aspect ratio for fibre volume fractions of 30%. Numerical results were compared with analytical micromechanical models and were plotted as a function of the AR.

2. METHODOLOGY

A general definition of the problem under discussion in this paper is the characterisation of mechanical and thermal behaviour of a short fibre composite for various AR and FO. This characterisation can be approached experimentally, analytically and numerically. In this study the characterisation of the materials was established through the concept of RVE. The choice of simulating a representative structure in order to derive effective properties, gave the opportunity to study micromechanical parameters which can affect the macroscopic behaviour of the material. In order to implement that, two variables were introduced into the system. FO and AR were varied through the analysis along with RVE size. To obtain the average homogenised mechanical and thermal properties, local measurements of stress, strain or thermal flux were integrated through the volume. The obtained properties for each size form a uniform distribution as shown in Fig. 1 and were tested statistically to ensure the representative size. To testify the results from numerical models, well established analytical models were considered for comparison.

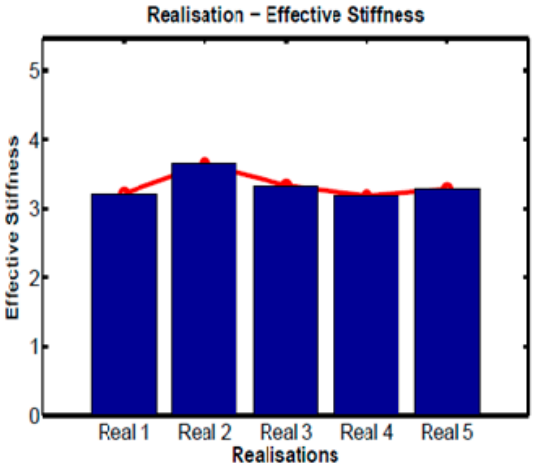

Fig. 1. Distribution of longitudinal stiffness over five realisations for a single size, AR, FO, and V_f.

3. PACKING PROBLEM

Packing problems are a class of optimisation problems in mathematics that involve a method to pack objects together (often inside a container), as efficiently as possible. In order to solve the packing problem of elliptical inclusions with different aspect ratio, contained in a square, an algorithm was developed. The algorithm was able to create periodic micro-geometries with inclusions of constant uniform length, a variety of aspect ratio and random orientations. The introduction of stochastic parameter made the packing problem more difficult to be solved because mainly it was more challenging to attain the desirable volume fraction. To overcome this barrier, a bisection method was introduced in order to agglomerate more fibres towards the centre of RVE. Fig. 2 shows the flow chart of the algorithm. The code was developed in Matlab environment and introduced to Abaqus for meshing and further analysis through Python scripting. The code uses the coordinates of the perimeter of the ellipse to check for any intersection, if there is no intersection, a bisection method is implemented in order to gather fibres towards the centre. The need to implement a bisection method rises once randomly oriented inclusions were introduced, and it was more difficult to have the desired V_f.

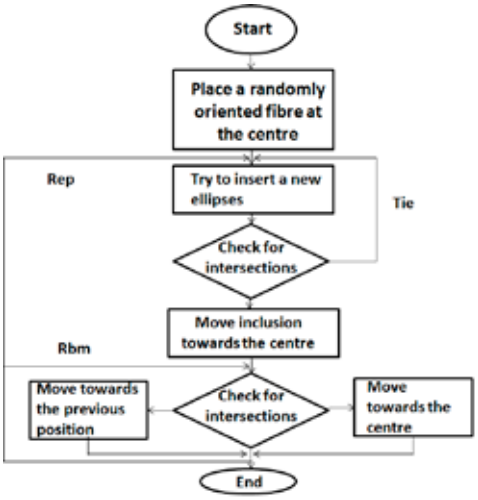

Fig. 2. Flow chart of the developed algorithm to solve the packing problem.

4. NUMERICAL MODELS

The cases of aligned, misaligned and randomly oriented fibres were analysed for AR = 1, 5, 10. As a result we examine a variety of sizes in order to ensure that positioning or orientation (realisation) does not affect the final result. If the final results depend on the position of the inclusions in space, then the selected size is not representative of the structure, and it has to be rejected. In order to classify representative cases, five different realisations were developed; for each size (2.5, 3.75, 5), for AR (1, 5, 10), and for fibre orientations (aligned, misaligned and randomly oriented). Fig. 3 shows the cases of three AR, three orientation cases, and three different sizes. For all the possible combination of those variables, five different realisations were developed, as it can be seen on the very right side of Fig. 3. Once the microstructure was introduced into Abaqus, samples were subjected to periodic boundary conditions (Eq. (1)) and meshed by plane stress triangular elements.

In Eq. (1) u_i^R,u_i^L represents displacement on the longitudinal direction where x_i^L,x_i^R represents longitudinal coordinates. In Eq. (2) v_j^T, v_j^B represents displacement on the transverse direction, where y_j^T,y_j^B represents transverse coordinates. In both equations, $\bar{\varepsilon}$ represents strain. The use of rectangular elements was not a solution due to the stochastic position of the inclusions in RVE, and a more efficient shape than rectangle was needed. The CS test was able to define the independency of the results with the stochastic parameter, by comparing the observed and the expected value of the property under investigation.

$$u_i^L - u_i^R = \bar{\varepsilon}_{11}(x_i^L - x_i^R) = u_i^{L-R} \tag{1}$$

$$v_j^T - v_j^B = \bar{\varepsilon}_{22}\left(y_j^T - y_j^B\right) = v_j^{T-B} \tag{2}$$

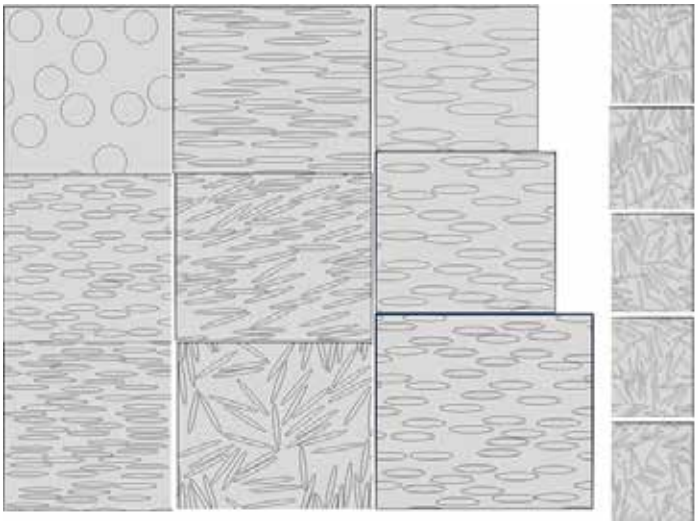

Fig. 3. Realisations for AR = 1, 5, and 10, for aligned, misaligned and random orientations, and for sizes 2.5, 3.75, and 5.0.

5. AVERAGE HOMOGENISED PROPERTIES

Homogenisation can be interpreted as a description of the behaviour of a material that is inhomogeneous on a lower length scale, and in terms of energetic equivalent, homogeneous reference material on a higher length scale.

In order to describe the responses of the models under simple uniaxial loading conditions such as uniaxial longitudinal tensile, transverse tensile and shear test, we implemented a homogenisation method. Average stresses and average strains can be defined in a similar way by integrating local micro-stresses or micro-strains over the entire volume of the specimen by implementing the average stress theorem (Eq. (3)) and the average strain theorem (Eq. (4)).

$$\overline{\langle\sigma\rangle}_{ij} = \frac{1}{V}\int_V \sigma_{ij}(x)dV \tag{3}$$

$$\overline{\langle\varepsilon\rangle}_{ij} = \frac{1}{V}\int_V \varepsilon_{ij}(x)dV \tag{4}$$

The results from Eqs. (3) and (4) are introduced into the generalised Hooke's law (Eq. (5)) in order to derive one element of the stiffness tensor for each virtual experiment.

$$\sigma_{ij} = C_{ijkl}\varepsilon_{kl} \tag{5}$$

6. RESULTS AND DISCUSSION

Numerical models have been developed in order to simulate the behaviour of short fibre composite. Finite element analysis was implemented, and results were achieved for the linear elastic response. Developed models were able to count the reinforcing parameters of orientations and AR. The effect of RVE size was considered. In general, models show higher stiffness in respect with higher degree of alignment and higher AR. Transverse stiffness and effective shear modulus shows an independency with AR for all the cases of orientation, except for the case of randomly oriented fibres. Results for the stress and strain fields were obtained after applying kinematic uniform boundary conditions and solving the boundary condition problem of an RVE. Un-deformed and deformed models presenting the stress field for AR = 1, AR = 5 and AR = 10 are presented in Fig. 4. Sizes are dimensionless, as their values are normalised by the length of the inclusion.

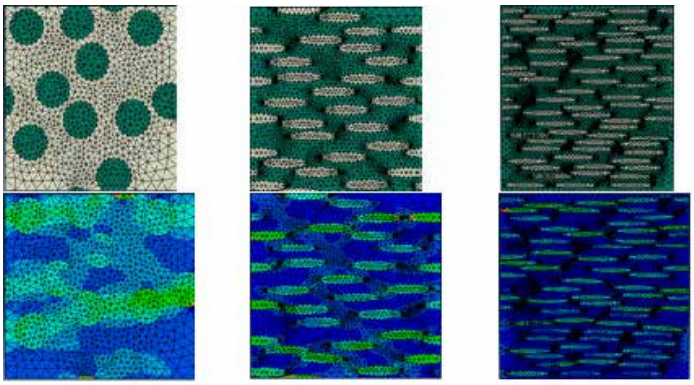

Fig. 4. Deformed and un-deformed aligned samples of various AR.

ACKNOWLEDGEMENTS

The authors wish to acknowledge Qatar Science and Technology Park for their funding of the project.

REFERENCES

Astrom, T.B. (1997). Manufacturing of polymer composites. 1st edition, Chapman & Hall, UK.

Eshelby, J.D. (1957). The determination of the elastic field of an ellipsoidal inclusion, and related problems. Proceedings of the Royal Society, London, UK.

Fu, S-Y., Lauke, B., Mai, Y-W. (2009). Science and engineering of short fibre reinforced polymer composites. 1st edition, Woodhead Publishing, UK.

Gitman, I, Askes, H. (2007). Representative volume: Existence and size determination. Engineering Fracture Mechanics, Vol. 74, 2518-2534.

Mori, T., Tanaka, K. (1973). Average stress in matrix and average elastic energy of materials with misfitting inclusions. Acta Metallurgica, 21,571-573.

Tucker, C.L., Liang, E. (1998). Stiffness predictions for unidirectional short fibre composites: Review and evaluation. Composites Science and Technology.

Proceedings of the 34th Risø International Symposium on Materials Science:
Processing of fibre composites – challenges for maximum materials performance
Editors: B. Madsen, H. Lilholt, Y. Kusano, S. Fæster and B. Ralph
Department of Wind Energy, Risø Campus
Technical University of Denmark, 2013

MATERIALS CHARACTERISATION OF GLASS/EPOXY COMPOSITES – FOCUSING ON PROCESS CONDITIONS

Johnny Jakobsen[1], Anders Lyckegaard[2],
Erik A. Jensen[1], Jens H. Andreasen[1]

[1] Dept. of Mechanical and Manufacturing Engineering,
Aalborg University, Denmark
[2] National Oilwell Varco, Denmark

ABSTRACT

Predicting the behaviour of fibre reinforced polymer composites taking the process conditions into account involves advanced modelling techniques and an extensive materials characterisation. The materials characterisation of a chopped strand mat glass/epoxy composite has been the focus of this paper. The resin gelation has been investigated with two different experimental setups and the measurements are compared. A thermo-chemical material model for the in-plane Young's modulus has been developed based on multiple DMA experiments and further presented in a modulus-temperature-transformation diagram. The viscoelastic behaviour for the fully cured composite materials was investigated and a master curve of the relaxation modulus was established.

1. INTRODUCTION

The solidification process of polymer fibre composite materials based on a thermoset matrix has been of interest to industry and academia during the past years. During this process the material properties are formed and they may to some extent be influenced by how the materials were processed. Properties such as the glass transition temperature, Young's modulus, Poisson's ratio and fatigue endurance are some of the properties that may be influenced by the processing. Understanding these influences is of great importance for a further optimisation of fibre composite material.

The transformation of a liquid resin matrix, linking to the fibre reinforcement and forming into a solid occurs over time at given process conditions. Moreover during this transformation the resin material passes several transitions and the first is gelation. Gelation of thermoset resins has been studied by several authors in the past. Hu, Fan and Yue (2001) conducted an experimental investigation of the gelation of a bismaleimide/cyanate ester applying different definitions to determine the point of gelation and the authors found dependence on the gel point definition.

Often the gel point is measured on the neat resin material and not on the composite materials. Results presented in this paper compares gelation measured on a neat epoxy resin with measurements conducted on a glass/epoxy composite.

Characterising the reaction of thermosets and further developing cure kinetic models of the reaction can be done by two approaches; a mechanistic or a phenomenological. The mechanistic models are generated by balancing the reactive species and require knowledge of the chemistry involved. Phenomenological models can however be established without a detailed knowledge of how the species react with each other. An excellent review on cure kinetics for thermosets was conducted by Yousefi, Lafleur and Gauvin (1997). Later Gotro and Prime (2002) followed with another thorough chapter on thermosets and cure kinetic models. The current paper presents cure kinetics of the epoxy used to fabricate glass fibre composite samples. The cure kinetic model will be used in the model development of the Young's modulus.

For unidirectional composites the Young's modulus during the transition will in the fibre direction be governed by the fibre itself and only a minor change in modulus will occur. However in the transvers direction the modulus is controlled by the matrix which through the curing will go through a radical change. Simon, Mckenna and Sindt (2000) developed a viscoelastic model of an epoxy resin during cure. Their model was able to predict the change in modulus from gelation and through vitrification and good agreements with measurements were obtained. Additional types of fibre mat architecture which are often used in fibre composite products are the chopped strand mat (CSM). This type of fibre architecture gives a nearly isotropic in-plane elastic response. In addition the CSM fibres are typically used in between directional fibre layers to increase the interlayer fracture toughness. Christensen and Waals (1972) developed analytical models of randomly orientated fibre composite and in comparison with experimental data a reasonable agreement was obtained. They further stated that the rule of mixture model would produce non-conservative predictions. Sk and Chakraboty (2004) developed their model based on a statistical approach. The CSM glass/epoxy composite has been given the attention of this paper and a material model characterising the change in elastic modulus during curing will be presented together with a model of its fully cured viscoelastic response.

2. EXPERIMENTAL METHOD

Modulated differential scanning calorimetry (MDSC) measurements are conducted on the neat epoxy resin aiming on collecting reaction data for the establishment of a cure kinetic model. Several isothermal measurements were made followed by a post cure sequence at a constant heating rate of 5K/minute. The heat of reaction from the isothermal and post cure measurements were evaluated by time integration of the non-reversing heat flow. The extent in the chemical conversion (c) of the reaction is formulated mathematical from the integrated heat flows (cf. Eq-1).

$$c = \frac{\int_0^t \Delta H_{iso}\, dt}{\Delta H_{tot}} \tag{1}$$

where ΔH_{iso} is the enthalpy of the isothermal measurement and ΔH_{tot} is the total enthalpy and is the sum of enthalpies from the isothermal and post cure measurements.

Measurements of the gelation for the neat epoxy were done in a parallel plate setup applying a small shear oscillation. For the CSM glass/epoxy a small oscillating bending setup was used.

The temperature conditions subjected to the samples were identical.

Measurements of the Young's modulus and the stress relaxation behaviour of the CSM glass/epoxy composite were done utilising dynamic mechanical analysis (DMA). A tension loading setup is used for the measurements. All samples were pre-cured to a conversion state just above gelation and the development of the Young's modulus during a post curing of the samples was monitored. The post curing was conducted at different isothermal temperatures. The cure kinetic model of the neat resin was used to convert the time data into conversion states. A model of the Young's modulus is presented depending on temperature and the conversion state only. Moreover the model is presented in a modulus temperature and transformation diagram (MTT diagram).

The viscoelastic model of the Young's modulus was developed for fully cured CSM glass/epoxy. Measurements were performed in a DMA during a stepwise heating of the several samples.

3. RESULTS

Gelation. For the composite sample which was subjected to a bending loading the gelation was defined as the onset in the storage / Young's modulus (E'). Onset is defined as the crossing of the tangents before and after the transition (cf. Fig-1 top graph). For the neat epoxy sample gelation was defined as the crossover of the storage and loss shear modulus (G'=G''). In Fig-1 it can be seen that identical times of gelation has not been measured.

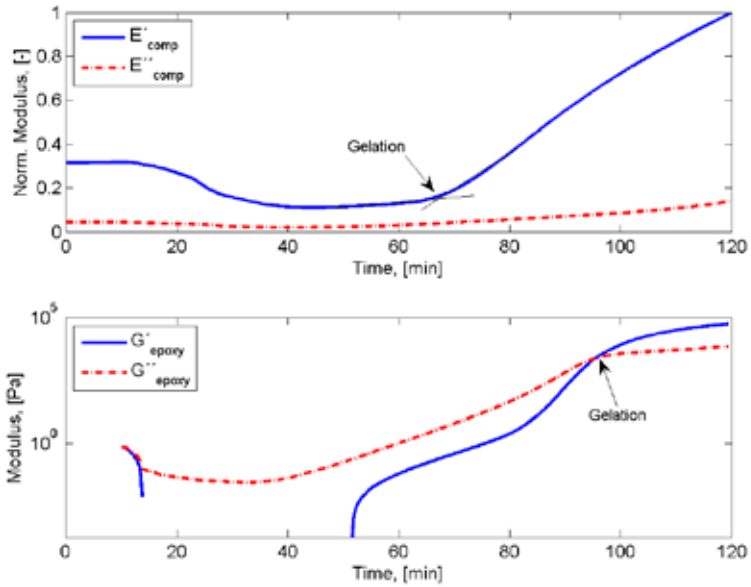

Fig 1. Point of gelation measured on the glass/epoxy composite (top graph) is compared with similar measurements conducted on the neat epoxy resin (lower graph).

It is believed that presence of the fibre reinforcement affects the chemical reaction and this originates from the sizing coated onto the fibre material. The gelation time measured for the composite sample which has been recorded to 68min will be used in the following of this paper.

Cure Kinetic Model. The cure kinetic model presented by Sourour and Karmal (1976) was used in a slightly extended version to describe the reaction rate of the epoxy. The model includes the effect of incomplete curing through the function (c_{max}) which could arise from to low curing temperature or too short curing time (see Eq-2).

$$\dot{c}(c,T) = \begin{cases} K_1 \, (c_{max}(T) - c)^{m_1} + \sum_{j=2}^{3} K_j \, c^{n_j} (c_{max}(T) - c)^{m_j} & , \quad for \; 0 \le c < c_{max}(T) \\ 0 & , \quad for \; c = c_{max}(T) \end{cases} \tag{2}$$

$$K_i(T) = A_i e^{\frac{-E_i}{RT}} \quad , \quad i = 1..3$$

In Eq-2, *c* is the state of conversion and *K* is the Arrhenius function. The model parameters *A, E, m* and *n* are found by non-linear regression analysis on the MDSC data from several isothermal experiments were used. A reasonable agreement with measured data has been achieved (see Fig-2). For the 373ºK curing the model under predicts the conversion rate with about 10%.

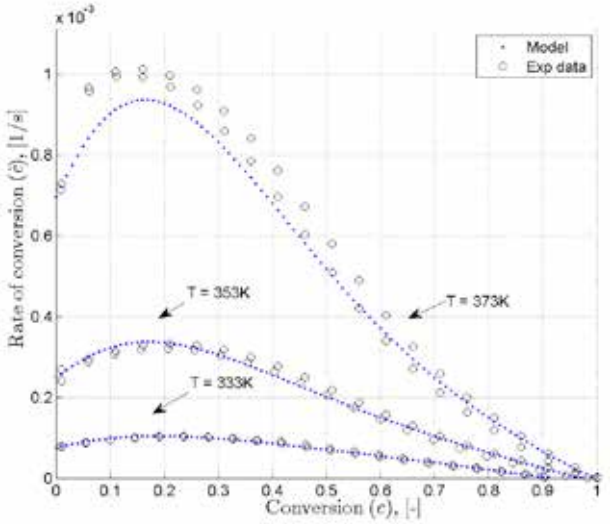

Fig 2. The cure kinetic model illustrated together with experimental data.

It may further be seen from Fig-2 that the model captures the incomplete cure for the 333ºK and 353ºK curing.

In-plane Young's Modulus. The development of the in-plane Young's modulus during curing is modelled with depending variables *c* and *T* which denotes conversion and temperature

respectively (see Eq-3). The model decouples modulus increments which is associated with time (or progress in conversion) from increments driven by a temperature change.

$$E = E_0 + \int_{t_{gel}}^{t} \frac{\partial E}{\partial t} dt + \int_{T_{gel}}^{T} \frac{\partial E}{\partial T} dT \tag{3}$$

Prior to gelation the modulus is relatively small for this type of fibre architecture and is accounted for in E_o. t_{gel} and T_{gel} denotes the time and temperature at gelation respectively. The time and temperature increments of the Young's modulus may be determined from a series of DMA experiments. Experimental data of the Young's modulus at three isothermal temperatures are presented in Fig-3.

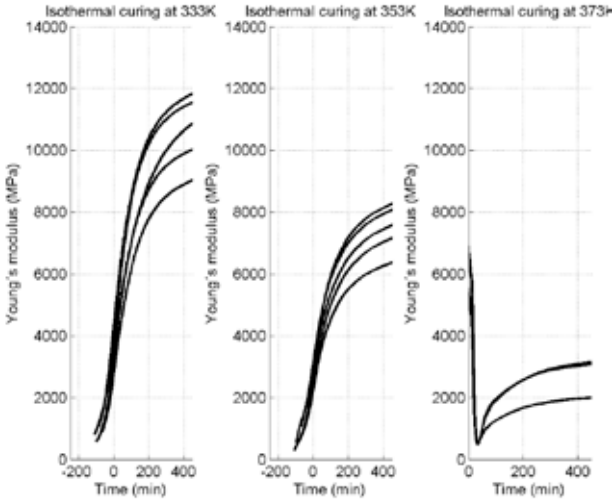

Fig 3. The development in Young's modulus at three different isothermal temperatures.

For the 333ºK and 353ºK data in Fig-3 time shifts have been imposed thus zero equals vitrification. The data presented has some scatter which may be due to fact that the samples had different conversion states prior to the experiment and this will influence modulus development. An additional source to the scattering may be related to the sample size and a representative volume of the fibre architecture. Even with a rather large data scattering it is possible to identify a temperature dependence of the Young's modulus during curing as expected.

The proposed model for the Young's modulus during curing may be displayed in a modulus temperature transformation (MTT) diagram (see Fig-4). Model predictions (solid black lines) show a reasonable agreement with experimental data (o). The solid black curves are the isothermal modulus response and the area enclosed by the green curve is the conversion range where modulus may increment due to the chemical reaction and by a temperature change. The area between the green and blue curves a modulus increment can only take place if the temperature is lowered.

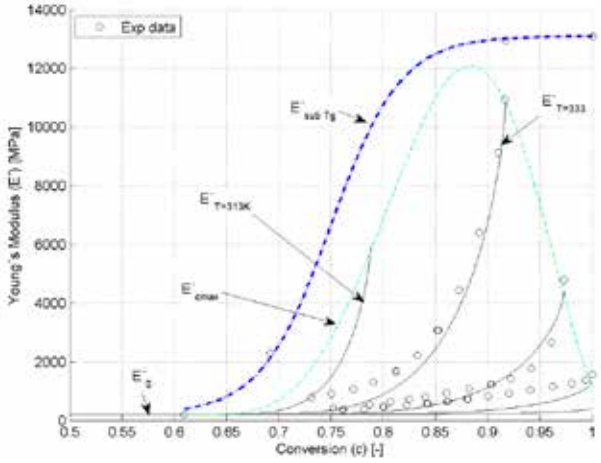

Fig 4. Modulus temperature transformation (MTT) diagram for a CSM glass/epoxy composite.

In-plane Viscoelastic Model. The material behaviour in the visoelastic phase is modelled as a linear viscoelastic solid. The relaxation modulus is determined based on measurements. The combined behaviour of the materials can be described by an additive decomposition of strain increments, which is defined as follows.

$$d\varepsilon(t,T) = d\varepsilon_{ve}(t,T) + d\varepsilon_{th}(T) + d\varepsilon_{ch}(t) \tag{4}$$

Here the total strain increment $d\varepsilon$ is a sum of; $d\varepsilon_{ve}(t,T)$ the viscoelastic contribution, $\varepsilon_{th}(T)$ the thermal contribution and $d\varepsilon_{ch}(t)$ the strains due to chemical reaction.

The strain increment terms due to thermal expansion and chemical shrink are assumed to be known functions of time by virtue of a known temperature and chemical potential relation with time. Also the total strain is assumed to be known.

Application of the Bolzman superposition principle, which implies a linear material behaviour, yields the following constitutive relation.

$$\sigma(t) = \int_0^t E(t-\tau)\,\frac{d\varepsilon(\tau) - d\varepsilon_{th}(\tau) - d\varepsilon_{ch}(\tau)}{d\tau}\,d\tau \tag{5}$$

Here $\sigma(t)$ represent the stresses and $E(t)$ is known as the relaxation modulus. Notice, that the current measurements are conducted on fully cured samples at isothermal conditions. This excludes thermal and chemical strain contributions in Eq-5. However these contributions have previously been reported by Kim and White (1996) to have an effect on the stress state and the relaxation modulus during curing of neat epoxy materials.

Relaxation Modulus. The in plane relaxation modulus was measured by stepwise thermal increments at an imposed constant strain of 0.04%. The measurements were conducted in a Q800 DMA from TA-Instruments and the samples were loaded in tension. All specimens were fully cured and the relaxation modulus was determined after isothermal conditions in each step were reached. This made neglecting of the thermal and chemical strain contributions valid. A few samples were also tested at a higher strain level. The measurements are subsequently collected to form a master curve for the material by using time-temperature scaling.

The scaling of the relaxation modulus is based on the time shift hypothesis (see e.g. Christensen

1971), i.e.

$$E(t \cdot a_T(T_1), T_1) = E(t, T_R) \tag{6}$$

where T_1 denotes a temperature, T_R is the reference temperature, and $a_T(T_1)$ is the shift factor, which is a temperature dependent constant.

The measured relaxation modulus is time shifted by the factors $a_T(T_1)$ shown in Fig. 6, and the resulting master curve is given in Fig. 5. The time shift factors are determined by manual fitting.

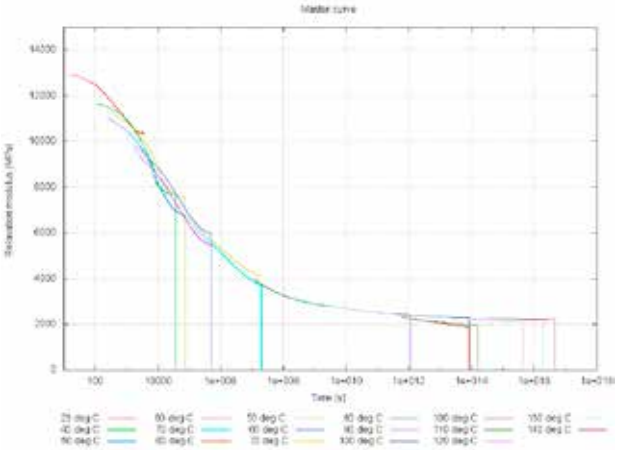

Fig 5. The measured relaxation modulus master curve.

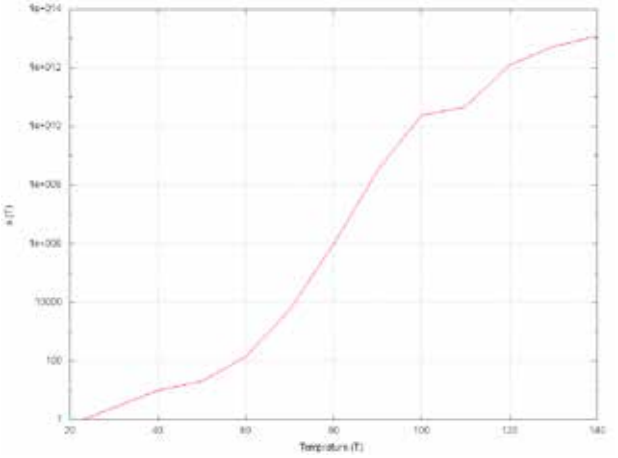

Fig 6. The obtained time shift factors for the master curve.

Fitting models to the above relations could be done. A Prony series fit is often used to approximate the relaxation modulus, whereas the time shift factor is often described by the Williams-Landel-Ferry (1955) relation. This task will be left for further research.

4. CONCLUSIONS

Materials characterisation of a CSM glass/epoxy composite has been conducted with respect to gelation, cure kinetics, in-plane Young's modulus during curing and the viscoelastic behaviour of the fully cured materials has been studied. Interesting but non consistent observations for the time at gelation were made when the measured sample consisted of either neat epoxy resin or epoxy with glass fibre embedded. It is proposed that the sizing of the fibre affects the chemical reaction and further the gelation.

The cure kinetics of the epoxy used was measured and a model of the conversion rate was established. The cure kinetic model is an extension of the well-known Sourour-Karmal equation.

The development and dependence on the chemical conversion and temperature of the in-plane Young's modulus was measured and characterised. Based on DMA measurements a model which decouples the modulus increment associated with chemical reaction from increments associated with a temperature change was presented.

Viscoelastic behaviour of the fully cured materials was measured and a master curve of the relaxation modulus was generated.

ACKNOWLEDGEMENTS

The work presented has been sponsored by the Danish Council for Independent Research, Technology and Production Sciences, Grant Award 10-093339. The materials used were provided by Siemens Wind Power A/S, Denmark. The support received is gratefully acknowledged.

REFERENCES

Christensen, R. & Waals, F. (1972), 'Effective Stiffness of Randomly Oriented Fibre Composites', *Journal of Composite Materials* **6**(3), 518-535.

Christensen, RM, (1971), Theory of viscoelasticity – An introduction, Academic press.

Gotro, J. & Prime, R. B. (2002), *Thermosets*, John Wiley & Sons, Inc..

Hu, X.; Fan, J. & Yue, C. Y. (2001), 'Rheological study of crosslinking and gelation in bismaleimide/cyanate ester interpenetrating polymer network', *Journal of Applied Polymer Science* **80**(13), 2437--2445.

Kim, Y. K. & White, S. R. (1996), 'Stress relaxation behavior of 3501-6 epoxy resin during cure', *Polymer Engineering & Science* **36**(23), 2852--2862.

Simon, S. L.; Mckenna, G. B. & Sindt, O. (2000), 'Modeling the evolution of the dynamic mechanical properties of a commercial epoxy during cure after gelation', *Journal of Applied Polymer Science* **76**(4), 495--508.

Sk, L. & Chakraborty, S. (2004), 'Effective Moduli of Random Short Fiber Composite: A Probabilistic Study', *Journal of Reinforced Plastics and Composites* **23**(7), 751-760.

Sourour, S. & Kamal, M. (1976), 'Differential scanning calorimetry of epoxy cure: isothermal cure kinetics', *Thermochimica Acta* **14**, 41 - 59.

Yousefi, A.; Lafleur, P. G. & Gauvin, R. (1997), 'Kinetic studies of thermoset cure reactions: A review', *Polymer Composites* **18**(2), 157--168.

Williams, M. L.; Landel, R. F. & Ferry, J. D. (1955), 'The Temperature Dependence of Relaxation Mechanisms in Amorphous Polymers and Other Glass-forming Liquids', *Journal of the American Chemical Society* **77**(14), 3701-3707.

Proceedings of the 34th Risø International Symposium on Materials Science:
Processing of fibre composites – challenges for maximum materials performance
Editors: B. Madsen, H. Lilholt, Y. Kusano, S. Fæster and B. Ralph
Department of Wind Energy, Risø Campus
Technical University of Denmark, 2013

AN ADAPTIVE MODULAR MONITORING & CONTROL SYSTEM FOR COMPOSITES MANUFACTURING PROCESSES

S. Konstantopoulos*, E. Fauster**, R. Schledjewski*,**

*Christian Doppler Laboratory for Highly Efficient Composites Processing, Otto Glöckel-Straße 2/I, 8700 Leoben, Austria
**Chair of Processing of Composites, Department of Polymer Engineering and Science, Montauniversität, Otto Glöckel-Straße 2/III, 8700 Leoben, Austria

ABSTRACT

Polymeric based fiber reinforced composite materials are most intriguing when components with high performance and low weight are aimed at. The increased demand for light weight structures is driving a trend toward fully controlled, automated Composites Manufacturing Processes (CMPs) which in the last few years have included numerous forms of software assisted control systems. Although the algorithmic contribution tends to increase due to the compelling advantages it offers, there is no common ground in terms of equipment or software development; every author struggles to create on his own pieces of code that serve specific hardware configurations. The aim of this study is the development and implementation of an algorithm-assisted control system designed specifically for CMPs, based on the latest advancements of industrial automation and software engineering. The hardware components and software modules constituting the proposed system are flexible enough to be used in numerous occasions and meanwhile new and more complex modules are constantly added to the basic set. In the context of this paper, continuous pultrusion and permeability measurement processes will be served by the proposed control solution which shows excellent results in real-time Degree-of-cure evaluation, process monitoring, temperature regulation, adaptivity to different CMPs, hardware-PC connectivity, and data recording.

1. INTRODUCTION

Composites manufacturing processes (CMPs) are highly dynamical and demand monitoring capabilities in order to ensure the best possible behavior of the system with respect to quality and costs. The natural consequence of monitoring is controlling the process whether this is achieved manually or through commands within a software module. In any case, based on the feedback the system demands decisions concerning parameters of the process, many of which

can be changed real-time. Changes of this nature undoubtedly favor the use of software tools that will make the interaction fast and accurate.

Exploring previous work in monitoring & control systems specifically addressing CMPs, one encounters several efforts. Matsuzaki et al. (2011) performed multiple point dielectric analysis (DEA) during a VARTM process using an area sensor appropriate for flow front & dry spots detection. During this process a connection to the PC was established thus allowing full process manipulation (relay switching, measuring & drawing) via an algorithm created from the authors for this purpose. Hegg et al. (2005) performed a 3 point DEA during non-heated RTM but the interpretation of the incoming measurements was performed by a custom made code built on existing models instead of an interrogation kit. Lawrence et al. (2002) after using DC sensors as feedback source during an RTM process of a complex 3-D mold, developed a program to optimize flow front advancement by utilizing multiple injection points. Fink et al. (1999) used material embedded DC sensors to monitor flow front & cure during RTM (SMARTweave^{TM}). The software contribution in this case was a code that converted voltage measurements to a virtual flow front advancement that simplified monitoring significantly. A similar interface was developed by Yenilmez & Sozer (2009) in order to interpret electrical permittivity measurements into a visual representation of the flow front advancement during multiple point DEA of an RTM process. Luo, Zhu & Zhao (2012) developed a novel signal processing algorithm to analyze ultrasonic waves generated on-line by a wave probe within a composites specimen in order to detect Degree-of-cure (DOC).

The above approaches are only a sample of a great number of publications in the field of composites where control oriented software implementations slowly find their way in all aspects of composites processing: Manufacturing, Structural Health Monitoring (SHM), off-line simulations & optimization. Focusing however in manufacturing on-line monitoring & control, what previous papers have in common is their singularity. Evidently, every scientist struggles on his own to create control systems that serve his own purposes (pieces of custom made software that are compatible only with specific equipment). The resulting situation is a chaotic universe of different control systems often meant to serve the same CMPs. In this paper a more universal approach is proposed; an adaptive software-assisted monitoring & control system designed specifically for CMPs with respect to modern control and software engineering. The benefits of the proposed approach as compared to other regional implementations are:

- High adaptivity to different processes and flexibility (transferability or addition of modules) guaranteed by selecting certain software (section 2.2) and hardware (section 3.1) structures.
- The substitution of hardware components (e.g. temperature controllers, interrogation units) by software is feasible or easier due to the selected structure; ergo there is a higher cost reduction potential.
- The software tools and hardware configurations are designed based on appropriate control theory modeling (section 2.1) that guarantees long term stability and reliability.
- Real-time DOC evaluation is provided by means of analyzing reliable curing kinetics models, an analysis optimized by the input of live temperature measurements.

2. THEORETICAL BACKGROUND

The project at hand focuses in developing a control solution able to perform essential operations during various composite manufacturing processes. This definition implies the need to use theoretical elements from three distinct origins: *(i) Control & Automation* so that a solid theoretical basis is established which will allow the development of basic or advanced control tools, *(ii) Software Engineering* in order to make use of the appropriate software structures that offer adaptivity to many processes and *(iii)* a subtopic of Material engineering, *Reaction Modeling,* in order to direct the knowledge acquired by the first two areas into CMPs.

2.1 Control & Automation. The development of any software or hardware control system must abide to the laws of control & automation theory (Dunn 2005; Paraskevopoulos 2002). In case a computer is involved in controlling an operation the appropriate theoretical background is the field of *Digital control*. A common control structure for a PC controlled industrial system is defined by its state-space equations (eq.1, 2) and transfer function (eq.3):

$$x[(k+1)T] = Ax(kT) + Bu(kT) \tag{1}$$

$$y(kT) = Cx(kT) + Du(kT) \tag{2}$$

$$H(z) = z^{-1}C\phi(z)B + D \tag{3}$$

where $u(k) \in R^m$, $x(k) \in R^n$, $y(k) \in R^p$ are input, state and output vectors respectively, $\boldsymbol{A}$,$\boldsymbol{B}$,$\boldsymbol{C}$,$\boldsymbol{D}$ are constant matrices of appropriate dimensions, $\boldsymbol{T}$ the sampling period and $\phi(z) = z(zI - A)^{-1}$ is the transition matrix. A topic that always carries great significance when designing a control system is the system stability. Particularly in composites manufacturing where the target is to be able to maintain a stable manufacturing process for hours, establishing stability is considered a priority. In case of digital control, asymptotic stability is achieved when:

$$|\lambda_i| < 1 \tag{4}$$

where λ_i are the roots of the Characteristic equation $|\lambda I - A| = 0$ and I the identity matrix. A number of different criteria are then used to determine stability. Ruth, Jury, Lyapunov, Bode, Nyquist or even the root Locus method are used depending on the problem. However these governing laws offer merely an initial description of the problem at hand. The next step is to use more sophisticated control system designs in order to develop the best possible controller for specific equipment in given conditions. To this day numerous publications on two sub-categories of Intelligent Control (Fuzzy and Neural control) have been reported in the field of composites (Heider et al. 2003; Chen et al. 2010; Frazão, Oliveira & Dias 2009; Boime & Filleul 2001) and one of the subsequent targets of the present study is to include these two designs in the proposed monitoring and control method.

2.2 Adaptive Software Structure. A selection of three key structural elements that make the proposed method highly adaptive to many processes has been made. These architectures were formulated appropriately and included in a multi- dimensional code oriented to serve any CMP: *(i) The Multi-thread Structure* that provides independency (Sundell & Tsigas 2005; Shin, Lee & Gaudiot 2006) and high efficiency (Varoglu & Jenks 2011), *(ii) The Functional global temporary repository* that eliminates race conditions and performs unlimited operations other than the traditional *read* and *write* (Binkley et al. 2010; Lotz 2010)*, (iii) The TDMS output* that includes detailed information, various types of data and offers efficient 3D data categorizing (Czerwinski & Oddershede 2011).

2.3 Reaction Modeling Considerations. In the previous section, the operation of interrogation was presented as one of the duties of the Controller. In this operation lies the hard core of sensing in CMPs as it basically is an interpretation of the measurement to a quantity of interest. During interpretation of digital systems two different transformations occur:

- A first level mathematical model is being used in order to transit from the *Measured Property* (Bragg wavelength, sound wave velocity, electrical impedance etc.) to the *Controlled Property* (temperature, strain, Young's modulus, el.permitivity etc.).

- A second level mathematical model is being used in order to transit from the *Controlled Property* to the *Process property* (DOC, flow front, Viscosity, etc.)

The first transition is typically highly dependent on the sensor and is usually provided by the sensor manufacturer. Nevertheless, independent efforts to determine mathematical models governing sensing have been reported as well, for example by Hegg et al. (2005). The selection of the *software & optionally hybrid control configuration* proposed in the section 3.1, guarantees the flexibility to work in both ways. As far as the second transition is concerned, one of the most cited examples that correlates absolute temperature (T) with the DOC (a) is the Kamal-Sourour (Kamal & Sourour 1973) curing kinetics model of thermosetting matrices:

$$\frac{da}{dt} = (k_1 + k_2 a^m)(1-a)^n \quad \longrightarrow \quad m \,\&\, n \text{ are constants of order unity} \tag{5}$$

where k_i follows an Arrhenius dependence on temperature:

$$k_i = A_i exp\left(-\frac{E_i}{RT}\right) \quad \longrightarrow \quad A_i \text{ is the pre-exponential factor, } E_i \text{ the activation energy and } R \text{ is the universal gas constant} \tag{6}$$

In literature one can find more 1st or 2nd level models as this is a field of constantly growing interest. The proposed method supports the embodiment of any mathematical model as an independent algorithmic module and the experiments presented in section 4 use the model (eq. 5,6) in interpreting incoming temperature measurements during pultrusion.

3. PROPOSED CONTROL SYSTEM INSIGHT

The central hypothesis of this project revealed by a close study of common manufacturing setups (Mazumdar 2002; Hoa 2009) is that all processes share a certain hierarchy of identical circumstances:

- A connection between the hardware and the software needs to be established.
- A sensor (or array of sensors) that is installed for monitoring purposes, produce measurements that need to be appropriately interpreted.
- A heating system assisting Polymerization is involved and needs to be regulated.
- Recording all run-time data is in any case essential.
- Monitoring and interacting with all the above operations through a comprehensive application (Graphical User Interface) is crucial to the controllability of the system.

This section contains the main characteristics of a set of hardware and software modules designed to cover the five basic operations corresponding to the mentioned CMPs similarities.

3.1 Connectivity module. Establishing a connection with a digital device (e.g. PC) is a central demand of Digital Control. For that purpose appropriate software and equipment is required (e.g. Analog-to-Digital and Digital-to-Analog converters, a heat regulator, a measurement interrogation kit) which can be connected in various ways. In all controlling operations three choices emerge (Ibrahim 2006): Microcontrollers, hybrid or software controllers. Each of these three configurations has pros and cons summarized in Table 1. Every purpose has a different ideal but in the context of this project *the software controller with optional hybrid operation* is considered the best choice as it offers the best case scenario for a CMP. Low costs, high observability (monitoring & visualization), low measurement variance when the hybrid option is used, and high adaptivity that in correlation with the adaptive software structure presented in section 2 will result to the overall high universality. An EtherCAT technology based system (Beckhoff) was assessed to serve the above purposes and therefore was installed in both case studies presented in the experiments section. Moreover an algorithm to redirect full functionality to Labview based on mapping of the *.dll* file provided by the EtherCAT system manufacturer has been developed.

Table 1. Qualitative attributes of controller configurations.

	Controller		
	Software	Hybrid	Micro
Simplicity of implementation	low	middle	high
Costs	low	middle	high
Adaptivity	high	middle	low
Observability	high	high	low
Measurement Variance*	high	low	low

*Measurement Variance is an indicator of the possibility to see different results using different controllers for the same system. Apparently, the high variance suggested for software tools is a result of their adaptivity & flexibility to incorporate different laws and perspectives.

3.2 Process monitoring module. This is a software module that contains all information about the process by use of a combination of visual (virtual indicators & graphs appropriate for monitoring quickly the areas of major interest) and analytical elements (numerical values appropriate for further analysis). The information each independent module produces is directed to the monitoring module where it is visually depicted via graphs such as the *Time-sweep graph* (measured property vs. time), the *Space-sweep graph* (measured property vs. 1D or 2D represented die) or the *Error graph* (desired – acquired value). Moreover, the module contains a *graphical user interface (GUI)*, where a virtual representation of the equipment combined with a set of indicators is used in order to simplify monitoring further and offer various control possibilities. As a result, the user can interact real-time by changing the values of key parameters which are then distributed to their corresponding modules accordingly.

3.3 Temperature controller module. As explained in section 3.1, three are the possible choices for controlling a heating system. The advantages of a software controller however, are compelling: Cost reduction by avoiding the expensive microcontroller, absolute flexibility during the controller development, advanced monitoring capabilities as the process is being monitored via the custom made monitoring module presented in section 3.1. There is however a big challenge in developing the temperature controller module: Every type of heating system has its own particular needs and there is no way around preparing a controller for every type.

Typical industrial applications in composites involve many different types of heaters for curing and forming (Thekdi 2007). Ovens, Infrared, UV, Electron Beam, Induction, Fuel-Based Dryers, Infrared, Resistance, Microwave are only some of them. In this paper a choice of one of the most common heating systems has been made, the *Resistance Electric Heater (REH)*. It is the simplest and oldest electric-based method of heating with efficiency values close to 100% and maximum temperatures exceeding 3.600 °F. Its robustness, low cost and controllability makes it an ideal candidate for composites curing industrial applications where the indirect REH version (heat transfer from a heating element to the area of interest) is commonly used. In the dominant REH version (Switching) an array of resistor based heating devices produce heat when driven by an electrical current which can take only two values: Zero and a non-zero one (the second value varies depending on the manufacturer). The desired temperature is achieved by regulating how long the circuit is closed (non-zero current) with respect to heat transfer delays and power supply specifications.

Based on the above, a novel algorithm - governed by the structural innovations described in section 2 - that automatically opens or closes the circuit according to the needs has been developed. This decision making module takes into account various parameters of the process like ΔT, Phase change ΔT, heating elements T tolerance, % of the available power used, hardware T limit, circuit reaction time and control cycle time. As a result, the system approximates within an accepted margin of error (±2°C) the target temperature. Furthermore, in case the heat system consists of an array of independent heating devices (as is the case in the experiments presented in the next section) formulating either a constant or a variable temperature profile along the die is possible.

3.4 Measurement interpretation module. As explained in section 2.3 many different interpretations can be made for the same measurement. For this project, direct temperature values acquired real-time are used in solving the Kamal-Sourour differential equation (eq. 5,6) based on the Runge-Kutta numerical method. A publication containing all aspects of this approach (e.g. thermal analysis, kinetic parameters determination by DSC measurements, algorithmic techniques to handle many concurrent measurements) is scheduled as a next step. The result outline is that multiple point sensing can be interpreted simultaneously, resulting this way in a DOC real-time distribution along the curing component. The visual element that simplifies monitoring in this case is an *Intensity graph* (in Labview programming terms) or a graph comprising of pixels that represent the position of the sensors in the material (user selected resolution based on the number of the sensors) whose color change as curing progresses. The module supports any type and number of temperature measurements consequently it can be used not only for point (e.g. thermocouples inserted in a die or the MUT) but also for area sensing (e.g. Infrared Thermo-sensitive camera capturing frames of a visible curing operation which are then used for a DOC calculation) contributing this way to the overall system universality.

3.5 Record module. Detailed records of the process are vital for any monitoring or control approach. Not only for troubleshooting but also for connecting theory with practice or designing the next steps in developing the process. A module to serve these purposes has been developed; It creates a TDMS database that carries high quality recording options such as: Lingual elements recording (parameter names, comments describing the experiment or even the lingual rule base of a Fuzzy system), high observability by categorizing under user-defined groups, conversion to MATLAB (.mat extension) data file and three recording modes: *Periodical recording* (user defined period), *Record when Written* (eliminates unwanted records) and *Manual Record* (saves values only when commanded by the user).

4. EXPERIMENTAL PROCESS

To verify the functionality of the system presented in the previous section, it was tested in a pultrusion process and an optical permeameter. A series of experiments were conducted in both systems and a selection of the most representative are studied in the following sections.

4.1 Pultrusion experiments. The pultrusion line comprises of a 60 position spool base, a sealed injection box for fume restricted impregnation (Fig.5b), a steel die (Fig.5e) and the puller/cutter (Fig.5c). The die has a 32x4x800 mm cavity and proportional steel die holders secure the die and contain the heating elements. A total sum of 16 heating elements inserted in the die holder perpendicularly to the material movement, are the central components of a Switching REH system that ensures the proper heat flux within the cavity. A power board containing the electrical equipment (The Switching REH system current generator, main and peripheral power supplies) and two bus couplers (for EtherCAT based A/D & D/A conversion) are the connecting links between the process and the PC. The feedback loop that conducts the sensor measurement back-propagation has been designed based on the principles of digital control (eq.1-4) presented in section 2.1 and the board has been designed based on the control strategy discussed in section 2.3. Although it can offer pure software or hybrid controllers, for the needs of the current experiment the software controller was used.

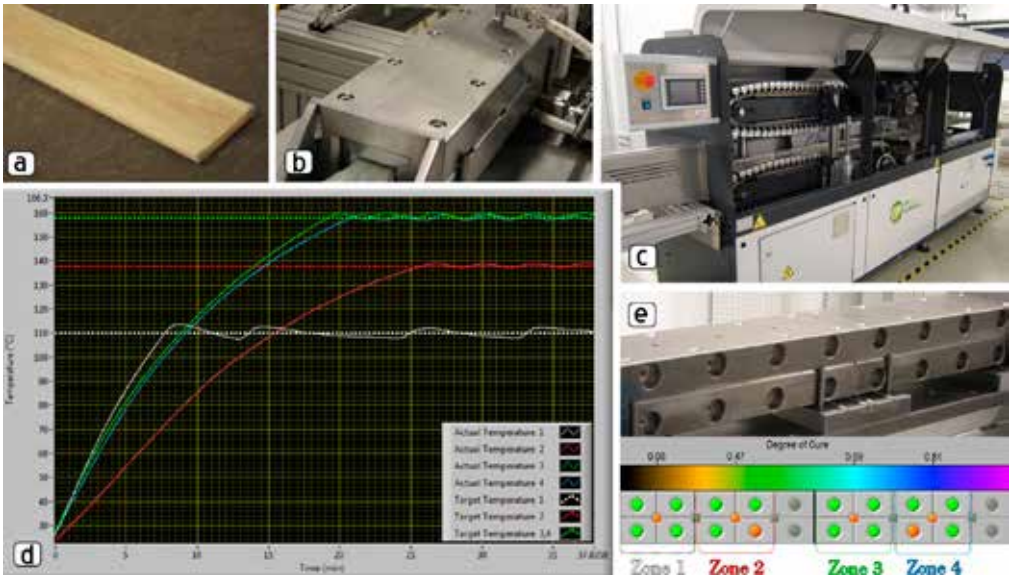

Fig. 5. (a) Pultruded Glass/Epoxy profile, (b) Injection box for resin impregnation, (c) Pulling & Cutting machine, (d) T(t) graph appearing in the monitoring module during a variable T profile (T_{Zone1}=110, T_{Zone2}=138, $T_{Zone3,4}$=158 °C) process. In all cases ripple remains within ±2°C. (e) The actual and virtual pultrusion die, part of the Graphical User Interface with model-based live DOC evaluation.

Each heating element contains a temperature sensor (thermocouple) and furthermore, 8 individual thermocouples are inserted in great proximity to the cavity. All 24 sensors are used to control the heating system based on the controller described in section 3.3. Moreover, real-time DOC information can be deduced by the 8 temperature measurements close to the cavity under

the assumption that the surface of the material proximal to these thermocouples will share the same temperature. For each of these locations the Kamal-Sourour ODE (eq. 5,6) is being solved using the Runge-Kutta 4th order method, giving a real-time evaluation of the DOC distribution along the die (Fig.5e).

The evaluation was based on two experiments, one with constant (158 °C) and one with variable temperature profile (110, 138, 158 °C) while both shared the same pulling speed (0.4 m/minute) and materials (Glass/Epoxy). After establishing a hard-soft connection using the connectivity module, all other user-defined operational parameters were set. The heat controller was set to use approximately 30% of the total available Power, a limit imposed to avoid the steel die temperature induced corrosion. The controlling cycle time was set to 20ms so that optimal synchronization between equipment and software is achieved, while the recording module performed a recording operation of all parameters of interest (heating elements temperatures, cavity temperatures DOC, etc.) every 1 sec.

4.2 Optical permeameter experiments. Unsaturated permeability measurements based on radial injection within a rectangular 300x400x1,5-5mm cavity can be conducted by a custom made permeameter (Fig.6a). The flow front is being captured by a high analysis digital monochromatic camera placed above the transparent lid. To reduce the deflection effect of the transparent lid a weight frame specifically designed not to deter the camera visibility (Fig.6b) was placed on it. A pressure sensor placed in series on the liquid tube returns real time pressure values used to control the injection profile (constant flow or pressure).

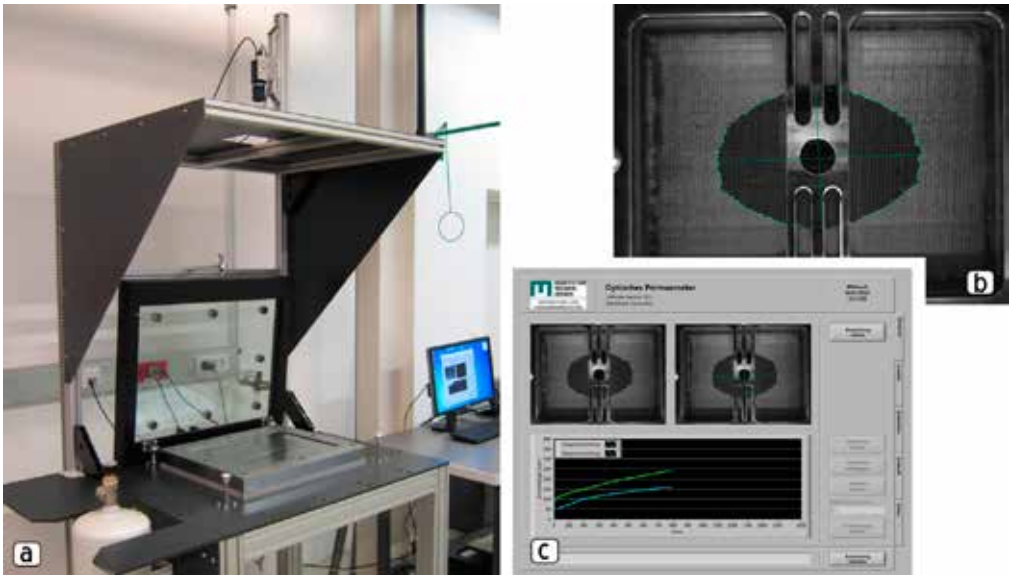

Fig. 6. (a) optical permeameter. (b) Image captured by digital camera. Detectable flow front through the weight frame used to reduce the deflection effect. (c) Graphical user interface for lid & pressure control as well as recording operations.

A permeameter is a rather different case in terms of monitoring & control. As it is not a system to host a manufacturing process, no curing takes place and no heating system is required. Therefore, only the recording and the connectivity modules are common with the pultrusion

line. New modules controlling the injection, hydraulic lid of the mold and interpreting the images were developed in order to create a complete permeameter management interface (Fig.6c). The implementation of the method in a permeability measurement serves the purposes of testing the flexibility of the system in adding new modules and testing the performance of the existing modules in a system different than pultrusion, thus ultimately expanding the cases taken into consideration in the package.

5. RESULTS AND DISCUSSION

The modules showed generally satisfactory results and high compatibility with the processes. All main targets (hard-soft connectivity, effective visual & detailed monitoring, temperature regulation, DOC real-time calculation and data recording) were successfully reached. Assiduous investigation of the module individual operation modes showed accurate and synchronous data representations or interactions.

However the critical point in this study is the universality: The reusability of the method in as many manufacturing methods as possible. Investigation of the proposed method potential in this direction shows that:

- The control system is a combination of two parts: The dependent on the equipment and the independent part. In any given application the equipment defines the first which means that 100% reusability (no alteration from system to system) cannot realistically be achieved.
- The true question lies in finding an efficient way to maximize the independent part of the system, keeping the potential changes from system to system in a few essential-only changes in pre-defined & non-structural elements and parameters.

On that basis, the implementations included in the proposed method succeed in achieving a fully independent structure, leaving specific components, parameters or small code segments to be altered when a different component demands it (something that happened during modifications for the permeameter). Extensive reusability examination reveals that every module has a different *Equipment Dependency* (ED). For example, the Record data module has the lowest ED as compared to other modules, a consequence of the fact that recorded information (e.g. an incoming measurement) is often a value whose origin (different sensory systems) is of no relevance to the recording operation. Similar circumstances emerge in other modules as well and as a next step, further investigation on ways to use these circumstances as means to lower the ED need to be made.

Exploring the opposite extreme, the paradigm that carries the highest ED is the two level interrogation process of the sensor measurements which as explained in section 2.3 is the hard core of process controlling software implementations. Here the dependency is undoubtedly the strongest as equipment specifications define in a great degree the mathematical models used to interpret information. The obvious way to reduce the ED in this case would be to include more case studies and modify appropriately the code in order to achieve the desired simultaneous compatibility with all of them. The proposed structure however, minimizes and simplifies significantly such alterations by (a) introducing independency techniques between modules and (b) by separating the algorithm to structural and non-structural elements that force any changes into a predictable pattern.

6. CONCLUSIONS

This project proposes an algorithm-assisted control system consisting of independent software and hardware modules that contribute in performing usual operations during CMPs: Polymerization progress indication by measurement-based DOC calculation, directing full control to the PC using an EtherCAT based connectivity kit and appropriate associative code, real-time process monitoring, temperature control and run-time data recording are successfully implemented through a control package flexible enough to be used in many different manufacturing processes. This flexibility is a direct result of developing highly adaptive software & hardware structures and keeping all modules independent. The latter is a key point in the proposed method, as more modules serving different purposes and experimental setups are constantly added. Experiments on pultrusion and an optical permeameter showed excellent results in the operations mentioned above while experimenting on an RTM process, including more kinetics models for measurement processing and decision making modules based on Intelligent Control are planned expansions of the project.

ACKNOWLEDGEMENTS

The authors kindly acknowledge the financial support provided by the Bundesministerium für Wirtschaft, Familie und Jugend. They also wish to thank MSc Maximilian Tonejc and MSc Harald Grössing for their contribution in developing the pultrusion graphical user interface and the custom made optical permeameter respectively.

REFERENCES

Binkley, D.; Harman, M.; Hassoun, Y.; Islam, S.; Li, Z. (2010): Assessing the impact of global variables on program dependence and dependence clusters. In *Journal of Systems and Software* 83 (1), pp. 96–107.

Boime, B.; Filleul, D. (2001): Apparatus for manufacturing composite parts produced by resin transfer molding. Patent no. US6,168,408B1.

Chen, X.; Xie, H.; Chen, H.; Zhang, F. (2010): Optimization for CFRP pultrusion process based on genetic algorithm-neural network. In *Int J Mater Form* 3 (S2), pp. 1391–1399.

Czerwinski, F.; Oddershede, L. B. (2011): TimeSeriesStreaming.vi: LabVIEW program for reliable data streaming of large analog time series. In *Computer Physics Communications* 182 (2), pp. 485–489.

Dunn, W. (2005): Fundamentals of industrial instrumentation and process control. New York: McGraw-Hill.

Fink, B.; Don, R. C.; Gillespie, J. W. JR. (1999): Development of a Distributed Direct Current Sensor System for Intelligent Resin Transfer Molding. Ft. Belvoir: Defense Technical Information Center.

Frazão, O.; Oliveira, R.; Dias, I. (2009): A simple smart composite using fiber Bragg grating sensors for strain and temperature discrimination. In *Microw. Opt. Technol. Lett.* 51 (1), pp. 235–239.

Hegg, M. C. (2005): Remote Monitoring of Resin Transfer Molding Processes by Distributed Dielectric Sensors. In *Journal of Composite Materials* 39 (17), pp. 1519–1539.

Heider, D.; Piovoso, M. J.; Gillespie, J. W. (2003): A neural network model-based open-loop optimization for the automated thermoplastic composite tow-placement system. In *Composites Part A: Applied Science and Manufacturing* 34 (8), pp. 791–799.

Hoa, S. V. (2009): Principles of the manufacturing of composite materials. Lancaster, PA: DEStech Publications.

Ibrahim, D. (2006): Microcontroller based applied digital control. Chichester, England, Hoboken, NJ: John Wiley.

Kamal, M. R.; Sourour, S. (1973): Kinetics and thermal characterization of thermoset cure. In *Polym. Eng. Sci.* 13 (1), pp. 59–64.

Lawrence, J. M.; Hsiao, K.; Don, R. C.; Simacek, P.; Estrada, G.; Sozer, E; Murat et al. (2002): An approach to couple mold design and on-line control to manufacture complex composite parts by resin transfer molding. In *Composites Part A: Applied Science and Manufacturing* 33 (7), pp. 981–990.

Lotz, P. (2010): Object-Oriented Messaging, Command Pattern, and State Pattern in LabVIEW.

Luo, Z.; Zhu, H.; Zhao, J. (2012): In Situ Monitoring of Epoxy Resin curing Process Using Ultrasonic Technique. In *Experimental Techniques* 36 (2), pp. 6–11.

Matsuzaki, R.; Kobayashi, S.; Todoroki, A.; Mizutani, Y. (2011): Full-field monitoring of resin flow using an area-sensor array in a VaRTM process. In *Composites Part A: Applied Science and Manufacturing* 42 (5), pp. 550–559.

Mazumdar, S.K. (2002): Composites manufacturing. Materials, product, and process engineering. Boca Raton, Fla: CRC Press.

Mijovic, J.; Yee, C. F. W. (1994): Use of Complex Impedance To Monitor the Progress of Reactions in Epoxy/Amine Model Systems. In *Macromolecules* 27 (25), pp. 7287–7293.

Paraskevopoulos, P. N. (2002): Modern control engineering. New York: Marcel Dekker.

Shin, C.; Lee, S.; Gaudiot, J. (2006): Adaptive dynamic thread scheduling for simultaneous multithreaded architectures with a detector thread. In *Journal of Parallel and Distributed Computing* 66 (10), pp. 1304–1321.

Sundell, H.; Tsigas, P. (2005): Fast and lock-free concurrent priority queues for multi-thread systems. In *Journal of Parallel and Distributed Computing* 65 (5), pp. 609–627.

Thekdi, A. (2008): Improving Process Heating System Performance. A Sourcebook for Industry. Eds. Weinhold et al. 2nd. Washington, D.C, Oak Ridge, Tenn: United States. Dept. of Energy.

Varoglu, S.; Jenks, S. (2011): Architectural support for thread communications in multi-core processors. In *Parallel Computing* 37 (1), pp. 26–41.

Venghaus, H. (2006): Wavelength filters in fibre optics. Berlin, New York: Springer (Springer series in optical sciences, 123).

Yenilmez, B.; Murat S. (2009): A grid of dielectric sensors to monitor mold filling and resin cure in resin transfer molding. In *Composites Part A: Applied Science and Manufacturing* 40 (4), pp. 476–489.

Proceedings of the 34th Risø International Symposium on Materials Science:
Processing of fibre composites – challenges for maximum materials performance
Editors: B. Madsen, H. Lilholt, Y. Kusano, S. Fæster and B. Ralph
Department of Wind Energy, Risø Campus
Technical University of Denmark, 2013

ADHESION IMPROVEMENT OF FIBRES BY CONTINUOUS PLASMA TREATMENT AT ATMOSPHERIC PRESSURE

Yukihiro Kusano, Tom L. Andersen, Bent F. Sørensen, Helmuth L. Toftegaard, Steluta Teodoru, and Charles M. Hansen*

Department of Wind Energy, Section of Composites and Materials Mechanics, Technical University of Denmark, Risø Campus, Frederiksborgvej 399, DK-4000 Roskilde, Denmark
*Jens Bornøs Vej 16, DK-2970 Hørsholm, Denmark

ABSTRACT

Carbon fibres and ultra-high-molecular-weight polyethylene (UHMWPE) fibres were continuously treated by a dielectric barrier discharge plasma at atmospheric pressure for adhesion improvement with epoxy resins. The plasma treatment improved wettability, increased the oxygen containing polar functional groups at the surface, and subsequently improved adhesion to the epoxy and fracture resistance of epoxy composites. Hansen solubility parameters (HSP), quantitatively describing physical interactions among molecules, were measured for the UHMWPE fibre surfaces. The result identifies two distinct types of surfaces in both the plasma treated and the untreated fibres. One type is typical of polyethylene polymers while the other is characteristic of the oxygenated surface at much higher values of HSP.

1. INTRODUCTION

Carbon fibres and ultra-high-molecular-weight polyethylene (UHMWPE) fibres are extensively used for improving the mechanical properties and reducing the weight of fibre reinforced polymer (FRP) composites. In order to achieve high mechanical strength of the FRP composites, fibre distribution, alignment, damage, and interface between fibre surfaces and a polymer matrix need to be understood and properly controlled. In particular strong adhesion between the fibre surfaces and the polymer matrix is one of the key issues for improving the longitudinal tensile strength of FRPs (Dilsiz 2000). An epoxy resin is often preferred for the host matrix due to excellent electrical properties, high mechanical strength, high resistance against aging/hydrolysis, and high bond strength to many polymer materials (Jones 1991). However, the non-polar nature of many fibres means that they are difficult to wet and almost impossible to chemically bond to generally used polymer matrices. Adhesion can be improved by surface treatment of many fibres, mainly by oxidation of the surfaces, introducing reactive polar functional groups onto the fibre surfaces.

Extensive research has been devoted to the surface treatment of carbon fibres and UHMWPE fibres in order to improve their bonding to the polymer matrix. Among various surface treatment techniques, plasma treatment is attractive due to its environmental friendliness and high treatment efficiencies without affecting the textural characteristics of the bulk material. These plasmas are often generated at low pressures. Plasma surface modification at low pressures, however, suffers from the drawbacks that they require expensive vacuum systems, and methods are only well-developed for batch or semi-batch treatments. To overcome these drawbacks an atmospheric pressure plasma treatment system can be used. This not only avoids the need for vacuum equipment but also permits the treatment of large objects, and continuous treatment on production lines (Kogoma, Kusano and Kusano 2011).

After the plasma treatment, there is a major change in the surface morphology accompanied by the inclusion of large amounts of oxygen, chain scission and local elimination of crystallinity. Surface characterization of the treated fibres is important in order to understand the effect of the treatment and the mechanism of the interaction with the polymer matrix. X-ray photoelectron spectroscopy (XPS) is a good candidate and widely used for this purpose, since it is surface-sensitive, and provides the quantitative information on atomic composition and chemical structure at the surface. The noticeable disadvantage of the XPS is that it is a localized analysis and does not give information on the uniformity and the overall character of the surfaces by a single measurement. XPS cannot tell exactly where the analysis took place, and in order to obtain a full understanding, one has to repeat the expensive and time-consuming analyses and then rely on statistical methods. On the other hand, Hansen solubility (cohesive energy) parameters (HSP) can be used to characterize the surface and can give the macroscopic information (Kusano, Teodoru and Hansen 2011). Here HSP are thermodynamic quantities that can quantitatively describe physical interactions among molecules. The HSP consist of three parameters; δ_D (dispersion), δ_P (polar) and δ_H (hydrogen bonds). More detailed discussions of the HSP concept are found elsewhere (Hansen 2007). Matching the HSP of fibres and matrix polymer will optimize the physical adhesion (Teodoru et al. 2009). Therefore, it is important to know the HSP of the oxygenated surfaces of the fibres. It is reported that HSP of an epoxy resin are δ_D, δ_P, and δ_H being 20.0, 10.0, and 8.0, while those of oxidized, unsized, chopped carbon fibres are δ_D, δ_P, and δ_H being 21.3, 8.7, and 11.5, all in $MPa^{½}$, respectively, and that they are very similar, thus contributing to good physical adhesion in such systems (Launay, Hansen and Almdal 2007).

In the present study, carbon fibres (Kusano, Andersen and Michelsen 2008, Kusano et al. 2012) and UHMWPE fibres (Teodoru et al. 2009, Kusano et al. 2011) were continuously treated by a dielectric barrier discharge (DBD) plasma at atmospheric pressure. Adhesive properties of treated and untreated fibres were evaluated and the fibre surfaces were characterized.

2. EXPERIMENTAL METHODS

Poly(acrylonitrile) (PAN) based unsized electrochemically-treated carbon fibres (TOHO TENAX HTA5001, 800tex) were used without pre-cleaning. UHMWPE fibres (1300 filament yarn with a tex number of 145, 12 μm diameter of a monofilament) were purchased from Goodfellow, UK, and were ultrasonically cleaned in acetone twice for 5 minutes and in methanol for 5 minutes to remove the silicon containing contaminants from the surfaces. After the cleaning, the Si content at the UHMWPE fibre surface was typically less than 1 atomic % measured by XPS.

The atmospheric pressure DBD was used to continuously treat fibres as shown in Figure 1. The feed speed of carbon fibres was 150 or 300 cm $minute^{-1}$, corresponding to 2- or 1-s treatment,

while that of UHMWPE fibres was 10 cm minute^{-1}. The high feeding speeds were chosen for carbon fibres so as to manufacture fibre reinforced composites which require several hundred metre carbon fibres. The DBD consists of parallel plate water cooled metal electrodes (50 mm × 50 mm) covered with alumina plates (100 mm × 100 mm × 3 mm). The DBD was generated by an alternating current power supply (Generator 6030. SOFTAL Electronic GmbH). The driving frequency was approximately 40 kHz and the average power was approximately 100-110 W. He gas was fed into the DBD at a flow rate of 1 L minute^{-1}. It is noted that contamination and the leakage of N_2, O_2, and H_2O from ambient air to the discharge is often inevitable, resulting in the introduction of oxygen and/or nitrogen at the exposed surfaces in a discharge, even if no oxygen or nitrogen containing gas is apparently supplied. In fact such a leakage sometimes plays an important role in oxidizing and nitriding the surface. The reproducibility of the treatment associated with the level of the leakage was indirectly ensured by confirming that the measured voltage and power were reproducible under the same conditions.

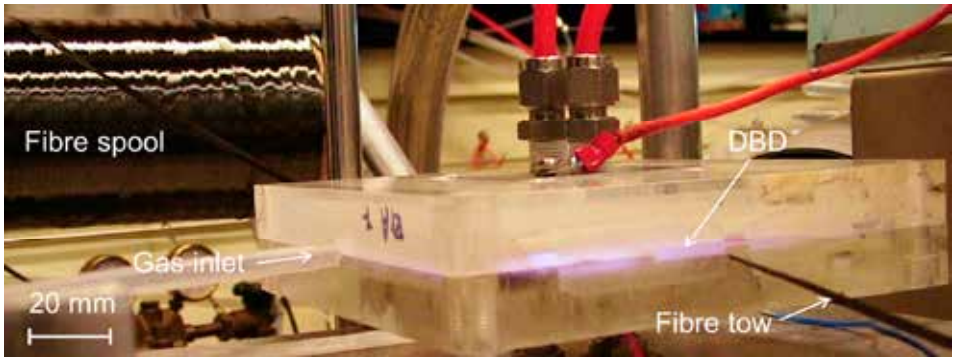

Figure 1. The atmospheric pressure DBD plasma treating carbon fibres continuously.

Carbon fibre reinforced epoxy (CFRE) plates for double cantilever beam (DCB) specimens were manufactured by filament winding followed by vacuum infusion, using untreated, 1- and 2-s plasma-treated carbon fibres with an epoxy resin (Prime 20. SP Systems) (Kusano et al. 2008). The thickness of the CFRE plate was 2 mm. Steel beams were glued to the outside of each composite plate with epoxy adhesive (Scotch Weld 460). The DCB specimens were loaded by pure bending moments and the fracture resistance was calculated using the J integral. The fibre adhesion of the CFRE plates was evaluated using fracture resistance values at steady state.

Another simple mechanical test was performed for the preliminary evaluation of the plasma treatment effect on adhesion of UHMWPE fibres with another epoxy (Strong Epoxy Rapid 2806, Casco). The 200-mm long fibres were aligned in parallel on a metal plate. Approximately 3-mm thick mixture was applied onto the plate so that it covered the fibre surfaces completely. After curing 90º peeling test was performed to evaluate the adhesive property of the fibres with the epoxy by gently pulling the fibres from the epoxy composites manually (Teodoru et al. 2009).

XPS was performed for the measurement of the oxygen/carbon (O/C) ratio of the carbon-fibre and UHMWPE-fibre surfaces using a SPECS Sage 100 and K-Alpha, ThermoFischer Scientific, respectively.

The basis of the HSP characterizations was to determine differences in interactions when fibre samples were immersed in a suitable set of test solvents. The fibre samples used for these characterizations were taken from a short piece of a much longer fibre either as supplied or after

plasma treatment. Interactions with the fibres were visually rated based on the extent to which the filaments were removed from each other thus increasing their apparent volume. The scale used for the rating was "1" for strongest interaction to "6" for very little interaction (Kusano et al. 2011). The interaction evaluated was the extent to which the fibres expanded in the vials. The fibre samples immersed in the solvents were stored at room temperature for at least 20 days after which there was no further change. 20 mg sample was placed in 13 mL of liquid in small vials such that the height of the liquid was approximately 5 cm. The fibres expanded to completely fill the vials when the interactions were strongest.

3. RESULTS AND DISCUSSION

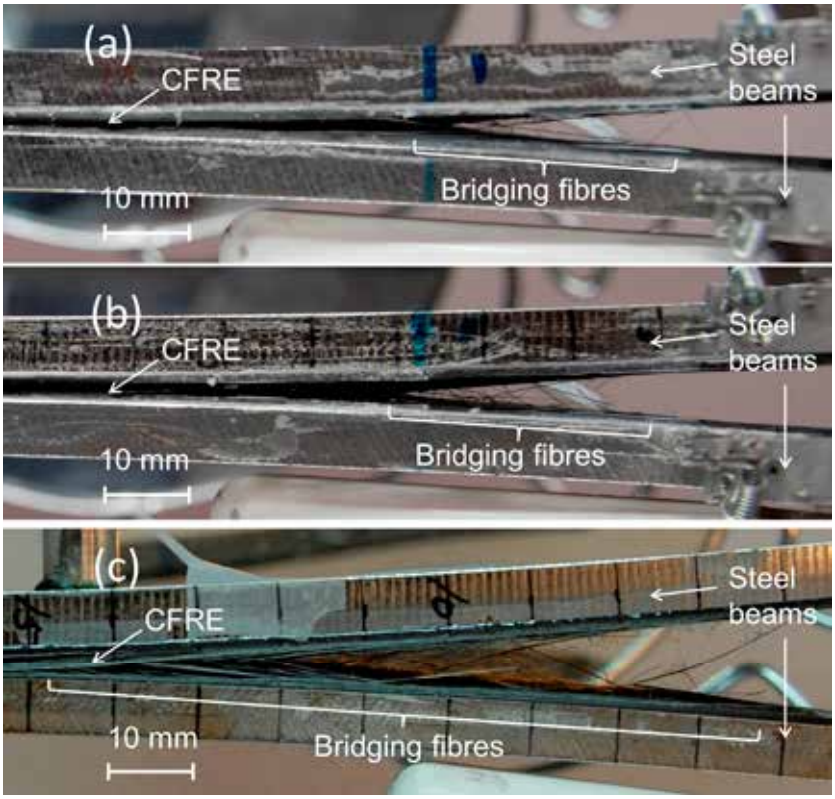

Figure 2. Photos of CFRE plates during the adhesion test. Untreated (a), 1-s (b) and 2-s (c) plasma treated.

Figure 2 shows photos of representative DCB specimens during the fracture mechanics test. All specimens show fibre bridging, which is a known toughening mechanism. The number of bridging fibres increases as the treatment time is longer. The fracture resistance of the CFRE with untreated and 1-s treated carbon fibres initially increased as the end-opening increased, and approached steady-state values. The CFRE with 1-s treated ones shows higher steady-state values (1700-2200 J m^{-2}) than those of the untreated ones (1400-1800 J m^{-2}) (Kusano et al. 2012). The fracture energy of the 2-s treated specimens steadily increased as the end-opening increased (1700-2400 J m^{-2} at the end opening of approximately 5 mm). It is therefore concluded that the plasma treatment improved the fracture resistance of the CFRE composites,

and that the longer treatment further improved them.

It is tempting to speculate that since the number density of bridging fibres increases as the treatment time is longer, the increase in macroscopic fracture resistance is due to a change in the adhesion properties of the fibre/matrix interface (Kusano et al. 2008, 2011).

The simple adhesion test for the UHMWPE fibres indicated that the untreated fibres were easily pulled off from the epoxy, showing a low adhesion between the fibres and the epoxy. The plasma treated fibres showed high interaction with the epoxy and were difficult to pull off (Teodoru et al. 2009).

The major effect of the conventional electrochemical treatments on carbon fibres for fibre/resin adhesion is believed to be the removal of weakly bound crystallites at the fibre surfaces, while the number of functional groups introduced onto the fibre surfaces by those treatments is too small to have a significant effect (Farrow and Jones 1994). They are less effective when they are applied to highly graphitised surfaces (Montes-Morán, Martínez-Alonso, Tascón and Young 2001). It is therefore interesting to know whether the plasma treatment can effectively oxygenate the fibre surfaces. The elemental composition of the carbon fibre surfaces before and after the plasma treatments was analyzed using XPS. The typical O/C ratio at the carbon fibre surface before plasma treatment is approximately 0.16, while it increases to approximately 0.18 after the treatment for 1 or 2 s. On the other hand, the O/C ratio of untreated UHMWPE fibre is 0.01, while that of the treated one is approximately 0.15, indicating that plasma treatment can efficiently oxidize the UHMWPE surface.

HSP correlations showed that there were two distinct regions of interaction on the untreated UHMWPE fibres. There was one region at high δ_P and moderately high δ_H characteristic of oxygenated species. The strong interaction, that is, a similar and clear effect of separating the fibres, is found in three solvents with very close HSP, N,N-Dimethyl formamide, N,N-Dimethyl acetamide, and N-Methyl-2-pyrrolidone. The oxygenated surface has δ_D, δ_P, and δ_H equal to 15.8, 13.4, and 6.0, all in $MPa^{½}$. There is a second distinct region characteristic of general polyethylene (PE) at higher δ_D and low δ_P and δ_H shown by the strong interaction with aromatic solvents. This PE surface has δ_D, δ_P, and δ_H equal to 18.0, 1.2, and 1.4, all in $MPa^{½}$. These HSP for the PE-type surface are based on literature values and could not be confirmed in this study because of too few data points in this region (Kusano et al. 2011).

Strong aromatic-solvent interaction with the UHMWPE fibres is characteristic of interaction with PE surfaces. This was also found for the plasma treated fibres. The data for benzene, toluene, and trimethylbenzene have therefore been deleted in the further analysis, since the primary interest here is the nature of the oxygenated surfaces and the simultaneous consideration of the two distinctly different surfaces only leads to a confusing result from the optimization software used to evaluate the HSP. There is a very good correlation with a high data fit for the strong interaction of solvents with the oxygenated surface of the plasma treated UHMWPE fibres. This correlation confirms a region with high δ_P and moderately high δ_H on the surface of the plasma treated UHMWPE fibres. For the plasma treated surface, this region is characterized by δ_D, δ_P, and δ_H being 16.5, 15.3, and 8.2, all in $MPa^{½}$. The differences between these HSP and those of the surface on the untreated samples are not large. However, the HSP of the treated fibres is higher than those of the untreated ones, indicating that the treated fibres contain more oxygen in basically the same functional groups of the untreated surfaces (Kusano et al. 2011).

4. CONCLUSIONS

Carbon fibres and UHMWPE fibres were continuously treated by atmospheric pressure DBD plasma for adhesion improvement with epoxy resins. Plasma treatments oxygenated the fibre surfaces, significantly increased the adhesion between fibres and epoxy resins and enhanced the fracture resistance of the fibre/epoxy composites. HSP characterizations appeared to be a useful technique to evaluate the potential fibre surfaces for wetting and physical adhesion.

ACKNOWLEDGEMENTS

This work was supported partly by a grant from the Danish Technical Research Council (STVF. Grant no. 26-04-0251) and the Danish Centre for Composite Structure and Materials for Wind Turbines (DCCSM), grant no. 09-067212, from the Danish Strategic Research Council (DSF).

REFERENCES

Dilsiz, N. (2000). Plasma surface modification of carbon fibers: a review. J. Adhesion Sci. Technol. 14(7), 975-987

Farrow, G.J., and Jones, C. (1994). The effect of low power nitrogen plasma treatment of carbon fibres on the interfacial shear strength of carbon fibre/epoxy composites. J. Adhesion 45, 29-42.

Hansen, C.M. (2007). Hansen solubility parameters: A user's handbook. CRC Press.

Jones, C. (1991). The chemistry of carbon fibre surfaces and its effect in interfacial phenomena in fibre/epoxy composites. Comp. Sci. Technol. 42(1-3), 275-298.

Kogoma, M., Kusano, M., and Kusano, Y. (ed.) (2011). Generation and applications of atmospheric pressure plasmas. Nova Science Publishers, Inc.

Kusano, Y., Andersen, T.L., and Michelsen, P.K. (2008). Atmospheric pressure plasma surface modification of carbon fibres. J. Phys. Conf. Series. 100, 012002.

Kusano, Y., Mortensen, H., Teodoru, S., Drews, J.M., Andersen, T.L., Sørensen, B.F., Rozlosnik, N., Goutianos, S., Kingshott, P., Mitra, S., Leipold, F., Almdal, K., Michelsen, P.K., and Bindslev, H. (2012). Plasma surface modification of glassy carbon plates, carbon fibres and UHMWPE fibres for adhesion improvement. in "Fiber-reinforced composites" Nova Science Publishers, Inc. 251-296.

Kusano, Y., Teodoru, S., and Hansen, C.M. (2011). The physical and chemical properties of plasma treated ultra-high-molecular-weight polyethylene fibers. Surf. Coat. Technol. 205 2793-2798.

Launay, H., Hansen, C.M., and Almdal, K. (2007). Hansen solubility parameters for a carbon fiber/epoxy composite. Carbon. 45, 2859-2865.

Montes-Morán, M.A., Martínez-Alonso, A., Tascón, J.M.D., and Young, R.J. (2001). Effects of plasma oxidation on the surface and interfacial properties of ultra-high modulus carbon fibres. Composites A 32, 361-371.

Teodoru, S., Kusano, Y., Rozlosnik, N., and Michelsen, P.K. (2009). Continuous plasma treatment of ultra high molecular weight polyethylene (UHMWPE) fibres for adhesion improvement. Plasm. Proc. Polym. 6, S375-S381.

Proceedings of the 34th Risø International Symposium on Materials Science:
Processing of fibre composites – challenges for maximum materials performance
Editors: B. Madsen, H. Lilholt, Y. Kusano, S. Fæster and B. Ralph
Department of Wind Energy, Risø Campus
Technical University of Denmark, 2013

VOLUMETRIC COMPOSITION IN COMPOSITES AND HISTORICAL DATA

Hans Lilholt and Bo Madsen

Composites and Materials Mechanics, Department of Wind Energy,
Technical University of Denmark, Risø Campus,
DK-4000 Roskilde, Denmark

ABSTRACT

The obtainable volumetric composition in composites is of importance for the prediction of mechanical and physical properties, and in particular to assess the best possible (normally the highest) values for these properties. The volumetric model for the composition of (fibrous) composites gives guidance to the optimal combination of fibre content, matrix content and porosity content, in order to achieve the best obtainable properties. Several composite materials systems have been shown to be handleable with this model. An extensive series of experimental data for the system of cellulose fibres and polymer (resin) was produced in 1942 – 1944, and these data have been (re-)analysed by the volumetric composition model, and the property values for density, stiffness and strength have been evaluated. Good agreement has been obtained and some further observations have been extracted from the analysis.

1. INTRODUCTION

The volumetric composition in composites is of importance for their performance and it includes the fiber, matrix and porosity content. The interrelation between these parameters has been described and evaluated in a series of papers, partly by the present authors, (Madsen and Lilholt 2002, Madsen, Thygesen and Lilholt 2007, Madsen, Thygesen and Lilholt 2009). The models are based on a maximum obtainable fibre *volume* content, which can be related to the packing ability of a fibre assembly under a given pressure (applied typically during processing of the composite). At fibre contents below the maximum the composite can be fully compacted to, ideally, no porosity, while at fibre contents above the maximum the composite will (inevitably) contain structural porosity caused by the inability of the matrix content to fill the voids in the fully compacted fibre assembly. The optimum composition is the one where the fibre content just equals the maximum value (under the given pressure), and the matrix content is just sufficient to fill the voids of the fibre assembly. This optimum composition corresponds to the best obtainable properties, such as (highest) density, stiffness and strength. The modeling of these aspects is based on the fibre *weight* fraction of the composite, which can be varied from

zero (pure matrix) to one (only fibres, in an assembly).

The model has been developed in the above papers, and illustrated by data for the volumetric composition, as well as by data for density and stiffness, for a series of composites with different fibres, matrices and fibre orientations. The effect of (processing) pressure on the volumetric composition is also studied in some cases. A recent closer study of the effect of (processing) pressure on the volumetric composition is given in the paper Madsen (2013) in these proceedings.

In composites the traditional view is that the fibres give a reinforcement of an otherwise weak (less stiff) matrix, and therefore the concept starts with a pure matrix and the fibres are added to this matrix. It is thus natural to use the (added) fibre fraction as a parameter for the composition of the composite. This approach is taken in the above analyses, and in particular the fibre *weight* fraction is used as the guiding parameter.

Actually, in most composites the fibres are the strength- and stiffness- dominating constituents, and it might therefore also be argued that the starting position is the fibres, normally in the form of some sort of preform (aligned bundle, aligned tape, bi-directional woven fabric, randomly oriented fibre mat e.g. paper, or other geometrical arrangements). Then *matrix is added* to the fibre assembly to allow concerted action of the fibres, and to keep the fibres together in the form of a solid (composite).

This thinking and approach was taken (unknown to the present authors) many years ago (1942 – 1944) by a research group under the British Ministry of Aircraft Production. During the second world war the aircrafts were to a large extent based on natural materials like wood, glue, and canvas, and a very large number of successful Mosquito aircrafts were manufactured (Gordon 1968). The focus of the research was on "the preparation of reinforced plastics from paper and phenol-formaldehyde resin" (Cox and Pepper 1944). The research was carried out jointly by the Engineering Department, National Physical Laboratory, and the Chemical Research Laboratory in England, thus including both engineering and chemical knowledge and expertice. It is interesting to note the threefold objects of the research: " (a) to study the effect of method of manufacture on the mechanical properties of phenolic paper-base plastics, (b) to assess the relative contributions of the resin and the paper-fibres, and (c) to provide information whereby improvements in existing materials might be affected." (Cox and Pepper 1944). It is also interesting to note one of the conclusions of this first paper, as quoted in the abstract: "The optimum resin content is that which just fills the air voids in the paper at any given pressure. This optimum resin content is indicated by a maximum in the density – resin content curve". In the second paper (Pepper and Barwell 1944) the studies are extended with "attempts to elucidate further the dependence of the mechanical properties on such factors as resin content, voids in the paper, and particularly on the pressure applied during bonding". In the abstract the conclusions are quoted: "…… although the tensile strength of reinforced plastics increases with the proportion of the stronger component, the fibre, the improvement is sharply limited by the need to fill all the voids in the paper; when the resin content is insufficient to fill the voids, the strength of the material is seriously reduced. It is demonstrated that the main function of the pressure applied during bonding is to reduce the voids in the paper ……".

The present evaluation is aimed at analyzing the extensive experimental results of this war-time research effort in the light of the concepts introduced in the above modern-time research on volumetric composition of fibre containing composites. The focus will be on the following elements of the materials and of the model: (i) volumetric composition, (ii) density, (iii) stiffness, (iv) strength, (v) compaction of paper/fibre assemblies.

2. BASIC MATERIALS AND PARAMETERS

The research group of Ministry of Aircraft Production used papers of various types, and phenol-formaldehyde resin, which was used either in an alcoholic solution or in a aqueous solution for impregnation of the paper. The basic materials are listed in table 1.

Table 1. Basic materials.

Paper	Manila Hemp paper
	Kraft paper
	High Density Kraft paper
Resin	Phenol-Formaldehyde, alcoholic solution (PF alc)
	Phenol-Formaldehyde, aqueous solution (PF aqu)

The preparation procedure is through four steps: (i) stacking of paper sheets, (ii) impregnation of paper with phenol-formaldehyde solution, (iii) drying of the impregnated paper, (iv) pressing of the laminated sheets. The pressing is typically done with pressure of 2000 or 2500 lbs per sq.in., at a temperature of 145 ^{o}C, and for a time 30 minutes.

The stacking of the paper sheets is done in two different ways. For Manila hemp paper the sheets are stacked with same orientation for all sheets. Although nominally with random fibre orientation, the production of paper sheets induces some alignment in the "machine" direction. The data for tensile strength in the "machine" direction and in the "cross-wire" direction, quoted by Cox and Pepper (1944) in their table 1, are used to calculate an effective fibre orientation factor in the "machine" direction for these composites (Lilholt and Bjerre 1997), the factor becomes $\eta = 0.389$. For Kraft paper and for High density kraft paper, the paper sheets are "crossed", such that the composite (on average) has random fibre orientation, and the fibre orientation factor for this case is $\eta = 0.333$.

The stiffness and strength data are quoted in imperial units in the original tables and diagrams (Cox and Pepper 1944, Pepper and Barwell 1944), and the conversion factors to SI units are the following:

stiffness in 10^6 lbs per sq.in.: 1×10^6 psi = 7.03 GPa

strength in tons per sq.in.: 1 tsi = 15.75 MPa

The composition of the different composites are quoted in resin weight fraction (percent) for data and diagrams on stiffness and on strength, while the composition is quoted in resin volume fraction (percent) for data and diagrams on density, (Cox and Pepper 1944, Pepper and Barwell 1944). The modern-time models are based on *fibre weight* fraction and the conversions are the following:

$$W_f = 1 - W_m$$

$$W_f = 1 / [\, 1 + (V_m / V_f) \cdot (\rho_m / \rho_f) \,]$$

where W is weight fraction, V is volume fraction and ρ is density, and f and m are fibre and matrix, respectively. The second equation is valid for no porosity in composites.

The evaluation will be made by presenting (the copy of) the historical diagrams and comparing them directly with the analysis and diagrams according to the volumetric composition model. In

the historical diagrams the authors have analysed their data by trend lines.

3. EXPERIMENTS AND MODELS

The experimental data are presented by their original diagrams, which include the (many) experimental points. The data points are read off the diagram in their original (imperial) units and the data are then converted to SI-units. This allows the data to be plotted according to the volumetric composition model, in the form used by the present authors, examples of "modern" data plotted in this manner are given in Madsen (2013) in these proceedings.

3.1. Density of Manila hemp paper / phenol-formaldehyde (alcoholic). These data are presented in Fig. 1a, which is copied directly from Cox and Pepper (1944) as their figure 3, and gives density in g/cm^3 as function of resin content by volume in percent. The 15 data point are converted to SI units and plotted as red points in Fig. 1b. With their paper fibre (cellulose) density of 1.53 g/cm^3, (which agrees with their linearly extrapolated trend line to zero resin content), and their phenol-formaldehyde density of 1.27 g/cm^3, the maximum fibre volume fraction $V_{f,max}$ is estimated to be 0.70, with the corresponding fibre weight fraction at transition $W_{f,trans}$ = 0.738. With these parameters the volumetric composition model curve is calculated and is plotted as the blue curve in Fig. 1b.

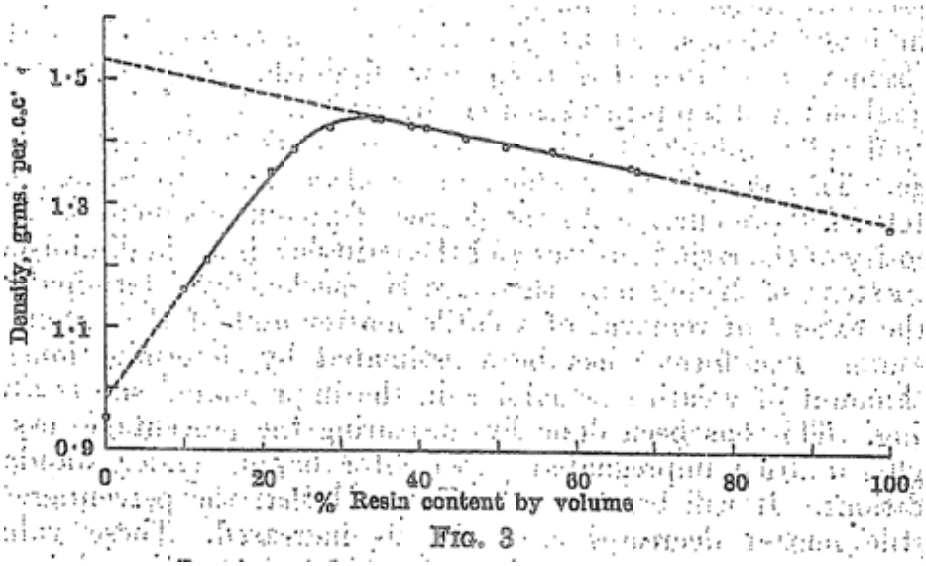

Fig. 1a. Density of Manila hemp paper / phenol-formaldehyde (alcoholic) in g/cm^3 as a function of resin content by volume in percent (Cox and Pepper 1944).

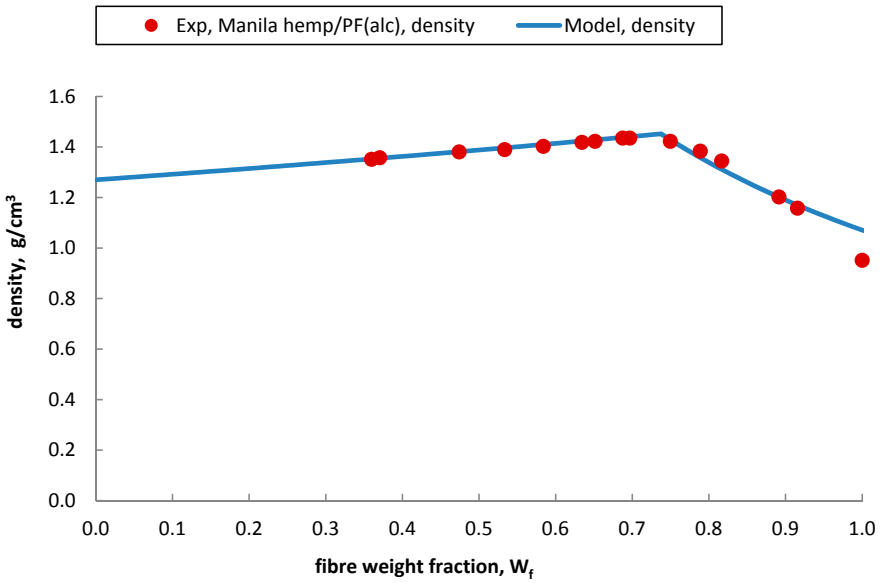

Fig. 1b. Density experimental data re-plotted as a function of fibre weight fraction, model calculated for $V_{fmax} = 0.70$.

The agreement of the experimental data with the model curve is satisfactory, especially at low fibre contents. The density value at $W_f = 1$ corresponds to the density of the dry (containing no matrix) fibre assembly compacted at the given pressure, in this case the experimental value is 0.952 g/cm^3, while the model implies a value of 1.084 g/cm^3. This probably indicates a situation where the fibre assemblies are compacted to higher density which is maintained during composite fabrication, while (part of) the compaction is released after compaction of a dry fibre assembly.

3.2. Density of High density kraft paper / phenol-formaldehyde (aqueous). These data are presented in Fig. 2a, which is copied directly from Pepper and Barwell (1944) as their figure 1, and gives density in g/cm^3 as function of resin content by volume in percent. The 12 data point are converted to SI units and plotted as green points in Fig. 2b. With their paper fibre (cellulose) density of 1.53 g/cm^3 and their phenol-formaldehyde density of 1.27 g/cm^3, the maximum fibre volume fraction $V_{f,max}$ is estimated to be 0.82, with the corresponding fibre weight fraction at transition $W_{f,trans}$ = 0.846. With these parameters the volumetric composition model curve is calculated and is plotted as the blue curve in Fig. 2b.

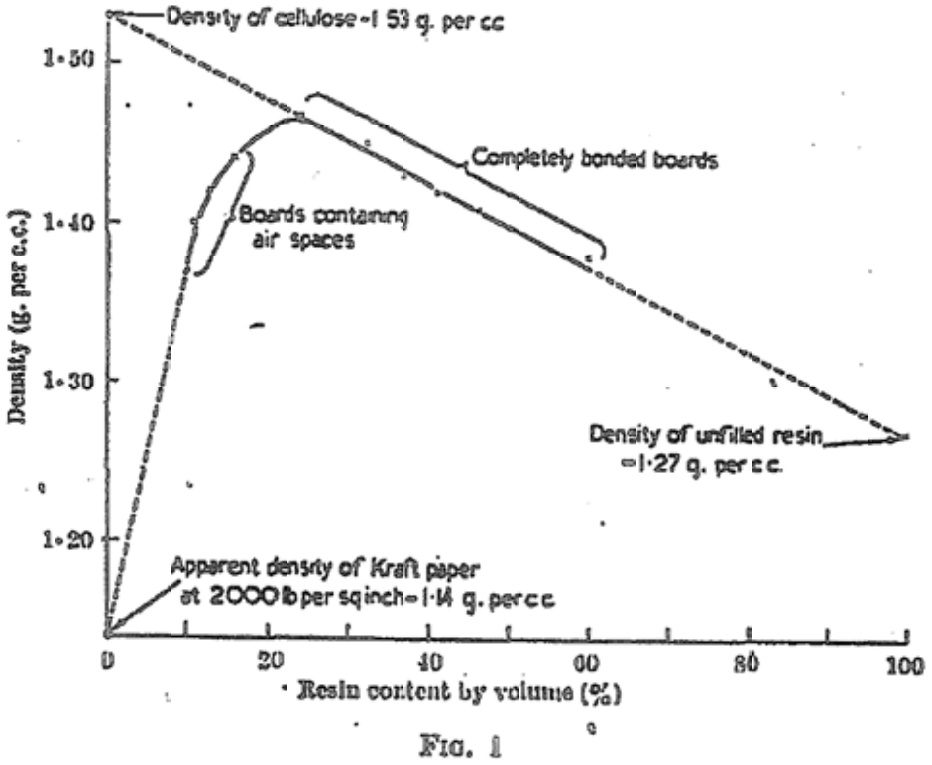

Fig. 2a. Density of High density kraft paper / phenol-formaldehyde (aqueous) in g/cm^3 as a function of resin content by volume in percent (Pepper and Barwell 1944).

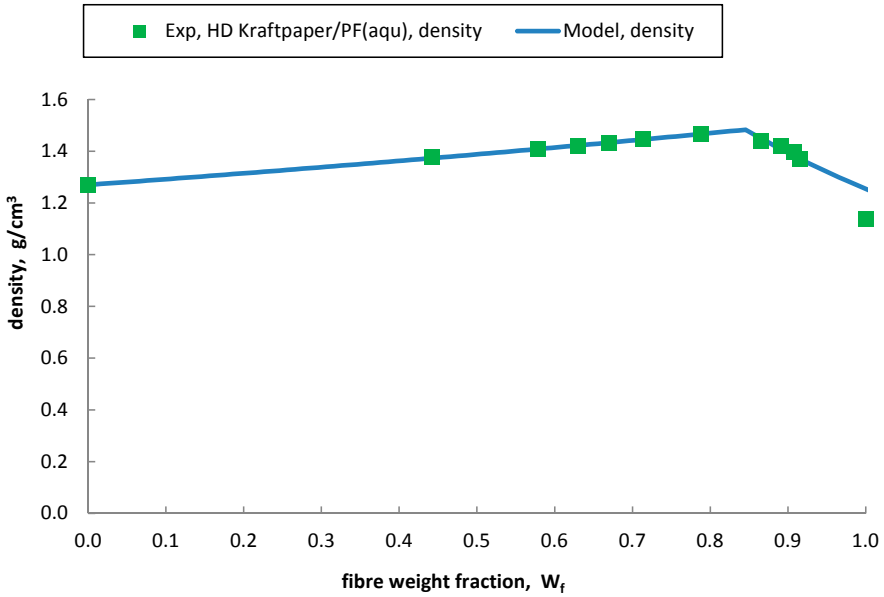

Fig. 2b. Density experimental data re-plotted as a function of fibre weight fraction, model calculated for $V_{fmax} = 0.82$.

The agreement of the experimental data with the model curve is satisfactory, especially at low fibre contents. The density value at $W_f = 1$ corresponds to the density of the dry (containing no matrix) fibre assembly compacted at the given pressure, in this case the experimental value is 1.140 g/cm^3, while the model implies a value of 1.260 g/cm^3. This probably indicates a situation where the fibre assemblies are compacted to higher density which is maintained during composite fabrication, while (part of) the compaction is released after compaction of a dry fibre assembly.

3.3. Stiffness of Kraft paper / phenol-formaldehyde (aqueous). These data are presented in Fig. 3a, which is copied directly from Pepper and Barwell (1944) as their figure 16, and gives stiffness in 10^6 lbs per sq.in. as function of resin content by weight in percent. The 7 data point are converted to SI units and plotted as green points in Fig. 3b. The calculation of the composite stiffness is made by the modified rule of mixtures (Madsen et al 2009):

$$E_c = (\eta \cdot V_f \cdot E_f + V_m \cdot E_m) \cdot (1 - V_p)^n \quad (1)$$

where E is stiffness, V is volume fraction, and f is fibre, m is matrix and p is porosity, η is the fibre orientation factor, and n is the exponent for porosity effect. The composites are made with "crossed" paper sheets, so the fibre orientation factor is $\eta = 0.333$, as described in section 2. The exponent n is set to 2.0, as used by Madsen et al (2009).

With the phenol-formaldehyde stiffness of 4.8 GPa (experimental value), the paper fibre (cellulose) stiffness is estimated to be 62 GPa and the maximum fibre volume fraction $V_{f,max}$ is estimated to be 0.77, with the corresponding fibre weight fraction at transition $W_{f,trans} = 0.801$. With these parameters the volumetric composition model curve is calculated and is plotted as the blue curve in Fig. 3b.

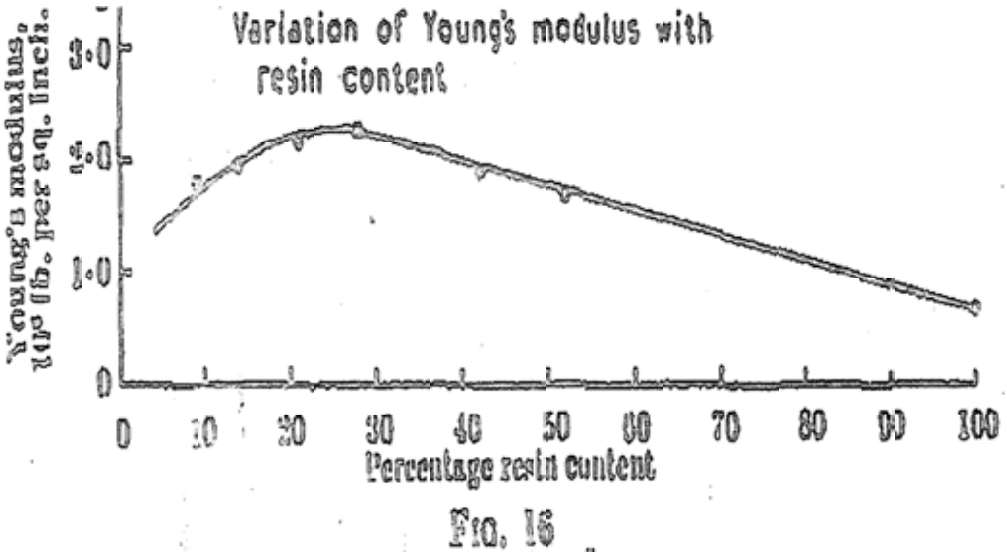

Fig. 3a. Stiffness of Kraft paper / phenol-formaldehyde (aqueous) in 10^6 lbs per sq.in. as a function of resin content by weight in percent (Pepper and Barwell 1944).

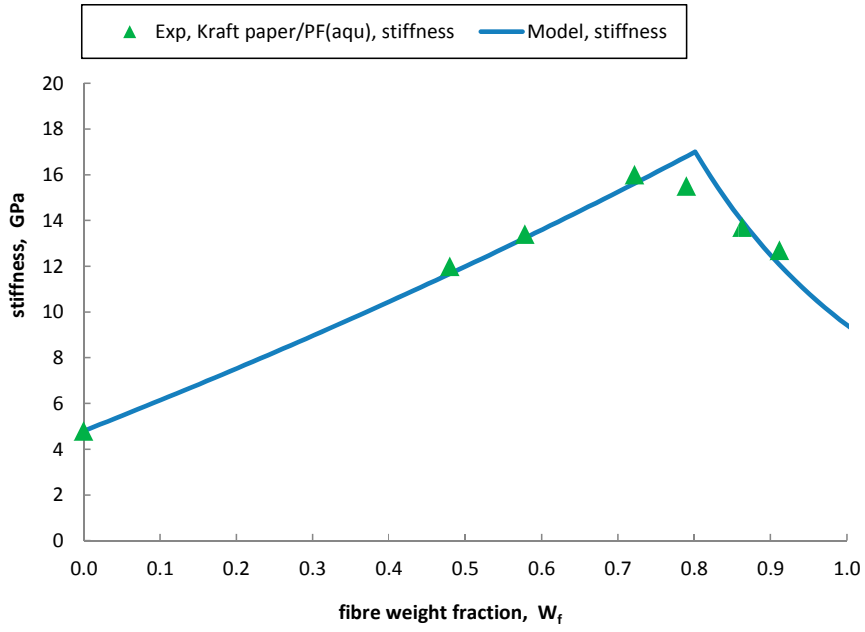

Fig. 3b. Stiffness experimental data re-plotted as a function of fibre weight fraction, model calculated for V_{fmax} = 0.77, fibre stiffness 62 GPa, matrix stiffness 4.8 GPa, fibre orientation factor 0.333, porosity exponent 2.0.

The agreement of the experimental data with the model curve is satisfactory. The stiffness value at $W_f = 1$ corresponds to the stiffness of the dry (containing no matrix) fibre assembly, i.e. the paper sheets, compacted at the given pressure, in this case the model implies a value of 9.65 GPa. This value might be compared to an experimental value for stiffness of the relevant Kraft paper sheets, (no data are available).

3.4. Stiffness of High density kraft paper / phenol-formaldehyde (aqueous). These data are presented in Fig. 4a, which is copied directly from Pepper and Barwell (1944) as their figure 4, and gives specific stiffness in km, as function of resin content by weight in percent. The specific stiffness is the stiffness divided by density, therefore the density data of Pepper and Barwell (1944) figure 1 are implied in the conversion to stiffness. The 9 data point are converted to SI units and plotted as green points in Fig. 3b. The calculation of the composite stiffness is made by the modified rule of mixtures (Madsen et al 2009), as eq. (1).

The composites are made with "crossed" paper sheets, so the fibre orientation factor is $\eta = 0.333$, as described in section 2. The exponent n is set to 2.0, as used by Madsen et al (2009).

The experimental value of phenol-formaldehyde stiffness is 3.5 GPa, the best fit of all data points is obtained with a matrix stiffness of 4.0 GPa, the paper fibre (cellulose) stiffness is estimated to be 63 GPa and the maximum fibre volume fraction $V_{f,max}$ is estimated to be 0.78, with the corresponding fibre weight fraction at transition $W_{f,trans} = 0.810$. With these parameters the volumetric composition model curve is calculated and is plotted as the blue curve in Fig. 4b.

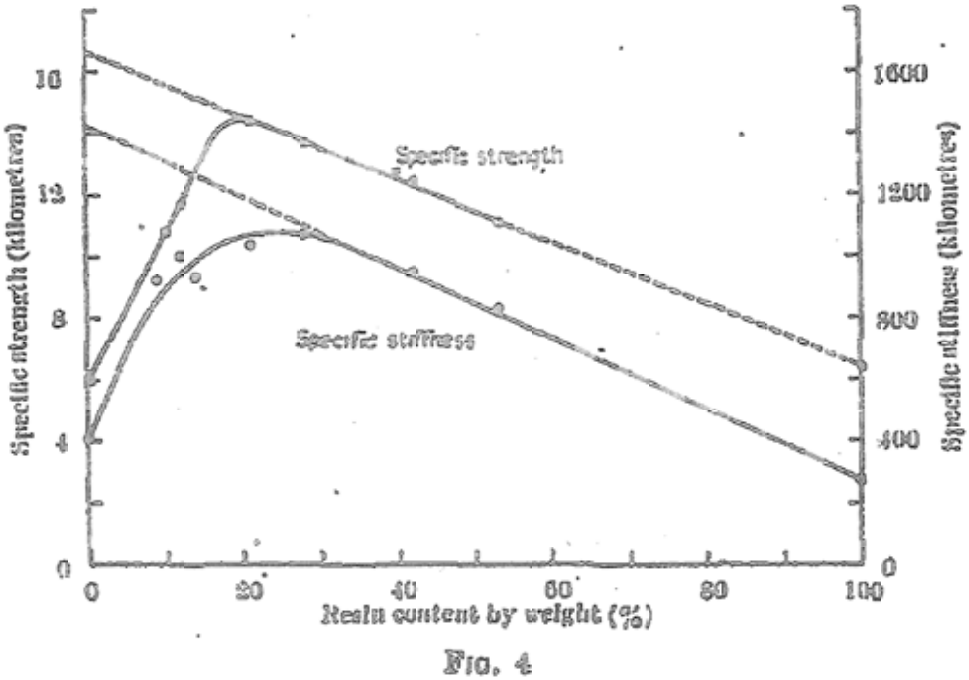

FIG. 4

Fig. 4a. Specific stiffness (right-hand axis) of High density kraft paper / phenol-formaldehyde (aqueous) in km as a function of resin content by weight in percent, (Pepper and Barwell 1944).

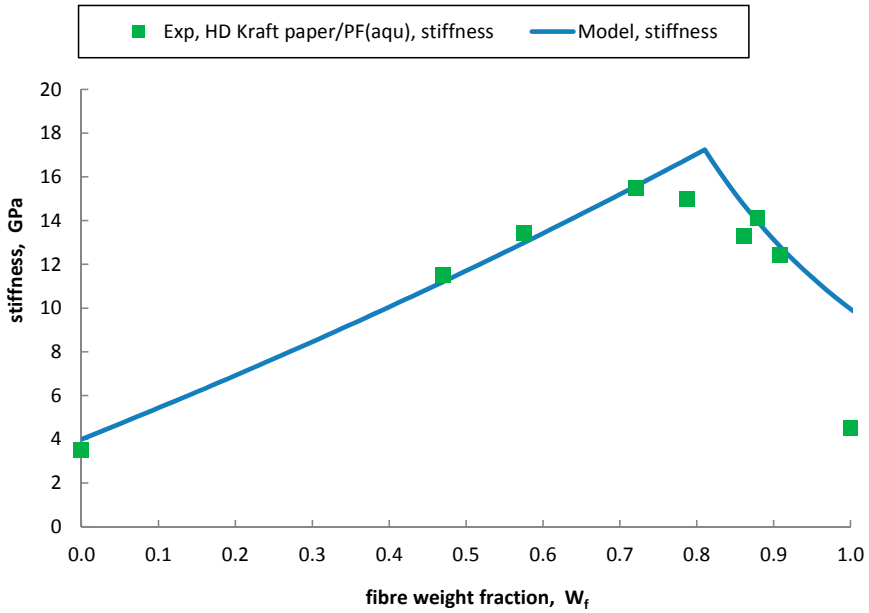

Fig. 4b. Stiffness experimental data re-plotted as a function of fibre weight fraction, model calculated for V_{fmax} = 0.78, fibre stiffness 63 GPa, matrix stiffness 4.0 GPa, fibre orientation factor 0.333, porosity exponent 2.0.

The agreement of the experimental data with the model curve is satisfactory. The stiffness value at W_f = 1 corresponds to the stiffness of the dry (containing no matrix) fibre assembly, i.e. the paper sheets, compacted at the given pressure, in this case the model implies a value of 10.2 GPa. This value might be compared to the experimental value of 4.49 GPa for stiffness of the High density kraft paper sheets (Pepper and Barwell 1944). As for density, the compaction of fibre assemblies are probably maintained, leading to higher stiffness, during composite fabrication, compared to the compaction of dry High density kraft paper sheets.

3.5. Strength of Manila hemp paper / phenol-formaldehyde (alcoholic). These data are presented in Fig. 5a, which is copied directly from Cox and Pepper (1944) as their figure 1, and gives strength in tons per sq.in. as function of resin content by weight in percent. The 12 data point are converted to SI units and plotted as red points in Fig. 5b. The calculation of the composite strength is made in analogy with the stiffness as given in eq. (1):

$$\sigma_c = (\eta \cdot V_f \cdot \sigma_f + V_m \cdot \sigma_m) \cdot (1 - V_p)^n \qquad (2)$$

where σ is strength, V is volume fraction, and f is fibre, m is matrix and p is porosity, η is the fibre orientation factor, and n is the exponent for porosity effect. The composites are made with paper sheets all in the same orientation, so the fibre orientation factor is η = 0.389, as described in section 2. The exponent n is set to 2.0, as used by Madsen et al (2009).

The phenol-formaldehyde strength is 48.5 MPa (experimental value), the best fit of all data points is obtained with matrix strength of 65 MPa. With this value, the paper fibre (cellulose) strength is estimated to be 1100 MPa and the maximum fibre volume fraction $V_{f,max}$ is estimated to be 0.70, with the corresponding fibre weight fraction at transition $W_{f,trans}$ = 0.738. With these parameters the volumetric composition model curve is calculated and is plotted as the blue curve in Fig. 5b.

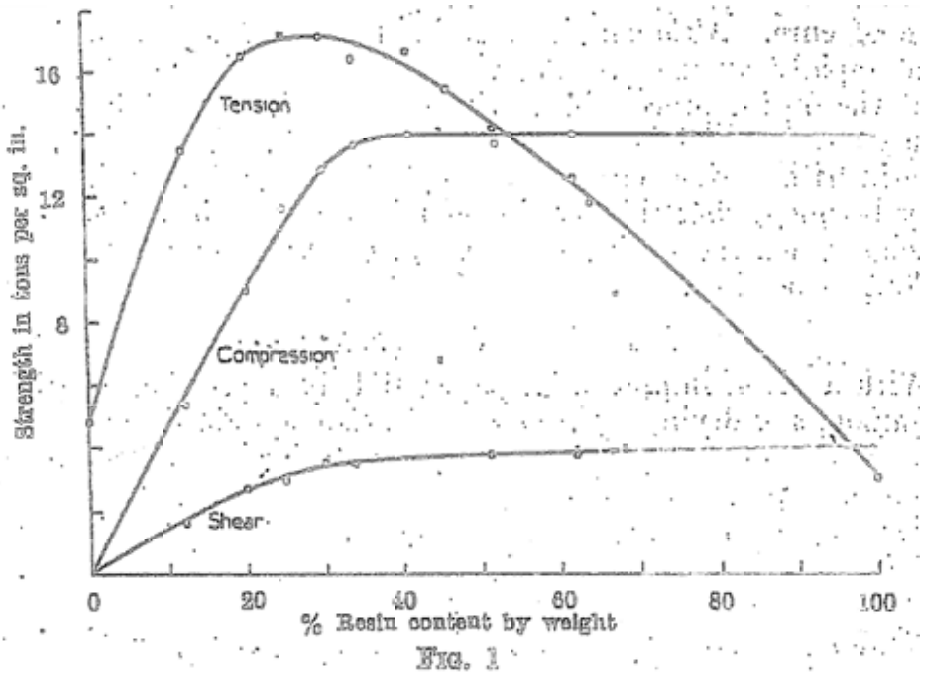

Fig. 5a. Strength of Manila hemp paper / phenol-formaldehyde (alcoholic) in tons per sq.in. as a function of resin content by weight in percent (Cox and Pepper 1944). (Only the tension strength data are analysed).

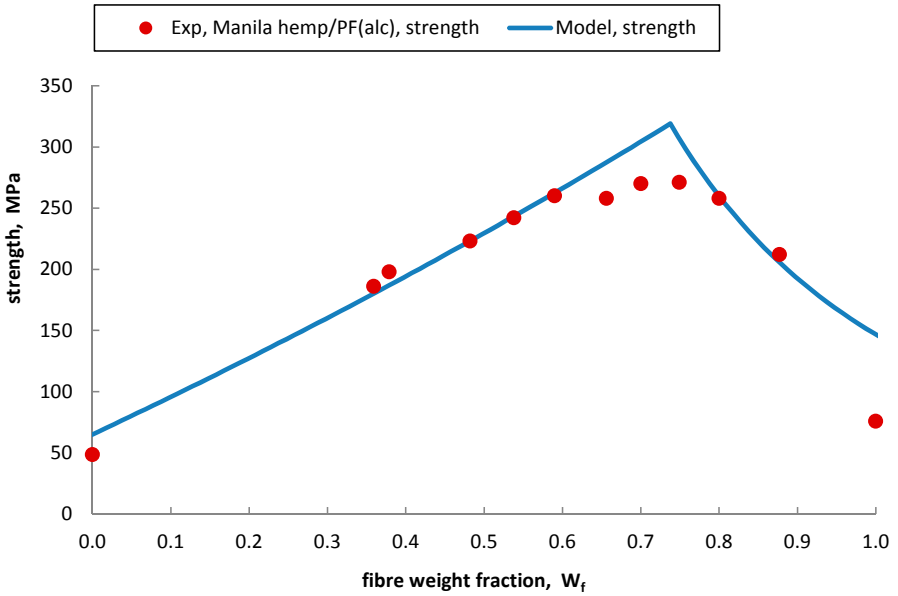

Fig. 5b. Strength experimental data re-plotted as a function of fibre weight fraction, model calculated for V_{fmax} = 0.70, fibre strength 1100 MPa, matrix strength 65 MPa, fibre orientation factor 0.389, porosity exponent 2.0.

The agreement of the experimental data with the model curve is satisfactory. The strength value at $W_f = 1$ corresponds to the strength of the dry (containing no matrix) fibre assembly, i.e. the paper sheets, compacted at the given pressure, in this case the model implies a value of 151 MPa. This value might be compared to the experimental value of 75.7 MPa for strength of the Manila hemp paper sheets (Cox and Pepper 1944). As for density and stiffness, the compaction of fibre assemblies are probably maintained, leading to higher strength, during composite fabrication, compared to the compaction of dry Manila hemp paper sheets.

3.6. Strength of High density kraft paper / phenol-formaldehyde (aqueous). These data are presented in Fig. 6a, which is copied directly from Pepper and Barwell (1944) as their figure 3, and gives strength in tons per sq.in. as function of resin content by weight in percent. The 11 data point are converted to SI units and plotted as green points in Fig. 6b. The calculation of the composite strength is made in the same way as in section 3.5, using eq. (2).

The composites are made with "crossed" paper sheets, so the fibre orientation factor is $\eta = 0.333$, as described in section 2. The exponent n is set to 2.0, as used by Madsen et al (2009).

With the phenol-formaldehyde strength of 72 MPa (experimental value), the paper fibre (cellulose) strength is estimated to be 800 MPa and the maximum fibre volume fraction $V_{f,max}$ is estimated to be 0.78, with the corresponding fibre weight fraction at transition $W_{f,trans} = 0.810$. With these parameters the volumetric composition model curve is calculated and is plotted as the blue curve in Fig. 6b.

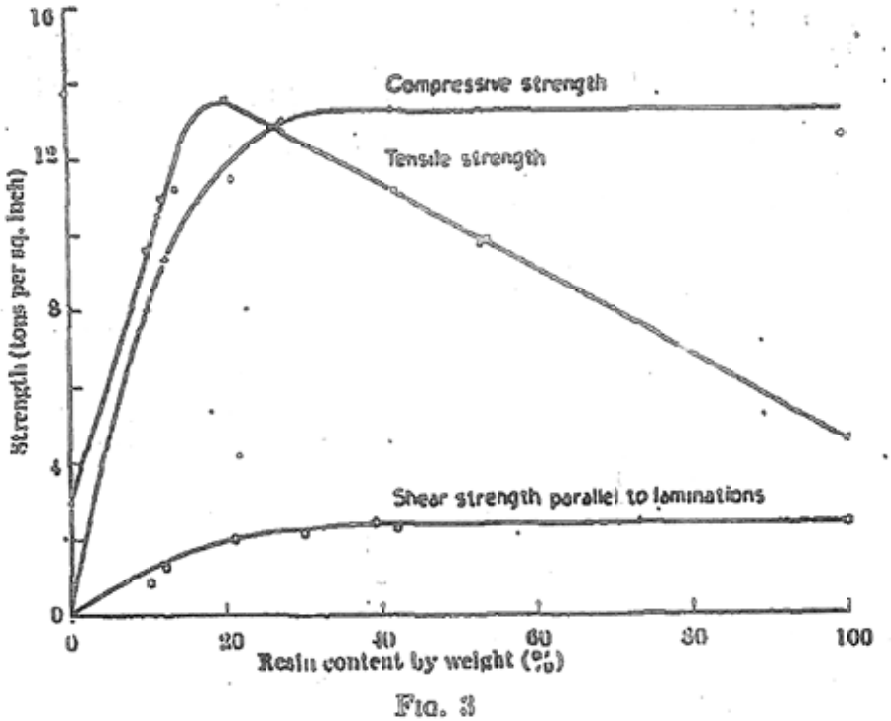

Fig. 6a. Strength of High density kraft paper / phenol-formaldehyde (aqueous) in tons per sq.in. as a function of resin content by weight in percent, (Pepper and Barwell 1944). (Only the tension strength data are analysed).

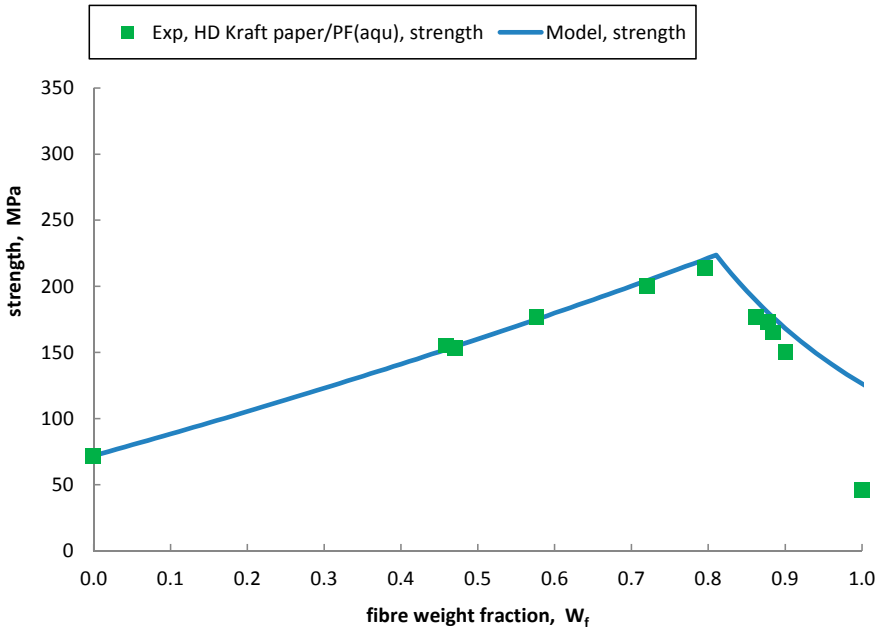

Fig. 6b. Strength experimental data re-plott ed as a function of fibre weight fraction, model calculated for V_{fmax} = 0.78, fibre strength 800 MPa, matrix strength 72 MPa, fibre orientation factor 0.333, porosity exponent 2.0.

The agreement of the experimental data with the model curve is satisfactory. The strength value at W_f = 1 corresponds to the strength of the dry (containing no matrix) fibre assembly, i.e. the paper sheets, compacted at the given pressure, in this case the model implies a value of 130 MPa. This value might be compared to the experimental value of 46 MPa for strength of the High density kraft paper sheets (Pepper and Barwell 1944). As for density and stiffness, the compaction of fibre assemblies are probably maintained, leading to higher strength, during composite fabrication, compared to the compaction of dry High density kraft paper sheets.

3.7. Comparison of the paper sheet / phenol-formaldehyde composites. The model curves established in the Figs. 1b to 6b, are all based on the best fitted values for those free parameter(s) which were not given experimentally. In an attempt to compare the three composite materials systems, fitted parameters are established to achieve the best agreement between model and experimental data simultaneously for both density, stiffness and strength (not all three properties were recorded for all composites). These values are collected in Table 2.

Table 2. Parameter to obtain *best agreement* with experimental data.

Property	Manila Hemp / PF(alc)	HD Kraft paper / PF(aqu)	Kraft paper / PF(aqu)
Fibre density, g/cm^3	1.53	1.53	1.53
Matrix density, g/cm^3	1.27	1.27	1.27
$V_{f\,max}$	0.70	0.82 & 0.78	0.77
$W_{f\,trans}$	0.74	0.85 & 0.81	0.80
Fibre stiffness, GPa	-	63	62
Matrix stiffness, GPa	-	4.0	4.8
Fibre strength, MPa	1100	800	-
Matrix strength, MPa	65	72	-
Fibre orientation, η	0.389	0.333	0.333
Porosity exponent, n	2.0	2.0	2.0

There is no clear tendency in the values of the materials parameters. The higher fabrication pressure (2500 psi) used for the Manila hemp composites does not lead to e.g. a higher maximum fibre volume fraction. The fibre stiffness of about 65 GPa is similar to the value estimated by the previous authors, from slightly different data and evaluations. The strength value for Manila hemp of about 1100 MPa is relatively high, and higher than the nominal fibre strength of Kraft paper(s) of about 800 MPa. The origin of the cellulose fibres of these papers is not clear, it may be based on wood, which generally has a lower cellulose content (about 40 %) than that of hemp (about 70%), and this may tentatively explain the lower strength for Kraft paper, because cellulose fibre strength is generally increasing with increasing cellulose content. The porosity exponent is about 2, but no clear indications can be derived from these data.

The density, stiffness and strength of the pure dry paper sheets were estimated above from the model, and compared to the available experimental data of Cox and Pepper (1944) and Pepper and Barwell (1944). These values are shown in Table 3.

Table 3. Density, stiffness and strength of dry paper sheets.

Density, g/cm^3	Fabr. pressure, psi	Value, model, $W_f = 1$	Exp. value
Manila hemp	2500	1.084	0.952
HD Kraft	2000	1.260	1.140
Stiffness, GPa			
Kraft	2000	9.65	-
HD Kraft	2000	10.2	4.49
Strength, MPa			
Manila Hemp	2500	151	75.7
HD Kraft	2000	120	46

The compaction of the fibre paper sheets during composite fabrication seems to be more efficient than compaction of dry fibre paper sheets, in terms of giving higher values for density, stiffness and strength, as discussed in the sections on the individual composite systems above. The effect on density is small, about a 10% increase, while the effect is much more significant for stiffness and strength, i.e. mechanical properties. This may be expected qualitatively, because mechanical performance of materials is rather sensitive to defects, in the present case the fact that the fibre paper sheets are not a solid but an assembly of fibres with air voids in between.

4. DISCUSSION AND CONCLUSIONS

The extensive study by Cox, Pepper and Barwell in 1942 – 1944 was emphasizing the need to just fill the air voids in the fibre assembly of the various papers with resin in order to make efficient composite materials. The volumetric composition model and the concept of a maximum fibre volume fraction addresses the same situation. The extensive amount of data for the three materials systems and the three properties investigated, were analyzed by the volumetric composition model and in general good agreement was established. The individual analyses for density, stiffness and strength give rather good fit between experiments and model. It is perhaps interesting to note that the situation for fibre contents at, and especially above, the maximum fibre volume fraction (fibre weight fraction transition point) the agreement is relatively good, as demonstrated in figures 1 to 6 with index b.

The model overestimates the value for density, stiffness and strength as the resin content approaches zero (fibre content approaches $W_f = 1$). For density the overestimate is about 10%, while the overestimate is by a factor of about 2 for stiffness and strength. This indicates, perhaps not surprisingly, that the mechanical performance drops extraordinarily, when the resin content is vanishing and the dry fibre assembly becomes not a true solid.

The combined modeling of the three materials systems allows reasonable best obtainable agreement with the common (same) parameters, listed in table 2, to describe density, stiffness and strength for each materials system.

REFERENCES

Cox, H.L. and Pepper, K.W. (1944). Paper-base plastics. Part I. The preparation of phenolic laminated boards. Journal of the Society of Chemical Industry, Transactions and Communications. 63, 150-154.

Gordon, J.E. (1968). The new science of strong materials – or why you don´t fall through the floor. Penguin Books Ltd., p 121 and 155.

Lilholt, H. and Bjerre, A.B. (1997). Composites based on jute-fibres and polypropylene matrix, their fabrication and characterization. In the Proceedings of the 18th Risø International Symposium on Materials Science. Polymeric Composites – Expanding the Limits. Risø National Laboratory, Roskilde, Denmark, p. 411-423.

Madsen, B. (2013). Process conditions and volumetric composition in composites, in these proceedings.

Madsen, B., and Lilholt, H. (2002). Compaction of plant fiber assemblies in relation to composite fabrication. In the Proceedings of the 23rd Risø International Symposium on Materials Science. Sustainable natural and polymeric composites – Science and technology. Risø National Laboratory, Roskilde, Denmark, p. 239-250.

Madsen, B., Thygesen A., and Lilholt H. (2007). Plant fiber composites – porosity and

volumetric interaction. Composites Science and Technology. 67, 1584-1600.
Madsen, B., Thygesen, A., and Lilholt, H. (2009). Plant fibre composites – porosity and stiffness. Composites Science and Technology. 69, 1057-1069.
Pepper, K.W. and Barwell, F.T. (1944). Paper-base plastics. Part II. Production at low pressure. Journal of the Society of Chemical Industry, Transactions and Communications. 63, 321-329.

PERFORMANCE OF COMPOSITE LAMINATES WITH EMBEDDED THERMOPLASTIC ADDITIVES FOR SELF-HEALING

E.H. Lim and K.L. Pickering

Faculty of Science and Engineering, University of Waikato
Private Bag 3105, Hamilton, New Zealand

ABSTRACT

Composites are susceptible to containing hidden damage. Repair of such damage has been a long running challenge in the composites industry with great demands of skilful workers and complex repair procedures. A recent development of self-healing composites has given a new method to manage composite repair; damage can potentially be autonomously repaired at the preliminary stage without involvement of a worker. In this paper, composite laminates made of a polymer blend containing epoxy resin diglycidyl ether of bisphenol A and thermoplastic poly(bisphenol-A-co-epichlorohydrin) at different weight ratios as the composite matrices were evaluated for mechanical performance and the potential of self-healing. Fabrication of the composite laminates and methodology of assessing the healing properties are also presented. The results show that not only healing is achievable, the embedded thermoplastic additives with reasonable amount also do not significantly disadvantage the mechanical performance of composites.

1. INTRODUCTION

Polymer composites are susceptible to premature damage that is invisible to the naked eye such as delamination and matrix cracking (Talreja, 1989; Voyiadjis, 1993). This type of hidden damage commonly forms inside the composite making detection and repair difficult to establish. One of the proven effective repair methods to overcome this problem involves the use of autonomic healing polymers as the composite matrices. A number of workers (Bogue, 2012; Zhang & Rong, 2011; Zwaag & Schmets, 2007) have been involved in developing polymeric matrix composites with the capability to self-heal. Hayes (Hayes, Jones, Marshiya, & Zhang, 2007; Hayes, Zhang, Branthwaite, & Jones, 2007) pioneered the method of making composite matrices consisting of both thermoset and thermoplastic in which the latter functions as healing agent that melts upon heating to fill matrix cracks and bonds the crack surfaces to arrest further propagation when solidified. This characteristic allows the composite matrices to undergo repeated healings. In this paper, fabrication of composite laminates by impregnating balanced

plain weave (PW) carbon fibre fabrics with the healable polymer blends at different weight ratios and curing in a vacuum oven is reported. Effects of thermoplastic inclusion on the composite mechanical properties were evaluated by tensile testing and three-point flexural testing. The healing ability was assessed by inducing damage on composites under cyclic loading before being subjected to three-point flexural test.

2. MATERIALS AND EXPERIMENT

Materials. The raw materials used for fabricating the composite laminates are epoxy resin, diglycidyl ether of bisphenol A (DGEBA or Epikote-828) (Fraser Brown & Stratmore Ltd, New Zealand), thermoplastic poly(bisphenol A-co-epichlorohydrin) (PBE) (Sigma-Aldrich Co. LLC, New Zealand), hardening agent, nadic methylene anhydride (NMA) (Hunstman International LLC, Australia) and 200gsm unidirectional carbon fibre fabric, designated as Gurit UT-C200 (Gurit Ltd., Australia). All materials were used as received.

Fabrication of composite laminates. Three groups of composite laminates with different compositions of polymer blends (Epikote-828 and PBE) were fabricated; laminates in Group A contained no thermoplastic, whereas laminates in Group B and Group C contained 10wt% and 20wt% thermoplastic, respectively. For fabrication of laminates without thermoplastic, Epikote-828 blended with curing agents was heated on top of a hot plate to about 40°C to reduce the viscosity of the mixture for ease of wetting the carbon fibre fabrics. During fabrication, a total of six 280 mm x 220 mm precut carbon fibre fabric layers were stacked on top of each other with polymer mixture spread evenly between the fabric layers. The laminate was sandwiched between Teflon cloth layers and flat glass panels for ease of removal after cure and to ensure a smooth and even laminate is fabricated (see Figure 1). A dead weight giving a pressure of 3kPa was applied to the laminate during degassing (80°C for 30 minutes) and curing (80°C for 4 hours followed by 130°C for 3 hours) in a vacuum oven. For fabrication of laminates containing thermoplastic (Group B and C), the PBE pellets were first dissolved in Epikote-828 at 80°C (on top of a hot plate) by continuously stirring the mixture until pellets had dissolved (assessed visually) in the mixture; the entire dissolution process could take up to over 24 hours depending on the concentration of PBE. Curing agents were then added to the polymer blend in preparation for laminate fabrication. Similar procedures were then carried out as in fabrication of Group A laminates.

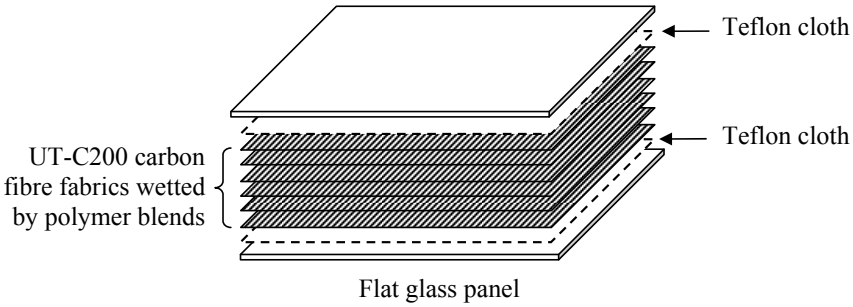

Fig. 1. Stacking sequence of carbon fibre fabrics, Teflon cloth and flat glass panel during composite laminate fabrication.

Sample preparation. Through the fabrication method described above, 230 mm x 200 mm (after trimmed) unidirectional composite laminates with a 1.40 ± 0.10 mm thickness were produced. The laminates were cut to the tensile specimen geometry recommended in ASTM

D3039/D3039M: Standard test method for tensile properties of polymer matrix composite materials (ASTM_D3039/D3039M, 2000) and flexural specimen geometry in ASTM D790: Standard test methods for flexural properties of unreinforced and reinforced plastics and electrical insulating materials (ASTM_D790, 2010). For tensile samples, additional tabs made of glass fibre reinforced composite (fabricated with the similar method as the samples) were adhered to both ends of the samples to prevent damage at the grip areas during testing. The end tabs were chamfered to improve tensile stress transmission to the gauge areas (see Fig. 2). All samples were conditioned in accordance to ASTM D618: Standard practice for conditioning plastics (ASTM_D618, 2000) prior to testing.

Fig. 2. Tensile test samples with end tabs mounted at the grip areas.

Testing. All tests were performed with an Instron 4204 universal tester. To evaluate the effect of thermoplastic additives on the composite tensile properties, the tabbed tensile samples were mounted in the wedge grips and loaded at 8 x 10^{-6} $m.s^{-1}$. Displacement of the sample gauge length was measured with a 50 mm extensometer and the corresponding load applied was recorded. For the evaluation of composite flexural properties, a three-point flexural test was performed; each flexural sample was placed on the support noses of a standard three-point loading fixture and loaded with a loading nose in the middle of sample top at 3.33 $mm.min^{-1}$. The fixtures of both tensile test and flexural test are shown in Fig. 3 and Fig. 4.

To assess the healing efficiency of composite, another batch of flexural samples from the three different laminate groups were subjected to 10 cycles of repeated loading up to 70, 80 and 90 per cent of average fracture load (obtained from earlier flexural tests), respectively. The procedure was carried out to induce damage within the samples. Healing was then performed by sandwiching the samples between two flat steel plates and heated in an oven at 130°C for 3 hours. Later, the samples were retested to obtain the ultimate flexural properties.

Fig. 3. Tensile test fixture; left: a sample gripped and mounted with a 50 mm extensometer, right: a sample end tabbed to prevent damage at grip areas.

Fig. 4. Three-point flexural fixture.

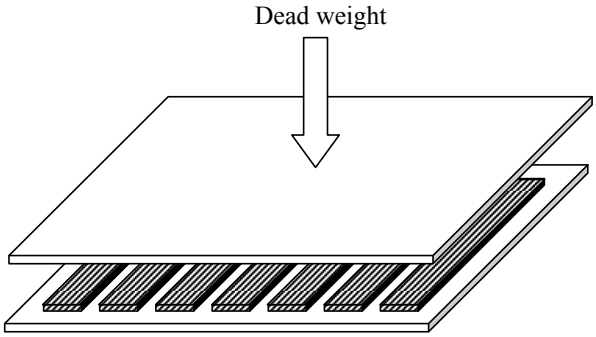

Fig. 5. Flexural samples sandwiched between two flat steel plates for healing; a dead weight was placed on the top to keep the samples flat during healing.

3. RESULTS AND DISCUSSION

Effect of thermoplastic additives on composite properties. Assessment of composite laminates with and without addition of thermoplastic was obtained from the tensile testing and the three-point flexural testing of composite samples. The tensile results in Fig. 6 show that Group A samples (without thermoplastic) have an average tensile strength of 1620 MPa, Young's modulus 123.2 GPa and 1.29 per cent failure strain, respectively. Compared to Group A, Group B (with 10wt% thermoplastic) samples have insignificant differences on overall tensile properties, whereas Group C with twice the concentration of thermoplastic (20wt% thermoplastic) presents 18 per cent decrease in tensile strength and 16 per cent decrease in tensile modulus, respectively. Similar results were found from flexural testing (see Fig. 7); Group C composite flexural strength and modulus decrease by 8 per cent and 17 per cent compared to Group A (1585 MPa, 113.5 GPa), whilst Group B composite flexural properties vary by less than 4 per cent.

Healing efficiency of composite. Table 1 shows the comparison of the retained flexural strength of undamaged composite samples and damage-induced samples subjected to 10 cycles of repeated loading at 70, 80 and 90 per cent of average fracture load (obtained from averaging fracture loads of all composite samples) to assess the efficiency of the thermoplastic additives in triggering healing of premature damage. The decrease of flexural strength with an increase of

the nominal maximum cyclic load indicates the increase of composite damage. Significant strength reduction was observed for all composite groups cyclic-loaded at 90% flexural load, as compared with the strength for other samples shows that damage caused at this stage is severer. The results also show that the strength restoration upon healing was achievable with strength reduction in Group A decreases from 35 per cent to 22 per cent in Group B and 10% in Group C. Retained flexural modulus as displayed in Table 2 also shows similar trend in healing efficiency, with modulus reduction reduces from 42 per cent (Group A) to 19 per cent (Group B) and 10 per cent (Group C).

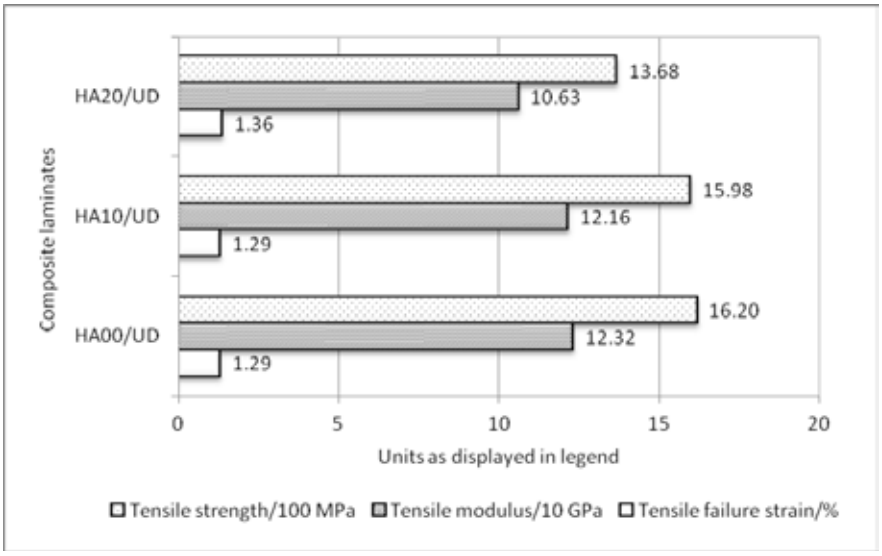

Fig. 6. Comparison of tensile properties from different groups of laminates.

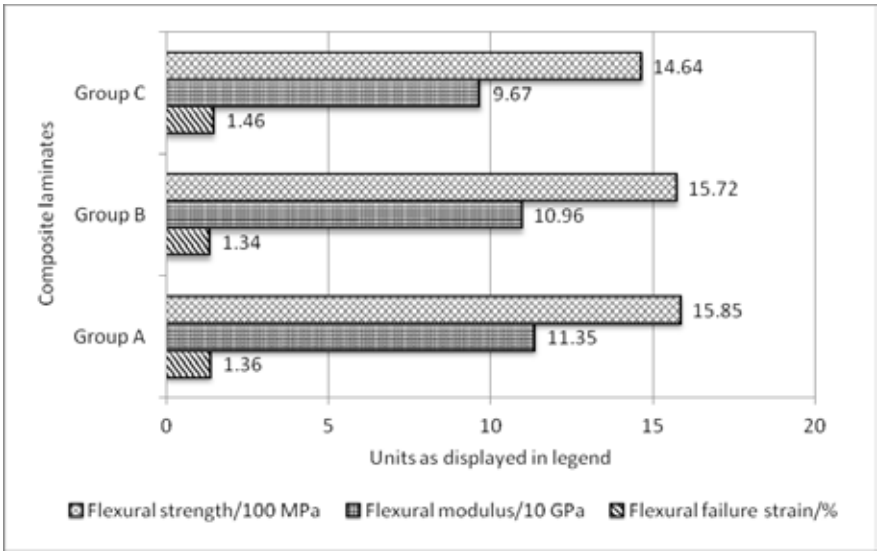

Fig. 7. Comparison of flexural properties from different groups of laminates.

Table 1. Flexural strength after healing of composite subjected to cyclic loading (standard deviations in parentheses).

Composite laminates	*Flexural strength (MPa), post-healing after subjected to cyclic loading at a proportion of maximum flexural load*			
	Undamaged	70%	80%	90%
Group A (without thermoplastic)	1585 (37)	1576 (29)	1512 (67)	1172 (129)
Group B (with 10wt% thermoplastic)	1572 (142)	1554 (117)	1514 (98)	1285 (68)
Group C (with 20wt% thermoplastic)	1464 (95)	1458 (116)	1426 (94)	1329 (77)

Table 2. Flexural modulus after healing of composite subjected to cyclic loading (standard deviations in parentheses).

Composite laminates	*Flexural modulus (GPa), post-healing after subjected to cyclic loading at a proportion of maximum flexural load*			
	Undamaged	70%	80%	90%
Group A (without thermoplastic)	113.5 (3.5)	113.4 (8.4)	105.9 (8.1)	79.7 (19.2)
Group B (with 10wt% thermoplastic)	109.6 (7.1)	106.4 (8.5)	103.9 (7.5)	92.1 (10.2)
Group C (with 20wt% thermoplastic)	96.7 (6.1)	91.1 (7.6)	91.1 (10.2)	88.1 (7.5)

4. CONCLUSIONS

Based on the tensile and flexural tests on unidirectional carbon fabric composites, the following conclusions were drawn. Inclusion of thermoplastic healing agent at 10wt% does not have a significant effect on the mechanical performance of composites. Property restoration of composites with damage is achievable with the proposed healing method; higher concentrations of thermoplastic in a composite give a better healing efficiency.

ACKNOWLEDGEMENTS

The authors wish to thank the Ministry of Higher Education, Malaysia and the Faculty of Science and Engineering (FSEN), University of Waikato for the sponsorship and support in this research.

REFERENCES

ASTM_D618. (2000). Standard practice for conditioning plastics for testing. United States: ASTM International.

ASTM_D790. (2010). Standard test methods for flexural properties of unreinforced and reinforced plastics and electrical insulating materials. United States: ASTM International.

ASTM_D3039/D3039M. (2000). Test method for tensile properties of polymer matrix composite materials. United States: ASTM International.

Bogue, R. (2012). Smart materials: A review of recent developments. *Assembly Automation, 32*(1), 3-7. doi: 10.1108/01445151211198674

Hayes, S. A., Jones, F. R., Marshiya, K., & Zhang, W. (2007). A self-healing thermosetting composite material. *Composites Part A (Applied Science and Manufacturing), 38*(4), 1116-1120. doi: 10.1016/j.compositesa.2006.06.008

Hayes, S. A., Zhang, W., Branthwaite, M., & Jones, F. R. (2007). Self-healing of damage in fibre-reinforced polymer-matrix composites. *Journal of the Royal Society Interface, 4*(13), 381-387. doi: 10.1098/rsif.2006.0209

Talreja, R. (1989). Damage development in composites: mechanisms and modelling. *Journal of Strain Analysis for Engineering Design, 24*(4), 215-222.

Voyiadjis, G. Z. (1993). *Damage in composite materials* (Vol. 34). Amsterdam ;New York: Elsevier.

Zhang, M. Q., & Rong, M. Z. (2011). *Self-healing polymers and polymer composites*. Hoboken, N.J.: Wiley.

Zwaag, S. v. d., & Schmets, A. J. M. (2007). *Self healing materials: An alternative approach to 20 centuries of materials science*. Dordrecht, The Netherlands: Springer.

Proceedings of the 34th Risø International Symposium on Materials Science:
Processing of fibre composites – challenges for maximum materials performance
Editors: B. Madsen, H. Lilholt, Y. Kusano, S. Fæster and B. Ralph
Department of Wind Energy, Risø Campus
Technical University of Denmark, 2013

QUANTITATIVE ANALYSIS OF LENGTH-DIAMETER DISTRIBUTION AND CROSS-SECTIONAL PROPERTIES OF FIBERS FROM THREE-DIMENSIONAL TOMOGRAPHIC IMAGES

Arttu Miettinen[1], Roberts Joffe[2], Bo Madsen[3], Kalle Nättinen[4], Markku Kataja[1]

[1]Department of Physics, University of Jyväskylä, FI-40014, Finland
[2]Luleå University of Technology, Division of Materials Science SE-97187 Luleå, Sweden
[3]Department of Wind Energy, Technical University of Denmark, Risø Campus, P.O. Box 49, DK-4000 Roskilde, Denmark
[4]VTT Technical Research Centre of Finland, Sinitaival 6, P.O. Box 1300, FI-33101 Tampere, Finland

ABSTRACT

A number of rule-of-mixture micromechanical models have been successfully used to predict the mechanical properties of short fiber composites. However, in order to obtain accurate predictions, a detailed description of the internal structure of the material is required. This information is often obtained from optical microscopy of polished cross-sections of a composite. This approach gives accurate yet local results, but a rather large number of optical images have to be processed to achieve a representative description of the morphology of the material. In this work a fully automatic algorithm for estimating the length-diameter distribution of solid or hollow fibers, utilizing three-dimensional X-ray tomographic images, is presented. The method is based on a granulometric approach for fiber length distribution measurement, combined with a novel algorithm that relates cross-sectional fiber properties to fiber length. The work opens up a possibility to assess multivariate distributions of fiber length and diameter, cross-sectional area or other microstructural fiber properties. As an example, the description of the microstructure of different composites with natural fibers is presented, along with verification of the results.

1. INTRODUCTION

Mechanical properties of short fiber composites have been successfully estimated using rule-of-mixtures based models (Madsen, Joffe, Peltola and Nättinen 2011; Neagu, Gamstedt and Berthold 2006; Andersons, Joffe, and Spārniņš 2006). In addition to mechanical properties of constituents, a significant amount of information about the geometrical structure of the material

is required for successful modeling. Part of this information can be measured using traditional methods, e.g. the volume fractions of the constituents, whereas more intricate techniques are required to measure, e.g., the length, diameter and orientation distributions of fibers and their correlations.

In addition to mechanical modeling, information about a composite structure may be used by composite manufacturers. The manufacturing process typically includes multiple steps, e.g. pelletization of fibers, compounding and injection moulding. Each of these potentially affects the geometry of individual fibers, thus rendering useless any measurements done on intact, non-processed fibers (Peltola, Madsen, Joffe and Nättinen, 2011). However, the morphology of the fibers affects the mechanical properties of the final product. Thus, information about the effect of processing on the fiber geometry is of interest and helps in the optimization of the manufacturing steps.

Traditional methods for measuring the microstructural and geometrical parameters of composites are microscopy of polished cross-sections, and dissolution of matrix to leave only fibers. Both of these traditional methods are time-consuming and they may further affect the geometry as large chemical or mechanical forces must be applied to the samples to transform them into analyzable form. Additionally, in the case of short fiber composites, the dissolution process hides information about e.g. fiber orientation and agglomeration.

X-ray microtomography (X-μCT) is a non-invasive technique for obtaining the three-dimensional internal structure of a sample. It is based on taking a large number of X-ray projection images of the sample, from different angles, and using that data to computationally reconstruct the three-dimensional structure. The result of the process is, roughly speaking, a three-dimensional density map of the sample with a typical resolution around 2 μm.

The two phases, fibers and matrix, can be separated in and X-μCT image of a fibrous composite sample. Without loss of generality it can be assumed that the result of the separation process is an image where the value of each voxel is the volume fraction of fiber material in that particular voxel. Then, voxels entirely in the fiber wall and entirely in the matrix are given values 0 and 1, respectively. We will call such an image semi-binarized.

In the present work, image analysis methods to quantify the microstructure of a composite sample are presented, given a three-dimensional semi-binary image as a starting point. Particularly, a method is given to estimate the multivariate distribution of length and cross-sectional properties of fibers. As a side-effect, other microstructural parameters become straightforward to measure, e.g. the fiber orientation distribution, which can be used to calculate the fiber orientation efficiency factor (Krenchel, 1964).

A similar method has previously been presented by Miettinen and Kataja (2011) and by Miettinen, Luengo Hendriks, Chinga-Carrasco, Gamstedt and Kataja (2012) where it has been assumed that the fibers are geometrically similar, i.e., the volume of a single fiber V_1 is proportional to lD^2, where l is fiber length and D is the smallest dimension of the cross-section of the fiber. In this work we relax this assumption, thereby improving the practical usability of the method considerably. Additionally, the method introduced in this work is capable of measuring many geometrical features of a fiber cross-section, not limited to D, e.g., cross-sectional area.

The results are verified using a computer-generated test data from Miettinen et al. (2011). The method is applied to measure the microstructure of flax fiber composites, whose mechanical properties are then estimated by a micromechanical model and compared to measured values.

2. ESTIMATION OF COMPOSITE MICROSTRUCTURE

Let us first represent the three-dimensional semi-binary image as a function $I(x_1, x_2, x_3)$, whose value is the volume fraction of fiber material in that particular point. Let us now approximate the partial derivatives of I with

$$I_i(\vec{p}) = \frac{\partial I(\vec{p})}{\partial x_i} \approx \left(\frac{\partial G(\sigma_s)}{\partial x_i} * I\right)(\vec{p}), \tag{1}$$

where $G(\sigma)$ is a three-dimensional Gaussian function with zero mean and σ variance in all directions, and $*$ denotes convolution operation. The structure tensor is then defined as (Jähne 2004)

$$S_{ij} = G(\sigma_t) * (I_i I_j). \tag{2}$$

To quantify the orientation of cylindrical structures at $\vec{p}$, the eigenvector of $S_{ij}(\vec{p})$ corresponding to the smallest eigenvalue is calculated.

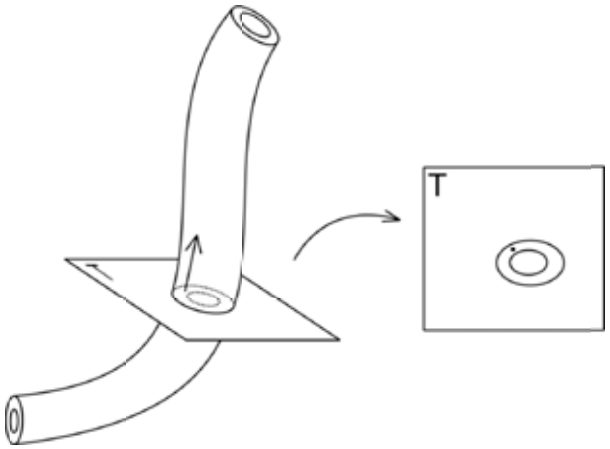

Fig. 1: Slicing a single fiber. The slice T is taken such that its normal (straight arrow) points to the local orientation of the fiber at point $\vec{x}$.

The image I is now sampled uniformly at random locations $\vec{x}_n$, where $n = 1, \ldots, N$ is the index of the location. If $I(\vec{x}_n) < 1$, i.e., the sampled voxel contains matrix material, the point is discarded. Otherwise, a slice around $\vec{x}_n$ is extracted such that the normal of the slice is the local orientation vector, see Fig. 1. The corresponding fiber cross-section is extracted from the slice and desired features are measured; in this work we consider the area of the cross-section A_n and the nominal diameter of the cross-section $d_n = \min(d_{n1}, d_{n2})$, where d_{n1} and d_{n2} are lengths of the projections of the cross-section to the directions of its principal axes. As also other features, in excess of fiber length, can be measured if desired, we denote all of them collectively by ξ_{kn}, where $k = 1, \ldots, K$ indexes a total of K features for the n:th cross-section. See e.g. (Jähne 2004) for a survey on some possible features.

To facilitate calculation of fiber length for the n:th cross-section, we denote by $O(I, l)$ the result of a constrained path-opening operation for image I with length parameter l (Luengo Hendriks

2010). The image $O(I,l)$ thus contains only structures whose longest dimension is less than l. The area of the cross-section corresponding to structures whose length is less than l is then

$$A_n(l) = \int_{A_n} O(I,l)dA, \tag{3}$$

where the integral is taken over the cross-section n. The length distribution of the cross-sectional area is given by

$$\phi_n(l) = \frac{\partial A_n(l)}{\partial l}. \tag{4}$$

We define fiber length L_n as the mode of the length distribution $\phi_n(l)$.

Having now determined the elementary data sets (ξ_{kn}, L_n) for $n = 1, \dots, N$, the sets can be used to create various multivariate distributions of the features ξ_{kn} and L_n. As the probability to sample a fiber is proportional to the volume of the fiber, the resulting distributions will be of type

$$\frac{\partial^{K+1} V}{\partial \xi_1 \partial \xi_2 \dots \partial \xi_K \partial L}, \tag{5}$$

i.e. (ξ_k, L)-distribution of total fiber volume V.

An interesting side-effect of the above process is that information about the point wise orientation makes it possible to use fiber orientation as one of the features ξ_{kn}. This enables construction of e.g. well-defined fiber orientation distribution. Note that most existing methods give, more or less, the orientation distribution of fiber-matrix interfaces. However, for micromechanical modeling of composites the Krenchel orientation efficiency factor η_o (Krenchel 1964) is more often used. It is defined by

$$\eta_o = \sum_m a_m \cos^4 \alpha_m, \tag{6}$$

where a_m is the ratio between volume of fibers whose orientation direction forms angle α_m with the loading force, and the total volume of all fibers. In the present method, in particular the cross-sectional area A_m and the angle α_m can be selected as measurable features. Approximating that $a_m \approx A_m / \sum_m A_m$ then enables direct application of the definition to approximate the value of η_o.

3. VERIFICATION WITH COMPUTER-GENERATED DATA

As a first test of the method, computer-generated images with a priori known bivariate fiber length and diameter distribution were created, as in (Miettinen et al. 2011). The images were generated using a specific deposition algorithm that modeled the fibers as long rods with small curvature, see Fig. 2 for an example. A total of eight images were generated such that the total number of fibers in them was 1600.

The method in Section 2 was applied to the images and the results were compared to the known distributions, see Fig. 3. The data shows good correspondence between true and measured distributions. The measured length distribution contains more large length values than it should because fibers that are connected to each other form long structures. One should note that in a real composite material there are typically less fiber intersections than in the test structure,

generated by a deposition process where fiber contacts are the only method for the structure to carry its own weight.

Fig. 2: Computer-generated test data. Reproduced from Miettinen and Kataja (2011).

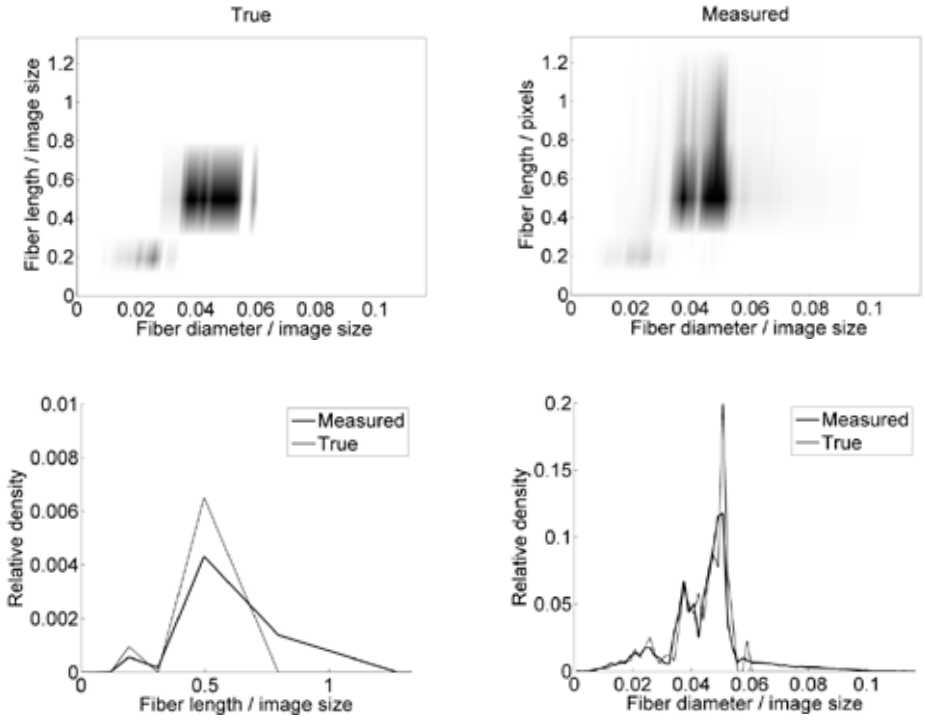

Fig. 3: Comparison between true (top-left) and measured (top-right) distributions of fiber length and diameter, black corresponding to high relative density. Marginal distributions of length (bottom-left) and diameter (bottom-right), with the corresponding true distributions (thin line).

4. APPLICATION TO COMPOSITES

For testing the method, four types of flax fiber composite samples, denoted below by C15, C16, C28 and C29, were manufactured with varying fiber and plasticizer content. The gravimetric composition of these composite samples is given in Table 1. Flax fibers were supplied by Ekotex, Poland. Amylose rich corn starch was supplied by Gargill, USA (Cerestar Amylogel 03003: 65 w-% amylose, 35 w-% amylopectin). The processes of fiber pelletizing, starch acetylation and plasticization are described in more detail in earlier work (Nättinen, Hyvärinen, Joffe and Wallström 2010). The compounding, post processing and injection molding of composite tensile specimens were performed as described earlier, except that in the present work compounds and composites were all compounded with the same temperature gradient from 60 °C in the feeding section to 200 °C in the melting zones and the die.

For X-μCT imaging, cylinders of about 2 mm diameter were cut from the middle part of the tensile specimens. X-μCT images of the samples were taken using an XRadia μCT-400 -device. The pixel size was 1.24 μm, giving a field of view corresponding roughly to the diameter of the cylindrical sample. The images were denoised using variance weighted mean filter and semi-binarized by linear contrast mapping, yielding an image that could be processed as described in Section 2. The results, along with comparison to independently measured values, are given in Table 2. The fiber length distributions and fiber diameter distributions for the four samples are shown in Fig. 4.

Table 1: Gravimetric composition of the flax/PSA composite compounds.

Sample	PSA matrix type	Weight fractions, nominal			Plasticizer content in matrix (w-%)
		Fiber	Starch acetate	Plasticizer	
C15	PSA2.1	0.100	0.720	0.180	20.0
C16	PSA2.1	0.400	0.480	0.120	20.0
C28	PSA5.1	0.100	0.608	0.293	32.5
C29	PSA5.1	0.400	0.405	0.195	32.5

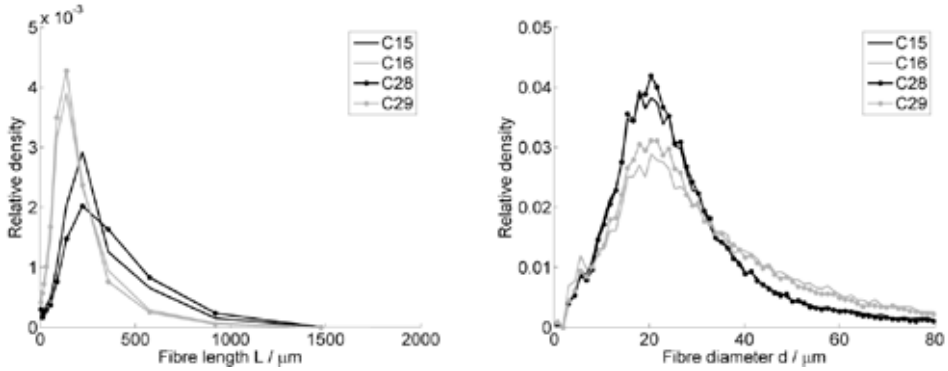

Fig. 4: Fiber length distributions (left) and fiber diameter distributions (right) for the four flax composites obtained using the X-μCT method.

Table 2: Comparison between quantities determined using X-μCT and independent method. Superscript *t* stands for X-μCT method, *g* for gravimetric method, *d* for dissolvement followed by manual microscopic analysis and *m* for value from micromechanical modeling (Nättinen et al. 2010; Madsen et al. 2011). Brackets ⟨·⟩ stand for average value. V_f, V_m and V_v are volume fractions of fibers, matrix and void, respectively. L is fiber length, d is fiber diameter and η_o is Krenchel's orientation efficiency factor.

Sample	V_f^t	V_f^g	V_m^t	V_m^g	V_v^t	V_v^g	$\langle L^t \rangle$	$\langle L^d \rangle$	$\langle d^t \rangle$	$\langle d^d \rangle$	η_o^t	η_o^m
C15	0.11	0.11	0.89	0.89	0	0.00	371±167	347±257	16±10	18±7	0.54	0.61
C16	0.31	0.36	0.69	0.62	0	0.01	262±120	151±105	20±14	19±7	0.73	0.61
C28	0.10	0.09	0.90	0.91	0	0.00	431±196	334±262	16±10	19±7	0.54	0.61
C29	0.27	0.36	0.73	0.64	0	0.01	243±110	293±256	19±13	19±7	0.56	0.61

As mentioned above, the stiffness of short fiber composites with randomly oriented fibers can be predicted with fairly good accuracy by a simple rule-of-mixtures model. The porosity effect can also be easily taken into account. According to (Madsen et al. 2009), the Young's modulus E_c of the composite is thus given by

$$E_c = \left(\eta_o \eta_l V_f E_f + V_m E_m\right)(1 - V_v)^2, \tag{7}$$

where V_f, V_m and V_v are the volume fractions of fibers, matrix and void, and η_o and η_l are the fiber orientation and length efficiency factors, respectively. The stiffness of matrix, E_m, has been measured to be 1.66 GPa for PSA2.1 matrix and 0.45 GPa for PSA5.1 matrix (see also Table 1). The fibers are assumed to be isotropic with E_f = 50 GPa (Lilholt and Lawther 2000). The length efficiency factor η_l is defined as (Cox 1952)

$$\eta_l = 1 - \frac{\tanh(\theta)}{\theta}, \quad \text{where} \quad \theta = 2\frac{\langle L \rangle}{\langle d \rangle}\sqrt{\frac{G_m}{E_f \ln(\frac{\kappa}{V_f})}}. \tag{8}$$

The shear modulus of matrix, G_m, is calculated from the stiffness and Poisson´s ratio ν, assuming an isotropic material with ν = 0.3. Fibers are assumed to be packed hexagonally, thereby implying value of geometrical packing pattern constant $\kappa = \frac{\pi}{2} \cdot \sqrt{3} \approx 0.907$.

The average fiber length $\langle L \rangle$, average fiber diameter $\langle d \rangle$, volume fractions and fiber orientation efficiency factor η_o are obtained from the X-μCT method or the independent measurements, see Table 2. The modeled values of the Young's modulus of the composites are presented in Fig. 5 for either case. Further information about methods used in the independent measurements is found in (Nättinen et al. 2010; Madsen et al. 2011). It must, however, be noted that in the case of independent measurements, the model has been fitted to the experimental data in Fig. 5 using the orientation efficiency factor as a fitting parameter. Such a procedure has been conducted because it is hard to obtain reliable independent measurement for orientation efficiency factor without the X-μCT method.

Based on Table 2, the X-μCT method gives results similar to the independent measurements. However, it must be noted that average fiber diameters $\langle d^t \rangle$ and $\langle d^d \rangle$ are not measured exactly the same way as the fiber cross-section is not perfectly circular. In the manual measurement the fibers are laid down on a microscope slide, so d^d is the diameter of the fiber in an unknown, poorly defined direction. In the X-μCT method, d^t is the diameter of the fiber in such a

direction that the value of d^t is minimal. It is then reasonable to assume that $d^t \lesssim d^d$, a condition that is fulfilled in three cases of four.

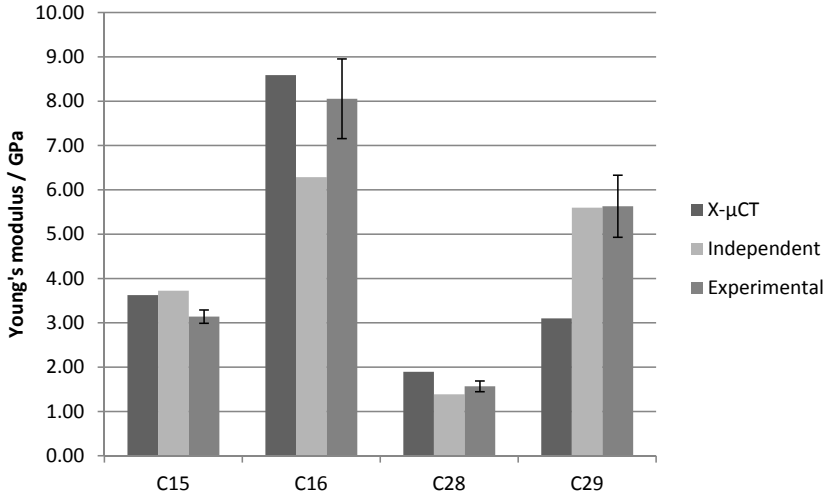

Fig. 5: Comparison between Young's modulus given by the model and tensile test. Bars labeled by 'X-µCT' and 'Independent' are calculated using the model with parameters from X-µCT method or the independent methods, respectively. Bars labeled as 'Experimental' are the results of tensile tests.

5. SUMMARY

Application of the X-µCT method to the computer-generated structure in Section 3 shows good correspondence between true and measured fiber length and diameter distributions. As the test structure contains a lot of fiber intersections, the X-µCT method overestimates the relative number of long fibers. The effect should, however, be much smaller in a real composite sample where there are less fiber intersections.

For real composite samples in Section 4 the X-µCT method gives plausible estimates of the microstructural parameters. Average fiber lengths and diameters measured by the X-µCT method and the independent methods are within one standard deviation from each other.

The modeled and measured stiffness values in Fig. 5 are generally in good agreement, showing the performance of the model, the X-µCT method and the independent measurements. However, it should be noted that X-µCT data fails to predict the Young's modulus of the sample material C29. The difference between volume fractions $|V_f^t - V_f^g|$ is largest in the case of C29, suggesting that the sample for the X-µCT method has been taken from such a location where there are less fibers than on average, thereby hindering effective measurement.

ACKNOWLEDGEMENTS

This work has been partially funded through the Finnish Bioeconomy Cluster FuBio JR2 program.

REFERENCES

Andersons J., Joffe R., Spārniņš E. (2006). Stiffness and strength of flax fiber/polymer matrix composites, Polymer Composites, 27:221-229.

Cox H.L. (1952). The elasticity and strength of paper and other fibrous materials. British Journal of Applied Physics, 3:72-79.

Jähne, B. (2004). Practical handbook on image processing for scientific and technical applications. CRC Press.

Krenchel, H. (1964). Fibre reinforcement. Akademisk forlag. Copenhagen.

Lilholt, H. and Lawther, J.M. (2000). Natural organic fibres. In: Kelly A and Zweben C (eds) Comprehensive composite materials (6 Vols). Vol. 1; Chap. 10. Amsterdam: Elsevier Science, 2000:303–325.

Luengo Hendriks, C.L. (2010). Constrained and Dimensionality-Independent Path Openings. IEEE Trans. Im. Proc. 19, 1587-1595.

Madsen, B., Thygesen A., Lilholt H. (2009). Plant fibre composites – porosity and stiffness, Composite Science and Technology, 69:1057-1069.

Madsen, B., Joffe, R., Peltola, H., Nättinen, K. (2011). Short cellulosic fiber/starch acetate composites - micromechanical modeling of Young's modulus. Journal of Composite Materials, 45 (20): 2119-2131.

Miettinen, A., Kataja M. (2011). Non-destructive analysis of fiber properties using 3D X-ray microtomographic data. Proceedings of the 32nd Risoe International Symposium on Materials Science, Risoe, Denmark, ISBN 978-87-550-3925-4.

Miettinen, A., Luengo Hendriks C.L., Chinga-Carrasco G., Gamstedt E.K., Kataja M. (2012). A non-destructive X-ray microtomography approach for measuring fibre length in short-fibre composites, Comp. Sci. Tech., Volume 72, Issue 15, Pages 1901–1908, http://dx.doi.org/10.1016/j.compscitech.2012.08.008.

Neagu, C., Gamstedt, E.K., Berthold, F. (2006). Stiffness contribution of various wood fibers to composite materials. Journal of Composite Materials. 40: 663-699.

Nättinen, K., Hyvärinen, S., Joffe, R., Wallström, L., Madsen, B. (2010). Naturally compatible: Starch acetate/cellulosic fiber composites. I. Processing and properties *Polymer Composites*, 31(3), 524-535.

Peltola, H., Madsen, B., Joffe, R., Nättinen, K. (2011). The influence of biocomposite processing and composition on natural fiber length, dispersion and orientation Journal of Materials Science and Engineering. Vol. 1 No: 2 , 190-198

Proceedings of the 34th Risø International Symposium on Materials Science:
Processing of fibre composites – challenges for maximum materials performance
Editors: B. Madsen, H. Lilholt, Y. Kusano, S. Fæster and B. Ralph
Department of Wind Energy, Risø Campus
Technical University of Denmark, 2013

FABRICATION AND CHARACTERISATION OF CARBON/BENZOXAZINE COMPOSITES WITH IMPROVED FRACTURE TOUGHNESS USING LIQUID RESIN INFUSION

N. Nash, D. Roy, T.M. Young, W.F. Stanley

IComp (Irish Centre for Composites Research), MSSI (Materials and Surface Science Institute), Department of Mechanical, Aeronautical & Biomedical Engineering, University of Limerick, Limerick, Ireland

ABSTRACT

This research aims to use Vacuum Assisted Resin Transfer Moulding (VARTM) as an alternative processing strategy to manufacture composite components with superior impact resistance through the incorporation of polyamide (nylon) interlayers while reducing overall costs and increasing the speed of manufacture. The veils enhanced the Mode-I interlaminar fracture toughness and apparent interlaminar shear strength with concurrent small reductions in T_g and flexural stiffness. Fibre bridging and fibre pull-out were the main mechanisms by which the veils assisted in resisting delamination while also blunting matrix crack tips. It was shown that the incorporation of veils at the surface of the composite reduces both mechanical and thermal properties. DMA tests showed that the crosslink density was reduced in relation to the concentration of nylon within the composite and hence caused increased toughness and decreased stiffness. Further in-depth investigations into the inclusion of nylon interlayers will include damage tolerance via open-hole compression testing and environmental effects on thermo-mechanical properties by moisture ingress.

1. INTRODUCTION

Composite materials are used increasingly in the aircraft industry as they boast higher specific strength and stiffness than their metallic counterparts. However, composites are susceptible to impact damage which may limit their use in structural applications. Also, the cost of the materials required to manufacture a composite part using preimpregnated (prepreg) material based processes, represents an estimated 25-40% of the total cost; the remainder is processing costs. Liquid resin infusion (LRI) is a generic title for processes which involve the infusion of liquid resin into dry fibre preforms, thus the composite material and final part are manufactured in a one-shot process. LRI processes eliminate the expensive prepreg material manufacture and energy-consuming autoclave processing steps, reduce the amount of labour required in the lay-up and enable complex and integrated net-shape parts to be made in one step. LRI has

historically been limited to making composite parts employing relatively brittle resin systems, leading to composites susceptible to impact damage. The aim of the research is to manufacture high quality composites of increased fracture toughness using low viscosity resin formulations via LRI processes.

Studies have shown that toughening the bulk matrix system with particles, such as carbon nanotubes (Davis and Whelan, 2011) and rubber (Kaynak, Sipahi-Saglam and Akovali, 2001), can enhance the fracture toughness of the composite; however, these modifiers can increase the viscosity of the resin – making it more difficult to infuse - and can adversely affect other mechanical and thermal properties. The use of thermoplastic fibres within a thermosetting composite is an area of toughening that has yielded significant results. Hogg (2005) found that the use of commingled thermoplastic fibres in glass and carbon fibre fabrics enhanced the impact and fracture toughness properties of the composite. It was also shown that the incorporation of thermoplastic interlayers was effective in increasing toughness and impact properties. Tzetzis and Hogg (2005) has shown that the use of thermoplastic veils to toughen the bond line of infused repairs can increase the fracture toughness of the repaired structure dramatically. Wong, Lin, McGrail, Peijs and Hogg (2010) reported dramatic increases in fracture toughness, with little effect on Young's Modulus and thermal stability, for small concentrations of a chopped phenoxy fibre interleaf which phase separates in the epoxy matrix during curing. The effects of polyester, polyamide, carbon and hybrid non-woven interlaminar veils on the Mode-I fracture toughness of carbon fibre laminates manufactured using different fabric architectures and different resin systems (epoxy and vinyl ester) were investigated by Kuwata and Hogg (2011). The thermoplastic veils were proven to be the most effective interlayers in increasing the fracture toughness. Yasaee, Bond, Trask and Greenhalgh (2012) has also reported an increase in fracture toughness through the use of thermoplastic interlayers in glass/epoxy composites, and Khan and Kim (2012) observed 31% and 104% improvements in interlaminar shear strength (ILSS) through the inclusion of carbon nanofibre interlayers.

The improvements achieved through the use of thermoplastic interlayers – specifically in carbon/epoxy composites – in toughness, using both autoclave and out-of-autoclave manufacturing methods, are well documented. Thermoplastic veils have the potential to be incorporated into LRI manufacturing processes to realise low-cost composites with superior impact resistance. The inclusion of veils does not involve resin modification and hence a potential rise in viscosity. However, the effects on other mechanical properties, such as stiffness, and thermal properties, such as T_g, have not been investigated in depth. The influences of thermoplastic veils on the manufacturing process, e.g. resin flow and curing kinetics, is also not fully understood. This research aims to investigate the effects of non-woven nylon interlaminar veils on the ILSS and Mode-I fracture toughness of carbon/benzoxazine composites manufactured using the VARTM technique. In addition to this, the stiffness and thermal properties of the modified composites will be compared to the baseline values.

2. EXPERIMENTAL

2.1 Materials. Carbon fibre panels were manufactured using 0/90 Non-Crimp Fabric (NCF) supplied by Saertex (Germany). The resin was a commercially available benzoxazine resin (Epsilon 99120) supplied by Henkel (Germany). To increase the fracture toughness of the panels, thermoplastic veils were incorporated at the interlaminar regions. Non-woven PBN-II nylon veils, with low areal weights of 17 g/m² and 34 g/m², supplied by Cerex Advanced Fabrics (USA) were used in this study.

2.2 Specimen Manufacture. Carbon/Benzoxazine panels were manufactured using the VARTM process. Prior to resin infusion, the resin was degassed in a vacuum oven at 110°C, 850mb for two hours. All nylon veils were dried in the vacuum oven at 90°C for one hour at 850mb to remove moisture. The degassed resin was heated to the infusion temperature of 110°C and infused by vacuum pressure through the dry fabric preform on a heated mould (schematic given in Figure 1). The temperature of the mould was maintained by a bank of insulated ceramic heaters and three PID controllers. Resin, mould and panel temperature are recorded using a thermocouple data logger in conjunction with PicoLog data acquisition software. Once the infusion was completed, a second vacuum bag was placed over the infused area for the duration of the curing process. The temperature of the tool was then increased to 180°C for a dwell time of 90 minutes.

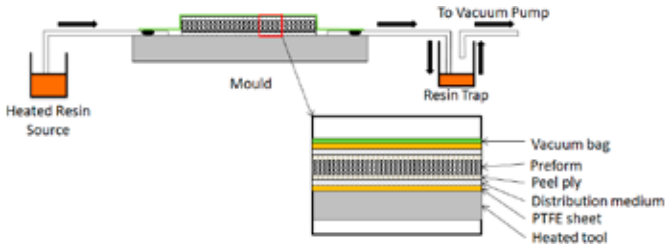

Fig. 1: Schematic of the VARTM manufacturing process; the lay-up of the ancillary materials is mirrored about the preform.

2.3 Characterisation. 2.3.1 Double Cantilever Beam. Mode-I fracture toughness tests, using Double Cantilever Beam (DCB) test specimens, were conducted in accordance with ASTM D5528. A schematic of the test specimen can be seen in Figure 2. For toughened specimens, the nylon veil was placed aft of the film insert i.e. pre-crack. The side of the specimen was sprayed with white primer paint and the first 5mm after the pre-crack marked in 1mm increments and the subsequent 40mm marked in 5mm increments to track crack growth throughout the test. Specimens were loaded at a rate of 3mm/min using a Tinius Olsen Bench-top Tester (model H25KS) with a 10kN load cell. The test was recorded using LaVision Strain Master 2D Digital Image Correlation (DIC) equipment. Using Modified Beam Theory (Figure 2), this test gives initiation and propagation values for Mode-I interlaminar fracture toughness, G_{IC}, the critical value of G for delamination growth as a result of an opening load or displacement.

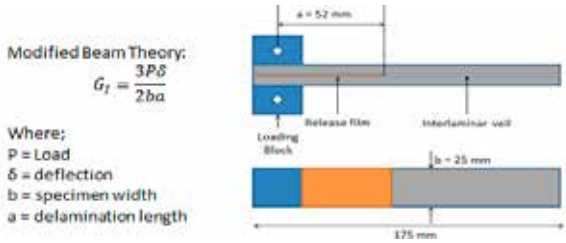

Fig. 2: Modified Beam Theory equation used to calculate G_{IC} and the geometry of DCB test specimens.

2.3.2 Short Beam Shear. Short Beam Shear (SBS) tests were conducted in accordance with BSEN2563 to find the Apparent ILSS. These tests were conducted at a rate of 1mm/min using a three-point bend fixture. Specimen dimensions were 25 mm x 10 mm x 2-3 mm, with thickness

dependent on the veil used. For SBS, flexure and Dynamic Mechanical Analysis (DMA) tests the following abbreviations are used: baseline – B, 34gsm interlaminar veils – 34I, 34gsm interlaminar and surface veils – 34IS, 17gsm interlaminar veils – 17I, and 17gsm interlaminar and surface veils – 17IS.

2.3.3 Flexure. The flexural stiffness was calculated in accordance with ASTM 7264. Tests were conducted at a rate of 1mm/min using a three-point bend fixture. A span-to-thickness ratio of 20:1 was used for each specimen.

2.3.4 Dynamic Mechanical Analysis. DMA was conducted using a TA Instruments Q800 and three point bend fixture. Samples were 60 mm x 10 mm x 2-3 mm in size and the span was 50 mm. Prior to testing, samples were conditioned for 40 hours at 25°C and 50% relative humidity. The specimens were heated from ambient temperature to 250°C at a rate of 5°C/min, amplitude of 10 μm and frequency of 1 Hz. The storage modulus, loss modulus and tan delta were recorded. Crosslink density (ν) was calculated using the equation: $\nu = E'/3RT$, where R is the universal gas constant (8.314 J/K-mole), T is the temperature in Kelvin, and E' is the storage modulus at 50°C above the T_g (Cardona et al. 2010). The T_g is taken as the tan delta peak temperature.

2.3.5 Differential Scanning Calorimetry. Preliminary Differential Scanning Calorimetry (DSC) tests, using a Perkin Elmer Setaram DSC, were conducted to observe the effect of the nylon on the curing reaction of the benzoxazine resin. A temperature sweep test was conducted whereby the sample and reference pan were held isothermal at 30°C for 30 minutes, the temperature was then ramped to 250°C at a rate of 2°C/min and then allowed to cool. The curing onset, enthalpy and offset were recorded.

3. RESULTS

3.1 Double Cantilever Beam. DCB results are presented in Figure 3. Figure 3a shows the load-extension curves for the three variations tested. The point at which the load-displacement curve becomes nonlinear is used as the point to calculate the initiation value for $G_{IC\ (NL)}$. Figure 3b illustrates the 25% reduction in G_{IC} for both toughened laminates and 46% increase in the propagation G_{IC} value for the 34gsm sample. The 17gsm sample showed a reduction of 16%. Toughened samples exhibited steadier crack propagation.

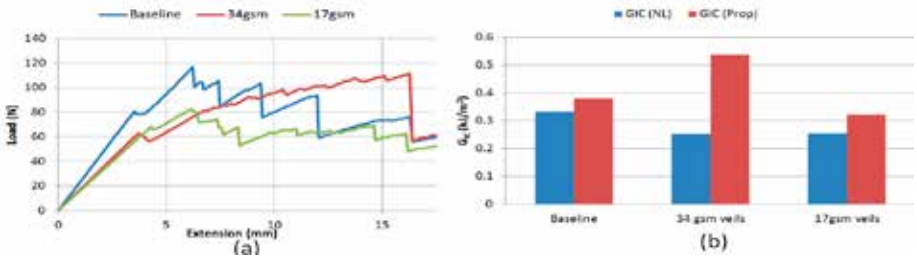

Fig. 3: (a) Load extension graph for baseline, 34gsm nylon veil toughened and 17gsm nylon veil toughened laminates; (b) chart comparing the initiation and propagation G_{IC} value.

3.2 Short Beam Shear. The results for the SBS test are presented in Table 1. Jagged load-extension curve followed initial yield, indicating a multiple shear failure mechanism. Veils were placed both at interlaminar regions and on the surface; however, the apparent ILSS was reduced by the presence of surface veils.

3.3 Flexure. Table 1 also shows that the flexural stiffness was reduced using all configurations of toughener. Samples with surface veils yielded the largest decreases. The reduction in stiffness of the samples with 34gsm interlaminar veils was negligible.

Table 1: SBS, Flexure and Crosslink Density results (relative increase/decrease with respect to the baseline are shown in parentheses).

Sample	Apparent ILSS (MPa)	Flexural Modulus of Elasticity (GPa)	Crosslink Density (moles of chains/cm^3)
B	46.16	49.18	0.9055
34I	46.91 (+8%)	48.30 (-2%)	0.9591 (-43%)
34IS	42.29 (-8%)	39.85 (-19%)	0.4122 (-61%)
17I	46.50 (+1%)	43.31 (-12%)	0.6065 (-12%)
17IS	45.51 (-1.5%)	35.84 (-27%)	0.4895 (-45%)

3.4 Dynamic Mechanical Analysis. Table 1 shows the results for the crosslink density calculated using the equation in section 2.3.4. It can be seen that the nylon significantly reduces the crosslink density of samples with the highest concentrations.

Tan delta is known as the damping parameter and is an indication of the material toughness. Figure 4 shows increases in the tan delta with slight decreases in the peak temperature, i.e. T_g for modified samples. The largest increase in tan delta was produced by the 34gsm interlaminar samples (16%). Reductions in T_g were negligible for all samples.

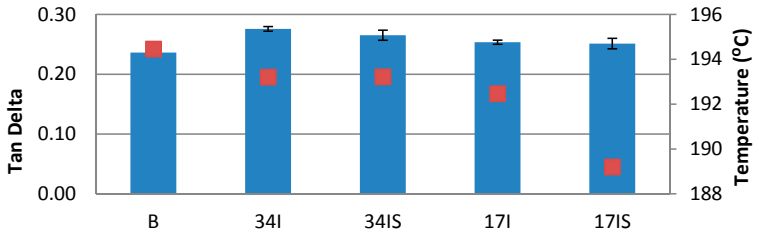

Fig. 4: Comparison of the tan delta values (blue) and tan delta peak temperatures (red) for each type of sample.

The loss modulus (Figure 5) describes the viscous properties of the material and relates to the material's ability to dissipate energy as heat. The peak loss modulus values were increased slightly by the addition of interlaminar veils, but decreased as a result of the surface veils (-27.7% for 34gsm and -17% for 17gsm). The peak loss modulus temperature was not reduced significantly. Figure 6 presents the storage modulus and onset temperature results. The storage modulus is a measure of the material's elasticity and the onset temperature is the temperature at which the storage modulus drops dramatically indicating a loss in rigidity and hence the service temperature ceiling of the material. Small reductions in storage modulus were reported for samples with interlaminar veils, while the samples with interlaminar and surface veils experienced larger decreases (-28.1% for 34gsm and -18.4% for 17gsm). The onset temperature was also decreased for the samples with surface veils and increased for samples without.

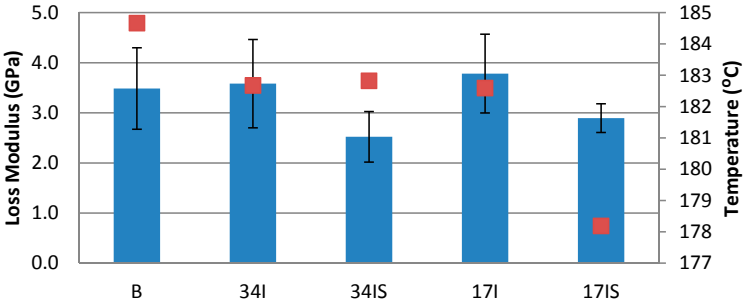

Fig. 5: Comparison of the loss modulus values (blue) and loss modulus peak temperatures (red) for each type of sample.

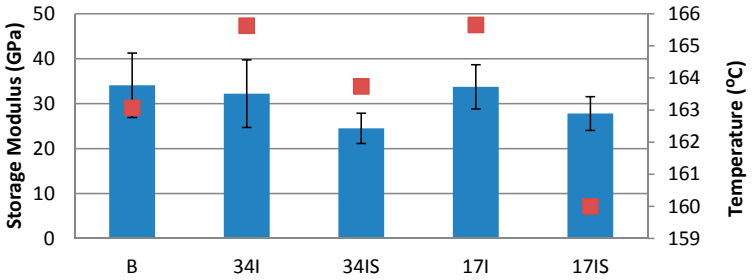

Fig. 6: Comparison of the storage modulus values (blue) and onset temperatures (red) for each type of sample.

3.5 Differential Scanning Calorimetry. Table 2 summarises the main results of the DSC temperature sweep of benzoxazine and benzoxazine modified with nylon. It can be seen that the curing enthalpy is dramatically reduced while the curing onset is greatly increased. The offset temperature and peak are only slightly increased for the sample containing nylon. These preliminary results indicate that the addition of nylon reduces the heat energy emitted during curing (this would make a large scale curing reaction much safer) and also accelerates the reaction.

Table 2: Summary of DSC results.

	Curing Onset (°C)	Curing Enthalpy (J/g)	Curing Offset (°C)	Curing Peak (°C)
Benzoxazine	166.44	-3339.9440	219.01	200.49
Nylon and Benzoxazine	199.36	-229.0912	222.02	210.89

4. DISCUSSION

It was observed in the DCB test that the 34gsm veil increased the fracture toughness of the carbon/benzoxazine composite while the 17gsm laminate did not. This increase can be attributed to the increased level of fibre bridging due to the nylon fibres. The crosslink density results show that the 34gsm interlaminar veils yielded the lowest value and hence the lowest level of bonding between the matrix, toughener and carbon fibres, allowing fibres to be pulled out much easier and bridge crack tips.

The inclusion of both areal weights of nylon interlaminar veils increased the apparent ILSS. As

the samples failed due to a multiple shearing mechanism, cracks travelled through each interlayer. The presence of the thermoplastic veils made the sample capable of blunting the crack tips and also deflected the crack path out of plane, unlike the baseline sample where cracks propagated directly through the brittle matrix. The reduction of apparent ILSS in the samples with surface veils may have been due to the now reduced between the matrix, toughener and carbon fibres at the surface, causing the sample to yield at lower loads than samples without surface veils.

Flexural tests showed small reductions in stiffness for samples with interlaminar veils and larger reductions for samples with interlaminar and surface veils. The reduction in stiffness can be explained again due to the reduction in crosslink density within the composite as a result of the presence of the nylon. However, whereas the lowest crosslink density is found in the 34gsm toughened composites, it is the 17gsm toughened composites that show the greater reduction in stiffness. This is due to the fact that the damage in the flexural sample travels through the composite as matrix cracking and delamination to which, as previously demonstrated in SBS and DCB tests, the 34gsm veil has a higher tolerance than the 17gsm. The crosslink density values were derived from a test where the sample was not subjected to high loading or tested to failure and hence does not fully agree with the results from destructive testing.

Tan delta results show that the inclusion of the veils greatly enhances the toughness of the material. This increase can be explained by the reduction in crosslink density due to the presence of nylon, allowing greater motion of the chains and hence improved damping. This is in line with the DCB and SBS results which show that the greatest improvement is produced by the sample with 34gsm interlaminar veils. It does not agree however, with the results for the samples with interlaminar and surface veils. This, again, is due to the fact that the DMA samples were not tested to failure and hence these samples increased the toughness for samples tested within the elastic limit. Incorporating the veils at interlaminar regions of the samples enhanced the ability of the composite to dissipate energy as heat and was shown by the increase in loss modulus. Further investigation into the thermal and curing properties of the resin and toughener are required to understand why the inclusion of surface veils reduced the loss modulus values, as well as the effect of the nylon on the peak tan delta and onset temperatures. The storage modulus results are directly mirrored by the crosslink density results. This is due to the stiffness being directly proportional to the level of crosslinking. These results agree with the flexure test results for the samples with interlaminar veils only.

5. CONCLUSIONS

It has been shown that the inclusion of non-woven nylon veils at interlaminar regions increases the Mode-I fracture toughness and apparent ILSS of carbon/fibre benzoxazine composites with small reductions in flexural stiffness. DMA testing showed that peak tan delta values, onset temperatures and peak loss modulus values all increased due to the interlaminar veils while the storage modulus and crosslink densities were reduced. The T_g was not reduced significantly. The higher areal weight veil of 34gsm proved to be more effective than the 17gsm veil. This was due to the low level of interaction between the toughener, resin and carbon fibres, allowing a greater level of fibre bridging in the DCB tests and hence producing a composite with higher delamination resistance. The higher concentration of nylon was also more effective in crack-tip blunting during flexural and SBS tests. The incorporation of surface veils was not effective in toughening the composite and actually produced composites with deteriorated properties due to low levels of crosslink density and local premature yielding at the surface in SBS and flexure tests.

6. FUTURE WORK

Further mechanical testing will be conducted in the area of Open-Hole Compression (OHC) testing. Through the introduction of defined damage to the laminate, via a hole, the residual compressive strength of a damaged composite can be measured and damage tolerance inferred. This is a crucial test to conduct as composites can have relatively poor compressive strength and hence it is a limiting property in their application. Characterisation of the interfacial interaction between benzoxazine and nylon will be conducted via Fourier Transform Infrared (FTIR) spectroscopy. DSC curing cycles will be conducted on different concentrations of nylon in benzoxazine. Rheology will be used in conjunction with the DSC results to determine the effect of nylon on the onset of curing. Permeability measurements, using a bespoke permeability rig, and computational flow simulations will be conducted to determine the influence of interlaminar veils on the in-plane and through thickness permeability of a preform. Finally, nylon is widely known to absorb moisture readily. Moisture ingress tests will be conducted to determine the degree of moisture absorption in composites toughened with nylon and its effect on material stiffness and T_g.

ACKNOWLEDGEMENTS

The authors wish to thank Cerex Advanced Fabrics (USA) for supplying the nylon veils, the Irish Research Council for Science Engineering and Technology (IRCSET) for funding and Ms. Inga Rosca and Dr. Anthony Comer for their invaluable help.

REFERENCES

ASTM International (2007a). D5528 Standard Test Method for Mode I Interlaminar Fracture Toughness of Unidirectional Fiber-Reinforced Polymer Matrix Composites. Pensylvannia, USA.

ASTM International (2007b). D7264 Standard Test Method for Flexural Properties of Polymer Matrix Composite Materials. Pensylvannia, USA.

British Standards Institution (1997). EN2563: Carbon fibre reinforced plastics — Unidirectional laminates — Determination of the apparent interlaminar shear strength. United Kingdom.

Cardona, F., Aravinthan, T., Fedrigo, J. & Moscou, C. (2010). Synthesis of Phenolic Bio-resins For Advanced Composites in Civil Engineering Structures. *Southern Region Engineering Conference.* Toowoomba, Australia.

Davis, D. C. & Whelan, B. D. (2011). An experimental study of interlaminar shear fracture toughness of a nanotube reinforced composite. *Composites Part B: Engineering,* 42**,** 105-116.

Hogg, P. J. (2005). Toughening of thermosetting composites with thermoplastic fibres. *Materials Science and Engineering: A,* 412**,** 97-103.

Kaynak, C., Sipahi-Saglam, E. & Akovali, G. (2001). A fractographic study on toughening of epoxy resin using ground tyre rubber. *Polymer,* 42**,** 4393-4399.

Khan, S. U. & Kim, J.-K. (2012). Improved interlaminar shear properties of multiscale carbon fiber composites with bucky paper interleaves made from carbon nanofibers. *Carbon,* 50**,** 5265-5277.

Kuwata, M. & Hogg, P. J. (2011). Interlaminar toughness of interleaved CFRP using non-woven veils: Part 1. Mode-I testing. *Composites Part A: Applied Science and Manufacturing,* 42**,** 1551-1559.

Tzetzis, D. & Hogg, P. J. (2006). Bondline toughening of vacuum infused composite repairs.

Composites Part A: Applied Science and Manufacturing, 37**,** 1239-1251.

Wong, D. W. Y., Lin, L., McGrail, P. T., Peijs, T. & Hogg, P. J. (2010). Improved fracture toughness of carbon fibre/epoxy composite laminates using dissolvable thermoplastic fibres. *Composites Part A: Applied Science and Manufacturing,* 41**,** 759-767.

Yasaee, M., Bond, I. P., Trask, R. S. & Greenhalgh, E. S. (2012). Mode I interfacial toughening through discontinuous interleaves for damage suppression and control. *Composites Part A: Applied Science and Manufacturing,* 43**,** 198-207.

Proceedings of the 34th Risø International Symposium on Materials Science:
Processing of fibre composites – challenges for maximum materials performance
Editors: B. Madsen, H. Lilholt, Y. Kusano, S. Fæster and B. Ralph
Department of Wind Energy, Risø Campus
Technical University of Denmark, 2013

IMPROVEMENT OF THE INTERFACE AND COMPOSITE STRENGTHS OF FLAX FIBRE REINFORCED BIO-EPOXIES: EFFECTS OF ALKALI AND SILANE TREATMENTS

D. Perremans, Y. Guo, J. Baets, A.W. Van Vuure, I. Verpoest

Department of Metallurgy and Materials Engineering, Katholieke Universiteit Leuven, Kasteelpark Arenberg 44 bus 2450, 3001 Heverlee, Belgium

ABSTRACT

In this paper, the joined effects of an alkalization and a silane treatment are explored to improve the durability of flax fibre reinforced bio-epoxies. Additionally, to separate the effect of the solution components, the effect of a water treatment on the interface strength is investigated. Transverse 3 point bending tests have been performed to estimate the efficacy of each of the treatments. Both alkali treatment and silane treatment lead to a threefold increase in interface strength, given the right processing parameters. Water treatment only mildly increases the interface strength. In all cases, the improvement in transverse bending properties is linked to changes in the flax fibre composition, increasing the reactivity with the bio-epoxy matrix. It is further shown that all treatments increase the longitudinal tensile stiffness by around 15%. This improvement is supported by an increase in fibre/matrix interface strength, as confirmed by SEM microscopy. However, only alkali treatment is able to increase the longitudinal tensile strength. The water and silane treatment decrease the plasticity of the composites, which opposes the improvement in fibre/matrix interface strength.

1. INTRODUCTION

Nowadays, more and more attention is diverted to the use of sustainable materials. In that sense, natural fibre reinforced bio-composites, being composed of fully naturally derived building blocks, offer an enormous potential. The potential is further reflected in the mechanical properties and the embodied energy of the composites. The latter is exemplified in Table 1 for construction materials.

Due to their low density of around 1.4g/cm³, the specific mechanical properties of natural fibres are rather high. Flax fibres are for instance reported to outmatch synthetic glass fibres in terms of specific stiffness (Moreno et al. 2007). However, the excellent mechanical properties of natural fibres are only transferred to the composite level in case the interfacial shear strength is

sufficiently high. A study by Van De Weyenberg et al. (2005) proves that for untreated flax fibre reinforced synthetic epoxy composites the interfacial shear strength is limited to 12MPa.

Table 1: Embodied energy of a 1x1m² facade panel with equivalent mechanical performance. The use of natural fibre reinforced synthetic matrix composites reduces the embodied energy by a factor of 8. The substitution of the synthetic matrix by a bio-derived polymer is presumed to further decrease the embodied energy (Hammond 2008).

Material	Embodied energy per unit mass (MJ/kg)	Embodied energy (MJ)
Bricks	8	1968
Aluminium	218	1177
Timber plywood	15	594
Glass/polyester	100	540
Hemp/polyester	69	249

Moreover, most natural fibres consist of similar molecular building structures (pectines, hemicellulose, cellulose and lignines), albeit in various quantities and compositions. These molecular entities, apart from lignines, are rich in hydroxyl groups and thereby prone to heavy water absorption. The diffusion of water molecules weakens the inter-fibre bonds and therefore leads to natural fibres with an increased strain-to-failure and an unfavorable decrease in stiffness. Assarar et al. (2011) show that the longitudinal tensile stiffness of flax fibre reinforced synthetic epoxy composites is reduced by 40% after room temperature immersion in water until saturation. Similarly, the ultimate strain-to-failure is increased by 60%. Equivalent glass fibre composites only yield a reduction in longitudinal tensile stiffness of around 8%.

So, despite their enormous potential, the industrial implementation of natural fibre reinforced bio-composites is currently to a major extent limited by their high sensitivity towards moisture absorption and their low interfacial shear strength. These two effects result in the degradation of the mechanical properties over time. Usually, the moisture resistance and the interfacial shear strength are increased through the application of fibre treatments (Baley et al. 2005; Fery et al. 2011). In this paper, the joined effect of an alkalization and a silane treatment are explored to improve the durability of flax fibre reinforced bio-epoxies. Additionally, to separate the effect of the solution components, the effect of a water treatment on the interface strength is investigated. For all treatments, the effect of concentration and immersion time will be handled. In a last section, it is explored whether the increase in interfacial shear strength as well procures an increase in the longitudinal tensile strength of the unidirectional composites.

2. MATERIALS AND METHODS

This research uses UD hackled flax fibres with an area weight of 250g/m². The flax starting material is kindly delivered by Terre de Lin. In order to treat the fibres, the UD fibres are taped on both ends and immersed in water (water treatment), a NaOH water solution (alkali treatment) or a (3-Aminopropyl)triethoxysilane water solution (silane treatment) respectively. The treatment time and solution concentration are the investigated parameters. In case of the alkali treatment, the fibres are subsequently heavily rinsed with water to ensure neutrality. After treatment, the fibres are dried for at least 24h at 60°C.

The composite samples are produced through vacuum infusion, in which a top plate controls the thickness and surface quality of the samples. The matrix consists of an EPIKOTE 828 LVEL epoxy resin and a NOVOCARD XRF-1400 bio-based novolac hardener in a mass ratio of 320/80. After mixing for 15minutes, the matrix is degassed for 20minutes at 60°C. The infusion

takes place at 75°C. The curing cycle comprises of 2h curing @135°C and 1h post-curing @150°C. The obtained degree of cure is measured with DSC and yields 99.7%.

Transverse three-point bending tests are performed in accordance with the ASTM D790 standard. The dimensions of the samples are 100mm x 10 mm x 1.5 mm. The tests are applied on an Instron 5567 with a 1kN load cell, a sample cross-head velocity of 1.3mm/min and a span length of 64mm. Longitudinal tensile tests are executed according to the ASTM D3039 standard on an Instron 4505 with a load cell of 100kN. The cross-head velocity is set at 1mm/min and an extensometer with a gauge length of 50mm is applied. The dimensions of the samples are 250 mm x 20 mm x 1.5 mm.

A Philips SEM XL30FEG equipped with a Schottky based field emission gun is used to investigate the fracture area of the longitudinal tensile samples. The applied voltage is around 10kV and the scanning mode is to set to detect secondary electrons. Prior to scanning, the composite samples are covered with a thin gold layer by using a S159A Sputter Coater to prevent charging effects. After coating, the samples are placed in a degassing chamber with a pressure of 350 mbar for at least 12 hours to remove moisture.

3. RESULTS AND DISCUSSION

3.1 Transverse three-point bending tests

Figure 1 represents the results of the transverse three-point bending tests that are performed on the alkali treated fibre composites. The untreated composites are included as a reference. For untreated flax reinforced bio-epoxy composites, the transverse flexural strength is around 11.9 MPa with a corresponding average transverse flexural stiffness of 1.1 GPa. The transverse flexural strength is similar to the one measured in the study by Van De Weyenberg et al. (2005).

Figure 1 further indicates that moderate concentrations and short treatment times of alkali treatment lead to the most beneficial improvements in transverse three-point bending results. A 4wt% 5 min alkali treatment is sufficient to improve the transverse three-point bending strength by a factor 2.5 and the transverse three-point bending stiffness by a factor 3.

The improvements in composites' transverse three-point bending strength after alkali treatment are dedicated to a higher interface strength between the flax fibres and the bio-epoxy matrix. This increase in interface strength is linked to the removal of various organic substances with low mechanical properties, inherent to the flax fibre structure. According to several authors, a small amount of water containing solution is already sufficient to remove pectin components (Bledzki and Gassan 1999; Fernyhough et al. 2011). The removal of fibre hemicellulose is forwarded by an increasing alkali concentration, giving rise to a maximal removal content of 3.5 % (Hinrichsen et al. 2000). This leads to an increased amount of hydroxyl groups at the surface of the flax fibres that increase the interaction with the bio-epoxy matrix. The increased interaction can be chemically or physically. The latter is explained by a larger extent of hydrogen bonding. However, given the magnitude of the increase in transverse flexural strength, it is more likely that a chemical reaction takes place. In this light, the moderate improvements at lower concentrations can be linked to an incomplete wax layer removal.

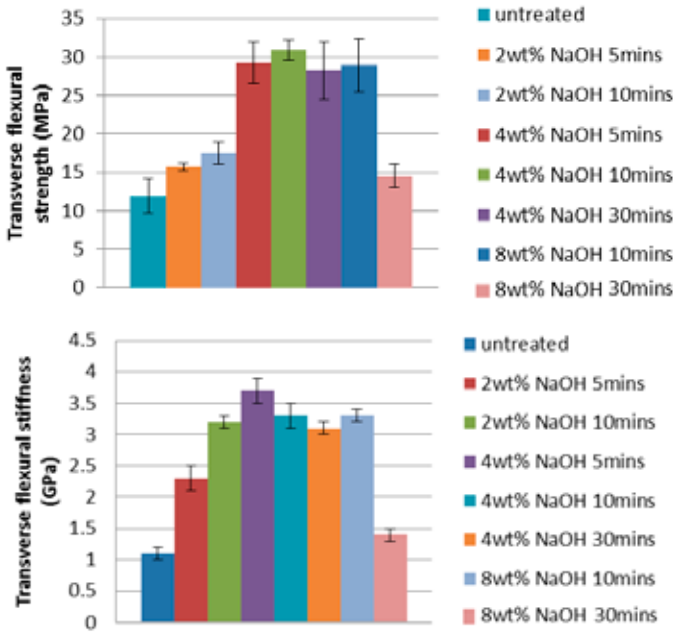

Fig. 1: Overview of the transverse flexural strength (top) and stiffness (bottom) of the alkali treated composite samples. Moderate concentrations and short treatment times of alkali treatment lead to the most beneficial improvements in transverse flexural properties. ($V_f = 35\%$).

The improvements in composites' transverse flexural modulus after alkali treatment are similarly accounted to an increase in interface strength. This increase in interface strength leads to a better load transfer between fibres and matrix, even at smaller strains, and can thus positively influence the transverse flexural modulus. It is further hypothesized that a second effect is present: the improvement in transverse three-point bending stiffness by removal of flax fibre components with low transverse moduli (pectines, waxes). Indeed, the transverse modulus of the composites roughly follows a relationship with the transverse moduli of the components as shown below, in which V_i refers to the volume fraction of the i^{th} component:

$$\frac{1}{E_C} = \frac{1}{V_1 E_1} + \frac{1}{V_2 E_2} + \ldots + \frac{1}{V_n E_n} \quad (1)$$

Table 2 indicates the results of the transverse three-point bending tests of the combined alkali and silane treated samples. It shows that application of silane treatment after alkali treatment does not lead to further improvements in the transverse flexural properties. The reason behind this lies in the fact that the silane molecules that constitute the surface layer of the fibres after treatment are already quite well bonded to the untreated flax fibres, as will be explicated in next paragraphs.

Table 2: Overview of the transverse flexural strength and stiffness of the alkali + silane treated composite samples. Application of silane treatment does not lead to further improvements in the transverse flexural properties. (V_f = 35%).

Treatment	Transverse flexural strength (MPa)	Transverse flexural stiffness (GPa)
4wt% NaOH 5mins	29.2±2.7	3.7±0.2
+2vol% silane 10mins	22.3±1.7	2.1±0.1
+2vol% silane 30mins	28.3±0.9	2.2±0.2
+10vol% silane 30mins	28.1±1.1	2.2±0.1

Figure 2 visualizes the results of the transverse three-point bending tests that are performed on the silane treated fibre composites. The untreated composites are as well included as a reference. From this figure, it is clear that silane treatment is able to improve the transverse flexural strength of the flax bio-epoxy composites to the same extent as alkali treatment. The transverse flexural stiffness is only improved by 66% compared to the alkali treated specimens. A 10wt% 10min silane treatment is sufficient to improve the transverse three-point bending strength by a factor of 2.5 and the transverse three-point bending stiffness by a factor of 2.5.

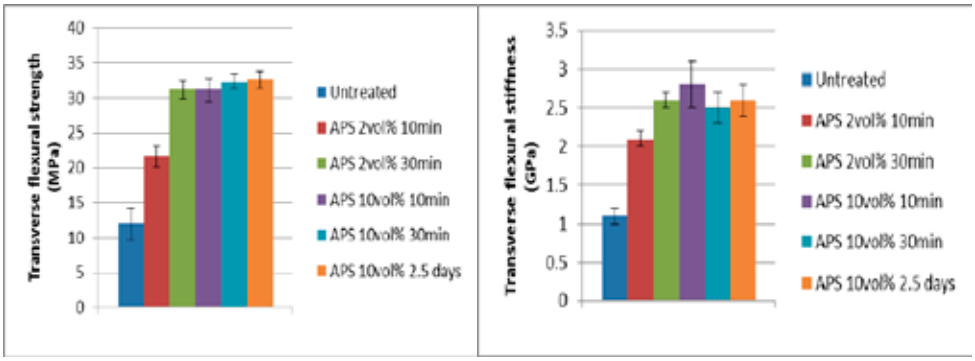

Fig. 2: Overview of the transverse flexural strength (left) and stiffness (right) of the silane treated composite samples. Moderate concentrations and short treatment times of silane treatment already constitute a maximal improvement in transverse flexural properties. (V_f = 35%).

The authors assume that the fortifying mechanism implies the formation of an amorphous coating structure at the surface of the flax fibres. Presumably, on the one hand the hydrolyzed silane molecules physically adhere to or chemically react with the exposed hydroxyl groups at the surface of the flax fibres, while on the other hand they chemically react with the bio-epoxy matrix. During treatment, diffusion kinetics determine the thickness of the coating layer, implying that longer treatment times or increased concentration magnify the silane deposition rate. With long treatment time and/or high concentration, this coating presumably consists of multiple layers of silane molecules that form an open network, held together by weak Van Der Waals forces and hydrogen bridges. Under application of a transverse tensile load to the coated fibres, the weakly held silane molecules will easily adjust their position to accommodate the imposed deflection, procuring a low stiffness. At higher strains, the mobility of the silane molecules is more restricted. In this case, the interface strength will be governed by the extent of hydrogen bonds within the coating.

To undoubtedly link the improvements in transverse three-point bending strength to the

presence of silane molecules in the solution, the effect of water treatment is verified. Table 3 summarizes the results of the transverse three-point bending tests that are performed on the water treated fibre composites. The untreated composites are as well included as a reference. Comparison of Table 3 and Figure 2 reveals that the major improvement in transverse flexural properties is assigned to the presence of silane molecules in the solution. Water treatment allows for a 50% increase in transverse flexural stiffness and strength compared to the untreated composites. This improvement is linked to the removal of pectin components in the flax fibre structure, which follows the above stated strategies to account for an increase in interface strength and by weakest link extrapolation an increase in transverse three-point bending strength.

Table 3: Overview of the transverse flexural strength and stiffness of the water treated composite samples. Water treatment leads to moderate improvements in the transverse flexural properties. (V_f = 35%).

Treatment	Transverse flexural strength (MPa)	Transverse flexural stiffness (GPa)
Untreated	11.9±2.2	1.1±0.1
Water 30mins	18.2±0.6	1.4±0.2
Water for 2 days and a half	18.9±1.1	1.7±0.2

3.2 Longitudinal UD tensile tests

The previous sections indicate that the treatments succeed in improving the interface quality of the flax fibre reinforced bio-epoxy composites. The improvement in interface strength should lead to a better load transfer between adjacing fibres and should therefore also constitute an improvement in the final tensile properties of the treated composites, albeit to a smaller extent. In order to investigate this hypothesis, a series of longitudinal tensile tests is performed on both treated and untreated composites. The result of this tensile test series is visible in Table 4.

Table 4: The longitudinal tensile properties of both treated and untreated flax fibre reinforced bio-epoxy composites. The longitudinal tensile properties are back-calculated to a fibre volume fraction of 40 % using the rule of mixtures. The table shows that all treatments succeed in increasing the longitudinal tensile stiffness due to improved interfacial adhesion between the technical flax fibres and the matrix.

treatment	Longitudinal tensile stiffness (GPa)	Longitudinal tensile strength (MPa)	Longitudinal strain-to-failure (%)
Untreated	25.1±0.9	224±7	1.2±0.1
Water (30min)	29.2±1.0	225±20	0.9±0.1
Silane (10vol% 10min)	28.8±1.0	230±18	0.9±0.1
Alkali (4wt% 5min)	28.5±0.9	256±16	1.1±0.1

Table 4 validates that the different treatments lead to a significant improvement in the longitudinal tensile stiffness of the composites. In analogy with the previous observations, these improvements are supported by better interfacial adhesion between the flax fibres and the bio-epoxy matrix. All treatments seem to improve the longitudinal tensile stiffness by around 15%. Regarding the longitudinal tensile strength of the composites, only alkali treatment yields a significant improvement of around 15%. Both water and silane treatments decrease the plasticity of the fibre composites, which opposes the improvement in flax bio-epoxy interface strength.
The improvement in fibre/matrix interfacial shear strength is also observed under SEM microscopy. Figure 3 shows SEM images of the cross-section of an untreated (A) and various

treated (B-D) flax fibre composites after tensile test failure. Figure 4 further reveals that the fibre/matrix interface is broken in untreated composites after tensile testing. This debonding is presumed to happen at low strains, giving rise to a global decrease in longitudinal tensile stress-strain response. The debonding between flax fibres and matrix is absent in the SEM microscopy analysis of the cross-section of treated flax fibre composites after tensile test failure.

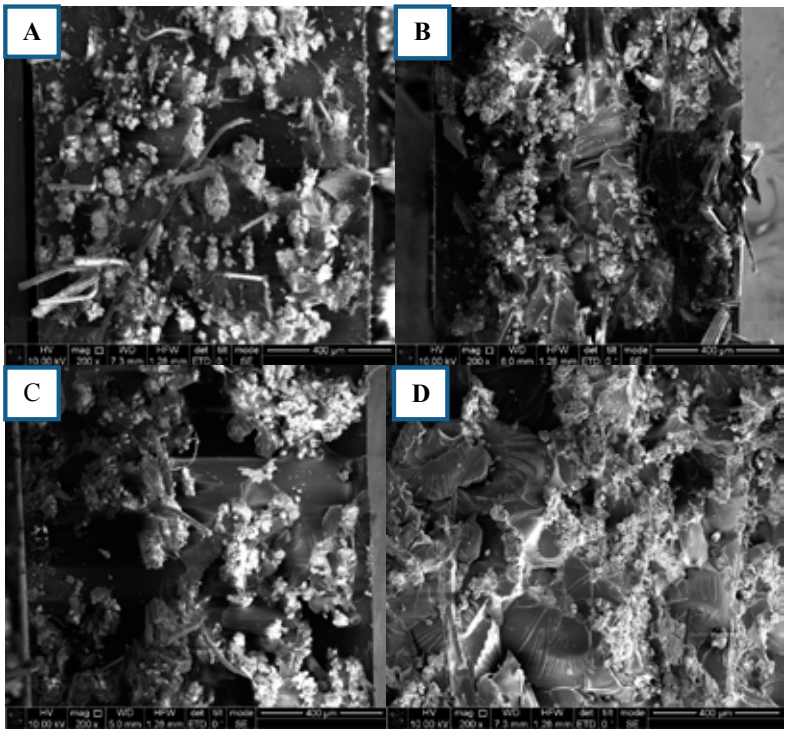

Fig. 3: SEM images of the cross-section of untreated (A), alkali treated (B), water treated (C) and silane treated (D) composites after tensile test failure. All images indicate a brittle failure with fibre pull-out.

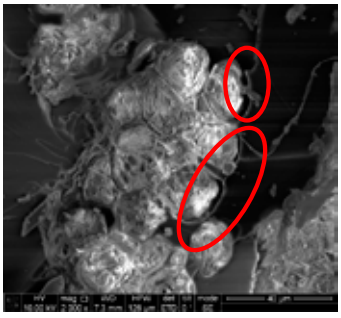

Fig. 4: SEM image of the cross-section of an untreated composites after tensile test failure at larger magnification. The image indicates that the technical fibres primarily debonded from the matrix, implying a weak technical fibre/matrix interface.

4. CONCLUSIONS

In this paper, the effect of silane, alkali and water treatment on the mechanical properties of flax fibre reinforced bio-epoxies is investigated. Transverse three-point bending tests are applied to investigate the optimal treatment parameters for each treatment. For alkali treatment, immersion of the fibres in a 4 wt% water solution for 5mins leads to an optimal improvement in the transverse flexural strength from 11.9±2.2 to 29.2±2.7 MPa and stiffness from 1.1±0.1 to 3.7±0.2 GPa. The optimal silane treatment is able to statistically yield the same transverse flexural strength (31.1±1.7 MPa), but cannot rise up to the same transverse flexural stiffness (2.8±0.3 GPa). Furthermore, the best water treated composites shows a transverse flexural strength of 18.2±0.6 MPa with corresponding flexural stiffness of 1.4±0.1 GPa. In all cases, the improvement in transverse bending properties is linked to changes in the internal flax fibre composition, increasing the reactivity with the bio-epoxy matrix.

In order to investigate the improvement of the fibre treatments on the longitudinal tensile properties of UD flax fibre reinforced bio-composites, a series of tensile tests is carried out. It is shown that all treatments increase the longitudinal tensile stiffness by around 15%. This improvement is supported by an increase in fibre/matrix interface strength, as confirmed by SEM microscopy. However, only alkali treatment is able to increase the longitudinal tensile strength. The water and silane treatment decrease the plasticity of the composites, which opposes the improvement in fibre/matrix interface strength.

ACKNOWLEDGEMENTS

The authors wish to thank the EU-FP7-financed BioBuild project for their contribution.

REFERENCES

Assarar, M., Ayad, R., El Mahi, A., Poilâne, C., Scida, D. (2011). Influence of water ageing on mechanical properties and damage events of two reinforced composite materials: Flax–fibres and glass–fibres, Materials and Design 32, 788–795.

Baley, C., Busnel, F., Grohens, Y., Sire, O., (2005). Influence of chemical treatments on surface properties and adhesion of flax polyester resin, Composites: Part A 37, 1626–1637.

Bledzki, A.K., Gassan, J., (1999). Possibilities for improving the mechanical properties of jute/epoxy composites by alkali treatment of fibres, Composites Science and Technology, 59(9): p. 1303-1309.

Fernyhough, A., Pickering, K.L., Sawpan, M.A., (2011). Effect of fibre treatments on interfacial shear strength of hemp fibre reinforced polylactide and unsaturated polyester composites, Composites: Part A 42, 1189–1196.

Fery, A., Kafta, O., Le Troëdec, M., Max, E., Peyratout, C., Rachini, A., Rossignol, S., Smith, A., (2011). Influence of chemical treatments on adhesion properties of hemp fibres, Journal of Colloid and Interface Science 356, 303–310.

Hammond, Jones, Inventory of Carbon and Energy (ICE), University of Bath, 2008.

Hinrichsen, G., Khan, M.A., Mohanty, A.K., (2000). Influence of chemical surface modification on the properties of biodegradable jute fabrics—polyester amide composites, Composites Part A: Applied Science and Manufacturing, 31(2): p. 143-150.

Ivanova, O.N., Lebedeva, T.N., Prusov, A.N., Voronova, M.I., Zakharov, A.G., (2003). Structural Changes Induced in Flax Cellulose by Alkaline Treatment, Russian Journal of Applied Chemistry, 76(12): p. 1993-1997.

Moreno, L., Osorio, L., Trujillo, E. (2007). Estudio de las caracteristicas fisicas de los haces de

fibra de Guadua angustifolia Kunth. Revista Scientia et Technica, N° 34 , 613-617.
Van De Weyenberg, I., De Corte, B., Van Acker, J., Stevens, M., Stevens, C.V., Verpoest, I. (2005). A quantitative evaluation of the interface of flax fibre composites through microdroplet tests. In the Proceedings of ICCM-15, Durban, South Africa, p. 535-536.

Proceedings of the 34th Risø International Symposium on Materials Science:
Processing of fibre composites – challenges for maximum materials performance
Editors: B. Madsen, H. Lilholt, Y. Kusano, S. Fæster and B. Ralph
Department of Wind Energy, Risø Campus
Technical University of Denmark, 2013

PRELIMINARY CHARACTERIZATION OF GLASS FIBER SIZING

Helga Nørgaard Petersen, Yukihiro Kusano*,
Povl Brøndsted*, and Kristoffer Almdal

Department of Micro- and Nanotechnology, Technical University of Denmark, Ørsteds Plads, Building 345E,
DK-2800 Kgs. Lyngby, Denmark
*Department of Wind Energy, Section of Composites and Materials Mechanics, Technical University of Denmark, Risø Campus,
Frederiksborgvej 399, DK-4000 Roskilde, Denmark

ABSTRACT

Glass fiber surfaces are treated with sizing during manufacturing. Sizing consists of several components, including a film former and a silane coupling agent that is important for adhesion between glass fibers and a matrix. Although the sizing highly affects the composite interface and thus the strength of the composites, little is known about the structure and chemistry of the sizing. A part of sizing was extracted by soxhlet extraction. The fibers were subsequently burned and some fibers were merely burned for analysis of glass fiber and sizing. The results showed that the analyzed fibers had amounts of bonded and physisorbed sizing similar to what has been presented in literature. An estimated sizing thickness was found to be approximately 100 nm. It is indicated that an epoxy-resin containing film former and a polyethylene oxide lubricant are present, yet no silanes or other sizing components were identified in the extractant.

1. INTRODUCTION

Reinforcements in fiber composites are mainly glass or carbon fibers, although aramid, polyethylene and cellulose fibers are also used. Carbon fibers are superior by having the highest stiffness and tensile strength as well as a rather low density. However carbon fibers have the disadvantage of the price due to expensive raw materials and a complicated manufacturing process. Glass fibers are not as strong as carbon fibers but much cheaper to manufacture. This is the reason why glass fiber composites take a first place as the most widely used material for wind turbine rotor blades (Brøndsted, Lilholt and Lystrup 2005). When looking into manufacturing of a mechanically strong material to be used for wind turbine blades, certain requirements should be met: high material stiffness, a low density and a long fatigue-life. These

properties are crucial to obtain optimal performance regarding aerodynamic, gravity forces and material degradation (Stevens 1999).

The handling and the performance of glass fibers and glass fiber reinforced composites both depend highly on the applied surface treatment (sizing) of the fibers. Despite the importance, the nature and properties of the sizing and the interface in the composites are poorly understood and documented in the literature (Thomason 2012). Sizing is an important part of composite materials and its chemistry is considered to be crucial to the properties of the composites. The exact composition of the full sizing is often hidden as commercial recipes by manufacturers. It can be the reason why comprehensive understanding of the full sizing structure is not reported in the literature. Only a simplified structure is suggested by Liu, Thomason and Jones (2008) consisting of a mixture of silane polymer chains bonded to the fiber surface and physisorbed in the sizing layer together with a film former. Figure 1 shows a conceptual view of a cross section of sizing on a glass fiber.

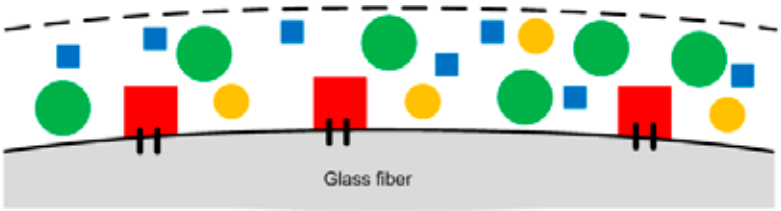

Fig. 1: Simplified illustration of the sizing layer. (■) Bonded organosilane polymer, (■) free organosilane oligomer, (●) film former and (●) other sizing components.

Little is known about the chemistry of the full multi-component sizing as the focus in the literature is often on one component: the silane coupling agent which is believed to be primarily responsible for the adhesion between glass fibers and a matrix (Plonka, Mäder, Gao, Bellmann, Dutschk and Zhandarov 2004). Organosilanes are obvious as coupling agents between the inorganic surface of glass fibers and the organic matrix since they contain both silica and organic functional groups being capable of forming bonds to both materials (Plueddemann 1981; Shokoohi, Arefazar and Khosrokhavar 2008). Many organosilanes have been investigated for their adhesive properties towards matrices used in composite materials (Ivashchenko 2009). Organosilanes with amino or epoxide groups are suggested to be especially well functioning with epoxy matrices (Shokoohi et al. 2008; Jones 2010).

The organosilanes can bond to each other by condensation reactions of the hydrolyzed alkoxy groups (silanol groups) and to silanol groups on the glass fiber surface. The possibility of crosslinking arises since functionalized trialkoxysilanes are the most used. The reaction of organosilanes forms polymers of different lengths while the reaction between organosilanes and silanol groups on the glass fiber surface leads to a chemical bond between them. Non-bonded polymers will be physisorbed in the sizing layer. The bonding of organosilanes as small oligomers and larger polymer chains in the sizing layer governs a complex network (Wang and Jones 1994; Liu et al. 2008; Jones 2010).

Organosilanes dominate only 10% of the many-component sizing. In fact the main component is the film former that represents approximately 79 % (Gorowara, Kosik, McKnight and McCullough 2001). The film former is added to ease the handling by providing good processing characteristics. The film former protects against fiber-fiber damage but also keeps the fibers together in a strand. The film former along with organosilanes set the efficiency of the wetting.

The choice of film former depends on the compatibility with the utilized polymer matrix. So the number of different film formers is connected to the number of available polymer matrices. The most commonly utilized film formers are: polyurethanes, polyvinyl acetates, polyesters, polyalkenes and epoxies (Dwight 2000; Thomason 2001; Zinck 2001; Rudzinski, Häussler, Harnisch, Mäder and Heinrich 2011). The extractable part of the silane is considered to be able to diffuse into the matrix together with the film former (Jones 2010).

In this paper, a preliminary characterization result of the glass fiber sizing is presented. To investigate the sizing, commercially available fibers as received are compared with fibers washed in a soxhlet for 24 h to remove extractable sizing and/or with fibers burned at 565°C for 3 h to remove organic components.

2. EXPERIMENTAL METHODS

The fibers used in this investigation were E-glass fibers (a tex number of 1200, 17 µm diameter of monofilament, moist content ≤ 0.10% and sizing content in the range of 0.45-0.70%) supplied by Jushi (Chengdu, China). Attenuated Total Reflectance Fourier Transform Infrared (ATR-FTIR) spectroscopy was conducted on a Perkin Elmer spectrum 100. The analyses were performed from 4000 to 650 cm^{-1} with a resolution of 4 cm^{-1} and 16 scans per sample. Extracted samples were dissolved in acetone before placed on the ATR crystal. The acetone was subsequently evaporated prior to analysis. Two pure organosilanes were used as reference materials to identify characteristic bands: 3-aminopropyltrimethoxysilane (abbreviated 3-APTMS, 97%, ρ_{APTMS} = 1.03 g/ml) and 3-glycidoxypropyltrimethoxysilane (abbreviated 3-GPTMS, ≥98%, ρ_{GPTMS} = 1.07 g/ml) both from Sigma-Aldrich (Steinheim, Germany).

Extraction of sizing combined with burning of glass fibers is often used as a method to obtain values of the amount of loosely bound and physisorbed sizing. Extraction will remove the physisorbed organosilanes and a film former. Burning the fiber will remove all organic materials and organic functional groups leaving the part of the sizing that is strongly bonded to the fiber surface e.g. through Si-O bonds. By comparing the obtained value with the value of the amount of sizing that can be extracted, a distribution of loosely bound and physisorbed sizing can be calculated. The amount of strongly bonded sizing can be calculated only if the total amount of sizing is stated by the manufacturer (Tanoglu, Ziaee, McKnight, Palmese and Gillespie 2001).

The burn-off experiment was performed with fivefold determination. Before burning, the fibers were dried in a vacuum oven at 0.2 bars and 80°C for 2 h. Five dry crucibles with 10 g of dry fibers were placed in a furnace at 565°C for 3 h. The fibers were weighed to determine the moist content and loss on ignition (LOI) after burn off.

The acetone extraction was based on the work of Tanoglu et al. (2001), see Fig. 2. A similar approach is taken by Zhuang, Burghardt and Mäder (2010), Mallarino, Chailan and Vernet (2005), Feih, Wei, Kingshott and Sørensen (2005), Gorowara et al. (2001) and Liu et al. (2008). The extractable sizing was removed from the fibers by soxhlet extraction in spectroscopic grade acetone (Sigma-Aldrich, Steinheim, Germany) for 24 h. Each extraction was done with approximately 10 g of fibers. The fibers were weighed before and after the extraction and the drying to calculate the amount of the extracted sizing.

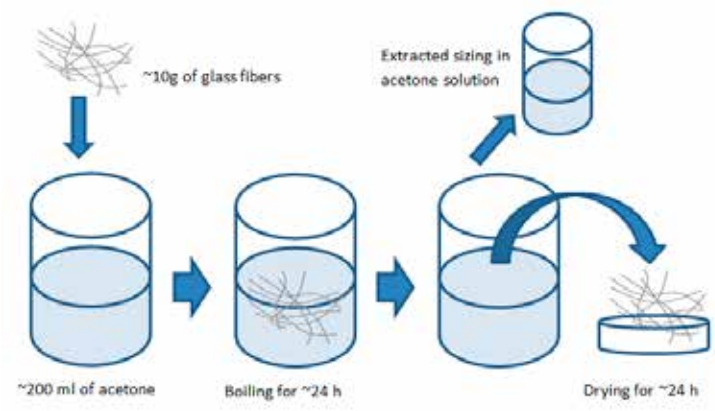

Fig. 2: A schematic presentation of the extraction process.

3. RESULTS AND DISCUSSION

It is reported that the amount of sizing varies and is in general in the range of 0.2-2 wt.% (Wu, Dwight and Huff 1997). The extractable part of sizing is mostly film former. This is supported by an extensive investigation of different commercial E-glass rovings by Thomason (1995) showing that the extractable amount of sizing was around 80-90 % of the total amount of sizing, which was in the range of 0.2-1.0 wt.%.

The results of acetone extraction and burn-off experiments are summarized in Table 1 and Fig. 3. It was observed that after extraction the fibers seemed softer and electrostatically charged. After burning they seemed more fragile and brittle. The observations correspond with the extraction of the film former and burn off of the organic parts of the sizing on the fibers.

Table 1: Results of weight loss from burn off and acetone extraction experiments. The values are given as weight percentages, the mass loss compared to the weight before burning and/or extraction.

	As received fibers	**Extracted fibers**
LOI	0.630% ± 0.007	0.070% ± 0.001
Moist	0.024% ± 0.060	0.050% ± 0.041
Extracted	0.502% ± 0.098	-

The amount of removable sizing can be estimated from values given by the manufacturer; however the sizing content is presented as a range. Using the highest value it is estimated that up to 25 wt.% cannot be removed by extraction or burning at 565°C.

The extractable amount of sizing (green area in Fig. 3) can be calculated as the share that the extracted sizing represent of the total amount of removable sizing (yellow area in Fig. 3) to be in the range of 80-90 wt.%. The amount of removable sizing on the fibers is consistent with values reported by Thomason (1995); the same is valid for the amount of extractable sizing. Comparing the mass losses indicated that the amount of oligomers is negligibly small. The moist contents show a good agreement to the value given by the manufacturer.

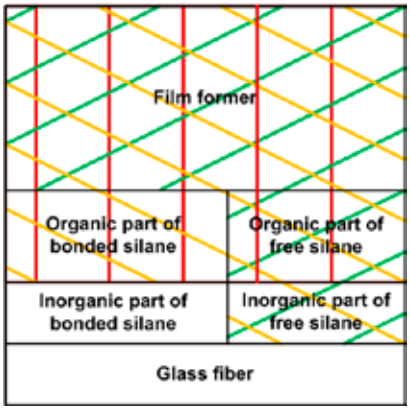

Fig. 3: A schematic presentation of the experimental results. The area covered by (||) equals the 0.63 wt.% that is lost by burning at 565°C. The area covered by (//) equals the 0.50 wt.% that is extracted by soxhlet extraction of the fibers. The area covered by (\\) equals the sum of the mass loss from the extraction and the subsequently burning which is 0.50 + 0.07 = 0.57 wt.%.

From the diameter of the fibers and the sizing content the sizing thickness can be estimated with Equation 1 to be approximately 60 nm, assuming the densities of sizing and glass fiber to be 1 and 2.5 g/cm^3, respectively (Brøndsted et al. 2005). This thickness is reasonable, compared with the report by Thomason (1999) stating that the sizing layer is unevenly distributed with thicknesses in the range of 1 nm-1 µm.

$$t = \frac{(sizing{-}wt\%) \cdot r \cdot \rho_{glass\ fiber}}{2 \cdot \rho_{sizing}}, \quad (1)$$

where t, r, $\rho_{\text{glass fiber}}$ and ρ_{sizing} are sizing thickness, fiber radius, density of sizing and density of glass fiber, respectively. The sizing-wt.% is the weight of sizing compared to the glass fiber.

Commonly used organosilanes have either an amino, epoxy or a vinyl group attached when used with polymer matrices of epoxy or unsaturated polyester. It is reported that especially 3-aminopropylsilane, 3-glycidopropylsilane, 3-aminoethylaminepropylsilane and chlorine-substituted aminosilane have the ability to enhance the adhesion of glass fibers to epoxy resins (Shokoohi et al. 2008; Jones 2010). Thus an aminosilane (3-APTMS) and an epoxysilane (3-GPTMS) were chosen as references for comparison of FTIR spectra.

The FTIR spectra of analysed fibers are shown in Fig. 4. The spectra from analysis of fibers are not shown below 1200 cm^{-1} since any other bands are dominated by strong absorption from Si-O-Si bonds in the glass fiber that are in the region of 900-1100 cm^{-1}. The signal from silicon oxide is much stronger since the weight percentage of sizing is as low as around 0.6 wt.%. The spectra of burned and extracted fibers exhibit none of the characteristic bands found in the spectra of extracted or reference silanes. It is therefore indicated that the concentration of the extracted silanes could be below the detection limit.

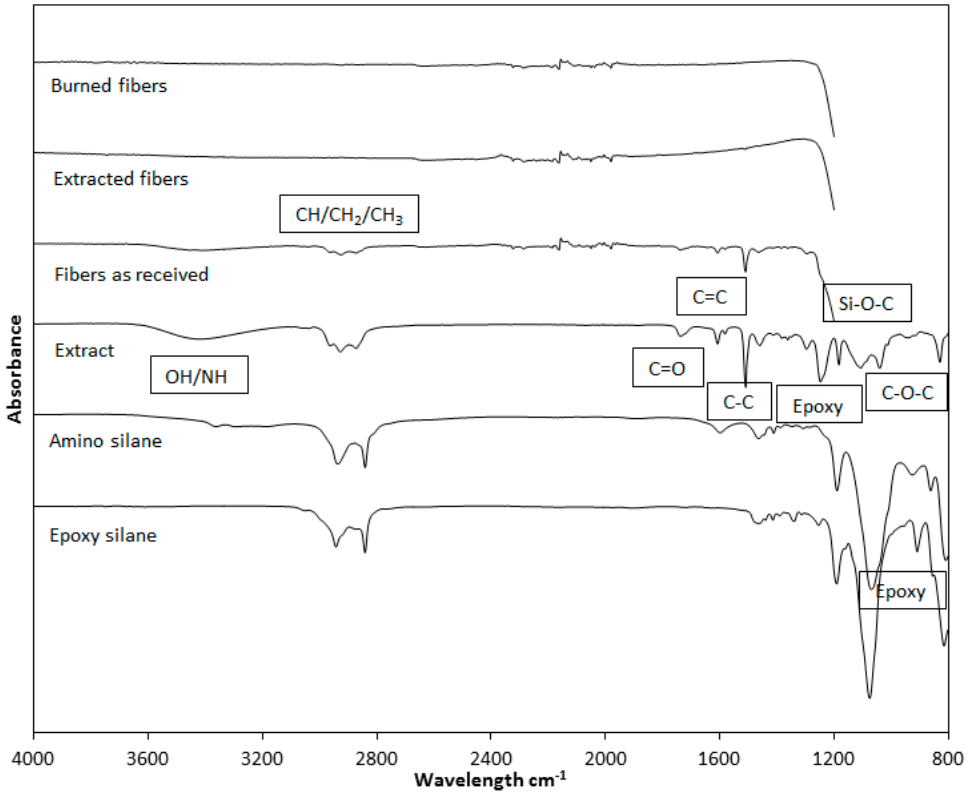

Fig. 4: FTIR spectra of as received, burned and acetone extracted fibers, the extractant and the two reference organosilanes.

The broad band between 3200 and 3600 cm^{-1} in the spectrum of both fibers as received and after extraction is assigned to stretching in N-H/O-H bonded to C and Si alike. The collection of bands around 2965-2873 cm^{-1} is attributed to stretching in C-H of CH, CH_2 and CH_3, both in aromatic and aliphatic compounds. The band at 1735 cm^{-1} corresponds to stretching of C=O in esters/carbonyl. The bands around 1100 cm are assigned stretching of C-O and Si-O which could indicate the presence of polyethylene and/or some kind of silicon oxide compounds. The bands at 1608, 1509, 1040 and 830 cm^{-1} all correspond to an epoxy resin and can be assigned to stretching in C=C of aromatic rings, C-C in aromatics, C-O-C of ethers and C-O-C in oxirane group, respectively. The bands at 1248 and 1183 cm^{-1} are also attributed to the epoxy resin. The spectrum of epoxy silane displays the characteristic epoxy band at 916 cm^{-1}. The presence of the C-O-C band can also originate from polyethylene oxide which is used as lubricant and surfactant in sizing (Salmon, Thorminette, Pays, and Verdu 1997; Dwight 2000; Gorowara et al. 2001; Macan, Ivanković, Ivanković and Mencer 2004; Zhuang et al. 2010; Rudzinski et al. 2011; Öhman and Person 2011).

4. CONCLUSIONS

The removed amounts of sizing correspond well with the values found in the literature. Likewise is the amount of extractable sizing of 80-90 wt.% considered common in commercially available glass fibers. Comparing the sizing content to the one stated by the manufacture it was estimated that up to 25 wt.% of the sizing is not removable and must be considered strongly chemically bonded to the surface.

The absorption bands in the ATR-FTIR spectra of as received fibers and extracted sizing correspond reasonable with the presence of an epoxy-resin containing film former and a polyethylene oxide lubricant/surfactant compared to band values found in the literature.

ACKNOWLEDGEMENTS

This work was supported by the Danish Centre for Composite Structures and Materials for Wind Turbines (DCCSM) from the Danish Research Council for Strategic Research (grant number: 09-067212).

REFERENCES

Brøndsted, P., Lilholt, H., and Lystrup, A. (2005). Composite materials for wind power turbine blades. Annu. Rev. Mater. Res. 35, 505–538.

Dwight, D.W. (2000). Glass Fiber Reinforcements. In: Comprehensives Composite Materials 2000. Eds. Kelly A., Zweiben C. (Elsevier, Amsterdam), vol. 1 chapter 8, 231 – 261.

Feih S., Wei, J., Kingshott, P., and Sørensen, B.F. (2005). The influence of fibre sizing on the strength and fracture toughness of glass fibre composites. Composites Part A: Applied Science and Manufacturing 36, 245–255.

Gorowara, R.L., Kosik, W.E., McKnight, S.H., and McCullough, R.L. (2001). Molecular characterization of glass fiber surface coatings for thermosetting polymer matrix/glass fiber composites. Composites Part A: Applied Science and Manufacturing 23, 323–329.

Ivashchenko, E.A. (2009). Sizing and finishing agents for basalt and glass fibers. Technology of polymeric and composite materials 43, 511–516.

Jones, F.R. (2010). A review of interphase formation and design in fibre-reinforced composites. Journal of Adhesion Science and Technology 24, 171–202.

Liu, X., Thomason, J. L., and Jones, F.R. (2008). XPS and AFM study of interaction of organosilane and sizing with E-glass fibre surface. The Journal of Adhesion 84, 322–338.

Macan, J., Ivanković, H., Ivanković, M., and Mencer, H.J. (2004). Study of cure kinetics of epoxy-silica organic–inorganic hybrid materials. Thermochimica Acta 414, 219-225.

Mallarino, S., Chailan, J.F., and Vernet, L.J. (2005). Glass fibre sizing effect on dynamic mechanical properties of cyanate ester composites. I. Single frequency investigations. European Polymer Journal 41, 1804–1811.

Öhman, M., and Persson, D. (2011). ATR-FTIR Kretschmann spectroscopy for interfacial studies of a hidden aluminum surface coated with a silane film and epoxy I. Characterization by IRRAS and ATR-FTIR. Surface and Interface Analysis 44, 133-143.

Plonka, R., Mäder, E., Gao, S.L., Bellmann, C., Dutschk, V., and Zhandarov, S. (2004). Adhesion of epoxy/glass fibre composites influenced by aging effect on sizings. Composites Part A: Applied Science and Manufacturing 35, 1207–1216.

Plueddemann, E.P. (1981). Principles of interfacial coupling in fibre-reinforced plastics. International Journal of Adhesion and Adhesives Oct., 305–310.

Rudzinski, S., Häussler, L., Harnisch, Ch., Mäder, E., and Heinrich, G. (2011). Glass fibre reinforced polyamide composites: Thermal behaviour of sizings. Composites Part A: Applied Science and Manufacturing 42, 157-164.

Salmon, L., Thorminette, F., Pays, M.F., and Verdu, J. (1997). Hydrolytic degradation of model networks simulating the interfacial layers in silane-coupled epoxy/glass composites. Composites Science and Technology 57, 1119-1127.

Shokoohi, S., Arefazar, A., and Khosrokhavar, R. (2008). Silane coupling agents in polymer-based reinforced composites: A review. Journal of Reinforced Plastics and Composites 27, 473–485.

Stevens, M.P. (1999). Polymer Chemistry an Introduction. Oxford University Press.

Tanoglu, M., Ziaee, S., McKnight, S.H., Palmese, G.R. and Gillespie, J.W. (2001). Investigation of properties of fiber/matrix interphase formed due to the glass fiber sizings. Journal of Materials Science 36, 3041–3053.

Thomason, J. L. (1995). The interface region in glass fibre-reinforced epoxy resin composites: 3. Characterization of fibre surface coatings and the interphase. Composites 26, 487–498.

Thomason, J.L., and Adzima, L.J. (2001). Sizing up the interphase: an insider's guide to the science of sizing. Composites Part A: Applied Science and Manufacturing 32, 313-321.

Thomason, J.L. (2012). Glass Fibre Sizings – A Review of the Scientific Literature. Publisher: J.L.Thomason, University of Strathclyde, Scotland.

Wang, D., and Jones, F. (1994). TOF SIMS and XPS study of the interaction of aminosilanised E-glass fibres with epoxy resins. Part I: Diglycidyl ether of bisphenol S. Composites Science and Technology 50, 215-228.

Wu, H.F., Dwight, D.W., and Huff, N.T. (1997). Effect of silane coupling agents on the interphase and performance of glass-fiber-reinforced polymer composites. Composites Science and Technology 57, 975–983.

Zhuang, R.-C., Burghardt, T. and Mäder E. (2010). Study on interfacial adhesion strength of single glass fibre/polypropylene model composites by altering the nature of the surface of sized glass fibres. Composites Science and Technology 70, 1523–1529.

Zinck, P., Mäder, E., and Gerard, J.F. (2001). Role of silane coupling agent and polymeric film former for tailoring glass fiber sizings from tensile strength measurements. Journal of materials science 36, 5245-5252.

Proceedings of the 34th Risø International Symposium on Materials Science:
Processing of fibre composites – challenges for maximum materials performance
Editors: B. Madsen, H. Lilholt, Y. Kusano, S. Fæster and B. Ralph
Department of Wind Energy, Risø Campus
Technical University of Denmark, 2013

EXPERIMENTS AND ANALYSES FOR DETERMINING FIBRE/MATRIX INTERFACE PARAMETERS – UNDERSTANDING DEBONDING PROBLEMS

R.T. Durai Prabhakaran, Mohit Gupta*, Hans Lilholt,
Bent F. Sørensen, and Puneet Mahajan*

Composites and Materials Mechanics, Department of Wind Energy,
Technical University of Denmark, Risø Campus,
DK-4000 Roskilde, Denmark
*Department of Applied Mechanics, Indian Institute of Technology,
IIT Delhi Campus, Hauz Khas, New Delhi, India

ABSTRACT

A new experimental technique is developed to monitor the initiation and propagation of a debond crack during a fibre pull-out experiment. The advanced experimental setup consists of a high resolution video camera and a laser extensometer mounted at a tensile test machine. The test setup enables the measurement of the fibre/matrix displacement and debond length. A micromechanical model is used for analysing the experimental data. It allows the evaluation of the following parameters: the interface debond energy G_{IIc} and the frictional sliding shear stress τ_s at the fibre/matrix interface, and the misfit strain $\Delta\varepsilon^T$, accounting for initial residual stresses. Specimens of a single steel fibre embedded centrally in a polyester matrix are tested using the experimental setup and the model. A practical experimental procedure for establishing the interface parameters is suggested, and an example demonstrates the procedure and yields a set of interface parameters.

1. INTRODUCTION

Interfacial properties of a composite are of utmost importance for an understanding of composites overall properties. The stress transfer between fibre and matrix occurs through the fibre/matrix interface. To characterize and understand the interface phenomena, several techniques are available like single fibre fragmentation test, fibre peel test, single fibre pull out test and micro indentation test. Out of these, single fibre pull out test is one of the best suited for the study of composite interfacial behavior. The two most important mechanisms that take place are interfacial debonding and frictional sliding along the debonded interface. The parameters that control these mechanisms are the interfacial sliding shear stress, the debond energy and residual stresses for any fibre/matrix composite system.

Marshall (1992) used the advanced shear-lag models derived by Hutchinson and Jensen (1990) for evaluating the interface properties for ceramic matrix composites experimentally. Kharrat et al. (2006) used an analytical model based on shear lag analysis (for elastic load transfer) for a stainless steel/epoxy system. The shear lag model is effective as long as the fibre has not debonded, after complete debonding the fibre is extracted against interfacial friction. The SiC-Glass system was used by Kerans and Parthasarathy (1991) to extract the interface parameters such as frictional resistance, residual axial strain considering the Poisson's effect. They found that after debond initiation the curve of load versus fibre/matrix displacement show nonlinear behaviour, and unstable failure occurs when the debond initiation load is high or when residual stress is low. Levasseur et al. (1997) obtained the interfacial parameters of a SiC/pyrex composite from pull out tests.

This paper targets the latest advancements made in the fibre pull out process to measure debond lengths and fibre/matrix displacements in a steel/polyester system. The procedure defined in this study aims to determine the interface parameters and to evaluate the mechanical effects of surface coatings applied on fibre surface. This evaluation procedure has been derived from the basic model of Hutchinson and Jensen (1990), applying the fibre debond-length measurements and correlating the analytical results with the experimental data. The calculation of the frictional shear stress is done using the load versus debond length measurements. The data obtained can be used further to calculate the residual stresses and the debond energy G_{IIc} (fracture toughness).

2. MATERIALS AND MANUFACTURING

The steel fibres used in the current research study are high carbon steel fibres with a fibre diameter of 0.21mm. The surface coating on the steel fibre is zinc layer (to protect from corrosion). The fibre surfaces are otherwise untreated (no sizings). The fibre was cleaned with acetone before infusing the polyester resin. The fibre was embedded in a thermoset polymer, a standard polyester resin (Polylite 400-499). Test specimens designed for pullout experiments have a matrix block with dimensions 100 mm x 5 mm x 5mm. A silicone mould was designed having a cavity 5 mm x 5 mm with a pin hole to place the steel fibre exactly at the centre line of the cavity. The test setup for processing the specimens is shown in Fig. 1.

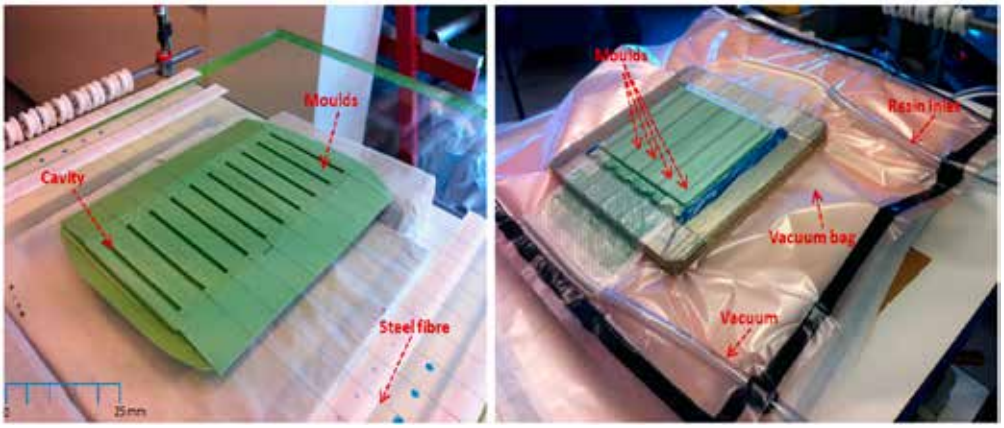

Fig. 1. Processing setups for pull-out specimens: placement of fibre in the mould and closed silicone moulds with vacuum bagging.

Specimens were made using vacuum infusion in order to obtain high quality specimens for pullout test avoiding processing issues like bubbles, voids or shrinkage problems. The silicone mould has cavities for producing 10 samples. In order to obtain perfectly placed steel fibre at centre of the specimen, a weight of 200 grams is used to preload the steel fibre after the fibre has been placed at the centre of the mould cavity. This ensures steel fibre placement and straightness of the fibre after processing. After demoulding, the specimens are inspected for bubbles and damages in the fibres. Finally the specimens are post cured in an oven at 60℃ for 24 hours. This is to ensure total cure of the matrix material.

3. EXPERIMENTAL SETUP

3.1 State of the art – pull-out test: The test method chosen to characterize the fibre/matrix interface is single fibre pullout using fixed bottom gripping as shown in Fig. 2. The testing method was chosen to fit to the boundary conditions of the advanced micromechanical models of Hutchinson and Jensen (1990).

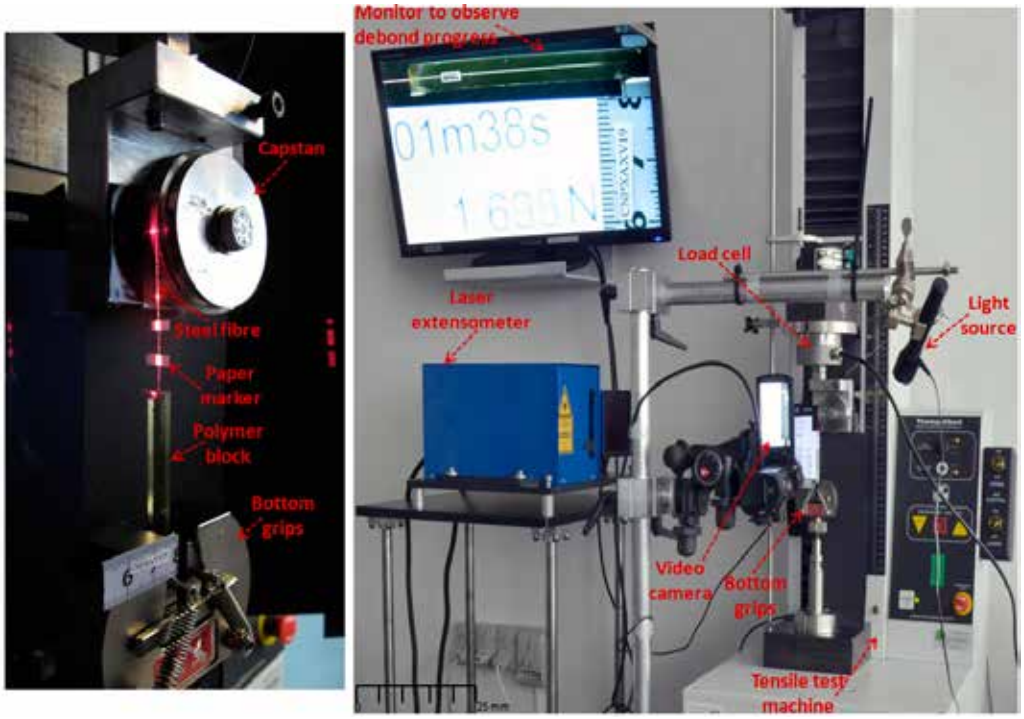

Fig. 2. Pull-out test – Advanced experimental setup.

3.2 Advanced experimental setup: The polyester block is gripped from the bottom and the fibre is pulled using a circular capstan having a radius 25 mm at the top. A laser extensometer (P-50, Fiedler Optoelektronik GmbH) is used for measuring fibre/matrix displacements. A video camera (Panasonic, HDC–TM 900) is used to record the interface crack initiation and progression while loading the specimen as shown in Figure 2. The resolution of the image is 1920 x 1080 pixels, and images were recorded with 50 frames per second. The target is to measure the debond lengths from the video clips. Tests are performed at a displacement rate of 1

mm/min with a data sampling rate of 10 Hz. The experiments are terminated, when the debond length approaches the clamped end (i.e. within 10mm from the bottom grip).

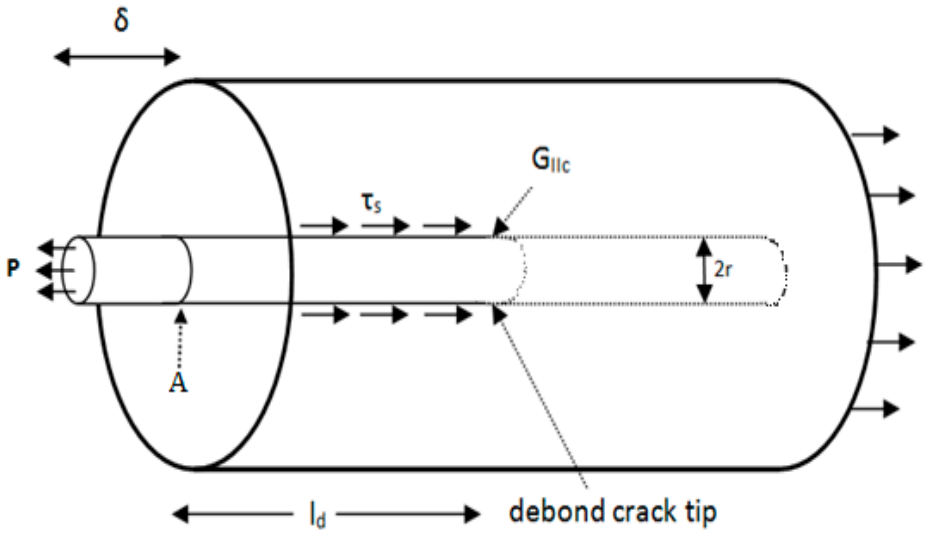

Fig. 3. The model for a fibre in a block of matrix, with debond and pull-out conditions. The parameters recorded during the pullout experiment are the applied force, P, the fibre/matrix displacement δ, and the debond length, l_d.

4. MODEL FOR DEBOND AND PULL-OUT

The experiments are designed to correlate closely with the model for the single fibre debond and pull-out mechanism, the model and analysis is based on the theoretical work of Hutchinson and Jensen (1990).

The material system parameters which characterize the basic materials and geometry are: fibre stiffness E_f, matrix stiffness E_m, fibre radius r, specimen cross sectional area A_c, fibre volume fraction V_f, matrix volume fraction V_m, and composite stiffness E_c. The composite stiffness is calculated from the law of mixtures for unidirectional composites.

The parameters which characterize the debond and pull-out mechanism are the misfit strain $\Delta\varepsilon^T$, accounting for initial residual stresses, the mode II interface debond energy G_{IIc}, and the frictional sliding shear stress τ_s acting along the fibre/matrix interface after debonding.

4.1 Model geometry: The model constitutes a single cylindrical fibre in a block of matrix, and is axisymmetric with respect to the fibre axis, see Fig. 3. The fibre sticks out at one end of the specimen, such that load can be applied to the fibre. At the other end of the specimen the matrix (composite) is held by a conventional gripping system, as shown in Fig. 2.

4.2 Experimental aspects: The experiment is carried out by applying the load axially along the fibre at a constant loading rate. The steps during the experiment are the following: (i) elastic loading of the composite (fibre and matrix), (ii) at load P_o initiation of a mode II debond crack occurs at position A, and controlled by debond energy G_{IIc}, (iii) displacement δ increases with

load P, and debond length l_d increases with load P. The analysis of experimental data are the following: (i) the debond lengths l_d as a function of load P are measured from the video recordings, (ii) the relative displacements between fibre and matrix δ as a function of load P are calculated from the laser extensometer recordings.

4.3 Analysis of data: The procedure for deriving the (three) parameters τ_s, $\Delta\varepsilon^T$, and G_{IIc} is based on equations of the micromechanical model.

1) The relation between load P and debond length l_d is:

$$P = \left(2\pi\, r \tau_s \frac{E_c}{V_m E_m} \right) l_d \;+\; 2\pi\, r \sqrt{\left(r\, G_{IIc} \frac{E_f E_c}{V_m E_m} \right)} \;-\; \pi\, r^2 E_f \Delta\varepsilon^T \tag{1}$$

According to the micromechanical model P is linearly related to l_d. The slope of a P versus l_d curve (dP/dl_d) is only dependent on τ_s and thus allows evaluation of τ_s.

2) The equation for $\Delta\varepsilon^T$ is related to both the displacement δ and the debond length l_d and τ_s :

$$\Delta\varepsilon^T = \frac{\delta}{l_d} + \frac{\tau_s}{r} \frac{E_c}{E_f V_m E_m}\, l_d \;-\; \frac{1}{E_f} \frac{P}{\pi r^2} \tag{2}$$

Knowing τ_s from the first analysis step, the above equation is used to calculate $\Delta\varepsilon^T$ for combined sets of δ, l_d and P (all known experimental data), and to plot $\Delta\varepsilon^T$ versus P. This should give a constant value for $\Delta\varepsilon^T$.

3) The final step is then to use $\Delta\varepsilon^T$ together with P_o, in the equation for G_{IIc}:

$$G_{IIc} \;=\; \left(\frac{P_0}{\pi\, r^2 E_f} + \Delta\varepsilon^T \right)^2 \frac{r\, E_f V_m E_m}{4 E_c} \tag{3}$$

4) Finally, the experimentally determined values for τ_s, $\Delta\varepsilon^T$, and G_{IIc} are used in Eq. (4) to calculate the curve of load P versus displacement δ, for comparison with the experimental curve of P versus δ. The relation between the load P and the displacement δ is:

$$P = \pi\, r^2 E_f \sqrt{\left(\delta\; \frac{4\,\tau_s E_c}{r\, E_f V_m E_m} \;+\; \frac{4\, G_{IIc}}{r} \frac{E_c}{E_f V_m E_m} \right)} \;-\; \pi\, r^2 E_f \Delta\varepsilon^T \tag{4}$$

Eq. (4) shows that P is expected to be related to the fibre/matrix displacement δ, with a nearly square-root dependence (i.e. $P \sim \sqrt{\delta}$).

5. AN EXPERIMENTAL EXAMPLE

To illustrate the evaluation procedure, one experiment is used in the following paragraphs. The basic material system parameters are listed in Table 1. Fig. 4 shows a plot of load P versus debond length l_d, and the slope of the line yields a value for τ_s using Eq. (1). Fig. 5 shows a plot of $\Delta\varepsilon^T$ versus load P calculated by Eq. (2) (using the determined value of τ_s and simultaneous values of δ, P and l_d); this yields a (nearly) constant value for $\Delta\varepsilon^T$. The initial debond load P_o is obtained by extrapolation of the P-l_d relationship to $l_d = 0$ as shown in Fig. 4. Having determined

τ_s, $\Delta\varepsilon^T$, and P_0, the debond energy G_{IIc} is then calculated from Eq. (3). Fig. 6 is the plot of load P versus displacement δ, based on Eq. (4) using the determined the interface parameters. This curve is compared with the direct experimental curve of P versus δ.

The procedure seems to be operational, and gives reasonable results, although at present the actual values for τ_s, $\Delta\varepsilon^T$, and G_{IIc} cannot be evaluated against independent measurements or other data, nor against more experiments which will give a statistical qualification of the values.

Table 1. Material and interface parameters – (steel fibre/polyester system, CNPXAXV08).

Material parameters			
Fibre stiffness	E_f	GPa	210
Matrix stiffness	E_m	GPa	3
Fibre radius	r	mm	0.155
Specimen area	A_c	mm^2	25
Fibre volume fraction	V_f		0.003
Matrix volume fraction	V_m		0.997
Composite stiffness	E_c	GPa	3.625
Interface parameters			
Shear stress	τ_s	MPa	1.24
Misfit strain	$\Delta\varepsilon^T$		0.0029
Initial load	P_0	N	13
Debond energy	G_{IIc}	J/m^2	93

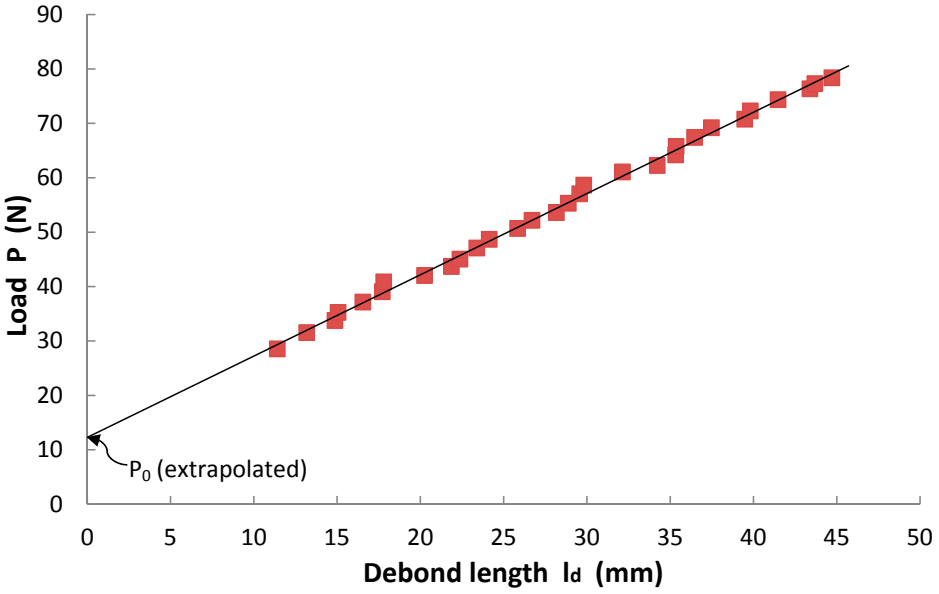

Fig. 4. Load as a function of debond length; the slope is used to evaluate interfacial frictional sliding shear stress τ_s, and the intersection with the y-axis P_o is used in the calculation of G_{IIc}.

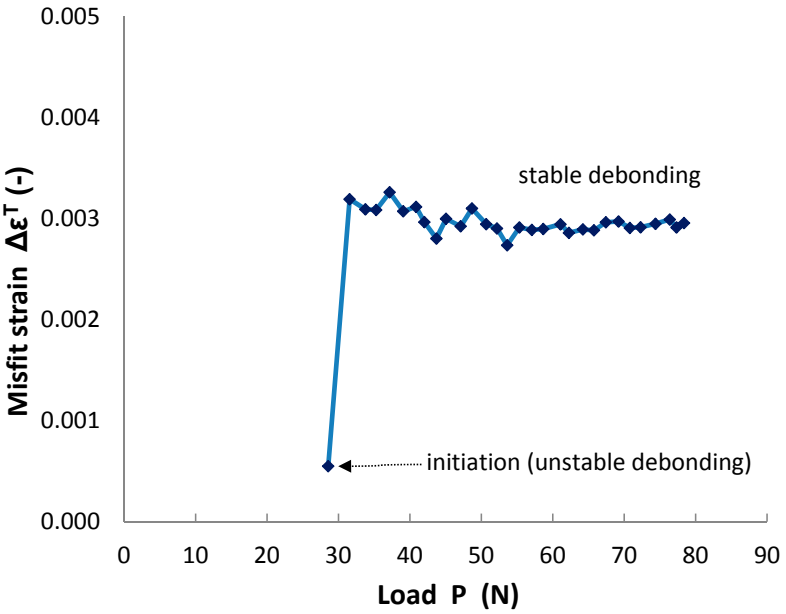

Fig. 5. Misfit strain as a function of load, the (nearly) constant value establishes $\Delta\varepsilon^T$ for the material system.

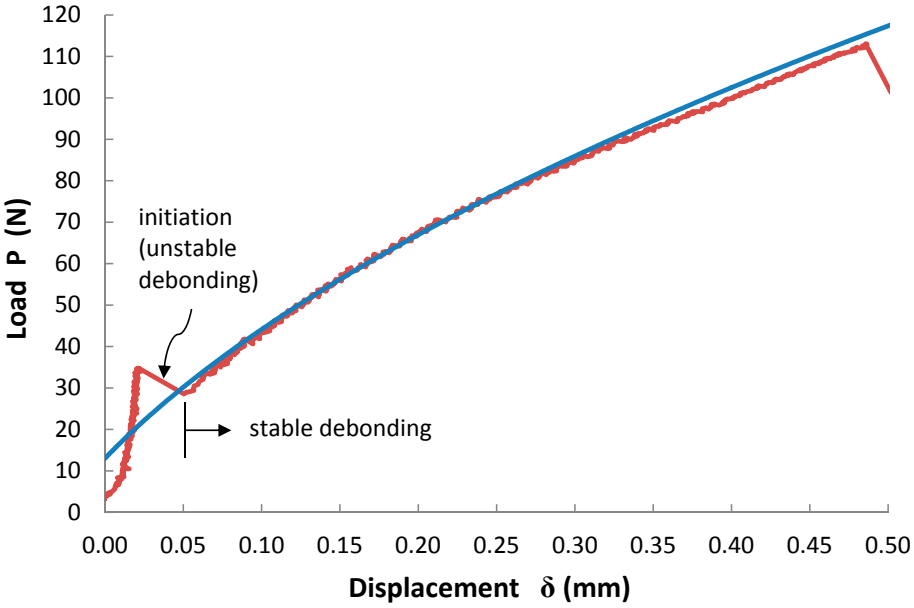

Fig. 6. Load as a function of displacement, the blue curve is calculated on the basis of experimental values for τ_s, $\Delta\varepsilon^T$, and G_{IIc}, and the red curve is based on the experimental data from the laser extensometer.

6. SUMMARY AND CONCLUSIONS

A new experimental technique is developed to monitor the initiation and propagation of a debond crack during a fibre pull-out experiment. The advanced experimental setup consists of a high resolution video camera and a laser extensometer. The test setup enables the measurement of the fibre/matrix displacements and the debond length. A micromechanical model is used for analyzing the experimental data. It allows the evaluation of the following interface parameters: the misfit strain $\Delta\varepsilon^T$, the interface debond energy G_{IIc} for mode II cracking, and the frictional sliding shear stress τ_s acting along the fibre/matrix interface during the debonding. Specimens of a single steel fibre embedded centrally in a polyester matrix are used to demonstrate the experimental setup and the use of the micromechanical model. A practical experimental procedure for establishing the interface parameters is suggested, and an example demonstrates the procedure and yields a set of parameters. At present, the validity of these results cannot be established.

ACKNOWLEDGEMENTS

The work reported was conducted in a research project sponsored by the Danish National Advanced Technology Foundation. The authors would also like to thank the material suppliers for their support. The authors would like to thank Erik Vogeley, Steffen Rasmussen, Thor Meyer, Tom L. Andersen, Povl Brøndsted, Christen Malte Markussen, and research technicians from materials testing laboratory for supporting the experimental work.

REFERENCES

Hutchinson, J. W., and Jensen, H. M. (1990). Models of fiber debonding and pullout in brittle composites with friction, Mechanics of Materials, 9, 139 – 163.

Kerans, R.J., and Parthasarathy, T.A., (1991). Theoretical analysis of fiber pull-out and push-out tests, J. American Ceramic Society, 74(7), 1585-1596.

Kharrat, M., Dammak, M., and Charfi, A. (2006). Mechanical characterisation of interface for steel/polymer composite using pull-out test: shear-lag and frictional analysis, J. Mater. Sci. Technol., 22(4), 552-558.

Marshall, D. B., (1992). Analysis of fiber debonding and sliding experiments in brittle matrix composites, Acta Metallurgica et Materialia, 40 (3), 427 – 441.

Levasseur, P., Sudre, O., Chaboche, J. L. and Sangleboeuf, J.C. (1997). Identification of interfacial parameters with analytical and numerical models from pull-out tests on a micro-composite, Damage and Failure of Interfaces, Vienna (Austria), September 24-26, 97-168.

Proceedings of the 34th Risø International Symposium on Materials Science:
Processing of fibre composites – challenges for maximum materials performance
Editors: B. Madsen, H. Lilholt, Y. Kusano, S. Fæster and B. Ralph
Department of Wind Energy, Risø Campus
Technical University of Denmark, 2013

FIBRE WAVINESS AND MISALIGNMENT MEASUREMENT OF UNIDIRECTIONAL GLASS/LPET COMMINGLED COMPOSITES – EFFECT ON MECHANICAL PROPERTIES

R.T. Durai Prabhakaran, Hans Lilholt, Francis Aviles[*]
Tom Løgstrup Andersen, and Hans Knudsen[**]

Composites and Materials Mechanics, Department of Wind Energy,
Technical University of Denmark, Risø Campus,
DK-4000 Roskilde, Denmark
[*1] Centro de Investigación Científica de Yucatán, Unidad de
Materiales, Calle 43 No. 130 Col. Chuburná de
Hidalgo, Mérida, Yucatán, México
[*2] Department of Mechanical and Manufacturing Engineering,
Aalborg University, Fibigerstræde 16,
DK-9220 Aalborg East, Denmark
[**] Comfil ApS, Karolinelundsvej 2, DK- 8883 Gjern, Denmark

ABSTRACT

An experimental investigation was conducted to study the effect of fibre misalignment and waviness on stiffness and strength of unidirectional glass fibre/LPET composites under tensile and compression loading. Analytical models were developed for predicting the fibre misalignment angles and tex factor for three levels of waviness generated during yarn formation. It is shown that the stiffness and strength in both tension and compression loading is reduced as the fibre misalignment angle and tex factor (waviness) increase. The stiffness in both tension and compression are analysed on the basis of the fibre angle dependence calculated for laminate plates with straight fibres (in each ply). The tension strength of the composites is analysed on the basis of the three composite failure modes, tension failure along fibres, shear failure along fibres, and tension failure transverse to fibres. The dominating failure is the shear failure, and an increase of the shear strength is implied from the tension data, and indicates a possible *shear strengthening* effect of wavy fibres. The compression strength of the composites is analysed on the basis of a model for elastic shear buckling with a further assumption of perfect plasticity in shear beyond the yield stress. The use of the improved shear strength values obtained from the tension data and the fibre angle dependence of the shear modulus, gives calculated compression data which show the same trend in fibre angle dependence as the experimental data, but at a lower level. The difference is 50-100 MPa, such that the experimental data indicates a possible *shear strengthening* effect for wavy fibres, similar to the observation for the tension data.

1. INTRODUCTION

Many researchers are challenged with trying to find cost-effective solutions for designing large structures by optimizing the materials properties and achieving high end benefits from polymer composites. Composites are made from its constituent materials, such as polymers and synthetic or natural fibres. Processing or mixing of polymer and fibre reinforcements can be done at various levels, which include fibre-fibre, bundle-bundle, and ply-ply level. The process of mixing polymer fibres and fibre reinforcements at filament level by the air texturing method forming a single tow or yarn is called commingling. The resultant yarn is hybrid in nature and normally woven into a fabric form. The other possibility could be winding up the commingling yarns on to a metal frame which can finally form a purely unidirectional pattern. Another advantage with commingled yarns include that during processing the molten polymer inside the fibre preforms can flow shorter distances and allow the material to be moulded with low pressures. The air texturing process (commingling) inevitably introduces some misalignment of the (two or more) fibres. This is of particular importance for the reinforcement fibres and the term fibre waviness is used to describe this situation. Fibre misalignment, i.e. fibres with orientation angles larger than zero relative to the loading direction, normally will reduce mechanical properties such as stiffness and strength. It is therefore of importance to control, measure and evaluate the effect of (normally small) fibre misalignments on mechanical properties. Composites with unidirectional fibre orientation may be particularly sensitive to fibre misalignment under compression loading.

Few researchers studied the role of fibre waviness and misalignment on composite properties. For example, Hsiao and Daniel (1996) investigated the effect of fibre waviness on stiffness and strength reduction of unidirectional composites under compressive loading. Both Young's modulus and compressive strength decrease as the fibre waviness increases. Material anisotropy is also shown to influence the stiffness and strength reduction with the carbon/epoxy material being much more sensitive to fibre waviness than the glass/epoxy material. The experimental results were in good agreement with the analytical predictions. Similarly, Piggott (1995) reviewed the effect of fibre waviness on the mechanical properties. Apart from strength and stiffness under compression, shear strength and delamination resistance were considered. Due to lack of sufficient experimental data there are no conclusions from the analysis. Yurgartis (1987) studied fibre misalignment and its influence on mechanical properties such as longitudinal compression strength and modulus. The technique presented was able to measure fibre misalignment angle, and can provide a full bivariate distribution such as in-plane and out-of-plane misalignments. Three laminates with a lay-up sequence 0/90, unidirectional, and prepreg carbon fibre/epoxy were considered to study the effect of misalignment on properties. The misalignment angle measurement varies between 0.693 and 1.936 degrees. For measuring the fibre waviness and misalignment experimentally, none of the authors considered fibre level mixing forming a commingled yarn.

Therefore the current study considers glass fibres mixed by commingling with low temperature based polyethylene terephthalate (LPET) polymer fibres at filament level. To study the effect of fibre waviness and misalignment on tensile and compression properties three levels of misalignment are introduced into glass fibres. The commingled yarns are used to produce unidirectional composites in the form of plates. The three levels of fibre waviness aim to give three levels of increasing glass fibre misalignment. The fibre volume fraction of the composites is nominally 30 vol% in order to ensure a high quality material, i.e. low porosity.

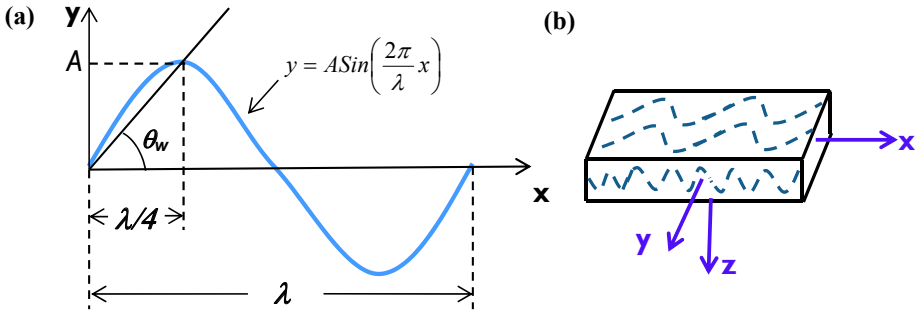

Fig. 1. Schematic representation of sinusoidal fibre waviness. (a) sinus curve and definition of geometric parameters, (b) definition of *xy* and *xz* planes.

2. METHODOLOGY

Fibre bundles and yarns are normally characterized by their tex value, i.e. weight in grams per 1000m. For straight fibres in the yarn the tex value can be measured directly by weighing, and it can be calculated from fibre diameter and density. For yarns with "overfeed" it may be difficult to calculate the tex value, while it is fairly simple to measure the tex value by weighing. The "overfeed" can be characterized by a tex factor defined as the actual tex value relative to the tex value for the corresponding straight fibre bundle. The higher tex value tex(n) of the bundle with "overfeed" can be described as a wavy fibre bundle confined to the same reference length as the straight fibre bundle with tex(0). The wavy shape of the fibre bundle is justified by the observations of the yarns in Fig. 2, with three levels of "overfeed" (nominally 1%, 5%, 10%). The wavy shape implies a longer bundle length '*s*', relative to the length 's_o' of the straight fibre bundle, therefore the tex factor is

$$\text{Tex factor} = \frac{tex(n)}{tex(0)} = \frac{s}{s_0} \tag{1}$$

The transformation of the waviness of the fibre bundle into a fibre misalignment (in the composite) can be done by using a simple (planar) *sinus curve* to characterize the fibre bundle waviness. The sinus curve is reasonably justified by the observations in Fig. 2. The formal sinus curve is characterized by its wave length λ and amplitude A, as shown in Fig. 1. Furthermore the length of (one period of) the sinus curve is 's'. This establishes a relation to the tex factor:

$$\text{Tex factor} = \frac{tex(n)}{tex(0)} = \frac{s}{s_0} = \frac{s}{\lambda} \tag{2}$$

because the wavelength λ corresponds to the (period) length of the straight fibre bundle.

The sinus curve allows calculation of the (local) fibre orientation angle θ relative to the length direction (x-axis). The angle θ varies between zero and a maximum value, which is determined by the amplitude A relative to the sinus curve wave length λ, and thus by the fibre waviness.

The fibre angle θ can be described by its distribution $0 < \theta < \theta_{max}$, by the average value θ_{av}, and by the maximum value θ_{max}.

From the sinus curve the θ can be found (by simple mathematical derivations), and are

$$\tan\theta_{\max} = \frac{2\pi A}{\lambda} \tag{3}$$

$$\tan\theta_{av} = \frac{4A}{\lambda} \tag{4}$$

It is noted that $$\tan\theta_{\max} = \frac{\pi}{2}\tan\theta_{av} \tag{5}$$

From the arc length of the sinus curve it is derived that

$$\frac{s}{\lambda} = \sqrt{1 + \frac{256}{\pi^2}\left(\frac{A}{\lambda}\right)^2} \tag{6}$$

This establishes a relation between tex factor ($\frac{s}{\lambda}$) and fibre angle:

$$\tan\theta_{\max} = \frac{\pi^2}{8}\sqrt{\left(\frac{s}{\lambda}\right)^2 - 1} \tag{7}$$

$$\tan\theta_{av} = \frac{\pi}{4}\sqrt{\left(\frac{s}{\lambda}\right)^2 - 1} \tag{8}$$

These equations allow an estimate of fibre angles, based on a planar sinus curve as an approximation for the fibre waviness in a bundle. The estimate can be based directly on the wavy fibre bundle via the tex factor, or based on (microscopical) observations of the sinus curve approximation for the fibre waviness, either on the bundles (Fig. 2) or on the composites (Fig. 3). It should be noted that the potential non-straightness of fibre (typically in unidirectional fibre composites) conveniently can be characterized by "microscopic fibre misalignment" which is small deviations from zero angle in otherwise straight fibres, and "macroscopic fibre waviness" which is numerically larger deviations of angle over larger distances, as described above. The microscopic fibre misalignment could be overlayed on the fibre waviness. The microscopic fibre misalignment can be estimated by methods as described by Kratmann et al. (2009). The "macroscopic fibre waviness" can potentially be treated as described above.

It should be noted that the direct measurement of tex values and thus the tex factor gives an essentially three-dimensional (3D) description of fibre waviness. The observation of the (dry) fibre bundles (Fig. 2) gives a projection of the 3D nature of the bundle onto a plane of observation, and thus the description may be called 2-3D. The composites are normally studied on planar sections of the composites (Fig. 3), and thus the description is clearly 2D, with a well defined plane. This is typically the xy plane or the xz plane, as defined in Fig. 1b. The choice of plane may depend on e.g. the sample cross sectional geometry, where specimens with rectangular cross sectional area may be sensitive to compression loading in particular in the "thin" direction of the specimen, and therefore the fibre waviness on the xz plane will probably be most critical for compressive strength.

Fig. 2. Glass/LPET fibre yarns with three levels of "overfeed".

3. EXPERIMENTAL MEASUREMENTS

Glass fibres commingled with LPET fibres made into yarns by the air texturing method will have a tendency to become slightly wavy. The wavy states of the yarns depend on the practical setting and other parameters for the air texturing machine. The interaction between the manufacturing parameters and the resulting (compression) properties have been studied in a series of composites made from glass fibres and LPET as matrix. To ensure a low (near zero) porosity the composites are designed to have about 30 vol % of fibres. Deliberately three levels of waviness of fibres are created for the yarns (made by Comfil ApS, DK).

The fibre yarns produced are shown in Fig. 2 and are labeled with nominal overfeed: 1%, 5%, and 10%. The three groups of glass/LPET unidirectional composites with V_f = 31% were manufactured at Comfil ApS, DK, who also performed the morphological characterization.

3.1 Measurement of waviness. The fibre yarns are characterized by weighing and by microscopy, to obtain tex factors and calculate related fibre orientation angles, both average fibre angles and maximum fibre angles. The results for the microscopy observations and measurements (Figs. 2 and 3) are given in Table 1, where data for sample DDD04 could not be estimated reliably. All data are collected in Table 2, where especially the fibre angles (average and maximum) are listed.

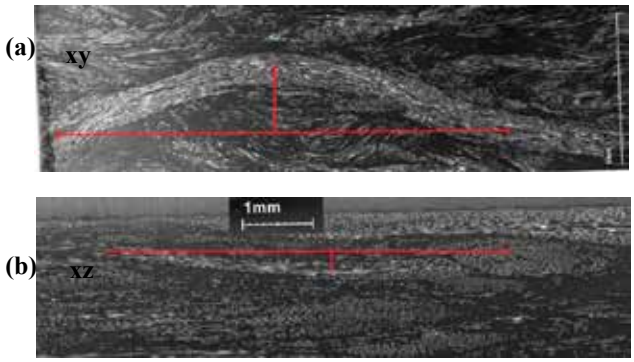

Fig. 3. Optical images (merged from several smaller images) of polished Glass/LPET composites for quantification of fibre waviness, (a) in-plane (xy), b) through-thickness (xz).

Table 1. Evaluation of fibre waviness parameters of the glass/LPET composites.

Plane	**xy**			**xz**		
Sample	**DDD04**	**DDD05**	**DDD06**	**DDD04**	**DDD05**	**DDD06**
Nominal tex increase	1%	5%	10%	1%	5%	10%
λ (mm)	-	16.7	28.0	-	6.16	11.3
A (mm)	-	1.09	2.20	-	0.221	0.262
θ_{av} (°)	-	14.7	17.5	-	8.2	5.3
Tex Factor (measured) $\frac{s}{\lambda}$	-	1.063	1.075	-	1.011	1.021
Tex Factor (calc) A & λ	-	1.054	1.077	-	1.016	1.007
θ_{max} (°)	-	22.3	26.3	-	12.6	8.3

Table 2. Measurement of tex factor and fibre misalignment angles.

Method	**Sample**	**DDD04**	**DDD05**	**DDD06**	**DDD04**	**DDD05**	**DDD06**
		Tex factor			**Average fibre angle (deg)**		
Fibre weighing	3D	1.011	1.029	1.054	6.7	10.8	14.7
Fibre microscopy	2-3D, s/λ	1.012	1.035	1.081	7.0	11.8	17.9
Fibre microscopy	2-3 D, A & λ	1.007	1.023	1.066	5.3	9.6	16.2
Average		***1.010***	***1.029***	***1.067***	***6.3***	***10.7***	***16.3***
Composite microscopy	2 D, **xy**, s/λ	-	1.063	1.075	-	15.8	17.2
Composite microscopy	2 D, **xy**, A & λ	-	1.054	1.077	-	14.7	17.4
Average		***-***	***1.058***	***1.076***	***-***	***15.3***	***17.3***
Composite microscopy	2 D, **xz**, s/λ	-	1.011	1.021	-	6.7	9.2
Composite microscopy	2 D, **xz**, A & λ	-	1.016	1.007	-	8.0	5.3
Average		***-***	***1.013***	***1.014***	***-***	***7.4***	***7.3***

3.2 Measurement of tex factor and misalignment angles. The fibre angle values can be estimated directly from the tex factors, i.e. before composite fabrication, or from microscopy measurements (sinus curve), i.e. after fabrication on the final composites themselves. The tex factor determined by weighing of the yarns directly is attractive because the measurement is simple. The various estimates of the tex factor are summarized in Table 2. The signatures of 3-D, 2-3-D and 2-D indicate that the measurements give waviness in 3, 2-3, and 2 dimensions.

The data show for fibres and yarns that the weighing method and the microscopy method are rather similar, with values from weighing being slightly smaller. The tex factors measured on the xy plane are larger than the 3-D tex factor, which again is larger than the tex factor for the xz plane, this is expected from the fabrication procedures of (pressing) flat composite plates. The fibre misalignment angles are calculated from the procedures described above, and the values are listed in Table 2. The fibre angles are used to correlate with the mechanical properties of glass/LPET composite i.e. strength and stiffness (Table 3).

Table 3. Tensile and compression properties of three glass/LPET composites.

Composite Parameters	Units	DDD04	DDD05	DDD06
Fibre vol fraction	%	31.1	30.9	31.3
Matrix vol fraction	%	68.5	68.6	68.2
Porosity vol fraction	%	0.4	0.5	0.5
Fibre based θ_{av}	degree	6.3	10.7	16.3
θ_{max}	degree	8.1	14.7	24.5
Composite based				
xy – plane, θ_{av}	degree	-	15.3	17.3
xy –plane, θ_{max}	degree	-	22.3	26.3
xz – plane, θ_{av}	degree	-	7.4	7.3
xz – plane, θ_{max}	degree	-	12.6	8.3
Tensile Properties				
E-modulus	GPa	25.8 ± 0.5	22.1 ± 0.3	20.4 ± 0.5
Strength	MPa	619 ± 26	450 ± 19	367 ± 19
Strain	%	0.0262	0.0228	0.0208
Compression Properties				
E-modulus	GPa	25.1 ± 0.4	22.6 ± 0.3	20.6 ± 0.8
Strength	MPa	-530 ± 43	-424 ± 36	-349 ± 15
Strain	%	-0.0214	-0.0197	-0.0178

4. MECHANICAL CHARACTERIZATION

In order to quantify the effect of fibre waviness and misalignment on strength and stiffness reduction of (nominally unidirectional) composites, both tensile and compression tests were conducted. Both tensile and compression tests were conducted as per standards ISO 527 and ISO 14126.

Tension tests are performed in a standard Instron machine, and mechanical extensometers were mounted back-to-back on the specimen surface within the gauge section to measure strain data. The stress-strain curves indicate the performances of three laminate series. All test samples showed specimen failure as expected within the gauge region.

Compression tests are conducted with a test fixture designed and developed by Risø DTU. This fixture is basically a Mechanical Combined Loading (MCL) fixture which can transmit both shear loading and end loading. The end loading is accomplished by inserting metal shims in the gap between the ends of the specimen and the base of the fixture. The test fixture is accepted in composite community to test the structural materials with a minimum specimen buckling and more accuracy in test results (see Bech et al. 2011). Strain gauges were mounted to measure specimen deformation during compression loading.

The experimental test results from tension and compression loading for the three series of glass/LPET laminates is summarized in the following Table 3.

5. RESULTS AND DISCUSSIONS

The results are presented in Figs. 4, 5, 6, and 7 as the mechanical properties versus the fibre misalignment angle as measured above for the three composite systems. The stiffness in tension, the stiffness in compression, and the strength in tension and the strength in compression all show a decrease in values with increasing fibre angle. The various estimates for the fibre angle are shown, to indicate the range for the average angle, the maximum angle, as well as the

estimates from the xy-plane and the xz-plane. There does not seem to be any special measure which could be preferred for a rational analysis of the data. The average values will be used in the further analysis, in order to simplify the models for the stiffness and strength as a function of fibre angle.

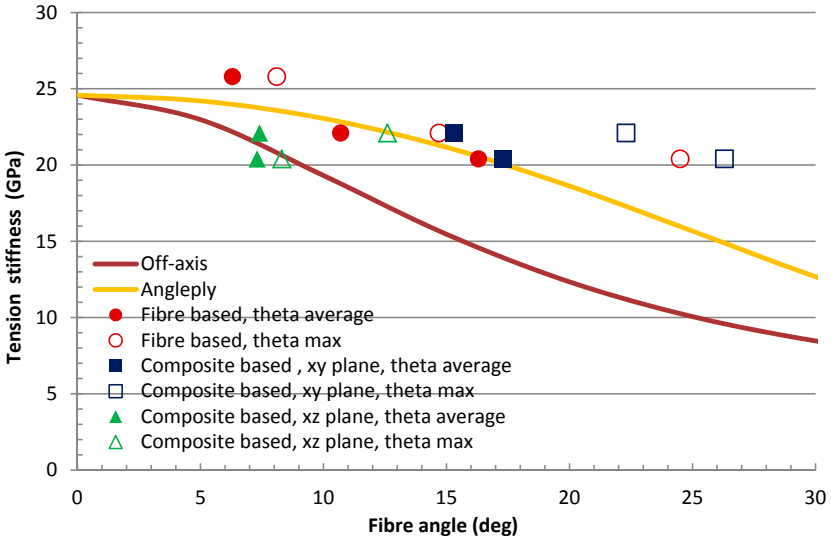

Fig. 4. Tension stiffness as a function of fibre angle; the various estimates for fibre angles are shown. The curves are based on the laminate plate calculations.

5.1 Stiffness in tension and in compression. There exists no model for stiffness as a function of fibre angle for wavy fibres. Therefore the traditional laminate plate calculation for ply-based laminates will be used as a first attempt to describe the stiffness as a function of fibre angle. The laminate calculation is performed both for off-axis fibre angle (+ θ), and for angle-ply fibre configuration (± θ). The theoretical curves for ply-based laminate stiffness are calculated with fibre stiffness: E_f = 72 GPa and matrix stiffness E_m = 3.1 GPa, and with composite fibre volume fraction V_f = 0.31. In Fig. 4 and Fig. 5, the brown curve represents the off-axis laminate (+ θ), and the yellow curve represents the angle-ply laminate (± θ). It is assumed that for stiffness at small strains, the stiffness will be the same in tension and in compression, and therefore the same calculated curves are used for tension data in Fig. 4 and for compression data in Fig. 5. The figures show a general agreement between data, both for tension and for compression, with the laminate based calculation for angle ply fibre configuration. It does not seem unreasonable that the wavy fibres give a similar "blocking" of the deformation as does the angle-ply configuration for laminate plates.

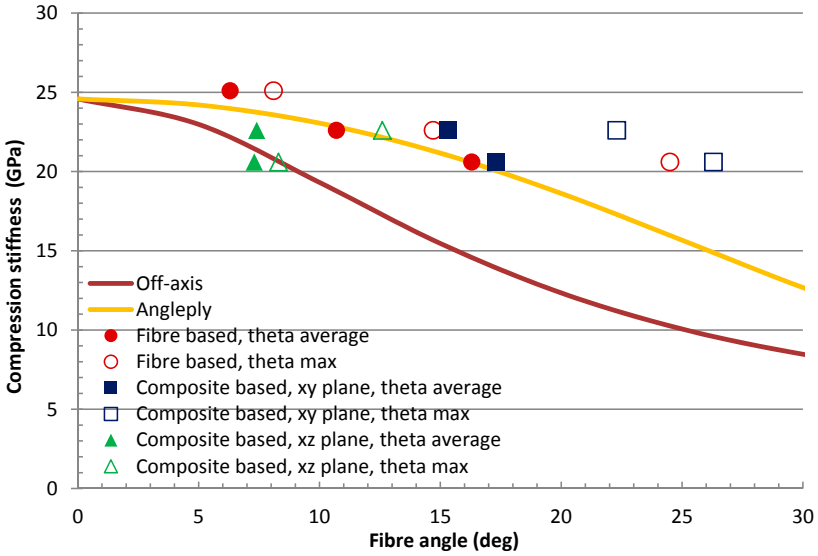

Fig. 5. Compression stiffness as a function of fibre angle; the various estimates for fibre angles are shown. The curves are based on the laminate plate calculations.

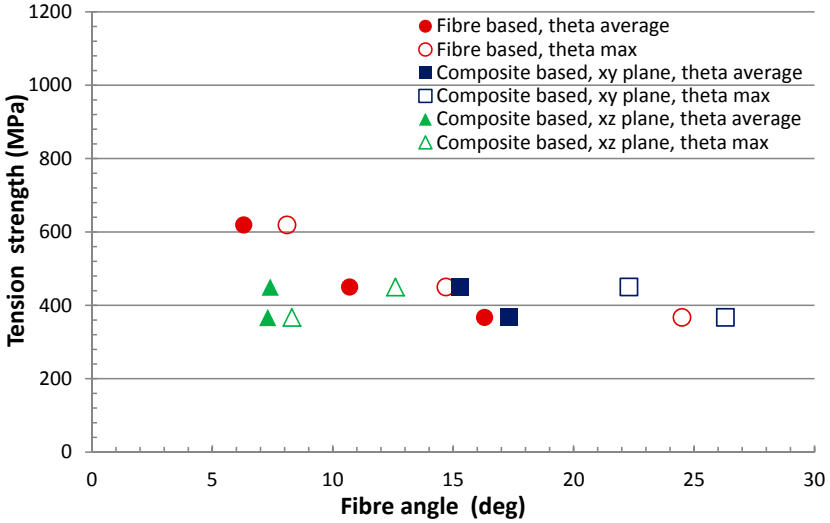

Fig. 6. Tension strength as a function of fibre angle; the various estimates for fibre angles are shown.

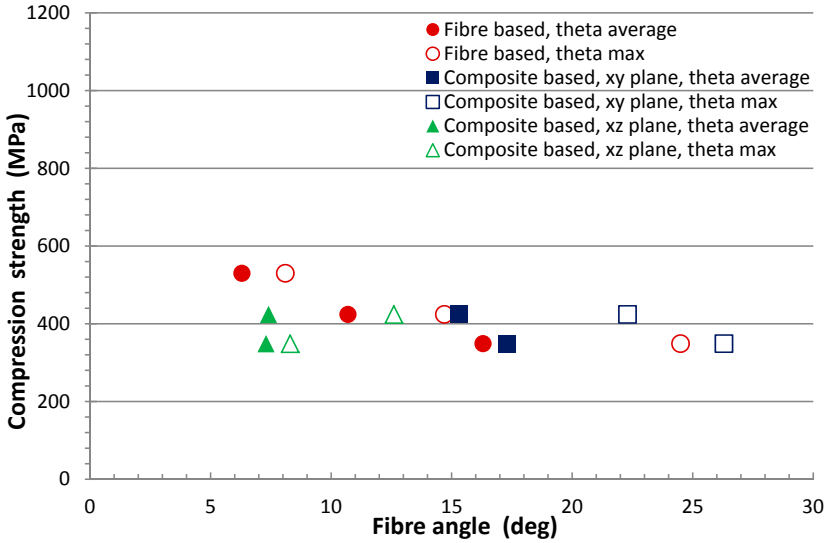

Fig. 7. Compression strength as a function of fibre angle; the various estimates for fibre angles are shown.

5.2 Strength in tension. A simple model exists for the off-axis strength of unidirectional composites, where maximum stresses for three failure modes are implied (Stowell and Liu 1961).

Tension failure of the composite along fibre direction is given by

$$\sigma_{11} = \frac{\sigma_{11}(0)}{(\cos\theta)^2} \tag{9}$$

Shear failure of the composite parallel to the fibres is given by

$$\sigma_{12} = \frac{\tau_{12}(0)}{(\sin\theta\cos\theta)} \tag{10}$$

Tension failure of the composite transverse to fibre direction is given by

$$\sigma_{22} = \frac{\sigma_{22}(0)}{(\sin\theta)^2} \tag{11}$$

Since the actual fibre angles are in the range 0^{o} to about 30^{o}, the focus will be on this fibre angle range, i.e. the first two equations and in particular the equation for shear failure. For the tension failure the constant $\sigma_{11}(0)$ is the strength of the unidirectional composite; the value is estimated from the simple law of mixtures, and is calculated to be 1120 MPa. For the shear failure the constant $\tau_{12}(0)$ is estimated from the lower bound equation for shear strength of the composite, and is calculated to be 36 MPa. The curves calculated with these two constants are shown in Fig. 8 as the blue curve (tension failure) and the green curve (shear failure). It is clear that the experimental data show higher strength values than the green curve. The shear failure equation has been used to estimate (by back calculation) the effective value of $\tau_{12}(0)$ for the individual

data points. As an attempt to quantify this fibre angle dependence, the $\tau_{12}(0)$ values are plotted as a function of sin θ, including the theoretical lower bound of 36 MPa at θ = 0. The data form approximately a linear relationship which can be written

$$\tau_{12}(0) = \tau_{12}(0)_{(th)}(1 + 7 \sin \theta) \tag{12}$$

With this value in the shear failure equation, the curve for off-axis strength is shown in Fig 8 as the red curve. As expected this empirical equation gives an improved description of the experimental off-axis tension strength for composites with wavy fibres. This observation indicates that the wavy fibres give a *shear strengthening* effect to the composite, so that the shear properties are expected to be above the simple estimate for shear strength of composites.

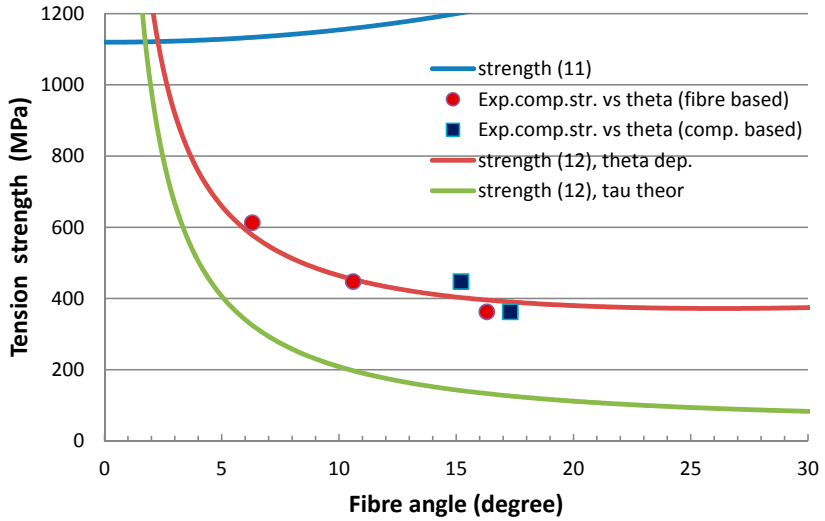

Fig. 8. Tension strength as a function of fibre angle; only fibre angle average values are shown. The curves are based on the model(s) for off-axis tension strength; the green curve is based on the calculated lower bound for unidirectional composite shear strength; the red curve is based on the θ dependence of equation (12) for composite shear strength.

5.3 Strength in compression. A model for strength in compression has been developed, based on the observation of highly localized kinking of small fibre bundles. This mechanism was analyzed by elastic shear buckling by Rosen (1965) and further developed by Budiansky (1983) with the assumption of perfect plasticity in shear beyond the yield stress. The equation for this mechanism is given by

$$\sigma_{11}(B) = G_{12}/(1 + \theta/\gamma) \tag{13}$$

where G_{12} is the composite shear modulus, θ is fibre misalignment angle, and γ is the shear yield strain of the composite. The challenge is to establish reliable values for the shear modulus and in particular the shear yield strain.

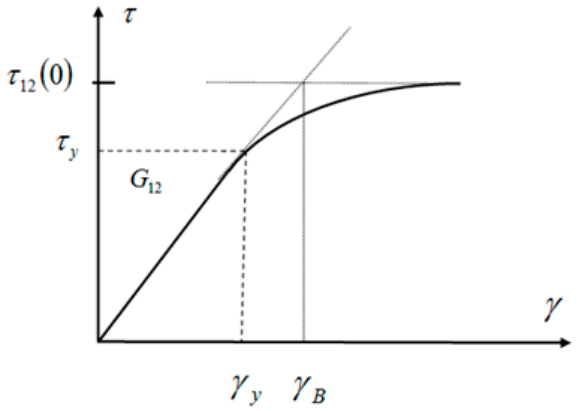

Fig. 9. Schematic shear stress – shear strain curve with the estimate of shear yield strain values γ_y and γ_B.

Table 4. Composite parameters estimated for fibre angles (off-axis and angle ply laminates).

Composite Parameter	Units	Fibre angle, θ (degree)		
		6.3	10.7	16.3
τ_{12} (0)*	MPa	67	79	98
G_{12} (+ θ)	GPa	2.14	2.23	2.46
G_{12} (± θ)	GPa	2.31	2.73	3.48
τ_y (+ θ)	MPa	42	53	64
τ_y (± θ)	MPa	50	60	67
γ_y (+ θ)		0.020	0.023	0.026
γ_y (± θ)		0.022	0.022	0.019
γ_B (+ θ)		0.031	0.035	0.040
γ_B (± θ)		0.029	0.029	0.028

* Estimated from tension strength data in Fig. 8, see section 5.2.

The shear modulus for the composite is estimated from the laminate plate calculation for increasing fibre angle, both for off-axis fibre angle (+ θ), and for angle-ply fibre configuration (± θ). The shear modulus values for the three (average) fibre angles (6.3°, 10.6°, 16.3°) are listed in Table 4. Since shear deformation is not part of a distinction between tension and compression loading, it is assumed that the shear properties estimated from the tension strength in section 5.2, are also usable in the context of compression loading. The maximum shear strength values $\tau_{12}(0)$ estimated from the tension data are also listed in Table 4. The estimate of the shear yield strain is based on the schematic shear stress – shear strain curve shown in Fig 9. The maximum shear strength values are combined with the shear modulus (+ θ) and the shear modulus (± θ), respectively, to establish the curve(s) in Fig 9. The shear yield strains estimated are listed in Table 4, together with the shear strain based on perfect plasticity (Budiansky 1983). The shear modulus values and the shear strain values are used in eq.(13) to establish the (four) curves in Fig. 10. The general trend for the model curves follows the experimental data, but at lower (numerical) levels. The effect of shear modulus values for off-axis and for angle-ply fibre configurations, respectively, is rather small, while the effect of definition of shear yield strain has a larger effect. In all cases there is a positive additional effect of the fibres being wavy. The

tension data indicate (Fig 4 and 5) that the shear modulus (± θ) for angle-ply configuration is most realistic. For these curves in Fig 10, the numerical differences between experiments and models are about 120 MPa for yield strain γ_y, and about 40 MPa for shear yield strain γ_B based on perfect plasticity.

To illustrate the complete curve for compression strength, the θ dependence of the shear modulus $G_{12}(+\theta)$ is estimated from the analytical equation for the shear modulus for off-axis fibre configuration. A good approximation (less than 5% error) in the range of 0^o to 25^o, is:

$$G_{12}(+\theta) = G_{12}(0)/(\cos\theta)^4 \tag{14}$$

The value of $G_{12}(0)$ is taken as the calculated value (2.07 GPa) from the laminate plate calculation, and this value is higher than the lower bound calculation (giving 1.58 GPa). The θ dependence of the shear strength is given by eq. (12). With these expressions the plasticity based yield strain can be calculated and the (complete) curve for compression strength can be calculated as a function of fibre angle, and is plotted in Fig. 11. The general trend of curve and data points is approximately the same, with a numerical difference of about 50 MPa. This may be a yet un-identified effect of the waviness of the fibres.

A calculation of the compression strength with the use of the shear modulus $G_{12}(\pm\theta)$ for angle-ply fibre configuration gives a very similar curve, shifted upwards by about 10 MPa, see Fig. 11. Thus the effect on compression strength is rather small for the fibre configuration with respect to "blocking" of deformation.

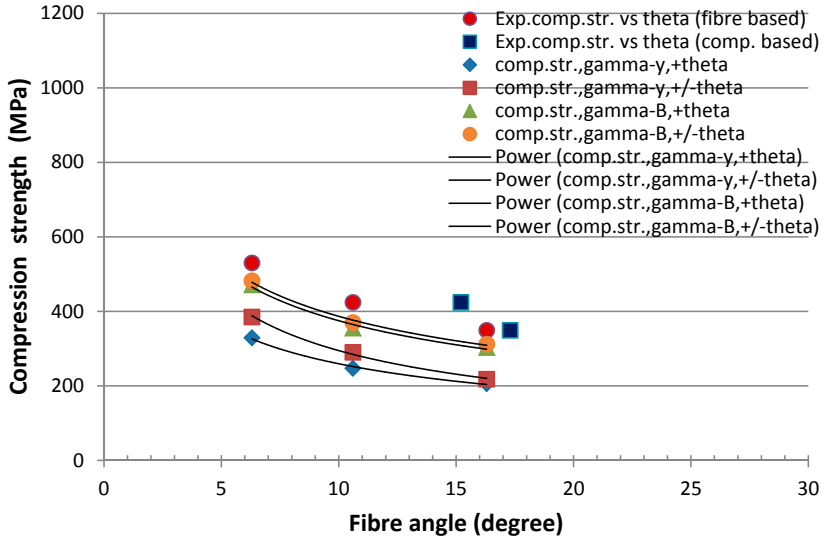

Fig. 10. Compression strength as a function of fibre angle; only fibre angle average values are shown. The four groups of (three) data points, connected by lines, represent the two definitions of shear yield strain, and the two estimates of shear modulus (off-axis and angle-ply fibre configurations).

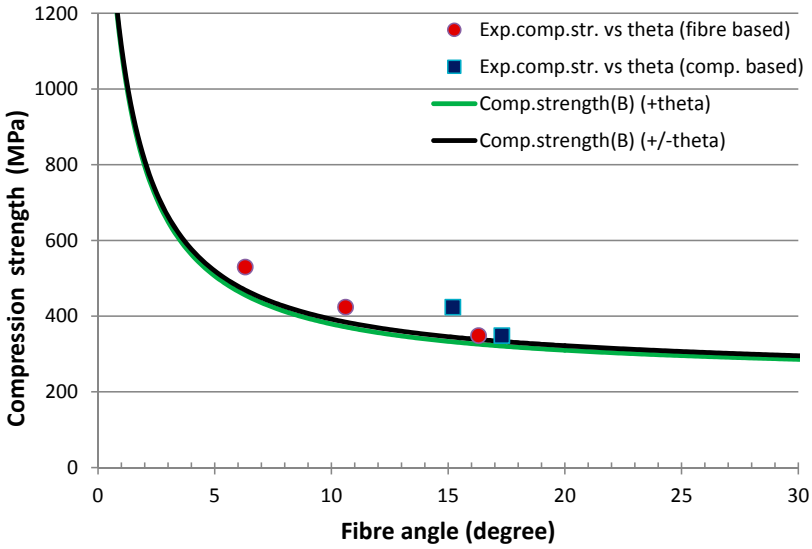

Fig. 11. Compression strength as a function of fibre angle; only fibre angle average values are shown; with the complete curves for the shear plasticity model, with the two estimates of shear modulus (off-axis and angle-ply fibre configurations).

6. CONCLUSIONS

An experimental investigation was conducted to study the effect of fibre misalignment and waviness on stiffness and strength of unidirectional glass fibre/LPET composites under tensile and compression loading. Analytical models were developed for predicting the fibre misalignment angles and tex factor for three levels of waviness generated during yarn formation. It is shown that the stiffness and strength in both tension and compression loading is reduced as the fibre misalignment angle and tex factor (waviness) increase. The stiffness in both tension and compression are analysed on the basis of the fibre angle dependence calculated for laminate plates with straight fibres (in each ply). The experimental data agree reasonably well with the angle-ply fibre configuration, indicating that the wavy fibres (partly) "block" the shear deformation in a manner similar way to the + θ plies and the – θ plies in laminates with straight fibres. The tension strength of the composites is analysed on the basis of the three separate failure modes, tension failure along fibres, shear failure along fibres, and tension failure transverse to fibres, each mechanism being active in separate fibre angle ranges. The dominating failure is the shear failure of the composite, and an increase of the shear strength is implied from the tension data, and indicates a possible *shear strengthening* effect of wavy fibres. The compression strength of the composites is analysed on the basis of a model for elastic shear buckling with a further assumption of perfect plasticity in shear beyond the yield stress. The use of the improved shear strength values obtained from the tension data and the fibre angle dependence of the shear modulus, gives calculated data which show the same trend in fibre angle dependence as the experimental data, but at a lower level. The calculation of the complete curve of compression strength versus fibre angle gives a difference of about 50 MPa, such that the experimental data indicates a possible *shear strengthening* effect for wavy fibres, similar to the observation for the tension data.

ACKNOWLEDGEMENTS

This work was conducted in a research project sponsored by the Danish National Advanced Technology Foundation. The authors would also like to thank the material suppliers for their support and useful discussions in carrying out this study. The authors would like to thank Helmuth Toftegaard for the laminate plate calculations, and Christen Malte Markussen and laboratory technicians for supporting the experimental work.

REFERENCES

Budiansky, B. (1983). Micromechanics, Computers and Structures, 16, 3-12.

Bech, J. I., Goutianos, S., Andersen, T.L., Torekov, R.K. and Brøndsted, P. (2011). A new static and fatigue compression test method for composites, Strain, 47, 21-28.

Fibre-reinforced plastic composites – Determination of compressive properties in the in-plane direction, International Standard ISO 14126: 1999, International Organization Standard, Geneve 20, Switzerland.

Hsiao, H.M. and Daniel, I.M. (1996). Effect of fibre waviness on stiffness and strength reduction of unidirectional composites under compressive loading, Composites Science and Technology, 56, 581 – 593.

Kratmann, K.K., Sutcliffe, M.P.F., Lilleheden, L.T., Pyrz R. and Thomsen, O.T. (2009). A novel image analysis procedure for measuring fibre misalignment in unidirectional fibre composites, Composites Science and Technology, 69, 228-238.

Piggott, M.R. (1995), The effect of fibre waviness on the mechanical properties of unidirectional fibre composites: A review, Composites Science and Technology, 53, 201 – 205.

Rosen, B.W. (1965), Mechanics of composite strengthening, Fiber Composite Materials, American Society of Metals Seminar.

Stowell, E. Z. and Liu, T.S. (1961), On the mechanical behaviour of fibre reinforced crystalline materials. J. Mech. Phys. Solids, 9, 242-260.

Yurgartis, S.W. (1987), Measurement of small angle fibre misalignments in continuous fibre composites, Composites Science and Technology, 30, 279 – 293.

Proceedings of the 34th Risø International Symposium on Materials Science:
Processing of fibre composites – challenges for maximum materials performance
Editors: B. Madsen, H. Lilholt, Y. Kusano, S. Fæster and B. Ralph
Department of Wind Energy, Risø Campus
Technical University of Denmark, 2013

AUTOMATED GEOMETRIC CHARACTERISATION OF WOVEN REINFORCING TEXTILES USING IMAGE ANALYSIS TECHNIQUES

E.E. Swery[*], P. Kelly[**], R. Sharma[***], S. Bickerton[*]

[*]Centre for Advanced Composite Materials, Department of Mechanical Engineering, University of Auckland, Private Bag 92019, Auckland, New Zealand
[**]Department of Engineering Science, University of Auckland, Private Bag 92019, Auckland, New Zealand
[***]Department of Mechanical Engineering, University of Auckland, Private Bag 92019, Auckland, New Zealand

ABSTRACT

An automated geometric characterisation tool for woven reinforcement textiles has been developed and is presented. This tool is used to obtain the in-plane geometry of woven textiles. The image of the textile is captured using a standard office scanner, eliminating the need for complex set up and specialised equipment. The controlled lighting provided by the scanner also enables any fibre material to be analysed, and examples of glass and carbon textiles are presented. The steps used in the processing technique are discussed, along with the resulting geometric information for the materials studied. The extracted information can be used to provide a better understanding of the reinforcing material properties, for example, compaction response and permeability. A study has been conducted, which shows how the geometric characteristics can be used to predict the fabric permeability.

1. INTRODUCTION

Fibre Reinforced Polymer Composite (FRPC) materials are used in a large number of industrial applications. FRPCs are formed by combining two or more distinct materials (generally a fibre reinforcement and a matrix) of significantly different physical and/or chemical properties, forming a material with more desirable properties. For applications where parts are mass produced and high levels of accuracy and repeatability are required, Liquid Composite Moulding (LCM) processes are the preferred manufacturing methods (Johnson 1988; Trochu, Ruiz, Achim and Soukane 2006). Resin is injected into a mould containing the dry compacted fibrous reinforcements and is left to cure before the final part is removed from the mould.

LCM simulations are being used more extensively as process design tools in order to accurately predict fill time, flow front advancement and dry spot formation, ultimately enabling the production of high quality parts under the most efficient conditions (Trochu, Gaubin and Gao 1993). These simulations require further knowledge about the reinforcing material permeability and compaction response. These properties may be predicted utilising simulation based methods; however it is crucial to first obtain the reinforcing textiles geometric information and associated variability in order to compute these.

The reinforcing materials are generally made out of glass or carbon fibres, bundled into tows. The tows can be woven, knitted, braided or stitched together to create the fibre preform. Each of these manufacturing techniques results in different reinforcing architectures and consequently different permeability and compaction properties. Additionally, variability and the presence of defects within the reinforcement architecture influence these properties and must be taken into consideration. There are a number of methods in which the geometric characteristics of the reinforcing materials may be obtained, ranging from manual measurements to automated techniques. Utilising automated image analysis techniques eliminates the potential influence of human error, increasing the accuracy and reliability of the final results (Desplentere, Lomov, Woerdeman, Verpoest, Wevers and Bogdanovich 2005).

The geometric models assume that the reinforcing material consists of solid tows. The individual fibres are not modelled, as this substantially increases the complexity of the models without any significant increase in result accuracy. To fully define the textile, each tow's path (x,y,z) and cross section at different locations have to be obtained. Focus has been placed on gathering in plane geometric data; tow's path (x,y) and width. In further applications, where required, the through thickness data may be estimated from simple microscopy tests.

2. IMAGE ACQUISITION

The geometric information was gathered from scanned 2D images of the reinforcement material. A Ricoh Aficio MP C2550 colour photocopier was used, scanning images at 600 dpi scan resolution. Sample images of textiles of different materials are presented in Fig. 1. It is important to note that for good quality images, the fibre tows must be parallel to the longitudinal axis of the moving light tube of the scanner, and a black surface placed behind all non-carbon textiles.

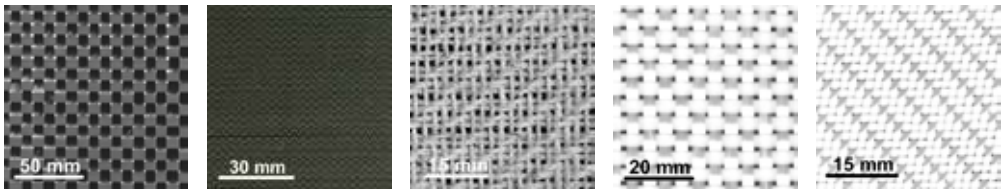

(a) (b) (c)

Fig. 1. Scanned images of different textiles. (a) Carbon, (b) flax and (c) glass.

Using a standard office scanner eliminates the need for complex set up and specialised equipment. The controlled lighting provided by the scanner also enables any fibre material to be analysed as complications due to reflections are not present.

3. IMAGE ANALYSIS TECHNIQUE

A MATLAB® code has been developed in order to analyse scanned images of different woven textiles. This code identifies the individual tows' path and edges, which can then be used to extract desired information about the textiles. The image analysis code comprises of the following steps:

1. *Import and prepare image*
   A scanned image of the textile surface is imported. The image is converted to grayscale in order to simplify the computation and a calibration factor is defined.

2. *Identify weft and warp tow directions*
   The average weft and warp tow directions are identified by the user. The direction is defined in terms of the average angle of the tows from the horizontal axis.

3. *Tow edge detection*
   Using the MATLAB ® edge function, the tows' edges are identified. The vertical and horizontal edges are isolated and separated into two separate matrices. (Fig. 2).

4. *Identify location of tow edges*
   The edge matrix of each of the weft and warp tows is used to automatically identify the approximate location of the edge. (Fig. 3).

5. *Edge curve fitting*
   A polynomial curve is fitted to the locations identified with high intensity of edge pixels. This is undertaken for both the weft and warp tow edges.

6. *Creation of full tow matrix*
   Using the fitted curves, a matrix containing data about the location of every edge point of a tow is formulated. From this information, the central path of each tow is computed.

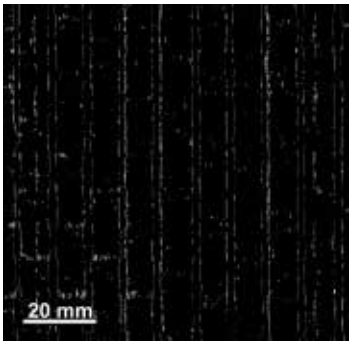

Fig. 2. Vertical edges of textile identified.

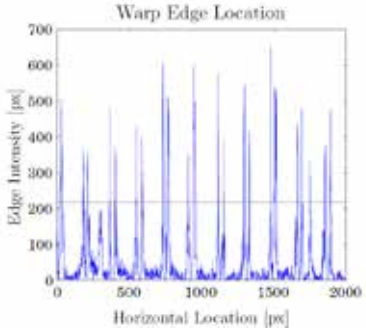

Fig. 3. Identifying locations of vertical tow edges.

4. CASE STUDY

A case study was conducted on two different reinforcing textiles, in order to assess the validity and accuracy of this automated geometric analysis tool as well as to evaluate its applicability in further uses. Each material had the image analysis process performed on it as well as a set of microscopy images taken, to manually confirm the geometric measurements obtained.

4.1 Materials. Two glass fibre reinforcements were studied; a plain weave (PW) and a 2x2 twill weave (TW). The material data is presented in Table 1 and schematics of the materials' architectures are presented in Fig. 4, showing the parameters of interest. Both reinforcement materials were E Glass fibres, with a fibre density of 0.00254 g/mm^3 and supplied by SP High Modulus New Zealand. Five uncompacted samples of each textile were used, where each sample measured approximately 100 x 100 mm.

Table 1. Material Data.

Reinforcement Type	Code	Areal Weight [g/m^2]	Architecture
0°/90° Biaxial Woven	PW	800	Balanced Plain Weave
0°/90° Biaxial Twill Woven	TW	300	2x2 Twill Weave

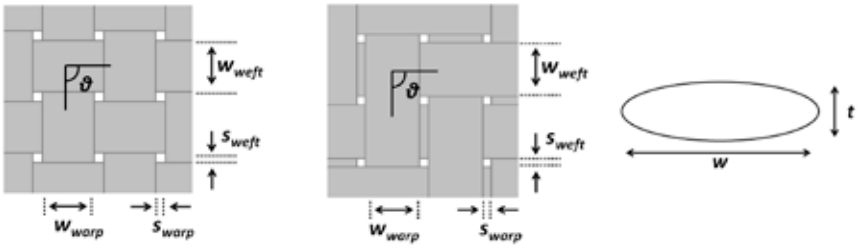

(a) (b) (c)

Fig. 4. Material architecture schematics and measurement scheme. (a) Plain Weave, (b) Twill Weave and (c) Tow cross section.

4.2 Image Analysis Results – PW. Fig. 5 shows two examples of the analysed PW samples. It can be seen that the image analysis program worked well, recognising the location of the weft and warp tows. Figs. 6 to 9 illustrate the geometric data obtained from all the samples, highlighting the presence of variation within and between the samples. The median measurement is shown by the middle red line, the upper and lower quartile values by the box outlines, and the data range by the whiskers. Outliers are shown on the plot as the red crosses.

The results illustrate that on average, the weft tows are wider than the warp tows by 6%. The size of gaps between the weft tows (0.36mm) is significantly smaller than the size of gaps between the warp tows (1.51mm). There is a large inter-sample variation in the angle between the weft and warp tows. This is because the material has a low resistance to in-plane shear, and the samples were taken at different locations on the roll.

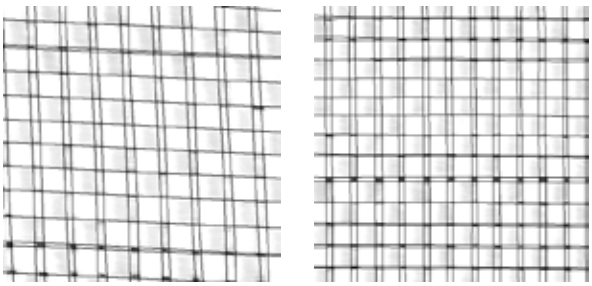

Fig. 5. Examples of analysed PW images.

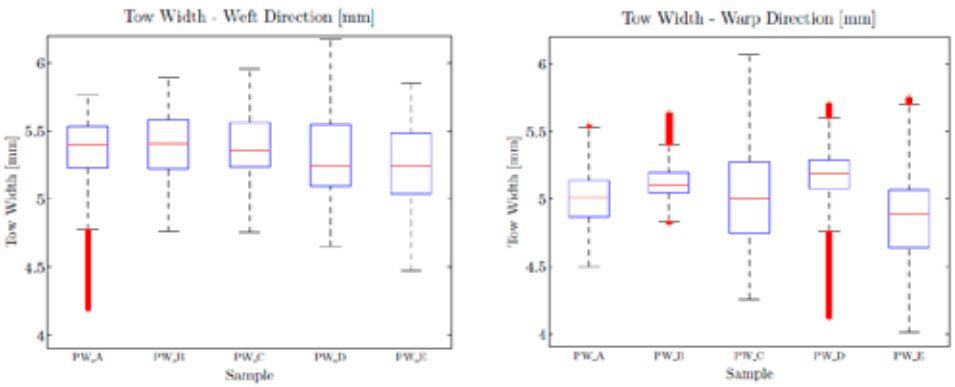

Fig. 6. Tow width – weft and warp directions.

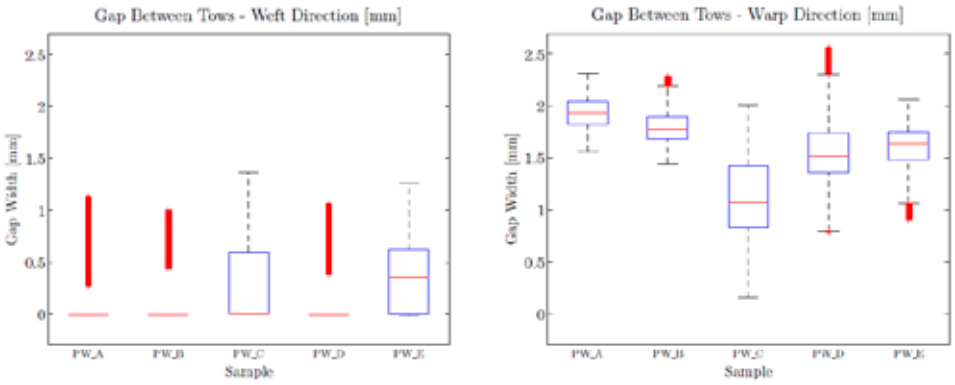

Fig. 7. Gap width – weft and warp directions.

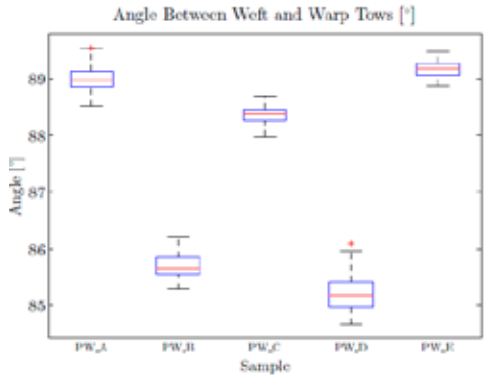

Fig. 8. Angle between weft and warp tows.

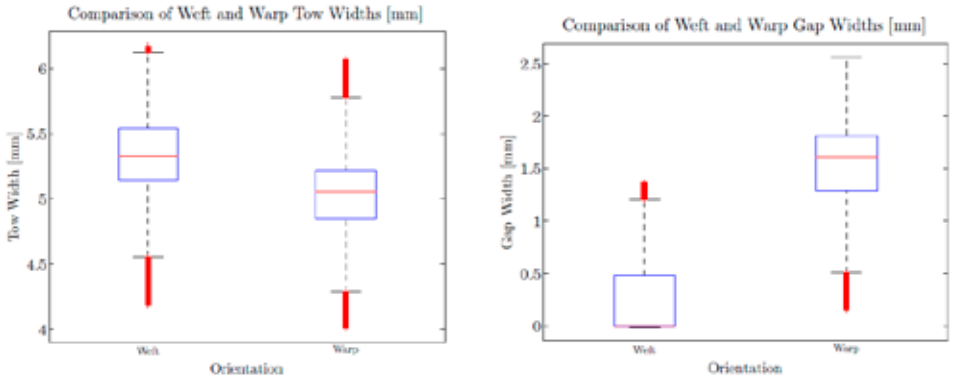

Fig. 9. Comparison of weft and warp measurements – Tow widths and gap widths.

4.3 Image Analysis Results – TW. The TW material was woven substantially tighter than the PW. Due to this, a "*no gap"* function was implemented in the image analysis code, so as to avoid locating shared edges twice. This textile was noticeably more consistent, with fewer variations, making the image analysis process significantly faster and simpler. Fig. 10 shows two examples of the analysed TW material. Figs 11 to 13 illustrate the geometric data obtained from all the samples, highlighting the variations between and within the samples.

The results illustrate that there is little variation in the tow width measurements across samples. The weft tow widths measured across the five samples are very similar and the warp tows widths are similar in each of the samples too. In addition to this, the average weft tow width is similar to the average warp tow width measured in all the samples. There is a large inter-sample variation in the angle between the weft and wrap tows. This is due to the fact that the material has a low resistance to in-plane shear and the samples were taken at different locations on the roll.

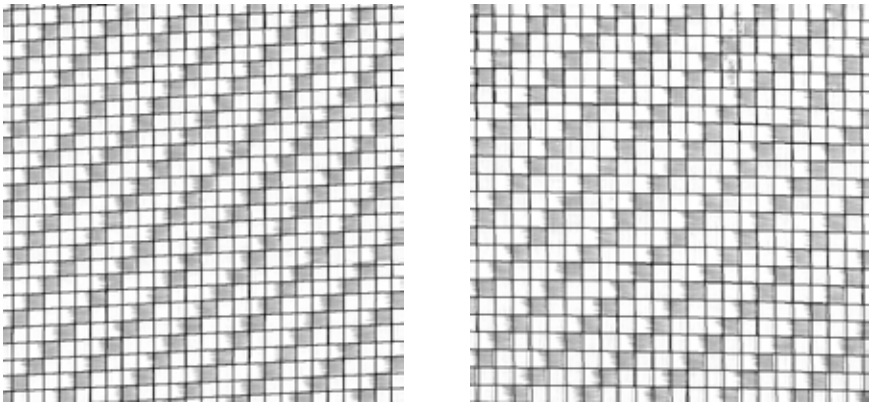

Fig. 10. Examples of analysed TW images.

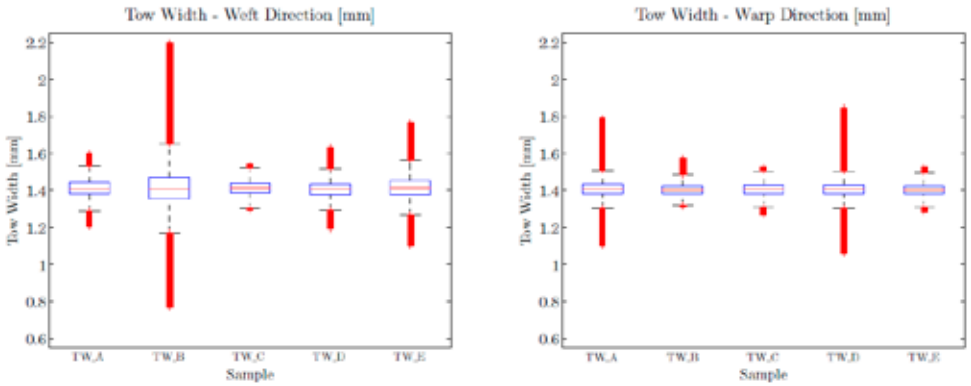

Fig. 11. Tow width – weft and warp directions.

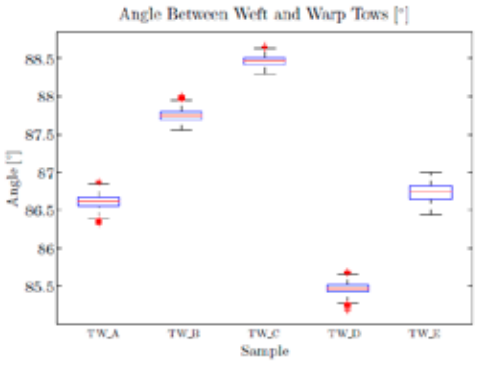

Fig. 12. Angle between weft and warp tows.

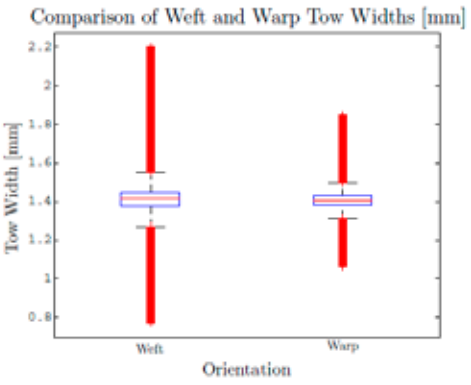

Fig. 13. Comparison of weft and warp widths.

5. VERIFICATION OF IMAGE ANALYSIS RESULTS

The cross sections of the PW and TW weft and warp tows were examined using microscopy images of the reinforcements impregnated in a polymer resin. A total of 10 images in each of the weft and warp direction PW material were taken and 15 images in each of the weft and warp direction of the TW material. These images were processed to determine the tows' width. Tables 2 and 3 provide a summary comparison of the geometric measurements. It can be seen that the measurements obtained using the two methods are in good agreement. The small discrepancies could be accounted for due to the limited number of samples examined in microscopy.

Table. 2. PW Microscopy validation.

Tow Width [mm]	Mean	Stdev
Weft – image Analysis	5.33	0.30
Weft – microscopy	5.03	0.32
Warp – image Analysis	5.03	0.31
Warp – microscopy	5.02	0.22

Table. 3. TW Microscopy validation.

Tow Width [mm]	Mean	Stdev
Weft – image Analysis	1.41	0.08
Weft – microscopy	1.33	0.10
Warp – image Analysis	1.4	0.04
Warp – microscopy	1.27	0.09

In addition to the agreement of the image analysis measurements with the microscopy measurements obtained, confidence was gained through the matching of the tow edge paths recognized by the code with the scanned image.

6. APPLICATIONS OF EXTRACTED INFORMATION

The presented image analysis technique may be used in a number of applications, predominantly in cases where information about the textile architecture is required. It enables statistical characterisation and quality control of the reinforcement, permeability and compaction predictions carried out through simulations and studying the effects of manual handling.

A permeability prediction study was carried out using the image analysis technique discussed. Various unit cell geometries of the fabrics studies were created using TexGen (Fig. 14), a textile generation software (University of Nottingham 2012), capturing the different geometric variations that were present in the material. These geometries were then used in flow simulations (Fig. 15) to predict the permeability of the unit cell which will later aid in optimising the manufacturing process by being used in LCM simulations. The simulation results obtained are in close agreement with experimental permeability results, thus providing further validation that the image analysis technique produced accurate results.

Fig. 14. Unit cell model of TW in TexGen.

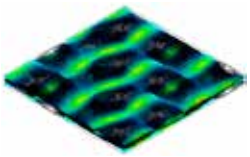

Fig. 15. Flow simulation on TW unit cell.

7. CONCLUSIONS

An automated method has been developed that enables the geometric characterisation of woven reinforcement textiles. The tool is able to be used on fabrics of different materials, such as glass, carbon and flax. The tool works efficiently, capturing the variability of important geometric features, which is crucial when the material is to be used in further simulations to predict the material behaviour properties.

REFERENCES

Desplentere, F., Lomov, S. V., Woerdeman, D. L., Verpoest, I., Wevers, M., and Bogdanovich, A.E. (2005). Micro-CT characterization of variability in 3D textile architecture. Composite Science and Technology. 65(13). 1920-1930.

Johnson, C. F. (1988). Engineering Composites Book: Engineering Plastics (ASM International, Ohio).

Trochu, R., Gauvin, R., and Gao, D. M. (1993). Numerical analysis of the resin transfer molding process by the finite element method. Advances in Polymer Technology. 12(4). 329-342.

Trochu, R., Ruiz, E., Achim, V., and Soukane, S. (2006). Advanced numerical simulation of liquid composite molding for process analysis and optimization. Composites Part A: Applied Science and Manufacturing. 37(6). 890-902.

University of Nottingham. (2012). TexGen (Version 3.5.1). https://texgen.sourceforge.net. (Retrieved 14 May 2012).

Proceedings of the 34th Risø International Symposium on Materials Science:
Processing of fibre composites – challenges for maximum materials performance
Editors: B. Madsen, H. Lilholt, Y. Kusano, S. Fæster and B. Ralph
Department of Wind Energy, Risø Campus
Technical University of Denmark, 2013

HEMP FIBRES: ENZYMATIC EFFECT OF MICROBIAL PROCESSING ON FIBRE BUNDLE STRUCTURE

A. Thygesen[*], M. Liu[*], A.S. Meyer[*] and G. Daniel[**]

[*]Center for Bioprocess Engineering, Department of Chemical and Biochemical Engineering, Technical University of Denmark, 2800 Lyngby, Denmark.
[**]Department of Forest Products/Wood Science, Swedish University of Agricultural Sciences, 750-07, Uppsala, Sweden

ABSTRACT

The effects of microbial pretreatment on hemp fibres were evaluated after microbial retting using the white rot fungi *Ceriporiopsis subvermispora* and *Phlebia radiata* Cel 26 and water retting. Based on chemical composition, *P. radiata* Cel 26 showed the highest selectivity for pectin and lignin degradation and lowest cellulose loss (14%) resulting in the highest cellulose content (78.4%) for the treated hemp fibres. The pectin and lignin removal after treatment with *P. radiata* Cel 26 were of the order 82% and 50%, respectively. Aligned epoxy-matrix composites were made from hemp fibres defibrated with the microbial retting to evaluate the effects on their ultrastructure. SEM microscopy of the composites showed low porosity on the fibre surfaces after defibration with *P. radiata* Cel 26 and *C. subvermispora* indicating good epoxy polymer impregnation. In contrast, fibres treated by water retting and the raw hemp fibres were badly impregnated due to porosity caused by surface impurities such as epidermis and other pectin rich plant cells. The pectin and lignin mainly located in the outer part of the fibres were assumed to be extracted and degraded by pectinase and peroxidase enzymes produced by the fungi.

1. INTRODUCTION

Hemp fibres can be used as reinforcement agents in biocomposites due to their good mechanical properties including low density and high stiffness (Thygesen, Thomsen, Daniel and Lilholt 2007). The principal constituent of hemp fibres is cellulose, which has a high theoretical strength (8 GPa) and functions as the reinforcing component in the fibres. Currently, the largest demand for cellulosic fibres is for the production of string, twine, cord and ropes (Sankari, 2000). These applications require primary processing of raw materials into yarn with a series of steps including retting, scutching, carding, cottonization and spinning. Retting is the term used for the removal of non-cellulosic components from natural fibers and separation of the fibres from the plant stem structure, to obtain cellulose-rich fibers. It is performed by microbiological

methods. Retting precedes mechanical separation (scutching) of the fibre from the stem and is essential for reduction of fibre breakage (Franck, 2005). However, recent data suggest that the gentle microbial retting process can enzymatically create defects in the fibre structure during the processing of hemp stems into single fibres. (Thygesen et al., 2007; Thygesen, Madsen, Thomsen and Lilholt, 2011).

Parenchyma cells rich in pectin and hemicellulose, which bind the hemp bast onto the stem surface, are located between the fibre bundles (Garcia-Jaldon, Dupeyre and Vignon, 1998; Franck, 2005). This binding must be degraded to obtain useful fibres for strong composites. As explained in more detail below, hemp fibres are classically separated from the plant stems by "water retting", which in essence is a microbial process. In this process, indigenous bacteria and notably fungi present on the plant stems degrade pectin between the fibres and the stem surface at temperatures of around 15 ºC to 30 ºC within six to ten days (Franck, 2005; Thygesen et al., 2007). It has been shown that bacterial species of *Achromobacter*, *Clostridium* and *Pseudomonas* dominate (Rosember, 1965). Despite its long use, the process is still largely empirical, and obviously depends on the microbial flora present on the fibres. In order for the process to be successful, it is of crucial importance that the cellulose is not degraded. Knowledge about changes in hemp fibre ultrastructure and chemical composition during processing is of great importance to produce high-quality fibres.

In this study, the basidiomycete white-rot fungi *Ceriporiopsis subvermispora* (Akhtar, Attridge, Blanchette, Myers, Wall, Sykes, Koning, Burgess, Wegner and Kirk, 1992) and mutant strain (cellulase less) *Phlebia radiata* Cel 26 (Nyhlen and Nilsson, 1987), which have a limited ability to degrade cellulose were used to treat hemp stems and investigate their effect on the fibre microstructure and chemical composition compared with traditional water retting. These fungi have been used for microbial separation of woody fibres. Results were analyzed based on knowledge of the cell wall active enzymes produced by the two fungi.

2. MATERIALS AND METHODS

2.1 Raw material. The investigated hemp fibres are presented in Table 1. The H0, H1, H2, H3 fibre samples were produced from the same original hemp plants (*Cannabis Sativa* L, Felina 34) grown at Flakkebjerg Research Station, Aarhus University, Denmark (Thygesen et al., 2007). H0 fibres were manually peeled from the un-retted stems and were considered as non-processed. H1, H2 and H3 fibres were obtained from H0 by water retting as well as by fungal treatment with *C. subvermispora* (Akhtar et al., 1992) and *P. radiata* Cel 26 (Nyhlen and Nilsson, 1987), respectively. The fibre yield was determined by separation of the fibres by hand peeling followed by weighing. The yield was between 28 – 38 g fibres per 100 g plant stem and between 68 – 100 g per 100 g untreated fibres as shown in the table.

Table 1. Overview of the investigated hemp fibres.

Fibre type	Code	Treatment	Fibre yield	
			(g/100 g stem)	(g/100 g raw fibres)
Loose hemp fibre bundles	H0	Untreated	38±1	100
	H1	Water retting	27±1	68
	H2	*C. subvermispora*	29±1	75±4
	H3	*P. radiata* Cel 26	28±1	70±1

2.2 Chemical composition analysis. A gravimetric method was used to determine the content of wax, water-soluble components, pectin, lignin, hemicellulose and cellulose in the hemp fibres (Thygesen, Daniel, Lilholt and Thomsen, 2005). The method consists of five steps: (1) Wax was soxlet extracted in chloroform, (2) water soluble extractives were extracted in water, (3) pectin was extracted in 30 g/L ethylene-diamine-tetra-acetic acid (EDTA), (4) lignin was oxidized and extracted in 33 g/L $NaClO_2$ + 6 g/L CH_3COOH, and (5) hemicellulose was extracted in 120 g/L NaOH + 20 g/L H_3BO_3. The remaining residue, unaffected by the extraction steps was cellulose. The mineral content was determined by incineration of 0.5 g sample at 550 ºC for 3 h.

2.3 Fungal treatment and water retting. Cultures of the white rot fungi *C. subvermispora* and *P. radiata* Cel 26 were applied on hemp stems as described by Thygesen et al. (2007). The fungi were kindly supplied from the Swedish Agricultural University, Dept. Forest Products. They were stored and pre-cultivated on 2% (w/v) malt agar plates at 20 ºC. For inoculation, the mycelia grown on one agar plate was homogenized into 100 mL water. A solution of 1.5 g/L NH_4NO_3, 2.5 g/L KH_2PO_4, 2g/L K_2HPO_4, 1 g/L $MgSO_4 \cdot 7H_2O$ and 2.5 g/L glucose was used as growth medium in the fungal treatment experiments. The growth medium (625 mL) and hemp stem pieces (50 g) were sterilized in Erlenmeyer flasks at 120 ºC for 30 min. After cooling to ambient temperature, the mycelium suspension (70 mL) was added aseptically and the fungal treatment experiments conducted at 28 ºC for 14 days (72 kg hemp stem m^{-3} liquid). Following fungal treatment, the hemp stem pieces were washed in water to remove epidermal and fungal material from the stem surfaces and to separate the fibres from the woody cores of the stems. Water retting was performed with 20 kg hemp stems in 750 L water (26 kg hemp stem m^{-3} liquid) at 35 ºC for 4 days. Water-retted hemp fibres became separated from the stem core during the retting process.

2.4 Staining pectin and use of light microscopy. Sections of hemp stem were stained with 1 g/L ruthenium red (Sigma-Aldrich #R2751; ammoniated ruthenium oxychloride [Linear formula: $[(NH_3)_5RuORu(NH_3)_4ORu(NH_3)_5]Cl_6$]). Transverse sections of hemp stem (30 µm thickness) were viewed using light microscopy at 100 times magnification (Strivastava, 1996; Thygesen et al., 2005).

2.5 Epoxy composites and scanning electron microscopy (SEM). The hemp fibres were wetted in water in order to keep them aligned followed by vacuum drying. The hemp fibres were embedded in epoxy polymer (SPX 6872 + SPX 6873; Ekomposit, Denmark) to form composites by press consolidation. A low viscosity epoxy resin (SPX 6872) and a hardener (SPX 6873) were mixed in the ratio of 100 g resin to 36 g hardener. The final composites contained 20 – 40 weight-% fibres corresponding to 80 – 60 weight-% epoxy. The lay-up was pre-cured at 40 ºC for 16 h and thereafter cured at 120 ºC for 6 h. Composite pieces were polished perpendicular to the fibre axis using wetted silicon carbide paper (Thygesen et al., 2007). Platinum coated samples were observed using a Philips XL30 ESEM scanning electron microscope.

3. RESULTS AND DISCUSSION

3.1 Chemical composition of the fibres. Pectin is the main component that closely binds the fibres to the other constituents of the hemp stem. Reducing the content of pectin and hemicellulose helps to expose the highly ordered crystalline structure of cellulose and facilitates separation of the flexible fibres for subsequent mechanical processing. The effects of biological treatments on the chemical composition of the investigated hemp fibres are shown in Table 2. All the fibre components were to some extent degraded with the investigated treatments and pectin to the highest extent.

The pectin loss in hemp fibres caused by fungal treatment with *C. subvermispora*, *P. radiata* Cel and or by water retting was 57%, 82% and 77%, respectively. The weight loss of hemicellulose in samples treated with water retting (44%) and *P. radiata* Cel 26 (36%) were not significantly different. *C. subvermispora* caused the lowest hemicellulose degradation (25%), while water retting caused a significant loss in cellulose with 22%. However, *P. radiata* Cel 26 and *C. subvermispora* treatment caused only 14% and 12% weight loss in cellulose, respectively.

The results showed that *P. radiata* Cel 26 had the highest selectivity for pectin degradation. The selectivity value is defined as the ratio of pectin degradation to cellulose degradation and is used to describe the depectinization efficiency. According to the definition, a higher selectivity value reflects improved preferential depectinization. On the contrary, a lower selectivity value means relatively high amount of cellulose degradation during the biological treatment resulting in a loss. As shown in Table 2, *P. radiata* Cel 26 demonstrated higher selectivity (6.0) than water retting (3.5) and *C. subvermispora* (4.6). Besides best depectinization, *P. radiata* Cel 26 also caused the highest lignin (50%) and hemicellulose degradation (36%) confirming its limited cellulase activity and that the strain can produce pectinase and hemicellulase enzymes (Nyhlén, Nilsson, T. 1987; Daniel, Volc and Niku-Paavola, 2004). The highest (50%) weight loss in lignin resulting from the fungal treatment with *P. radiata* Cel 26 on the stem indicates the highest activity of Pyranose oxidase (POD) and Mn-dependent peroxidases (MnP). This was suggested due to the presence of much higher concentration of H_2O_2 (1-5 mg/L) in the fungal treatment broth, since H_2O_2 produced by POD has a crucial role in the ligninolytic systems and is necessary for the ligninolytic peroxidases (Daniel et al, 2004; Kantelinen, Hatakka and Viikari, 1989).

Table 2. Process results obtained by fungal treatment and water retting of hemp.

Fibre code	H_2O_2 (mg/L)	Selectivity value*	Weight loss (%)			
			Cellulose	Hemicellulose	Lignin	Pectin
H1	n.a.	3.5	22	44	0	77
H2	0-1	4.6±2	12±5	25±5	-12±12	57±5
H3	1-5	6.0±1	14±2	36±1	50±22	82±2

* Selectivity value = Pectin loss / Cellulose loss.

Table 3. Chemical composition and structural properties of the investigated hemp fibres.

Fibre code	Chemical composition					Structure
	Cellulose (% w/w)	Hemicellulose (% w/w)	Lignin (% w/w)	Pectin (% w/w)	Residuals (% w/w)	Transverse section (μm^2)
H0	64.4±0.8	14.4±0.1	3.4±0.2	7.3±0.5	10.5	160000
H1	73.8	11.8	5.0	2.5	6.9	10000
H2	72.4±1.4	13.8±0.8	4.9±0.4	4.0±0.6	4.9±0.2	50000
H3	78.4±1.0	13.0±0.1	2.4±1.0	1.9±0.3	4.3±0.2	3000

Table 4. ANOVA table for cellulose content of the investigated hemp fibres.

Source of variation	Sums of squares	DF	Mean square	F	P value
Treatments	19.9	2	9.929	6.336	0.136
Error	3.13	2	1.567		
Total	23.03	4			

The defibration of hemp treated by water retting and cultivation of *C. subvermispora* and *P. radiata* Cel 26 resulted in hemicellulose, pectin and lignin degradation (Table 2). The cellulose content increased compared to un-retted hemp fibres (H0) though there were slight cellulose losses caused by these treatments. Overall, the principle constituent of the four samples was cellulose, at 64 – 78% of total weight. The remainder consisted of 11 – 14% hemicellulose, 2 – 5 % lignin, 2 – 7% pectin and 4 – 11% residuals. *P. radiata* Cel 26 treatment resulted in the highest cellulose (78.4%) and lowest contents of lignin and pectin due to the preferential attack of *P. radiata* Cel 26 for pectin and lignin (Tables 2, 3). However, according to Table 4, the content of cellulose in samples pretreated by cultivation with *C. subvermispora* (72.4%), *P. radiata* Cel 26 (78.4%) or by water retting (73.8%) was not statistically significant different ($P=0.136>0.05$ ANOVA, $F(2, 2)$). Moreover, smaller hemp fibre bundles were obtained with *P. radiata* Cel 26 (3000 μm^2) (H3) than by water retting (10000 μm^2) (H1) and with *C. subvermispora* (50000 μm^2) (H2), due to the greater degradation of the lignin and pectin rich middle lamellae between the fibres. Based on the transverse section data the fibres treated with *C. subvermispora* (H2) were best despite that *P.radiata* Cel 26 (H3) has the highest selectivity for pectin and lignin degradation.

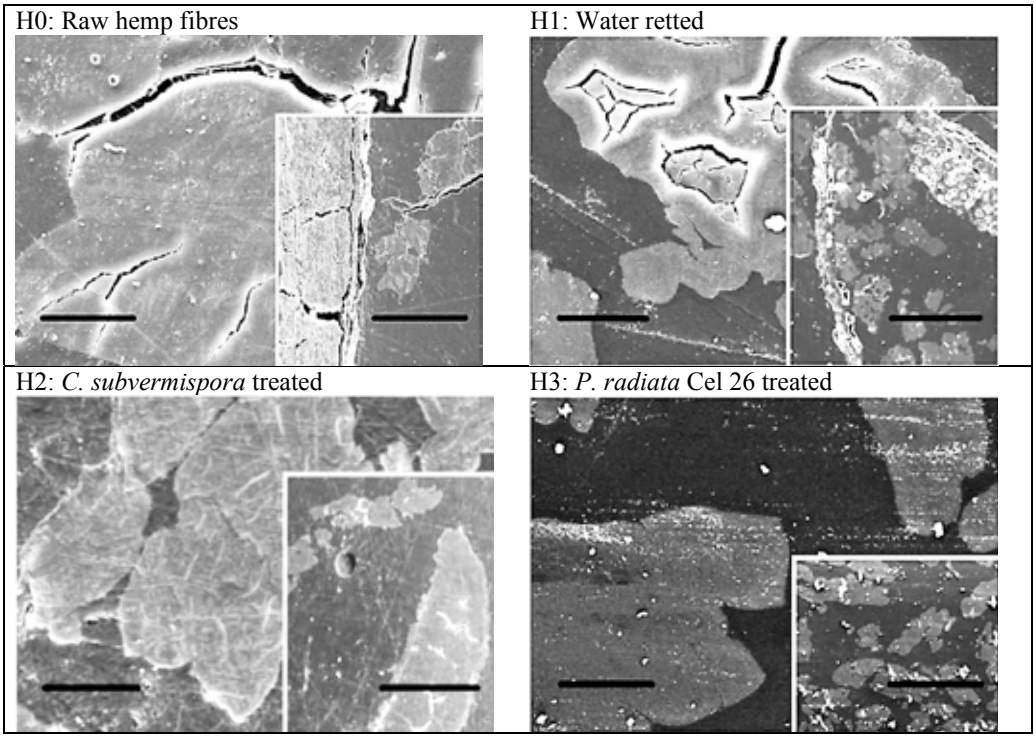

Figure 1. SEM images of transverse composite sections recorded at low and high magnification with the investigated hemp fibres. Inset images have scale bars of 200 μm and the background images 20 μm (Thygesen et al., 2007).

3.2 Microstructure of fibre bundles and epoxy impregnation. In lignocellulosic materials, hemicellulose and lignin are considered to be amorphous components, while cellulose is partly crystalline (Gharpuray, Lee and Fan, 1983). Since there was significant lignin and hemicellulose degradation during the treatments, it was of interest to investigate the effect of different treatments on the microstructure of treated hemp fibres. The microstructure was observed in transverse cross sections using SEM (Figure 1). The figure shows the fibres (light grey areas), the matrix (dark grey areas) and the air filled voids described as porosity areas (black areas).

Increased porosities and cracks appeared inside the epidermis on the fibre bundle surfaces of raw hemp fibres (H0) and water retted (H1) hemp fibres (Figure 1). This resulted in incomplete impregnation of the fibre bundles forming gaps between the matrix and the fibres. This increase in porosity appeared to the highest extent in composites reinforced with raw hemp bast and water-retted hemp fibres due to surface impurities such as epidermis and other pectin rich plant cells. In contrast, hemp fibres defibrated by cultivation of *C. subvermispora* (H2) and *P. radiata* Cel 26 (H3) were well impregnated in epoxy since no porosity was observed on the surfaces of the fibres due to fewer impurities (Figure 1). It was in accordance with the chemical composition analysis in Table 3 showing that residuals were higher in the raw fibres (10.5%) and water retted fibres (6.9%) as compared to the fibers retted with *P. radiata* Cel 26 (4.9%) and *C. subvermispora* (4.3%).

3.3 Pectin distribution in the fibres. Pectin was stained using ruthenium red by reaction with carboxylic acid side groups and shown as a red colour in Figure 2. Both the parenchyma cells and the single fibre compound middle lamellae contained pectin, while the secondary cell wall appeared to lack pectin. It shows that the pectin rich parenchyma cells in the cross section were degraded resulting in smaller fibre bundles. Parenchyma cells have large lumina and will in a composite give high porosity content. The treatment with *P. radiata* Cel 26 resulted in complete detachment of the fibres from the stem surface so fabrication of cross sections was not possible. Therefore an example of stained whole fibres is shown instead.

Pectin is commonly regarded as intercellular glue having important functions in cell growth and differentiation. However, in order to separate fibres from a hemp stem, it is essential to remove pectic contents by selective attack by bacteria and/or fungi. As shown in Figure 2, compared to the raw hemp fibres (Figure 2a), significant amounts of pectin were degraded by water retting (Figure 2b) as well as by cultivation of *C. subvermispora* (Figure 2c) and *P. radiata* Cel 26 (Figure 2d). To be more specific, large amounts of dark red staining materials surrounding white areas are shown in Figure 2a. This indicated that a lot of pectin existed in the raw hemp fibres. A large amount of the same dark red area outside the cell wall existed in Figure 2c, but the vast majority of the dark red area between fibres has been removed compared to Figure 2a. This indicated that a large amount of pectin was degraded by cultivation of *C. subvermispora*.

In Figure 2b, there was also a small area of dark red on the fibre surface. However, there were almost no dark areas remaining around individual fibres while small dark areas appeared on the surface of the fibres (Figure 2d). This result suggests that most pectin was degraded by treatment with *P. radiata* Cel 26, which corresponds to the results discussed in Section 3.1 that the largest pectin loss (82%) was caused by *P. radiata* Cel 26 compared to water retting (77%) and *C. subvermispora* (57%).

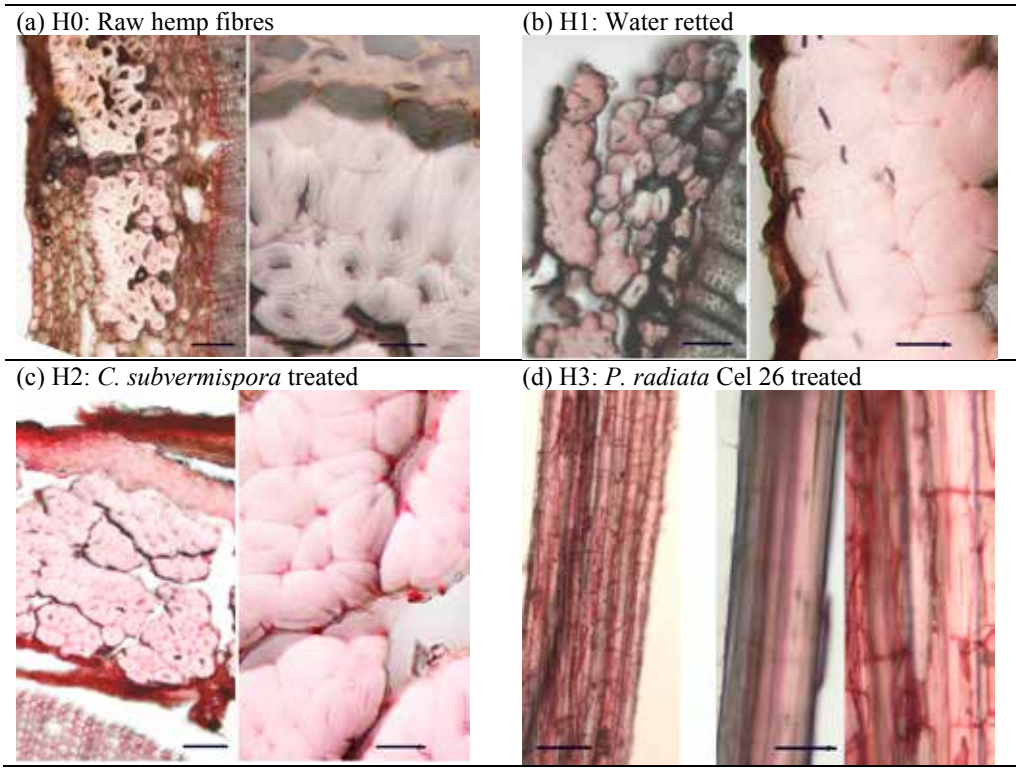

Figure 2. Pectin stained in hemp transverse sections and hemp fibre surfaces using ruthenium red. Scale bars: left side: 200 μm and right side: 50 μm.

4. CONCLUSIONS

1. Compared to water retting and fungal treatment with *C. subvermispora,* fungal treatment with *P. radiata* Cel 26 was most preferable with highest selectivity for pectin degradation. This resulting in 36% hemicellulose, 50% lignin and 82% pectin degradation and a minimal loss of cellulose (14%).
2. SEM microscopy of hemp fibre reinforced composites showed good epoxy impregnation after fungal treatment with *P. radiata* Cel 26 and *C. subvermispora*. In contrast, hemp samples treated by water retting and the raw hemp fibres were badly impregnated due to porosity caused by surface impurities. The surface impurities were in accord with the chemical composition showing that residuals were higher in the raw and water retted fibres as compared to the fibers retted in a controlled fashion with *P. radiata* Cel 26 and *C. subvermispora*.

ACKNOWLEDGEMENTS

Tomas Fernqvist (DTU Chemical Engineering) is thanked for technical support. Dr. Bo Madsen and Dr. Hans Lilholt (DTU Wind Energy) are acknowledged for composite materials related support. The Danish Council for Independent Research is acknowledged for supporting the CelFiMat project (IP No. 12-127446: “High quality cellulosic fibres for strong biocomposite materials”).

REFERENCES

Akhtar, M., Attridge, M.C., Blanchette, R.A., Myers, G.C., Wall, M.B., Sykes, M.S., Koning, J.W., Burgess, R.R., Wegner, T.H., Kirk, T.K. (1992). The white-rot fungus *Ceriporiopsis subvermispora* saves electrical energy and improves strength properties during biomechanical pulping of wood. In: Kuwahara, M., Shimada, M. (Ed.), Biotechnology in pulp and paper industry, Uni Publishers CO., Tokyo, Japan. 5, pp 3-8.

Daniel, G., Volc, J., Niku-Paavola, M.L. (2004). Cryo-FE-SEM & TEM immuno-techniques reveal new details for understanding white-rot decay of lignocellulose. C. R. Biol. 9-10, 861-871.

Franck, R.R. (2005). Bast and other plant fibres (CRC Press, New York) p.185-186.

Garcia-Jaldon, C., Dupeyre, D., Vignon, M.R. (1998). Fibres from semi-retted hemp bundles by steam explosion treatment. Biomass Bioenerg. 14, 251-260.

Gharpuray, M., Lee, Y.H., Fan, L. (1983). Structural modification of lignocellulosics by pretreatments to enhance enzymatic hydrolysis. Biotechnol. Bioeng. 25, 157-172.

Kantelinen, A., Hatakka, A., Viikari, L. (1989). Production of lignin peroxidase and laccase by *Phlebia radiata*. Appl. Microbiol. Biotechnol. 31, 234-239.

Nyhlen, L., Nilsson, T. (1987). Combined T.E.M. and UV-microscopy on delignification of pine wood by *Phlebia radiata* and four other white rotters. In: Odier, E. (Ed.), Proc. of Lignin Enzymic and Microbial Degradation Symposium, INRA Publications, pp. 277-282.

Rosember, J.A. (1965). Bacteria responsible for retting of Brazilian flax. Appl. Microbiol. 13, 991-992.

Sankari, H.S. (2000). Comparison of bast fibre yield and mechanical fibre properties of hemp (*Cannabis sativa* L.) cultivars. Ind. Crops Prod. 11, 73-84.

Strivastava, L. (1996). Histochemical studies on lignin. Tappi. 49, 173-183.

Thygesen, A., Daniel, G., Lilholt, H., Thomsen, A.B. (2005). Hemp fibre microstructure and use of fungal defibration to obtain fibres for composite materials. J. Nat. Fibres 2-4, 19-37.

Thygesen, A., Thomsen, A.B., Daniel, G., Lilholt, H. (2007). Comparison of composites made from fungal defibrated hemp with composites of traditional hemp yarn. Ind. Crops Prod. 25, 147-159.

Thygesen A, Madsen B, Thomsen AB, Lilholt H (2011). Cellulosic fibres: Effect of processing on fibre bundle strength. J Nat Fibres, 8, 161-175.

Proceedings of the 34th Risø International Symposium on Materials Science:
Processing of fibre composites – challenges for maximum materials performance
Editors: B. Madsen, H. Lilholt, Y. Kusano, S. Fæster and B. Ralph
Department of Wind Energy, Risø Campus
Technical University of Denmark, 2013

MULTI-NON-CRIMP: COMPOSITES BASED ON NON-CRIMP 3D INTERLOCK WEAVES

M. Urbanus*, B. Wendland**, L. Van der Schueren* and L. Ruys*

*Centexbel, Technologiepark 7 9052 Gent, Belgium
**Institut für Textiltechnik (ITA) der RWTH Aachen University,
Otto-Blumenthal Strasse 1 – D – 52074 Aachen, Germany

ABSTRACT

The advantages of 3D interlock fabric composites are known to lie mainly in the increased impact resistance and reduced crack propagation. On the other hand, in-plane properties like modulus, strength and fatigue are reduced by the increased amount of crimp in yarns in 3D fabrics. Other disadvantages of 3D interlock weaves are poor impregnation performance and low production speeds. In this research project "Multi-NonCrimp", it is shown that multilayer 3D interlock weaves with minimal warp and weft crimp can be produced on full width weaving looms with much greater production speed than conventional 3D weaving. Weaves with different warp, weft and pile yarn densities were impregnated and mechanically characterised by 3-point flexural and bending after impact tests. Results show good impact resistance, but limited bending strength due to incomplete impregnation. Further work will be carried out to optimise weaving pattern and impregnation methods for 3D textile reinforced composites.

1 INTRODUCTION

Fibre reinforced composites are being used in an ever increasing amount of applications where lightweight, corrosion resistance, impact resistance and other specific performances are necessary. The most common class of composites is glass fibre reinforced thermosets, with the fibres in a certain form of textile architecture: nonwoven, woven fabric, noncrimp fabric (NCF), etc. Traditionally, a composite plate consists of multiple layers of fabric, i.e. a laminate. Due to substantial in-plane orientation of the fibres, especially NCF reinforced composites show very high in-plane mechanical properties. The 'crimp' (out-of-plane orientation) in woven fabrics somewhat reduces the in-plane mechanical properties in a composite. On the other hand, due to the interlocking (weaving) of different yarns the resistance to delamination is increased, thus also increasing the resistance to impact. However, laminates of multiple layers of 2D weaves still remain vulnerable to impacts through delamination between the different plies.

Composites based on 3D woven fabrics offer some significant advantages compared to traditional 2D textile composites. There is a score of different types of 3D weaves, as was summarized by Gloy, Neumann, Wendland, Stypa and Gries (2010), see Figure 1.

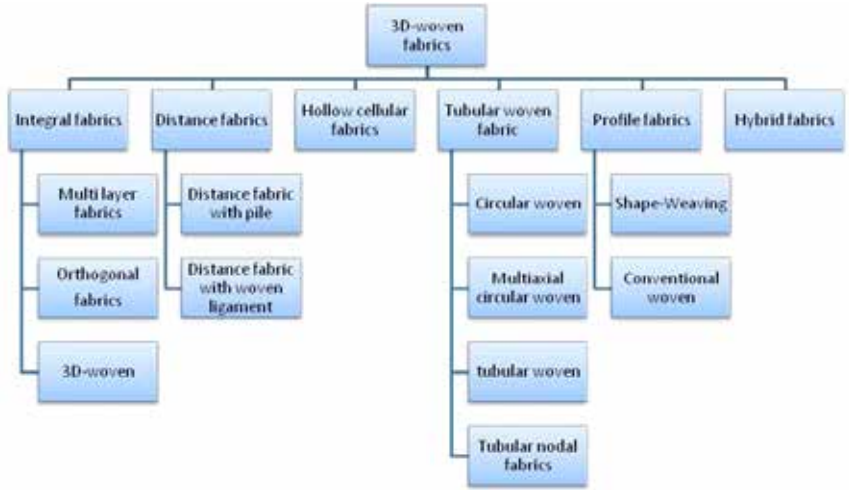

Figure 1: Overview of different types of 3D woven fabrics (Gloy et al. (2010).

The most interesting class of 3D fabrics for the replacement of 2D fabrics in large and/or thick parts, is 3D multilayer interlock weaves. These combine multiple layers of fabric, which are connected by the interlock – or pile – yarns. There are thus 3 types of yarn in a 3D interlock weave:

1. Warp yarns that stay within one layer of fabric
2. Warp yarns that interlock different layers: interlock yarns or pile yarns
3. Weft yarns that are inserted during weaving and always stay within one layer

The interlock yarns can be characterized on the one hand by either going straight up and down (orthogonal interlock), or at an angle (angle interlock). Secondly, the interlock yarns can connect different layers “layer-to-layer” or go through the whole fabric “through-the-thickness”. Figure 2 shows the main differences between conventional 2D weaving and 3D interlock weaving.

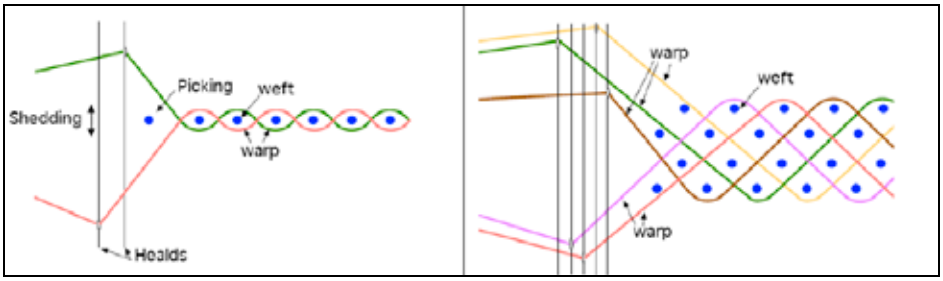

Figure 2: Conventional (2D) weaving (left) compared to 3D weaving (right). In the latter, there are multiple warps and multiple wefts above each other. In the figure on the right, all the warp yarns are *through-the-thickness interlock* yarns.

The main advantages of 3D woven fabrics over 2D fabrics as reinforcement are an increase in crack propagation and impact resistance. Due to high amounts of fibres in out-of-plane directions (mainly the interlock yarns), the in-plane mechanical properties on the other hand, are typically lower than in 2D fabric composites. Various studies investigating the influence of 3D textile architecture on properties of composites have already been carried out, among others: Brandt, Drechsler and Arendts (1996); Chen, Spola, Paya and Mollst (1999); Gu and Zhili (2002). The portion of pile yarn increases interlaminar shear strength (as depicted in Figure 3), but decreases in-plane modulus and strength (see Figure 4) (Soden and Weissenbach 1999). In order to minimise the loss in in-plane properties, Multilayer *noncrimp* 3D woven fabrics have been developed. These are essentially 0/90 noncrimp fabrics with multiple layers, connected by the pile yarns during the 3D weaving process (see Figure 5).

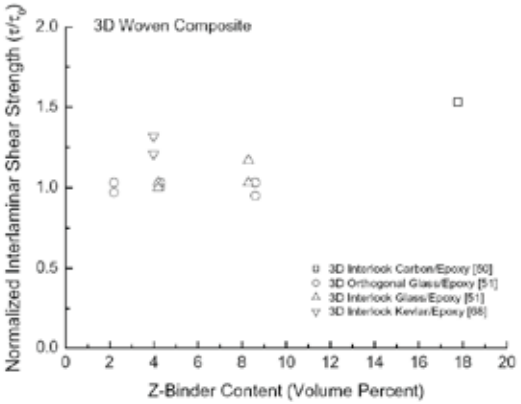

Figure 3: Increase in interlaminar shear strength with increasing amount of pile yarn ("Z-binder").

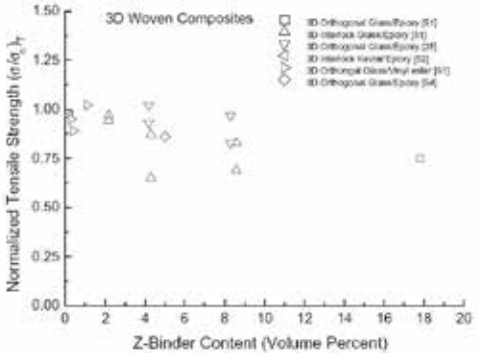

Figure 4: Decrease in tensile strength due to increased out-of-plane fibre content ("Z-binder").

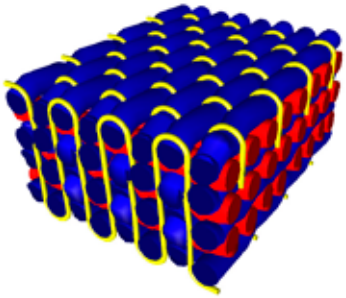

Figure 5: Multilayer 3D interlock weave with the weft yarns in blue, the single layer warp yarns in red and the interlock yarns (through-the-thickness) in yellow.

There are already multilayer noncrimp 3D textiles for composite reinforcement on the market; by companies such as 3Tex, Cary (USA) or Biteam AB, Bromma (Sweden). However, these are produced as narrow fabrics (max. 60 cm width) and at low speeds (20 – 60 tpm). This limits actual applications to specific (smaller) parts in aerospace industry, where impact resistance and crack propagation resistance are of prime importance.

This research further optimizes a technique for 3D weaving on a modified face-to-face multirapier loom, traditionally used for velvet or carpet weaving (De Clercq, Van Haezebrouck, Vasile, Gries and Gloy 2010). These looms produce textiles between 1.3 m and 5 m wide (depending on type and application). This is a huge advantage in terms of production efficiency when comparing to currently available 3D fabrics.

The research presented in this paper is conducted in the Eranet Era-SME project "Multi-noncrimp", with 3 industrial partners: VDS Weaving, 3D Weaving, Novacom and 2 R&D institutions: Centexbel, ITA (RWTH Aachen) [1].

[1] www.vdsweaving.com, www.novacom.de, www.3dweaving.com, www.centexbel.be, http://www.ita.rwth-aachen.de/

2 MULTIRAPIER 3D WEAVING

Traditional multirapier weaving is used to make velvet or carpets, which are in essence two layers of woven fabric connected by pile yarns. It is distinguished from standard weaving, mainly by the use of multiple weft insertions (hence the name *multirapier*) and multiple warp beams: one for the interlock yarns and 2 for the warp layers. In standard carpet or velvet weaving, the pile yarns are cut prior to rolling up the fabric in order to produce two fabrics (see Figure 6). Essentially, if the cutting is omitted, a 3D spacer fabric could be produced. In order to make 3D multilayer fabrics, the space between the top and bottom of the fabric is also filled up with woven layers. In order to make this possible on a standard multirapier loom, some modifications have to be made (De Clercq et al. 2010) and special warp beams are needed.

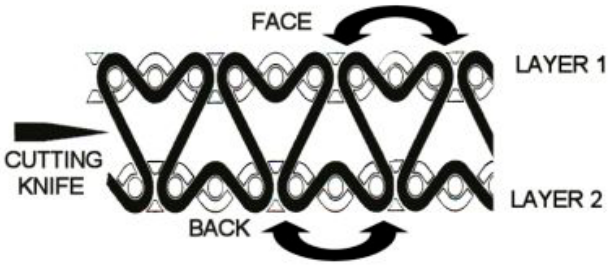

Figure 6: Schematic view of woven velvet with cutting knife on the left.

One of the major advantages of using the multirapier technique for 3D weaving is the hugely increased production speed, compared to current commercial narrow 3D fabrics for composite reinforcements. In order to show this, a calculation of production rate for multirapier 3D fabrics and narrow 3D fabrics is made in Table 1. The production rate R (m²/hr) is calculated with the parameters listed in Table 1 as follows:

$$R = V_m * W_t * W_{cm} * b \quad (1)$$

Table 1 compares typical production parameters for a narrow woven 3D fabric (currently commercial) and production on a modified multirapier of a 3D fabric with following parameters:

- 3 warp layers, 4 weft layers
- 4 yarns/cm in each layer (warp and weft)
- 4 interlock yarns/cm

This means that for each woven cm, 16 weft insertions are needed (4 in each of 4 layers). As can be seen in Table 1, the multirapier technique is obviously the real full industrial scale process, with a hugely increased production rate.

Table 1: Comparison of typical production parameters for a 7-layer 3D fabric.

	Narrow woven 3D	**Multirapier 3D**	**Unit**
Machine RPM (V_m)	60	200	rpm
Weft insertion per revolution (W_t)	1	2	
Weft insertions per cm (W_{cm})	16	16	/cm
Width (b)	0.6	1.25	cm
Production rate (R)	1.35	18.75	m²/hr

Besides the increased production speed and capacity, the multirapier technique also opens up the way for application of 3D textile composites in larger applications, like parts of wind mills, leaf springs and large ballistic panels. In this research, specific developments are done for a leaf spring (550 mm length, 60 mm width and 16 mm thickness) that would serve as suspension for a small trailer (design load of 300 kg). Replacing 2D fabric laminates by 3D fabrics in such large scale applications has two specific benefits:

- Improved impact resistance and damage tolerance
- Reduced low-skilled labour and handling costs in the lay-up phase of production

The 3D interlock fabrics developed here typically have 7 to 11 layers (4 or 6 weft layers, combined with respectively 3 or 5 warp layers). Using 1200 tex glass yarns at around 4 yarns/cm, it quickly becomes clear that 1 layer of 3D fabric can replace multiple layers of standard weave. Taking the 16 mm thick leaf spring, made from polyester composite with 40 vol% glass fibre with density of 1800 kg/m³, following lay-up would be feasible with standard 2D textile (480 g/m²): 34 layers (0,47 mm thickness per layer). On the other hand a 3D fabric can be designed to have a much higher thickness per ply. In the example of a leaf spring, an 11-layer 3D textile (5 warp layers, 6 weft layers) with 3 yarns/cm in warp and weft direction (4104 g/m²) would require just 4 layers to achieve 16 mm thickness.

It thus becomes clear that in certain applications a lot of lay-up labour can be avoided by using 3D fabrics. On the other hand, this does cause a lower degree of freedom in lay-up design (variation of angles in respective plies) and 3D textiles have much lower deformability and drapability, thus limiting the achievable shapes.

3 MATERIALS AND METHODS

Materials
For preliminary trials, already available weaving beams with 136 tex glass fibre were used to avoid excessive labour in beam preparation. Weft yarns used were 1200 tex with SE3030 sizing from 3B and interlock yarns were 68 tex glass fibre. This combination creates quasi-unidirectional composites with a large fraction of the fibres in weft direction. 3D interlock fabrics were made in various constructions with the multirapier technique. The weft density was varied from 3 yarns/cm to 5 yarns/cm and the amount of weft layers from 4 to 6. Composite plates were produced from the textiles using a vacuum infusion technique and room temperature curing epoxy resin.

Microscopy
Cross-sections of consolidated composite plates were made and investigated to view the internal structure and impregnation of the material.

Mechanical testing
3-point bending tests were performed on composites samples according to ISO 14125. Bending after impact was done using EN 6038 norm for barely visual impact and ISO 14125 for bending strength. Barely visual impact damage is defined as an indentation below 0.3 mm and no visual fibre breakage on the composite surface.

Permeability
In the composites industry permeability tests are done using a resin, or other liquid with similar characteristics. This resin is usually vacuum infused into the preform (weave, NCF, nonwoven) and the time for infusion is measured. To define the permeability constant K, the Darcy equation is used:

$$Q/A = K/\eta * \Delta P/l \quad (2)$$

with η the viscosity of the flow liquid (Pa.s), Q/A the flow per unit area ($m^3.s^{-1}.m^{-2}$) and $\Delta P/l$ the pressure drop over the length of the flow path ($Pa.m^{-1}$). The permeability constant K has unit m^2. Due to capillary effects, there are two distinct resin flow types: saturated and unsaturated. The latter involves the existence of a flow front where the resin meets the dry fabric. The capillary effect, caused by a good wetting of the fibres, causes the resin to flow slightly faster. The fabric therefore seems to have a higher permeability. Saturated flow occurs when the fabric is fully impregnated in a certain area and in some cases is less important for composite production, which mainly involves impregnating the fabric and then holding the liquid for curing. However, saturated flow measurements can be more accurate and do not involve the influence of fibre-matrix compatibility and thus can also be very useful.

Centexbel has a large array of testing equipment that is specifically designed for textile testing in the 'classical' textile industry. Even though test methods used for composite preforms are often different, the textile tests can still be used or, if necessary, adapted for preform testing. Therefore, the 'classical textile' test ISO 9237 for air permeability was used to define the permeability constant. Darcy's law is valid for any saturated fluid flow through a permeable medium, thus also for air given the input of the correct viscosity, which is $1{,}18*10^{-5}$ Pa.s at room temperature and atmospheric pressure.

In the air permeability test (ISO 9237), a pressure drop of 0,999 bar over the fabric thickness is applied. The resulting air flow through the fabric in the thickness direction is recorded. This directly shows the major difference with resin flow methods, which usually record the *in-plane* permeability (x and y direction), whereas ISO 9237 records the *through-the-thickness* permeability. The latter is always lower due to the lack of flow in yarn direction, but can still be used as a comparative parameter for different textile designs.

4 RESULTS

Permeability
Air permeability tests on fabric with 6 weft layers (1200 tex) and 4 wefts/cm showed a permeability constant of $4.3x10^{-7}$ cm². This is in the same order of magnitude as results reported by Parnas, Flynn and Dal-Favero (1997) from through-the-thickness permeability measurements using a saturated resin flow. This result shows that the air permeability measurement can be effectively used to aid the further development of easily impregnable 3D fabrics.

Mechanical properties
3-point bending tests on samples with the previously listed fabric constructions are shown in

Figure 7. As expected, strength in the warp direction – perpendicular to the 1200 tex yarns – is much lower. Apart from higher strength in samples with 4 layers and 3 or 3,5 wefts/cm, no real trends could be identified.

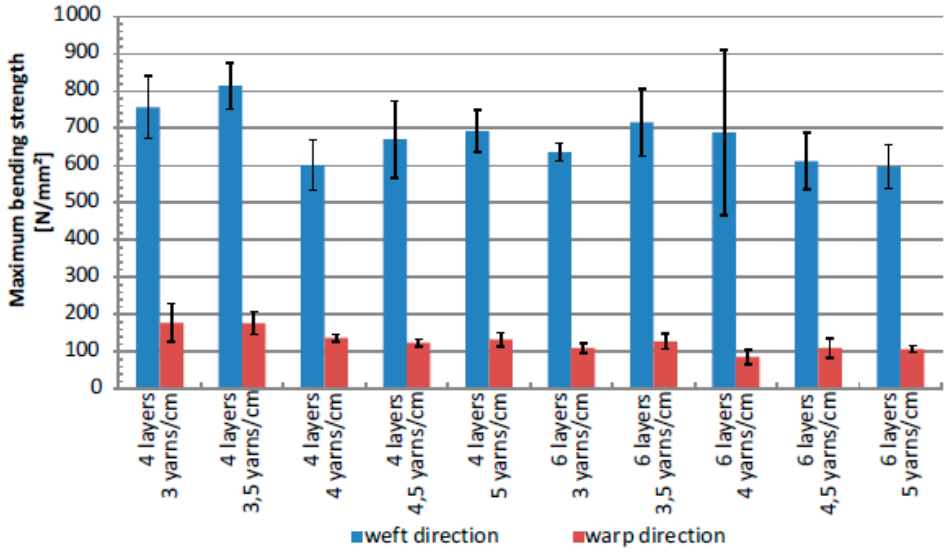

Figure 7: Bending strength in weft and warp direction.

Results of bending tests after impact with "barely visual damage" are shown in Figure 8. Samples with 5 wefts/cm showed a slightly lower decrease in strength due to impact, indicating higher tolerance to damage. In general, bending strength after impact was quite high, with an average decrease of 14%.

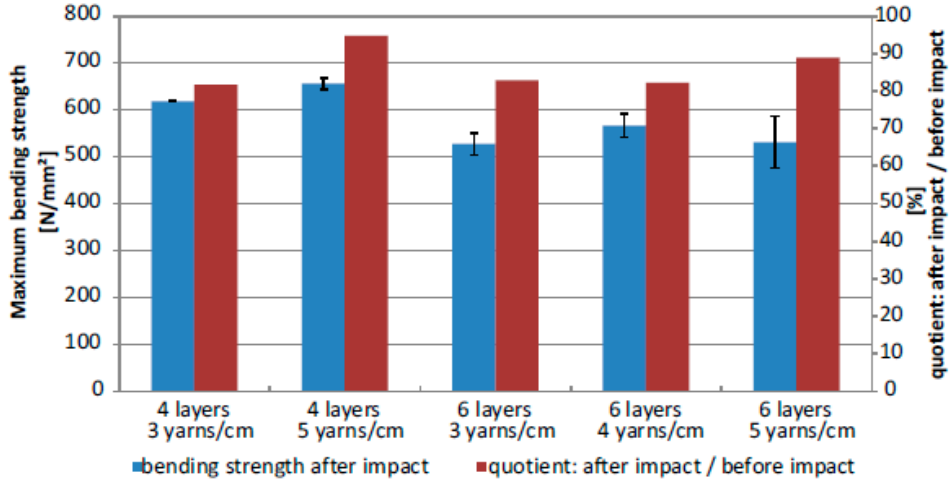

Figure 8: Results of bending after impact tests.

Microscopy
Microscopy of the cross-section showed air pockets between yarns and some intra-yarn voids (see Figure 9). The resin impregnation methods need to be improved in further parts of this research.

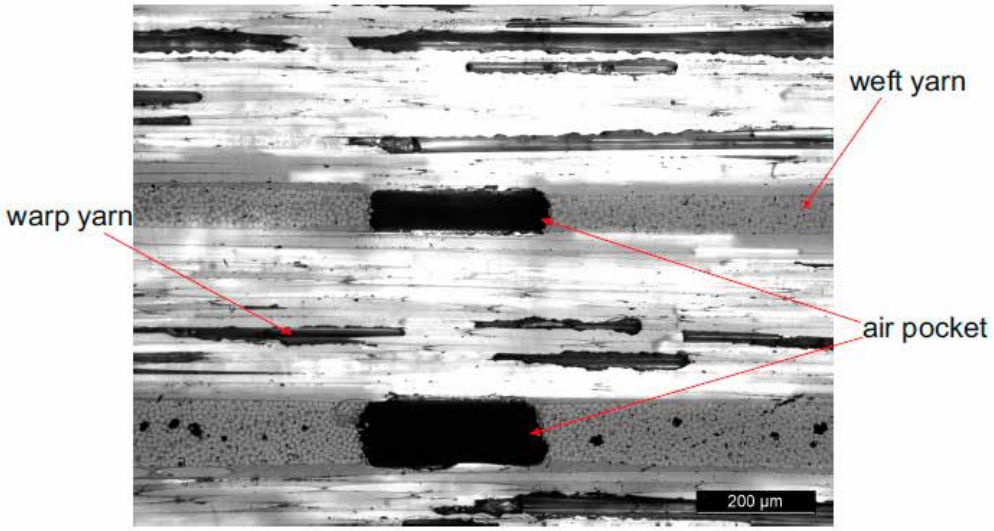

Figure 9: Microscopy image of the composite cross section of "4 layers, 4,5 wefts/cm".

5 DISCUSSION & CONCLUSIONS

3D interlock fabrics for composite reinforcement, produced on a full-width multi-rapier weaving machine, combine good in-plane mechanical properties, impact resistance and excellent productivity. This research shows that the production capacity of the multi-rapier weaving process is a magnitude higher than conventional 3D weaving processes. Secondly, a large amount of lay-up labour can be avoided when 3D fabrics are used for thick composite sections.

The composite panels produced here were based on fabrics with 4 or 6 layers of weft yarn, with 3 to 5 weft insertions per cm. Mechanical testing showed limited flexural strength, especially in composites with higher amount of yarns per cm. Microscopy showed the presence of large inter-yarn air pockets and smaller intra-yarn voids. However, bending strength after impact showed only a decrease of 14% on average. These results show that there is still some development work to be done, especially on the impregnation methods used for 3D fabrics.

6 FURTHER WORK

Further work in this on-going project will involve following tasks with the goal of developing 3D textile composites with optimal in-plane properties combined with high impact resistance and damage tolerance:

- Optimisation of weaving process and machinery for 3D glass fabrics
- Optimisation of vacuum impregnation process for 3D fabrics

- Further investigation into effect of 3D fabric architecture on mechanical properties and impregnation

ACKNOWLEDGEMENTS

The authors wish to thank the Eranet (CORNET) consortium, AiF (Germany), IWT (Belgium) for making this research possible.

REFERENCES

Brandt, J.; Drechsler, K.; Arendts F.J. (1996), Mechanical performance of composites based on various three-dimensional woven-fibre preforms, Composites Science and Technology, 56 , S. 381–386.

Chen, X; Spola, M; Paya, J.; Mollst, P. (1999), Experimental Studies on the Structure and Mechanical Properties of Multilayer and Angle-interlock Woven Structures, Journal of the Textile Institute, Part 1&2, S. 91-99.

De Clercq, G., Van Haezebrouck, G., Van Langenhove, L., Vasile, S.-I., Gries, T. & Gloy, Y.-S. (2010). Use of multirapier technology for woven 3-D fabrics. In P. Kiekens, R. Rossi, & A. M. Grancaric (Eds.), Defense related intelligent textiles and clothing for ballistic and NBC (nuclear, biological, chemical) protection (pp. 119–120). Presented at the Defense related intelligent textiles and clothing for ballistic and NBC (nuclear, biological, chemical) protection, NATO Advanced Study Institute.

Gloy, Y.; Neumann, F.; Wendland, B.; Stypa, O.; Gries, T. (2010): Overview of developments in technology and machinery for the manufacture of 3D-woven fabrics, Proceedings of the 3rd World Conference on 3D Fabrics and Their Applications.

Gu, H.; Zhili, Z. (2002), Tensile behavior of 3D woven composites by using different fabric structures, Materials and Design, 23(7): S. 671–674.

Parnas R., Flynn K., Dal-Favero M. (1997), A permeability database for composites manufacturing, Pol Comp, Vol. 18 No. 5

Soden J.A., G. Weissenbach, B.J. Hill (1999), The design and fabrication of 3D multi-layer woven T-section reinforcements, Composites Part A: Applied Science and Manufacturing, Vol. 30 No. 3.

Previous Publications

Proceedings of the 1st Risø International Symposium on
"Recrystallization and Grain Growth of Multi-Phase and Particle Containing Materials"
Editors: N. Hansen, A.R. Jones, T. Leffers
Risø National Laboratory 1980

Proceedings of the 2nd Risø International Symposium on
"Deformation of Polycrystals: Mechanisms and Microstructures"
Editors: N. Hansen, A. Horsewell, T. Leffers, H. Lilholt
Risø National Laboratory 1981

Proceedings of the 3rd Risø International Symposium on
"Fatigue and Creep of Composites Materials"
Editors: H. Lilholt, R. Talreja
Risø National Laboratory 1982

Proceedings of the 4th Risø International Symposium on
"Deformation of Multi-Phase and Particle Containing Materials"
Editors: J.B. Bilde-Sørensen, N. Hansen, A. Horsewell, T. Leffers, H. Lilholt
Risø National Laboratory 1983

Proceedings of the 5th Risø International Symposium on
"Microstructural Characterization of Materials by non-Microscopical Techniques"
Editors: N. Hessel Andersen, M. Eldrup, N. Hansen, D. Juul Jensen, T. Leffers, H. Lilholt, O.B. Pedersen, B.N. Singh
Risø National Laboratory 1984

Proceedings of the 6th Risø International Symposium on
"Transport-Structure Relations in Fast Ion and Mixed Conductors"
Editors: F.W. Poulsen, N. Hessel Andersen, K. Clausen, S. Skaarup, O. Toft Sørensen
Risø National Laboratory 1985

Proceedings of the 7th Risø International Symposium on
"Annealing Processes – Recovery, Recrystallization and Grain Growth"
Editors: N. Hansen, D. Juul Jensen, T. Leffers, B. Ralph
Risø National Laboratory 1986

Proceedings of the 8th Risø International Symposium on
"Constitutive Relations and Their Physical Basis"
Editor: S.I. Andersen, J.B. Bilde-Sørensen, N. Hansen, T. Leffers, H. Lilholt, O.B. Pedersen, B. Ralph
Risø National Laboratory 1987

Proceedings of the 9th Risø International Symposium on
"Mechanical and Physical Behaviour of Metallic and Ceramic Composites"
Editors: S.I. Andersen, H. Lilholt, O.B. Pedersen
Risø National Laboratory 1988

Proceedings of the 10th Risø International Symposium on
"Materials Architecture"
Editors: J.B. Bilde-Sørensen, N. Hansen, D. Juul Jensen, T. Leffers, H. Lilholt, O.B. Pedersen
Risø National Laboratory 1989

Proceedings of the 11th Risø International Symposium on
"Structural Ceramics – Processing, Microstructure and Properties"
Editors: J.J. Bentzen, J.B. Bilde-Sørensen, N. Christansen, A. Horsewell, B. Ralph
Risø National Laboratory 1990

Proceedings of the 12th Risø International Symposium on
"Metal Matrix Composites – Processing, Microstructure and Properties"
Editors: N. Hansen, D. Juul Jensen, T. Leffers, H. Lilholt, T. Lorentzen, A.S. Pedersen,
O.B. Pedersen
Risø National Laboratory 1991

Proceedings of the 13th Risø International Symposium on
"Modelling of Plastic Deformation and Its Engineering Applications"
Editors: S.I. Andersen, J.B. Bilde-Sørensen, N. Hansen, D. Juul Jensen, T. Leffers, H. Lilholt,
T. Lorentzen, O.B. Pedersen, B. Ralph
Risø National Laboratory 1992

Proceedings of the 14th Risø International Symposium on
"High Temperature Electrochemical Behaviour of Fast Ion and Mixed Conductors"
Editors: F.W. Poulsen, J.J. Bentzen, T. Jacobsen, E. Skov, M.J.L. Østergård
Risø National Laboratory 1993

Proceedings of the 15th Risø International Symposium on
"Numerical Predictions of Deformation Processes and the Behaviour of Real Materials"
Editors: S.I. Andersen, J.B. Bilde-Sørensen, T. Lorentzen, O.B. Pedersen, N.J. Sørensen
Risø National Laboratory 1994

Proceedings of the 16th Risø International Symposium on
"Microstructural and Crystallographic Aspects of Recrystallization"
Editors: N. Hansen, D. Juul Jensen, Y.-L. Liu, B. Ralph
Risø National Laboratory 1995

Proceedings of the 17th Risø International Symposium on
"High Temperature Electrochemistry: Ceramics and Metals"
Editors: F.W. Poulsen, N. Bonanos, S. Linderoth, M. Mogensen, B. Zachau-Christensen
Risø National Laboratory 1996

Proceedings of the 18th Risø International Symposium on
"Polymeric Composites – Expanding the Limits"
Editors: S.I. Andersen, P. Brønsted, H. Lilholt, Aa. Lystrup, J.T. Rheinländer, B.F. Sørensen, H. Toftegaard
Risø National Laboratory 1997

Proceedings of the 19th Risø International Symposium on
"Modelling of Structure and Mechanics of Materials from Microscale to Product"
Editors: J.V. Carstensen, T. Leffers, T. Lorentzen, O.B. Pedersen, B.F. Sørensen, G. Winther
Risø National Laboratory 1998

Proceedings of the 20th Risø International Symposium on
"Deformation-Induced Microstructures: Analysis and Relation to Properties"
Editors: J.B. Bilde-Sørensen, J.V. Carstensen, N. Hansen, D. Juul Jensen, T. Leffers, W. Pantleon, O.B. Pedersen, G. Winther
Risø National Laboratory 1999

Proceedings of the 21st Risø International Symposium on
"Recrystallization – Fundamental Aspects and Relations to Deformation Microstructure"
Editors: N. Hansen, X. Huang, D. Juul Jensen, E.M. Lauridsen, T. Leffers,
W. Pantleon, T.J. Sabin, J.A. Wert
Risø National Laboratory 2000

Proceedings of the 22nd Risø International Symposium on
"Science of Metastable and Nanocrystalline Alloys – Structure, Properties and Modelling"
Editors: A.R. Dinesen, M. Eldrup, D. Juul Jensen, S. Linderoth,
T.B. Pedersen, N.H. Pryds, A. Schrøder Pedersen, J.A. Wert
Risø National Laboratory 2001

Proceedings of the 23rd Risø International Symposium on
"Sustainable Natural and Polymeric Composites – Science and Technology"
Editors: H. Lilholt, B. Madsen, H.L. Toftegaard, E. Cendre,
M. Megnis, L.P. Mikkelsen, B.S. Sørensen
Risø National Laboratory 2002

Proceedings of the 24th Risø International Symposium on
"Superconductivity and Magnetism: Materials Properties and Developments"
Editors: N.H. Andersen, N. Bay, J.-C. Grivel, P. Hedegård, D. McMorrow, S. Mørup, L.T. Kuhn, A. Larsen, B. Lebech, K. Lefmann, P.-E. Lindelof, S. Linderoth, N.F. Pedersen
Risø National Laboratory 2003

Proceedings of the 25th Risø International Symposium on
"Evolution on Deformation Microstructures in 3D"
Editors: C. Gundlach, K. Haldrup, N. Hansen, X. Huang, D. Juul Jensen, T. Leffers, Z.J. Li, S.F. Nielsen, W. Pantleon, J.A. Wert, G. Winther
Risø National Laboratory 2004

Proceedings of the 26th Risø International Symposium on
"Solid State Electrochemistry"
Editors: S. Linderoth. A. Smith, N. Bonanos, A. Hagen, L. Mikkelsen, K. Kammer, D. Lybye, P.V. Hendriksen, F.W. Poulsen, M. Mogensen, W.G. Wang
Risø National Laboratory 2005

Proceedings of the 27th Risø International Symposium on
"Polymer Composite Materials for Wind Power Turbines"
Editors: H. Lilholt, B. Madsen, T.L. Andersen, L.P. Mikkelsen, A. Thygesen
Risø National Laboratory 2006

Proceedings of the 28th Risø International Symposium on
"Interface Design of Polymer Matrix Composites – Mechanics, Chemistry, Modelling and Manufacturing"
Editors: B.F. Sørensen, L.P. Mikkelsen, H. Lilholt, S. Goutianos, F.S. Abdul-Mahdi
Risø National Laboratory 2007

Proceedings of the 29th Risø International Symposium on
"Energy Materials – Advances in Characterization, Modelling and Application"
Editors: N.H. Andersen, M. Eldrup, N. Hansen, D. Juul Jensen, E.M. Nielsen, S.F. Nielsen, B.F. Sørensen, A.S. Pedersen, T. Vegge, S.S. West
Risø National Laboratory 2008

Proceedings of the 30th Risø International Symposium on
"Nanostructured Metals. Fundamentals to Applications"
Editors: J.-C. Grivel, N. Hansen, X. Huang, D. Juul Jensen, O.V. Mishin, S.F. Nielsen, W. Pantleon, H. Toftegaard, G. Winther, T. Yu
Risø National Laboratory 2009

Proceedings of the 31st Risø International Symposium on
"Challenges in Materials Science and Possibilities in 3D and 4D Characterization Techniques"
Editors: N. Hansen, D. Juul Jensen, S.F. Nielsen, H.F. Poulsen, B. Ralph
Risø National Laboratory 2010

Proceedings of the 32nd Risø International Symposium on
"Composite Materials for Structural Performance: Towards Higher Limits"
Editors: S. Fæster, D. Juul Jensen, B. Ralph, B.F. Sørensen
Risø National Laboratory for Sustainable Energy,
Technical University of Denmark, 2011

Proceedings of the 33rd Risø International Symposium on
"Nanometals – Status and Perspective"
Editors: S. Fæster, N. Hansen, X. Huang, D. Juul Jensen, B. Ralph
Department of Wind Energy
Technical University of Denmark, 2012

AUTHOR INDEX

ISBN 978-87-92896-51-3
ISSN 0907-0079

CENTERTRYK A/S, Holbæk